SMALL-SCALE CYCLOGENESIS

DURING THE GENESIS OF ATLANTIC LOWS EXPERIMENT

by

John William Nielsen

S. B., Earth and Planetary Sciences, MIT
(1984)
S. M., Meteorology, MIT
(1987)

Submitted to the Department of
Earth, Atmospheric, and Planetary Sciences
in partial fulfillment of the requirements for the Degree of

DOCTOR OF PHILOSOPHY
IN METEOROLOGY

at the

MASSACHUSETTS INSTITUTE OF TECHNOLOGY

June 1990

Signature of Author_____
Center for Meteorology and Physical Oceanography
25 May 1990

Certified by_____
Randall M. Dole, Thesis Supervisor

Accepted by_____
Thomas H. Jordan, Chairman, Departmental Committe on Graduate Students

SMALL-SCALE CYCLOGENESIS DURING THE GENESIS OF ATLANTIC LOWS EXPERIMENT

by
JOHN WILLIAM NIELSEN

Submitted to the Department of Earth, Atmospheric, and Planetary Sciences
on May 25, 1990 in partial fulfillment of the reqirements for the Degree of
Doctor of Philosophy in Meteorology

ABSTRACT

The objective of this thesis is to describe the horizontal and vertical structure, dynamics, influence on local weather, and predictability of small-scale (500 km) extratropical cyclones which form in warm advection regions during wintertime. Our dataset consists of the enhanced surface and upper air observations taken in the eastern United States during the Genesis of Atlantic Lows Experiment (GALE), from 15 Jan 1986 to 15 Mar 1986, as well as grid point data from operational forecast runs of the Nested Grid Model (NGM). A statistical climatology of North American low centers analyzed during GALE shows that two-thirds of the cyclones were small-scale, but that most small-scale cyclones were stationary and apparently forced by orography.

We select for detailed analysis a non-stationary small-scale cyclone which formed off the southeast coast of the United States on 19 Jan 1986 and was associated with localized precipitation of 75 mm in eighteen hours. Techniques used to investigate the small-scale cyclone include potential vorticity analysis and inversion, filtered surface analyses, omega equation inversion, and vertical grid point profiles of tendency terms in the vorticity, divergence, and thermodynamic equations.

The observed small-scale cyclone possessed a horizontal width of about 400 km and a central surface pressure 2-3 mb lower than the surrounding environment, while the NGM forecast small-scale cyclone was broader and weaker. Both the actual and NGM small-scale cyclones are found to have a warm-core structure, with low-level vorticity produced by localized moist ascent. The NGM updraft was driven by mid- and upper-level convective instability, and vertical or slantwise convective adjustment is determined to have also occurred in the atmosphere. The convective instability was generated by a combination of large-scale ascent and low-level advection of boundary-layer air being warmed and moistened by the Atlantic Ocean. Adiabatic instability processes, such as baroclinic instability, were not important in either the NGM or the atmosphere.

A second small-scale cyclone which formed on 10 Feb 1986 is compared to the 19 Jan 1986 cyclone. Although the second small-scale cyclone formed in a strongly baroclinic environment under the influence of an upper-level short wave, locally unstable or neutral vertical and slantwise moist ascent are again found to be directly responsible for the development of vorticity at low levels.

Successful prediction of this type of small-scale cyclogenesis depends upon knowledge of the potential for upright or slantwise instability, which in turn depends upon accurate analysis of the low-level moisture field.

Thesis Supervisor: Dr. Randall Dole, Associate Professor of Meteorology

TABLE OF CONTENTS

CHAPTER ONE

INTRODUCTION

Section 1.1 : Scope

Many types of cyclonic circulations with scales of 200 km to 1000 km exist in the atmosphere. We shall be concerned primarily with mobile cyclonic circulations which form during the wintertime in mid-latitudes. Hurricanes, which form in the tropics (with very rare exceptions), most commonly during summer and early fall, will not be considered. Nor will stationary lows which form over arid areas in summertime and are a product of differential solar heating. We shall also not consider, except for contrast or in the context of influence on smaller scales, synoptic-scale mid-latitude cyclones, which form through baroclinic instability and/or the interaction of finite-amplitude waves at different levels of the troposphere.

The above initial attempt to narrow the scope of the weather phenomenon under study must be regarded as unsuccessful. The family of cyclones which are known as polar lows or comma clouds includes cyclones which occur in mid-latitudes (Reed 1979). At least two basic instability mechanisms have been found to lead to the development of polar lows (Rasmussen 1983, Reed and Duncan 1987, Craig and Cho 1988, Peltier *et al.* 1990), in varying proportions depending on the particular initial conditions. At one end of the spectrum, baroclinic processes can be important if the cyclone develops within a narrow baroclinic zone, possibly under the influence of an upper-level trough. At the other end of the spectrum lies processes related to CISK (Conditional Instability of the Second Kind), in which the release of latent heat in an environment unstable to moist convection leads to spinup. This spectrum is complicated by the presence of heating at the surface, which can

lead both to shallow baroclinic growth (Orlanski 1986) and to a hurricane-like convective circulation (Emanuel and Rotunno 1989). Polar lows, therefore, share attributes of all three types of cyclonic circulations which we originally attempted to exclude.

Because this study will be observational in nature, the example of polar lows shows us that a dynamically-based statement of scope will be nearly impossible, because even mesoscale circulations which are considered to be a single class of cyclone can owe their existence to a wide range of dynamical processes. Conversely, since most mesoscale circulations incorporate a variety of dynamical processes, most such processes have already been the subject of substantial theoretical and observational research in isolation or in combination. The observationalist who wishes to make a worthwhile contribution to the body of work on mesoscale circulations must either add incrementally to the knowledge of a particular type of circulation or identify an unstudied type of circulation which incorporates the potential dynamical contributors to mesoscale cyclogenesis in an interesting and scientifically significant way. We choose the latter alternative.

The search for an unstudied class of mesoscale cyclone begins with an attempt to determine whether such a class does indeed exist. Chapter Two is a climatology of cyclones occurring over North America and the adjacent Atlantic Ocean between 10 Jan 1986 and 21 Mar 1986. This time period was chosen to coincide with the period of the Genesis of Atlantic Lows Experiment, which is described in Section 1.3. The enhanced surface and upper air observations during GALE permit analyses on scales two to four times finer than conventional observations permit. We will use this enhanced data set for our case studies, and the comprehensive map search required to construct the climatology will permit us to identify potential cases of interest.

The geographical area and time period of the climatology by design exclude hurricanes and avoid favored regions for the genesis of polar lows and comma clouds. The primary objective of the climatology is to determine whether it is appropriate to make a distinction between synoptic-scale baroclinic cyclones and mesoscale cyclones. A clear

scale separation would imply that mesoscale cyclones are qualitatively different from synoptic-scale cyclones, while a smooth distribution would imply that any differences might only be quantitative. Such a determination might be difficult and inconclusive (see, for example the question of separation of deepening rates raised by Roebber (1984)). Even if a clear scale separation cannot be inferred, we at least would like to determine the geographical distribution of mesoscale cyclones and confirm that they are plentiful and influential enough to warrant further study.

As it turns out, a clear, apparent scale separation will be found in the two-month climatology. Anticipating this result, we will here introduce the terminology "large-scale cyclone" to refer to ordinary synoptic-scale cyclones, and "small-scale cyclone" to refer to mesoscale circulations with a typical radius of circulation (to be defined later) of 150 km to 750 km. The upper end of the scale range corresponds to the local minimum of frequency in the climatology, which, while convenient for our immediate purposes, might not emerge from a larger population of cyclones. The lower end of the scale is partly artificial, and corresponds to the minimum size at which NMC (the United States National Meteorological Center) will analyze a low center based on regular surface airways observations, offshore ship and buoy observations, or satellite images. But the lower end of this scale may also be considered to have a physical basis, being roughly that scale at which the surface winds attain a substantial Coriolis deflection such that a circulation results which can be detected by normally-spaced observations. In dynamical terms, this is the minimum scale at which it is reasonable to apply the invertibility principle (Hoskins *et al.* 1985) for potential vorticity. From examination of the three-hourly synoptic maps, it appears that analysts tend to identify and locate small-scale cyclones on the basis of circulation rather than pressure, so this dynamical interpretation is a valid one.

As the climatology reveals a wide range of small-scale cyclones, we next seek to select a particular class of cyclone to study in detail, preferably one not yet well-documented. Since a considerable body of literature already exists on polar lows and

comma clouds, we shall ignore lows forming within cold air masses or in regions of cold advection, under the influence of an upper-level trough, with embedded convective activity. Such cyclones were rare within the climatology area. We will also ignore those lows which appear to be the product of lee cyclogenesis, although the details of lee cyclogenesis are extremely dependent upon the local orography and are not well understood in all regions. Rocky Mountain lee cyclogenesis occurs too far west to be covered by the special GALE observing network. Appalachian lee cyclogenesis, while accounting for a local maximum of cyclogenesis events in the GALE region, tended to produce dry, shallow cyclones which remained weak and did not appear to influence large-scale cyclogenesis.

We choose, for detailed study, mobile, small-scale cyclones which form along warm or stationary fronts or within the warm sector of large-scale cyclones. These are cyclones which form in the absence of large-scale cyclogenesis or ahead of the mobile large-scale cyclone. Perhaps because they form in regions of warm advection, they tend to be associated with precipitation, with the heaviest precipitation apparently associated with the small-scale cyclones.

We consider this particular class of cyclones worthy of study for the following reasons. Their apparent influence on mesoscale precipitation variations makes them of obvious potential importance for local forecasting. Their position ahead of large-scale cyclones makes them of potential importance for large-scale cyclogenesis, either by developing into large-scale cyclones themselves, or by enhancing or inhibiting large-scale cyclone development. Their small scale makes it unlikely that they would be handled correctly by current numerical weather prediction models, making it particularly important that the processes leading to small-scale cyclogenesis be understood. A brief overview of physical and dynamical processes which can potentially contribute to the development of warm-sector small-scale cyclones will be given in Section 1.2.

Chapter Two consists of the cyclogenesis climatology, in which we obtain an estimate of the size distribution and behavior characteristics of small-scale cyclones. In

order to conduct this climatology, it was necessary to record the locations and sizes of every cyclone at every map time during GALE. We make use of this data set to compare cyclogenesis climatology results obtained by using differing definitions of cyclogenesis, to compare cyclone frequency maps based upon cyclone occurrences and cyclone tracks, and to examine the geographical variation of cyclone deepening rates. We also compare the intensities, durations, and cyclogenesis locations of small-scale and large-scale cyclones.

In Chapter Three, we select a particular small-scale cyclone, that of 19 Jan 1986, and use surface, sounding, and radar data to define the horizontal and vertical structure of the small-scale cyclone, and describe the apparent effect of the small-scale cyclone on local weather. In Chapter Four, we examine a similar small-scale cyclone which was forecasted by the NMC's Nested Grid Model. This model became the primary operational 48-hour forecasting model during GALE. As it happens, the NGM produced small-scale cyclones bearing similarities to the small-scale cyclones selected for case studies. The NGM simulations will be studied along with the actual cases, with the objective of determining what causes small-scale cyclogenesis in the operational model, and to what extent these processes may be considered to occur in the real atmosphere. As a principal diagnostic tool, we use potential vorticity inversion techniques to determine whether baroclinic development played a role in the formation of the small-scale cyclone. We find that the small-scale cyclone was a site of potential vorticity production at low levels by localized moist ascent.

Chapter Five is concerned with the statement and testing of hypotheses for the cause of the localized ascent regions in the NGM, and assessment of differences in dynamical processes between the small-scale cyclones in the NGM and the real atmosphere. We conclude that unstable middle and upper level moist ascent generated the cyclone in the NGM. Moist adjustment to upright and slantwise neutrality is also identified as the process responsible for generation of the actual small-scale cyclone, with a possible contributing role played by surface sensible and latent heat fluxes. To assess whether these

mechanisms are generally applicable in their respective environments, we examine a second small-scale cyclone in Chapter Six for which heat fluxes were apparently unimportant and the relative intensities of the NGM and actual small-scale cyclones are reversed. Chapter Seven contains the conclusions and a discussion of the implications of the primary results.

Section 1.2 : Overview of Processes Contributing to Small-Scale Cyclogenesis

We restate our lower limit on cyclone scale as being that scale at which winds approach an approximate non-linear balance between the pressure gradient force and the fictitious Coriolis and centrifugal forces. At such scales, it is appropriate to consider the dynamics of vortex generation to be related to a redistribution or generation of Ertel potential vorticity (Ertel 1942a, Ertel 1942b), which may be approximately written as

$$Q = -g\frac{(\zeta_\theta + f)}{\frac{\partial p}{\partial \theta}} \qquad (1.1)$$

Symbols, except where noted, will have their standard meteorological meanings. A list of symbols and their meanings is given in Appendix A. Here ζ_θ is the vertical component of the vorticity of the horizontal wind, evaluated along surfaces of constant potential temperature. We will henceforth refer to the quantity Q as, simply, "potential vorticity". We shall also take the general concept of potential vorticity to include surface potential temperature, which is mathematically equivalent to an infinitesimally thin layer of potential vorticity (Bretherton 1966, Eliassen 1983). Finally, we will use the term "tropopause potential vorticity" to refer to potential vorticity anomalies along isentropic surfaces associated with excursions of the dynamical tropopause, the boundary between low potential vorticity air in the troposphere and high potential vorticity air in the stratosphere (Danielson and Hipskind 1980). The use of maps of potential temperature on the

dynamical tropopause for diagnosis of cyclogenesis was suggested by K. Emanuel (pers. comm.) and has been employed by Hoskins and Berrisford (1988) and Davis (1990).

The first candidate process we will consider is deep baroclinic instability. Simple continuous models for deep baroclinic instability in the troposphere may be divided into two classes: the Charney model (Charney 1947), in which the instability occurs through interaction of a surface potential temperature gradient with a potential vorticity gradient distributed through the troposphere, and the Eady model (Eady, 1949), in which the surface potential temperature gradient interacts with a potential temperature gradient at an upper lid. While the imposition of a lid in the Eady model seems artificial, it is equivalent to assuming that the potential vorticity of the stratosphere, which is an order of magnitude larger than in the troposphere, is infinite.

For typical mid-latitude atmospheric conditions, both models give maximum growth rates for baroclinic waves at wavelengths of about 4000 km. The original authors recognized that this wavelength was larger than that of most observed cyclones, but the structure of mature cyclones is reproduced reasonably accurately in both the linear and nonlinear regimes (*e. g.*, Simmons and Hoskins 1978). Consequently, a large amount of research has been devoted to shortening the most unstable wavelength, increasing the growth rate, or both. This may be accomplished adiabatically by increasing the low-level shear or decreasing the low-level stratification (Staley and Gall 1977, Orlanski 1986), diabatically by including the effects of water vapor (Gall 1976, Tokioka 1973, Emanuel *et al.* 1987), or artificially by reducing the depth of the troposphere (Mansfield 1974).

Smaller-scale baroclinic instability is found from the stability analysis of a discontinuous frontal boundary, a problem first examined by Solberg (1928) and solved for a wide range of parameter values by Orlanski (1968). Besides supporting deep baroclinic instability, the front supports a shallow baroclinic mode involving an interaction between the surface potential temperature and the vorticity maximum along the front. The nonlinear evolution of both the deep and shallow baroclinic waves has been shown to lead

to further, smaller-scale wave development as thin bands of potential vorticity are injected into the frontal region (Sinton and Mechoso 1984).

An apparently similar type of shallow baroclinic instability was found by Moore & Peltier (1987), who examined the stability of a finite-width, constant potential vorticity frontal zone. The new instabilities had a wavelength near 1000 km and were trapped at the top or bottom boundary. Although possible manifestations of this instability in the atmosphere have been examined (Peltier *et al.* 1990, Ford and Moore 1990), its prevalence in the atmosphere is still open to debate.

In the context of adiabatic motions, instabilities other than the deep baroclinic or shallow baroclinic-barotropic modes are not expected to be important in the generation of small-scale cyclones. Inertial instability should be unimportant near the surface, where generation of cyclone-scale regions of negative absolute vorticity should be difficult to generate. Somewhat less unlikely to occur is dry symmetric instability, but the cross-shear scale of such instabilities in the atmosphere tends to be much less than 100 km. Vertical shear instability (Kelvin-Helmholtz instability) has much too small a horizontal scale.

Diabatic processes, in particular latent heat release, act to redistribute potential vorticity within the fluid or along the boundaries. Moist ascent, although it conserves equivalent potential vorticity,

$$Q_e = -g\frac{(\zeta_{\theta e} + f)}{\frac{\partial p}{\partial \theta_e}} \qquad (1.2)$$

causes potential vorticity generation at low levels and potential vorticity destruction at high levels, or, more precisely, a transport of potential vorticity across isentropic surfaces which conserves total mass-weighted potential vorticity (Haynes and McIntyre 1987).

As with the smaller-scale dry instabilities, moist convective and moist slantwise instabilities in their simplest configurations are not of the proper scale to produce what we are calling small-scale cyclones. An upright convective cloud has a typical horizontal scale

of less than 10 km, and supercells are not much larger. Moist symmetric instability rainbands have typical cross-shear scales of about 100 km. Mesoscale convective systems can attain horizontal scales of 200 km, and their surface signatures include both a mesohigh and a mesolow (Fujita 1963). This scale makes some convective systems large enough to be included in our scale-based definition of small-scale cyclones (*cf.* Brandes 1990), and indeed one of the cyclones in the Chapter Two climatology was produced by a squall line. However, the characteristic surface pressure patterns were not found in any other cyclones during the climatology period.

Acting in concert, moist convection can be associated with another form of instability, known as Conditional Instability of the Second Kind, or CISK (Charney and Eliassen 1964, Ooyama 1964). CISK relies on an ensemble of convective clouds being associated with low-level vorticity and being fed by Ekman pumping; the ensemble vertical motion leads to vortex stretching and spinup, which feeds back on the Ekman pumping (Fraedrich and McBride 1989). This type of organization requires widespread conditional instability, and is unlikely to be found in its pure form in the baroclinic, highly disturbed wintertime midlatitudes, although it may contribute to certain cyclogenesis events. An alternative to CISK for hurricanes and polar lows is air-sea interaction theory, which depends upon surface heat fluxes over water in a nearly conditionally neutral environment (Emanuel 1986). However, the requirement of a large initial perturbation to trigger the instability (Rotunno and Emanuel 1987, Emanuel 1989) makes this instability an unlikely candidate for the comparatively weak small-scale cyclones observed in the climatology.

Local horizontal inhomogeneities in the basic state introduce a wide range of additional potential sources of small-scale cyclogenesis, including many which are modifications of previously-discussed instabilities. From the cyclone climatology, it appears that the phenomenon which produces the greatest number of small-scale cyclones is variations in surface orography, which leads to a class of phenomena known as lee cyclogenesis (Pierrehumbert 1986). However, except for noting its ubiquity in many

regions of the study area, we will limit our study to cyclones which are not directly affected by orography.

Another direct effect of the lower boundary involves inhomogeneities in surface heat fluxes. Such inhomogeneities will be most pronounced along discontinuities in snow cover, along coastlines, and near regions of strong sea surface temperature gradient. However, any circulations which develop would be of the nature of land and sea breezes, confined to the planetary boundary layer, and unlikely to grow to significant amplitude except in weak wind regimes. As stated earlier, we are excluding heat lows from further discussion.

Potentially, much larger amplitudes and deeper systems may be obtained if the differential heating can be distributed throughout the troposphere. The mechanism for such a redistribution is latent heat release through stable ascent, moist symmetric instability, or upright convection. This process has been linked to explosive cyclogenesis statistically (Davis and Emanuel 1988, Sanders and Davis 1988), observationally (Nuss and Kamikawa 1990), and numerically (Anthes *et al.* 1983, Nuss 1989). Most simulations have shown such latent heat release to be maximized along the warm front. These studies are not directly applicable to the small-scale cyclogenesis problem because they consider inhomogeneities of the basic state atmosphere or surface thermal field on scales as large or larger than the scale of the cyclone. But localized cyclogenesis could presumably take place if the localized heating region were at some distance from the center of the developing baroclinic wave. Also, Orlanski (1986) has shown that localized heating can trigger small-scale baroclinic instability.

In the absence of surface heating, the effect of moist neutrality in the presence of large-scale forcing is to enhance and localize the updraft (Thorpe and Emanuel 1985), producing a local maximum of vorticity at the ground. Again, horizontal variations in moist stratification in an environment nearly neutral to slantwise ascent would lead to variations in the production of surface vorticity. Even inhomogeneities in the moisture

field, with or without moist instability present, would tend to enhance vertical motion in the region of saturation and lead to enhanced local vorticity production (Manabe 1956).

Baroclinic development might be enhanced or hindered locally by variations in the basic state. However, we would expect any deep baroclinic cyclone which intensifies on a small scale as a result of enhanced local instability to quickly become the dominant cyclone at large scales as well, and would therefore appear as a small-scale cyclone only temporarily.

The basic state could be important in the absence of baroclinic instability by increasing the penetration depth of upper-level troughs (Hoskins *et al.* 1985). If a small-scale upper-level trough moved into a region of reduced stability such that its associated cyclonic circulation penetrated to the surface, an apparent small-scale cyclogenesis event would result. Another way in which the basic state could increase the circulation associated with a trough in the absence of baroclinic instability processes is by the action of deformation upon an elongated trough such that the potential vorticity anomaly becomes more circular (Farrell 1989).

Stable, locally unforced motions, such as mesoscale gravity waves or inertia-gravity waves, are a potential source of apparent small-scale cyclogenesis, when cyclogenesis is defined on the basis of the appearance of surface pressure minima. Such processes are capable of producing large-amplitude perturbations at the low end of the scale range, which, given suitable background conditions, could become analyzable low centers.

Finally, we must include as small-scale cyclogenetic effects a variety of phenomena which are more appropriately thought of as anticyclogenetic. For example, cold-air damming east of the Appalachians (Forbes *et al.* 1987, Bell and Bosart 1988) produces anomalous high pressure between the mountains and the coastal plain. The superimposition of a large-scale cyclonic pressure pattern centered just west of the Appalachians would create an additional local minimum of pressure at the eastern edge of the damming region opposite the large-scale cyclone.

Of even less dynamical interest are those cyclones which are produced by bad data. Since, in our climatology of Chapter Two, we shall adopt a map-based definition of cyclones and cyclogenesis, we cannot necessarily eliminate on dynamical grounds those cyclones produced by a faulty anemometer, a misplaced ship, or an overzealous analyst. Over land, false cyclones should almost never appear in the analyses, but ephemeral cyclones over the Atlantic may "occur" sporadically. We will therefore be suspicious of short-lived, small-scale cyclones appearing offshore beyond "buoy range" (400 km from the coast), although it is likely that attempts by analysts to avoid creating false cyclones may cause an underestimate of small-scale cyclones offshore beyond that expected from the reduced data density.

The above list of potential small-scale cyclogenetic mechanisms is necessarily brief. A comprehensive description and critical evaluation of such mechanisms would make a good subject for a book. We will let more detailed discussions be motivated by the results of case study analyses, and we will also postpone discussion of other small-scale cyclone case studies until they may be directly compared with the present cases. For now, it will be sufficient to note that most of the above mechanisms may be distinguished on the basis of potential vorticity and parcel stability. Deep baroclinic instability implies an interaction of potential vorticity gradients of opposite sign located at two different levels; frontal instability implies a potential vorticity (temperature) gradient at the lower boundary with localized vorticity above; surface heating implies generation/destruction at the lower boundary; latent heat release implies vertical redistribution of potential vorticity across isentropic surfaces. Absolute moist instability is marked by unstable stratification in a vertical column; moist symmetric instability is marked by unstable stratification along an M surface (Emanuel 1983), and stable moist ascent is marked by stable stratification along an M surface. Our procedure in the case studies will be to use potential vorticity analyses to narrow down the range of possible cyclogenetical mechanisms, before performing detailed

diagnostic analyses in an attempt to isolate the mechanism or mechanisms responsible for the particular cases of small-scale cyclogenesis.

Section 1.3 : Description of Data from the Genesis of Atlantic Lows Experiment

An overview of the Genesis of Atlantic Lows Experiment may be found in Dirks *et al.* (1988) and Raman and Riordan (1988). Details of the design, operations, observations, and data may be found in a set of technical publications (GALE Project Office 1985, GALE Project Office 1986, Mercer and Kreitzberg 1986, Mercer and Hartnett 1988). We present here a description of the data collected during the experiment which will be used in the case studies which follow.

GALE was conducted between 15 Jan 1986 and 15 Mar 1986 in the southeastern United States. The distribution of observing facilities is shown in Fig. 1.1. Most special observing sites were concentrated in North and South Carolina and neighboring coastal waters (the "inner GALE area"). Many observing systems were continuously operating; others functioned only during IOPs (Intensive Observing Periods), when interesting cyclogenesis events were expected to occur.

Over land, the normal complement of hourly observations was supplemented by a network of fifty PAM (Portable Automated Mesonet) stations, which transmitted observations every five minutes of temperature, wet bulb temperature, pressure, wind components, peak wind, and rainfall. By analogy with surface airways observations, we corrected the pressures to sea level using a standard atmospheric lapse rate and the mean of the temperatures at observation time and twelve hours prior to observation time.

Because of inaccuracies in barometer calibrations and reported station elevations, it was necessary to also eliminate station-specific systematic errors. This was done by constructing individual station mean pressures from a set of ten days characterized by weak pressure gradients, a variety of geostrophic wind directions, and an apparent lack of

mesoscale variation. Pressure observations from two synoptic times for each of the ten days were averaged together and plotted on a map. The field was then analyzed subjectively, under the constraints that the field be smooth, that it not deviate in a systematic manner from observed mean pressures over large areas of the map, and that it most closely match the mean pressures from the primary hourly observing stations. Systematic pressure errors were then obtained by subtracting the station mean pressure from the pressure interpolated to the station location of the smooth analyzed field. Corrections of less than 0.5 mb were disregarded. Corrections for PAM stations which were missing during part of the ten-day sample were inferred from nearest-neighbor checks on days in which both were available.

Supplementing the standard ship and buoy observations was a set of eight specially-deployed buoys which recorded data at half-hourly intervals. These buoys were especially critical for diagnosing the small-scale cyclone event during IOP 1. In the same near-shore area, hourly observations were also available from the research vessel Cape Hatteras (RVC). Pressure corrections were attempted for the buoy data in the same manner as for the PAM data, but the data were incomplete and pressure errors were found to vary with time. Instead of applying pressure corrections during the decoding process, we have plotted the raw pressures and have inferred corrections from buddy checks at adjoining map times before performing pressure analyses.

Of greater importance on the scales of interest is the enhanced rawinsonde observing network. The standard rawinsonde network is indicated in Fig. 1.1 by squares; additional sites used during GALE are indicated by circles. All sites in this figure, as well as other NWS rawinsonde sites in the region, took three-hourly observations during selected IOPs. The greatest improvement in upper-air coverage was due to the deployment of eight CLASSes (Cross-chain LORAN Atmospheric Sounding Systems). Seven of the CLASS sites are indicated by open circles in Fig. 1.1; the eighth site was on RVC, which was usually deployed near 35.5N, 76.8W. The shipboard system was not installed until

IOP 2; for IOP 1, the ship used a minisonde system which measured temperature and humidity but not winds. During certain periods, the CLASS sites made sounding observations at 90 minute intervals.

The CLASS soundings and other non-NWS soundings were examined individually for regions in which the kinematic or thermodynamic variables, or both, were interpolated over large vertical ranges. Data in such ranges were then manually set to missing values. NWS sounding data was generally assumed to be correct. Special sounding data from Petersburg, Virginia, was found to be of low quality, possessing oddly skewed wind observations, and was automatically deleted by the decoding program.

Doppler radar sites are indicated on Fig. 1.1 by open triangles. For a variety of reasons, the only Doppler radar data useful for this study is from CP4, located on Cape Hatteras. CP3 tended not to be operating during small-scale cyclogenesis events, and the MIT radar (near Wilmington) was not recording usable velocity data during the periods of interest.

Aircraft were widely deployed during GALE but were of little direct use to us. Because the subject of the first case study was unforecasted, no aircraft were deployed in or ahead of the small-scale cyclone. The second case study makes limited use of aircraft data from the NCAR Electra, but the primary purpose of that flight was to study coastal fronts.

Most of the data we use for the case studies has been obtained from the GALE Compact Disk. The final version of the offshore surface data file, the RVC IOP 1 minisonde data, and the NGM forecast run data (described in Section 4.2) were obtained separately from the GALE Data Center, located at Drexel University. The CP4 radar data was obtained from files stored at NCAR.

We will have cause at various times to refer to the distribution of sea surface temperatures near the GALE region. For future reference, we present in Fig. 1.2 a map of the NMC operational sea surface temperature analysis for the latest time available preceding

the first studied case of small-scale cyclogenesis. Characteristic features of the sea surface temperature distribution in the GALE region which are visible in Fig. 1.2 include the far offshore waters with a relatively flat temperature field of between 19 C and 23 C, the tongue of warmer water 50 km to 150 km offshore associated with the Gulf Stream, and the much cooler coastal waters between the Gulf Stream and the coastline.

A horizontal scale will not in general be provided in the figures. Please refer back to Fig. 1.1 for approximate distances, or make use of the fact that the distance from the northern border of North Carolina to the southern tip of South Carolina is approximately 500 km.

CHAPTER TWO

A CLIMATOLOGY OF CYCLONE SIZES

Section 2.1 : Introduction and Discussion of Cyclone Size Estimation Techniques

The gross climatological behavior of cyclones in the Northern Hemisphere is well known from the work of Petterssen (1956) and Klein (1957). Both authors presented maps of cyclone frequency and cyclogenesis locations. Klein also constructed mean monthly storm tracks from cyclogenesis and cyclone frequency maps and from previous work by other investigators.

More recently, several studies have been conducted which extend the work of Petterssen and Klein regarding North American cyclones. Some of these studies have been concerned with the interannual variation of cyclogenesis (Reitan 1974, Reitan 1979, Zishka and Smith 1980, Hayden 1981) or with an updated hemispheric climatology (Whittaker and Horn 1984). Improved spatial resolution (one to two degrees) has been employed over the entire continent (Zishka and Smith 1980) and over smaller areas such as the eastern United States (Colucci 1976) and the lee of the Rocky Mountains (Chung *et al.* 1976). These studies have typically included maps of cyclogenesis frequency, cyclone frequency, and/or storm tracks.

Less attention has been paid to the question of statistical or geographical relationships among various cyclone characteristics. Colucci (1976) investigated the geographical distribution of cyclone deepening characteristics. Zishka and Smith (1980) briefly compared the minimum pressure of cyclones forming in the lee of the Rockies and off the East Coast. Explosively deepening cyclones were examined by Roebber (1984) and their locations of formation and deepening were compared to other cyclones. Gyakum *et*

al. (1989), in a study of North Pacific cyclones, compared the temporal evolution of cyclones with maximum deepening rates, locations, and lifetimes.

In this chapter, we document the characteristics and behavior of North American cyclones as observed during GALE. We shall extend the techniques used by previous investigators and consider a variety of cyclone characteristics, such as cyclogenesis locations, deepening rates, lifetimes, motion, and maximum intensity. The methods used, and the ability to compute correlations between various cyclone parameters, are sufficiently novel that we shall address the general problem of climatological cyclone behavior in some detail.

Our primary interest is with the distribution of cyclone sizes and the relationships between cyclone size and other cyclone characteristics. To our knowledge, the sizes of wintertime North American cyclones have not been systematically examined with an extensive surface data set. This may in part be due to the difficulty in assigning a length scale to particular cyclones appearing on surface weather maps.

There are few measures of cyclone size which may be applied visually to subjectively-analyzed surface pressure maps. They include (1) the distance from the cyclone center to the nearest high pressure center, (2) the distance from the cyclone center to the nearest low pressure center, (3) the distance from the cyclone center to the nearest col (saddle point) of sea level pressure, or (4) the horizontal area encompassed by the largest closed isobar. Under particular idealized conditions, these methods would produce size estimates proportional to the wavelength or square of the wavelength of development. In practice, all of these methods have advantages and disadvantages, which we will illustrate by means of three simple examples.

Consider a cyclone family (Fig. 2.1a) consisting of a series of cyclones of equal wavelength but varying intensities. The cyclone family is located along a frontal zone which is a local minimum of pressure. Method 1 will yield a scale for the width of the baroclinic zone rather than the cyclone wavelength. Methods 3 and 4 will incorrectly infer

that the more intense cyclones have a larger scale. Only method 2 properly estimates the cyclone size in this case. On the other hand, if the cyclones actually had equal intensities but varying wavelengths, methods 3 and 4 would be correct and method 2 would be in error.

Our next example (Fig. 2.1b) is taken from 0300 UTC 15 Jan 1986. The weak low pressure center in South Carolina is a quasi-stationary lee cyclone resulting from a cold front passing across the southern Appalachians. Assuming that its scale is determined locally by the orography, methods 1 and 2 will produce a scale dependent entirely on the (irrelevant) distances to nearby highs and lows. Methods 3 and 4 will tend to produce imperfect but reasonable estimates of cyclone size.

Our final example (Fig. 2.1c), from 0600 UTC 20 Jan 1986, further illustrates the problem of what is meant by cyclone size. Two distinct low centers are present within a larger circulation. It cannot be determined by inspection whether this is a large-scale cyclone with an imbedded small-scale cyclone (and which low is the small-scale cyclone?), or whether two small-scale cyclones are present, masking the pressure minimum due to the large-scale cyclone. Method 1 would consider both lows to be large-scale cyclones, while the other three methods would consider both to be small-scale cyclones, unless we arbirtrarily assign a larger cyclone scale to one of the lows.

From consideration of a variety of scenarios, we conclude that methods 3 and 4 tend to produce the most consistent estimates of cyclone size and are least influenced by the scales of adjacent cyclones and anticyclones. Because of its comparative ease of implementation, we have adopted method 3 for estimating cyclone size. The distance measurement it produces (hereafter called the "radius" because it is a distance from the cyclone center to the outermost closed isobar) may be interpreted as an estimate of the half-wavelength of the cyclone. For waves along a frontal zone (Fig. 2.1a), it is precisely one-half the cyclone wavelength. For more general wavelike geometries, but with no background pressure gradient, the radius is given by

$$r = \frac{\pi}{2}\sqrt{\frac{1}{k^2} + \frac{1}{l^2}} \tag{2.1}$$

where k and l are the zonal and meridional wavenumbers.

To keep r roughly proportional to half the cyclone wavelength, we modify the definition of radius such that it is taken to be the minimum of the distance to the nearest col and the distance to the nearest high pressure center. For purely wavelike pressure patterns, this puts a maximum value for r as one-half the shortest wavelength. The minimum value for r occurs with a square wave configuration, and is roughly 0.35 times the shortest wavelength. Within the climatology, it was necessary to use the distance to the nearest high pressure center about 5% to 10% of the time.

In practice, it was found that the problem of the masking of larger cyclone centers, presented in example 3 (Fig. 2.1c), could be avoided by computing the maximum radius during the lifetime of each low. During the period of study, all of the cyclones with a closed circulation of four millibars or greater had single low centers within the large-scale circulation regions for at least part of their lifetimes, so that their existence and size is properly recorded by using the maximum radius. The problem of whether this masks some small-scale cyclogenesis events will be considered below.

We discuss the data set, study region, other details of the methodology, and terminology in Section 2.2. The representativeness of the two-month cyclone sample is assessed in Section 2.3. In Section 2.4, the preferred cyclogenesis and cyclolysis locations of stationary and travelling cyclones are presented, and the geographical distribution of storm tracks and cyclone frequencies is discussed. Cyclone intensification and deepening rates are discussed in Section 2.5. In Section 2.6, cyclone size distributions are examined and related to other cyclone characteristics. It is found that more than half the cyclones have maximum radii distances of only a few hundred kilometers. In Section 2.7, the

principal results are summarized and the implications for case studies of small-scale cyclones are discussed.

Section 2.2 : Data and Methods

The principal data sources for this study are the three-hourly North American and six-hourly North Atlantic and North Pacific surface analyses produced by the National Meteorological Center, transmitted in real time via DIFAX, and archived at the Massachusetts Institute of Technology. A description of the techniques used by NMC to construct the surface analyses is given by Corfidi and Comba (1989). The analyses are subjective, but make use of an model initial guess field over oceans. On rare occasions, MIT received a fully automated analysis. Because of the lack of a time continuity constraint on these automated analyses, we re-analyzed these maps subjectively to determine cyclone parameters wherever data was available. We note that a similar climatology could not be performed with current maps, because NMC has switched to entirely automated pressure analyses over North America.

All cyclones found within regions A, B, and C (see Fig. 2.2) between 0000 UTC 13 Jan. 1986 and 0000 UTC 17 Mar. 1986 were tracked *for the duration of their existence* using these surface analyses. This time period encompasses the Genesis of Atlantic Lows Experiment, but with an exception mentioned below, none of the special data collected for GALE were used for constructing the cyclone climatology. By this means, any cyclone frequency maxima which appear in the GALE region may be regarded as being free from biases caused by unusual inhomogeneous data coverage.

Each low pressure center was assigned an index number, and the its associated characteristics were recorded at three-hourly intervals within region A and at six-hourly intervals elsewhere. Among the parameters recorded were: day and hour, position (to the nearest degree), distance from the cyclone center to nearest col (cyclone radius), types of

associated fronts (if any), central pressure, and the difference between the central pressure and the pressure of the lowest col. The latter parameter may be thought of as the number of closed isobars at 1 mb increments which may be drawn around a low pressure center. The pressure of the lowest col was subjectively estimated from the plotted data (over land) or from the analyses (over the ocean), and was generally easy to estimate because the pressure gradient within a col is weak by definition.

To be counted, a pressure minimum was required to be present on two consecutive three-hourly surface maps in region A or on two consecutive six-hourly surface maps in regions B and C, and to have been analyzed as a low on at least one map. This requirement is much less restrictive than that of other cyclone climatologies, and permits the counting of a cyclone even if no closed isobar has been drawn around it. The purpose of this was to avoid establishing an *a priori* criterion for minimum intensity, and to include in the sample smaller-scale lows which would tend to have fewer closed isobars for a given perturbation geostrophic wind.

During inspection of the surface maps, it became apparent that the analysts often did not identify a developing surface low until it was two or three millibars lower than its surroundings. Consequently, plotted data on the surface maps immediately preceding cyclogenesis (and immediately following cyclolysis) were examined, and if a well-defined 1 mb deep (or greater) surface low was present, or if an apparent surface low was accompanied by an obvious circulation, the lifetime of the low was extended accordingly. Particular attention was paid to attempting to enforce continuity in cases in which a low vanished in one analysis but reappeared a few hours later in another analysis. Spurious and erroneous lows were avoided by requiring that NMC analyze a low center, by checking contiguous maps for temporal continuity, and by using supporting data from several stations when extending the lifetime of a low. The complete set of three-hourly analyses, which cover regions A and B, were used when available to determine cyclogenesis and cyclolysis locations and times.

Over the Atlantic Ocean, the lack of a dense network of surface observations required a modified approach. In most cases, the NMC analyses were accepted. On about five occasions when consecutive analyses of low pressure systems off the East Coast were inconsistent and specific low centers could not readily be tracked, the ship and buoy data from the GALE Compact Disk were used to construct subjective analyses with as much temporal and spatial continuity as possible.

For the sake of brevity and clarity, we define the following terms. "Deepening" will refer to the fall in central pressure of a cyclone; a rise in central pressure is equivalent to negative deepening and will be referred to as "filling". "Intensification" will be used to refer to various measures of spinup or vorticity increase associated with a cyclone. "Cyclogenesis" will refer to the initial formation of a low pressure center, while "cyclolysis" will refer to the disappearance of a low pressure center. The "duration" of a cyclone will be the period of time between cyclogenesis and cyclolysis. "Radius", as discussed in the Section 2.1, is the distance from a cyclone center to the nearest col. The difference in pressure between a cyclone and the lowest col (the col with the lowest pressure, not necessarily the nearest col) will be referred to as a cyclone's "pressure deficit".

Section 2.3 : Representativeness of the Cyclone Sample

A total of 216 cyclones were tracked during the 61-day period. Because of the shortness of the period, the cyclone sample might not be representative of typical conditions during that time of year, particularly with regard to geographic distributions.

The mean 500 mb geopotential heights during the period of study, the climatological geopotential heights, and the anomalous geostrophic winds are shown in Fig. 2.3. The strength of the mean jet stream over the western Atlantic was close to normal, although the jet was oriented more southwest-northeast than usual and displaced

northward four degrees. Over western North America, there was an enhanced time-mean ridge, resulting in weaker than normal flow over northern Mexico and a more northerly than normal jet across the central United States. If jet strength is correlated with eddy activity, one would expect enhanced activity in central Canada and near Newfoundland, and reduced activity in the southern United States.

The observed anomalies in 1000 mb bandpass (2.5-6 day) height variations, expressed as a percentage of normal, are shown in Fig. 2.4. This statistic, which was developed by Neilley (1990) and is interpreted as a measure of anomalous synoptic-scale eddy activity, has been constructed by first applying a bandpass filter to local time series of 1000 mb heights and computing the local standard deviation of the filtered data over ten day periods. These standard deviations have been averaged over the GALE period and are compared to a twenty-five year vstat climatology for the same period.

Positive anomalies greater than 120% are present in northern Canada and near Iowa, while negative anomalies are present in the southwestern United States, over the Gulf of Mexico, and over the central North Atlantic. Most of the study region had eddy activity within 20% of normal. Based on these anomalies and the anomalies in Fig. 2.3, we infer that the cyclone sample should be grossly representative of typical conditions for the period, but with a less than normal amount of cyclones in the southwestern United States or originating in the Gulf of Mexico, and a greater than normal amount of cyclones in Canada and a possibly enhanced number of "Alberta clippers".

For independent verification for these inferences, we have attempted to construct a map comparable to the January cyclogenesis climatology of Zishka and Smith (1980), which is reproduced as Fig. 2.5b and was constructed using storm track maps. To mimic the criteria for a cyclone to be associated with a storm track, we excluded all cyclones which did not travel at least 500 km or attain a pressure deficit of 3 mb or more. We also excluded all cases of redevelopment in which the old and new cyclone centers were present together for six hours or less. The resulting cyclogenesis map (Fig 2.5a) should retain

some differences, apart from sample size, because of different portions of the year, different bin sizes, and the decreasing bin size with latitude of Zishka and Smith. Despite this, the two maps are quite similar, with differences due mainly to frequency variations rather than differences in the locations of key cyclogenetical regions. The magnitudes cannot be compared directly, but by looking at relative strengths, it can be seen that the GALE sample has relatively less cyclogenesis in southern Colorado, the Gulf of Mexico, or far off the East Coast, and relatively more cyclogenesis in northern and central Canada. Elsewhere, the variations in cyclogenesis are comparable in magnitude to what would be expected simply from the different periods of the year (see, for example, the monthly cyclogenesis maps of Klein 1957), and are surprisingly small considering that this GALE cyclogenesis map is composed of only 46 cyclones.

The above three methods of estimating anomalous cyclone activity during GALE produce similar predictions of the geographical distribution of anomalous activity. Although the lack of a major East Coast snowstorm during GALE is well known, the evidence indicates that on the whole the GALE period encompassed a reasonably typical set of cyclones. We shall assume, then, that the GALE cyclone sample is a representative set of wintertime cyclones, but we shall avoid inferences which depend on small portions of the sample or which may be contaminated by the known departures from cyclone climatology.

Section 2.4 : Geographical Distributions of Cyclones, Cyclogenesis, and Cyclolysis

Figure 2.6 shows the tracks of the 216 cyclones included in the climatology. It is immediately apparent that the vast majority of cyclones exhibited an eastward component of motion throughout their lifetimes, and that their paths curve to the left. One interesting exception is that many cyclones forming along the East Coast initially travel northeast, but

soon turn sharply eastward. Most cyclones passing through a given area exhibit a preferred direction of motion, and it was this observation which led to the use of storm tracks as a forecasting tool. In present parlance, the term "storm track" often refers to bands of maximum band-pass or high-pass eddy activity, as discussed by Wallace *et al.* (1988). We shall retain the original meaning of storm track here as a preferred path of cyclones.

The specification of the western boundary of the climatology region was motivated by the desire to include all continental lee cyclone developments while excluding Pacific cyclogenesis events. From Fig. 2.6 it can be seen that this boundary is a natural one: only two cyclones were judged to have travelled intact from the Pacific to the interior of North America. Similar boundary effects can be noted at other mountain ranges and ice caps. In particular, the Appalachians act as an effective barrier to cyclones. Only one cyclone center originating west of the Appalachians was able to propagate eastward across the mountains to the coast, indicating that redevelopment occurs within almost all large-scale cyclonic circulations in this area. Some of the low centers actually make it most of the way across the Appalachians before dying on the leeward side, suggesting that the effect might not be entirely orographic and that the increased baroclinicity and reduced stratification offshore may be the primary cause of redevelopment in some cases. In contrast to lows forming over the continent, offshore cyclones are free to travel unimpeded by orography, and a few cyclones traversed great distances. One cyclone travelled due eastward to southeastern Spain. Another cyclone formed over the balmy Sargasso Sea, traversed the east coast of Greenland, and eventually froze to death over the Arctic Ocean north of Siberia.

Previous studies of cyclone frequency have used one of two methods for counting cyclones. Older studies, such as Petterssen (1956) and Klein (1957), have tended to count the total number of times a low center was analyzed within a grid box, or bin. More recent studies such as Zishka and Smith (1980), which use recorded cyclone tracks, have counted the number of times a cyclone passed through a grid box. The former method emphasizes

climatological locations of stationary cyclones, such as the southwestern United States. The latter method emphasizes travelling cyclones, and is therefore more closely related to storminess or baroclinic wave activity. However, the cyclone track method is sensitive to aliasing problems associated with the orientation of grid boxes relative to climatological directions of cyclone propagation (Taylor 1986) (see Fig. 2.7).

While previous researchers have noted the differences in cyclone frequency maps produced by the two methods, nobody has yet applied both methods to a single collection of cyclones. We do that here in Figs. 2.8 and 2.9. We also avoid the aliasing problem by using circular bins, with the radius of each bin typically specified as 150 km or 300 km. According to Taylor (1986), this method was first suggested by Kelsey (1925) and was first employed by Neumann and Pryslak (1981).

Previous climatologies also have been forced to deal with the problem of contouring discretized fields. In general, a method is adopted which is equivalent to assuming that cyclones are distributed uniformly within each bin. We elect to use heavily overlapping bins, with a resolution of one degree by one degree. Because the spacing between bin centers is so small, our horizontal resolution is determined by the spacing between bin centers and the original resolution of the surface pressure analyses and is independent of bin size. This represents a significant improvement in previous methods and avoids the need for smoothing or assuming uniform distribution within bins. The resulting maps are much more detailed and accurately represent the actual cyclone distributions during the studied time period.

The cyclone frequency map (Fig. 2.8) is dominated by local maxima in Alberta, Wyoming, and Colorado. These maxima are probably due to quasi-steady lee orographic effects in the presence of certain large-scale wind regimes. The map of cyclone tracks (Fig. 2.6) shows that many cyclones in these areas tend to remain close to the mountains while following erratic, slow paths. Other local maxima may be found associated with other mountain barriers, such as the maxima in Washington and South Carolina. Previous

cyclone frequency maps have generally shown only the maxima in Alberta and Colorado. This discrepancy may simply be due to our smaller sample size, but contributing heavily to the cyclogenesis frequency in the new areas are weak, small, short-lived cyclones which would not have been included in previous climatologies.

The overall noisiness of the plotted field is a consequence of the small (two-month) sample period. We elected not to smooth the field so as to depict clearly those local maxima due to lee cyclogenesis which we regarded as realistic and probably representative of the long-term cyclone climatology. Some of the weaker local maxima, such as those in the Alabama Panhandle, Iowa, northern Minnesota, and across portions of south-central Canada, not being adjacent to any notable orographic features, are undoubtedly artifacts of the small sample period. Other maxima, such as those in Ohio-Kentucky and over Lake Superior, can be related to mountain barriers and warm bodies of water, respectively. However, their magnitudes are not significantly above the noise levels in these regions and their matches to the orography are not perfect. Thus, without confirmation with a much larger sample size, they can only be regarded as suggestive of possible actual climatological maxima. Similar statements apply to cyclone minima: the cyclone voids in western Colorado and south of 30 N in the Atlantic are realistic, whereas those in Louisiana and south of Hudson's Bay are not.

While it is difficult to discern from Fig. 2.8 a preferred large-scale region of cyclone activity across the central United States, such a large-scale region is quite prominent in the Atlantic, extending from Cape Hatteras along an arc across the northwestern Atlantic to north of Newfoundland. This well-defined maximum is probably also an artifact of the two-month sample, because it is coincident with the local maximum in anomalous height variance for the same period (Fig. 2.4).

Although the same bin size was used for Fig. 2.9, the map of cyclone track frequency is much smoother than the map of cyclone frequency (Fig. 2.8), for two reasons. First, where travelling cyclones predominate, such as over the Atlantic, rapidly

moving cyclones which might cross two adjoining bins in a six-hour period are recorded in every bin in Fig. 2.9 but only in every other bin for Fig. 2.8. Second, where stationary cyclones predominate, cyclones only record single hits in a given bin for Fig. 2.9 but record multiple hits in Fig 2.8. In an approximate sense, the ratio of the plotted fields in Fig. 2.9 and Fig. 2.8 is proportional to the average local velocity of cyclone centers.

Thus the lee cyclone centers from Fig. 2.8 become weak maxima in Fig. 2.9 which extend eastward or southeastward away from the mountains along the preferred tracks of cyclones (compare Fig. 2.6). The band of cyclone activity off the Atlantic coast in Fig. 2.9 is at least as large as any region of orographic cyclogenesis. The local maxima in Wisconsin and Ohio have the appearance of being locations where storm tracks intersect, an impression which is confirmed by Fig. 2.6. But close inspection of Fig. 2.9 also shows the danger of inferring preferred cyclone tracks from a cyclone track frequency map. The storm track over the Atlantic appears to originate in the Carolinas and extend northeastward to Newfoundland. The raw cyclone track map (Fig. 2.6) shows, however, that only one cyclone originating in the storm track region west of 75 W actually followed the "storm track" all the way to Newfoundland.

Which way of counting cyclones is better? It depends upon what one's purpose is. Cyclone frequency maps (Fig. 2.8) are excellent indicators of favored locations for stationary cyclones, while cyclone track frequency maps (Fig. 2.9) emphasize the travelling cyclones. Where cyclones tend to be mobile, such as over the Atlantic, the differences between the two methods are generally quantititive, but Fig. 2.9 is superior because of the "cyclone hopping" effect when the bin sizes are smaller than the typical travel distances of cyclones between map times. Also, Fig. 2.9 seems to better depict the orientation of cyclone tracks over the central United States and over the Atlantic, although we emphasize that this sort of cyclone track information must be interpreted cautiously.

The distribution of all cyclogenesis events during the study period is shown in Fig. 2.10. Compared to Fig. 2.5a, the relative number of lows is much greater (213 to 46), but

the overall pattern is roughly similar. The preferred areas of cyclogenesis are along the East Coast of the United States and along the eastern slopes of the Rocky Mountains. The greatest cyclogenesis density is in the Carolinas, surprisingly far west and near the center of the inner GALE region. A second prominent maximum is located in southern Alberta. Areas with little or no observed cyclogenesis activity include eastern Canada and the offshore Atlantic south of 30 degrees.

Inspection of Figs. 2.6-2.9 indicates that many of the lows which formed along the Rocky Mountains or in the Carolinas were quasi-stationary, short-lived lee cyclones. To separate such cyclones from the remainder of the sample, we define two classes of cyclones. "Stationary cyclones" are defined as those cyclones whose cyclolysis positions are less than 400 km from their cyclogenesis positions. Conversely, "travelling cyclones" are those cyclones whose cyclolysis positions are 400 km or more from their cyclogenesis positions.

Although broadly similar, the cyclogenesis distributions for travelling (Fig. 2.11) and stationary (Fig. 2.12) cyclones differ substantially in the details. The maximum in the Carolinas is found to be primarily due to local cyclones, which inspection of synoptic maps reveals to be cyclones forming in the lee of the southern Appalachians. This cyclogenesis maximum is not an artifact of possible increased attention paid to the area by analysts; most cyclones forming there attained maximum pressure deficits of 2-3 mb, distinct enough on a surface map but too weak to meet most cyclone climatology criteria. The East Coast maximum for mobile cyclones is offshore, just northeast of Cape Hatteras, North Carolina, and downstream of the inner GALE region. This notable difference near the GALE region partially accounts for the lack of cyclones which formed west of 75 W and travelled to Newfoundland.

Along the Rockies, stationary cyclones also tend to form farther west than travelling cyclones. Travelling cyclones predominate in Colorado and Wyoming, to the lee of the Sierra Nevada, in Southern Alberta, and in the vicinity of Great Slave Lake. Stationary

cyclones have cyclogenesis maxima in eastern Washington, central Montana, and in New Mexico and Texas. Elsewhere, the vast majority of cyclones forming in featureless areas such as the open Atlantic Ocean and the Plains states are travelling cyclones, suggesting that almost all stationary cyclones during this time period are orographically related.

The travelling cyclogenesis maximum off Cape Hatteras is greater than the maximum in Alberta. This contrasts with the results of Zishka and Smith (Fig. 2.5b), in which the maximum in Alberta was higher. This difference is due in part to our considering all appearences of a new low pressure center as a separate cyclogenesis event. As a result, lows which "hop" the Appalachians and would have been counted as a single cyclone by Zishka and Smith are counted as two cyclones by us. As stated before, only one low pressure center during GALE successfully passed over the Appalachians and moved offshore, the rest having clearly redeveloped with both old and new low pressure centers present during redevelopment.

The cyclolysis distribution of travelling cyclones (Fig. 2.13) is dominated by cyclones which die upon reaching the Appalachians. The maximum cyclolysis frequency is located in West Virginia, with a band of cyclolysis extending northeastward into Quebec. The maximum is located over the mountains rather than on the upslope side as other researchers have found, a distinction apparently due to our following low centers until they disappear completely. Lesser maxima are located along the shore of Baffin Bay and downstream of the cyclogenesis maxima associated with the Rockies, the Sierra Nevada, and the Gulf of Mexico.

By definition, the cyclolysis distribution of stationary cyclones (not shown) resembles the corresponding cyclogenesis distribution (Fig. 2.12).

Section 2.5: Cyclone Deepening and Intensification

Cyclone intensification is commonly estimated on weather maps by the change in central pressure (*e. g.*, Sanders and Gyakum 1980). We have called this "deepening", and its usefulness as a measure of intensification depends on the assumption that the pressure of a cyclone's environment remains roughly constant. This assumption is often violated when, for example, a weak cyclone propagates toward a region of lower pressure such as the Aleutian or Icelandic Low. Although the cyclone may remain weak, its central pressure will fall in response to the changing environmental pressure it experiences.

The validity of cyclone deepening as a measure of intensification may be investigated by comparing deepening with pressure deficit (defined in Section 2.2). Figure 2.14 is a scatter diagram of maximum 24-hour deepening versus maximum pressure deficit for all travelling cyclones which formed within the study region during the study period. If the environmental pressure were constant along the path of a cyclone, the maximum pressure deficit attained by a cyclone would be at least as large as the maximum 24-hour deepening it experiences, and all points would lie to the right of the diagonal. As can be seen, this assumption is violated by many cyclones. Eleven of the thirty-three cyclones which deepened at least 12 mb in 24 hours failed to attain a pressure deficit as large as their maximum change in central pressure.

While strong deepening does not necessarily imply a large pressure deficit, a large pressure deficit is a good indicator of rapid deepening. Of the eight cyclones which attained a maximum pressure deficit of at least 40 mb, all deepened at a maximum rate of at least 20 mb in 24 hours. For this limited sample, rapid deepening was a prerequisite for attaining a large pressure deficit.

Unfortunately, in the context of the present study, deepening rate is the only available measure of intensification. The alternative, change in pressure deficit, often

varies rapidly with the birth or death of adjacent cyclones and is therefore not useful as a general measure of cyclone intensification.

The maximum 12 hour deepening rates are shown in histogram form in Fig. 2.15 for stationary and travelling cyclones. The stationary cyclones are tightly clustered and their average most rapid intensification is a filling of 1.7 mb. The travelling cyclones approximate the deepening distribution found by Roebber (1984), but the two distributions are not strictly comparable because of differences in geographical area, map frequency, and season. The GALE sample has a greater proportion of cyclones which deepen more than 15 mb in 12 hours, but this is to be expected because six-hourly rather than twelve-hourly maps were used, increasing the likelihood of the period of most rapid deepening being detected. The outlying travelling cyclone which filled 18 mb in 12 hours (an anti-bomb) was the redevelopment over Alaska of a large-scale cyclone which was undergoing rapid cyclolysis as it passed over the Gulf of Alaska.

It has been suggested (Roebber 1984, Roebber 1989) that oceanic cyclones possess different deepening rate characteristics than continental cyclones. To investigate this hypothesis, we divided the cyclone sample into Atlantic and Continental cyclones based on whether they formed east or west of the line [Latitude N + Longitude W = 120 degrees] (see Fig. 2.2). This line was chosen because it lies along the western slopes of the Appalachian Mountains. Cyclones forming to the east of this line are presumed to have access to Atlantic moisture and to have the capacity to be influenced by sea surface temperature gradients during their lifetime. Recall that only one cyclone formed west of the Appalachians and successfully crossed over them and reached the coast. Also, because of the lack of notable cyclogenesis in the vicinity of the Gulf of Mexico, the question of whether the Gulf should be considered part of the Atlantic for deepening rate purposes was moot.

When the cyclones are thus segregated by formation position, marked differences are found. The two deepening distributions are shown in Fig. 2.16. All of the rapid

deepeners (greater than 15 mb in 12 hours) are Atlantic cyclones, consistent with the findings of Sanders and Gyakum (1980) and Roebber (1984) that explosive cyclogenesis is almost exclusively an oceanic phenomenon. A second cluster of Atlantic deepening is centered near 4 mb. The Continental cyclones are distributed about a mean of 3.0 mb. This deepening rate is 28% of the mean Atlantic deepening rate of 10.8 mb, a difference significant at the 99% confidence level using the large sample Z test (Devore 1982). The Z test assumes that the individual cyclones represent independent samples of deepening rate, an assumption which becomes poor if the study period is short. However, similar differences in continental versus oceanic deepening rates have been observed in other samples (Roebber, 1989).

Section 2.6 : Comparison of Small-Scale and Large-Scale Cyclones

As discussed in Section 2.1, we shall use the distance from a low pressure center to the nearest col as a measure of cyclone size. This radius should tend to be one-third to one-half the wavelength associated with the cyclone. For typical theoretical wavelengths associated with the maximum growth rate of baroclinic instability, 2000 km to 4000 km, the expected radius is 700 km to 2000 km.

The actual distribution of maximum cyclone radius during GALE (Fig. 2.17) is highly skewed, with the median cyclone radius being 500 km. Two-thirds of the cyclones have a maximum radius of 700 km or less, in the mesoscale or subsynoptic-scale range. There is a local minimum in maximum cyclone radius near 750 km, and we will adopt this as the cut-off point between small-scale and large-scale cyclones. As indicated in Fig. 2.17, about half of the small-scale cyclones are stationary cyclones, including most of the cyclones having a maximum radius of 300 km or less.

The travelling cyclones in Fig. 2.17 have a median maximum radius of 725 km and a mean maximum radius of 875 km. These sizes are still small compared to what one

thinks of as a typical cyclone size. We recover the "normal" cyclone size in Fig. 2.14 by selecting only those cyclones which attain at least a 12 mb pressure deficit, that is, those cyclones which would be surrounded by at least three closed isobars. These cyclones, which might be called prominent cyclones, are the cyclones which are most noticeable on a weather map. The distribution of maximum radius of the prominent cyclones follows an approximate Gaussian curve, with the average radius of 1500 km implying a cyclone wavelength of about 3000 km, consistent with both synoptic experience and baroclinic instability theory. But these charactistics apply to less than one-fifth of the cyclones which occurred during GALE, and most cyclones are of the small-scale variety.

Compared to large-scale cyclones, small-scale cyclones tend to be short-lived phenomena. Fig. 2.18 is a scatter diagram of maximum cyclone radius versus cyclone duration. Most of the small-scale cyclones have durations of 48 hours or less, with the mean duration being 18.2 hours. The large-scale cyclones are scattered about a wide range of lifetimes, with a mean duration of 83 hours and a standard deviation of 56 hours. Larger cyclones tend to last longer; the correlation between maximum radius and duration is 0.74. When the cyclone population is split into two groups by size, the correlation becomes 0.49 for the small-scale cyclones and 0.43 for the large-scale cyclones.

The maximum pressure deficit of cyclones is also correlated with maximum radius (Fig. 2.19). The scatter is not as large as in Fig. 2.18, and the overall correlation is 0.81. Again, a clustering of small-scale cyclones is observed in the small radius-small pressure deficit region. However, maximum pressure deficit is a poor measure of cyclone intensity in this instance. Given two cyclones with equal pressure deficit but radii differing by a factor of two, the smaller storm will tend to have twice the geostrophic wind speeds and mean geostrophic vorticity of the larger storm. Hence, we shall estimate intensity by dividing the maximum pressure deficit by the maximum radius. Because maximum deficit and maximum radius do not necessarily occur simultaneously, this is only a lower bound on the largest mean pressure gradient attained by a cyclone.

The scatter diagram of cyclone intensity, as defined above, versus cyclone radius is shown in Fig. 2.20. Overall, a correlation of 0.53 is present, but points are widely scattered throughout most of the figure. The most intense storms are seen to have maximum radii between 1200 km and 1800 km. The mean maximum intensity for the large-scale, travelling cyclones is 14 mb $(1000 \text{ km})^{-1}$. The small-scale cyclones tend to be weaker, with a mean of 8 mb $(1000 \text{ km})^{-1}$, but are still comparable in intensity to many larger cyclones. Rather than being overwhelmed by the larger cyclones, small-scale cyclones over their generally short lifetimes attain significant amplitudes. Their contribution to eddy kinetic energy, however, would be much less than their intensity indicates, because of their short lifetimes and small sizes.

A difficulty in comparing this figure to baroclinic instability theory is that the maximum cyclone scale is not necessarily the scale at which the most rapid intensification occurs. The radius of a typical cyclone changes considerably during its lifetime. Figure 2.21 is a scatter diagram of maximum cyclone radius versus the radius of cyclones six hours after cyclogenesis. By definition, all points must lie in the lower right half of the diagram. Aside from the tendency of cyclones (particularly short-lived cyclones, as would be expected) to cluster near the diagonal, little coherent pattern is evident. Of the nineteen cyclones which attained a maximum radius of 1500 km or more, fourteen would still be classified as small-scale cyclones (radius of less than 750 km) after six hours, and eight of those had a six-hour radius of less than 400 km.

Because of our definition of cyclone radius, a large portion of these apparent changes in scale are due to large-scale cyclogenesis occuring when more than one small-scale cyclone is present. In a typical scenario, such as that depicted in Fig. 2.1c, two small-scale cyclones are located along a front, separated from each other by 450 km and from other lows by 1250 km. If one of the small-scale cyclones intensifies rapidly, or if development takes place on a larger scale, eventually one of the low centers will be absorbed into the other. When that happens, the col distance of the developing cyclone

increases from 225 km to ~800 km instantaneously. Thus, the individual points toward the right in Fig. 2.21 may indicate either the sudden initiation of cyclogenesis on a large scale or the gradual increase in scale or intensity of a smaller cyclone.

Section 2.7 : Discussion

In the above climatology, we have shown that the class of cyclones which attains a maximum radius of 750 km or less includes most stationary cyclones and many travelling cyclones. In contrast to large-scale cyclones, most small-scale cyclones vanish from the weather map less than a day after they first appear. The pressure deficits of small-scale travelling cyclones, when normalized by radius to obtain a measure of intensity, are comparable to most large-scale cyclones. Most large-scale cyclones appear initially as small-scale cyclones, and although this fact may not be of dynamical significance, it prompts the question of how one can distinguish between a future large-scale cyclone and a permanent small-scale cyclone.

The existence and frequent occurence of travelling small-scale cyclones was noted by Willett and Sanders (1959), who gave the following general description:

> "Many minor cyclonic or anticyclonic circulations occur unaccompanied by any significant counterpart in the form of a trough or ridge in the flow aloft. The pattern of vertical motion and weather phenomena associated with these circulations is similar to that ... of the more fully developed cyclonic and anticyclonic circulations, except that the horizontal and vertical extent and the vigor of the circulation is limited. If frontal structure is present within such a cyclonic circulation, the low center at the surface appears as a small, poorly defined frontal wave. The essential difference lies in the fact that a pronounced upper-level counterpart to the surface circulation center is necessary to the intensification of the latter ... [and is probably] necessary even for the maintenance of the circulation at low levels against the dissipative effect of friction. Consequently, these

> features rarely can be identified longer than one or two days and frequently persist for only a few hours. The geographical distribution of such features probably resembles that of the more fully developed cyclonic and anticyclonic circulations, though the data are frequently insufficient for their accurate detection. The minor frontal waves are nevertheless often of great importance since they are capable of producing marked fluctuations of weather conditions over short periods of time."

As has been discussed, small-scale cyclones indeed rarely last more than one or two days. The prediction of the geographical distribution of small-scale cyclones may be checked by means of Fig. 2.22, which shows the cyclogenesis regions of travelling small-scale cyclones (a subset of the cyclogenesis events in Fig. 2.11). The overall pattern is indeed similar to larger-scale cyclogenesis, but there are some suggestive differences. In particular, maxima are noted east of Georgia (south of the maximum in the lee of the southern Appalachians) and southeast of Texas. These locations are both south of the main bands of cyclone activity (Figs. 2.6-2.9), and they are both positioned over the northwestern edges of warm bodies of water. This implies that the local maximum of surface and latent heating, displaced from the track of primary cyclones, may be leading to small-scale cyclogenesis. The local geometry favors cyclogenesis, both by ensuring a local negative Laplacian of surface heating (Petterssen, 1956), and by causing those areas to be the first areas of low-level latent heating to be affected by eastward-travelling regions of large-scale forcing.

Aside from these maxima, and other maxima related to orographic features discussed earlier, sporadic cyclogenesis events occur throughout the domain, indicating that many travelling small-scale cyclones are not triggered by variations in the topography. The differences between stationary and travelling small-scale cyclones, and the existence of occasional small-scale cyclogenesis throughout the domain with a few maxima apparently related to the topography, suggests a broad range of small-scale cyclogenetic mechanisms.

Beyond their direct effects on local weather, Fig. 2.21 showed that small-scale cyclones can also be precursors to larger-scale cyclone development. From these statistics, it cannot be determined whether the small-scale cyclones play an important role in larger-scale cyclogenesis. A direct role, in which a pre-existing small-scale cyclone interacts with an approaching upper-level potential vorticity anomaly, would require that the upper-level trough not be much larger in size than the small-scale cyclone and that the stratification be much weaker than normal. Such an interaction should not produce a cyclone much larger than the initial small-scale cyclone. An indirect role might involve the triggering of latent heat release, the enhancement of the surface baroclinic zone, and the development of localized surface vorticity which experiences rapid spinup as large-scale ascent begins. Alternatively, the presence of small-scale cyclones might merely indicate the existence of a region favorable for large-scale baroclinic development.

The maximum in small-scale cyclogenetic activity along the southeast Atlantic coast is of particular interest for case study purposes. Most of the small-scale cyclones which formed there formed within regions of warm advection, satisfying the criteria for study established in Chapter One. This was also the region of formation of the Presidents' Day cyclone (Bosart 1981, Uccellini *et al.* 1987), and GALE was set up to observe cyclogenetic processes in this region. Because this is the site of the enhanced observations, we will limit our study to small-scale cyclones which formed in this area.

The selection of candidates for case study depends upon four factors: the data coverage, the influence of the small-scale cyclone on the local weather, the degree to which the small-scale cyclone was not forecasted correctly, and the degree to which the small-scale cyclone does not fit preexisting paradigms of cyclogenesis.

Of the smallest warm-sector travelling cyclones forming in this area, two are of particular interest because they had strong apparent influences on local rainfall patterns, they were difficult to forecast or were not forecasted at all, and they were present within the three-hourly rawinsonde network as they developed. These cyclones formed on 19 Jan

1986 and 25 Jan 1986. The main apparent difference between the two cases is that the 25 Jan cyclone formed along a coastal front while no coastal front was present on 19 Jan.

We elect to study the 19 Jan cyclone rather than the 25 Jan cyclone. The deciding factor was that the 25 Jan cyclone was already being studied within the context of IOP 2 by several groups, while little investigation was being made of events during IOP 1. Thus, the results of the IOP 1 case study may be compared to other case studies of IOP 2, the purpose being to delineate alternative explanations or differences in mesoscale processes.

As a second small-scale cyclone, we elected to study a cyclone which formed on 10 Feb 1986. This cyclone was not associated with the large rain amounts over land of the 19 Jan and 25 Jan cyclones, but preliminary analyses indicated that it may have merged with another cyclone to form a large-scale cyclone after leaving the GALE area. The data coverage for this case was also superior to that of the other remaining candidate small-scale cyclones.

CHAPTER THREE

SMALL-SCALE CYCLONE 1: OBSERVATIONS

Section 3.1: Surface Data and Analyses

a) Conventional surface analyses and time series

Six-hourly weather maps are shown in Fig. 3.1 for the case of the 19 Jan 1986 small-scale cyclone. These maps include NMC analyses of pressure and frontal structure taken from the regular three-hourly analyses received by facsimile, with additional subjective analyses of temperature based on the data on the original maps. This set of maps is intended to show the synoptic conditions within which the small-scale cyclone formed, as well as to illustrate the difficulty NMC analysts encountered in analyzing the small-scale cyclone.

The primary synoptic-scale cyclone of interest had just formed in Kentucky at 19/00. (We abbreviate dates and times according to the convention *dd/hh* or *dd/hhmm*, where *dd* is the date, *hh* is the hour (UTC), and *mm* is minutes.) During the subsequent 36 hours, the cyclone deepened at a moderate rate as it travelled slowly east-northeastward. The first low center is last seen in the analyses over Pennsylvania at 20/00, with redevelopment occurring to its southeast. This second, redeveloped low center was first analyzed in Virginia at 19/21 (not shown); it soon became the primary center and subsequently moved north along the mountains to eastern Pennsylvania by 20/06. The Kentucky low formed along a cold front which extended southward from a non-intensifying cyclone over the Great Lakes. The northern portion of this front was analyzed as having dissipated over the following 24 hours. The portion of the front south of the

developing cyclone moved eastward at a speed of 10-12 m/s, passing across the Carolina coast between 19/18 and 20/00.

At 19/00, the only analyzed warm front was the dissipating warm front extending eastward from the Great Lakes low. At 19/12, a second warm front is analyzed from North Carolina to southeast of Cape Cod. This warm front moves northward and becomes stationary along the coast as it extends northeastward. We interpret this front as a coastal front (Bosart *et al.* 1972, Nielsen 1989, Nielsen and Neilley 1990) which formed between Maryland and Maine during 19 Jan. The portion of the analyzed warm front extending eastward was not colocated with a specific surface temperature gradient. As seen in Fig. 3.1, the analyzed front progressed rapidly northward while individual isotherms moved much more slowly. Individual offshore buoy observations also fail to support the analysis of a warm front offshore. The southward extension of the analyzed warm front into the Carolinas at 19/12 is believed to be an attempt by the analysts to assign frontal wave characteristics to the developing small-scale cyclone, to be discussed below.

To summarize the important points from the synoptic weather pattern: the Carolina coastal region between 19/00 and 19/18 was 500 km to the southeast of a developing large-scale cyclone. This region can fairly be characterized as being in the "warm sector" of the developing cyclone, even though no classical warm front was present. The temperature analyses indicate a broad northwest-southeast temperature gradient extending from Canada to between 25N and 30N.

A small-scale cyclone is present on the 19/00 analysis in the Gulf of Mexico. This cyclone had been wandering around the Gulf of Mexico for over a day, and analyses of it rely heavily on the three regularly-spaced buoys in the Gulf. There is not enough data available for a detailed analysis, but NMC has analyzed two troughs (marked "trof") in a warm front-cold front configuration. Satellite pictures showed a large subtropical cloud shield over the Gulf during the period. The cyclone is analyzed over northern Florida at 19/06, and is not present in the analyses at 19/09 (not shown). It is not apparent from the

NMC analyses whether this cyclone is continuous with the small-scale cyclone which appeared later along the Carolina coast, and we will examine a time series of hourlies from Florida to show that this cyclone did not cross the Florida Peninsula. This point is of interest both for the sake of determining the rate of intensification of the small-scale cyclone and for helping to determine what role local mechanisms, such as surface heating, may have played in the small-scale cyclogenesis.

The small-scale cyclone of interest first appears on the three-hourly NMC maps at 19/12 (Fig. 3.1c) in North Carolina, at the junction between the previously-discussed "warm front" and a cold front which is analyzed as in the process of forming and which extends southwest across Florida. No actual pressure minimum is analyzed; however, a closed low is analyzed at 19/15 (not shown) along the North Carolina coast in the same position relative to the two fronts. At 19/18 (Fig. 3.1d) there is again no closed low, but the frontal intersection remains in what is clearly an area of high geostrophic vorticity. At 19/21 (not shown) the cold front was re-analyzed as a trough, which may be seen well offshore in the 20/00 analysis. We will discuss this cold front/trough at some length below.

When it became apparent to us that a small-scale cyclogenesis event had occurred, we re-analyzed the sea level pressure field on an hourly basis using surface and marine data available on the GALE Compact Disk. A more complete version of the offshore data file was then used to enhance the analyses shown in Figs. 3.2-3.4, which correspond to the synoptic times in Fig. 3.1b-d. We refrained from explicitly analyzing fronts and troughs, as we did not wish to assume that a particular frontal configuration should be expected with the small-scale cyclone.

In Fig. 3.2, the small-scale cyclone had been analyzed to have just formed off the South Carolina coast. In our initial hourly maps, the analysis of an actual low center at 19/06 was based primarily on extrapolation from subsequent hourly analyses in which the cyclone was more intense and better resolved by the data. The revised analysis shown in

Fig. 3.2 includes an additional key observation from a ship near the low center (20 C, 25kt SE wind). The surface pressure observation was 1010.9 mb, and a check of this particular ship's pressure observations at other times indicates a possible systematic error of about -0.8 mb. This observation caused us to shift the low southeast slightly and deepen it by a millibar. The revision in central pressure was substantial, considering that the revised low is still only about 1.5 mb lower than the environmental pressure to its northwest. We have described the effect of an additional observation in detail to show that the offshore surface analyses are prone to poor data coverage and differences in interpretation of the observations which are available, and we regard these analyses as less reliable than any other analyses we will present. Nevertheless, the small-scale cyclone is generally adequately resolved by the data, particularly at later times.

Although we have drawn a closed isobar around the small-scale cyclone, no closed circulation is apparent. Winds to its east are strong and tend to be spiraling inward toward the cyclone, while winds to its west are much weaker. It appears that a small-scale cyclonic circulation would be present if the large-scale wind pattern were removed, and we shall employ filtering below to isolate the wind field associated with the small-scale cyclone. Over land, winds are calm or light from the southeast. Nocturnal cooling has produced a land-sea temperature contrast of about 5 C, and temperatures over water are generally homogeneous at about 19 C to 20 C.

By 19/12 (Fig. 3.3), the small-scale cyclone is clearly present in the observations. The cyclone is still not intense enough to have a closed circulation in a stationary frame of reference with the available spacing of observations, but some observations just north of the cyclone indicate calm or a slight northerly component. The analyzed pressure deficit of the small-scale cyclone with respect to the col to its northwest is about 2.5 mb, and the mean difference between the central pressure and the pressure at a 125 km radius is about 2 mb. Both these numbers were smaller at 19/06.

Beyond this time, the cyclone weakened as a local pressure minimum, through some combination of weakening of the small-scale cyclone and intensification of the ambient pressure gradient due to the large-scale cyclogenesis centered over Virginia. At 19/18 (Fig. 3.4), which is the final time the small-scale cyclone can be identified as a pressure minimum, it is located over land near Cape Hatteras, with a pressure trough and shear line extending to its south. The shear line is not colocated with either of the two NMC-analyzed cold fronts at 19/18 (Fig. 3.1d), although the eastern analyzed front appears to have been drawn along the shear line up to and including the 19/15 weather map. The plotted temperatures and winds in Figs. 3.3-3.4 do not confirm the analysis of a warm front extending to the north of the small-scale cyclone.

Beyond 19/18, the extrapolated track of the cyclone would have taken it over open ocean east of Chesapeake Bay. Ship and buoy observations (not shown) from times up to and including 20/00 detected neither a closed circulation nor a local pressure minimum, but a circulation center of 100 km to 150 km radius could possibly have been present between observation locations.

Because the track of the cyclone only occasionally took it over regions of good data coverage, it is useful to examine time series of selected stations in the path of the cyclone to discern its detailed horizontal structure. The locations of the time series cross sections are given in Fig. 3.5. The southwestern cross section, from Valdosta (VAD) to Miami (MIA), is intended to determine whether the Gulf of Mexico cyclone crossed Florida to become the small-scale cyclone of interest. The other four cross sections are located downstream of the apparent cyclogenesis region of the small-scale cyclone and show the surface weather variations associated with the passage of the cyclone. Becaues we plot the earliest observations at the top of the figures and the later observations at the bottom, the figures may be interpreted as two-dimensional surface maps of features passing from southwest to northeast across the cross sections. If one were to take full advantage of this time-space correction, the vertical spacing between consecutive hourly observations would need to be

scaled by the horizontal station spacing and the assumed speed of weather features. We keep the vertical spacing constant, but we do shift by one hour the observations from certain stations located too far off the line of the cross section, based on an assumed weather system translation of 0.3 degrees latitude and 0.3 degrees longitude to the northeast. These corrections are indicated spatially in Fig. 3.5. One of the stations used in the cross sections was ship NLFI, which was travelling from northeast to southwest during the time of cyclone passage. Because of the variable displacement of the ship from the line of the cross section, we shifted the plotted ship observations by between one and three hours.

Were we to plot the actual sea level pressure observations, the cross sections would be dominated by falling large-scale pressures and by systematic station pressure errors. To remove both these effects and to isolate the small-scale, short-lived pressure variations, we have adjusted the plotted pressures as follows. First, the pressure observations at each station from the first two and last two hours of the time series were averaged together, and a straight line was fitted to the average pressures at two stations, chosen by their assumed reliability, located near either end of the cross section. Differences between the average pressures at the remaining stations and the straight-line fit were interpreted as systematic pressure errors and were subtracted from the particular station's pressure observations at all times in the time series. The mean pressure tendency was then removed by computing the difference between a station's corrected pressure and the mean corrected pressure of all stations in the time series at a particular hour. The resulting pressures will show pressure perturbations associated with small-scale cyclone passages only if the cyclone passes over some stations but not others. For completeness, the mean pressures are plotted next to each string of hourly observations.

The Florida time series (Fig. 3.6) depicts a situation of light winds and generally falling pressures. We are concerned with identifying the passage of a vorticity center with a scale of about 200 km, or about twice the spacing between stations. The cyclone should

be manifested as a north-south dipole of the north-south pressure gradient, as well as an east-west dipole in northerly winds and a north-south dipole in easterly winds. If the large-scale flow is weak, this leads to the well-known situation of winds backing to the left of the track of the low and veering to the right of the track of the low.

Inspection of the time series for such cyclone signatures reveals two pressure gradient dipoles. The first, between VAD and MCO from 18/23 to 19/03, is accompanied by a backing of the wind at the southern station, MCO, which is opposite of what would be expected. The second dipole, between VRB and MIA at about the same time, is coincident with a windshift at PBI and a slight veering at MIA. Although the signature is not very strong, it appears that a weak low may have passed across the southern Florida coast at about 19/02. However, this cannot have been the incipient small-scale cyclone of interest because it is too far removed from the analyzed position and track of the cyclone at later times. Finally, a general shift from southerlies to westerlies is found near the end of the period, but this appears to be due to larger-scale flow variations. Periods of rain occur at all stations, but generally take the form of brief, light showers at one station at a time. We thus find no evidence that a small-scale cyclone of detectable magnitude passed across Florida upstream of the small-scale cyclogenesis event in the Atlantic.

The next set of observations (Fig. 3.7) is from airports and buoys near South Carolina. This set is the first to show the passage of the small-scale cyclone. Between 19/06 and 19/12 at station BY5, the wind backs, weakens, then shifts to west-northwest before strengthening and becoming southwesterly. As this occurs, the pressure at BY5 relative to BY4 decreases. This is the signature of a low passing over or just south of the station.

Station BY4 also has a period of light northwesterly winds. There, oddly, the winds veer as the disturbance passes. This would suggest a low passing just to the north, but for the increasing pressure toward the north. The coastal station, MYR, is calm until the southwesterly winds kick in after 19/14.

Farther downstream, cross sections are available from farther offshore which show the passage of the cyclone in greater detail. In Fig. 3.8, cyclone passage is observed at all three offshore stations. The wind at BY2 shifts from southerly to northerly before backing to westerly, indicating a cyclone passing to the south as expected. At FPSN, the wind backs at first, then goes calm before becoming westerly, suggesting a cyclone passage just to the south. At NLFI, the wind remains strong and veers from southerly to westerly, implying that the cyclone passed to the north of NLFI. The time delay between cyclone passage at BY2 and NLFI indicates that the cyclone was elongated from north to south, since the cross section is oriented northwest-southeast. Pressure variations at BY2 and FPSN are consistent with the cyclone passage, but the pressure observations at NLFI do not indicate a pressure variation associated with the windshift. This was found to be a general characteristic of the observations of cyclone passage: about one-third of the stations did not show a clear pressure variation. We did not investigate the cause of this inconsistency, but we attribute it to the modifying effects of inhomogeneities in precipitation.

Farther downstream, the cyclonic wind variation associated with the small-scale cyclone is confined to three hours or less. Fig. 3.9 shows the time series for stations from RVC northwest. At the southeastern stations, the passage of the SSC is marked by a sudden change in wind direction from southerly to westerly and, except for RVC itself, a relative minimum in pressure. NKT is the first land station to show cyclone passage, with falling pressures, a cessation of rainfall, and a weak indication of backing. Otherwise, it is difficult to determine whether the cyclone passed to the south or north of individual stations. Along with the differences in cyclone time found in this and the preceeding cross section, this implies that the cyclone is not circular but highly elongated, as depicted in Figs. 3.2-3.4.

The final set of stations influenced by the cyclone before it moved out of the data-rich inner GALE region experienced an even narrower region of cyclonic vorticity (Fig.

3.10). The windshift from strong southerlies to strong southwesterlies at about 19/18 takes place within two hours at both DSLN and HAT. The wind shift is coincident with the end of the precipitation at HAT, but no indication of the trough passage is found in the hourly pressure observations. For this particular cross section time series, the lack of a pressure perturbation may be attributed to the near-simultaneity of the passage of the cyclone at the four stations. The inland stations, ECG and P48, show weak wind shifts at about the same time as the stronger wind shift along the coast. The pressure signature of the cyclone appears instead in the cross section mean pressures, plotted on the left of the cross section, which show a sudden drop before the time of the wind shift and a steady pressure afterwards.

Overall, the time series show that the small-scale cyclone formed over the Atlantic somewhere between Florida and South Carolina. It appeared to undergo a narrowing in the east-west direction as it intensified and moved northeastward. (An increase of propagation velocity would also cause an apparent narrowing of scale, but the cyclone appeared to pass the cross sections at a steady speed.) The long axis of the cyclone also rotated from north-south to northwest-southeast. After 19/12, it formed the dividing line between southerly and southwesterly to westerly winds. This windshift line has not been identified as a cold front because temperatures after trough passage were not systematically colder than temperatures before trough passage.

Using data from time series of high-frequency station observations, such as half-hourly buoys and PAM data, it is possible to construct detailed surface analyses of the cyclone while it was over land. We show in Fig. 3.11 the analyses of temperature and wind for 19/15 and 19/18. The center of circulation is indicated by a "C", and travels from the central North Carolina coast at 19/15 to the northeast corner of North Carolina at 19/18. Two windshift lines (dashed lines) have been analyzed. The southern windshift line is the shift from southerlies to westerlies discussed earlier. The northern line associated with a shift from weak southeasterlies to strong southerlies, as observed at 19/14 at CLKN and

41007 (Fig. 3.9) and at 19/17 at P48 (Fig. 3.10). This windshift was accompanied by a 1-2 C temperature increase, but no change in weather. Soundings indicate that it was a shallow feature, and we interpret it as the trailing edge of a surface-based inversion separating air which had been cooled by the near-shore waters from air which had been heated by the Gulf Stream. The configuration of the two windshift lines give the cyclone the superficial (and incorrect) appearance of a frontal wave.

The temperature analyses show that while a temperature gradient is present offshore, the center of circulation is not propagating along it, having moved inland after 19/15. Over land, temperatures have increased during the day, so that by 19/18 temperatures are as warm over land as they are over water. In fact, a sea breeze has developed along the southern North Carolina coast. Thus, neither the windshift line nor the circulation center appear to have been linked directly to the local surface baroclinicity.

b) Bandpass filtered surface analyses

We now desire to separate the small-scale cyclone from the larger-scale weather patterns. Characteristics of the small-scale cyclone which are masked by its environment include:

1) Intensification. The central pressure of the small-scale cyclone decreased from 1011 mb at 19/06 to 1001 mb at 19/18 (Figs. 3.2-3.4). This deepening rate, if extended through 24 hours, would qualify the small-scale cyclone as a "bomb" (Sanders and Gyakum 1980). But inspection of the synoptic maps shows that most or all of this deepening was due to the cyclone moving toward lower pressure while pressures were falling everywhere.

2) Scale. The method of estimating cyclone scale employed in Chapter Two is not well suited to cyclones embedded in a large-scale pressure gradient. Furthermore, we wish to determine whether the shape of the cyclone is circular or elongated.

3) Position. The analyses in Fig. 3.11 tracked the center of circulation of the small-scale cyclone. However, when embedded in a large-scale flow, the center of circulation will tend to be displaced to the left (relative to the downwind direction) of the vorticity center, and this tendency varies with the intensity of the cyclone and the strength of the large-scale flow.

In order to remove the large-scale, slowly-varying field components, observations may be filtered either spatially or temporally. In order to avoid problems relating to systematic pressure errors and inhomogeneous data density, we elect to apply a temporal filter to the observations.

From the station time series data, it appears that the small-scale cyclone took about three to four hours to completely pass individual stations. We therefore wish to remove all variations with periods of about eight hours or longer. It is also desirable to filter short-time-scale noise from the observations. The filter employed is a simple bandpass discrete Fourier filter, operating on 32-hour time series of observations (19/00 to 20/07) whose systematic trend has been removed. The filter completely removes the time mean as well as Fourier components with periods of 32 and 16 hours and half of the 8-hour component, and filters out periods of 2.7 hours or less. The filter was applied separately at each station.

The input data included mean sea level pressure and the two horizontal wind components. If data was missing for a particular hour or two contiguous hours, it was linearly interpolated from adjacent times; stations with data missing for longer periods of time were deleted from the dataset. After filtering, it was found that spatially systematic pressure variations were still present in the data, apparently due to a relatively large amplitude of the semidiurnal tide during the day of Jan 19. The hourly mean bandpass pressure for all stations was therefore subtracted from the hourly bandpass pressure at each station. Because the small-scale cyclone was much smaller than the station domain, this

permits us to infer intensity variations from the central bandpass pressure of the cyclone on successive maps.

The response of the filter is shown in Fig. 3.12 for various input curves. The first input curve is a wedge, in which the pressure drops for ten hours and then rises for ten hours. The input curve mimics the pressure behavior associated with a windshift line. The filter removes the large-period variation, producing weak responses only at the "corners" of the input curve, such as at the base of the wedge.

The second input curve is one complete period of a cosine curve superimposed on a constant field. The cosine has a period of eight hours, well within the range of the bandpass. This input curve mimics the behavior of an isolated small-scale cyclone. The filtered curve compensates for the isolated cosine by producing a positive response at the periphery of the cosine and a strong negative response in the center. If our small-scale cyclone has this form, the filtered maps will show a pressure minimum preceded and followed by two pressure maxima of about half the amplitude of the minimum. If the cyclone were part of a periodic wave (not shown), the maxima and minima would have comparable amplitudes.

The final graph shows the filtered response to an isolated bad data point. The response curve shows that the filter removes less than half of the amplitude of the bad data, and produces decaying waves on either side of the bad data point with a period of about three hours, at the short end of the bandpass spectrum. This response may be distinguished from the response to the isolated cosine by the length of the characteristic period of the response. An isolated data point, or an isolated pressure minimum with a period shorter than the cutoff period, will produce a response with a wavelength of about three hours. An isolated pressure minimum within the range of bandpass periods will produce a response with a wavelength comparable to the period of the pressure minimum itself.

Subjective analyses of filtered winds and pressures for the period 19/09 to 19/21 are shown in Fig. 3.13. The station data plotted on the maps are from the nominal time as well as one hour before and after the nominal time. Data not from the nominal time are plotted displaced from the actual station locations by 0.3 degrees of latitude and 0.3 degrees of longitude in the appropriate direction. This displacement was determined iteratively from the analyzed propagation velocity of the bandpass pressure minimum, and was also applied to the time series cross sections as discussed earlier.

At 19/09, based on continuity with later maps, the cyclone is located somewhere to the south of BY5 (see hypothetical location of -0.4 mb contour), out of range of most station observations. Offshore to the northeast, however, substantial pressure variations are apparent in the observations. In particular, an east-west band of anomalously high pressure is present off the southern North Carolina coast. This high propagated toward the northeast in succeeding maps.

The cyclone is easily seen on the 19/12 map as an area of cyclonic winds and low pressure south of North Carolina. The wind pattern suggests a nearly circular shape for the small-scale cyclone at this time. The lowest anomalous hourly pressure observed was -1.1 mb, and the winds suggest that the actual central pressure was lower.

At 19/15, the cyclone has moved to near Cape Lookout. the estimated central pressure is -1.4 mb, and the velocities of the bandpass winds have increased. The cyclone has also changed in shape, becoming more elongated in the north-south direction. The southward extent of the pressure perturbation cannot be determined because of the inhomogeneity of the data coverage and the likely nonrepresentativeness of RVC to the southeast of the plotted cyclone position.

The evolution of the small-scale cyclone continued in a similar fashion over the next three hours. At 19/18, the east-west scale of the low, as measured by the size of the -0.4 mb contour, had shrunk to 100 km, while the north-south scale was at least 150 km. At 19/21, the data coverage was poorer, but the central pressure was at least -1.0 mb. Behind

the cyclone, a region of anomalously high pressure may be seen following the same track as the pressure minimum.

The amplitude of the pressure maxima that preceded and followed the small-scale cyclone was about half that of the small-scale cyclone itself. This is consistent with the expected response to an isolated pressure minimum. The wavelength of this quasi-periodic response, estimated from the 19/12 and 19/18 maps, was 350-400 km, and the local period was about 12 hours. This is near the high end of the periods allowed by the filter, so this phenomenon is not a response to a high-frequency pressure perturbation. Based on the response to the cosine curve in Fig. 3.12, we estimate the magnitude of the isolated pressure minimum by determining the peak-to-trough amplitude of the response. This amplitude, 1.8-2.0 mb, probably underestimates the actual amplitude of the small-scale cyclone because its period is near the edge of the bandpass region, and from Fig. 3.2, it appears that the actual amplitude of the small-scale cyclone is more like 3 mb.

Because the southward extent of the cyclone cannot be determined from the filtered surface data, the track of the cyclone is ambiguous. We can say with confidence that the northern edge of the pressure minimum tracked toward the northeast, near the northern margin of the Gulf Stream, at a speed of approximately 10 m/s, and the pressure perturbation was limited in its northward extent to about 100-200 km northwest of the north wall of the Gulf Stream. The shear line, or at least that portion of the shear line which was along the North Carolina coast, was oriented approximately NNW-SSE and propagated toward 80 degrees at 7 m/s. An alternative way of considering the motion of the small-scale cyclone is to regard it as propagating northward along the shear line at a speed of 7 m/s.

Given the small size of the cyclone, it is interesting that the bandpass winds tend to be oriented along the pressure contours rather than being directed down the pressure gradient. Clearly, this phenomenon is a vortex in actual wind as well as in geostrophic wind, although filtered wind speeds are less than that expected from gradient wind balance.

c) Kinematic properties of the offshore wind field

To better determine the southern extent of the small-scale cyclone, to estimate the kinematic properties of the surface wind field, and to see whether the track of the cyclone was related to any noticeable feature of the large-scale surface wind field, we constructed analyses of the offshore wind field south to 25 N and east to 60 W. Both subjective and objective analyses were attempted. It was found that even when bogusing of data was used to fill in gaps in data coverage, the objective analyses suffered from numerous dipoles in derivative quantities of magnitudes comparable to the large-scale fields themselves. The subjective analyses were broadly similar to the objective analyses, but without the dipoles introduced by anomalous stations, and we show only the subjective analyses here.

The subjective analyses were constructed by hand-analyzing each component of wind separately on a surface map. The analyzed fields were then manually interpolated to a 1x1 degree grid and input into a computer, which then computed vorticity and divergence and performed a streamfunction analysis.

The wind speed and streamfunction analyses (Figs. 3.14a-3.18a) are dominated at early times by strong anticyclonic flow around the high pressure center located northeast of Bermuda. Wind speeds are greater than 10 m/s over a large area at each six-hourly time, although weaker winds tend to be found near the coast. During the period covered by the maps, a region of westerly flow appears off the Florida coast and spreads eastward, and a dramatic confluence zone forms between the two wind regimes. We have noted the northern end of this confluence line earlier (for example, Fig. 3.10), describing it as a windshift line between southerly and westerly flow, with the small-scale cyclone located at its northern end. These analyses show that the windshift line extended southward all the way to the Bahamas.

Was the small-scale cyclone likewise as extensive? Figs. 3.14b-3.18b show the vorticity associated with this analyzed wind field. According to these analyses, the largest vorticity tends to be located within 300 km of the coast, consistent with the previous analyses of the cyclone track. This result must be viewed with caution, however, because these analyses were performed by somebody who expected to find a small-scale cyclone near the coast. The objective analyses do show a broadly similar vorticity pattern, although the vorticity maximum along the coast is not as distinct. Further south, along the confluence line, the subjective analyses indicate typical vorticities of $1x10^{-5}$ sec^{-1} to $2x10^{-5}$ sec^{-1}.

As for the intensification of the small-scale cyclone, the vorticity analyses show a broad region of weakly positive vorticity at 19/00 in the region of incipient cyclogenesis off the Georgia-Florida coast. At 19/06 a closed vorticity maximum is present off the coast of South Carolina. Because these analyses were performed before data from the key ship discussed earlier was available, a more current analysis would have a stronger vorticity maximum located farther to the southeast. At later times a gradual intensification is indicated through 19/18, after which time the analysis suffers from a decrease of data density near the cyclone center. The actual magnitude of maximum vorticity at these later times is strongly dependent upon the horizontal resolution of the analysis; plugging in numbers from the DSLN time series and the propagation velocity of the small-scale cyclone, the vorticity of the windshift line which passed DSLN was at least $3x10^{-4}$ sec^{-1}.

The patterns of divergence (Figs. 3.14c-3.18c) are consistent with the near-shore radar observations to be discussed later. At 19/00, a broad region of weak convergence is located near the coastline. This convergence region intensifies and expands southward during the following twelve hours, becoming (not surprisingly) colocated with the confluence line, which we may now properly call a convergence line. Beginning at 19/12, the maximum convergence (about $5x10^{-5}$ sec^{-1}) tends to be located south of the region of

maximum surface vorticity, and the convergence tends to be less localized than the vorticity.

Section 3.2: Upper Air Data and Analyses

a) Potential vorticity analyses and upstream cross sections

In addition to determining the vertical structure of the cyclone, the analysis of upper air data should show whether or not the small-scale cyclone was directly associated with an upper-air disturbance. Both these tasks turn out to be somewhat difficult, because the small-scale cyclone remained offshore. Adequate upper-air coverage is only present in the northern portions of the cyclone. However, because of the large-scale flow structure, upper air data is available both upstream and downstream of the cyclone. This fact is particularly useful for isentropic potential vorticity analyses, which depict a quasi-conserved quantity. In effect, what we will be doing is seeing what ingredients (potential vorticity gradients and anomalies) went into the cyclogenesis region and what products (intensification of anomalies, diabatic transport of potential vorticity across isentropic surfaces) came out the other side.

The evolution of the potential vorticity structure of the troposphere is depicted in Figs. 3.19-3.27, which show potential temperature at the ground and at the tropopause and potential vorticity within the 295-305 K and 315-325 K layers. The dynamical tropopause is arbitrarily defined as the 1.5 PVU (10^{-6} m^2 K kg^{-1} s^{-1}) surface. The 295-305 K layer is representative of the lower troposphere in the vicinity of the small-scale cyclone, while the 315-325 K layer is representative of the upper troposphere. The ground potential temperature analysis was constructed using only sounding data, in order to be consistent with the other maps in data coverage and resolvable scales. The interpretation of maps of this type is outlined by Hoskins *et al.* (1985).

The sequence of maps shows a baroclinic development produced by the superposition of an upper level trough and a surface temperature gradient. The tropopause map shows the trough cutting off over Missouri and Iowa between 18/12 and 19/00, well before the main cyclogenesis at the surface. After 19/00, no intensification of the upper level anomaly can be expected from advection of large-scale potential temperature gradients at the tropopause. The cutoff trough is embedded in a background deformation field, however, and does undergo some intensification as a result of its shape becoming more circular.

While cutting off, the core of the anomaly appears to grow colder. While some potential vorticitiy generation may have occurred, we believe that it is more likely that the coldest anomaly, initially being long and narrow, was located between upper air stations as it plunged southward and only becomes apparent as it reaches a nearly circular shape over a data-rich region. As the cutoff cyclone travels slowly eastward, the coldest temperatures rotate around to the eastern side of the cutoff. This superposition at the tropopause is another mechanism for finite-amplitude intensification of the upper-level anomaly.

At the ground, the approaching upper level trough induces a wavelike perturbation in a preexisting cold front over the Ohio River at 19/06. The resulting warm anomaly is held at nearly constant phase with respect to the cold anomaly aloft as they both progress eastward. The apparent strength of the warm anomaly gradually increases with time, and the analyses of surface pressure (Fig. 3.1) indicate a gradual continuous deepening of the surface cyclone.

Aside from the primary trough, the tropopause map does not show any significant small-scale troughs. One upper level trough not apparent in the tropopause temperatures may be seen in Fig. 3.19b over southeastern Louisiana. IPV maps at other levels indicate that this trough was a potential vorticity anomaly within the upper troposphere rather than at the tropopause itself. This trough, being an isolated feature, was sheared both vertically and horizontally by the approaching primary trough. At 19/00, the center of the potential

vorticity anomaly in the 315-325 K layer has advected to northern Georgia. Analyses show it weakening in intensity as the anomaly becomes narrower than the station spacing.

These analyses suggest that the small-scale cyclone was not directly associated with an upper level trough. No viable candidate troughs were seen in either the tropopause map or the 315-325 K layer map. The winds aloft, as shown on these maps, imply that any small-scale wave or anomaly, such as the one over Louisiana on 18/12, would have rapidly advected northeastward ahead of the primary trough, contrary to the known motion of the small-scale cyclone.

The upper tropospheric analyses do not extend into the Gulf of Mexico. To make certain of the conclusion that the small-scale cyclone was not induced by an advancing small-scale upper level trough, cross sections of wind from Nashville to West Palm Beach were constructed for the period preceeding the development of the small-scale cyclone. Station locations are shown in Fig. 3.28. Any inducing trough would have passed through this cross section near AYS and TBW and left a wind signature in the form of enhanced shear vorticity and/or anomalous northward wind followed by anomalous southward wind.

The cross sections, at three-hourly intervals, are shown in Figs. 3.29-3.30. The cross section normal wind is dominated by a subtropical jet with a maximum wind speed over AYS of over 50 m/s. South of AYS, anticyclonic shear vorticity predominates. A region of positive shear vorticity is present throughout the period between AYS and TBW below 800 mb. Positive shear vorticity does appear aloft between AYS and TBW at 19/03, but the positive vorticity does not extend downward below the 600 mb level. The cross section parallel wind has a complicated pattern, but it evolves slowly and no passing upper level troughs may be seen.

Given the small scale of the cyclone at the surface, it was unlikely to have been part of a deep baroclinic development caused by an advancing upper level trough. The potential vorticity analyses have confirmed that the small-scale cyclone was not a deep baroclinic

cyclone. There was also no strong potential vorticity gradient in the upper troposphere at early times for the small-scale cyclone to interact with.

We now return to the discussion of Figs. 3.19-3.27. At the surface, little temperature perturbation is evident over land. Over water, where the cyclone was located, trajectories had taken the air parcels over water for several days. Interactions with sea surface temperatures would act to damp any transported thermal anomalies quickly, so air temperature anomalies are only expected near the location of a sea surface temperature anomaly or where heat fluxes may have been increased by high winds. The latter effect, an important element in hurricanes, is apparently not due to interaction with the small-scale cyclogenesis in this case. Figs. 3.14-3.18 showed that the region of high winds extended well offshore and was not oriented or colocated with the region of strongest surface vorticity.

Another possibility for surface vorticity production is the generation or mean-gradient advection of low-level potential vorticity. The generation of potential vorticity cannot be neglected, and we shall see that vigorous precipitation was occurring in the vicinity of the small-scale cyclone. The 295-305 K layer is suitable for investigating the possible presence of both large gradients and generation.

Because the layer winds were parallel to the coast during the time of the small-scale cyclone, it is necessary to look upstream to determine the initial potential vorticity structure. The 18/12 map (Fig. 3.19d) shows that the potential vorticity values over Florida were between 0.25 and 0.5 PVU. Later maps through 19/09 show the potential vorticity both over Florida and downstream over the GALE region as being between 0.25 and 0.4 PVU. There is little reason to expect an ambient potential vorticity gradient in the unsampled layer offshore without the effect of diabatic potential vorticity generation.

Later in the period, at 19/18, the potential vorticity within the primary cutoff trough reaches the 1.5 PVU threshhold. Because this high potential vorticity air is localized and nearly circular, it provides a useful Lagrangian reference point for air parcels ahead of it.

At 19/06, the air ahead of the cutoff is generally below 0.5 PVU (indicated by the highlighted line), with no evidence of significant potential vorticity gradients apart from those connected to the cutoff. Over the next several hours, and particularly between 19/18 and 20/00, most of the layer converts from less than 0.5 PVU to greater than 0.5 PVU. This increase was not due directly to advection of high potential vorticity air horizontally, as can be verified by inspection of the airflow patterns in Figs. 3.19d-3.27d. Rather, the increase represents non-conservation of potential vorticity, which we attribute to vertical transport of potential vorticity across potential temperature surfaces through diabatic processes. The highest values of potential vorticity ahead of the cutoff cyclone appear over southern New England at 20/06. The potential vorticity of this air is greater than 0.75 PVU, and it appears downstream of the heavy precipitation region ahead of the small-scale cyclone.

The diabatic transport of potential vorticity should appear as a negative potential vorticity tendency in the 315-325 K layer. This tendency may be seen in the motion of the 0.5 PVU contour (highlighted) between 19/00 and 20/00. The contour moves across the wind field rather than being advected by it. This tendency may be seen most clearly between 19/12 and 20/00, when the contour first travels westward to Lake Ontario, counter to the observed winds, and then becomes stationary over Chesapeake Bay in the presence of 100 kt winds advecting it northward. We would normally hesitate to draw conclusions based on the wiggles of a single contour from map to map, but in this case the tendency is one of a steady decrease of potential vorticity aloft and the details of the evolution are confirmed by the three-hourly intermediate maps (not shown).

If the diabatic effect is deep enough, or if the precipitation is a result of deep convective or slantwise instability, there should be a diabatic warming of the tropopause as well. Indeed, while no region of the tropopause upstream of the Atlantic coast is warmer than 335 K between 18/12 and 19/00, such a region does first appear over Cape Hatteras at 19/12 and propagate toward New England through 19/18.

The potential vorticity analyses have shown that the small-scale cyclone apparently developed independent of prolonged dynamical interaction with a small-scale upper trough. They have also indicated that the vorticity of the small-scale cyclone was most likely due to the generation of potential vorticity at low levels rather than due to an internal or edge Rossby wave or baroclinic superposition of two or more potential vorticity anomalies. Because of the lack of data coverage offshore, the analyses were not useful for directly determining the structure of the small-scale cyclone.

b) Vertical structure of the small-scale cyclone

The track of the cyclone was such that only three sounding sites experienced a bandpass surface pressure anomaly of 0.5 mb or more. These sites were HAT, MRH, and RVC. Upper air data fron these three sites are less than complete, for reasons which we now discuss.

MRH was one of the six CLASS sites operating during this IOP. Soundings were performed every 3 hours before 19/15 and every 1.5 hours thereafter. Winds from MRH were frequently missing below 700-900 mb, so the nearly complete temperature record is hindered by poor wind data.

HAT was more directly in the path of the small-scale cyclone, and also experienced the heaviest rainfall. Because it was a NWS sounding site, rawinsonde observations were taken at most every 3 hours. Also, the 19/09 and 19/18 soundings were missing. Wind data is also available at HAT from the CP4 Doppler radar, but a variety of circumstances have prevented us from making use of it.

RVC was located offshore, and was in the best position to obtain time series data of the passage of the small-scale cyclone. For IOP 1, RVC was equipped only with minisondes. These sondes do not record winds and tended to reach only 500-700 mb. Also, the sounding observations are missing between 19/12 and 19/21.

Using this abbreviated but nevertheless valuable dataset, we will first consider the thermal structure of the small-scale cyclone. Initially, maps of temperatures on particular pressure levels were constructed, but these maps were hindered by the undesired noise produced by small-scale vertical temperature variations. Ordinarily, such variations are not a problem, but because of the small size of both the cyclone and the observing network, typical station-to-station variations in the temperature field are often less than 1 C.

The vertical noise is eliminated by considering thickness rather than temperature. Not only is small-scale vertical noise eliminated, but by dividing the troposphere into four or five layers, the complete (coarse) temperature field may be depicted using a small number of maps. We shall convert thickness into mean temperatures using the thickness formula

$$\bar{T} = -\frac{g}{R}\frac{\delta(Z)}{\delta(\ln p)} \tag{3.1}$$

in which Z is the geopotential height.

Because of missing observations, it is difficult to construct a time series of thickness maps. Instead, we show in Table 3.1 a time sequence of selected thicknesses from MRH (located near NKT in Fig. 3.3). Using our standard time-space conversion of 33 km/hr, each three-hour interval between soundings may be regarded as a 100 km spatial separation. Because the 19/09 MRH sounding is missing, we have replaced it with the 19/12 HAT sounding, taken 100 km downstream. From Fig. 3.13, we judge the small-scale cyclone to have passed MRH at about 19/15 with an amplitude of 2.0 mb.

Table 3.1 shows that the passage of the small-scale cyclone was approximately coincident with a maximum in temperatures in all layers between 800 mb and 300 mb. Temperatures tended to rise at a regular rate between 19/06 and 19/12, apparently reached a peak between 19/12 and 19/15, and then fell after 19/15. Below 800 mb, the maximum temperature was not reached until 19/1930, most likely because of diurnal heating over

land. Above 800 mb, there is no noticeable tilt to the temperature wave. Given the temporal resolution of the data and the speed of the small-scale cyclone, the actual vertical tilt, if any, must have been 50 km or less.

Similar temperature tendencies were found at other stations, though no other stations in the path of the small-scale cyclone had a complete temperature record. To indicate the horizontal extent of the temperature wave, we show in Fig. 3.31 the pattern of mean 300-400 mb temperature at the nominal time of 19/15. We have plotted data from both the nominal time and from times before and after, using the usual time-space conversion of 0.3 degrees of latitude and longitude per hour to offset the observations from the station locations. The subjective analysis follows the observations at the nominal times when possible.

The analysis shows that the amplitude of the temperature perturbation was strongest near the coast, with the maximum temperatures located over or just downstream of the surface position of the small-scale cyclone. Estimating the magnitude of the perturbation relative to the background temperature field, it appears that the perturbation decreases from about 4.5 degrees near the coast to at most 2 degrees along a line extending from Delaware to central South Carolina.

A warm core structure like the one apparent in Table 1 and Fig. 3.31, in which the amplitude of the warm core is nearly constant with height, is characteristic of a positive potential vorticity anomaly at low levels coupled with a negative potential vorticity anomaly at high levels. This is consistent with the potential vorticity maps (Figs. 3.19-3.27), which implied a diabatic transport of potential vorticity from high levels to low levels in the general area of the small-scale cyclone.

With this warm-core structure, we expect to find the vorticity of the small-scale cyclone decreasing with height. The relative vorticity should be negative above mid-levels as the influence of the inferred negative potential vorticity anomaly aloft becomes stronger. Maps of relative vorticity at selected levels, constructed by objective analysis of rawinsonde

winds, are shown in Fig. 3.32. At this time (19/15), the small-scale cyclone, according to filtered and unfiltered surface analyses, was located just south of Cape Lookout. The contours of vorticity offshore in Fig. 3.32 are a consequence of the extrapolation of onshore data offshore by the Barnes objective analysis program, and are not to be trusted. Over eastern North Carolina, where observations are available, the relative vorticity is seen to be a maximum at the lowest level, becoming negative above 750 mb.

A standard technique in case study analysis is the computation of vertical profiles of vorticity and divergence from triangles of upper air stations (e. g., Keshishian and Bosart 1987). Because critical observations were missing at certain times, that technique was not available to us here. Even construction of single-time triangles about the small-scale cyclone proved to be difficult. The best available profile of vorticity (Fig. 3.33) ends at 400 mb and shows an erratic vorticity structure superimposed on a trend of decreasing vorticity with height. The small-scale variations may indicate real atmospheric structures, but it is more likely that they are an artifact of the small size of the triangle, as sensitivity to wind errors varies inversely with triangle size.

Because the small-scale cyclone was elongated from north to south, most of the vorticity associated with the cyclone should take the form of shear vorticity in the northerly component of wind. The problem of missing observations is mitigated by interpolation or by using observations displaced slightly from the cross section if necessary. Cross sections through northern North Carolina, normal to the track of the small-scale cyclone, are shown in Figs. 3.34-3.35. Station locations are shown in Fig. 3.28. These cross sections suffer from the lack of upper air wind observations offshore, and therefore only show the left flank of the small-scale cyclone. Also, the sounding from HAT at 19/18 is missing, so that the region of largest vorticity is not sampled by these cross sections.

The plots of wind normal to the axis of the cross section (Fig. 3.34) show a subtropical jet at 200 mb similar to the one found in Fig. 3.29. Below 800 mb, a low-level jet first appears at 19/06 over MRH and HAT. This jet, with velocities greater than 15 m/s,

expands eastward to PGV at 19/09 before retreating to MRH at 19/12. The low-level winds from MRH are missing at 19/15, but the low-level jet is still strong over HAT at 19/15. HAT is missing at 19/18, and the low-level jet has disappeared off the right edge of the cross section.

We associate this jet with the strong southerly winds seen at the surface ahead of the small-scale cyclone and the confluence zone to its south. Plots of time sequences of upper air winds at low levels over the GALE region (not shown) indicate that the wind maximum strengthened with time. The trailing edge of the wind maximum was oriented north-south, was narrower than 100 km, and propagated steadily toward the east. The position of this shear zone, if extrapolated southward, matched the position of the offshore surface shear line. The strong winds apparently did not penetrate to the surface at inland stations because of the combination of surface friction and low-level inversions.

Positive (negative) shear vorticity may be inferred from these cross sections wherever the normal wind speed increases toward the right (left). Shear vorticity on the western side of the low-level jet may be seen below 900 mb at 19/06, below 850 mb at 19/09, and below 800 mb at 19/12 and 19/15. At 19/15, the wind shear between PGV and HAT is as large as 10 m/s. Since the station spacing between PGV and HAT is about 165 km, this yields an estimate of the shear vorticity downstream of the small-scale cyclone of 6×10^{-5} s^{-1}. Aloft, anticyclonic shear prevails from 700 mb to above the level of the subtropical jet at 200 mb, and a wind minimum at 650 mb is found at HAT at 19/15.

The horizontal winds in the plane of the cross section (3.35) indicate winds toward the left ahead of the small-scale cyclone (at 19/09, 19/12, and 19/15) and winds toward the right behind the small-scale cyclone (at 19/18). This is in the expected sense for cyclone passage. These veering winds, like the low-level jet, are confined to below 800 mb, except for a possible deeper wind shift at HAT between 19/15 and 19/18, which cannot be verified without 19/18 data from HAT. The remainder of the cross sections are dominated by increasing winds to the left, as the upper-level trough seen in Figs. 3.19-3.27 begins to cut

off southeast of the northwestern edge of the cross section. Both sets of cross sections confirm that the positive vorticity associated with the small-scale cyclone was confined to low levels, as was anticipated from both the potential vorticity and thickness analyses.

Section 3.3: Observations of Precipitation Distribution

Our purpose in this section is to document the horizontal distribution of precipitation during the small-scale cyclone event. As previous sections have shown, the cyclone is closely related to the diabatic generation of potential vorticity through latent heat release, and precipitation provides an estimate of the magnitude and horizontal distribution of potential vorticity generation. Also, because the variations in precipitation will be seen to be substantial, the relationship between the cyclone and the precipitation is of forecasting as well as theoretical interest. Finally, accumulated precipitation is a standard method of verifying model forecasts and simulations, and the comparison with forecasted rainfall totals will demonstrate the degree to which the operational models failed to accurately capture the development of the small-scale cyclone.

Over the inner GALE region, the precipitation distribution had considerable mesoscale variability. The observed 6-hourly precipitation distribution for 19 Jan 1986 is shown in Fig. 3.36. These maps were constructed using surface airways observations, PAM station observations, and observations from state climatological stations. The precipitation may be seen to be particularly heavy over extreme eastern North Carolina, while the least precipitation over the 24-hour period was observed less than 200 km to the west along a strip extending from ILM northward. West of that strip, local precipitation maxima are scattered about, with the precipitation generally heavier toward the mountains. Overall, 24 hour totals were over 75 mm at Cape Hatteras, less than 10 mm in other coastal regions, and 15-25 mm along the southern Appalachians.

Near Cape Hatteras, accumulated precipitation increased monotonically toward the southeast, and the magnitude and offshore extent of the heavy precipitation cannot be determined from the surface observations. An estimate of the horizontal extent of the offshore precipitation is available from Martin *et al.* (1988). They estimated accumulated precipitation from satellite images using a technique described by Arkin and Meisner (1987), which gives a linear relationship between fractional cloud cover and precipitation. As implemented by Martin *et al.*, the fractional cloud cover f_r in 1x1 degree boxes of clouds with infrared brightness temperatures below 235 K is related to rainfall rate *RR* by

$$RR = C\, f_r \ , \tag{3.2}$$

where C is specified as 72 mm d^{-1}. The 6-hourly maps for 19 Jan are shown in Fig. 3.37, and indicate that the heavy precipitation extended over a wide area offshore. Of course, these maps must be viewed with considerable caution, but allowing for the box size, the agreement is acceptable over land, where independent confirmation of the accumulated rainfall is available.

National Radar Summaries for 18/1135 to 20/1135 are shown in Fig. 3.38. At 18/1135, well before the initial appearance of the small-scale cyclone at the surface, scattered precipitation has already broken out in the cyclogenesis region along the South Carolina, Georgia, and Florida coasts. The offshore precipitation spread northward, and by 19/0535 already extended well north of Cape Hatteras. The highest cloud tops of the heavier offshore precipitation were reported at 25,000 ft. The 0535 radar summary does not indicate precipitation in the immediate vicinity of the developing small-scale cyclone, but the cyclone at this time is beyond the range of the coastal radars.

On succeeding maps, the heavy offshore precipitation travels northeastward and is beyond Cape Hatteras by 19/1735. Six hours later, deep convection is present over the Gulf Stream, with cloud tops to 41,000 ft. Much lightning was reported within these clouds by observers on the scene, but the shallower, heavy precipitation that fell on Cape

Hatteras earlier was not accompanied by reports of thunder or lightning, even though much of the rain fell during the night. The small-scale cyclone, which moved within range of the coastal radars at 19/1135 and 19/1735, appears to have been located at the trailing edge of the heavy precipitation rather than being embedded within it.

Elsewhere, the large-scale cyclone which formed at 19/00 over Kentucky is accompanied by precipitation throughout the period of these maps. However, there does not seem to be a correlation between the intensity of the cyclone and the areal coverage and intensity of the rainfall. The horizontal separation between the heavier precipitation along the coast and the inland cyclogenesis event is also quite unlike standard models of extratropical cyclones, which have the primary precipitation regions adjacent to the cyclone or its trailing cold front.

The precipitation distribution measured directly over land, observed by radar along the coast, and deduced from clouds well offshore, does not agree with the precipitation forecasted by the LFM (Limited-area Fine Mesh model, an operational model with coarser resolution than the NGM), by the NGM, or by the GALE forecasters (including the author). The 12-hour accumulated precipitation forecasts from the LFM and NGM, based on an initialization time of 19/00, are shown in Fig. 3.39. Both models forecasted generally light precipitation through the first 12 hours, with maximum accumulations of about 15 mm. After that time, heavier precipitation was forecasted to occur offshore south of Cape Hatteras.

Based mostly on the numerical guidance, the GALE forecasters recommended that aircraft be in the vicinity of HAT starting at 19/21, in order to observed the heaviest precipitation within range of the coastal radars. The actual precipitation was not only much heavier than expected, but it had ended at HAT by 19/18. This was one of the largest forecast busts of the experiment.

The structure of the radar echo pattern at CP4 varied considerably during the period of heavy precipitation. Between 19/06 and 19/12, the precipitation was remarkably

amorphous, considering the intensity of rainfall. A typical 1.5 km CAPPI (constant-altitude plan-position indicator) is shown in Fig. 3.40a. Nearly the entire range is filled with echo varying irregularly between 20 and 40 dbZ. The only indication of organized structure is along the western edge of the figure, where the precipitation ends abruptly along a rough northeast-southwest line. This margin fluctuated by less than 30 km between 19/06 and 19/12 and is reflected in the large, localized accumulated precipitation gradient shown in Fig. 3.36b.

Between about 19/12 and 19/14, the echo pattern evolved from an amorphous mass of echo into a broad band of precipitation 50-100 km wide oriented northeast-southwest and located over HAT. Fig. 3.40b shows the band when it was most coherent. Echo had decreased both inland and offshore of HAT before 19/15, and between 19/17 and 19/18 the southern end of the band passed across Cape Hatteras, bringing an end to significant precipitation in the region. CAPPIs from that period do not show any comma-shaped pattern or other feature which might indicate the presence of the small-scale cyclone as it travelled northward with the trailing edge of precipitation. The pattern of echo after 19/14 suggests that HAT was a local maximum of precipitation, with accumulated rainfall of perhaps less than 40 mm at locations 50-100 km offshore.

Section 3.4: Summary

The 19 Jan small-scale cyclone formed over water off the coast of Georgia between 19/00 and 19/06, in a region of large-scale southerly flow ahead southeast of a slowly-developing large-scale baroclinic cyclone. The small-scale cyclone had a horizontal radius of 200 km (total width of 400 km) along the axis of the cyclone track. The central pressure of the small-scale cyclone was 2-3 mb less than the ambient surface pressure at its maximum observed intensity at 19/15. The cyclone travelled toward the northeast, roughly parallel to the Gulf Stream, with a velocity of about 10 m s^{-1}.

The cyclone was located at the northern edge of a surface confluence-shear line, with strong southerly winds ahead of the cyclone and weak westerly winds behind the cyclone. The confluence line extended far southward, and subjective analyses of offshore winds indicated that convergence and vorticity were widespread offshore, with the strongest vorticity concentrated near the location of the analyzed small-scale cyclone. At sounding stations over land, the strong southerly winds took the form of a low-level jet with maximum wind velocities of greater than 15 m s^{-1} near the 900 mb level. The cyclone was elongated along the axis of the shear line, and appeared to become increasingly elongated with time.

The cyclone was also colocated with the trailing edge of a region of widespread heavy precipitation, with 75 mm of rainfall observed over Hatteras. The precipitation was highly localized; stations 100 km inland of Hatteras received less than 10 mm of rainfall. The radar data from Hatteras indicated that the precipitation was widespread and amorphous between 19/06 and 19/11, but later evolved into a NNE-SSW oriented band 75-100 km wide, oriented along the large-scale thermal wind.

A careful examination of upper air data revealed no small-scale upper-level trough which could have induced the surface development of the small-scale cyclone. Potential vorticity generation at low levels and potential vorticity destruction aloft were inferred to have occurred in the vicinity of the small-scale cyclone from examination of the potential vorticity fields upstream and downstream of the cyclone. This generation-destruction is consistent with the observed coastal and offshore precipitation.

The small-scale cyclone was warm-core, with a thermal perturbation of 2-4 C which extended throughout the troposphere. The vorticity was largest at low levels, with negative relative vorticity present above 700 mb. The small-scale cyclone formed and remained on the anticyclonic shear side of the jet.

These observations suggest that saturated ascent and latent heat release played a major role in the development of the small-scale cyclone. We shall postpone examination

of the vertical moist stratification until Section 5.5. First, we note that diagnosis of events offshore has been hampered by the general lack of upper air data in the region of small-scale cyclogenesis. In order to obtain a complete picture of the structure of the small-scale cyclone and its environment, we shall examine in Chapter Four the NGM forecast of the small-scale cyclone.

CHAPTER FOUR

THE NGM FORECAST OF A SMALL-SCALE CYCLONE

Section 4.1: Rationale for Studying the NGM Simulation

The NGM initialized at 19/00 did not forecast a closed mesoscale low to form offshore and pass over HAT at 19/18. However, the NGM did produce a small-scale low-level vorticity maximum whose motion, structure, and evolution were broadly similar to the observed small-scale cyclone. As an example of the similarity, Fig. 4.1 compares the 19/15 observed normal wind cross section (taken just ahead of the small-scale cyclone) to a 20/00 cross section through the NGM's low-level vorticity maximum at roughly the same orientation.

Both cross sections show a prominent upper level jet centered at about 250 mb. On the anticyclonic side of the jet, both cross sections also show a low-level jet centered at about 850 mb. The magnitude of the horizontal gradient of normal wind is about three times larger in the observed cross section than in the NGM, but the shear vorticity is distributed in the NGM over only four or five grid points. Both the observed small-scale cyclone and the NGM small-scale cyclone (located near grid point 32) are located at the western edge of the low-level jet. Above the region of cyclonic low-level shear, both cross sections show a macimum of anticyclonic shear centered near 400 mb.

One of the advantages of examining the NGM forecast in detail is apparent in Fig. 4.1. Rather than just the western edge of the low-level jet and the small-scale cyclone being resolved by the observations, the entire jet and small-scale cyclone are contained within the C grid of the NGM. In addition, the problems of observation errors and poor analyses are avoided, because the NGM data is in effect a set of dynamically and

temporally consistent analyses. The primary disadvantage is that the analyses are of a hypothetical weather event which is artificially prevented from having small mesoscale structure by the grid resolution and smoothing of the NGM. So while we will examine the NGM in detail under the assumption that the evolution of the NGM parallels the evolution of the real atmosphere, we will be alert to possible dynamically significant differences between the NGM and the atmosphere.

We do not at this point regard the threefold increase in scale and intensification time and decrease in maximum vorticity as a dynamically significant difference. The limited horizontal resolution of the NGM forces the cyclone to be larger than a half-wavelength of a couple of hundred kilometers. If the small-scale cyclone was produced by an instability mechanism which has a maximum growth rate at the smaller scale, its rate of intensification in the NGM will necessarily be slower, even if the initial conditions in the NGM are accurate. Also, the NGM cyclone is small enough that the horizontal smoothing of the model is acting to dissipate it. In summary, we shall assume that the process which produced the small-scale cyclone in the real atmosphere were also responsible for its development in the NGM. Our hope is that the processes important to the modeled intensification place specific constraints on the atmospheric observations which could then be tested.

Section 4.2 : Description of the Nested Grid Model Data Used in this Study

The NGM is the prognostic component of NMC's Regional Analysis and Forecast System. A description of the current RAFS is given in Hoke *et al.* (1989), and its state at the time of GALE may be inferred from a list of changes since GALE provided by Rogers *et al.* (1990). Further detail on the NGM is found in various technical reports, of which the primary source of information is Phillips (1979).

The NGM is a hydrostatic, primitive equation model with sixteen sigma-coordinate layers in the vertical with typical vertical spacing of 50 mb to 75 mb. The horizontal grids are mapped onto a polar stereographic projection; the largest grid covers the entire Northern Hemisphere, with superimposed grids of increasing resolution nested over North America. The highest-resolution grid, called the "C" grid, has a grid spacing of about 80 km at 35.0 N. Where grids overlap, forecasted variables are interpolated between grids in both directions. The consequence of this interpolation is that the rightmost four grid points on the C grid, for example, are actually interpolated values from the B grid, with a resulting decrease by a factor of two of horizontal resolution near the edge of the grid. The deepening rates of cyclones passing through these grid mesh regions has been found to be systematically underestimated by the NGM (Hoke *et al.* 1987).

The three velocity components are on a staggered grid relative to state variables. Time stepping (on the C grid, a full time step is 75 s) is by the two-step Lax-Wendroff method (Phillips 1962, Lax and Wendroff 1964), which has the desirable side effect of damping short-wavelength, rapidly propagating disturbances. Additional damping of short wavelengths, in lieu of explicit diffusion tems in the prognostic equations, is performed by applying a fourth-order horizontal smoother (Shapiro 1975) every thirty minutes. This smoother acts to damp wavelengths of four grid increments or less, or roughly 320 km on the C grid, and may therefore detrimentally affect the simulation of phenomena at the low end of our specified small-scale cyclone spectrum.

Surface fluxes of heat, water vapor, and momentum are parameterized by bulk aerodynamic formulae, with the drag coefficient a linear function of wind speed and proportional to the surface roughness. In the version of the NGM used during GALE, the suface roughness over the oceans did not vary with wind speed. Also, there was no surface radiation budget, so heat and water vapor fluxes over land were set to zero. Over water, heat fluxes are proportional to the air-sea temperature difference, while moisture

fluxes are proportional to the difference between the specific humidity of the air and the saturation specific humidity of the sea surface. Sea surface temperatures are held constant.

The parameterization of large-scale precipitation is by a method described by Phillips (1981). We describe this parameterization in detail here both because of the relative obscurity of the documentation and because of the importance of the large-scale moist processes to the dynamics of the NGM small-scale cyclones. The parameterization is modivated by the desire to initiate condensation within grid boxes at relative humidities below saturation, under the assumption that variable saturation exists within a given grid box area in the real atmosphere, and that requiring the entire box to reach saturation would overly delay the forecasted onset of precipitation.

In the atmosphere, when a parcel of air becomes supersaturated, a portion of its water vapor condenses, raising the temperature of the parcel. To a first approximation, the reduction of specific humidity to its saturated value and the corresponding increase in temperature may be expressed as (Haltiner and Williams 1980, pp. 313-314):

$$T_{new} - T = \frac{(q - q_s(T))}{\frac{C_p}{L} + \frac{L}{R_v T^2} q_s(T)} \tag{4.1}$$

$$q_{new} - q = -\frac{C_p}{L} (T_{new} - T) \tag{4.2}$$

where $q_s(T)$ is evaluated at the initial temperature T rather than the final temperature T_{new}. We note that the changes in q and T are linearly proportional to the supersaturation q - $q_s(T)$.

The parameterization supposes that the specific humidity q_o computed to be present in a grid box at the end of a full time step of model integration represents a uniform distribution of q over the range $(q_o - ¥ q_o) < q < (q_o + ¥ q_o)$, where ¥ has been set equal to 0.05 for the version of the parameterization implemented in the NGM. The value of q_s is computed from the grid point (mean) values of T and p.

If $q_S > (q_O + ¥ q_O)$, the entire grid box is subsaturated, so no condensation occurs. If $q_S < (q_O - ¥ q_O)$, the entire grid box is supersaturated, and (4.1)-(4.2) are used to compute a new (mean) T and q. If q_S lies within the assumed range of q, some fraction of the parcels within the grid box are saturated, as given by

$$F = \frac{q_O (1 + ¥) - q_S}{q_O (1 + ¥) - q_O (1 - ¥)} \tag{4.3}$$

The parameterization supposes that each supersaturated parcel experiences a change in its T and q given by (4.1)-(4.2), and that the total changes are averaged over the grid box to produce net changes in T and q, which from (4.1)-(4.3) are:

$$T_{new} - T = \frac{¥ F^2 q_O}{\frac{C_p}{L} + \frac{L}{R_v T^2} q_S} \tag{4.4}$$

$$q_{new} - q_O = - \frac{C_p}{L} (T_{new} - T) \tag{4.5}$$

The excess water vapor $(q_O - q_{new})$ falls out as rain, and in the version of the NGM used during GALE, falls to the ground without evaporating into lower levels.

If this adjustment were applied iteratively to a grid point, its relative humidity would converge to 100 (1 - ¥), or 95% in the NGM. In actuality, the parameterization is applied once per time step, so that ascending motion increases the relative humidity about as fast as the parameterization reduces it. For ascent rates characteristic of the cases studied, the relative humidity of air in a grid box undergoing moist ascent in the NGM tends to lie between 95% and 100%.

An important consequence of this parameterization is that air undergoing stable moist ascent, although approximately conserving θ_e (to the level of approximation of (4.1-4.2)), does not ascend along the appropriate moist adiabat. Rather, because its relative humidity is below 100%, grid boxes are slightly warmer than their corresponding moist adiabats. Furthermore, the deviation from moist adiabats is a function of ascent rate.

When vertical motion is weak, the parameterization is more efficient at keeping the relative humidity near 95%.

As a consequence, parcel theory does not apply directly within the NGM. For our calculations of lifted parcel temperatures when parcels are displaced over a small vertical distance, we will assume that a parcel greater than 95% saturation ascends along the saturation moist adiabat given by the parcel's temperature and pressure, while parcels with less than 95% saturation ascend along dry adiabats as usual. Phillips (1981) showed that this approximation is excellent for constant ascent rates. An additional complication is introduced by an apparently undocumented parameterization of $q_s(T)$ which differs substantially from the parameterization used by the analysis software we shall employ in our calculations. For purposes of displaying quantities associated with moisture, we will make use of the fact that the parameterization introduces a discontinuity in the gradient of relative humidity and in quantities which are functions of relative humidity, such as the difference between equivalent potential temperature θ_e and saturated equivalent potential temperature θ_e^*.

The moist convective parameterization is of the type introduced by Kuo (1965) and modeled after processes associated with large-scale regions of tropical convection. Our case studies will avoid regions in which parameterized convection is occurring, so we will not discuss the details of the convection scheme. Of importance, though, is that because of the computational inefficiency of the Kuo scheme, convective instability is checked only for those parcels originating in the lowest four layers of the NGM, so that convective instability above about 850 mb must be released through grid-scale processes.

The initial fields for the NGM forecast runs are obtained from an analysis system that uses six-hour global spectral model output as its first guess. The analysis (DiMego 1988) has a horizontal scale of 150-200 km and uses significant level rawinsonde data as well as satellite data, aircraft observations, and surface reports. Corrections are made to the first guess using optimum interpolation techniques. After the analysis is complete, a

nonlinear normal mode initialization is applied to the deepest two vertical modes. This initialization does not affect the specific humidity fields.

The NGM data obtained from the GALE Data Center consists of the initialized fields as well as forecast fields every six hours out to 48 hours, the full extent of the NGM run. Variables are provided on a 41x41 subset of the C grid centered over the southeastern United States and extending from about 103.5 W to the eastern edge of the C grid. In the vertical, variables have been interpolated from their sixteen initial sigma levels to evenly-spaced pressure levels 50 mb apart, from 1000 mb to 50 mb. This interpolation, performed separately for q and T, introduces a slight amount of vertical noise to θ_e and θ_e^* in regions of moist ascent.

Section 4.3: Description and Analysis of the NGM Small-Scale Cyclone

The NGM cyclone possessed maximum relative vorticity at 850-950 mb, with a tendency for the maximum vorticity to progress upward toward 850 mb with time. Fig. 4.2 shows the 850 mb relative vorticity for the 0-30 hour forecasts from an initial time of 19/00. (Since all model data in this section is from the 19/00 forecast run, times will be referred to by forecast hour. Thus, F18 is the 18-hour forecast valid at 19/18.)

At the initial time, a southerly to southwesterly low-level jet is situated offshore. Corresponding to this jet is a band of positive relative vorticity extending from off the coast of Florida north to Cape Hatteras. This region of positive vorticity is well detached from the larger high vorticity region associated with the intensifying cyclone over Tennessee.

After six hours, the magnitude of the wind offshore has decreased by 10-15 kt in most places. Near the Florida peninsula, winds have increased, a trend which would continue through F30. The band of weakly positive vorticity is still present over Cape Hatteras, and the vorticity over Tennessee is increasing.

At F12, the small-scale cyclone first appears in the 850 mb vorticity field as a bulge in the band of vorticity due east of Cape Hatteras. This bulge does not appear to have been produced from the band of vorticity by a barotropic instability process. The winds along that section of the band remain weakly confluent, so the bulge in vorticity was not produced by anomalous advection of the vorticity band.

During the next six hours, the maximum relative vorticity within the small-scale cyclone doubled. The cyclone overwhelmed the preexisting pattern of vorticity, and the strongest winds near the cyclone are feeding into it from the south. The small-scale cyclone was moving north-northeastward, roughly parallel with the 850 mb flow. The synoptic-scale cyclone to the west made its closest approach at that time. As the forecast run continued, the small-scale cyclone moved into southern New England, maintaining its rough triangular shape and continuing to intensify at the rate of about 2×10^{-5} sec^{-1}/(6 hours). To its south, a more prominent region of high vorticity suddenly developed. This region was associated with large amounts of convective precipitation. (Parameterized convective precipitation did not occur in the vicinity of the small-scale cyclone itself.) The system took the form of a line of convection, at least superficially resembling a cold front or squall line. Its evolution and dynamics will not be discussed here because of its likely interrelationship with the convective parameterization, and because it formed far enough south of the small-scale cyclone and late enough in the forecast run that it did not have any significant effect on the small-scale cyclone during its intensification.

An abrupt weakening of the offshore winds occurred between F00 and F06, while after F06, the winds near the eastern corner of the C grid changed little during the forecast. This appears to be an example of the model "adjusting itself", developing an internally dynamically consistent mass and flow field. Because of this phenomenon, we shall pay little attention to events occurring before F06. It is fortunate for two reasons that the small-scale cyclone does not form until F12. First, we do not have to worry about model startup effects contaminating the dynamics. Second, we can be sure that the model developed the

small-scale cyclone on its own, rather than being initialized with it or spinning it up suddenly in response to a poor initialization. The small-scale cyclone forms and develops as an internally consistent dynamical entity within the NGM.

The small-scale cyclone in the NGM developed in a similar manner to the observed small-scale cyclone. Both formed offshore well ahead of the synoptic-scale trough, moving toward the northeast at 10-15 m/s, and were small in scale compared to the larger cyclone to the west. Some quantitative differences are present, however, in its time of formation, scale, intensity, location, and motion. Errors associated with the timing and location are interpreted as dynamically insignificant, because the incipient small-scale cyclone was initialized over water, where observations of upper air conditions are generally lacking, especially on the scale of the small-scale cyclone. Furthermore, the boundary temperatures of the NGM are obtained from a much coarser analysis than the one shown in Fig. 1.2. Fig. 4.3 shows the initialized sea and land surface temperatures for the 19/00 NGM run. If the observed small-scale cyclone was influenced by the relatively warm Gulf Stream, the NGM would fail to capture the interaction. If the small-scale cyclone preferred to propagate along the western edge of the warmest water, the NGM would carry it farther offshore because the warmer water was farther offshore.

The other quantitative differences are not so easy to dismiss. The comparatively large scale of the NGM cyclone may be attributed to the horizontal resolution of the model, since the small-scale cyclone occupies a total of about twenty horizontal grid points. However, this only confirms that the NGM could not have correctly simulated the small size of the observed small-scale cyclone. It does not imply that the dynamics which produced the small-scale cyclone in the atmosphere would simply produce a larger-scale small-scale cyclone in the NGM. It is possible that a different dynamical mechanism is more important at the resolvable scales of the NGM.

Similar concerns apply to the intensification rate. The comparatively slow intensification in the NGM might imply that the dynamics of the small-scale cyclone are not

as efficient at this scale, that a critical part of the dynamics is being inhibited in the NGM, or that entirely different dynamics are operating. The discrepancy in motion is 5 m/s or less, and may be due to errors in the initialization of the wind field, but it also suggests the possibility that the structure of the small-scale cyclone, particularly the vertical structure, varies from the atmosphere to the NGM.

Before we proceed to investigate the structure and dynamics of the NGM small-scale cyclone, we first will consider whether the NGM small-scale cyclone possesses certain dynamically significant characteristics of the observed small-scale cyclone, particularly in regards to the vertical structure and the lack of an associated upper-level trough.

To consider the possibility of interaction with an upper trough, we shall examine time series of upper air thermal vorticity advection. Discussions of the potential vorticity pattern and omega equation calculations will be postponed until later. Fig. 4.4 shows temperature and relative vorticity at F6, F12, and F18. From the Sutcliffe (Sutcliffe 1947, Hoskins and Pedder 1980) formulation of the omega equation, quasi-geostrophic vertical motion forcing is proportional to the advection of vorticity by the thermal wind. Consequently, we are looking in this figure for a middle or upper tropospheric vorticity maximum with significant thermal wind advection which forces development on the scale of the small-scale cyclone. Because the small-scale cyclone was continually intensifying, we want this vorticity maximum to be displaced upshear from and moving in tandem with the small-scale cyclone for at least two six-hourly maps.

The most prominent trough in Fig. 4.4 is the synoptic-scale trough over Tennessee. Vertical motion forcing associated with this trough is quite large, as indicated, for example, by the very small rectangles over Alabama at 450 mb at F12. Frequently the assumption, valid for sinusoidal disturbances, is made that the vertical motion is proportional to the forcing. This assumption cannot be made here. The forcing is strongly localized, and the Laplacian operator in the response would produce a broad region of upward motion

extending eastward on a scale comparable to the Rossby radius. Such a response would imply positive vertical motion over the small-scale cyclone at F06 and increasing vertical motion through F18, but the vertical motion would not be localized on the scale of the small-scale cyclone unless additional factors were at work (as discussed in Chapter Five).

Other troughs in the vicinity of the small-scale cyclone, whose scales are more compatible with the small-scale cyclone's development, are located at F06 off South Carolina at 300 mb, 750 km east of Jacksonville at 450 mb, and 500 km southeast of Cape Hatteras at 600 mb. The 600 mb trough is associated with consistently weak thermal advection, and is located three-quarters of a wavelength too far to the east at F12 and F18 to be driving the small-scale cyclone. The 450 mb trough remains well to the southeast throughout the period. The 300 mb trough is the only trough associated with thermal vorticity advection over the small-scale cyclone center, at F12. However, the scale match appears to be poor, with the 300 mb trough being much larger than the small-scale cyclone. More importantly, the 300 mb trough is moving much too quickly to have a long-term effect on the small-scale cyclone. At F12 the 300 mb trough was located directly over the small-scale cyclone, while at F18 it had moved a complete half-wavelength downshear. During that period, the thermal vorticity advection over the small-scale cyclone was such as to force downward motion rather than upward motion. None of these three troughs was strong enough, deep enough, in the proper location, or moving at the proper velocity to have produced a dynamical interaction of six hours or more with the developing small-scale cyclone, which intensified over a time period of twenty-four hours in the NGM. In that sense, no upper-level troughs can be said to have been associated with the small-scale cyclone.

For a check on the vertical structure of the NGM small-scale cyclone, Fig. 4.5 shows the relative vorticity from 200 mb to 1000 mb at F18. Four regions of positive vorticity dominate this set of maps. The first, the synoptic-scale trough to the east, is seen to be a troposphere-deep system, extending along the left margin of the map at all levels.

Two other troughs, discussed in the preceding paragraph, appear as vorticity maxima well east of Norfolk at 300 mb and 600 mb. Their small horizontal scales are matched by small vertical scales. Neither trough has a total vertical extent of as much as 300 mb.

The fourth prominent vorticity anomaly is the small-scale cyclone itself. The small-scale cyclone may be seen as a prominent vorticity center just offshore of Norfolk at 1000 mb, 900 mb, and 800 mb. At 700 mb the plotted vorticity center appears to be a combination of the 600 mb trough above and the small-scale cyclone below. Although the patterns overlap at 700 mb, it is appropriate to consider them to be two distinct entities because they are separated by a half wavelength in the horizontal, are tilted downshear, and are moving apart from each other independently (Figs. 4.2 and 4.4). Thus the small-scale cyclone had maximum positive vorticity at low levels, had zero relative vorticity at 600 mb, and had negative relative vorticity in the upper troposphere. As implied by this vorticity structure, the thermal structure of the small-scale cyclone was warm-core (not shown). This vertical structure closely resembles that of the observed small-scale cyclone.

Section 4.4: Potential Vorticity Diagnostics and Dynamical Implications

a) Evolution of potential vorticity within the NGM

Having compared the NGM small-scale cyclone to observations and found close similarities in the area of formation, the vertical structure, and the lack of an associated upper-level trough, we now wish to examine the dynamics of the NGM small-scale cyclone. After examing the gross potential vorticity structure, we will use potential vorticity inversion techniques to deduce the method of intensification.

The tropopause, 320 K, 300 K, and surface maps for the NGM are shown in Figs. 4.6-4.11, and may be directly compared to the observed potential vorticity pattern in Figs. 3.19-3.24. One significant difference in the construction of the NGM tropopause maps is

that they were made by superimposing the 1.5 PVU contour from analyses on consecutive isentropic levels. This allows contours to cross in regions of tropopause folds, but prevents us from easily recovering tropopause winds to go with the temperatures. The winds (plotted in m/s rather than kt) at every fourth grid point have been overlain on the IPV maps as well as on the 1000 mb potential temperature map, which is taken as a proxy for the boundary layer potential temperature map. The NGM maps have the advantage over the observed potential vorticity maps of extending offshore, although this can also be considered a disadvantage because the data does not extend offshore. Also, while the NGM maps depict an accurate dynamical evolution of potential vorticity to the extent to which finite-differencing and physical parameterizations do not introduce undue errors, any errors present in the initialization may persist throughout the period. Although these factors affect the accuracy of the NGM potential vorticity maps, they are not of primary concern here, because we wish to examine the potential vorticity as it affected the small-scale cyclone in the NGM.

In many respects, the NGM potential vorticity turns out to be quite similar to the observed potential vorticity. The NGM shows the cutoff forming over Tennessee, and a warm tongue of surface air being advected northward ahead of it. This baroclinic development closely parallels the observed development. The 18/12 Louisiana trough is initialized at 19/00 over the southern Appalachians and is advected northward past New England by F18, well ahead of the small-scale cyclone. The 300 mb trough seen in Fig. 4.6b-4.8b also appears in the tropopause maps, where the anomaly can be seen as weakening rapidly with time, apparently because of grid-scale smoothing. In the 320 K (upper tropospheric) potential vorticity distribution, the previously discussed 450 mb vorticity maximum appears briefly at F06, before weakening and moving off the edge of the grid.

The observed development of a low potential vorticity region at 320 K along the Atlantic coast is seen in the NGM, which has its low potential vorticity region extending

well offshore. A small region of negative potential vorticity even appears at this level at F24, just downshear of the 850 mb small-scale cyclone position. This region expands and moves to the edge of the plotting region by F30.

At the 300 K level, the potential vorticity field is initialized smoother than in our objective analysis, and becomes even smoother during the first twelve hours of integration. The initial field includes a band of relatively high (>0.5 PVU) potential vorticity, which we associate with the vorticity and low-level jet discussed earlier at 850 mb. Other minor blobs of potential vorticity are scattered about, and the synoptic-scale trough is located near the left-hand margin. At six hours, all but two blobs have become smoothed out. At F12, even the blob over eastern Tennessee has vanished, but only temporarily.

Also at F12 is the first appearance of a new potential vorticity anomaly just southeast of Cape Hatteras. This anomaly increases in magnitude through F30, eventually acquiring a second closed contour at 0.75 PVU as it moves northward. Comparison with Fig. 4.2 shows that this anomaly is associated with the 850 mb small-scale cyclone throughout the period. It is also clear from this map sequence that the potential vorticity anomaly was produced non-conservatively, rather than by advection of a larger-scale gradient. Also appearing at F24 offshore is a second anomaly associated with the line of convection mentioned earlier.

The 1000 mb potential temperature evolution is comparatively uninteresting, aside from the thermal wave associated with the large-scale cyclogenesis. The offshore potential temperature is seen to adjust within 12-18 hours to the sea surface temperatures (Fig. 4.3), and remain static afterwards. No wavelets associated with the small-scale cyclone are readily apparent, even at smaller contour intervals (not shown).

The vertical structure of the potential vorticity in the vicinity of the small-scale cyclone at F24 is shown in Fig. 4.12, where the potential vorticity has been calculated over 5 K isentropic layers rather than 10 K as before. The lowest layer, 290-295 K, intersects the ground just southeast of the small-scale cyclone. This layer also has a potential

vorticity maximum of greater than 0.8 PVU. As discussed below, it is not clear whether this maximum was generated by interior latent heating or by boundary layer heat fluxes.

The three layers immediately above all have potential vorticity maxima of greater than 0.6 PVU. By comparison, the environmental values of potential vorticity surrounding the small-scale cyclone are less than 0.2 PVU, so the potential vorticity in the center of the cyclone was about a factor of three greater than its surroundings.

At the 315-320 K and 320-325 K layers, regions of negative potential vorticity are present over and to the north and west of the positive anomalies below. Negative potential vorticity was not present at these levels 6-12 hours prior to these maps, and their presence here indicate both diabatic non-conservation and the presence of negative moist potential vorticity (to be discussed in Chapter Five). These areas are larger than in the 315-325 K map (Fig. 4.10) because potential vorticity was calculated from finite differences and averages at the boundaries of the layers, and the negative absolute vorticity is primarily confined to the 320 K isentropic surface.

b) "Bitwise" potential vorticity inversion

Potential vorticity inversion may be used to assess the relative contributions of potential vorticity at various levels (a diagnostic technique first employed by Robinson 1988 with quasi-geostrophic potential vorticity) to the vorticity of the cyclone. The inversion technique we will use is a particular application to the technique of potential vorticity inversion using the non-linear balance equation which was developed by Davis (1990). We use potential vorticity from the NGM at eight evenly spaced pressure levels from 950 mb to 250 mb. The horizontal domain size is chosen to be 20x20 grid squares on the NGM C grid, and the domain is centered over the small-scale cyclone at each individual time of inversion. Boundary conditions are taken from the NGM forecasted winds and temperatures on the edges of the domain. For the sake of the following discussion, we will

use the terms "observed" or "actual" to refer to the NGM initial and forecasted fields and "inverted" to refer to fields obtained by inverting the actual NGM potential vorticity.

In addition to inverting the complete actual potential vorticity field, we shall perform inversions on potential vorticity fields constructed by setting the potential vorticity on certain pressure levels (and potential temperature at the upper or lower boundary) to its horizontal mean value throughout the domain. This method differs from the Green's function technique of Davis (1990) in that we are zapping potential vorticity by setting the fields to their domain-average values rather than their time-averaged values, and we are not explicitly considering the effect on the induced flow of one anomaly by the changes in stability induced by another anomaly. Both of these simplifications are permitted by the relatively small size of the inversion domain, which forces the effect of large-scale potential vorticity variations to be felt only through the boundary conditions. The remaining interior potential vorticity variations are necessarily small in scale, and the modifications to the induced flow from anomalies separated vertically and horizontally is as a result weak. The legitimacy of this technique is confirmed after the fact by noting that the total inverted flow is nearly identical to the sum of the individual flow fields obtained by inverting potential vorticity anomalies at various levels, with a suitable allowance made for the flow induced by the boundary conditions.

The objective of "bitwise potential vorticity inversion" in this case is to determine the relative importance of upper-level potential vorticity anomalies, low-level potential vorticity generation, and surface potential temperature variations in producing the NGM small-scale cyclone. To clearly separate regions of expected potential vorticity creation from regions of potential vorticity destruction, we choose the boundary between upper-level potential vorticity and low-level potential vorticity to be 500 mb. Upper-level potential vorticity will be treated as a unit, and is taken to include 450 mb, 350 mb, 250 mb, and the potential temperature at the upper boundary. Low-level potential vorticity will include the potential vorticity at 550 mb, 650 mb, 750 mb, and 850 mb.

Near the ground, the surface air temperatures have been shown to adjust rapidly toward sea surface temperatures. As a result, the initial surface potential temperature distribution is converted into a low-level potential vorticity distribution. Within the southerly offshore flow in the NGM, warm air which is advected over colder water cools rapidly. As it cools, its static stability and potential vorticity increase. Meanwhile, above the boundary layer, the atmosphere is relatively insensitive to the combined changes in surface potential temperature and boundary layer potential vorticity which have taken place. It is therefore appropriate to consider the 950 mb potential vorticity and the surface potential temperature together when the boundary layer air is being cooled from below; a diabatic change in one will tend to be coupled with an effectively equal and opposite change in the other. We shall refer to them collectively as "surface potential vorticity". While the diabatic tendency from surface heating on this combined term should be small, the inclusion of potential vorticity in the lowest 100 mb permits additional diabatic generation from, for example, moist ascent.

The induced relative vorticity at 850 mb produced by inverting upper-level potential vorticity, low-level potential vorticity, and surface potential vorticity are shown in Fig. 4.13-4.17. Depicted in Fig. 4.13a-4.17a is the induced flow calculated after setting the observed potential vorticity and boundary potential temperatures to their level-mean values everywhere. This shows the contribution of the winds along the lateral boundaries to the induced vorticity. Since the same lateral boundary conditions are used for all inversions, this induced vorticity contributes to the total induced vorticity in all the inversions. The boundary winds may be seen to result in a contribution of roughly 0.5×10^{-5} sec^{-1} at all times. The large gradients of vorticity near the edges of the domain are a consequence of the implicit discontinuities of potential vorticity along the boundaries which result from replacing potential vorticity by its mean value in the interior of the domain. Conversely, the lack of gradients in the interior, as well as the small absolute values of vorticity in the

are distant enough to have little artificial effect on the inversion in the neighborhood of the small-scale cyclone.

The inclusion of upper-level potential vorticity does not produce an easily noticeable change in the induced 850 mb vorticity (Fig. 4.13b-4.17b). This immediately indicates that the small-scale cyclone is not growing by means of superposition with an upper-level anomaly or an anomaly approaching from outside the inversion domain. The lack of mesoscale structure in the vorticity field also implies that upper-level anomalies are not inducing winds at low levels on the scale of the cyclone, and thus cannot be intensifying the cyclone by differential advection of a low-level potential vorticity field.

The low-level potential vorticity initially induces an elongated north-south vorticity structure (Fig. 4.13c), which we have seen is associated with the offshore low-level jet. During the next twelve hours (Fig. 4.14c-4.15c), vorticity on the eastern edge of the band increases and develops a closed contour. The induced vorticity continues to increase during the next twelve hours (Fig. 4.16c-4.17c), with the maximum value of relative vorticity increasing at the rate of nearly 1×10^{-5} sec^{-1} per 12 hours. Comparison with the total inversion shows that the mid-level potential vorticity induced over half of the vorticity associated with the cyclone at 850 mb.

The remainder of the vorticity is induced by the surface potential vorticity (the combination of 950 mb potential vorticity and surface potential temperature) (Fig. 4.13d-4.17d). Through the period there is a weak east-west induced vorticity gradient. Embedded within this gradient, a local vorticity maximum forms and intensifies at the location of the small-scale cyclone. Both the magnitude and rate of increase of the vorticity are roughly half that of the induced vorticity from mid-levels. Also, the induced vorticity is displaced southwestward along the thermal wind vector rather than northeastward. Both of these facts imply that the low-level contribution is due to saturated vertical motion rather than differential advection across the surface potential temperature gradient.

The total inverted vorticity (Fig. 4.13e-4.17e) is in good agreement with the actual vorticity pattern (Fig. 4.13f-4.17f). The primary difference is an underestimate of the vorticity amplitude of the small-scale cyclone by about 30%. As we have used the full nonlinear balance equation with Ertel potential vorticity, this discrepancy is attributed to the presence of unbalanced flow. The close match of vorticity *patterns* implies that the imbalance is being felt on a scale at least as large as that of the updraft/vortex itself. So while bitwise potential vorticity inversion has proven useful for confirming the lack of baroclinic superposition effects, the specific mechanism for the development of the small-scale cyclone may depend at least partly on inherently unbalanced dynamical processes.

Section 4.5: Vertical Motion Associated with the NGM Small-Scale Cyclone

Along with previous analyses, the potential vorticity inversion suggests that moist ascent was responsible for generating the potential vorticity anomaly associated with the small-scale cyclone. Alternatively, the vertical motion generated the small-scale cyclone through vortex tube stretching. These interpretations have nominally been made without direct examination of the vertical motion or moisture fields. We now examine those fields to confirm the presence of saturated vertical motion and to examine the horizontal and vertical structure of the updraft.

The vertical motion fields at 700 mb and 400 mb are shown in Fig. 4.18-4.19. At the initial time, there is a broad region of vertical motion over the cyclogenesis region. After six hours, a local maximum has developed southeast of Cape Hatteras, accompanied by large gradients of vertical motion, particularly to the northwest. Elsewhere in the area, vertical motion is generally weak but upward.

At F12, the vertical motion maximum has become stronger and is much less elongated toward the south. A noticeable tilt has also developed, with the 400 mb maximum displaced downshear from the 700 mb maximum. Also, there is a significant

vertical motion difference south of Cape Hatteras, with air moving upward at 700 mb and downward at 400 mb.

Between F12 and F18, a dramatic evolution has taken place. Instead of a single vertical motion maximum as at F12, there are four at F18. We shall demonstrate below that the easternmost vertical motion maximum is the original maximum, having progressed toward the northeast. At F18 the horizontal displacement between vertical motion maxima at 700 mb and 400 mb is more than twice the magnitude of the tilt at F12, and the magnitude of vertical motion has remained about the same. The maximum is located near the B-C grid mesh region, which seems to be adversely affecting it. The omega contours are visibly flattened along the edge of the mesh area, and six hours afterward this particular maximum was barely discernable.

The southernmost maximum is associated with the line of convection and will not be discussed. The northwestern maximum is short-lived and also will not be discussed. The remaining maximum is located just off Cape Hatteras at F18. It shows a slight upshear tilt, and is quite distinct from the original maximum, especially at 400 mb. Judging by its future track, this maximum first appeared as the tiny closed contour contour of constant omega at 700 mb off Wilmington, NC, at F12. Through F24 and F30, this area of upward motion expands in horizontal scale while moving northeastward. At F24, two maxima are present at 700 mb, while only one maximum is present at 400 mb. The time interval between grids (six hours) is too large to determine temporal continuity between these updrafts, and it seems that this updraft underwent variations on a time scale of six hours or less, while maintaining its overall identity.

Plots of lower and mid-level relative humidity are shown in Fig. 4.20. The 950 mb air is initially saturated over a large area offshore, but the area of saturation shrinks over six hours as the air is heated from below in the absence of sufficient compensating latent heat fluxes. At 800 mb, a fish-shaped region of near-saturation extends in a northeast-southwest direction. With the vertical motion present at that time (Fig. 4.18), this air soon

becomes saturated. In six hours, a moderately-sized area of saturation has developed offshore. Also at six hours, saturation has occurred at 650 mb along a similar banana-shaped tongue.

The F06 vertical motion pattern (Fig. 4.18) closely matches the relative humidity pattern. While a remnant of the original north-south vertical motion region remains, most of the vertical motion is concentrated within the region of saturation. This is still the case at F12, although the saturated air now extends farther to the southeast, beyond the vertical motion maximum.

At later times, most of the region has reached saturation. At F18, all four vertical motion maxima identified above are within regions saturated at both 800 mb and 650 mb. Because upward vertical motion is present even outside of the maxima, the areas of saturation continue to increase in extent.

The spatial relationship between the small-scale cyclone and the vertical motion field is explored in Fig. 4.21, which overlays selected contours of 850 mb relative vorticity and 700 mb vertical velocity (compare with Fig. 4.2 and Fig. 4.18). It is apparent that the small-scale cyclone comes under the influence of two separate vertical motion maxima during its lifetime. Between F06 and F18, the first updraft develops offshore and moves northeast. As a consequence, the vorticity increases beneath it, with the first closed contour developing at F12. There is an apparent drift of the low-level vorticity relative to the updraft, in the direction to be expected from thermal wind considerations.

The drift places the small-scale cyclone in position to be intensified by the second updraft, which develops to the south of the small-scale cyclone between F12 and F18. The second updraft, like the first, follows a course to the right of the small-scale cyclone, passing over it at F24. The surprising conclusion to be drawn from this figure is that not only was the small-scale cyclone not a modal structure, the lack of any semblance of a coherent phase relationship implies that the vertical motion was not being directly driven by the small-scale cyclone. Rather, it appears that the NGM small-scale cyclone was

essentially the integrated result of a series of updrafts forming and propagating over the same low-level air.

Section 4.6: Summary

The forecast run of the Nested Grid Model initialized at 19/00 included the development of an offshore small-scale cyclone which shared many of the features of the observed small-scale cyclone. As in the real atmosphere, the NGM small-scale cyclone was not directly associated with an upper level trough and was warm core with positive relative vorticity below 600 mb. The NGM small-scale cyclone developed later and was broader and weaker than the actual small-scale cyclone, but these errors may be attributed to the initialization and grid resolution of the NGM.

Using a potential vorticity inversion technique similar to that of Davis (1990), we determined that upper-level and large-scale potential vorticity anomalies did not contribute to the low-level vorticity of the NGM small-scale cyclone. Rather, the spinup was due entirely to potential vorticity anomalies at low and mid-levels which were produced diabatically in regions of localized moist ascent.

Two separate small-scale vertical motion maxima were found to contribute successively to the generation of low-level potential vorticity, and the first updraft was well-developed six hours before a significant vorticity or potential vorticity perturbation was present at low levels. These facts strongly suggest that the low-level vorticity played a passive role in the dynamics of the small-scale updrafts and spinup of the small-scale cyclone. In Chapter Five, we shall investigate a variety of hypotheses to explain the development of the localized updrafts in the NGM, and then consider whether the NGM updrafts and the actual small-scale cyclone were formed by similar mechanisms.

CHAPTER FIVE

THE GENERATING MECHANISM OF THE SMALL-SCALE CYCLONE: HYPOTHESIS TESTING

Section 5.1: Ordinary Quasi-Geostrophic Forcing

In this chapter, we will investigate a hierarchy of hypotheses to attempt to explain the formation and propagation of the small-scale cyclone described in the preceding two chapters. We will concentrate our attention on the small-scale cyclone appearing in the NGM forecast, because the dynamical causes of the forecasted small-scale cyclone are in principle perfectly knowable. Diagnosis of the real small-scale cyclone is made difficult by incomplete upper air data coverage and errors in observing systems, and our ability to explain the small-scale cyclone depends upon our ability to distinguish between viable mechanisms with the available data. Once the dynamics of the NGM small-scale cyclone have been satisfactorily explained, we shall examine the similarities and differences of the real small-scale cyclone from the perspective of the NGM dynamics.

The standard first hypothesis for large mesoscale or synoptic-scale vertical motion is that it is a secondary response to Lagrangian changes in the large-scale thermal wind. Although we do not expect this hypothesis to be appropriate in the case at hand, it is desirable to formally exclude this hypothesis. Also, the structure of the large-scale forcing will be relevant to later hypotheses of the cause of the vertical motion.

The quasi-geostrophic forcing of vertical motion may be expressed mathematically in a variety of ways. One of the most physically illuminating is the Q-vector approach (Hoskins and Pedder 1980), which has the advantages of having the forcing term calculable from data at a single level, and of suggesting the form of low-level irrotational

flow. The quasi-geostrophic omega equation in pressure coordinates on an f-plane may be written in Q-vector form as

$$f^2 \frac{\partial^2 \omega}{\partial p^2} + \bar{\sigma} \nabla^2 \omega = -2 \nabla \cdot \boldsymbol{Q} \quad , \tag{5.1}$$

where the components of the Q-vector $\boldsymbol{Q}$ (not to be confused with potential vorticity Q) are defined as

$$Q_x = -\overline{\frac{\alpha}{\theta}\left(\frac{\partial v_g}{\partial y}\frac{\partial \theta}{\partial x} + \frac{\partial v_g}{\partial x}\frac{\partial \theta}{\partial y} \right)} \tag{5.2a}$$

$$Q_y = -\overline{\frac{\alpha}{\theta}\left(\frac{\partial u_g}{\partial y}\frac{\partial \theta}{\partial x} + \frac{\partial u_g}{\partial x}\frac{\partial \theta}{\partial y} \right)} \tag{5.2b}$$

with

$$\bar{\sigma}(p) = -\overline{\frac{\alpha}{\theta}\frac{\partial \theta}{\partial p}} \quad , \tag{5.3}$$

where overbars denote a horizontal spatial average, and where other symbols have their usual meaning.

The Q-vector field at various levels for the forecast period are shown in Figs. 5.1-5.3. The field is dominated by the near cutoff at upper levels moving into the southeast. For a simple cutoff cyclone with isotherms parallel to geopotential height contours, the Q-vectors tend to rotate around the cutoff to the left of the potential temperature gradient vector. Thus, the rotation is cyclonic at 500 mb, below the potential vorticity anomaly, and anticyclonic at 300 mb, in the stratosphere above the potential vorticity anomaly.

Because the cutoff is moving southeastward relative to the low-level flow, there is also a southeastward contribution to the Q-vectors in the neighborhood of the cutoff below the potential vorticity anomaly. This is seen, for example, at 500 mb for F12 (Fig. 5.2b), where there is a net southeastward component of 3×10^{-12} m^2 s^{-1} kg^{-1} in the vicinity of the

cutoff. This produces a dipole in forcing, with upward forcing in the upper troposphere to the southeast of the cutoff and downward forcing to the northwest of the cutoff.

Outside of the vicinity of the cutoff, the Q-vectors have relatively small magnitudes. Offshore, at 700 mb and 900 mb, the Q-vectors generally have magnitudes of less than 2×10^{-13} m^2 s^{-1} kg^{-1}. At 300 mb and 500 mb, some convergence is seen offshore, along a north-south line that roughly corresponds to the broad band of vorticity seen in Fig. 4.2a. After F06, however, the Q-vector convergence aloft becomes much weaker.

To obtain the quasi-geostrophic vertical motion field for the NGM forecasts, we have inverted (5.1) using the boundary conditions of zero vertical motion at 1000 mb and 100 mb and actual NGM vertical motion at the sides of the domain. Typical quasi-geostrophic vertical motion fields are shown in Figs. 5.4-5.5. At F06, in addition to the small-scale cyclone offshore, the actual NGM vertical motion field (Figs. 5.4b and 5.4d) is dominated by what appear to be mesoscale gravity waves over the lower Mississippi River valley. Broadly, vertical motion is upward east of the Mississippi and downward west of the Mississippi. The quasi-geostrophic vertical motion contains neither the gravity waves nor the small-scale cyclone updraft, but does recover the broad upward-downward dipole. The lack of gravity waves is a natural consequence of the use of quasi-geostrophic equations to diagnose vertical motion. The lack of a vertical motion signature over the small-scale cyclone offshore contradicts the hypothesis that the small-scale cyclone is a simple response to adiabatic quasi-geostrophic forcing.

Even the large-scale quasi-geostrophic vertical motion shows large differences with the actual vertical motion field. The differences are larger at 400 mb, and are more easily seen at F24 (Fig. 5.5), after the mesoscale gravity waves have propagated away or dissipated. At 400 mb, the vertical motion dipole is overestimated from the quasi-geostrophic calculation by a factor of four, although the position estimate is correct. Our purpose is not to investigate the shortcomings of the quasi-geostrophic approach to diagnosing vertical motion on the primary cyclone scale, but we suggest that a major

contributing factor to this error is the excess of geostrophic vorticity over actual vorticity about the cutoff cyclone at upper levels.

Also at F24, the vertical motion maxima offshore do not appear as maxima in the quasi-geostrophic vertical motion field. Indeed, as at F06, there is a virtually flat quasi-geostrophic vertical motion field offshore, rather than the clearly defined maxima of the actual vertical motion field. In contrast to the quantitative difference near the cutoff, this is a qualitative difference which indicates a failure of the initial hypothesis.

Section 5.2: The Response of a Variably-Stratified Environment to Large-Scale Forcing

a) Statement of hypothesis

A variety of alternative hypotheses are available to account for the vertical motion maxima associated with the small-scale cyclone. To be considered viable, the hypotheses must incorporate an explanation of why the vertical motion was localized rather than wavelike. Throughout the forecast run, there was no downward vertical motion maxima of similar scale and amplitude to the upward motion maxima. Even areas of weak downward motion in the vicinity of the updrafts were rare.

One such hypothesis may be termed the "reduced effective stratification" hypothesis. Briefly, it states that the response to large-scale forcing is altered by the presence of water vapor, which provides a heat input when a saturated volume of air undergoes ascent. The direct result is that to bring about a given amount of cooling through upward motion, a greater amount of upward motion is needed in the presence of latent heat release. This effect is best thought of not as an additional additional energy input into the system, but rather an increased amplitude of the response required to produce a

change in geostrophic vorticity. This hypothesis has been successfully applied to synoptic-scale weather systems by Smagorinsky (1956), Aubert (1957), and Danard(1964).

b) Theoretical development of hypothesis

The thermodynamic equation may be written as

$$\frac{\partial\theta}{\partial t} + u\frac{\partial\theta}{\partial x} + v\frac{\partial\theta}{\partial y} + \omega\frac{\partial\theta}{\partial p} = H \quad . \tag{5.5}$$

The standard quasi-geostrophic assumptions involve replacing the horizontally advecting winds with the geostrophic wind, and replacing the static stability term by a suitable horizontal mean:

$$\frac{\partial\theta}{\partial t} + u_g\frac{\partial\theta}{\partial x} + v_g\frac{\partial\theta}{\partial y} + \omega\frac{\partial\bar{\theta}}{\partial p} = H \quad . \tag{5.6}$$

We wish to write the heating term H in a form which applies to latent heat release under conditions of stable moist ascent. To do this, we note, following Emanuel *et al.* (1987), that in regions of saturation, the saturated equivalent potential temperature θ_e^* is conserved:

$$\frac{\partial\theta_e^*}{\partial t} + u\frac{\partial\theta_e^*}{\partial x} + v\frac{\partial\theta_e^*}{\partial y} + \omega\frac{\partial\theta_e^*}{\partial p} = 0 \quad . \tag{5.7}$$

Since θ and θ_e^* are both state variables, we may write

$$\delta\theta = \left(\frac{\partial\theta}{\partial\theta_e^*}\right)_p \delta\theta_e^* + \left(\frac{\partial\theta}{\partial p}\right)_{\theta_e^*} \delta p \quad . \tag{5.8}$$

Using the result (Emanuel *et al.* 1987) that

$$\left(\frac{\partial(ln\ \theta)}{\partial(ln\ \theta_e^*)}\right)_p = \frac{\Gamma_m}{\Gamma_d} \quad , \tag{5.9}$$

where $\Gamma_m = \left(\frac{\partial T}{\partial z}\right)_{\theta_e^*}$ and $\Gamma_d = \left(\frac{\partial T}{\partial z}\right)_{\theta}$, we may write (5.7) as

$$\frac{\partial \theta}{\partial t} + u\frac{\partial \theta}{\partial x} + v\frac{\partial \theta}{\partial y} + \omega\frac{\theta}{\theta_e^*}\frac{\Gamma_m}{\Gamma_d}\frac{\partial \theta_e^*}{\partial p} = 0 \quad . \tag{5.10}$$

Comparison of (5.5) and (5.10) shows that in saturated ascent, (5.5) may be written as

$$\frac{\partial \theta}{\partial t} + u\frac{\partial \theta}{\partial x} + v\frac{\partial \theta}{\partial y} + \omega\frac{\partial \theta}{\partial p} = \left[\omega\frac{\partial \theta}{\partial p} - \omega\frac{\theta}{\theta_e^*}\frac{\Gamma_m}{\Gamma_d}\frac{\partial \theta_e^*}{\partial p}\right] \quad . \tag{5.11}$$

Bringing the heating term to the left hand side of the equation, the source of the "reduced effective stratification" terminology becomes clear:

$$\frac{\partial \theta}{\partial t} + u\frac{\partial \theta}{\partial x} + v\frac{\partial \theta}{\partial y} - \omega\tilde{S} = 0 \quad , \tag{5.12a}$$

where $$\tilde{S} = -\frac{\partial \theta}{\partial p} \quad , \qquad \text{unsaturated,} \tag{5.12b}$$

and $$\tilde{S} = -\frac{\theta}{\theta_e^*}\frac{\Gamma_m}{\Gamma_d}\frac{\partial \theta_e^*}{\partial p} \quad , \qquad \text{saturated.} \tag{5.12c}$$

A conceptually simpler way of expressing the same concept is to consider that the $\omega\tilde{S}$ term is simply measuring the local change in potential temperature caused by vertical transport of air. Thus, if we define $\theta_{lift}(p,\theta,q,p_o)$ as the potential temperature an air parcel at a particular pressure, potential temperature, and water vapor mixing ratio would have if brought adiabatically (or pseudoadiabatically) to a given pressure level p_o, (5.12) may be written, for the case of dry or moist adiabatic motion, as

$$\frac{\partial \theta}{\partial t} + u\frac{\partial \theta}{\partial x} + v\frac{\partial \theta}{\partial y} + \omega\left(\frac{\partial \theta_{lift}}{\partial p}\right)\Big|_{p=p_o} = 0 \quad . \tag{5.13}$$

The quasi-geostrophic approximation involves replacing the stratification with its mean value (5.6). If we are to include latent heat release, we will be effectively using two separate mean values of stratification. Since the actual horizontal variations in stratification will be dominated by the presence or absence of latent heat release, the inclusion of latent

heating is a much greater modification to the equations than the inclusion of other horizontal stratification variations. So we may as well retain the full effective stratification (5.12b-5.12c) rather than replacing it by two mean values which are conditional on the presence of saturation. Our modified quasi-geostrophic thermodynamic equation therefore becomes

$$\frac{\partial \theta}{\partial t} + u_g \frac{\partial \theta}{\partial x} + v_g \frac{\partial \theta}{\partial y} - \omega \tilde{s} = 0 \quad . \tag{5.14}$$

Equation (5.14) is not a valid component of the quasi-geostrophic system of equations. However, we are not presently interested in obtaining a complete dynamically and energetically consistent set of equations. Our objective is to attempt to determine in what way the flow response to forcing is modified by small-scale changes in effective stratification. While it is a bit presumptious to expect that an omega equation derived using (5.14) will give quantitatively correct answers for our small-scale cyclone case, we do expect that (5.14) will yield at least a qualitatively correct idea of how the addition of latent heating in a stably-stratified environment modifies the local response to the large-scale dynamics.

The quasi-geostrophic vorticity equation is not directly modified by the presence of latent heating. With the usual small Rossby number assumptions, and for mathematical simplicity restricting ourselves to an f-plane, the vorticity equation is:

$$\frac{\partial \zeta_g}{\partial t} + (\boldsymbol{u}_g \cdot \nabla)\zeta_g = f \frac{\partial \omega}{\partial p} \quad . \tag{5.15}$$

Equations (5.14)-(5.15) are coupled by the geostrophic relation

$$\zeta_g = \frac{1}{f} \nabla^2 \Phi \tag{5.16}$$

and by the hydrostatic equation for an ideal gas, neglecting the effect of moisture on density,

$$\frac{\partial \Phi}{\partial p} = -\alpha = -\frac{R\theta}{p}\left(\frac{p}{p_o}\right)^{\kappa} \quad , \tag{5.17}$$

so that (5.14) may be written

$$\frac{\partial}{\partial t}\left(\frac{\partial \Phi}{\partial p}\right) + (\boldsymbol{u}_g \cdot \nabla)\left(\frac{\partial \Phi}{\partial p}\right) + \tilde{\sigma}\,\omega = 0 \quad , \tag{5.18}$$

where

$$\tilde{\sigma} = \frac{\alpha}{\theta}\tilde{S} \quad . \tag{5.19}$$

Equations (5.15) and (5.18) may be combined to yield a single diagnostic equation for ω:

$$\boxed{f^2 \frac{\partial^2 \omega}{\partial p^2} + \nabla^2(\omega\,\tilde{\sigma}) = -2\,(\nabla \cdot \boldsymbol{Q})} \quad , \tag{5.20}$$

where $\boldsymbol{Q}$ is the quasi-geostrophic Q-vector defined in (5.2). A similar equation, with the forcing term written differently, was derived by Danard (1966). Equation (5.20) differs from the standard omega equation only in the definition (5.19) of the stratification parameter. In ordinary quasi-geostrophic theory, the stratification is only a function of pressure, so that σ may be moved outside the Laplacian operator and (5.1) results.

Our modified omega equation (5.20) may be regarded as diagnosing the linear modified local response to large-scale dynamics. In a physical sense, it will be valid for stable ascent as long as the vorticity and divergence variations produced by the local variations in stratification do not substantially alter the geostrophic vorticity field, either through horizontal advection or by geostrophic adjustment. The extent to which this occurs will depend on the strength and duration of any localized updrafts which develop. This makes (5.20) most applicable when a region of the atmosphere has just become saturated, before vorticity has had a chance to be modified by stretching and before the divergent flow has altered the temperature field. These conditions are best satisfied in the 19/00 NGM run over the ocean for the first twelve to eighteen hours, because the model was initialized unsaturated everywhere over the Atlantic, the small-scale vorticity variations were weak, and the temperature gradients were small.

For a given vertical depth scale P for variations of the forcing and the depth of the fluid, (5.1) has a single characteristic length scale, the Rossby radius of deformation, which in our notation is

$$L_R = \frac{P\,\bar{\sigma}^{1/2}}{f} \quad . \tag{5.21}$$

This length scale arises from a balance of the horizontal and vertical second derivative terms. Equation (5.20) has a second length scale, the horizontal scale of variation of stratification, which we shall call L_S. In order to gain an understanding of how the vertical motion depends upon the structure of the stratification variations, we now consider two asymptotic limits. When $L_S >> L_R$, it is readily seen that at lowest order, (5.20) reduces to (5.1) with the stratification parameter replaced by its local value:

$$f^2 \frac{\partial^2 \omega}{\partial p^2} + \sigma \nabla^2(\omega) = -2\,(\nabla \cdot Q) \quad . \tag{5.22}$$

For uniform forcing and zero omega at the upper and lower boundaries (p_T and p_B), (5.22) has the solution

$$\boxed{\omega = -\frac{(\nabla \cdot Q)}{f^2}(p - p_B)\,(p - p_T)} \quad . \tag{5.23}$$

The solution of more immediate interest occurs when the scale of variation of stratification is smaller than the Rossby radius. Setting $\varepsilon = L_S/L_R << 1$ and non-dimensionalizing, (5.20) becomes

$$\varepsilon \frac{\partial^2 \omega}{\partial p^2} + \nabla^2(\sigma\omega) = -2\,\varepsilon\,(\nabla \cdot Q) \quad . \tag{5.24}$$

Expanding ω in powers of ε ($\omega = \omega_0 + \varepsilon\omega_1 + \varepsilon^2\omega_2 + ...$), the lowest order equation is

$$\nabla^2(\sigma\omega_0) = 0 \quad . \tag{5.25}$$

If we assume a simple form for the lateral boundary conditions on ω, such as periodic boundary conditions, the solution to (5.25) is

$$\omega_0 = \frac{F(p)}{\sigma} \quad , \tag{5.26}$$

where $F(p)$ is an unknown function of pressure.

To recover $F(p)$, we need to consider the first order equation:

$$\frac{\partial^2 (F(p)/\sigma)}{\partial p^2} + \nabla^2(\sigma\omega_1) = -2(\nabla \cdot Q) \quad . \tag{5.27}$$

In order to simplify the equation, we shall assume $\sigma = \sigma(x,y)$ is not a function of pressure. Numerical experiments indicate that allowing σ to vary with pressure does not qualitatively affect the nature of the response. Rearranging (5.27) gives

$$\nabla^2(\sigma\omega_1) = -2(\nabla \cdot Q) - \frac{F''(p)}{\sigma} \quad . \tag{5.28}$$

Integrating over the domain in x and y and applying periodic horizontal boundary conditions on $\sigma\omega$, we obtain

$$\iint \{ -2(\nabla \cdot Q) \}\, dA = \iint \frac{F''(p)}{\sigma}\, dA \quad . \tag{5.29}$$

Because $F''(p)$ is not a function of x or y, it may be taken outside the integral. Defining the averaging operator

$$[\,*\,] = \iint * \, dA \quad , \tag{5.30}$$

we arrive at a simple equation for $F(p)$:

$$F(p) = \sigma\omega_0 = \frac{1}{2}\frac{[-2(\nabla \cdot Q)]}{\left[\frac{1}{\sigma}\right]}(p - p_B)(p - p_T) \quad . \tag{5.31}$$

After dimensionalizing and placing into a form analogous to (5.23),

$$\boxed{\omega = - \frac{\sigma - 1}{[\sigma - 1]} \frac{[\nabla \cdot Q]}{f^2} (p - p_B)(p - p_T)} \quad . \qquad (5.32)$$

Thus, only the smaller-scale stratification variations influence the vertical motion response to quasi-geostrophic forcing. From (5.23), the response depends directly on the local forcing, and is independent of the stratification when the stratification only varies on large scales. By contrast, when the stratification varies on small scales (5.32), the vertical motion is insensitive to small variations in the forcing. Rather, it depends directly on the inverse of the local value of the effective stratification.

c) Computation of vertical motion for prototypical test cases

We test the validity of the above asymptotic results by means of numerical inversion of the modified omega equation for particular simple distributions of forcing and stability. From performing the inversion on a full range of length scales, we also gain an understanding of the behavior of the vertical motion at intermediate scales, when neither asymptotic result is valid. To simplify the calculations and to facilitate understanding, we shall operate on the two-dimensional version of (5.20), which is obtained by replacing the Laplacian operator by a second derivative with respect to x.

We have chosen parameters of the inversion as follows. Our vertical domain ranges from 1000 mb to 200 mb, discretized into nine levels at 100 mb increments (seven levels in the interior, two on upper and lower boundaries where $\omega = 0$). We choose f - 1×10^{-4} sec^{-1}. We wish to have L_R = 1000 km, and by (5.21) this constrains the domain-mean stratification σ_o to be 1.56×10^{-6} m^4 s^2 kg^{-2}. If the stratification is constant at that value, a vertical velocity at 600 mb of -1 Pa s^{-1} would be obtained from a constant forcing of ($\nabla \cdot Q = - 6.25 \times 10^{-18}$ m^2 s^{-1} kg^{-1}), and we will choose this value for our constant

basic forcing. Since (5.20) is symmetric in p, and we will be doing nothing to break the symmetry, it will be sufficient for us to examine ω at only one level (we choose 600 mb).

Our horizontal domain will consist of forty-one evenly-spaced grid points, two on the lateral boundaries and thirty-nine in the interior. Designating the total domain length by L_D, we will specify a particular interior distribution of σ as a function of the fractional distance x/L_D. Holding this distribution fixed, we then allow L_D to vary over a range of values from $L_D >> L_R$ to $L_D << L_R$, to explore the dependence of the solutions on the length scale of the stratification distribution. Specifically, we shall perform calculations on seven domain length scales A-G, defined as A: $L_D = 8L_R$; B: $L_D = 4L_R$; C: $L_D = 2L_R$; D: $L_D = L_R$; E: $2L_D = L_R$; F: $4L_D = L_R$; G: $8L_D = L_R$.

For our first calculation, we choose a cosine function for the stability distribution:

$$\sigma = \sigma_o \left\{ 1 + \frac{1}{2} \cos(2\pi x/L_D) \right\} \tag{5.33}$$

We choose the constant basic forcing derived above, and we specify periodic boundary conditions on ω. Technically, (5.20) requires periodic boundary conditions on $(\sigma\omega)$, but we have already guaranteed periodicity in σ by (5.33).

The results of the inversion are shown in Fig. 5.6, with ω given by the solid curves. At long length scales, curve A shows that the vertical velocity is very nearly independent of the local stratification, as expected from (5.23). As the length scale of the stratification variations becomes narrower, the influence of the variable stratification becomes more and more prominent, with the largest vertical velocity (negative ω) occurring at $x/L_D = 0.5$, where the stratification is weakest by (5.33). At the smallest length scales, the graphs of ω appear to be approaching an asymptotic limit.

The nature of this asymptotic limit may be investigated by means of the dashed curves, which are plots of $\omega \frac{[\sigma - 1]}{\sigma - 1}$. At large length scales (curve A), where ω is nearly constant, the curve is effectively a normalized plot of the reciprocal local stability. At

smaller length scales (curve G), however, the dashed curves approach a constant value of 1 Pa s^{-1}, as expected from the short-scale limit (5.32). Thus, both theoretical asymptotic limits are confirmed.

We note that, because of the dependence of ω on the inverse stratification at the short length scale limit, the ω curve G describes an inverse cosine wave rather than a cosine wave. As a consequence, the region of enhanced upward motion is narrower than the region of inhibited upward motion, and the largest deviation from the mean vertical motion occurs within the reduced stratification region.

The results of this first calculation were interesting, but the chosen stratification pattern does not resemble the stratification pattern which would be produced by a localized region of saturation. Such a region would produce a zero-order discontinuity in the stratification. This is not a problem for the solution of (5.20), as long as the product $(\sigma\omega)$ remains continuous. This implies that a discontinuity in ω should develop which exactly cancels the stratification discontinuity. Such a discontinity appears naturally in the short length scale asymptotic solution (5.32), in which ω is proportional to the inverse stratification and the product $(\sigma\omega)$ is constant.

To investigate this behavior, we retain the same forcing and boundary conditions as before, but specify an upside-down top hat profile for the stratification:

$$\sigma = \frac{1}{4}\sigma_o \quad , \frac{3}{8} < \frac{x}{L_D} < \frac{5}{8}$$

$$\sigma = \frac{5}{4}\sigma_o \quad , \text{ otherwise.} \tag{5.34}$$

This stratification also satisfies the periodic boundary conditions.

The inversion results (Fig. 5.7) are again consistent with both asymptotic limits. At short scales (curves G), the dashed line is again constant at -1 Pa s^{-1}, while the vertical velocity curve attains an upside-down top hat profile which mimics the negative inverse of the stratification. As scales increase, the vertical motion itself tends toward the constant

value of -1 Pa s^{-1}. But even at the largest scales (solid curve A), there is significant variation of ω from a straight line in the vicinity of the stratification discontinuity. This is because the discontinuity has a length scale which depends on the grid spacing and is much smaller than the scale of the domain. The length scale over which the vertical velocity relaxes back to its constant asymptotic value is given by the Rossby radius L_R. Despite the discontinuity in stratification, the product ($\sigma\omega$) is continuous for all length scales, as expected. This can be seen by the dashed curves, which are smoothly varying even across the discontinuity.

We note a few points concerning these calculations. First, the vertical mass flux is equal in both the large and small length scale asymptotic limits. For small-scale stability variations, the additional upward motion in the weakly stratified region is compensated by a reduced vertical motion in the more strongly stratified region. However, at no parameter ranges is there any induced subsidence, in the sense that the local ω is positive. Thus, in the real atmosphere, we expect induced upward motion to be enhanced in saturated regions and suppressed in unsaturated regions. And in the absence of a strong feedback to the large-scale dynamics, the region of saturation should continue to expand with time.

The fact that ω at short length scales is independent of the local magnitude of the forcing, perhaps surprising at first sight, is actually a statement that in the quasi-geostrophic omega equation, short length scale variations of the forcing are not important, regardless of the stratification. To show this, we consider a variation of the upside-down top hat stratification configuration, for which the forcing within the domain is zero but the vertical motion is induced to be upward throughout the domain as a result of a specified non-zero ω on the lateral boundaries. We choose a negative half-sine profile for ω on each boundary, with an amplitude of 1 Pa s^{-1} at $x = 0$ and an amplitude of 0.5 Pa s^{-1} at $x = L_D$. This corresponds physically to localized forcing at some $x < 0$, a configuration which is similar to that found for the forcing distribution in the small-scale cyclone case (Figs. 5.1-5.5). We take the same stratification distribution (5.34) as before.

The results (Fig. 5.8) are similar to the earlier case with constant forcing (Fig. 5.7). At the shortest length scales, the dashed curve G is nearly a straight line connecting the fixed points at the two lateral boundaries, so that the solid ω curve indicates five times the upward motion inside the saturated region compared to outside the saturated region. As the length scale becomes larger, two effects combine to produce decreasing vertical motion in the saturated region. First, the solution is tending toward the large length scale limit, so that the jump in vertical velocity is decreasing. Second, the increasing domain size is tending to confine the vertical motion field to with one Rossby radius of the edges of the domain, with little or no vertical motion in the interior.

d) Induced vertical motion in the NGM

Having considered several prototypical cases, we are now prepared to calculate the response to forcing in the NGM case. We shall allow the stratification to vary according to (5.12b-5.12c), depending on whether the air is saturated, *i.e.*, at or above 95% relative humidity (see Section 4.2). We will also permit the stratification to vary within saturated and unsaturated regions according to the actual NGM values. We also include the variation of f with latitude, and as before use the actual ω along the boundaries as a boundary condition. The calculated vertical motion field was found not to be sensitive to whether the first guess ω field was taken to be the actual NGM ω field or was set to zero.

A sample stratification field, for F06 at 700 mb, is shown in Fig. 5.9a. The boundaries between saturated and unsaturated regions show up as discontinuities in the stratification field over portions of the Atlantic, North Carolina, and the west-central Appalachians. Parts of the saturated regions are seen to possess negative apparent stability. From the theoretical calculations in Section 5.2b, as the stability goes to zero the vertical motion should become infinite. To avoid this situation and guarantee that (5.20) remains elliptical, we shall arbitrarily set the effective stratification in weakly or negatively stratified

areas to a small value consistent with an effective lapse rate of potential temperature of 0.2 K per 50 mb.

It is not directly obvious whether the NGM actually sees these areas as being negatively stable. As discussed in Section 4.2, latent heat is released in updrafts at less than 100% relative humidity, which complicates assessments of vertical stability. Also, the vertical interpolation from sigma surfaces to fixed pressure surfaces, which was apparently a linear interpolation, introduces vertical variations in θ_e in an initially neutrally-stratified column. Certainly, though, the stratification in many regions is quite close to neutral. We will come back to this point in Section 5.3.

A second consideration for the sake of the inversion of the omega equation (5.20) is the small scale of the rapid stability variations. The grid point structure of the NGM is apparent from the shape of the stratification contours in Fig. 5.9a. From the preceding discussion, we anticipate that this will lead to similarly small-scale variations in ω. Since such grid-scale motion variations will not occur in the NGM because of horizontal smoothing, we shall filter the stratification field to remove the smallest-scale variations. This allows comparison with the actual NGM ω field, and also permits much more rapid numerical convergence for the inversion calculation. A final advantage to filtering is that it prevents the contouring program from crashing, which it would do about 30% of the time otherwise.

The sample stratification field, after filtering, is shown in Fig. 5.9b. The gradients are still localized around the saturated regions, but they are spread out over a broad area and the shapes are smoother. The relatively small saturated region in North Carolina suffers a large decrease in amplitude as a result of the smoothing; other amplitude variations are much less substantial.

The F06 inversion (Fig. 5.10a-b) represents a considerable improvement over the constant-stratification inversion (Fig. 5.4b, Fig. 5.4d) in its ability to reproduce the vertical motion field. In particular, the vertical motion maximum offshore resembles the actual

NGM vertical motion maximum in its size, shape, and amplitude. Farther inland, the band of vertical motion along the western side of the Appalachians appears in both the inverted and actual NGM fields, although the details of position and amplitude vary. The constant stratification inversion did not include this feature. The third reduced stability region produced a small vertical motion maximum over North Carolina that was not present in the actual NGM vertical motion field.

At later times, the agreement between the modified quasi-geostrophic vertical motion and the actual NGM vertical motion becomes progressively worse. At F12 (not shown), the offshore vertical motion maximum becomes split, unlike the actual maximum. Also, a pronounced but small-scale low-level maximum appears east of South Carolina which does not exist in the actual field (although, interestingly, it is directly upstream of the F18 vertical motion maximum). At F24 (Fig. 5.10c-d), the locations of the actual vertical motion maxima are readily discerned in the inverted field, but not in the manner intended: instead of vertical motion maxima, the inversion produces vertical motion dipoles oriented approximately across the shear. This is a clear breakdown of the quasi-geostrophic approximations, with the tendency for an increasing dipole amplitude with time being an indication that nonlinear effects of the small-scale updrafts are the cause of the breakdown. Even the first updraft has a dipole structure aloft in the quasi-geostrophic ω field at F18 (not shown).

For the moment putting aside the errors caused by the small scale and large amplitude of the stratification perturbations, the induced field is inconsistent with the problem as we have set it up, because downward motion is occurring within the reduced effective stratification regions. The cause of reduced stratification within these regions is of course latent heat release, which under circumstances applicable here requires upward motion. It is not implausible that if the stratification in regions of downward motion were required to take on its dry value, a locally different ω response would result, with a possible larger area of upward motion as a consequence.

The incorporation of this idea into the inversion of quasi-geostrophic forcing requires an iterative approach. After inverting the omega equation (5.20) with the actual effective stratification, one may replace the stratification in regions of descent with their dry stratification values and re-invert the omega equation. The process can then be repeated until no descent is occurring within a reduced stratification region. Depending on the details of the technique used, the result may be different, since more than one solution is possible. Alternatively, there may be no solution.

Another difficulty in this process is that in principle it would be necessary to re-filter the stability field after each iteration. To avoid complicating the problem more than is warranted, we carried out the experiment of an adjustable stratification using the unfiltered $\tilde{\sigma}$ field. Between one and four iterations were required before the ω field was consistent with the $\tilde{\sigma}$ field for F06 and F24. It was found that rather than changing the area covered by regions of upward and downward motion, the net effect of iteratively varying the stability was to produce weak descent rather than strong descent in the regions of vigorous descent in Fig. 5.10. Although this caused a decrease in the magnitudes of the errors of the quasi-geostrophic ω field, we do not regard this as a qualitative improvement.

Another location of discrepancy between the quasi-geostrophic and actual fields is over the southeast, in the vicinity of the digging, cutting-off trough. Both the inversion with constant stratification and the inversion with variable stratification grossly overestimate the magnitude of the ascent-descent couplet, and the magnitude of the error grows with time in the forecast. Again, we do not regard the variable stratification calculation as an improvement over the constant stratification calculation. The root cause of the discrepancy is the lack of geostrophic wind balance in the vicinity of the trough, owing to the large values of curvature vorticity there. At 350 mb at F24, for example, the maximum actual wind velocity around the base of the trough is about 40 m/s, while the maximum geostrophic wind velocity is nearly 90 m/s. This doubling of the wind by the geostrophic approximation may be expected to produce a quadrupling of the forcing over

that associated with the gradient wind. To the extent that more distant points are influenced by the forcing maximum at the base of the trough, a general overestimate of ω can be expected elsewhere as well.

Section 5.3: Sources of Error in the Quasi-Geostrophic and Geostrophic Momentum Omega Equations

a) Overview of the construction of the omega equations

An advantage to diagnosing model data as opposed to the actual evolution of the atmosphere is that one may accurately calculate those terms which have been neglected by the diagnoses. This can help determine, for example, whether the errors should be regarded as qualitative or quantitative, whether neglected terms are actually of similar or larger magnitude than retained terms, and whether the next higher level of approximation should be expected to yield qualitative agreement.

The basic premise of quasi-geostrophic diagnostics, whether with constant stratification or horizontally and vertically varying stratification, is that both the vorticity and the local rate of change of vorticity can be regarded as equal to the geostrophic vorticity and local rate of change of geostrophic vorticity. This allows the vorticity equation and the thermodynamic equation to be combined to eliminate the time derivatives, and with other appropriate approximations yields a diagnostic equation for ω.

The vorticity equation, neglecting friction, may be written in isobaric coordinates as:

$$\frac{\partial \zeta}{\partial t} = -(\boldsymbol{u} \cdot \nabla)\zeta - (\boldsymbol{u} \cdot \nabla)f - \omega\frac{\partial \zeta}{\partial p} + (f + \zeta)\frac{\partial \omega}{\partial p} + \frac{\partial \omega}{\partial y}\frac{\partial u}{\partial p} - \frac{\partial \omega}{\partial x}\frac{\partial v}{\partial p} \quad , \qquad (5.35)$$

where the vector wind $\boldsymbol{u}$ is understood to be the horizontal wind. This equation is interpreted as saying, term by term, that the local rate of change of vorticity (we will use the term "vorticity" to refer to the vertical component of relative vorticity, ζ, and use "absolute vorticity" when we mean absolute vorticity) is equal to the horizontal advection of vorticity, the advection of planetary vorticity, the vertical advection of vorticity, the vortex tube stretching, and two terms constituting the tilting of vortex tubes from the horizontal to the vertical.

Under the quasi-geostrophic (QG) approximation, all advecting winds are replaced by their geostrophic values, the vorticity is assumed small compared to the Coriolis parameter, and the tilting term is neglected. The equation becomes

$$\frac{\partial \zeta_g}{\partial t} = -(\boldsymbol{u}_g \cdot \nabla)\zeta_g - (\boldsymbol{u}_g \cdot \nabla)f + f\frac{\partial \omega}{\partial p} \quad . \tag{5.36}$$

Under the geostrophic momentum (GM) approximation, the total wind is used for advection of momentum and other quantities. The geostrophic momentum vorticity equation may be written as

$$\frac{\partial \zeta_g}{\partial t} = -(\boldsymbol{u} \cdot \nabla)\zeta_g - (\boldsymbol{u} \cdot \nabla)f - \omega\frac{\partial \zeta_g}{\partial p} + \left[(f+\zeta)\frac{\partial \omega}{\partial p} + \frac{\partial u}{\partial x}\frac{\partial v_a}{\partial x} - \frac{\partial v}{\partial y}\frac{\partial u_a}{\partial y}\right] + \frac{\partial \omega}{\partial y}\frac{\partial u_g}{\partial p} - \frac{\partial \omega}{\partial x}\frac{\partial v_g}{\partial p}, \tag{5.37}$$

where the extra ageostrophic terms written as part of the stretching term arise as a result of cross products of derivatives of the total and geostrophic wind and should be order Rossby number smaller than the stretching of relative vorticity.

The form of the GM equations is much simpler when a transformation is made to semi-geostrophic coordinates. In transformed space, the equations are similar to the QG equations, with slight differences in the definitions of various quantities. It has become customary to do diagnostic calculations in semi-geostrophic space and transform the results back to physical space. However, the transformation to semi-geostrophic space cannot be performed if there is a region within the domain in which the absolute geostrophic vorticity

is negative. As it turns out, this is the case for the upper portions of the updraft of interest. Therefore we shall restrict ourselves to physical space. Incidentally, besides preventing the semi-geostrophic coordinate transformation, the presence of negative absolute geostrophic vorticity is an indication that the GM approximation might not describe the updraft adequately.

The thermodynamic equation undergoes comparatively little modification under the QG and GM approximations. Neglecting diffusion, radiation, and boundary transfer, and incorporating latent heating into the stability term, the thermodynamic equation, using the hydrostatic equation (5.17), can be written as:

$$\frac{\partial}{\partial t}\left(\frac{\partial \Phi}{\partial p}\right) = - (\boldsymbol{u} \cdot \nabla)\left(\frac{\partial \Phi}{\partial p}\right) - \tilde{\sigma}\omega \quad , \tag{5.38}$$

where $\tilde{\sigma}$ is defined by (5.19) and (5.12b-c). This is also the form taken by the GM thermodynamic equation. In its normal QG form, the equation becomes

$$\frac{\partial}{\partial t}\left(\frac{\partial \Phi}{\partial p}\right) = - (\boldsymbol{u_g} \cdot \nabla)\left(\frac{\partial \Phi}{\partial p}\right) - \bar{\sigma}\omega \quad . \tag{5.39}$$

Replacement of $\bar{\sigma}(p)$ by its effective local value $\tilde{\sigma}$ yields the variable stratification QG equation (5.18). We shall refer to the three terms in the thermodynamic equation as the local tendency term, the advection term, and the heating term. The heating term in (5.38) incorporates latent heating as well as adiabatic heating and cooling.

Equations (5.36) and (5.39), (5.36) and (5.18), or (5.37) and (5.38), may be combined to form an omega equation. From the horizontal Laplacian of (5.17), the vertical derivative of geostrophic vorticity is locally proportional to the horizontal Laplacian of the potential temperature field. To form a QG omega equation, a modified QG omega equation with variable static stability, or a GM omega equation, (5.36) or (5.37) are differentiated with respect to pressure and the horizontal Laplacian is taken of (5.39), (5.18), or (5.38). When the resulting equations are added, the time derivatives cancel. The terms involving ω

take the form of a three-dimensional Laplacian in the QG case (5.1), and a form similar to a three-dimensional Laplacian in the QG with variable stratification or GM cases. The remaining terms are regarded as forcing terms.

b) Description of omega equation error tables

The extent to which the approximations are valid may be assessed by comparing the magnitude of the terms retained to the magnitude of the terms dropped. Even if neglected terms are of comparable magnitude to terms retained, it is possible that the QG or GM omega equations would still give qualitatively correct results. So we will also obtain a "bottom-line" estimate of the omega equation errors by comparing the magnitudes of the derivatives with respect to pressure and time of the geostrophic vorticity calculated from the vorticity equation and from the thermodynamic equation. All units in the following tables are mks.

We plot the magnitudes of various terms in the equation in table form (*e. g.*, Table 5.1). At each point, we evaluate the three vorticity equations (5.36), (5.37), and (5.35), term by term on separate lines (in boldface type), with each term identified at the top of each column by its full form. For example, in the column for the horizontal advection of relative vorticity term, $-(\boldsymbol{u}\cdot\nabla)\zeta$, we list the value of $-(\boldsymbol{u}_g\cdot\nabla)\zeta_g$ on the QG line and the value of $-(\boldsymbol{u}\cdot\nabla)\zeta_g$ on the GM line. Since, for example, the vertical advection term is neglected in the QG approximation, that column is left blank on the QG line. On each line, the tendency term (to the left of the equals sign) will equal the sum of the terms to the right of the equals sign, with slight differences possible due to roundoff error. Below each vorticity equation line, we also list the values of the partial derivatives of each term with respect to pressure (in italics), for the sake of comparison with the Laplacian of the thermodynamic equation. Again, the term on the left hand side will equal the sum of the terms on the right hand side.

The first part of the second half of each table (*e. g.*, Table 5.1b) consists of various terms in the thermodynamic equation. At each point, we list on a single line (in boldface) the time tendencies of the partial derivative of geopotential with respect to pressure Φ_p at various levels of approximation, along with the terms they were calculated from. The first three numbers are the time tendencies evaluated from (5.39), (5.18), and (5.38), and the remaining four numbers are the geostrophic advection term (used in (5.39) and (5.18)), the full advection term (used in (5.38)), the mean stratification heating term (used in (5.39)), and the actual stratification heating term with latent heating included (used in (5.18) and (3.28)). Below each line (in italics), we list the values of the horizontal Laplacian of the terms in the thermodynamic equations.

The final part of each table is a listing of the differences between the tendency terms computed from the derivative with respect to pressure of the vorticity equation and the horizontal Laplacian of the thermodynamic equation, at various levels of approximation. The QG error term is the pressure derivative of (5.36) minus the Laplacian of (5.39), the QG with variable σ error term is the pressure derivative of (5.36) minus the Laplacian of (5.18), and the GM error term is the pressure derivative of (5.37) minus the Laplacian of (5.38). Each of the individual terms (such as the pressure derivative of (5.36)) may be found elsewhere in the tables. For a given approximation to be considered to be accurate, the error term should be smaller in magnitude than either of the individual time tendency terms.

By inspecting the various terms in the tables, additional information may be gleaned. For example, the various approximations to the stretching term in the vorticity equation contain information on the local magnitude of the relative vorticity. The full stretching term divided by the QG stretching term is simply the ratio of absolute vorticity to planetary vorticity. Similarly, in the thermodynamic equation section of the tables, the full stratification heating term divided by the average stratification heating term gives the ratio of the effective local stratification to the mean stratification. Also, because the average

stratification by definition does not vary horizontally, the magnitudes of the average stratification heating term at various points at a given level may be used to infer the relative magnitudes of ω at those points.

Although we are plotting data for only selected grid points, maps of the full fields have been examined at various levels to confirm that the selected points are representative of conditions near the centers of the updrafts.

c) Omega equation error analysis, second updraft

A set of five points about the second updraft at F24 has been selected to examine the magnitudes of terms in the thermodynamic and vorticity equations. We look at terms at three levels: 850 mb, 600 mb, and 350 mb. The values for 850 mb (Table 5.1) show only fair agreement with QG and GM assumptions. In the vorticity equation, the dominant terms tend to be the horizontal advection of vorticity and the stretching of planetary vorticity. A comparison of the GM and complete equations indicates that the advection of geostrophic vorticity is also large. However, a comparison of QG and GM advection terms in both the vorticity and thermodynamic equations shows that advections are dominated by the geostrophic wind. The implication is that there is considerable small-scale disagreement between the geostrophic and actual winds, resulting in large local differences in the vorticity patterns.

The heating term is reduced by an order of magnitude when latent heating is included. While this has a large effect on the time tendency of the vertical derivative of geostrophic vorticity, the net result is not necessarily an improvement in the agreement with the approximate vorticity equations. At two of the five points, the QG approximation with constant effective stratification actually has the closest agreement. At two of the others, GM does best, while the moist quasi-geostrophic equation is closest at the fifth. Thus, the preliminary indication is that GM does not offer an improvement in approximation over QG

for this phenomenon. Indeed, the largest term neglected from the QG vorticity equation, the advection of ageostrophic vorticity, is also neglected in the GM approximation.

At 600 mb (Table 5.2), the approximations tend to do no better. In the vorticity equations, the dominant terms are the horizontal advection of geostrophic vorticity, the horizontal advection of ageostrophic vorticity, the stretching of planetary vorticity, and the vertical advection of vorticity. The vertical advection term is partially included in the GM approximation, so we might expect the GM approximation to show an improvement at this level. Again, it appears that the small-scale pattern of vorticity is significantly different from the pattern of geostrophic vorticity.

In the thermodynamic equation, the atmosphere again appears to be nearly neutral to vertical moist ascent, with the latent heating producing an order of magnitude reduction in the effect of vertical motion on temperature. This time, the effect is prominent in the geostrophic vorticity tendency term as well, with the result that the largest discrepancy in the vorticity tendency terms is always with the dry QG approximation. The hoped-for improvement with GM doesn't materialize, though, as no systematic improvement in agreement between the thermodynamic and vorticity equations is found.

At 350 mb (Table 5.3), the situation is dramatically different. Compared to other levels, the geostrophic vorticity advection by the geostrophic or total wind is quite large, but it tends to be balanced by the advection of agostrophic vorticity, suggesting considerable small-scale structure in the thermal field. Meanwhile, the stretching (or, in this case, shrinking) of planetary vorticity is balanced by the shrinking of relative vorticity. Partially because of these cancellations, the largest contributors to the horizontal Lagrangian rate of change of vorticity in the complete equation are the vertical advection and tilting terms, which are completely neglected in the QG equation and poorly approximated in the GM equation. In view of the size of the neglected terms and the difference between geostrophic and actual vorticity, it is no surprising that the omega equation gives qualitatively incorrect results for ω.

Furthermore, note that the stretching term changes sign when the relative vorticity term is included at one of the five points. This indicates that the absolute vorticity is negative at that location. Negative absolute vorticity, as discussed later, is found over a large area on the northern side of the updraft at 350 mb. Thus, the model atmosphere at these levels is inertially unstable, and the future evolution of the upper portion of the updraft should be qualitatively different from that predicted by either QG or GM.

In the thermodynamic equation, incorporation of latent heating induces a change in sign of the heating term. This implies that the model atmosphere is also absolutely unstable to moist vertical displacements. We therefore have a situation in which the normal effects of vertical motion at this level are reversed: instead of vertical motion producing a decrease in relative vorticity through vortex tube shrinking, it produces an increase in relative vorticity; instead of a maximum in vertical motion producing a decrease of geostrophic vorticity with pressure, it produces an increase. The QG and GM omega equations are wholly inappropriate to describe the dynamics of this phenomenon, which seems to more closely resemble a very large cumulus cloud than a cyclone wave.

Although the effect of reduced stratification within the omega equation should in isolation have been to suggest an updraft in the saturated region, the nonlinear consequences of the strong localized updraft within a region of unstable vertical stratification (and negative equivalent potential vorticity) apparently acted to overwhelm the large-scale forcing to produce an erroneous diagnosis of downward motion. To see this in Tables 5.1-5.3, consider the modified QG thermodynamic equation (5.18) with zero (or weakly stable) stratification. With the heating term equal to zero, the temperature tendency must come entirely from advection. When this equation is combined with (5.36) into an omega equation, the temperature advection term must balance the sum of the vorticity advection term and the stretching term. At the center point at 350 mb (Table 5.3b), we have the Laplacian of the QG temperature advection term (term 1) equal to $+1.79 \times 10^{-13}$, while the pressure derivative of the vorticity advection term (Table 5.3a) is $+6.53 \times 10^{-13}$.

Since the vorticity advection term is the larger, the pressure derivative of the stretching term must be negative to satisfy the omega equation. This implies downward motion, opposite to what is observed in the NGM. The vorticity advection term is larger than the temperature advection term at 600 mb and 850 mb (Tables 5.1-5.2) as well, and downward motion is diagnosed by the modified quasi-geostrophic omega equation at all levels in the center of the updraft, as seen in Fig. 5.5.

Despite this diagnosis of downward motion in the center of the updraft, the omega equation errors listed in Table 5.3b are surprisingly small. The reason for this is that the error calculations use the actual unstable stratification, rather than a stratification set equal to zero or some weakly stable value. The quasi-geostrophic omega equation inversion, constrained by ellipticity to substitute a weakly stable stratification for the actual unstable stratification, is doomed to failure in this case. A similar problem would have confronted the inversion of a semi-geostrophic omega equation, since most of the upper portion of the updraft is a region of negative equivalent potential vorticity.

We had earlier discounted convective instability because no convectively parameterized precipitation was produced by the model in the neighborhood of the small-scale cyclone. It turns out from the above calculations that convective instability was present, but that the parameterization was not invoked because the instability was only present above the lowest four layers of the NGM, or about 850 mb (see Section 4.2).

d) Omega equation error analysis, first updraft

We now proceed with a similar error diagnosis for points in the vicinity of the first updraft at F06. At 850 mb (Table 5.4), many of the characteristics found at low levels in the second updraft are found in the first updraft as well. In the vorticity equation, the dominant terms are again the stretching term, the horizontal advection of geostrophic vorticity, and the horizontal advection of ageostrophic vorticity. The heating term in the

thermodynamic equation is again strongly affected by the release of latent heat. On the whole, however, the updraft appears to be young enough that nonlinear, small-scale effects are comparatively unimportant: the agreement between the vorticity tendency terms in the GM equations is better than for the second updraft and represents an improvement over both QG and modified QG at four of the five points.

At 600 mb (Table 5.5), unlike the second updraft, the vertical advection of vorticity at most points is small. This is because the updraft and small-scale cyclone are young; significant perturbation vorticity has not yet developed to be advected upwards. The tilting term is as large as the advection terms, but this tilting is nearly completely captured in the GM approximation. But in the thermodynamic equation, we see that unstable stratification is present at four of the five points.

Aloft, the 350 mb terms show persistent disagreement between geostrophic and ageostrophic vorticity. As at 600 mb, the tilting term is significant but is captured by the GM equation, and the vertical advection term is small. We are well above the level of moist convective instability found at 600 mb, so ascent produces cooling at all points. The agreement of time tendency terms is worse than at 850 mb, and about the same as was found at the second updraft.

An analysis of the balance of terms in the omega equation, as was done for F24, also implies downward motion at the central point when the stratification is taken to be near zero. But surrounding points, unlike at F24, generally imply upward motion, so it appears that the small scale of the saturated region and the lack of a strong vorticity perturbation combine to produce the upward motion diagnosed in Fig. 5.4. This is not useful to our understanding of the situation, since the dynamics of both updrafts ought to be strongly influenced, if not controlled, by the presence of convective and inertial instability.

Section 5.4: The Effect of Unstable Stratification on Updraft Evolution in the NGM

a) Conceptual model

In the divergence equation, we can see how the dynamics of a weakly stable and weakly unstable isolated moist updraft will evolve differently. The divergence equation, neglecting the horizontal gradient of the Coriolis parameter f, may be written as:

$$\left(\frac{\partial}{\partial t} + \boldsymbol{u}\cdot\nabla\right)\omega_p = -\omega\omega_{pp} + f(\zeta_g - \zeta) + u_x u_x + v_y v_y + 2\,v_x u_y + \omega_x u_p + \omega_y v_p \quad (5.40)$$

For this discussion we will assume that $\nabla^2\theta' \sim -\theta'$, so that heating leads directly to the production of a vertical geostrophic vorticity gradient, with a tendency for negative relative geostrophic vorticity above the heating and positive relative geostrophic vorticity below the heating.

Suppose we start with a locally uniform upward motion field, that is, a motion field which varies slowly compared to the scale of variation of moisture. Now suppose that embedded within the area of upward motion is a region of saturation. This situation might correspond to the first stages of a numerical model, in which vertical velocities have been initialized to be weak, or a situation in which large-scale ascent has just brought an area to saturation. As the large-scale ascent is assumed to be forced quasi-geostrophically, in the absence of latent heat release the divergence tendency is nearly zero and the production of vorticity at low levels through stretching is balanced by the production of geostrophic vorticity by the forcing. If latent heating occurs in a small area, however, there will be an unbalanced production of positive relative geostrophic vorticity at low levels relative to the heating and of negative relative geostrophic vorticity at higher levels. Through the

divergence equation (5.40), this will lead to increased convergence at low levels, increased divergence aloft, and a resulting increase in vertical motion at the level of the heating.

Under stable moist ascent conditions, the increased ascent will act to inhibit further increases in convergence or divergence. From the vorticity equation (5.35), stronger ascent leads to anomalous vortex tube stretching at low levels and vortex tube shrinking aloft. From the thermodynamic equation (5.38), stronger ascent leads to greater cooling and a reduction in the anomalous geostrophic vorticity production. One can see that if the updraft is locally strong enough, the cooling by the sum of the diabatic and adiabatic terms in the moist region can just equal the cooling by the adiabatic term alone in the dry, reduced ascent region, resulting in no net production of geostrophic relative vorticity. This is precisely the situation considered in Section 5.2, where we found that for small-scale reduced-stratification regions, the product of the stability and the vertical velocity tends to be constant along pressure surfaces.

When the stratification is unstable, this balance is no longer so easy to obtain. As air ascends unstably, the direct effect on geostrophic vorticity is not much different from weakly stable ascent. However, as the vertical motion increases locally, the geostrophic vorticity production increases rather than decreases, causing a positive feedback on the divergence tendency. The velocity of the updraft is now given, for example, by parcel theory, although in the NGM the effects of compensating pressure forces, relative vorticity production, and grid-scale smoothing most likely lead to a complicated, unsteady, rough balance of forces.

b) Lagrangian diagnosis of updraft evolution

To diagnose quantitatively some of these effects, we have calculated the magnitudes of various terms in the divergence equation. The points have been selected to lie in the

center of the updrafts, so that Lagrangian rates of change may be interpreted as changes in strength of the updraft. The terms plotted are:

$$\omega = \frac{Dp}{Dt} \qquad \textit{vertical motion} \qquad (5.41)$$

(solid lines with circles)

$$\zeta = \frac{\partial v}{\partial x} - \frac{\partial u}{\partial y} \qquad \textit{relative vorticity} \qquad (5.42)$$

(solid lines with squares)

$$\zeta_g = \frac{\partial v_g}{\partial x} - \frac{\partial u_g}{\partial y} = \frac{\nabla^2 \Phi}{f} \qquad \textit{geostrophic relative vorticity} \qquad (5.43)$$

(solid lines with triangles)

$$\frac{D_H \omega_p}{Dt} = - \omega\omega_{pp} + f(\zeta_g - \zeta) + u_x u_x + v_y v_y + 2\, v_x u_y + w_x u_p + w_y v_p \qquad (5.44)$$

ω_p *tendency, filtered* *(dashed lines with circles)*

$$\frac{D_H \zeta_{gp}}{Dt} = - \frac{1}{f} (\nabla^2 \omega\tilde{\sigma}) - \frac{1}{f} \left[\nabla^2 (\boldsymbol{u} \cdot \boldsymbol{\nabla}) \Phi_p - (\boldsymbol{u} \cdot \boldsymbol{\nabla}) \nabla^2 \Phi_p \right] \qquad (5.45)$$

ζ_{gp} *tendency, filtered* *(dashed lines with triangles)*

$$\frac{D_H \zeta}{Dt} = - (\boldsymbol{u} \cdot \boldsymbol{\nabla}) f - \omega \frac{\partial \zeta}{\partial p} + (f + \zeta) \frac{\partial \omega}{\partial p} + \frac{\partial \omega}{\partial y} \frac{\partial u}{\partial p} - \frac{\partial \omega}{\partial x} \frac{\partial v}{\partial p} \qquad (5.46)$$

ζ *tendency* *(dashed lines with squares)*

Our tendency operator is the horizontal substantial derivative,

$$\frac{D_H}{Dt} = \left(\frac{\partial}{\partial t} + (\boldsymbol{u} \cdot \boldsymbol{\nabla}) \right) \quad . \qquad (5.47)$$

We do not include vertical advections in the Lagrangian tendency terms so that we may diagnose the intensification of the updraft as seen on given pressure levels.

Before evaluating terms in the time tendency equations, we apply horizontal filters to the ω_p tendency term (5.44) and the term involving stratification in the ζ_{gp} tendency

equation (5.45). In the ω_p tendency equation, the dominant term is the vorticity difference term, with the remaining terms, particularly the vertical advection term, becoming important as the intensity of the small-scale cyclone increases. We have neglected the β term in the divergence equation (5.40, 5.44), as it tends to be an order of magnitude smaller than the other terms.

Within the first updraft at F06 (Fig. 5.11), the vertical motion is upward everywhere, with a maximum at 550-600 mb. The ω_p tendency is negative above the level of non-divergence and positive below. Thus, this updraft is intensifying, and because ω_p and the tendency of ω_p are strongly correlated, we shall assume that the physical and dynamical processes which are intensifying the vertical motion maximum at this time are the same processes which produced the bulk of its prior intensification.

The ω_p tendency at this early time is dominated by the vorticity difference term. Both ζ_g and ζ are shown in Fig. 5.11, and it is easily seen that the ω_p tendency is roughly proportional to the difference between ζ and ζ_g at most levels.

The agreement between ω_p and the ω_p tendency may be seen indirectly in the ζ tendency term, which at this time is dominated by the stretching of planetary vorticity and is therefore roughly proportional to ω_p. The ω_p tendency and the ζ tendency curves nearly match each other, both being positive at low levels and negative at high levels. Besides showing the dominant terms in the respective equations, the two curves also indicate that the vorticity tendency is acting to reduce the rate of increase of the updraft.

The remaining curve, the ζ_{gp} tendency, is dynamically the most important term plotted, because the geostrophic vorticity variation is driving the vertical motion. Plots of ζ_g upstream at the initial time (not shown) indicate that ζ_g started out with little vertical variation, much like ζ at F06 (Fig. 5.11). The fact that ζ_g is more structured than ζ, that the tendency of ζ is to bring it toward ζ_g, and that the tendency of ζ_g is to bring it farther away from ζ (as discussed presently) all imply that ζ_g is producing a vorticity difference and ζ and ω are responding to it.

The ζ_{gp} tendency curve is the noisiest of the six curves, despite the field being passed through a horizontal filter. This is an indication of the sensitivity of the term to small changes in relative humidity, as well as the noisiness of the vertical partial derivatives. The curve can be broken up into three regions. Below 650 mb, the ζ_{gp} tendency is nearly zero. Because this grid point is at a local maximum of vertical motion, the small magnitude implies weak stratification. (At this time, the horizontal advection term is not contributing strongly to the tendency.) At 600 mb and 550 mb, the ζ_{gp} tendency is large and positive, implying a local heating maximum. As ω is strongly negative, this maximum is due to the unstable stratification discussed in Section 5.3. The plot implies that at this point, at least, the instability is limited to a 100 mb deep layer. Finally, at 500 mb and above, the tendency is for localized cooling. In Table 5.6 it may be seen that the stratification at 350 mb is a factor of three less than the mean stratification, but much larger than the effective stratification in the saturated air at 850 mb. We infer that the local maximum in ω is overwhelming any variations in σ to produce localized cooling, the "normal" consequence of upward motion. This generally tends to inhibit further vertical motion, since it is creating a tendency for convergence above and divergence below. But, as seen in Fig. 5.11, the geostrophic vorticity aloft, around 300 mb, is still smaller than the total vorticity, so this inhibition must still be a secondary effect.

From the vertical structure of the geostrophic vorticity, it appears that the heating at mid-levels has been more dominant than the cooling at upper levels during the existence of the updraft, since the positive ζ_{gp} at mid-levels is much more prominent than the negative ζ_{gp} above it. Even without changes in the vertical extent of the updraft, this should be expected, because the vertical motion is acting to increase the stability aloft by vortex tube shrinking. Thus, the cooling aloft should become larger even if the magnitude of vertical motion remains constant.

By F12 (Fig. 5.12), many of the anticipated changes have taken place. The vertical motion maximum is stronger, although the maximum of vertical motion has not moved

significantly higher. The vorticity has developed a maximum at 650 mb and a minimum at 400 mb, consistent with the F06 tendency term. The vorticity is nearly unchanged below 750 mb, a fact we attribute to advection of negative relative vorticity at low levels form the east and northeast by the shear. The vertical geostrophic vorticity gradient has amplified between 600 mb and 500 mb (warm core) and between 400 mb and 200 mb (cold core). Interestingly, local net warming has occurred between 500 mb and 400 mb, contrary to the ζ_{gp} tendency term at F06. The proximate cause of this may be seen in the ζ_{gp} tendency term at F12: the region of heating has moved upward to 500 mb, with positive heating up to 350 mb. We shall see later that differential advection of θ_e has reduced the effective stability and allowed the updraft to produce net warming. Finally, the ω_p tendency term, as implied by the difference between ζ_g and ζ, still shows intensification of the updraft, although not as much as at F06.

Meanwhile, upstream of the second updraft, six hours before it appears (Fig. 5.13), the vertical motion is comparatively weak and actually downward in the upper troposphere. But since the tendency is for convergence at low levels and divergence aloft, a stronger updraft appears to be developing. The origin of this tendency is not apparent from this snapshot, since the ζ_{gp} tendency appears to be uncorrelated with ζ_{gp} or with $(\zeta_g - \zeta)_p$.

Six hours later (Fig. 5.14), the second updraft is already well-developed. The maximum updraft of 0.9 Pa s^{-1} occurs at 550 mb, and there is a strong tendency for further development of divergence aloft, due to the difference between ζ_g and ζ between 300 mb and 500 mb. The ζ_{gp} tendency is for warming at all levels, particularly between 700 mb and 400 mb, implying unstable stratification aloft. The ζ tendency remarkably is positive at all levels, a consequence of the strength of the upward advection of vorticity.

By F24 (Fig. 5.15), the maximum updraft has moved to 450 mb. This is attributable to the change in ζ_{gp} tendency, which is now a maximum at 400 mb and has become much larger than before. This is consistent with the large point values of unstable

stratification found at 350 mb in Section 5.3. At low levels, the vorticity has grown larger than the geostrophic vorticity, and there is a resulting tendency for downward motion below 600 mb, even as the updraft continues to intensify above 600 mb.

To show that the important tendencies are not confined to particular grid points and are closely related to the updrafts, selected ζ_{gp} tendencies have been plotted in Figs. 5.16-5.17. We have broken the tendency up into the contributions due to vertical and horizontal processes, a distinction not made in the grid point soundings. The first set, Fig. 5.16, is at a level which had a large positive ζ_{gp} tendency at both F06 and F12 at the location of the updraft. The maps show that most of the ζ_{gp} tendency variation throughout the area is due to the vertical term.

In the first updraft, the vertical term is nearly perfectly co-located with the updraft, clearly indicating the close relationship between the tendency of ζ_{gp} and the tendency of ω_{pp}. At F12, the updraft is still producing warming over a scale comparable to its size. At both times the region of positive ζ_{gp} generation is surrounded by zones of negative ζ_{gp} generation. This might be expected from the sign of the Laplacian of ω alone, but the small-scale structure implies a contribution from variations in moist stratification or saturation. At F18, the updraft is dominated by negative ζ_{gp} tendency, implying that the updraft has become stable and is not significantly less stratified than its surroundings. The updraft itself has also weakened, but part of that weakening must be attributed to the updraft coming into proximity to the NGM grid meshing boundary.

The generation of ζ_{gp} in the second updraft was more prominent at 400 mb (Fig. 5.17). At F12, a heating maximum is nearly surrounded by a ring of cooling, suggesting a small-scale region of saturation triggered by the first updraft or reduced stratification advected from below. This pattern weakens and vanishes over the next 12 hours as the updraft dissipates. In its place, a similar doughnut-like couplet appears within the second updraft. The heating due to the second updraft is strong and localized, and appears to be the result of localized moist instability. The localized nature of the unstable region may be

seen by comparing Figs. 5.17f and 5.17i. In the mesoscle updraft, the ζ_{gp} tendency is positive where ω is a minimum (maximum upward), implying heating from below. Over Maryland and coastal North Carolina, the ζ_{gp} tendency is positive where ω is a maximum (miminum upward motion), implying cooling from below.

We have not discussed the possibility of symmetric instability. We would expect that, since the atmosphere is locally convectively unstable in the vertical, buoyancy effects would predominate. Since the inertial effects operate on longer time scales, they should play less of a role in the development of these particular updrafts.

The importance of symmetric instability may be deduced from Figs. 5.16-5.17. Physically, we expect that as air parcels ascend in a sheared environment, they will be subgeostrophic and will accelerate to the left as they drift back relative to the ambient flow. This will result in a localized region of warm advection, causing a maximum of ζ_{gp} generation displaced toward the cold side of the updraft. This effect should be dominant in the horizontal ζ_{gp} tendency near the level of non-divergence. In the upper troposphere, this effect could be even stronger, but it is necessary to separate it from the tendency of the divergence to cause heating on the cold side of the ω maximum and cooling on the warm side. An asymmetry in the divergence heating-cooling couplet will be inferred to be evidence of inertial advection.

At 550 mb in the first updraft (Fig. 5.16), which is near the level of non-divergence so that the divergence dipole is absent, we see that inertial advection appears to be making a small positive contribution to the ζ_{gp} tendency. The contribution is most apparent at F06; at later times, negative ζ_{gp} tendency centers appear in the vicinity of the updraft, making the total contribution on the scale of the updraft unclear. In any case, the effect at this level is minor compared to the effect of vertical instability.

At 400 mb (Fig. 5.17), the horizontal term is positive within the first updraft at both F12 and F18, and at F18 is strong enough that it compensates for the negative tendency in the vertical term. The effect of the grid mesh area in weakening the negative half of the

divergence dipole is not known, but could be substantial. The second updraft shows more of a dipole at F18, but by F24 the area of positive horizontal generation has moved to the north and west of the updraft, where it is being cancelled by the vertical term. This dislocation appears to be due to the formation of a temperature maximum within the updraft by moist unstable ascent, and the concomitant displacement of the strongest temperature gradient to the northwest.

c) The prediction of unstable updrafts in the NGM

Having established that upright instability was the proximate cause of both updrafts in the NGM, it is now appropriate to ask whether the location and evolution of the updrafts could have been inferred from the initial conditions of the NGM at 19/00.

One useful indicator of possible upright or slantwise overturning is the equivalent potential vorticity, Q_e, defined in (1.2). Negative Q_e indicates potential symmetric or upright instability which would be realized if the air were brought adiabatically to saturation without changing Q_e. The lower- and mid-tropospheric distribution of equivalent potential vorticity at F06 is shown in Fig. 5.18. Although Q_e in the vicinity of the updraft offshore is negative at 550 mb and 600 mb as expected, the unstable Q_e extends south and west over a broad area of the coastal regions of the southeast United States at many levels. This parameter alone is clearly insufficient to diagnose the location of vertical motion maxima, although Fig. 5.18 indicates that almost any region of saturation which develops would potentially be unstable.

The missing diagnostic is water vapor. In view of the problem of assessing saturation in the NGM discussed in Section 4.2, and the unimportance of slantwise convection for the present case, we choose to combine stability and moisture information by plotting maps of θ_e and θ_e* at selected vertical levels (Figs. 5.19-5.23). We have plotted θ_e (solid) and θ_e* (dashed) at 1 K increments from 318 K to 325 K. Regions of

saturation correspond to those areas in which the θ_e contours lie within 1 K of their respective θ_e* contour. For example, a region of saturation is present at 900 mb at F06 (Fig. 5.20) south of Cape Hatteras, where the θ_e and θ_e* lines are parallel and close together. Along the coast and further offshore, the θ_e and θ_e* lines diverge, indicating unsaturated conditions, with the relative humidity being roughly proportional to the difference between θ_e and θ_e* within a given level. In general, the model is initialized with unsaturated conditions, and the region of saturation increases with time in the subregion of interest so that most of the plotted domain is saturated by F30.

Since the model atmosphere is unsaturated at F00, a check of Fig. 5.19 does not show any regions of absolute instability. Potential instability may be seen at 900 mb over northern Florida and southern Georgia, as well as along the eastern edge of the map (θ_e at 900 mb higher than θ_e at 800 mb in those areas). Farther up, the closed θ_e contours at 700 mb and 600 mb are marginally unstable. Because relative humidities are higher in these potential instability regions, and because large-scale vertical motion will tend to be larger at these levels, we could deduce from these maps alone that an unstable updraft would be likely to form at mid-levels near the center of the plotted map. Potentially stable conditions prevail above 500 mb.

Six hours later (Fig. 5.20), the location of the updraft is marked at 600 mb by closed θ_e and θ_e* maxima at 600 mb. The close agreement between θ_e and θ_e* marks the updraft as saturated, and the region of saturation extends westward to a point south of South Carolina. The θ_e* field has the appearance of being a combination of the F00 θ_e fields at 600 mb and 700 mb, which is reasonable given the presence of vertical motion. As was seen in the grid point soundings, the air in the updraft is only unstable over a shallow region. Absolute instability exists between 600 mb and 500 mb, but above 500 mb the air is statically stable.

Elsewhere, a prominent region of potential instability has developed along the coast and offshore south of Wilmington, NC. Differential advection by the thermal wind

(parallel to the θ_e* contours) is advecting relatively low θ_e air over the higher θ_e air at 900 mb and 800 mb. At 1000 mb, the θ_e* field is in the process of rapidly adjusting to the sea surface temperatures, which are colder than initialized air temperatures near the coast and warmer than initial temperatures offshore. After F12 (Fig. 5.21), there is little further change in the 1000 mb θ_e*, despite 10 m/s winds, and the θ_e at 1000 mb remains at least a degree lower than the 900 mb θ_e* at all times.

Aloft, the evolution of the pattern proceeds slowly over the next six hours (Fig. 5.21). Instability is still present in the updraft at F12. Air over southern South Carolina is very potentially unstable but also very dry. At 800 mb, absolute instability appears to be present at extreme southern South Carolina, but with stable stratification above 700 mb and below 800 mb, the instability was apparently not strong enough to cause immediate formation of an updraft. Farther north along the southern coast of North Carolina, the 800 mb air has a θ_e of 319 K and is within one degree of being saturated. Inspection of the maps at higher levels indicates that lifted air would be warmer than θ_e* at 700 mb and 600 mb, and warmer even than θ_e at 500 mb and 400 mb. Because gradients are at least as strong at 800 mb as above, this developing region of instability extends offshore at least to the 322 K θ_e contour at 800 mb.

It was in this region that the second updraft formed. The large depth of the potential instability which was about to become absolute instability through the action of large-scale upward motion accounts for the rapid development and intensity of the second updraft, which attained nearly its full amplitude in less than six hours between F12 and F18.

By F18 (Fig. 5.22), the amplitude of the thermal anomaly at mid-levels associated with the first updraft has weakened considerably, a surprising occurrence which we attribute to smoothing and matching along the grid boundary. The formation of a second updraft has led to moistening at 500 mb and 400 mb through both cooling and vertical advection of warmer θ_e air from below. However, most of the updraft remains unstable,

as is confirmed by spot-checking of air parcels. For example, the parcel over Cape Hatteras at 800 mb has a θ_e of 321 K. This equals the θ_e* at 700 mb and exceeds θ_e* from 600 mb to 300 mb. The size of the unstable region is easily seen by comparing the maps at 700 mb and 400 mb. With saturation present at both levels, most parcels at 700 mb have θ_e's 1-2 degrees warmer than the corresponding parcels at 400 mb. This region of instability occupies a roughly circular area extending eastward from Cape Hatteras and corresponding fairly well to the area covered by the second updraft.

A feature of note at F24 (Fig. 5.23) is the rapid warming which has taken place at mid-levels as a result of the absolute moist instability and developing updraft. By this time the difference in unstable θ_e between 700 mb and 400 mb is much reduced from six hours earlier. Large regions of weak gradient have formed within the 321 K θ_e isotherm at 500 mb and 400 mb. This has caused the region of absolute instability to move upward, and air at 400 mb is now unstable when lifted to 300 mb.

In summary, the first updraft seems to have formed as a result of the initialization (using no offshore *in situ* observations) of a nearly saturated, potentially unstable θ_e maximum at 600 mb to 700 mb. The second updraft also depended on the initial conditions, but the instability was larger, deeper, and was generated by differential advection of the large-scale θ_e pattern rather than the presence of a localized θ_e maximum. Because air in the lowest layers was convectively stable, neither updraft had, as a contributing factor, surface fluxes of sensible and latent heat during the model run.

If these processes took place in the real atmosphere, they would be considerably different in character. First, the instability would have been released on convective scales, which are of the order of 10 km for the atmosphere. Thus, instead of having a single broad mesoscale updraft, many smaller updrafts would have formed, interspersed with downward motion. The net result, an atmosphere neutral to moist convection, should be the same in both cases, so we expect roughly similar patterns of geostrophic vorticity after six to twelve hours, with the instability being released sooner in the real atmosphere.

Section 5.5: Differences Between the Small-Scale Cyclone in the NGM and in the Real Atmosphere

The observations examined in Chapter Three implied that the actual small-scale cyclone was produced locally by generation of potential vorticity at low levels due to moist ascent and latent heat release. The complementary analyses and model simulations discussed in Chapter Four offered further evidence that baroclinic instability or superposition of preexisting anomalies was not directly responsible for the low-level vorticity spinup. The small-scale cyclone produced in the NGM was clearly a product of moist ascent. In the preceding sections of Chapter Five, we found that localized, stable ascent was a potential generator of small-scale cyclones, but that the NGM updrafts were due to mid- and upper-level convective instability. While confirming the likelihood that the actual small-scale cyclone was produced by moist processes, the structure of the NGM updraft was not realistic.

There are three key questions we now wish to address with regard to differences between the NGM and the real atmosphere:

1) What was the nature of the stratification in the real atmosphere? Given a localized region of saturation, ascent in either stable or unstable stratification could have produced small-scale cyclogenesis.

2) What was the role of surface heat fluxes? Because the small-scale cyclone developed on such a rapid time scale and never attained a closed, tropical storm-like circulation, it seems likely that the primary role, if any, of surface fluxes of sensible and latent heat was to precondition the boundary layer during the days and hours before the cyclone formed. The effect of surface fluxes depends strongly on the nature of the stratification (question 1), however, because unstable vertical or slantwise stratification would allow boundary layer air to ascend freely and cause the largest temperature changes

to be located in the upper troposphere where moist adiabats are farthest apart. Stable stratification would tend to prevent the troposphere from overturning and limit the effect of heat fluxes to the lower troposphere.

3) Why was the real small-scale cyclone located at the edge of the precipitation region? In the NGM, vorticity production was largest where the updraft was most intense, and the maximum vorticity was displaced only slightly downwind at low levels (i. e., to the northwest) of the updraft cores. But the evolution of the small-scale cyclone in the NGM was complicated by the fact that it was associated with two separate updrafts during its development.

All three of these questions are best addressed by means of examining temperature and dew point soundings in the vicinity of the small-scale cyclone. This task would be easier if there were sounding stations located where the small-scale cyclone formed (see Section 1.3), but we are not so lucky. Three sounding sites (RVC, MRH, and HAT) are located in the region of heavy precipitation, so we can begin to address the question of the nature of the stratification within that portion of the updraft. The small-scale cyclone itself either passed over RVC or passed between RVC and HAT at about 19/15, so we have decent data on the thermal structure of the small-scale cyclone at that stage in its evolution. The cyclone passed near HAT at 19/18, but that sounding was missing.

The RVC soundings are also useful for considering the effects of heat fluxes, because these soundings are the only ones which have not been affected by upstream cooling of the boundary layer by the nearshore waters. We will also make use of ship observations to assess the distribution and evolution of surface equivalent potential temperature upstream of and in the neighborhood of the small-scale cyclone, and use upstream soundings from West Palm Beach (PBI) to attempt to reconstruct the initial environmental conditions before upright or slantwise instability (if any) was released.

Comparisons between soundings will be facilitated by the 323 K equivalent potential temperature pseudoadiabat, which is part of our standard skew-T diagram and

which most of the temperature profiles tend to lie near. This pseudoadiabat intersects the bottom of the sounding diagrams near 18 C and is the leftmost pseudoadiabat to intersect the top of the sounding diagrams.

Fig. 5.24 shows the complete set of soundings from RVC between 18/12 and 20/00, encompassing the time period from before the onset of precipitation to after the passage of the small-scale cyclone. This sequence of soundings is the set of observations which most closely depicts the evolution of the vertical structure of the atmosphere in the vicinity of the small-scale cyclone. When examining this figure, it may also be useful to refer back to Chapter Three, particularly the radar summaries (Fig. 3.38) and the time series of hourly observations from RVC (Fig. 3.9).

The first few soundings are characterized by a 100 mb deep boundary layer with constant potential temperature and decreasing mixing ratio with height. Near 800 mb, an inversion is present, above which the air is generally much drier. The general trend with time in the boundary layer is for gradually increasing temperatures and mixing ratios. Above the boundary layer, between 800 mb and 600 mb, a gradual increase in humidity is occurring. By 19/03, dew point depressions are only about 5 C at least up to 700 mb. Most of these soundings show potential instability, with equivalent potential temperatures in the boundary layer warmer than equivalent potential temperatures above the boundary layer or above the inversion.

A major change occurs between 19/03 and 19/06, which we associate with the onset of precipitation. Most of the sounding becomes saturated and roughly moist-adiabatic, and the transformation of the boundary layer air from 19/03 to 19/06 is attributable to the evaporation of precipitation. Because of the cooling caused by the precipitation, the 19/06 boundary layer is colder than at any other time in the sounding sequence. Above the boundary layer, the combination of saturation and occasional lapse rates greater than moist-adiabatic cast suspicion that the temperature sensor is moist and that the sounding is effectively one of wet-bult temperature only. A similar problem is

encountered with the 19/12 sounding. However, this problem does not affect the determination of equivalent potential temperature, and in both soundings the nearly moist-adiabatic profile and slight remaining instability of low-level air indicate that upright or weakly slantwise convective adjustment is taking place.

The soundings from 19/09, 19/15, and 19/21 are hampered by a lack of altitude, and the 19/09 sounding additionally has an obviously bad data point near 750 mb. By 20/00, dry continental air has advected over RVC, and an inversion is again present at 700 mb.

The set of soundings from HAT during the period of precipitation (Fig. 5.25; note the change in vertical scale from the preceding figure) confirm the diagnosis of an adjustment to moist neutrality. The 19/00 sounding was taken prior to the onset of deep precipitation. An inversion is present below 980 mb which is caused by the low-level marine air being advected over colder shelf water before reaching the sounding site. Similar inversions are present in most other HAT soundings. Above this inversion is a deep, nearly moist-adiabatic moist layer, capped by a dry inversion at 600 mb. The temperature profile becomes superadiabatic just as the relative humidity decreases; this is an artificial feature of many soundings and is caused by evaporation of accumulated moisture from the rawinsonde as it leaves the cloud or precipitation layer. We note that this sounding also is either potentially unstable or nearly so.

The following four HAT soundings were all taken within areas of precipitation. All show similar dew point depression structure, with the dew point depression increasing smoothly and regularly with height. We infer that either the air is saturated or the rawinsonde observations have been contaminated by water on the instrument. As for the temperature structure, all four soundings have lapse rates steeper than moist adiabatic in the lowest 150 mb to 250 mb, and stabler than moist adiabatic above. In the "stable" region, the temperature profile shows a remarkable tendency to deviate just slightly to the stable side of moist adiabatic over depths of 400 mb to 500 mb. This tendency is clearest at

19/15. This particular sounding is tainted by a blip at 650 mb which is consistent with water covering the thermistor freezing as it passes through 0 C. Aside from the blip, the temperature profile follows a very regular curve, slightly stabler than moist adiabatic, all the way from 850 mb to 300 mb. This sounding in particular indicates moist unstable, moist slantwise, or moist neutral ascent rather than moist stable ascent, and implies that unstable overturning has occurred or is occurring. The temperature at mid-levels is also increasing with time from 19/03 to 19/15, as the small-scale cyclone approaches, and there has been a similar but not as regular increase in temperatures in the elevated boundary layer around 950 mb. The change in temperatures is greatest aloft, which is again consistent with moist convective overturning.

Much less precipitation was observed at MRH than at HAT, and the soundings from MRH (Fig. 5.26) do not show deep layers of saturation as were found at HAT, although the 19/09 MRH sounding is missing. Prior to the onset of precipitation, the familiar dry, potentially unstable inversion is found at mid-levels. Between 19/00 and 19/06, as precipitation begins, the dry air is replaced by a deep region of high relative humidity, and a HAT-like inversion forms at the surface.

The most interesting soundings are from 19/12, 19/15, and 19/1630. These soundings were all taken with MRH on the edge of, but just outside, the region of precipitation as seen by the CP4 radar. They also correspond to the time the small-scale cyclone apparently passed just to the south. Several features are worthy of note. First, the three soundings have deep regions of relative humidities greater than 70% in which the temperature and dew point lapse rates are anticorrelated, but equivalent potential temperatures are nearly constant. This is an indication of small-scale, slanting updrafts and downdrafts being penetrated by the rawinsonde, and is consistent with slantwise convective overturning occurring nearby. Second, despite the shallow variations, the overall soundings tend to follow lapse rates just slightly steeper than moist adiabatic, which is what the precipitation soundings were found to do at HAT. Finally, the temperatures

themselves also closely match the temperatures at HAT. This is true even of the 19/1630 sounding, which is effectively dry above 600 mb. We infer from these characteristics that air along the margins of the convective ascent regions is undergoing compensating subsidence so as to roughly match the temperatures of ascending moist parcels and thereby remove the instability.

As the soundings in the precipitation region all seem to indicate convective overturning, we now look upstream to see what ambient conditions were before the convective instability to confirm that potential instability should have been present. The best available sounding site is PBI, which is located a bit south of the cyclogenesis region and therefore may be a bit warmer than actual ambient conditions in the region of overturning. The soundings for 18/12 to 19/06 are shown in Fig. 5.27. They show the familiar dry layer at mid-levels before 19/00, with air possessing equivalent potential temperatures less than 323 K, and therefore colder after ascent than the warmer soundings from MRH and HAT. Below the dry layer, the air is nearly saturated, and the boundary layer air is warmer than any air in soundings in Fig.s 5.24-5.26 and has a warmer equivalent potential temperature temperature than any air aloft. Thus, potential instability is present upstream of the cyclogenesis region prior to the onset of widespread precipitation.

Final confirmation of potential instability is found in the equivalent potential vorticity maps from the NGM (Fig. 5.18). Those maps showed potential instability through much of the lower troposphere throughout the southeast, and the soundings we have examined have given us no cause to doubt this result.

The environmental winds were such that the PBI soundings were only located upstream of the cyclogenesis area with respect to the middle and upper troposphere. To infer the low-level upstream conditions, and to also consider the possible effect of surface heat fluxes, we have plotted maps of wind and equivalent potential temperature using filtered ship and land-based observations (Figs. 5.28-5.30). We have not attempted to contour these fields because of the noisiness of the data, the general unreliableness of ship-

based observations, and the tendency of equivalent potential temperature to magnify any errors which may be present.

The large-scale pattern of equivalent potential temperature offshore shows a systematic gradient from northeast to southwest, consistent with the anticyclonic trajectories of air parcels and the sea surface temperature distribution. The air flowing toward the small-scale cyclogenesis area at 19/00 has an equivalent potential temperature of about 330 K, with 335 K to 338 K found upstream to the south, near the Bahamas. At 19/06, data are sparse upstream of the cyclogenesis area, but observations off the Carolina coast show equivalent potential temperatures of 325 K to 328 K. These temperatures are not unambiguously colder than temperatures six hours before, since data coverage is not adequate, but a reduction in surface equivalent potential temperature would not be inconsistent with upright or slantwise convective overturning. The sounding sequences, however, did not show a reduced equivalent potential temperatures at the surface at the same time as the onset of precipitation.

At 19/12, surface equivalent potential temperatures in the neighborhood of the small-scale cyclone have become 330 K to 335 K. This represents an increase of about 4-8 K over twelve hours. Unfortunately, the available data is insufficient to determine what proportion of this increase was due to surface heat fluxes and what proportion was due to advection. Using the winds at 19/06, a simple back-trajectory would place the 19/12 air in a band without observations at 19/00, with equivalent potential temperatures below 330 K to the north and above 332 K to the south. Because the environmental air was unsaturated and tended to be a couple of degrees colder than sea surface temperatures, it is plausible that at least some of the observed temperature increase was due to surface fluxes.

Of more importance dynamically is to what extent the heat fluxes were modified by the small-scale cyclone. The direct effect of increasing heat fluxes by increasing winds at the surface appears to have been minor, because wind speeds were not any larger in the vicinity of the small-scale cyclone than they were over a large expanse of the Atlantic. At

most, the effect of the vorticity generation was to extend the band of high winds closer to shore. An alteration of wind direction might also lead to increased total heating of a portion of the boundary layer, if the winds shift to blow along the Gulf Stream. This effect may have contributed to the development of the small-scale cyclone, when the wind was blowing along the Gulf Stream off the Florida coast. However, this wind configuration was due mostly to large-scale processes. At later times, hourly observations from ships such as NLFI and RVC do not indicate a period in which the wind was blowing along the Gulf Stream. For the most part, the winds just ahead of the cyclone were southerly rather than southwesterly. A final modification of heat fluxes by the small-scale cyclone could be due to the effect of overturning and evaporative cooling at low levels at the onset of precipitation. However, this is probably a very minor effect, since it is not immediately obvious whether evaporative cooling would enhance or reduce the effect of fluxes on equivalent potential temperature.

Over Florida, Figs. 5.28-5.30 show equivalent potential temperatures generally between 320 K and 330 K. This is colder than offshore temperatures, and may help explain why widespread precipitation was limited to areas experiencing an inflow of air from the south or southeast rather than the southwest.

We have shown that the stratification in the neighborhood of the small-scale cyclone, within the region of widespread precipitation, was apparently convectively adjusted to a nearly neutral state with respect to parcels lifted from the boundary layer. We have also shown that during the development of the small-scale cyclone, high equivalent potential temperature air was flowing in from the south and southeast, possibly undergoing slight warming as it approached the cyclogenesis region. We are now in a position to answer the third question, and attempt to explain the location of the small-scale cyclone relative to the precipitation and convective overturning.

Consider the basic state shown in Fig. 5.31a. A large-scale cyclone is located to the north of the dashed area, and is presumed to be undergoing intensification while

moving closer to the dashed area. The intensification is due to an isolated upper-level potential vorticity anomaly approaching a region of warm surface temperatures and weak stratification. With this configuration, large-scale lifting would be occurring within the dashed area (as well as outside of it) as the cyclone approaches. Now suppose that because of the large scale lifting the air within the dashed area becomes unstable and undergoes convective adjustment, either through upright or slantwise convection. The adjustment is confined to the dashed area because that area is a location of anomalously high surface equivalent potential temperatures and high relative humidities. Suppose that the surface equivalent potential temperature increases toward the southwest, as in the observed case.

The convective adjustment produces a net heating, which will lead to a decrease in pressure in the lower troposphere and an increase in pressure in the upper troposphere which will be proportional to the amount of heating, as shown in Fig. 5.31b. The edges of the region experiencing a change in pressure would not be sharp, but would be smoothed somewhat by geostrophic adjustment.

Finally, allow this change in pressure to be superimposed on the ambient pressure field (Fig. 5.31c). The result, which has been produced conceptually by processes shown to have been occurring in the real atmosphere, is similar to the observed pressure pattern associated with the small-scale cyclone. According to this model, the small-scale cyclone is located near the southwest edge of the precipitation region because it is precisely this region which undergoes the greatest amount of warming. The cyclone is displaced toward the northwest because of the presence of an ambient pressure gradient. This second effect is an artificial one, in the sense that the location of the vorticity center should be unaffected.

Section 5.6: Summary

In this chapter, we investigated a variety of hypotheses to attempt to explain the development of localized updrafts within the NGM, and by extension the small-scale cyclone in the real atmosphere.

We first considered the hypothesis that the localized vertical motion was simply a result of large-scale quasi-geostrophic forcing. The vertical motion patterns obtained by inverting the quasi-geostrophic omega equation were found to be in only fair agreement with the actual large-scale NGM vertical motion fields, and no localized updrafts were found offshore where the small-scale cyclone developed. This hypothesis was rejected.

Motivated by the observation that the first NGM updraft encompassed a localized region of saturation in the lower troposphere, we next considered the hypothesis that the reduced effective stratification caused by latent heat release was producing a locally strong response to large-scale forcing. To attempt to qualitatively verify this hypothesis, we altered the quasi-geostrophic omega equation to include a variable effective stratification. While not energetically consistent within the quasi-geostrophic system of equations, our modified omega equation is still useful as a diagnostic tool.

To determine how a variable stratification should alter the response to forcing, we obtained asymptotic solutions to the omega equation for stratification length scales longer and shorter than the Rossby radius of deformation. These solutions, confirmed by numerical solution of prototypical stratification distributions, showed that for small-scale stratification variations, the local response should be inversely proportional to the local effective stratification.

Applying the modified omega equation to the NGM fields yielded vertical velocities which were generally superior to those obtained from the standard quasi-geostrophic omega equation. Early in the forecast, a localized vertical motion maximum was calculated which agreed with the actual NGM vertical motion in magnitude, horizontal scale, and

location. At later times, however, downward vertical motion was calculated over the location of the small-scale cyclone, in contrast to the actual maximum of upward motion in the same location. Allowing the effective stratification to be a function of the sign of the vertical motion did not remove the erroneous subsidence from the diagnosed vertical motion fields.

In order to isolate the cause of the breakdown of the modified quasi-geostrophic omega equation and to determine whether a formally superior approximation such as the geostrophic momentum approximation might be valid, the magnitudes of individual terms in the vorticity and thermodynamic equations were calculated for selected grid points surrounding the vertical motion maximum. It was found that the local vorticity distribution bore little resemblance to the geostrophic vorticity distribution. The magnitudes of several neglected terms were comparable to terms retained in the quasi-geostrophic and geostrophic momentum equations. Furthermore, the upper portion of the updraft was found to be both inertially and convectively unstable.

A similar diagnosis for the first updraft indicated that this updraft was also convectively unstable at certain levels. We therefore abandoned the hypothesis that the dynamics of the updrafts could be adequately diagnosed with a balanced system of equations and proceeded to evaluate terms in the full divergence equation.

Vertical profiles through both updrafts showed that the updrafts were driven by the generation of positive (negative) geostrophic vorticity below (above) the level of convective instability, as a consequence of the localized vertical motion. The imbalance between the geostrophic and actual vorticity served to strengthen the updraft, which in turn amplified the vertical geostrophic vorticity dipole as long as convective instability was present. The convective instability was not released by the NGM convective parameterization because the instability was located above the 850 mb level. Inspection of the horizontal and vertical distribution of θ_e and θ_e* confirmed that the development and horizontal distribution of vertical motion maxima was closely related to the existence of convective instability.

We then examined the atmospheric data to determine whether this type of development produced the actual small-scale cyclone. Widespread convective instability was found upstream of the small-scale cyclogenesis region. Time series of soundings indicated that an adjustment to upright or slantwise convective neutrality occurred within the heavy precipitation region ahead of the small-scale cyclone. Unlike in the NGM, heat fluxes from the sea surface may have aided the development, although it appeared that most of the boundary-layer warming in the vicinity of the small-scale cyclone was due to large-scale advection from the southeast. A simple hypothetical distribution of convective heating correctly implied that the small-scale cyclone should be located along the western edge of the region of convective adjustment.

We have shown that moist convective instability caused vertical motion and low-level potential vorticity generation in both the NGM and the real atmosphere, leading to the development of low-level small-scale vorticity maxima. We next wish to determine whether these processes may be expected to be a general characteristic of small-scale cyclones in warm advection regions.

CHAPTER SIX

A SECOND SMALL-SCALE CYCLONE: SIMILARITIES AND DIFFERENCES

Section 6.1: Observations

Up to this point we have been considering a particular small-scale cyclone. Single case studies rightfully invoke the question of generality. Any conclusions based on a single case may be peculiar to that case and not be generally applicable. In Chapter Two we found that many mobile small-scale cyclones over North America during a given winter season, and we wish to know whether the particular dynamical mechanisms responsible for the small-scale cyclone we examined in Chapters Three, Four, and Five are typical of small-scale cyclones or unusual.

We shall not present a complete case study of a second case. Instead, we shall make use of the observational and dynamical techniques which we developed for the first case study, and present selected highlights of the second case. From prior chapters, we know that the principal feature which distinguishes the dynamics of the first small-scale cyclone are the presence of strong, isolated moist vertical motion in a region of the atmosphere initially characterized by potential instability to upright or slantwise convection.

Our selection of small-scale cyclone of 10 Feb 1986 as the object of the second case study was based on utilitarian considerations. Among cyclones analyzed to have a radius of 200 km six hours into their lifetime, the data coverage for the 10 Feb cyclone ranked third. The best data coverage was for the 19 Jan cyclone, the object of our primary case study analyses. The second best coverage was for a cyclone which followed the same track as the 19 Jan cyclone and which is being or has been studied elsewhere. The 10 Feb

cyclone was the subject of three-hourly rawinsonde coverage in Georgia, South Carolina, and North Carolina while it passed over those areas.

As it happens, the 10 Feb cyclone had certain characteristics which make it particularly interesting in light of our first case study. Unlike the first case, the 10 Feb cyclone developed in a region of strong baroclinicity. Also unlike the first case, it formed within a precipitation region associated with a mobile upper-level trough. Finally, the precipitation over land was much weaker than the first case, while the updraft and vorticity in the NGM were much stronger.

Surface analyses of the 10 Feb small-scale cyclone are shown in Figs. 6.1-6.4. At 10/12 (Fig. 6.1), the particular small-scale cyclone of interest has not yet formed. The low center analyzed off Cape Hatteras is a preceding small-scale cyclone which formed offshore and quickly moved away from any ships which were taking observations. The low is embedded within a developing frontal zone running from southern Alabama across the coast of Georgia and east-northeast across the Atlantic. To the south of the frontal zone (particularly obvious at this time in the vicinity of Florida), large-scale southerly and southwesterly winds predominate. Temperatures in the warm air are generally 20-25 C. To the north of the frontal zone, from Georgia across the Carolinas and into Virginia, weak to moderate northeasterlies prevail, with temperatures of 0-10 C. This air is being trapped against the Appalachians by strong stratification and the large-scale geostrophic wind. Mobile cyclones passing over the area are masked at the surface by the anomalous high pressures associated with the trapped pool of cold air.

Six hours later (Fig. 6.2), the small-scale cyclone of interest has appeared off the coast of South Carolina. Analyzed with a central pressure of 1011 mb, it has formed on the offshore frontal zone. Close inspection indicates that it does not appear to be a frontal cyclone, as there is no discernable wave along the front and winds within the cold air have not been noticeably influenced by the presence of the small-scale cyclone. Within the warm air, substantial perturbations are present; the ship whose observation (west wind, 22 C

temperature) is plotted just south of the cyclone reported a wind shift from due south in the past hour, and would continue to veer to northwest during the following hour, with falling temperatures lagging the wind shift by two hours. The earlier small-scale cyclone off Cape Hatteras has vanished from the analysis; in its place is a large question mark, indicating insufficient data along the frontal zone to discern features with scales of less than a few hundred kilometers.

After forming, the small-scale cyclone moved swiftly along the frontal zone toward the east-northeast. At 11/00 (Fig. 6.3), the oddly-shaped low was located off Cape Hatteras, where the earlier small-scale cyclone had been located twelve hours previously. On the warm side of the front, substantial cyclonic vorticity and convergence is apparent in the nicely-distributed surface observations, while coastal and offshore stations to the north of the cyclone have undergone a strenghening of the winds, without noticeable backing. Those northeasterly winds remain in place during the following six hours (Fig. 6.4), while the cyclone further offshore toward the big question mark. To the west, a larger-scale cyclone is taking shape over Georgia. This cyclone would re-form along the coastal front off North Carolina six hours later (not shown), following the approximate track of the small-scale cyclone of interest as it deepened.

The radar summaries in Fig. 6.5 cover the period before and during the small-scale cyclogenesis. The show a large, roundish region of mostly light precipitation centered over Alabama and Mississippi at 10/0535, surrounding the southern Appalachians at 10/1135, and covering the coastline from New Jersey to South Carolina at 10/1735. At 10/2235, only the western margin of the precipitation region is detected, along the mid-Atlantic coast. The precipitation region was trackable as a steadily-moving, distinct entity in the hourly radar summaries from 09/18, when it was located over East Texas, until 11/03, when it had moved completely offshore. Behind it, a second, similarly-sized region of precipitation associated with the trailing cyclone is following a similar path and is centered over Alabama at 10/2235.

Several features on these radar summaries are worthy of note at this time. First, although generally light precipitation (VIP level 1) is found in most of the first precipitation region, a large region of heavier echo, apparently convective, with tops to 32,000 ft, is present south of North Carolina at 10/1735. This corresponds in position to the frontal zone as well as the location of the developing small-scale cyclone (Fig. 6.2). Although the data coverage is not as good, it appears that this cyclone, like the Jan 19 small-scale cyclone, traveled along the trailing edge of a region of heavy precipitation. Precipitation amounts as large as with the Jan 19 cyclone may well have fallen offshore. Second, the precipitation region at 10/1735 takes the striking form of three large bands, oriented ENE-WSW. (The first band extends from southern New Jersey to northeastern Tennessee, the second band extends from Cape Hatteras to central Georgia, and the third band extends from off the Carolina coast to the Florida panhandle.) Because the bands are oriented along-shear, the pattern is suggestive of symmetric instability. Finally, much upright convection is taking place along the Gulf Coast, with tops to 47,000 ft, and two tornado watch boxes have been posted in Alabama, Georgia, and Florida.

The vertical structure of the cyclone is difficult do determine from the observations. A weak upper level trough was known to be present and was tracked in real time across the southeastern United States, using primarily water vapor imagery, and was interpreted as producing the roundish precipitation region described above. Because the trough was fast-moving, time series of upper air observations are not as useful as in the first case study for discerning the structure of the cyclone. Considerable small-scale structure was also apparently present, so we shall employ compositing techniques to depict the upper-level structure.

The vorticity maximum appeared most prominently across the Carolinas at 800 mb, above the level of the coastal front. Fig. 6.6 shows the wind structure centered at 10/18, at which time the surface cyclone was just south of Wilmington, NC. This figure includes upper air observations for the period between 10/12 and 11/00. Observations not taken at

10/18 were shifted relative to the geography by a time-space conversion based on the velocity of the small-scale cyclone in the NGM. The need and utility of this conversion may be seen by considering a few selected "adjacent" observations. Plotted near the end of the Florida panhandle are two 11/00 observations, one having a 30 kt west wind and the other having a 35 kt south-southwest wind. These winds appear to be more in conflict than any other pair of winds on the map, yet because they were taken synchronously, they have not been shifted relative to each other. On the other hand, several pairs of observations which have been juxtaposed by the time-space conversion show quite good agreement, such as the observations in southern South Carolina, western West Virginia, and western Virginia. The conflicts induced by the time-space conversion are in general smaller than those inherent in the observations.

As for the small-scale cyclone, the map shows a vorticity structure elongated in the same direction as the bands noted in Fig. 6.5 for the same time. Across southern Georgia, southern South Carolina, and offshore southeast of South Carolina, winds are generally strong from the west-southwest at 35-50 kt. Lighter southwesterly winds prevail from northern South Carolina to the Cape Hatteras area. Most of the relative vorticity associated with the difference in wind between these two regimes is of the shear form, with a magnitude of about 5×10^{-5} sec^{-1}, although some curvature is apparent offshore near the location of the surface cyclone.

The vertical stratification of the environment has been investigated by Emanuel (1988), who reported data from a pair of M-surface aircraft soundings for this case. The locations of the two soundings, after applying the time-space conversion, are shown by the nearly vertical lines in Fig. 6.6. The earlier sounding (Fig. 6.7) was taken within the light precipitation region ahead of the vorticity center and shows high relative humidities and nearly neutral stratification with respect to moist slantwise ascent. A conventional vertical sounding, shown in the same figure for comparison, is much stabler. The contrast between the two soundings indicates the large amount of shear in the environment, as well

as the lack of upright convective instability over land. The later sounding (Fig. 6.8) was taken after the passage of the vorticity center and behind the region of precipitation. Although the temperature structure is grossly similar to the earlier M-surface sounding, the presence of deep unsaturated layers and temperature departures of several degrees from a moist adiabat indicate that slantwise convective adjustment was no longer occurring.

Section 6.2: The NGM Forecast

The NGM forecast of this small-scale cyclone, from the 0210/00 forecast run, was a much more accurate forecast of the location and intensification of the cyclone than the NGM forecast of the 19 Jan small-scale cyclone. In both large and small scale aspects, the 1000 mb level forecast maps (Fig. 6.9) are a close match to the subjectively analyzed surface maps (Figs. 6.1-6.4). At 10/12, both maps show the intense cyclone to the northwest, the weaker cyclone south of Bermuda, the col between them east of Cape Hatteras, the weak northeasterlies across the Carolinas, the broad southerlies in the warm air to the south, and the large cyclone (off the edge of the map in Fig. 6.1) which is present over the northern Gulf of Mexico. Missing from the F12 NGM map is the small-scale cyclone off Cape Hatteras, so we will not be able to use the NGM to find out what happened to the cyclone after it moved into the area of poor surface data coverage.

Although the NGM never manages to produce a closed height contour (drawn at 1.5 dam intervals), the developing circulation of the small-scale cyclone of interest is nicely captured by the NGM. At 10/18, a closed circulation center is evident just south of Wilmington NC, which is where the actual small-scale cyclone first appeared at this time. The wind field to the south of the small-scale cyclone is also a close match, with westerlies and southwesterlies over Florida and southerlies to the east of the cyclone. The presence of 1000 mb winds blowing toward higher heights at this and later times, seen here over northern Florida, is due to the downward transport of momentum.

At 11/00, the strongly-curved warm air flow field near the small-scale cyclone in Fig. 6.3 is mirrored nicely in the NGM. The cyclone itself is located 100-200 km too far south in the NGM, as is the larger cyclone to the west. Both errors appear to be due to an overestimate of the southward extent of the cold anticyclone to the north. Similar errors are present at 11/06 in the position of the western cyclone and the offshore surface trough. By F30, there is no longer a closed circulation center evident southeast of Cape Hatteras in the NGM; inspection of upper-level maps leads us to believe that this error is due to the cyclone impinging on the grid mesh area of the NGM and being smoothed out of existence. Aside from this difficulty and the positioning of the small-scale cyclone slightly too far south, the NGM made what can be considered an excellent forecast of the evolution of the small-scale cyclone and associated surface pressure pattern, certainly doing much better than it had for the 19 Jan small-scale cyclone.

A comparison of the 10/18 800 mb winds (Figs. 6.6 and 6.10) shows that the NGM was again correct with the gross features, although it suffered some shortcomings with regard to the detailed structure. In the NGM, the transition zone from strong westerlies to weaker southwesterlies occurs in the vicinity of the central coast of South Carolina, while in the atmosphere it occurred in the vicinity of Wilmington. This position error is consistent with the errors that were found at 1000 mb. In addition to a systematic overestimate of wind speeds, particularly to the north, the NGM also grossly overestimates the weak southwesterly winds north of the vorticity center. The maximum north-south velocity difference across the small-scale cyclone in the NGM is about 15 kt, while in the real atmosphere a typical number is more like 25 kt. Thus, like the first case, the local maximum intensity of the small-scale cyclone is underestimated by the NGM. The gross features, such as the curving southwesterly-to-westerly-to-southwesterly flow to the south of the small-scale cyclone, are handled well by the NGM.

For comparison with the first case, we present in Fig. 6.11 the six-hourly evolution of the 850 mb vorticity in the NGM. The small-scale cyclone first appears as a closed

vorticity center at F06 over southern Mississippi. This is much sooner than in the first case study, and indicates that the initial conditions of the NGM were suitable for immediate small-scale cyclogenesis. At the initial time, a back-trajectory of the small-scale cyclone would place the vorticity center in extreme Eastern Texas, and it can be seen that no vorticity center is initially present there. The closed center south of Alabama does not evolve into the small-scale cyclone, but rather weakens as it moves eastward across Georgia.

As the small-scale cyclone travels eastward, it intensifies. The highest closed isogon is $3x10^{-5}$ s^{-1} at F06, $5x10^{-5}$ s^{-1} at F12, and $7x10^{-5}$ s^{-1} at F18. Through this period the maximum vorticity of the small-scale cyclone in the NGM is larger than any point values of vorticity associated with the trailing larger-scale cyclone over the northern Gulf. The tendency for east-west elongation, seen earlier in the radar maps and 800 mb observed winds, may also be seen in these 850 mb vorticity maps, particulary at later times. After F18, the small-scale cyclone weakens and moves off the edge of the C-grid.

The potential vorticity evolution for this case, from the NGM, is shown in Figs. 6.12-6.15. Plotting formats are the same as were used earlier, except that the IPV maps are taken at slightly higher potential temperature levels. As before, they are chosen to be located in the upper and lower troposphere in the vicinity of the developing small-scale cyclone.

At initialization (Fig. 6.12), the tropopause map is dominated by a strong east-west band of potential temperature gradients stretching across the center of the country. The waviness of the band, particularly at higher temperatures, is not reflected in the upper-level winds (see the 325K-335K IPV map), and advects away after the first twelve hours. Because of the lack of a wind correlation and the rapid reduction in waviness by the dynamics of the NGM, we regard the initial waves to be an unrealistic consequence of the analysis.

The upper-level trough which we have mentioned above appears in the southwestern corner of both the tropopause map and the 325K-335K IPV map as a region of anomalously high potential vorticity. At both these levels, the trough appears as a cutoff region of high potential vorticity, detached from the region of strong gradient to the north, so that according to the NGM analysis this trough is not subject to intensification by the baroclinic instability mechanism of down-gradient advection of potential vorticity. At the surface, a strong potential temperature gradient is present ahead of the short wave. At low levels, potential vorticity over large areas of the map is quite small, less than 0.25 PVU, with slightly higher values in a band extending along the Gulf Coast.

In the next set of maps (Fig. 6.13), attention is immediately drawn to the circular feature in the upper-level maps over northern Louisiana. This is a region of negative absolute vorticity, which appears as a region of negative vorticity on an IPV map and as a region of high potential temperature on a tropopause map. As we have yet to find an actual region of negative potential vorticity on upper-level IPV maps, and as this feature does not appear in later observations or forecast initializations, we infer it to be another product of faulty initial analysis. Its location along the northern border of Mexico at initialization time (not shown) indicates that it was probably a consequence of erratic Mexican sounding data. The presence of this feature means that we cannot use this series of potential vorticity maps as an accurate representation of the real atmosphere, but the fact that the small-scale cyclone was accurately simulated and the difference in propatation speeds between the small-scale cyclone and the negative potential vorticity region allow us to assume that its presence does not detrimentally alter the dynamics of the small-scale cyclone.

The presence of this negative anomaly complicates the interpretation of the upper trough using these maps. The features at upper levels which we wish to concern ourselves with are those with horizontal lengths of 500-1000 km or greater, for it is these features which will be able to induce winds through the depth of the troposphere. With this in mind, we note that at the tropopause level, the 335 K contour makes a permanent deviation

from the central US jet to the subtropical jet over the Gulf of Mexico in the neighborhood of the negative potential vorticity, while at the 325-335 K layer, both the 0.5 PVU and 0.75 PVU contours deviate permanently to the south. We associate these features with the 1000 km-scale upper-level short wave. Thus, paradoxically, the center of the short wave is located near the southern edge of the region of negative potential vorticity.

At lower levels, little has happened during the first six hours. At the surface, the potential temperature contours have remained in place, while the changes in the wind field are as expected for a short-wave moving over southeastern Louisiana from the east. In the 300-310 K layer, the field has changed mostly through simple advection of the pre-existing potential vorticity field.

After another six hours (Fig. 6.14), the negative potential vorticity region has advected rapidly eastward, and the short-wave trough is centered roughly over western Georgia. At lower isentropic levels, a closed 0.5 PVU contour has appeared over southern Georgia, at the same location as the 850 mb vorticity maximum. This positive potential vorticity anomaly was obviously not produced by isentropic advection of potential vorticity.

The final set of maps (Fig. 6.15) shows that the low-level potential vorticity anomaly is amplifying rapidly. Already an 0.75 PVU contour is present, within an environment characterized by less than 0.25 PVU. Surface cooling, a candidate process for low-level generation of potential vorticity, did not produce this anomaly; the scale of the anomaly does not match the scale of the region of surface warm advection. As with the first small-cyclone case study, this potential vorticity was created in place by latent heat release within a localized saturated updraft. The expected decrease in potential vorticity aloft is found at the 325-335 K layer, where the 0.75 PVU contour has moved northward by non-conservative means into southern North Carolina. A trough is still present at tropopause level, though it is now slightly ahead of the position of the low-level potential vorticity anomaly.

Unlike the 19 Jan small-scale cyclone, this NGM cyclone was associated with a single vigorous updraft throughout most of its lifetime. The initial 600 mb vertical motion field (Fig. 6.16) shows the large-scale ascent pattern associated with the upper-level short wave. Upward vertical motion is present across Oklahoma, east Texas, and the northern Gulf of Mexico, with weaker upward motion to the east. The eastern edge of the downward motion half of the couplet may be seen over central Texas. Within the first six hours, two localized updrafts have formed. The northern updraft, in eastern Mississippi, was short-lived and apparently was inhibited by advection from the west of warm, dry air above 500 mb. The southern updraft, at the western edge of the Florida panhandle, would continue to intensify and rapidly evolve into the dominant updraft. The 850 mb vorticity maximum at this time is located in a compromise position between the two updrafts.

After 12 hours, the primary updraft has come to dominate the vertical motion field. This updraft, already stronger than the small-scale updrafts in the first case study, is partially surrounded by regions of downward vertical motion. The updraft continues to intensify, reaching a maximum value at 600 mb of 2.0 Pa s^{-1} at F18. During this period, the 850 mb vorticity center and low-level potential vorticity anomaly are located slightly to the west of the 600 mb vertical motion maximum. The updraft weakens after F18 as it reaches the edge of the grid.

Section 6.3: Diagnosis of vertical and slantwise stability in the NGM forecast

The updraft formed over a period of eighteen hours, much more slowly than the updrafts in the first small-scale cyclone case. Because of this gradual growth, we are able to examine the updraft in its development stage. Fig. 6.17 shows the θ_e and θ_e* fields during this development time, at 1 K increments between 325 K and 333 K. At this time, the updraft is centered over southeastern Georgia at 600 mb. At low levels, the intense surface frontal zone is apparent in the sharp gradients of θ_e*, but air in these frontal zones

is only saturated to the west of the updraft position. The lowest saturation in the updraft core appears at 800 mb, with the 328 K θ_e contour along the Georgia-Florida border and the 325 K contour at the latitude of Savannah.

Surprisingly, the absolute vertical instability in this case is confined to the southern portions of the updraft. A parcel originating on the 328 K contour is unstable when lifted through 700 mb, 600 mb, 500 mb, and 400 mb, but a parcel originating on the 325 K contour is at best neutral when lifted through those levels. To the west, very large potential instability is present for parcels lifted from 800 mb or 900 mb, but the subsidence occurring over these areas is helping to suppress updraft development. Nevertheless, a small updraft has formed to the east of the first updraft by F18 (Fig. 6.16), and this updraft intensified very rapidly during the following six hours.

A combination of factors caused us to investigate the hypothesis that this updraft was at least partly driven by symmetric instability. First, the updraft reached an intensity twice that of the second updraft in the first case study, even though the absolute vertical instability appeared to be much smaller. Second, the center of the updraft was displaced northward, away from the region of convective instability and over a region of convective neutrality. Finally, the updraft developed much more slowly than the updrafts in the first case, consistent with the slower time scale of symmetric instability.

This hypothesis was confirmed by several methods, including a direct diagnosis of air parcel accelerations. The clearest depiction of slantwise instability is a pair of cross sections taken normal to the shear across the developing updraft at F12 (Fig. 6.18), extending from eastern Tennessee on the left to Lake Okeechobee on the right. The upper panel shows M surfaces (M is defined here as $v_n + x/f$, where x is positive toward the right and v_n is the wind into the page) and lines of constant θ_e*. The strong shear of the environment is indicated by the large departures of the M surfaces (dashed lines) from the vertical. The presence of slantwise instability in saturated air (margin of saturation denoted by wavy line) is inferred when θ_e* surfaces have a steeper slope than M surfaces.

Similarly, the presence of upright instability is inferred when θ_e* surfaces pass through the vertical.

Four regions with differing stability characteristics may be found within the cloudy air. Above 300 mb toward the northern end of the cross section, the cloudy air is stable along the tropopause. In the lower northern part of the cloudy air, the θ_e* surfaces are aligned with *M* surfaces, so the environment is slantwise neutral. In the central portion of the cloud, to the left of the 326 K isotherm, the air is convectively stable to upright displacements but unstable to slantwise displacements. Finally, the southern portion of the cloud, to the right of the 326 K isotherm, is unstable to upright displacements. Consistent with the fact that no convectively parameterized precipitation was occurring in the vicinity of this updraft, the absolute upright convective instability is confined to 800 mb and above.

The bottom panel shows the two-dimensional flow in the plane of the cross section. Because this cross section was taken normal to the track of the small-scale cyclone, the vectors show the two-dimensional air motion relative to the cyclone. The inflow of the updraft is from the south at low and middle levels, while strong outflow is observed in both directions at the tropopause level. Most parcel trajectories slope to the left, as would be expected for slantwise instability. A specific prediction of symmetric instability theory which we look for here is that parcel trajectories lie between *M* surfaces and θ_e* surfaces. A comparison of the two cross sections confirms that this condition is satisfied in the most vigorous parts of the updraft. Solid circles have been drawn at the origins of vectors oriented between *M* surfaces and θ_e* surfaces, and these dots have been transcribed to the upper panel. It may be seen that updrafts with the expected slope are found throughout the middle and upper portions of the regions of slantwise and upright instability. Apparently, air is not accelerating upward sufficiently fast to attain a slope steeper than the *M* surfaces until it reaches the central portions of the updraft.

We conclude this analysis with a plot of vertical motion and vorticity tendencies for the updraft at F12 (Fig. 6.19). The point chosen is located in the center of the cross

sections of Fig. 6.18. We have retained the same scale as in Chapter Five, and this has caused the ω profile to extend off the left edge of the graph. We have allowed it to reappear on the right-hand side of the graph, where it may be seen that ω attains a value of nearly 1.4 Pa s^{-1}. Also nearly going off the edge of the graph is the plot of ζ_g, which is below -9×10^{-5} s^{-1} at 400 mb, implying a negative absolute geostrophic vorticity at that level. Furthermore, the ζ_{gp} tendency is positive at almost all levels between 800 mb and 300 mb, implying further warming and intensification of the ζ_g dipole at low and high levels. This tendency is consistent with our diagnosis from the cross sections of slantwise and possible convective instability at this point between 800 mb and the tropopause.

The relative vorticity ζ shows much less of a dipole than the geostrophic vorticity between low and high levels. Stretching and shrinking are acting to increase the vorticity perturbation at low and high levels, while vertical advection is inducing an increase of vorticity at mid-levels. So the vertical motion is acting in the proper sense on the relative vorticity, to try to bring it closer to the geostrophic vorticity. Finally, because the relative vorticity is still lagging the geostrophic relative vorticity, the updraft continues to intensify, as shown by the negative ω_p tendency below 700 mb and the positive ω_p tendency above 500 mb.

In summary, this updraft was much like the updrafts in the first small-scale cyclone case in that it was driven by latent heat release and convective instability. The primary difference in this updraft was that the bulk of the instability was slantwise in character. This apparently affected the updraft by resulting in a longer spinup time, but did not lead to a two-dimensional structure for the updraft, as would be expected for pure moist symmetric instability. We believe this was due to the presence of convective instability in a portion of the updraft. Banded structures were observed in other NGM forecast runs for this period in regions where symmetric instability was present but convective instability was not.

The symmetric neutrality observed in the real atmosphere for this case indicates that the atmosphere is much more efficient than the NGM at adjusting to symmetric instability.

This is not surprising, since the atmosphere is capable of supporting structures on a much smaller scale, and the observed cross-shear scale of the bands in the radar summary was only a couple of hundred kilometers. It implies, though, that the NGM will be subject to short-range forecasting errors in precipitation during slantwise adjustment events, producing the adjustment through updrafts on larger space and time scales than the atmosphere.

CHAPTER SEVEN

DISCUSSION

Section 7.1: Principal Conclusions

From a statistical climatology of all cyclones occurring over central and eastern North America and the adjacent Atlantic Ocean, it was found that the majority of cyclones were short-lived, small-scale cyclones, with apparent horizontal half-wavelengths of between 150 km and 750 km and durations of 48 hours or less. Most of these small-scale cyclones were quasi-stationary and appeared only in mountainous regions or along lee slopes. Those small-scale cyclones which were mobile exhibited a preference for cyclogenesis at the northwestern margins of warm bodies of water, specifically the Gulf of Mexico and the Atlantic Ocean between Florida and South Carolina.

A specific small-scale cyclone, which formed near the GALE region on 19 Jan 1986, was selected for case study analysis on the basis of its small scale, the availability of observations with high spatial and temporal resolution, and its apparent strong influence on local weather. This small-scale cyclone had a total width of 400 km and an observed surface pressure amplitude of 2-3 mb. The cyclone was warm-core, with positive relative vorticity confined to below 700 mb. In the absence of an upper level trough, the low-level vorticity was produced primarily through diabatic generation of potential vorticity at low levels through latent heat release. The destabilization which led to the convective overturning appeared to be due to a combination of large-scale ascent induced by a synoptic-scale development to the northwest and differential advection of high equivalent potential temperature boundary layer air from the south and southeast. The resulting precipitation was substantial, with 75 mm of rain falling in 18 hours over Cape Hatteras.

The operational NMC Nested Grid Model forecast run for 19 Jan 1986 also produced a small-scale cyclone, and the grid-point forecast data was employed extensively for diagnostic purposes. The three-dimensional pattern of vorticity and potential vorticity generation in the NGM, although weaker, was similar to the observed patterns. The vertical motion in the NGM was driven by upright convective instability at levels ignored by the convective parameterization, resulting in an updraft which was effectively a very large cumulus cloud.

A second small-scale cyclone, from 10 Feb 1986 was selected for comparison with the 19 Jan 1986 small-scale cyclone. This second cyclone formed within a strongly baroclinic region, but advection of potential vorticity was again found to be much less important than low-level diabatic generation of potential vorticity. In the atmosphere, moist adjustment occurred along M surfaces, while the NGM updraft was strongly unstable to slantwise ascent. Unlike the first case, the timing and location of small-scale cyclogenesis were well forecasted by the NGM.

Section 7.2: Studies of Related Phenomena

Until very recently, there have been few case studies on small-scale cyclones occurring in warm advection regions during wintertime in middle latitudes. The most extensive work has been done on springtime "medium-scale" disturbances along the Baiu Front in Japan and China (Matsumoto *et al.* 1970, Akiyama 1989 and refs.). These medium-scale disturbances appear to be similar to the small-scale cyclones examined here in that they are warm-core at middle and upper levels, have positive vorticity confined to 600 mb and below, form in the absence of moderate or strong upper level forcing, have little or no vertical tilt, have horizontal wavelengths of 1000 km or less, and are associated with large amounts of precipitation. Studies have indicated that latent heat release is critical to the development of these disturbances. In particular, the modelling study by Nitta and

Ogura (1972) describes the numerical simulation of a small-scale cyclone which is strikingly similar to the NGM forecasts of the GALE small-scale cyclones, but on a larger scale commensurate with the increased grid spacing.

In the United States, case studies of apparently similar phenomena have been performed by Bosart (1984), Keshishian and Bosart (1987), and Wash *et al.* (1990). A direct phenomenological comparison with these studies is difficult, however, because study of the small-scale cyclone was not the main concern of Keshishian and Bosart (1987) and the remaining two studies do not present detailed descriptions of vertical structure.

Several recent papers have dealt at least peripherally with the small-scale cyclogenesis event of GALE IOP 2 (Riordan 1990, Holt *et al.* 1990, Doyle and Warner 1990). Riordan (1990) was directed toward the coastal front development, but it includes detailed surface analyses of the small-scale cyclone, which formed off the coast of Georgia and followed a similar track up the East Coast as the 19 Jan 1986 small-scale cyclone. The study by Holt *et al.* was primarily a modelling sensitivity study, but the simulations showed a shallow small-scale cyclone and a deep vertical circulation. Also prominent was a strong southerly low-level jet on the right flank of the small-scale cyclone. These features are all similar to the 19 Jan 1986 cyclone examined in Chapters Three, Four, and Five. The numerical simulation of this jet was found to be sensitive to the boundary layer parameterization, with the strongest jet produced by what the authors considered to be the most accurate parameterization.

The most extensive analyses of this case were performed by Doyle and Warner (1990). They found that the small-scale cyclone had a horizontal width of 500 km and was apparently warm-core, with the positive relative vorticity a maximum 60 mb above the ground and negative above 700 mb. As with the 19 Jan cyclone, the small-scale cyclone was colocated with the trailing edge of a region of heavy precipitation. Vertical motion increased ahead of the small-scale cyclone and decreased very rapidly behind the small-scale cyclone. Heat fluxes from the sea surface were more important prior to the

cyclogenesis event, acting to precondition and destabilize the environment, than during the cyclogenesis event. The small-scale cyclone had similar effects on the coastal front as the cyclone studied by Keshishian and Bosart (1987).

A small-scale cyclone which formed in July over the Baltic Sea has recently been studied by Kristjansson (1990). The small-scale cyclone had a total diameter of about 300 km and formed within a larger-scale cyclone. Kristjansson found that although quasi-geostrophic forcing of vertical motion was present, most of the surface vorticity tendency was due to latent heat release. Large amounts of precipitation were observed, and the environment was characterized by weak conditional stability. In the model simulation of this case, the ascent region was confined to a horizontal distance of three or four grid points (150 km), and the region of maximum ascent was unstable to slantwise displacements. In contrast to the present case, large amounts of vorticity were present initially at the surface, and Kristjansson inferred a CISK-type mechanism for the maintenance of the cyclone.

Theoretical studies have not dealt specifically with surface vorticity spinup due to slantwise or upright convective adjustment displaced from the primary region of baroclinic cyclogenesis. Recent theoretical work on modal Eady-type baroclinic instability (Emanuel *et al.* 1987) or finite-amplitude baroclinic development (Montgomery and Farrell 1990) with ascent regions characterized by very weak slantwise stability have shown that substantial small-scale potential vorticity generation occurs near the ground in response to the strong localized ascent. Presumably, if the region of moist neutrality were taken to be displaced horizontally from the initial upper and lower temperature anomalies, small-scale cyclogenesis would occur ahead of the baroclinic wave within the moist-neutral region.

Section 7.3: Implications

The basic mechanism we have described for the development of extratropical wintertime small-scale cyclones, that of slantwise or upright convective adjustment, is a

common occurrence in the cyclone environment. Observations of slantwise stratification in wintertime mid-latitude cyclones have consistently shown that the ascent regions of baroclinic cyclones are frequently characterized by slantwise moist neutrality (Emanuel 1988, Nuss and Kamikawa 1990, Reuter and Yau 1990, Sanders and Bosart 1985, Sanders 1986). Model simulations of explosive oceanic cyclones have indicated that warm fronts are regions of vigorous slantwise neutral or slantwise unstable ascent, and that the low-level potential vorticity production from these warm frontal ascent regions makes a substantial contribution to the explosive growth of the surface cyclones (Kuo and Reed 1988, Kuo and Low-Nam 1990). The possible contribution to explosive development from convective adjustment near the center of cyclones has also been noted in observational studies (Tracton 1973).

The cases we have examined differ from the above combinations of baroclinic intensification and diabatic potential vorticity generation. In the 19 Jan 1986 small-scale cyclone, slantwise convective adjustment took place several hundred kilometers away from the primary cyclone development. The 10 Feb 1986 small-scale cyclone occurred in conjunction with a weak upper level trough but in the absence of significant baroclinic development. Because large-scale intensification was either spatially separate or nonexistent, we have been able to examine the effects of slantwise or upright convective adjustment in near-isolation. Even the 25 Jan 1986 small-scale cyclone (Doyle and Warner 1990) occurred in combination with a coastal front, making it difficult to isolate the important dynamical effects in that particular case.

This spatial separation or lack of large-scale baroclinic development is in fact critical to small-scale cyclogenesis. For example, if the 19 Jan 1986 slanwise convective adjustment had occurred 500 km to the northwest, it would simply have been interpreted as part of the synoptic-scale intensification. Consequently, assuming that the mid-latitude environment is characterized by regions of slantwise potential instability, small-scale cyclogenesis is contingent upon either the presence of spatial inhomogeneities of slantwise

potential instability or the lack of conditions favorable for adiabatic baroclinic growth. Since warm bodies of water such as the Gulf of Mexico or the Atlantic Ocean over and southeast of the Gulf Stream act to locally increase potential instability through surface fluxes of heat and moisture, small-scale cyclogenesis should be expected near those areas in cases where large-scale cyclogenesis occurs 500-1000 km to the north or northwest. If large-scale development occurs within 500 km of the coast, small-scale cyclogenesis could be masked by the large-scale growth; development farther than a Rossby radius from the coast could fail to induce sufficient vertical motion to allow the atmosphere to become destabilized simultaneously over a large area.

The NGM small-scale cyclones were characterized by 200-300 km wide updrafts. In the real atmosphere, the scale of the updrafts may be much smaller. Our data has not been sufficiently detailed to enable us to diagnose the small-scale structure of the slantwise updrafts. Two-dimensional moist instability theory and simulations of moist convective adjustment (Bennetts and Hoskins 1979, Xu 1989, Knight and Hobbs 1988) show that depending on the slopes of the M and θ_e surfaces, the horizontal scale of the updrafts should be on the order of 50-100 km. A fully non-linear study of two-dimensional dry symmetric instability (Thorpe and Rotunno 1989) has shown that if the initial instability is sufficiently large, the initial banded structure eventually breaks down into a turbulent overturning and mixing. To our knowledge, fully three-dimensional modelling studies of moist slantwise convection have not been performed.

The apparent lack of realism of the NGM updrafts suggests that the present convective parameterization scheme should be expanded to include higher levels in the vertical, and that a slantwise convective adjustment scheme (*e. g.*, Nordeng 1987) should be implemented. It is not clear, however, that the implementation of these additional parameterizations would necessarily improve the forecasts. We have already noted that the 10 Feb 1986 small-scale cyclone was well forecasted by the 10/00 NGM forecast run. Kuo and Low-Nam (1990) find that when the local forcing is strong, numerical simulations

which explicitly resolve convection tend to be superior to numerical simulations with simple cumulus parameterizations. R. Reed (personal communication) has noted that mesoscale models with high horizontal resolution (such as 30 km) can realistically resolve slantwise neutral or weakly unstable updrafts, obviating the need for a slantwise convective parameterization.

Finally, as was also concluded by Kristjansson (1990), the accurate forecast of these small-scale cyclones depends crucially on the initial analyzed distribution of specific humidity. The error in forecasting the 19 Jan 1986 cyclone was at least partly due to a poor initialization of humidity offshore, such that saturation was not analyzed close to shore in areas where radar indicated that precipitation was occurring. The initial unstable updraft formed several hundred kilometers offshore in the NGM, where large-scale ascent was finally able to produce saturation. NGM forecasts of the 10 Feb 1986 small-scale cyclone made prior to 10/00 had the small-scale cyclone passing over northern Virginia; examination of the model initializations (not shown) indicated that because the environment was potentially slantwise unstable everywhere, small-scale cyclogenesis occurred in whichever location was initialized as being saturated. This sensitivity to specific humidity is unfortunate, because new surface-based observing systems, such as wind profilers, do not measure specific humidity in an air column.

ACKNOWLEDGEMENTS

I wish to acknowledge the support and encouragement of Prof. Randall Dole, who directed me toward this research topic and provided continued scientific input throughout the course of the work. Prof. Kerry Emanuel provided the opportunity for me to become involved with the Genesis of Atlantic Lows Experiment, and offered many helpful ideas and suggestions on various aspects of the case studies. This research would not have been possible without the cooperation of all those who participated in GALE. The analysis software used for this study was GEMPAK, which was developed by NASA. The potential vorticity inversion software was provided by Chris Davis. The 1000 mb vstat anomalies were calculated by Peter Neilley, who also wrote various routines used in the preparation of figures. Finally, I wish to thank all the professors and students whom I have come to for advice and suggestions, particularly Peter Neilley, Joshua Wurman, and Chris Davis.

This research was partially supported by grant no. ATM-8617132 from the National Science Foundation.

APPENDIX A

List of Symbols

Symbol	Name	Definition and/or First Use
	Roman characters	
C	Rainfall parameterization constant	(3.2)
C_p	Heat capacity of air at constant pressure	
dA	Differential area	(5.29)
F	Fraction of parcels within grid box that are saturated	Section 4.2
$F(p)$	Unknown function of pressure	(5.26)
$F''(p)$	Second derivative of F(p) with respect to pressure	
f	Coriolis parameter	
f_o	constant Coriolis parameter	
f_r	Fractional cloud cover	(3.2)
g	Gravity	9.8 m s^{-2}
H	Diabatic heating rate	(5.5)
k	Zonal wavenumber	(2.1)
L	Latent heat of evaporation	
L_D	Total domain length	Section 5.2c
L_R	Rossby radius	(5.21)
L_S	Horizontal scale of stratification variations	(5.21ff)
l	Meridional wavenumber	(2.1)
M	Pseudoangular momentum	Section 6.3
P	Vertical depth (pressure)	(5.21)
p	Pressure	
p_B	Pressure at lower boundary	(5.22)
p_T	Pressure at upper boundary	(5.22)
p_o	Reference pressure level	(5.13)

$\boldsymbol{Q}$	Q-vector	(5.2a-b)
Q	Potential vorticity	(1.1) 1 PVU = 1×10^{-6} m^2 K kg^{-1} s^{-1}
Q_e	Equivalent potential vorticity	(1.2)
q	Specific humidity	(4.1)
q_{new}	Newly calculated specific humidity	(4.1)
q_o	Specific humidity computed in grid box	Section 4.2
q_s	Saturation specific humidity	(4.1)
R	Gas constant for dry air	287 J kg^{-1} K^{-1}
R_v	Gas constant for water vapor	461 J kg^{-1} K^{-1}
RR	Rainfall rate	(3.2)
r	Cyclone radius	Section 2.1
$\tilde{S}$	Effective stability	(5.12)
T	Temperature	
T_{new}	Newly calculated temperature	(4.1)
$\overline{T}$	Mean layer temperature	(3.1)
$\boldsymbol{u}$	Horizontal vector wind	(u, v)
$\boldsymbol{u_g}$	Horizontal vector geostrophic wind	(u_g, v_g)
u	Wind component in x-direction	
u_g	Geostrophic wind component in x-direction	
v	Wind component in y-direction	
v_g	Geostrophic wind component in y-direction	
v_n	Wind component normal to cross section	Section 6.3
¥	Half the fractional range of q in grid boxes	Section 4.2
Z	Geopotential height	

Greek characters

α	Specific volume	
β	$\partial f/\partial y$	
Γ_d	Dry adiabatic lapse rate	(5.9ff)
Γ_m	Moist adiabatic lapse rate	(5.9ff)
$\delta()$	Finite difference derivative operator	(3.1)
ε	L_S/L_R	(5.24)

ζ	Relative vorticity	$\partial v/\partial x - \partial u/\partial y$
ζ_g	Geostrophic relative vorticity	(5.15)
ζ_{gp}	Partial derivative of ζ_g with respect to pressure	(5.45)
ζ_θ	Isentropic relative vorticity	(1.1) Vorticity of the horizontal wind, evaluated on an isentropic surface
$\zeta_{\theta e}$		(1.2) Vorticity of the horizontal wind, evaluated on surfaces of constant θ_e
θ	Potential temperature	$T\left(\frac{1\text{x}10^5\ \text{Pa}}{p}\right)^{\frac{2}{7}}$
θ'	θ perturbation from large-scale mean	Section 5.4a
θ_e	Equivalent potential temperature	
θ_e^*	Saturated equivalent potential temperature	
θ_{lift}	Parcel lifted potential temperature	(5.13)
κ	R/C_p	
σ	Stratification	(5.6)
$\overline{\sigma}$	Level mean stratification	(5.2c)
$\tilde{\sigma}$	Effective stratification	(5.19)
$\tilde{\sigma}_o$	Domain mean stratification	Section 5.2c
Φ	Geopotential (gZ)	(5.16)
ω	Omega (vertical motion in pressure coordinates)	
ω_0	ω to lowest order in ε expansion	(5.25)
ω_1	ω to first order in ε expansion	(5.25)

Operators

∂/∂^*	Partial derivative operator	
$*_x$	Partial derivative with respect to x	
$*_y$	Partial derivative with respect to y	
$*_p$	Partial derivative with respect to p	
D^*/Dt	Substantial derivative	$\partial^*/\partial t + \partial^*/\partial x + \partial^*/\partial y + \partial^*/\partial p$
D_H^*/Dt	Horizontal substantial derivative	$\partial^*/\partial t + \partial^*/\partial x + \partial^*/\partial y$ (5.47)
∇	Horizontal grad operator	$(\partial/\partial x\ ,\ \partial/\partial y\ )$
∇^2	Horizontal (2-d) Laplacian operator	
$[*]$	Horizontal averaging operator	(5.30)

BIBLIOGRAPHY

Akiyama, T., 1989: Large, synoptic, and meso scale variations in the Baiu Front, during July 1982. Part I: Cloud features. *J. Meteorol. Soc. Japan* **67**, 57-81.

Anthes, R. A., Y.-H. Kuo, and J. R. Gyakum, 1983: Numerical simulations of a case of explosive marine cyclogenesis. *Mon. Wea. Rev.* **111**, 1174-1188.

Arkin, P. A., and B. N. Meisner, 1987: The relationship between large-scale convective rainfall and cold cloud over the Western Hemisphere during 1982-84. *Mon. Wea. Rev.* **115**, 51-74.

Aubert, E. F., 1957: On the release of latent heat as a factor in large-scale atmospheric motions. *J. Meteorol.* **14**, 527-542.

Bell, G. D., and L. F. Bosart, 1988: Appalachian cold-air damming. *Mon. Wea. Rev.* **116**, 137-161.

Bennetts, D. A., and B. J. Hoskins, 1979: Conditional symmetric instability - a possible explanation for frontal rainbands. *Quart. J. Roy. Meteorol. Soc.* **105**, 945-962.

Bosart, L. F., 1981: The Presidents' Day snowstorm of 18-19 February 1979: A subsynoptic-scale event. *Mon. Wea. Rev.* **109**, 1542-1566.

_____, 1984: The Texas coastal rainstorm of 17-21 September 1979: An example of synoptic-mesoscale interaction. *Mon. Wea. Rev.* **112**, 1108-1133.

_____, C. J. Vaudo, and J. H. Helsdon, Jr., 1972: Coastal frontogenesis. *J. Appl. Meteorol.* **11**, 1236-1258.

Brandes, E. A., 1990: Evolution and structure of the 6-7 May 1985 mesoscale convective system and associated vortex. *Mon. Wea. Rev.* **118**, 109-127.

Bretherton, F. P., 1966: Critical layer instability in baroclinic flows. *Quart. J. Roy. Meteorol. Soc.* **82**, 325-334.

Charney, J. G., 1947: The dynamics of long waves in a baroclinic westerly current. *J. Meteorol.* **4**, 135-163.

_____, and A. Eliassen, 1964: On the growth of the hurricane depression. *J. Atmos. Sci.* **21**, 68-75.

Chung, Y.-S., K. D. Hage, and E. R. Reinelt, 1976: On lee cyclogenesis and airflow in the Canadian Rocky Mountains and the East Asian mountains. *Mon. Wea. Rev.* **104**, 879-891.

Colucci, S. J., 1976: Winter cyclone frequencies over the eastern United States and adjacent western Atlantic. *Bull. Amer. Meteorol. Soc.* **57**, 548-553.

Corfidi, S. F., and K. E. Comba, 1989: The Meteorological Operations Division of the National Meteorological Center. *Wea. Forecasting* **4**, 343-366.

Craig, G., and H.-R. Cho, 1988: Cumulus heating and CISK in the extratropical atmosphere. Part I: Polar lows and comma clouds. *J. Atmos. Sci.* **45**, 2622-2640.

Danard, M. B., 1964: On the influence of released latent heat on cyclone development. *J. Appl. Meteorol.* **3**, 27-37.

_____, 1966: A quasi-geostrophic numerical model incorporating effects of release of latent heat. *J. Appl. Meteorol.* **5**, 85-93.

Danielson, E. F., and R. S. Hipskind, 1980: Stratospheric-tropospheric exchange at polar latitudes in summer. *J. Geophys. Res.* **85**, 393-400.

Davis, C. A., 1990: Cyclogenesis Diagnosed with Potential Vorticity. Ph. D. Thesis, Center for Meteorology and Physical Oceanography, MIT, Cambridge, MA. 171 pp. and counting.

_____, and K. A. Emanuel, 1988: Observational evidence for the influence of surface heat fluxes on rapid maritime cyclogenesis. *Mon. Wea. Rev.* **116**, 2649-2659.

DiMego, G. J., 1988: The National Meteorological Center Regional Analysis System. *Mon. Wea. Rev.* **116**, 977-1000.

Dirks, R. A., J. P. Kuettner, and J. A. Moore, 1988: Genesis of Atlantic Lows Experiment (GALE): An overview. *Bull. Amer. Meteorol. Soc.* **69**, 148-160.

Doyle, J. D., and T. T. Warner, 1990: Mesoscale coastal processes during GALE IOP 2. *Mon. Wea. Rev.* **118**, 283-308.

Eady, E. T., 1949: Long waves and cyclones waves. *Tellus* **1**(3), 33-52.

Eliassen, A., 1983: The Charney-Stern theorem on barotropic-baroclinic instability. *Pure Appl. Geophys.* **121**, 563-572.

Emanuel, K. A., 1983: On assessing local conditional symmetric instability from atmospheric soundings. *Mon. Wea. Rev.* **111**, 2016-2033.

_____, 1989: The finite amplitude nature of tropical cyclogenesis. *J. Atmos. Sci.* **46**, 3431-3456.

_____, M. Fantini, and A. J. Thorpe, 1987: Baroclinic instability in an environment of small stability to slantwise moist convection. Part I: Two-dimensional models. *J. Atmos. Sci.* **44**, 1559-1573.

_____, and R. Rotunno, 1989: Polar lows as arctic hurricanes. *Tellus* **41A**, 1-17.

Ertel, H., 1942a: Ein neuer hydrodynamischer Wirbelsatz. *Meteorol. Zeitschr.* **59**, 277-281.

_____, 1942b: Ein neuer hydrodynamischer Erhaltungssatz. *Die Naturwissenschaften* **30**, 543-544.

Farrell, B. F., 1989: Transient development in confluent and diffluent flow. *J. Atmos. Sci.* **46**, 3279-3288.

Forbes, G. S., R. A. Anthes, and D. W. Thomson, 1987: Synoptic and mesoscale aspects of an Appalachian ice storm associated with cold-air damming. *Mon. Wea. Rev.* **115**, 564-591.

Ford, R. P., and G. W. K. Moore, 1990: Secondary cyclogenesis -- comparison of observations and theory. *Mon. Wea. Rev.* **118**, 427-446.

Fraedrich, K., and J. L. McBride, 1989: The physical mechanism of CISK and the free-ride balance. *J. Atmos. Sci.* **46**, 2642-2648.

Fujita, T. T., 1963: Analytical mesometeorology: a review. Severe Local Storms, *Meteorol. Monogr.* **5**(27), American Meteorological Society, pp. 77-125.

GALE Project Office, 1985: Genesis of Atlantic Lows Experiment (GALE) Experiment Design. GALE Project Office, Boulder. 199 pp.

_____, 1986: Genesis of Atlantic Lows Experiment (GALE) Operations Plan. GALE Project Office, Boulder. 72 pp. plus appendices.

Gall, R. L., 1976: A comparison of linear baroclinic instability theory with the eddy statistics of a general circulation model. *J. Atmos. Sci.* **33**, 349-373.

Gyakum, J. R., J. R. Anderson, R. H. Grumm, and E. L. Gruner, 1989: North Pacific cold-season surface cyclone activity: 1975-1983. *Mon. Wea. Rev.* **117**, 1141-1155.

Haltiner, G. J., and R. T. Williams, 1980: Numerical Prediction and Dynamic Meteorology, second edition. John Wiley and Sons. 477 pp.

Hayden, B. P., 1981: Secular variation in Atlantic coast extratropical cyclones. *Mon. Wea. Rev.* **109**, 159-167.

Haynes, P. H., and M. E. McIntyre, 1987: On the evolution of vorticity and potential vorticity in the presence of diabatic heating or other forces. *J. Atmos. Sci.* **44**, 828-841.

Hoke, J. E., 1987: Improving the horizontal resolution of the Nested Grid Model. Tech. Procedures Bulletin 368, National Weather Service. 9 pp.

_____, N. A. Phillips, G. J. DiMego, J. J. Tuccillo, and J. G. Sela, 1989: The Regional Analysis and Forecast System of the National Meteorological Center. *Wea. Forecasting* **4**, 323-334.

Holt, T., S. Chang, and S. Raman, 1990: A numerical study of the coastal cyclogenesis in GALE IOP 2: Sensitivity to PBL parameterizations. *Mon. Wea. Rev.* **118**, 234-257.

Hoskins, B. J., and P. Berrisford, 1988: A potential vorticity perspective of the storm of 15-16 October 1987. *Weather* **43**, 122-129.

_____, M. E. McIntyre, and A. W. Robertson, 1985: On the use and significance of isentropic potential vorticity maps. *Quart. J. Roy. Meteorol. Soc.* **111**, 877-946.

_____, and Pedder, M. A., 1980: The diagnosis of middle latitude synoptic development. *Quart. J. Roy. Meteorol. Soc.* **106**, 707-720.

Kelsey, K., 1925: A new method of charting storm frequency. *Mon. Wea. Rev.* **53**, 251-252.

Keshishian, L. G., and L. F. Bosart, 1987: A case study of extended East Coast frontogenesis. *Mon. Wea. Rev.* **115**, 100-117.

Klein, W. H., 1957: Principal tracks and mean frequencies of cyclones and anticyclones in the Northern Hemisphere. Research Paper No. 40, U. S. Weather Bureau. 60 pp.

Knight, D. J., and P. V. Hobbs, 1988: MMSOCPMC XV: A numerical modeling study of frontogenesis and cold-frontal rainbands. *J. Atmos. Sci.* **45**, 915-930.

Kristjansson, J. E., 1990: Model simulations of an intense meso-ß scale cyclone: The role of condensation parameterization. *Tellus* **42A**, 78-91.

Kuo, H. L., 1965: On formation and intensification of tropical cyclones through latent heat release by cumulus convection. *J. Atmos. Sci.* **22**, 40-63.

Kuo, Y.-H., and S. Low-Nam, 1990: Prediction of nine explosive cyclones over the western Atlantic Ocean with a regional model. *Mon. Wea. Rev.* **118**, 3-25.

_____, and R. J. Reed, 1988: Numerical simulation of an explosively deepening cyclone in the eastern Pacific. *Mon. Wea. Rev.* **116**, 2081-2105.

Lax, P., and B. Wendroff, 1964: Difference schemes for hyperbolic equations with high order of accuracy. *Commun. Pure App. Math.*, 381-398.

Manabe, S., 1956: On the contribution of heat released by condensation to the change in pressure pattern. *J. Meteorol. Soc. Japan* **34**, 308-320.

Mansfield, D. A., 1974: Polar lows: The development of baroclinic disturbances in cold air outbreaks. *Quart. J. Roy. Meteorol. Soc.* **100**, 541-554.

Martin, D. W., B. Auvine, and B. Hinton, 1988: Atlantic Ocean Satellite Rain Maps for GALE. Space Science and Engineering Center, University of Wisconsin-Madison. 14 pp. plus figures.

Matsumoto, S., S. Yoshizumi, and M. Takeuchi, 1970: On the structure of the "Baiu Front" and the associated intermediate-scale disturbances in the lower atmosphere. *J. Meteorol. Soc. Japan* **48**, 479-491.

Mercer, T. J., and C. W. Kreitzberg, 1986: Genesis of Atlantic Lows Experiment (GALE) Field Program Summary. GALE Data Center, Drexel University. 152 pp. plus appendices.

_____, and E. Hartnett, 1988: Genesis of Atlantic Lows Experiment (GALE) Data Users Guide. GALE Data Center, Drexel University. 120 pp. (est.)

Montgomery, M. T., and B. F. Farrell, 1990: Moist surface frontogenesis associated with interior potential vorticity anomalies in a semi-geostrophic model. Submitted to *J. Atmos. Sci.*

Moore, G. W. K., and W. R. Peltier, 1987: Cyclogenesis in frontal zones. *J. Atmos. Sci.* **44**, 384-409.

Neilley, P. P., 1990: Interactions Between Synoptic-Scale Eddies and the Large-Scale Flow During the Life Cycles of Persistent Anomalies. Ph. D. Thesis, Center for Meteorology and Physical Oceanography, MIT. 220 pp. and counting.

Neumann, C. J., and M. J. Pryslak, 1981: Frequency and motion of Atlantic tropical cyclones. NOAA Tech. Report NWS 26. 64 pp.

Nielsen, J. W., 1988: Direct analysis of Ertel potential vorticity. Synoptic Meteorology: Notes from an NCAR summer colloquium F. H. Carr, NCAR, Boulder. pp. 38-47.

_____, 1989: The formation of New England coastal fronts. *Mon. Wea. Rev.* **117**, 1380-1401.

_____, and P. P. Neilley, 1990: The vertical structure of New England coastal fronts. *Mon. Wea. Rev.* **118**, in press.

Nitta, T., and Y. Ogura, 1972: Numerical simulation of the development of the intermediate-scale cyclone in a moist model atmosphere. *J. Atmos. Sci.* **29**, 1001-1024.

Nordeng, T. E., 1987: The effect of vertical and slantwise convection on the simulation of polar lows. *Tellus* **39A**, 354-375.

Nuss, W. A., 1989: Air-sea interaction influences on the structure and intensification of an idealized marine cyclone. *Mon. Wea. Rev.* **117**, 351-369.

_____, and S. I. Kamikawa, 1990: Dynamics and boundary layer processes in two Asian cyclones. *Mon. Wea. Rev.* **118**, 755-771.

Ooyama, K., 1964: A dynamical model for the study of tropical cyclone development. *Geofys. Int.* **4**, 187-198.

Orlanski, I., 1968: Instability of frontal waves. *J. Atmos. Sci.* **25**, 178-200.

_____, 1986: Localized baroclinicity: a source for meso-α cyclones. *J. Atmos. Sci.* **43**, 2857-2885.

Peltier, W. R., G. W. K. Moore, and S. Polavarapu, 1990: Cyclogenesis and frontogenesis. *Tellus* **42A**, 3-13.

Petterssen, S., 1956: Weather Analysis and Forecasting, Vol. 1, second edition. McGraw-Hill. 428 pp.

Phillips, N. A., 1962: Numerical integration of the hydrostatic system of equations with a modified version of the Eliassen finite-difference grid. Proceedings Intern. Symp. Numerical Weather Prediction, Meteorological Society of Japan, pp. 109-120.

_____, 1979: The Nested Grid Model. NOAA Tech. Report NWS 22. 80 pp.

_____, 1981: A simpler way to initiate condensation at relative humidities below 100 percent. Office Note 242, National Meteorological Center. 14 pp.

Pierrehumbert, R. T., 1986: Lee cyclogenesis. Mesoscale Meteorology and Forecasting, P. Ray, American Meteorological Society, pp. 493-515.

Raman, S., and A. J. Riordan, 1988: The Genesis of Atlantic Lows Experiment: The planetary-boundary-layer subprogram of GALE. *Bull. Amer. Meteorol. Soc.* **69**, 161-172.

Rasmussen, E., 1983: A review of mesoscale disturbances in cold air masses. Mesoscale Meteorology -- Theories, Observations and Models. D. K. Lilly and T. Gal-Chen, Reidel, pp. 247-283.

Reed, R. J., 1979: Cyclogenesis in polar air streams. *Mon. Wea. Rev.* **107**, 38-52.

_____, and C. N. Duncan, 1987: Baroclinic instability as a mechanism for the serial development of polar lows: a case study. *Tellus* **39A**, 376-384.

Reitan, C. H., 1974: Frequencies of cyclones and cyclogenesis for North America, 1951-1970. *Mon. Wea. Rev.* **102**, 861-868.

_____, 1979: Trends in the frequencies of cyclone activity over North America. *Mon. Wea. Rev.* **107**, 1684-1688.

Reuter, G. W., and M. K. Yau, 1990: Observations of slantwise convective instability in winter cyclones. *Mon. Wea. Rev.* **118**, 447-458.

Riordan, A. J., 1990: Examination of the mesoscale features of the GALE coastal front of 24-25 January 1986. *Mon. Wea. Rev.* **118**, 258-282.

Robinson, W. A., 1988: Analysis of LIMS data by potential vorticity inversion. *J. Atmos. Sci.* **45**, 2319-2342.

Roebber, P. J., 1984: Statistical analysis and updated climatology of explosive cyclones. *Mon. Wea. Rev.* **112**, 1577-1589.

_____, 1989: On the statistical analysis of cyclone deepening rates. *Mon. Wea. Rev.* **117**, 2293-2298.

Rogers, E., G. J. DiMego, J. P. Gerrity, R. A. Petersen, B. D. Schmidt, and D. M. Kann, 1990: Preliminary experiments using GALE observations at the National Meteorological Center. *Bull. Amer. Meteorol. Soc.* **71**, 319-333.

Sanders, F., 1986: Frontogenesis and symmetric instability in a major New England snowstorm. *Mon. Wea. Rev.* **114**, 1847-1862.

_____, and L. F. Bosart, 1985: Mesoscale structure in the megalopolitan snowstorm of 11-12 February 1983. Part I: Frontogenetical forcing and symmetric instability. *J. Atmos. Sci.* **42**, 1050-1061.

_____, and C. A. Davis, 1988: Patterns of thickness anomaly for explosive cyclogenesis over the west central North Atlantic Ocean. *Mon. Wea. Rev.* **116**, 2725-2730.

_____, and J. R. Gyakum, 1980: Synoptic-dynamic climatology of the "bomb". *Mon. Wea. Rev.* **108**, 1589-1606.

Shapiro, R., 1975: Linear filtering. *Math. Comput.* **29**, 1094-1097.

Simmons, A. J., and B. J. Hoskins, 1978: The life cycles of some nonlinear baroclinic waves. *J. Atmos. Sci.* **35**, 414-432.

Sinton, D. M., and C. R. Mechoso, 1984: Nonlinear evolution of frontal waves. *J. Atmos. Sci.* **41**, 3501-3517.

Smagorinsky, J., 1956: On the inclusion of moist adiabatic processes in numerical prediction models. *Ber. d. Deutsches Wetterd.* **5**(38), 82-90. [Referenced by Danard 1964]

Solberg, H., 1928: Integrationen der atmospharischen Storungsgleichungen. *Geophys. Publ.* **5**(9).

Staley, D. O., and R. L. Gall, 1977: On the wavelength of maximum baroclinic instability. *J. Atmos. Sci.* **34**, 1679-1688.

Sutcliffe, R. C., 1947: A contribution to the problem of development. *Quart. J. Roy. Meteorol. Soc.* **73**, 370-383.

Taylor, K. E., 1986: An analysis of the biases in traditional cyclone frequency maps. *Mon. Wea. Rev.* **114**, 1481-1490.

Thorpe, A. J., 1986: Synoptic scale disturbances with circular symmetry. *Mon. Wea. Rev.* **114**, 1384-1389.

_____, and K. A. Emanuel, 1985: Frontogenesis in the presence of small stability to slantwise convection. *J. Atmos. Sci.* **42**, 1809-1824.

_____, and R. Rotunno, 1989: Nonlinear aspects of symmetric instability. *J. Atmos. Sci.* **46**, 1285-1299.

Tokioka, T., 1973: A stability study of medium-scale disturbances with inclusion of convective effects. *J. Meteorol. Soc. Japan* **51**, 1-9.

Tracton, M. S., 1973: The role of cumulus convection in the development of extratropical cyclones. *Mon. Wea. Rev.* **109**, 573-593.

Uccellini, L. W., R. A. Petersen, K. F. Brill, P. J. Kocin, and J. J. Tuccillo, 1987: Synergistic interaction between an upper-level jet streak and diabatic processes that influence the development of a low-level jet and a secondary coastal cyclone. *Mon. Wea. Rev.* **115**, 2227-2261.

Wallace, J. M., G.-H. Lim, and M. L. Blackmon, 1988: Relationship between cyclone tracks, anticyclone tracks, and baroclinic waveguides. *J. Atmos. Sci.* **45**, 439-462.

Wash, C. H., S. M. Heikkinen, C.-S. Liou, and W. A. Nuss, 1990: A rapid cyclogenesis event during GALE IOP 9. *Mon. Wea. Rev.* **118**, 375-391.

Whittaker, L. M., and J. L. Horn, 1984: Northern Hemisphere extratropical cyclone activity for four mid-season months. *J. Climatol.* **4**, 297-310.

Willett, H. C., and F. Sanders, 1959: Descriptive Meteorology, second edition. Academic Press, New York. 355 pp.

Xu, Q., 1989: Extended Sawyer-Eliassen equation for frontal circulations in the presence of small viscous moist symmetric stability. *J. Atmos. Sci.* **46**, 2671-2683.

Zishka, K. M., and P. J. Smith, 1980: The climatology of cyclones and anticyclones over North America and surrounding ocean environs for January and July, 1950-1977. *Mon. Wea. Rev.* **108**, 387-401.

TABLE 3.1

Mean layer temperatures (C), derived from thicknesses, for a time series of soundings which includes the passage of the small-scale cyclone

	950-800 mb	800-600 mb	600-400 mb	400-300 mb
MRH 19/06	11.0	0.0	-16.3	-35.0
HAT 19/12	12.2	0.7	-15.5	-34.6
MRH 19/12	13.4	2.0	-14.9	-33.4
MRH 19/15	13.8	2.4	-15.1	-32.7
MRH 19/1630	13.4	1.8	-15.5	-34.4
MRH 19/18	13.6	1.9	-15.9	-35.2
MRH 19/1930	14.4	0.9	-16.8	-35.2
MRH 19/21	11.2	-1.1	-17.9	-36.5

TABLE 5.1A: VORTICITY EQUATION, 850 MB, 19/00 F24

$$\frac{\partial \zeta}{\partial t} = -(\boldsymbol{u}\cdot\nabla)\zeta \quad -(\boldsymbol{u}\cdot\nabla)f \quad -\omega\frac{\partial \zeta}{\partial p} \quad +(f+\zeta)\frac{\partial \omega}{\partial p} + \left[\frac{\partial \omega \partial u}{\partial y \partial p} - \frac{\partial \omega \partial v}{\partial x \partial p}\right]$$

tendency = adv(rel. ζ + plan. ζ) + vert.adv. + stretching + tilting

Center point: 33 x 31							
QG (x10^{-9})	**0.59**	=	**-0.63**	**-0.30**		**+1.52**	
∂(QG)/∂p (x10^{-13})	*0.58*	=	*-0.76*	*-0.01*		*+1.35*	
GM (x10^{-9})	**2.02**	=	**-0.66**	**-0.36**	**+0.55**	**+2.34**	**+0.14**
∂(GM)/∂p (x10^{-13})	*1.19*	=	*-0.61*	*-0.03*	*-0.29*	*+2.14*	*-0.02*
Full (x10^{-9})	**1.66**	=	**-0.76**	**-0.36**	**-0.17**	**+2.47**	**+0.47**
∂(Full)/∂p (x10^{-13})	*0.04*	=	*-1.52*	*-0.03*	*-0.56*	*+2.09*	*+0.05*
Northwest point: 32 x 32							
QG (x10^{-9})	**2.43**	=	**+1.02**	**-0.26**		**+1.68**	
∂(QG)/∂p (x10^{-13})	*2.29*	=	*+1.00*	*0.00*		*+1.29*	
GM (x10^{-9})	**4.53**	=	**+1.55**	**-0.31**	**+0.82**	**+2.51**	**-0.04**
∂(GM)/∂p (x10^{-13})	*2.80*	=	*+1.52*	*-0.01*	*-0.70*	*+2.08*	*-0.09*
Full (x10^{-9})	**6.39**	=	**+4.10**	**-0.31**	**+0.10**	**+2.58**	**-0.08**
∂(Full)/∂p (x10^{-13})	*-0.39*	=	*-0.50*	*-0.01*	*-1.40*	*+1.96*	*-0.45*
Northeast point: 34 x 32							
QG (x10^{-9})	**0.44**	=	**-1.09**	**-0.34**		**+1.88**	
∂(QG)/∂p (x10^{-13})	*-2.13*	=	*-2.97*	*-0.02*		*+0.86*	
GM (x10^{-9})	**1.14**	=	**-1.74**	**-0.39**	**+0.61**	**+2.69**	**-0.03**
∂(GM)/∂p (x10^{-13})	*-2.86*	=	*-4.06*	*-0.02*	*-0.25*	*+1.31*	*+0.16*
Full (x10^{-9})	**2.22**	=	**-0.23**	**-0.39**	**-0.21**	**+2.58**	**+0.46**
∂(Full)/∂p (x10^{-13})	*-0.50*	=	*-2.24*	*-0.02*	*-0.10*	*+1.09*	*+0.78*
Southeast point: 34 x 30							
QG (x10^{-9})	**-0.81**	=	**-2.17**	**-0.34**		**+1.70**	
∂(QG)/∂p (x10^{-13})	*0.67*	=	*+0.05*	*-0.03*		*+0.66*	
GM (x10^{-9})	**-0.58**	=	**-2.77**	**-0.40**	**+0.24**	**+2.41**	**-0.05**
∂(GM)/∂p (x10^{-13})	*0.51*	=	*-0.54*	*-0.03*	*-0.07*	*+1.03*	*+0.11*
Full (x10^{-9})	**-2.87**	=	**-4.60**	**-0.40**	**-0.29**	**+2.24**	**+0.17**
∂(Full)/∂p (x10^{-13})	*0.05*	=	*-1.36*	*-0.03*	*+0.23*	*+0.69*	*+0.52*
Southwest point: 32 x 30							
QG (x10^{-9})	**1.82**	=	**+1.76**	**-0.27**		**+0.32**	
∂(QG)/∂p (x10^{-13})	*1.23*	=	*-0.16*	*0.00*		*+1.39*	
GM (x10^{-9})	**2.39**	=	**+1.86**	**-0.29**	**+0.37**	**+0.47**	**-0.02**
∂(GM)/∂p (x10^{-13})	*2.22*	=	*+0.14*	*-0.03*	*-0.15*	*+2.13*	*+0.11*
Full (x10^{-9})	**-0.37**	=	**-0.96**	**-0.29**	**+0.13**	**+0.54**	**+0.22**
∂(Full)/∂p (x10^{-13})	*1.13*	=	*-0.18*	*-0.03*	*-0.64*	*+2.29*	*-0.31*

TABLE 5.1B: THERMODYNAMIC AND OMEGA EQUATIONS, 850 MB, 19/00 F24

	$\frac{\partial \Phi_p}{\partial t}(QG)$	$\frac{\partial \Phi_p}{\partial t}(QG_{VS})$	$\frac{\partial \Phi_p}{\partial t}(Full)$	$-(\boldsymbol{u_g}\cdot\nabla)\Phi_p$	$-(\boldsymbol{u}\cdot\nabla)\Phi_p$	$-\omega\bar{\sigma}$	$-\omega\breve{\sigma}$
	(1+3)	(1+4)	(2+4)	1	2	3	4
Tendencies:	*QuasiG*	*QG(VarStab)*	*Full(=GM)*	*Geos.Adv*	*FullAdv*	*AvStab*	*FullStab*
Center point: 33 x 31							
(*)x10^{-6}	**0.41**	**-0.20**	**-0.24**	**-0.23**	**-0.27**	**+0.64**	**+0.03**
$f^{-1}\nabla^2(*)x10^{-13}$	*-3.32*	*-1.03*	*-0.50*	*-1.15*	*-0.62*	*-2.18*	*+0.12*
Northwest point: 32 x 32							
(*)x10^{-6}	**0.42**	**-0.24**	**-0.34**	**-0.37**	**-0.44**	**+0.79**	**+0.09**
$f^{-1}\nabla^2(*)x10^{-13}$	*-7.49*	*-1.55*	*0.14*	*-0.76*	*+0.93*	*-6.73*	*-0.79*
Northeast point: 34 x 32							
(*)x10^{-6}	**0.41**	**-0.18**	**-0.17**	**-0.19**	**-0.19**	**+0.61**	**+0.02**
$f^{-1}\nabla^2(*)x10^{-13}$	*-5.29*	*-2.65*	*-2.89*	*-3.25*	*-3.49*	*-2.03*	*+0.60*
Southeast point: 34 x 30							
(*)x10^{-6}	**0.20**	**-0.26**	**-0.28**	**-0.26**	**-0.27**	**+0.46**	**0.00**
$f^{-1}\nabla^2(*)x10^{-13}$	*0.81*	*1.38*	*1.81*	*+1.19*	*+1.62*	*-0.39*	*+0.18*
Southwest point: 32 x 30							
(*)x10^{-6}	**0.20**	**-0.19**	**-0.21**	**-0.21**	**-0.23**	**+0.41**	**+0.03**
$f^{-1}\nabla^2(*)x10^{-13}$	*1.56*	*-0.38*	*-0.57*	*-0.37*	*-0.56*	*+1.93*	*-0.01*

ω-EQ. ERROR CALCULATIONS: $\partial/\partial p$(vorticity tendency) - $f^{-1}\nabla^2(\partial\Phi/\partial p$ tendency)

(*)x10^{-13}	***33 x 31***	***32 x 32***	***34 x 32***	***34 x 30***	***32 x 30***
Quasi-Geostrophic	**3.90**	**9.78**	**3.15**	**-0.14**	**-0.33**
QG with variable σ	**1.61**	**3.84**	**0.52**	**-0.70**	**1.62**
Geostrophic Momentum	**1.70**	**2.67**	**0.04**	**-1.30**	**2.79**

TABLE 5.2A: VORTICITY EQUATION, 600 MB, 19/00 F24

$$\frac{\partial \zeta}{\partial t} = -(\boldsymbol{u}\cdot\nabla)\zeta \quad -(\boldsymbol{u}\cdot\nabla)f \quad -\omega\frac{\partial \zeta}{\partial p} \quad +(f+\zeta)\frac{\partial \omega}{\partial p} + \left[\frac{\partial \omega \partial u}{\partial y\,\partial p} - \frac{\partial \omega \partial v}{\partial x\,\partial p}\right]$$

tendency = adv(rel. ζ + plan. ζ) + vert.adv. + stretching + tilting

Center point: 33 x 31							
QG (x10^{-9})	**2.36**	=	**+0.27**	**-0.27**		**+2.36**	
∂(QG)/∂p (x10^{-13})	*0.07*	=	*+1.15*	*+0.01*		*-1.09*	
GM (x10^{-9})	**5.08**	=	**+1.34**	**-0.29**	**+1.04**	**+2.73**	**+0.26**
∂(GM)/∂p (x10^{-13})	*-1.19*	=	*+0.94*	*+0.02*	*-1.25*	*-0.92*	*+0.02*
Full (x10^{-9})	**9.18**	=	**+4.90**	**-0.29**	**+1.60**	**+2.93**	**+0.04**
∂(Full)/∂p (x10^{-13})	*-4.04*	=	*-1.34*	*+0.02*	*-1.83*	*-0.78*	*-0.11*
Northwest point: 32 x 32							
QG (x10^{-9})	**0.67**	=	**-0.76**	**-0.25**		**+1.68**	
∂(QG)/∂p (x10^{-13})	*0.78*	=	*+0.60*	*+0.01*		*+0.18*	
GM (x10^{-9})	**2.73**	=	**+0.27**	**-0.26**	**+1.35**	**+1.47**	**-0.09**
∂(GM)/∂p (x10^{-13})	*1.33*	=	*+0.61*	*+0.01*	*-0.32*	*+0.48*	*+0.55*
Full (x10^{-9})	**7.78**	=	**+4.58**	**-0.26**	**+2.24**	**+1.36**	**-0.14**
∂(Full)/∂p (x10^{-13})	*0.58*	=	*-0.41*	*+0.01*	*-0.38*	*+0.59*	*+0.76*
Northeast point: 34 x 32							
QG (x10^{-9})	**3.95**	=	**+3.45**	**-0.28**		**+0.78**	
∂(QG)/∂p (x10^{-13})	*2.24*	=	*+2.36*	*-0.02*		*-0.10*	
GM (x10^{-9})	**3.95**	=	**+2.68**	**-0.27**	**+0.60**	**+1.02**	**-0.08**
∂(GM)/∂p (x10^{-13})	*1.26*	=	*+2.03*	*0.00*	*-0.73*	*-0.23*	*+0.18*
Full (x10^{-9})	**7.79**	=	**+5.34**	**-0.27**	**+1.80**	**+0.77**	**+0.15**
∂(Full)/∂p (x10^{-13})	*-1.78*	=	*-0.41*	*0.00*	*-0.85*	*+0.11*	*-0.63*
Southeast point: 34 x 30							
QG (x10^{-9})	**-3.49**	=	**-4.45**	**-0.30**		**+1.27**	
∂(QG)/∂p (x10^{-13})	*0.87*	=	*+1.22*	*+0.02*		*-0.38*	
GM (x10^{-9})	**-1.63**	=	**-4.72**	**-0.33**	**+1.79**	**+1.43**	**+0.20**
∂(GM)/∂p (x10^{-13})	*0.59*	=	*+2.06*	*+0.04*	*-1.27*	*-0.01*	*-0.22*
Full (x10^{-9})	**1.14**	=	**-1.61**	**-0.33**	**+1.42**	**+1.69**	**-0.02**
∂(Full)/∂p (x10^{-13})	*-2.63*	=	*-0.39*	*+0.04*	*-2.05*	*-0.18*	*-0.05*
Southwest point: 32 x 30							
QG (x10^{-9})	**4.51**	=	**+2.71**	**-0.30**		**+2.11**	
∂(QG)/∂p (x10^{-13})	*-1.57*	=	*-0.37*	*+0.04*		*-1.24*	
GM (x10^{-9})	**4.48**	=	**+2.70**	**-0.29**	**+0.45**	**+2.23**	**-0.61**
∂(GM)/∂p (x10^{-13})	*-1.53*	=	*-0.37*	*+0.04*	*-0.58*	*-0.98*	*+0.36*
Full (x10^{-9})	**3.71**	=	**+1.39**	**-0.29**	**+0.74**	**+2.50**	**-0.63**
∂(Full)/∂p (x10^{-13})	*-2.37*	=	*-1.17*	*+0.04*	*-1.00*	*-1.04*	*+0.79*

TABLE 5.2B: THERMODYNAMIC AND OMEGA EQUATIONS, 600 MB, 19/00 F24

	$\frac{\partial \Phi_p}{\partial t}(QG)$	$\frac{\partial \Phi_p}{\partial t}(QG_{VS})$	$\frac{\partial \Phi_p}{\partial t}(Full)$	$-(\boldsymbol{u_g}\cdot\nabla)\Phi_p$	$-(\boldsymbol{u}\cdot\nabla)\Phi_p$	$-\omega\bar{\sigma}$	$-\omega\tilde{\sigma}$
	(1+3)	(1+4)	(2+4)	1	2	3	4
Tendencies:	*QuasiG*	*QG(VarStab)*	*Full(=GM)*	*Geos.Adv*	*FullAdv*	*AvStab*	*FullStab*
Center point: 33 x 31							
(*)x10^{-6}	**1.18**	**-0.32**	**-0.39**	**-0.39**	**-0.46**	**+1.57**	**+0.07**
$f^{-1}\nabla^2$(*)x10^{-13}	-7.92	-0.64	1.48	-0.31	+1.81	-7.61	-0.33
Northwest point: 32 x 32							
(*)x10^{-6}	**1.34**	**-0.32**	**-0.35**	**-0.40**	**-0.44**	**+1.75**	**+0.08**
$f^{-1}\nabla^2$(*)x10^{-13}	-18.56	-1.78	-0.37	-1.69	-0.28	-16.88	-0.09
Northeast point: 34 x 32							
(*)x10^{-6}	**0.82**	**-0.55**	**-0.49**	**-0.68**	**-0.61**	**+1.50**	**+0.13**
$f^{-1}\nabla^2$(*)x10^{-13}	-2.83	+2.40	+1.29	+3.74	+2.64	-6.57	-1.35
Southeast point: 34 x 30							
(*)x10^{-6}	**1.07**	**-0.25**	**-0.33**	**-0.25**	**-0.33**	**+1.33**	**0.00**
$f^{-1}\nabla^2$(*)x10^{-13}	-6.15	0.15	2.35	+0.49	+2.69	-6.64	-0.34
Southwest point: 32 x 30							
(*)x10^{-6}	**0.57**	**-0.21**	**-0.23**	**-0.22**	**-0.23**	**+0.80**	**+0.01**
$f^{-1}\nabla^2$(*)x10^{-13}	8.55	0.23	-0.08	-0.13	-0.44	+8.68	+0.36

ω-EQ. ERROR CALCULATIONS: $\partial/\partial p$(vorticity tendency) - $f^{-1}\nabla^2(\partial\Phi/\partial p$ tendency)

(*)x10^{-13}	***33 x 31***	***32 x 32***	***34 x 32***	***34 x 30***	***32 x 30***
Quasi-Geostrophic	**7.99**	**19.35**	**5.07**	**7.02**	**-10.12**
QG with variable σ	**0.71**	**2.56**	**-0.15**	**0.71**	**-1.80**
Geostrophic Momentum	**-2.67**	**1.70**	**-0.03**	**-1.76**	**-1.45**

TABLE 5.3A: VORTICITY EQUATION, 350 MB, 19/00 F24

$$\frac{\partial \zeta}{\partial t} = -(\boldsymbol{u}\cdot\nabla)\zeta \quad -(\boldsymbol{u}\cdot\nabla)f \quad -\omega\frac{\partial \zeta}{\partial p} \quad +(f+\zeta)\frac{\partial \omega}{\partial p} + \left[\frac{\partial \omega \partial u}{\partial y\,\partial p} - \frac{\partial \omega \partial v}{\partial x\,\partial p}\right]$$

tendency = *adv(rel. ζ + plan. ζ)* + *vert.adv.* + *stretching* + *tilting*

Center point: 33 x 31							
QG (x10^{-9})	**-13.74**	=	**-9.70**	**-0.24**		**-3.80**	
∂(QG)/∂p (x10^{-13})	*9.38*	=	*+6.53*	*-0.03*		*+2.88*	
GM (x10^{-9})	**-9.12**	=	**-9.62**	**-0.40**	**+1.42**	**-0.63**	**+0.10**
∂(GM)/∂p (x10^{-13})	*15.62*	=	*+9.43*	*+0.06*	*+5.96*	*+0.29*	*-0.12*
Full (x10^{-9})	**7.76**	=	**+6.72**	**-0.40**	**+1.26**	**-0.65**	**+0.82**
∂(Full)/∂p (x10^{-13})	*3.82*	=	*-0.55*	*+0.06*	*+4.25*	*+0.20*	*-0.13*
Northwest point: 32 x 32							
QG (x10^{-9})	**-18.10**	=	**-14.50**	**-0.25**		**-3.35**	
∂(QG)/∂p (x10^{-13})	*8.23*	=	*+6.20*	*-0.02*		*+2.05*	
GM (x10^{-9})	**-19.32**	=	**-18.27**	**-0.47**	**+0.85**	**-0.09**	**-1.33**
∂(GM)/∂p (x10^{-13})	*13.66*	=	*+11.55*	*+0.11*	*+2.97*	*-0.32*	*-0.65*
Full (x10^{-9})	**1.38**	=	**+2.31**	**-0.47**	**+1.48**	**+0.62**	**-2.55**
∂(Full)/∂p (x10^{-13})	*1.60*	=	*-0.82*	*+0.11*	*+4.29*	*-0.90*	*-1.08*
Northeast point: 34 x 32							
QG (x10^{-9})	**-9.51**	=	**-6.37**	**-0.22**		**-2.93**	
∂(QG)/∂p (x10^{-13})	*3.74*	=	*+2.45*	*-0.02*		*+1.31*	
GM (x10^{-9})	**-10.24**	=	**-7.24**	**-0.32**	**-0.82**	**-1.44**	**-0.42**
∂(GM)/∂p (x10^{-13})	*4.71*	=	*+4.19*	*+0.04*	*+0.90*	*+1.30*	*-1.72*
Full (x10^{-9})	**6.40**	=	**+5.75**	**-0.32**	**+0.60**	**-0.46**	**+0.83**
∂(Full)/∂p (x10^{-13})	*-1.71*	=	*-3.30*	*+0.04*	*+1.96*	*-0.07*	*-0.34*
Southeast point: 34 x 30							
QG (x10^{-9})	**-4.92**	=	**-1.84**	**-0.25**		**-2.83**	
∂(QG)/∂p (x10^{-13})	*5.35*	=	*+4.30*	*-0.03*		*+1.08*	
GM (x10^{-9})	**-3.72**	=	**-1.42**	**-0.34**	**-0.52**	**-2.31**	**+0.87**
∂(GM)/∂p (x10^{-13})	*7.26*	=	*+6.69*	*+0.02*	*+1.42*	*+1.39*	*-2.26*
Full (x10^{-9})	**4.35**	=	**+2.63**	**-0.34**	**+0.06**	**-1.83**	**+3.83**
∂(Full)/∂p (x10^{-13})	*1.85*	=	*+1.74*	*+0.02*	*+0.75*	*+0.71*	*-1.38*
Southwest point: 32 x 30							
QG (x10^{-9})	**-0.25**	=	**+2.27**	**-0.39**		**-2.13**	
∂(QG)/∂p (x10^{-13})	*1.29*	=	*-0.57*	*0.00*		*+1.86*	
GM (x10^{-9})	**3.98**	=	**+2.97**	**-0.49**	**+1.41**	**+0.01**	**+0.09**
∂(GM)/∂p (x10^{-13})	*2.88*	=	*-0.95*	*+0.10*	*+4.42*	*-0.07*	*-0.61*
Full (x10^{-9})	**3.32**	=	**+3.72**	**-0.49**	**+1.45**	**-0.11**	**-1.24**
∂(Full)/∂p (x10^{-13})	*3.04*	=	*+0.86*	*+0.10*	*+3.87*	*-0.24*	*-1.54*

TABLE 5.3B: THERMODYNAMIC AND OMEGA EQUATIONS, 350 MB, 19/00 F24

	$\frac{\partial \Phi_p}{\partial t}(QG)$	$\frac{\partial \Phi_p}{\partial t}(QG_{VS})$	$\frac{\partial \Phi_p}{\partial t}(Full)$	$-(\boldsymbol{u_g}\cdot\nabla)\Phi_p$	$-(\boldsymbol{u}\cdot\nabla)\Phi_p$	$-\omega\bar{\sigma}$	$-\omega\sigma'$
	(1+3)	(1+4)	(2+4)	1	2	3	4
Tendencies:	*QuasiG*	*QG(VarStab)*	*Full(=GM)*	*Geos.Adv*	*FullAdv*	*AvStab*	*FullStab*
Center point: 33 x 31							
(*)x10^{-6}	**-0.31**	**-1.55**	**-1.91**	**-0.83**	**-1.19**	**+0.52**	**-0.72**
$f^{-1}\nabla^2$(*)x10^{-13}	*0.92*	*15.52*	*16.28*	*+1.79*	*+2.54*	*-0.86*	*+13.74*
Northwest point: 32 x 32							
(*)x10^{-6}	**-0.44**	**-1.44**	**-2.09**	**-0.92**	**-1.57**	**0.47**	**-0.52**
$f^{-1}\nabla^2$(*)x10^{-13}	*-2.90*	*7.02*	*12.63*	*+0.29*	*+5.91*	*-3.19*	*+6.72*
Northeast point: 34 x 32							
(*)x10^{-6}	**-0.17**	**-0.86**	**-1.11**	**-0.64**	**-0.89**	**+0.47**	**-0.22**
$f^{-1}\nabla^2$(*)x10^{-13}	*-4.13*	*2.34*	*3.73*	*+0.92*	*+2.31*	*-5.04*	*+1.42*
Southeast point: 34 x 30							
(*)x10^{-6}	**-0.12**	**-0.90**	**-1.10**	**-0.71**	**-0.91**	**+0.59**	**-0.19**
$f^{-1}\nabla^2$(*)x10^{-13}	*-9.52*	*-1.07*	*1.63*	*-1.40*	*+1.30*	*-8.12*	*+0.33*
Southwest point: 32 x 30							
(*)x10^{-6}	**-0.53**	**-1.45**	**-1.69**	**-0.91**	**-1.15**	**+0.38**	**-0.54**
$f^{-1}\nabla^2$(*)x10^{-13}	*0.93*	*4.35*	*2.86*	*-0.90*	*-2.39*	*+1.83*	*+5.25*

ω-EQ. ERROR CALCULATIONS: $\partial/\partial p$(vorticity tendency) - $f^{-1}\nabla^2(\partial\Phi/\partial p$ tendency)

(*)x10^{-13}	***33 x 31***	***32 x 32***	***34 x 32***	***34 x 30***	***32 x 30***
Quasi-Geostrophic	**8.45**	**11.13**	**7.87**	**14.87**	**0.36**
QG with variable σ	**-6.15**	**1.21**	**1.40**	**6.42**	**-3.06**
Geostrophic Momentum	**-0.66**	**1.03**	**0.98**	**5.63**	**0.02**

TABLE 5.4A: VORTICITY EQUATION, 850 MB, 19/00 F06

$$\frac{\partial \zeta}{\partial t} = -(\boldsymbol{u}\cdot\nabla)\zeta \quad -(\boldsymbol{u}\cdot\nabla)f \quad -\omega\frac{\partial \zeta}{\partial p} \quad +(f+\zeta)\frac{\partial \omega}{\partial p} + \left[\frac{\partial \omega}{\partial y}\frac{\partial u}{\partial p} - \frac{\partial \omega}{\partial x}\frac{\partial v}{\partial p}\right]$$

tendency = adv(rel. ζ + plan. ζ) + vert.adv. + stretching + tilting

Center point: 35 x 23							
QG (x10^{-9})	**1.95**	=	**+0.76**	**-0.20**		**+1.38**	
∂(QG)/∂p (x10^{-13})	*1.44*	=	*+0.46*	*-0.03*		*+1.01*	
GM (x10^{-9})	**2.61**	=	**+0.92**	**-0.24**	**+0.66**	**+1.57**	**-0.29**
∂(GM)/∂p (x10^{-13})	*1.58*	=	*+0.61*	*+0.01*	*-0.19*	*+1.31*	*-0.15*
Full (x10^{-9})	**0.42**	=	**+0.07**	**-0.24**	**-0.08**	**+1.38**	**-0.70**
∂(Full)/∂p (x10^{-13})	*1.12*	=	*+0.05*	*+0.01*	*+0.15*	*+0.96*	*-0.05*
Northwest point: 34 x 24							
QG (x10^{-9})	**-0.37**	=	**-0.82**	**-0.20**		**+0.65**	
∂(QG)/∂p (x10^{-13})	*2.31*	=	*+1.86*	*-0.04*		*+0.48*	
GM (x10^{-9})	**-1.08**	=	**-0.92**	**-0.23**	**+0.08**	**+0.59**	**-0.60**
∂(GM)/∂p (x10^{-13})	*2.23*	=	*+2.11*	*0.00*	*-0.14*	*+0.45*	*-0.20*
Full (x10^{-9})	**-0.76**	=	**-0.20**	**-0.23**	**-0.11**	**+0.69**	**-0.92**
∂(Full)/∂p (x10^{-13})	*0.96*	=	*+0.74*	*0.00*	*-0.01*	*+0.44*	*-0.21*
Northeast point: 36 x 24							
QG (x10^{-9})	**2.07**	=	**+1.10**	**-0.25**		**+1.23**	
∂(QG)/∂p (x10^{-13})	*0.16*	=	*-0.03*	*-0.05*		*+0.23*	
GM (x10^{-9})	**1.85**	=	**+1.02**	**-0.24**	**+0.43**	**+1.38**	**-0.74**
∂(GM)/∂p (x10^{-13})	*-0.58*	=	*-0.86*	*+0.02*	*-0.41*	*+0.36*	*+0.31*
Full (x10^{-9})	**0.37**	=	**+0.16**	**-0.24**	**-0.03**	**+1.11**	**-0.64**
∂(Full)/∂p (x10^{-13})	*1.04*	=	*+0.26*	*+0.02*	*+0.08*	*+0.19*	*+0.48*
Southeast point: 36 x 22							
QG (x10^{-9})	**-0.97**	=	**-2.15**	**-0.22**		**+1.40**	
∂(QG)/∂p (x10^{-13})	*-1.02*	=	*-1.55*	*-0.03*		*+0.56*	
GM (x10^{-9})	**-0.89**	=	**-2.52**	**-0.26**	**+0.29**	**+1.54**	**+0.06**
∂(GM)/∂p (x10^{-13})	*-0.52*	=	*-1.50*	*0.00*	*+0.15*	*+0.71*	*+0.12*
Full (x10^{-9})	**1.38**	=	**-0.29**	**-0.26**	**+0.01**	**+1.34**	**+0.57**
∂(Full)/∂p (x10^{-13})	*0.59*	=	*-0.34*	*0.00*	*+0.25*	*+0.54*	*+0.15*
Southwest point: 34 x 22							
QG (x10^{-9})	**1.86**	=	**+1.38**	**-0.20**		**+0.68**	
∂(QG)/∂p (x10^{-13})	*0.92*	=	*-0.09*	*-0.02*		*+1.04*	
GM (x10^{-9})	**2.17**	=	**+1.61**	**-0.23**	**+0.21**	**+0.63**	**-0.04**
∂(GM)/∂p (x10^{-13})	*0.46*	=	*-0.25*	*-0.01*	*-0.03*	*+1.12*	*-0.37*
Full (x10^{-9})	**0.08**	=	**-0.02**	**-0.23**	**-0.12**	**+0.75**	**-0.30**
∂(Full)/∂p (x10^{-13})	*0.02*	=	*-0.24*	*-0.01*	*-0.08*	*+1.08*	*-0.73*

TABLE 5.4B: THERMODYNAMIC AND OMEGA EQUATIONS, 850 MB, 19/00 F06

Tendencies:	$\frac{\partial \Phi_p}{\partial t}(QG)$ (1+3) QuasiG	$\frac{\partial \Phi_p}{\partial t}(QG_{vs})$ (1+4) QG(VarStab)	$\frac{\partial \Phi_p}{\partial t}(Full)$ (2+4) Full(=GM)	$-(\boldsymbol{u_g}\cdot\nabla)\Phi_p$ 1 Geos.Adv	$-(\boldsymbol{u}\cdot\nabla)\Phi_p$ 2 FullAdv	$-\omega\bar{\sigma}$ 3 AvStab	$-\omega\tilde{\sigma}$ 4 FullStab
Center point: 35 x 23							
(*)x10^{-6}	**0.36**	**-0.16**	**-0.22**	**-0.25**	**-0.31**	**+0.61**	**+0.09**
$f^{-1}\nabla^2(*)x10^{-13}$	-13.32	-4.07	-2.24	-2.08	-0.25	-11.24	-1.99
Northwest point: 34 x 24							
(*)x10^{-6}	**-0.19**	**-0.34**	**-0.39**	**-0.38**	**-0.43**	**+0.19**	**+0.05**
$f^{-1}\nabla^2(*)x10^{-13}$	1.56	0.71	1.97	+1.44	+2.70	+0.12	-0.73
Northeast point: 36 x 24							
(*)x10^{-6}	**0.01**	**-0.34**	**-0.33**	**-0.39**	**-0.38**	**+0.40**	**+0.04**
$f^{-1}\nabla^2(*)x10^{-13}$	-5.78	0.08	-1.31	+1.35	-0.04	-7.13	-1.27
Southeast point: 36 x 22							
(*)x10^{-6}	**0.31**	**-0.17**	**-0.18**	**-0.19**	**-0.20**	**+0.50**	**+0.02**
$f^{-1}\nabla^2(*)x10^{-13}$	-5.60	-0.24	-1.15	-0.81	-1.71	-4.79	+0.56
Southwest point: 34 x 22							
(*)x10^{-6}	**0.20**	**-0.14**	**-0.18**	**-0.21**	**-0.25**	**+0.41**	**+0.07**
$f^{-1}\nabla^2(*)x10^{-13}$	-4.63	-1.02	-0.38	-0.86	-0.23	-3.76	-0.15

ω-EQ. ERROR CALCULATIONS: $\partial/\partial p$(vorticity tendency) - $f^{-1}\nabla^2(\partial\Phi/\partial p$ tendency)

(*)x10^{-13}	***35 x 23***	***34 x 24***	***36 x 24***	***36 x 22***	***34 x 22***
Quasi-Geostrophic	**14.76**	**0.75**	**5.94**	**4.58**	**5.55**
QG with variable σ	**5.51**	**1.60**	**0.07**	**-0.78**	**1.93**
Geostrophic Momentum	**3.81**	**0.26**	**0.73**	**0.63**	**0.84**

TABLE 5.5A: VORTICITY EQUATION, 600 MB, 19/00 F06

$$\frac{\partial \zeta}{\partial t} = -(\boldsymbol{u}\cdot\nabla)\zeta \quad -(\boldsymbol{u}\cdot\nabla)f \quad -\omega\frac{\partial \zeta}{\partial p} \quad +(f+\zeta)\frac{\partial \omega}{\partial p} + \left[\frac{\partial \omega}{\partial y}\frac{\partial u}{\partial p} - \frac{\partial \omega}{\partial x}\frac{\partial v}{\partial p}\right]$$

tendency = adv(rel. ζ + plan. ζ) + vert.adv. + stretching + tilting

Center point: 35 x 23							
QG (x10^{-9})	**-0.28**	=	**-0.99**	**-0.17**		**+0.88**	
∂(QG)/∂p (x10^{-13})	*1.67*	=	*+0.43*	*+0.05*		*+1.19*	
GM (x10^{-9})	**0.73**	=	**-0.82**	**-0.21**	**+2.95**	**+0.59**	**-1.78**
∂(GM)/∂p (x10^{-13})	*1.26*	=	*+1.12*	*+0.03*	*-1.59*	*+1.28*	*+0.43*
Full (x10^{-9})	**2.03**	=	**+1.19**	**-0.21**	**+1.24**	**+0.85**	**-1.04**
∂(Full)/∂p (x10^{-13})	*1.88*	=	*-0.25*	*+0.03*	*-0.40*	*+1.32*	*+1.18*
Northwest point: 34 x 24							
QG (x10^{-9})	**-0.82**	=	**-1.24**	**-0.18**		**+0.61**	
∂(QG)/∂p (x10^{-13})	*-0.49*	=	*-0.30*	*+0.06*		*-0.25*	
GM (x10^{-9})	**-3.09**	=	**-1.27**	**-0.19**	**-0.05**	**+0.38**	**-1.97**
∂(GM)/∂p (x10^{-13})	*0.15*	=	*-0.21*	*+0.04*	*-0.13*	*-0.18*	*+0.62*
Full (x10^{-9})	**-1.12**	=	**-0.45**	**-0.19**	**+0.28**	**+0.56**	**-1.31**
∂(Full)/∂p (x10^{-13})	*1.12*	=	*+0.12*	*+0.04*	*-0.09*	*-0.13*	*+1.19*
Northeast point: 36 x 24							
QG (x10^{-9})	**0.74**	=	**+0.16**	**-0.19**		**+0.76**	
∂(QG)/∂p (x10^{-13})	*4.12*	=	*+2.47*	*-0.01*		*+1.66*	
GM (x10^{-9})	**3.53**	=	**+0.32**	**-0.22**	**+3.60**	**+0.68**	**-0.85**
∂(GM)/∂p (x10^{-13})	*3.24*	=	*+3.02*	*0.00*	*-2.32*	*+1.96*	*+0.58*
Full (x10^{-9})	**1.85**	=	**+1.43**	**-0.22**	**+0.87**	**+0.64**	**-0.87**
∂(Full)/∂p (x10^{-13})	*1.63*	=	*-0.06*	*0.00*	*-0.33*	*+1.49*	*+0.53*
Southeast point: 36 x 22							
QG (x10^{-9})	**1.30**	=	**+0.39**	**-0.17**		**+1.08**	
∂(QG)/∂p (x10^{-13})	*-0.97*	=	*-2.47*	*+0.01*		*+1.49*	
GM (x10^{-9})	**6.12**	=	**+1.17**	**-0.23**	**+3.91**	**+1.19**	**+0.09**
∂(GM)/∂p (x10^{-13})	*-3.78*	=	*-2.81*	*-0.01*	*-3.08*	*+2.05*	*+0.07*
Full (x10^{-9})	**4.12**	=	**+1.75**	**-0.23**	**+0.92**	**+1.19**	**+0.49**
∂(Full)/∂p (x10^{-13})	*-0.27*	=	*-1.02*	*-0.01*	*-0.69*	*+1.78*	*-0.33*
Southwest point: 34 x 22							
QG (x10^{-9})	**0.86**	=	**+0.49**	**-0.19**		**+0.56**	
∂(QG)/∂p (x10^{-13})	*0.34*	=	*+0.04*	*+0.07*		*+0.22*	
GM (x10^{-9})	**-1.24**	=	**+0.49**	**-0.20**	**+0.47**	**+0.31**	**-2.30**
∂(GM)/∂p (x10^{-13})	*0.79*	=	*+0.46*	*+0.06*	*-0.33*	*+0.16*	*+0.44*
Full (x10^{-9})	**-0.53**	=	**+0.24**	**-0.20**	**+0.47**	**+0.52**	**-1.57**
∂(Full)/∂p (x10^{-13})	*1.01*	=	*-0.51*	*+0.06*	*+0.08*	*+0.29*	*+1.10*

TABLE 5.5B: THERMODYNAMIC AND OMEGA EQUATIONS, 600 MB, 19/00 F06

	$\frac{\partial \Phi_p}{\partial t}(QG)$	$\frac{\partial \Phi_p}{\partial t}(QG_{VS})$	$\frac{\partial \Phi_p}{\partial t}(Full)$	$-(\boldsymbol{u_g}\cdot\nabla)\Phi_p$	$-(\boldsymbol{u}\cdot\nabla)\Phi_p$	$-\omega\bar{\sigma}$	$-\omega\tilde{\sigma}$
	(1+3)	(1+4)	(2+4)	1	2	3	4
Tendencies:	*QuasiG*	*QG(VarStab)*	*Full(=GM)*	*Geos.Adv*	*FullAdv*	*AvStab*	*FullStab*
Center point: 35 x 23							
(*)x10^{-6}	**1.22**	**-0.18**	**-0.27**	**-0.12**	**-0.21**	**+1.34**	**-0.06**
$f^{-1}\nabla^2$(*)x10^{-13}	*-19.69*	*-0.27*	*2.80*	*-0.96*	*+2.11*	*-18.74*	*+0.69*
Northwest point: 34 x 24							
(*)x10^{-6}	**0.23**	**0.05**	**0.02**	**-0.13**	**-0.15**	**+0.35**	**+0.17**
$f^{-1}\nabla^2$(*)x10^{-13}	*4.43*	*-13.32*	*-13.51*	*-1.23*	*-1.42*	*+5.66*	*-12.09*
Northeast point: 36 x 24							
(*)x10^{-6}	**0.96**	**-0.40**	**-0.46**	**-0.33**	**-0.38**	**+1.29**	**-0.08**
$f^{-1}\nabla^2$(*)x10^{-13}	*-16.16*	*22.67*	*23.65*	*+3.18*	*+4.16*	*-19.34*	*+19.49*
Southeast point: 36 x 22							
(*)x10^{-6}	**1.52**	**-0.07**	**-0.08**	**0.00**	**-0.02**	**+1.53**	**-0.06**
$f^{-1}\nabla^2$(*)x10^{-13}	*-25.12*	*7.66*	*7.78*	*-3.20*	*-3.07*	*-21.92*	*+10.86*
Southwest point: 34 x 22							
(*)x10^{-6}	**0.51**	**-0.14**	**-0.17**	**-0.10**	**-0.13**	**+0.61**	**-0.04**
$f^{-1}\nabla^2$(*)x10^{-13}	*0.51*	*0.59*	*0.76*	*+0.84*	*+1.01*	*-0.33*	*-0.25*

ω-EQ. ERROR CALCULATIONS: $\partial/\partial p$(vorticity tendency) - $f^{-1}\nabla^2(\partial\Phi/\partial p$ tendency)

(*)x10^{-13}	***35 x 23***	***34 x 24***	***36 x 24***	***36 x 22***	***34 x 22***
Quasi-Geostrophic	**21.37**	**-4.92**	**20.28**	**24.14**	**-0.17**
QG with variable σ	**1.94**	**12.83**	**-18.55**	**-8.63**	**-0.25**
Geostrophic Momentum	**-1.54**	**13.66**	**-20.41**	**-11.56**	**0.03**

TABLE 5.6A: VORTICITY EQUATION, 350 MB, 19/00 F06

$$\frac{\partial \zeta}{\partial t} = -(\boldsymbol{u}\cdot\nabla)\zeta \quad -(\boldsymbol{u}\cdot\nabla)f \quad -\omega\frac{\partial \zeta}{\partial p} \quad +(f+\zeta)\frac{\partial \omega}{\partial p} + \left[\frac{\partial \omega}{\partial y}\frac{\partial u}{\partial p} - \frac{\partial \omega}{\partial x}\frac{\partial v}{\partial p}\right]$$

tendency = adv(rel. ζ + plan. ζ) + vert.adv. + stretching + tilting

Center point: 35 x 23							
QG (x10^{-9})	**-5.39**	=	**-3.57**	**-0.27**		**-1.55**	
∂(QG)/∂p (x10^{-13})	*1.60*	=	*+1.83*	*+0.07*		*-0.29*	
GM (x10^{-9})	**-6.15**	=	**-3.89**	**-0.34**	**-0.26**	**-0.79**	**-0.88**
∂(GM)/∂p (x10^{-13})	*0.61*	=	*+1.82*	*+0.11*	*-0.58*	*-0.17*	*-0.57*
Full (x10^{-9})	**-0.87**	=	**+0.95**	**-0.34**	**+0.68**	**-1.08**	**-1.09**
∂(Full)/∂p (x10^{-13})	*1.07*	=	*+2.12*	*+0.11*	*-0.13*	*-0.53*	*-0.50*
Northwest point: 34 x 24							
QG (x10^{-9})	**-3.58**	=	**-2.90**	**-0.31**		**-0.37**	
∂(QG)/∂p (x10^{-13})	*1.31*	=	*+1.17*	*+0.07*		*+0.07*	
GM (x10^{-9})	**-4.86**	=	**-3.36**	**-0.36**	**+0.21**	**-0.22**	**-1.13**
∂(GM)/∂p (x10^{-13})	*1.39*	=	*+1.52*	*+0.12*	*+0.04*	*+0.07*	*-0.36*
Full (x10^{-9})	**-1.56**	=	**+0.30**	**-0.36**	**+0.26**	**-0.24**	**-1.53**
∂(Full)/∂p (x10^{-13})	*1.98*	=	*+2.19*	*+0.12*	*+0.09*	*-0.01*	*-0.40*
Northeast point: 36 x 24							
QG (x10^{-9})	**-4.26**	=	**-2.67**	**-0.22**		**-1.37**	
∂(QG)/∂p (x10^{-13})	*-2.49*	=	*-2.84*	*+0.06*		*+0.29*	
GM (x10^{-9})	**-4.70**	=	**-3.13**	**-0.30**	**-0.10**	**-0.73**	**-0.45**
∂(GM)/∂p (x10^{-13})	*-4.57*	=	*-3.61*	*+0.09*	*-1.02*	*+0.07*	*--0.11*
Full (x10^{-9})	**0.14**	=	**+1.42**	**-0.30**	**+0.39**	**-0.96**	**-0.41**
∂(Full)/∂p (x10^{-13})	*1.16*	=	*+1.54*	*+0.09*	*-0.33*	*+0.02*	*-0.16*
Southeast point: 36 x 22							
QG (x10^{-9})	**-3.93**	=	**-1.86**	**-0.25**		**-1.83**	
∂(QG)/∂p (x10^{-13})	*2.75*	=	*+2.75*	*+0.07*		*-0.07*	
GM (x10^{-9})	**-3.28**	=	**-1.85**	**-0.32**	**-0.04**	**-1.10**	**+0.03**
∂(GM)/∂p (x10^{-13})	*2.01*	=	*+2.88*	*+0.11*	*-0.78*	*-0.37*	*+0.18*
Full (x10^{-9})	**0.62**	=	**+1.71**	**-0.32**	**+0.83**	**-1.52**	**-0.08**
∂(Full)/∂p (x10^{-13})	*1.14*	=	*+1.59*	*+0.11*	*-0.22*	*-0.50*	*+0.15*
Southwest point: 34 x 22							
QG (x10^{-9})	**5.05**	=	**+5.98**	**-0.36**		**-0.57**	
∂(QG)/∂p (x10^{-13})	*-3.72*	=	*-3.62*	*+0.09*		*-0.19*	
GM (x10^{-9})	**3.84**	=	**+5.77**	**-0.36**	**-0.01**	**-0.41**	**-1.15**
∂(GM)/∂p (x10^{-13})	*-4.90*	=	*-3.72*	*+0.14*	*-0.31*	*-0.12*	*-0.88*
Full (x10^{-9})	**-0.76**	=	**+0.99**	**-0.36**	**+0.57**	**-0.39**	**-1.57**
∂(Full)/∂p (x10^{-13})	*0.34*	=	*+1.05*	*+0.14*	*0.00*	*-0.30*	*-0.56*

TABLE 5.6B: THERMODYNAMIC AND OMEGA EQUATIONS, 350 MB, 19/00 F06

	$\frac{\partial \Phi_p}{\partial t}(QG)$	$\frac{\partial \Phi_p}{\partial t}(QG_{VS})$	$\frac{\partial \Phi_p}{\partial t}(Full)$	$-(\boldsymbol{u_g}\cdot\nabla)\Phi_p$	$-(\boldsymbol{u}\cdot\nabla)\Phi_p$	$-\omega\bar{\sigma}$	$-\omega\tilde{\sigma}$
	(1+3)	(1+4)	(2+4)	1	2	3	4
Tendencies:	*QuasiG*	*QG(VarStab)*	*Full(=GM)*	*Geos.Adv*	*FullAdv*	*AvStab*	*FullStab*
Center point: 35 x 23							
(*)x10^{-6}	**0.80**	**0.13**	**-0.07**	**-0.32**	**-0.52**	**+1.13**	**+0.45**
$f^{-1}\nabla^2(*)x10^{-13}$	*-9.75*	*-4.71*	*-1.17*	*-0.37*	*+3.17*	*-9.38*	*-4.34*
Northwest point: 34 x 24							
(*)x10^{-6}	**0.26**	**-0.12**	**-0.26**	**-0.33**	**-0.46**	**+0.59**	**+0.21**
$f^{-1}\nabla^2(*)x10^{-13}$	*-0.24*	*2.02*	*3.93*	*-0.05*	*+1.85*	*-0.18*	*+2.08*
Northeast point: 36 x 24							
(*)x10^{-6}	**0.87**	**0.18**	**0.00**	**-0.20**	**-0.38**	**+1.08**	**+0.38**
$f^{-1}\nabla^2(*)x10^{-13}$	*-11.84*	*-8.31*	*-9.16*	*-5.01*	*-5.87*	*-6.83*	*-3.30*
Southeast point: 36 x 22							
(*)x10^{-6}	**0.87**	**0.08**	**-0.12**	**-0.45**	**-0.65**	**+1.32**	**+0.53**
$f^{-1}\nabla^2(*)x10^{-13}$	*-7.20*	*-2.48*	*-1.43*	*+2.13*	*+3.18*	*-9.33*	*-4.61*
Southwest point: 34 x 22							
(*)x10^{-6}	**0.39**	**-0.03**	**-0.05**	**-0.35**	**-0.38**	**+0.74**	**+0.32**
$f^{-1}\nabla^2(*)x10^{-13}$	*-0.48*	*3.92*	*1.79*	*+1.13*	*-1.00*	*-1.61*	*+2.79*

ω-EQ. ERROR CALCULATIONS: $\partial/\partial p$(vorticity tendency) - $f^{-1}\nabla^2(\partial\Phi/\partial p$ tendency)

(*)x10^{-13}	***35 x 23***	***34 x 24***	***36 x 24***	***36 x 22***	***34 x 22***
Quasi-Geostrophic	**11.36**	**1.55**	**9.35**	**9.95**	**-3.24**
QG with variable σ	**6.31**	**-0.71**	**5.82**	**5.23**	**-7.64**
Geostrophic Momentum	**1.78**	**2.53**	**4.59**	**3.44**	**-6.69**

APPENDIX B

PARTICULARLY LONG FIGURE CAPTIONS

Fig. 2.6: Observed individual cyclone tracks through the study region during GALE, 13 Jan 1986 to 17 Mar 1986. Cyclone tracks were smoothed by averaging the actual cyclone position with the average of its positions immediately before and after. Dashed lines indicate cyclone tracks which are retrograde (westward) for long distances. Figure does not depict the tracks of cyclones which did not pass within the study area, which is indicated by the double lines.

Fig. 2.7: Schematic diagrams showing the biases inherent in counting cyclones passing through bins (from Taylor 1986). Upper figure: Evenly-spaced cyclone tracks, oriented east-west and north-south. A simple count of cyclone tracks passing through the rectangular bins would erroneously give twice the cyclone track density for the north-south oriented cyclone track region, while the square bins would correctly show the same number of cyclones in both areas. Lower figure: Even the square bins are subject to biases based on prevailing cyclone track orientations. The number of cyclone tracks passing through box B is 1.4 times the number of cyclone tracks passing through box A, even though the actual cyclone track density is identical.

Figs. 3.6-3.11: Time series cross sections across or upstream of the track of the small-scale cyclone. Each box contains a single hourly observation, with the time of observations listed at the edge of the row of boxes. The station model is an abbreviated standard model, including winds and sky conditions, along with (clockwise from top): pressure (10ths of mb, corrected for systematic bias and with the cross-section mean pressure removed as described in the text), accumulated rainfall (in), ceiling (100s of ft), dew point (F), present weather, and temperature (F). The cross-section mean pressure

(10ths of mb, leading digits dropped) is listed at the edge of each row. The winds have been rotated to account for the orientation of the cross section, which is indicated in Fig. 3.5 and by the directional arrow (pointing toward north) on the side of the figure. For example, if north is toward the upper left corner of the page, a wind plotted as blowing from the top of the page is blowing from the northeast and directly normal to the cross section. Observations not directly on the cross section line have been shifted by one to three hours (as stated in the captions) to correct for the assumed motion of weather systems.

Figs. 3.19-3.27: Four-panel plots of potential vorticity and potential temperature. (a) Tropopause (1.5 PVU surface) winds (standard model) and potential temperatures (c.int. 5 K), calculated using the triangle method as described in Nielsen (1988). (b) Potential vorticity in the 315-325 K isentropic layer. Contour interval is 1.5 PVU (thick lines). Also contoured are intermediate contours (thin lines) every 0.25 PVU between 0.0 PVU and 1.5 PVU, to shown PV structure in the troposphere. The 0.5 PVU contour is highlighted. Also plotted are observed 320 K winds (standard model) and pressures (mb). (c) Surface potential temperature, analyzed from rawinsonde station observations (c.int. 5 K). (d) As in b), but for the 295-305 K layer, with observations at 300 K plotted.

Figs. 4.6-4.11: Four-panel plots of potential vorticity and potential temperature, from the 00 UTC 19 Jan 1986 NGM model run. Plotting conventions are similar to Figs. 3.19-3.27. (a) Potential temperature (c.int. 5 K, with 300 K, 320 K, and 340 K lines thick) on the 1.5 PVU (tropopause) surface. (b) Potential vorticity in the 315-325 K isentropic layer, with winds (standard model) on the 320 K surface. Contour interval is 1.5 PVU (thick lines). Also contoured are intermediate contours (thin lines) every 0.25 PVU between 0.0 PVU and 1.5 PVU, to shown PV structure in the troposphere. The 0.5 PVU contour is cross-hatched. (c) Potential temperature (c.int. 5 K, 280 K contour

thick) and wind (same model as in (b)), on the 1000 mb surface. (d) As in (b), but for 295-305 K layer (potential vorticity) and 300 K surface (wind).

Fig. 4.13: 850 mb relative vorticity (c.int. 1×10^{-5} sec^{-1}, negative contours dashed), constructed by bitwise inversion of potential vorticity (see text) from the 00 UTC 19 Jan 1986 NGM model run. (a) Vorticity from potential vorticity inversion of level mean values of potential vorticity at all levels and mean potential temperature at the upper and lower boundaries. (b) As in (a), but with actual NGM potential temperature on the upper boundary and actual NGM potential vorticity above 500 mb. (c) As in (a), but with actual NGM potential vorticity between 500 mb and 900 mb. (d) As in (a), but with actual NGM potential vorticity at 950 mb and actual NGM potential temperature on the lower boundary. (e) Vorticity from inversion of full forecasted potential vorticity and boundary potential temperature. (f) Actual forecasted NGM relative vorticity.

Fig. 5.11-5.15: Vertical profiles with respect to pressure (200 mb to 1000 mb) of various dynamical terms in the vorticity, thermodynamic, and divergence equations (see Section 5.4b for details), for points in the center of updrafts in the 00 UTC 19 Jan 1986 NGM forecast run. Solid line with circles: vertical motion (ω), units of 1×10^{-1} Pa s^{-1}; dashed line with circles: horizontal Lagrangian tendency $\left(\frac{\partial}{\partial t} + \boldsymbol{u} \cdot \boldsymbol{\nabla}\right)$ of the vertical derivative with respect to pressure of vertical motion (ω_p), horizontally filtered, units of 1×10^{-9} s^{-2}. Solid line with squares: relative vorticity (ζ), units of 1×10^{-5} s^{-1}; dashed line with squares: horizontal Lagrangian tendency of relative vorticity, units of 1×10^{-9} s^{-2}. Solid line with triangles: geostrophic relative vorticity (ζ_g), units of 1×10^{-5} s^{-1}; dashed line with triangles: horizontal Lagrangian tendency of the vertical derivative with respect to pressure of geostrophic relative vorticity, horizontally filtered, units of 1×10^{-13} s^{-2} Pa^{-1}.

Figs. 5.16-5.17: Comparison of terms in the geostrophic vorticity tendency equation (5.45), for pressure levels with maximum convective instability in the first updraft (Fig. 5.16), and second updraft (Fig. 5.17), 00 UTC 19 Jan 1986 NGM model run. Columns

are for successive six-hourly forecasts (6, 12, and 18 hours in Fig. 5.16; 12, 18, and 24 hours in Fig. 5.17. Row 1: $-\frac{1}{f}(\nabla^2\omega\tilde{\sigma})$, contour interval $1\text{x}10^{-13}$ Pa^{-1} s^{-2}, negative contours dashed. Row 2: $-\frac{1}{f}\left[\nabla^2(\boldsymbol{u}\cdot\nabla)\Phi_p - (\boldsymbol{u}\cdot\nabla)\nabla^2\Phi_p\right]$, contour interval $1\text{x}10^{-13}$ Pa^{-1} s^{-2}, negative contours dashed. Row 3: ω, contour interval $1\text{x}10^{-1}$ Pa s^{-1}, negative contours dashed.

Fig. 6.18: Cross sections through the updraft, NGM 12-hour forecast valid 12 UTC 10 Feb 1986. Cross section is oriented normal to the thermal wind and track of the small-scale cyclone, with north to the left and south to the right. Approximate length of cross sections: 920 km; vertical coordinate: pressure (mb). Margin of saturated region indicated by squiggly line. a) M (dashed lines) and saturated equivalent potential temperature (solid lines, contour interval 1 K in saturated regions and 2 K otherwise). b) Wind vectors in plane of cross section, appropriately scaled to show instantaneous parcel trajectories.

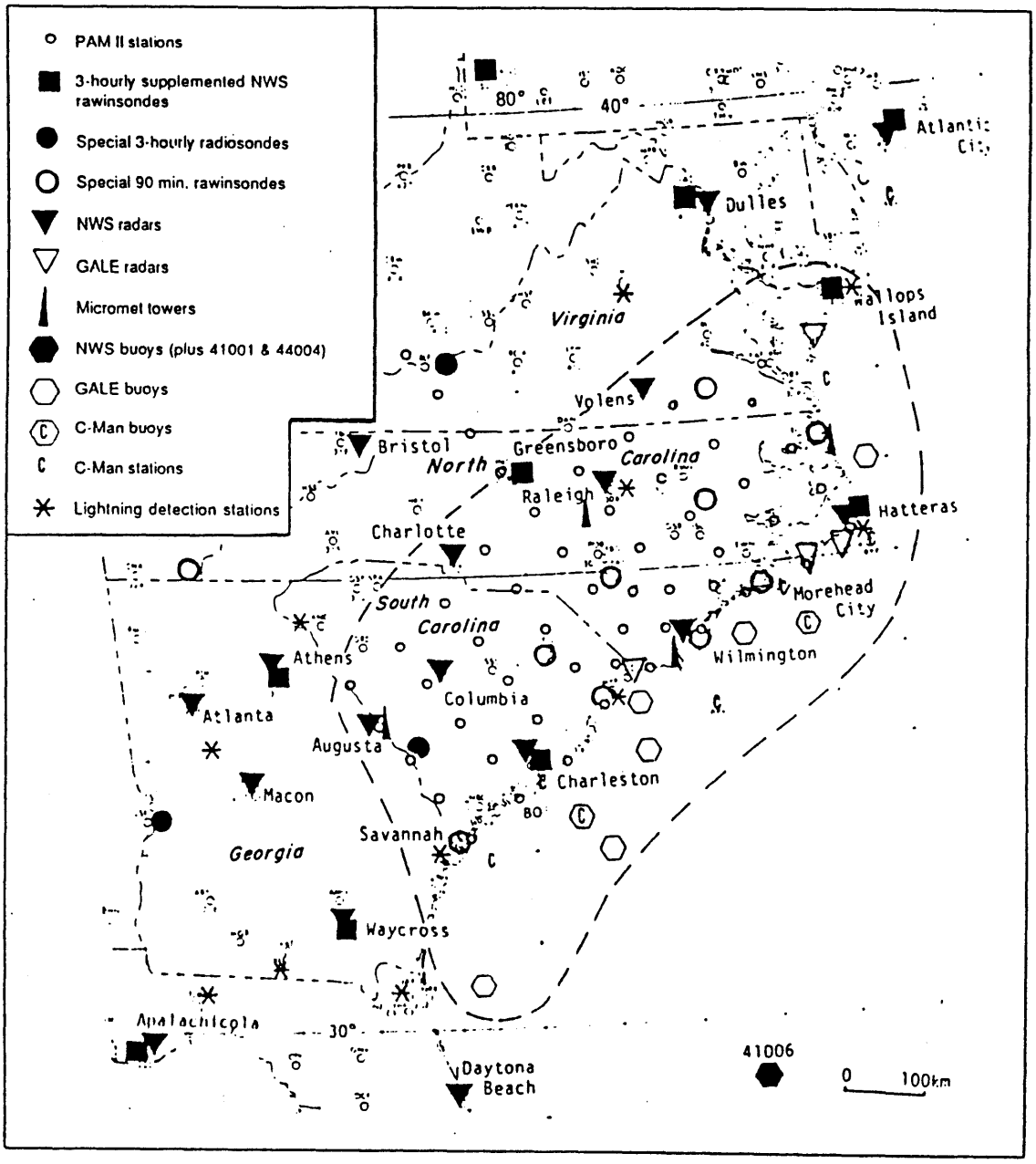

FIG. 1.1: GALE special surface-based observing facilities. Inner GALE area shown by dashed line.

From Dirks *et al.* (1988).

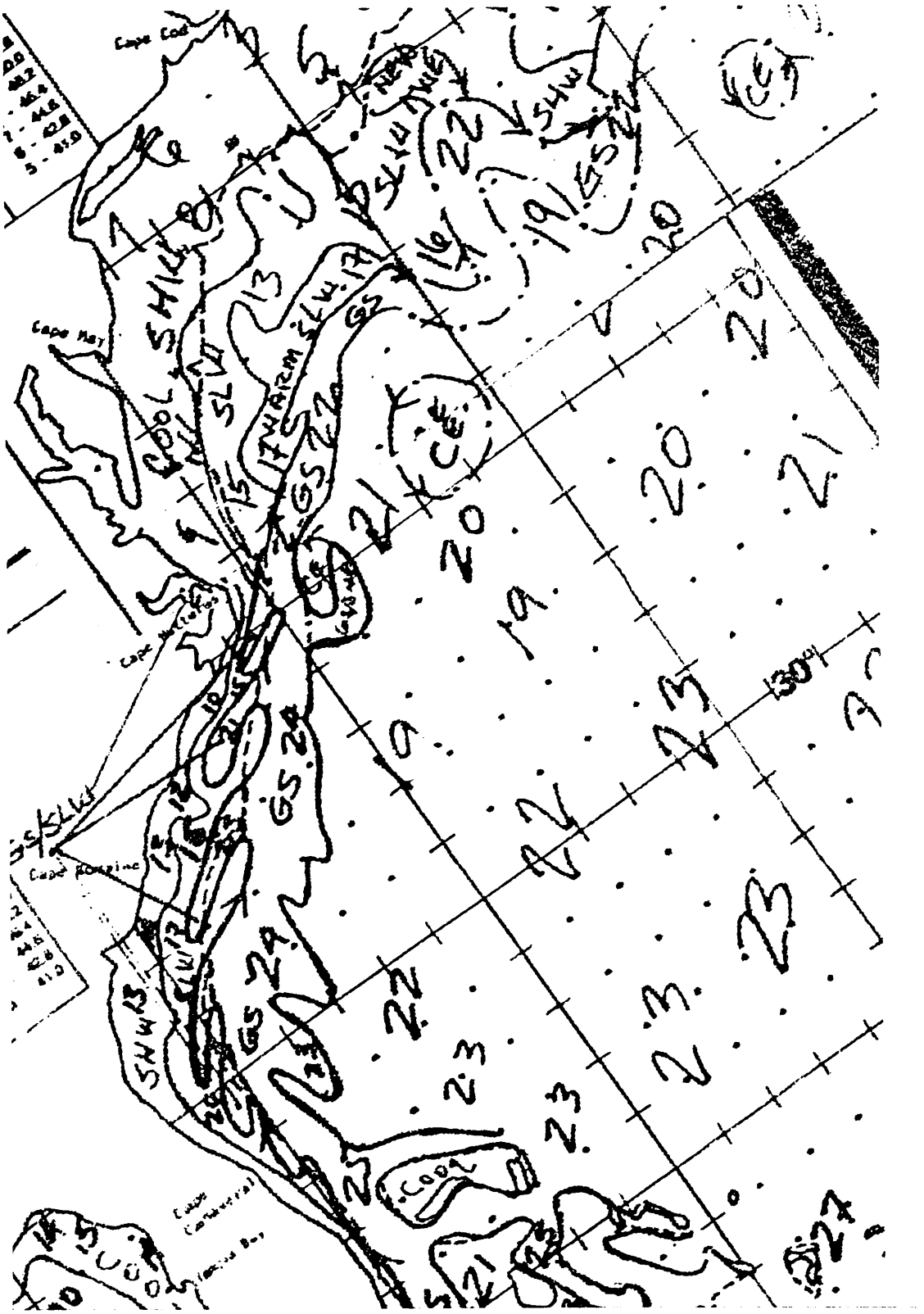

Fig. 1.2: NMC sea surface temperature analysis (Celsius), 16-17 Jan 1986. GS = Gulf Stream.

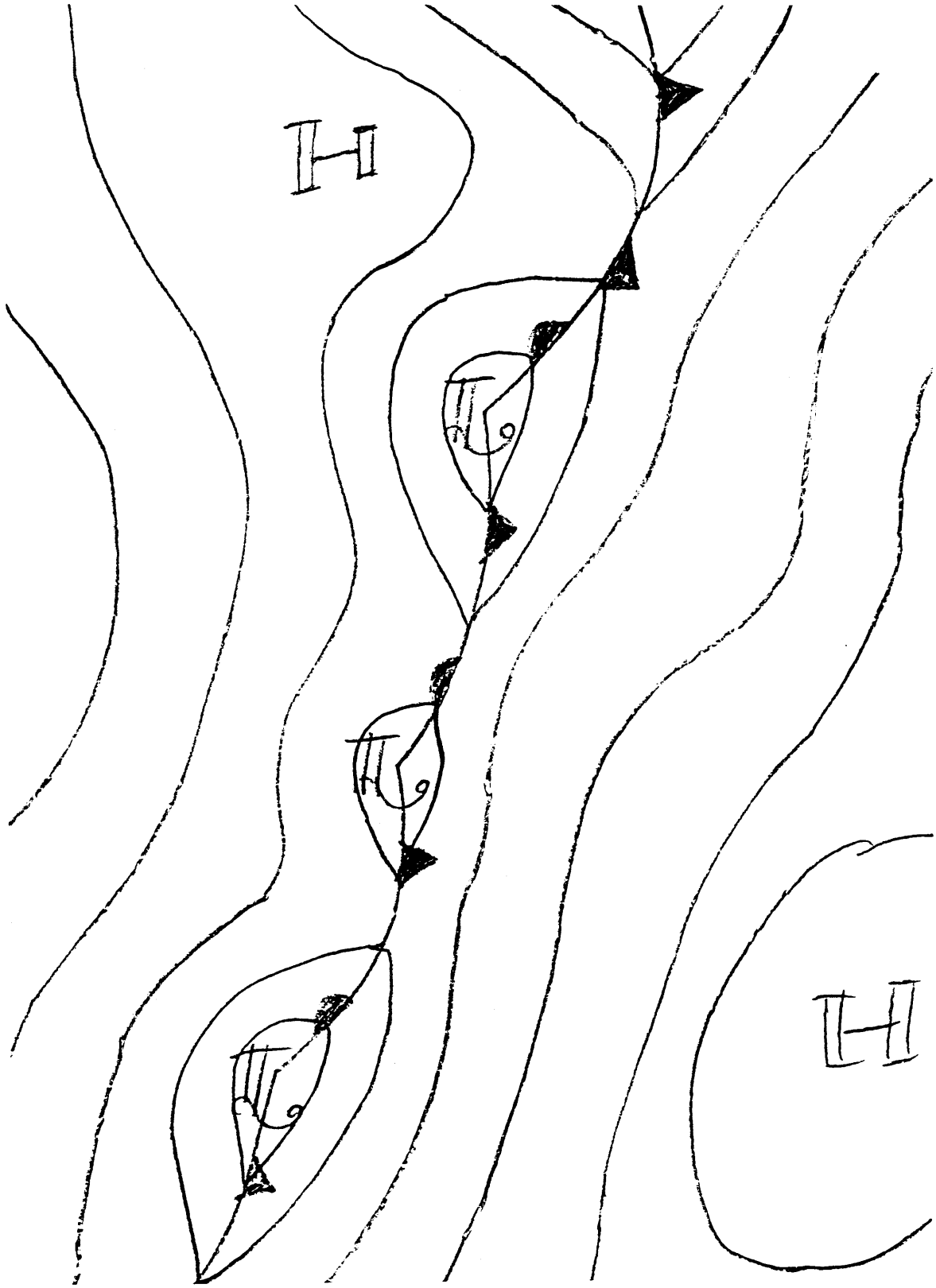

Fig. 2.1a: Schematic surface pressure analysis of a cyclone family along a front.

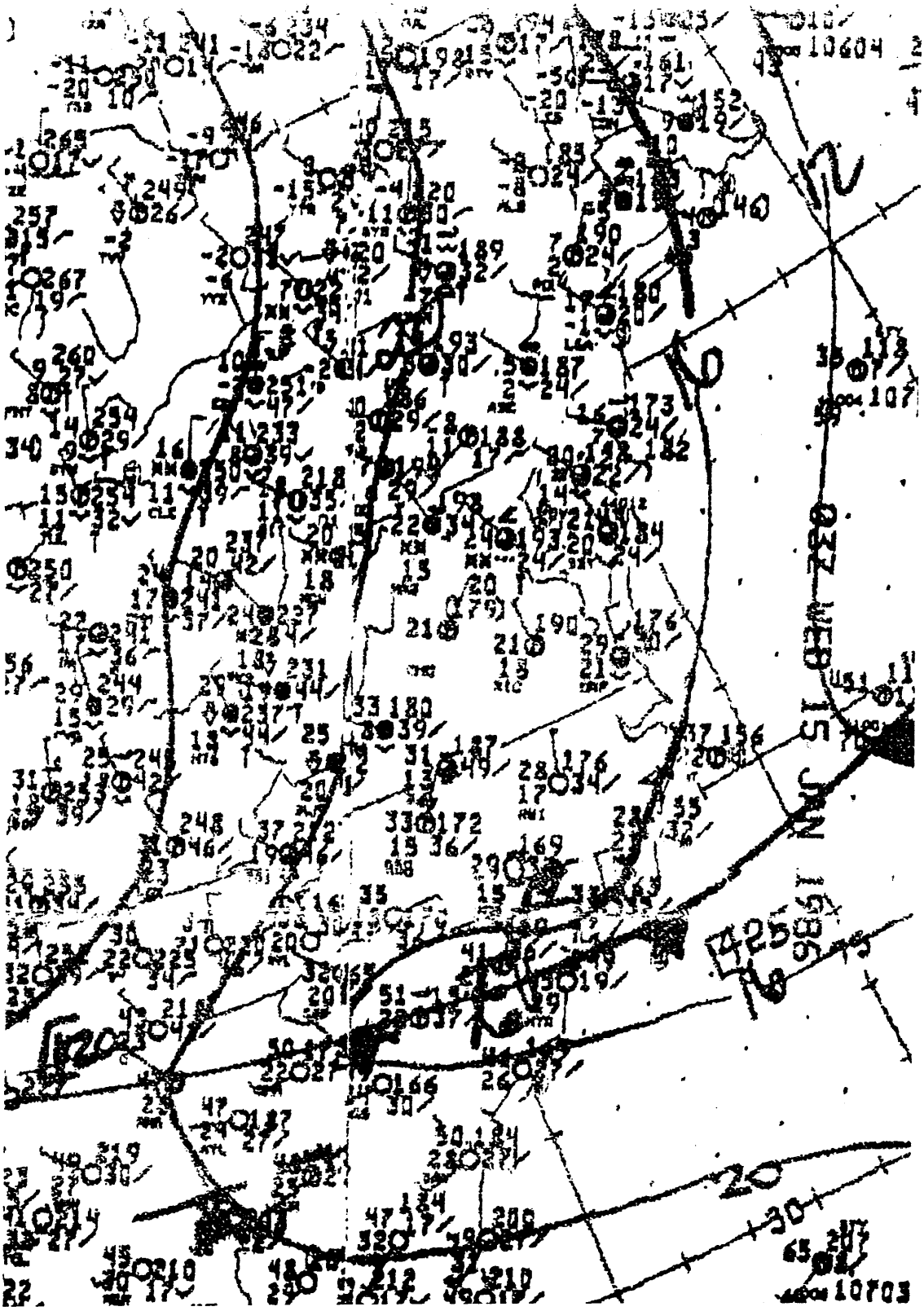

Fig. 2.1b: NMC surface pressure analysis (0300 UTC 15 Jan 1986), showing an example of a small-scale Appalachian lee cyclone.

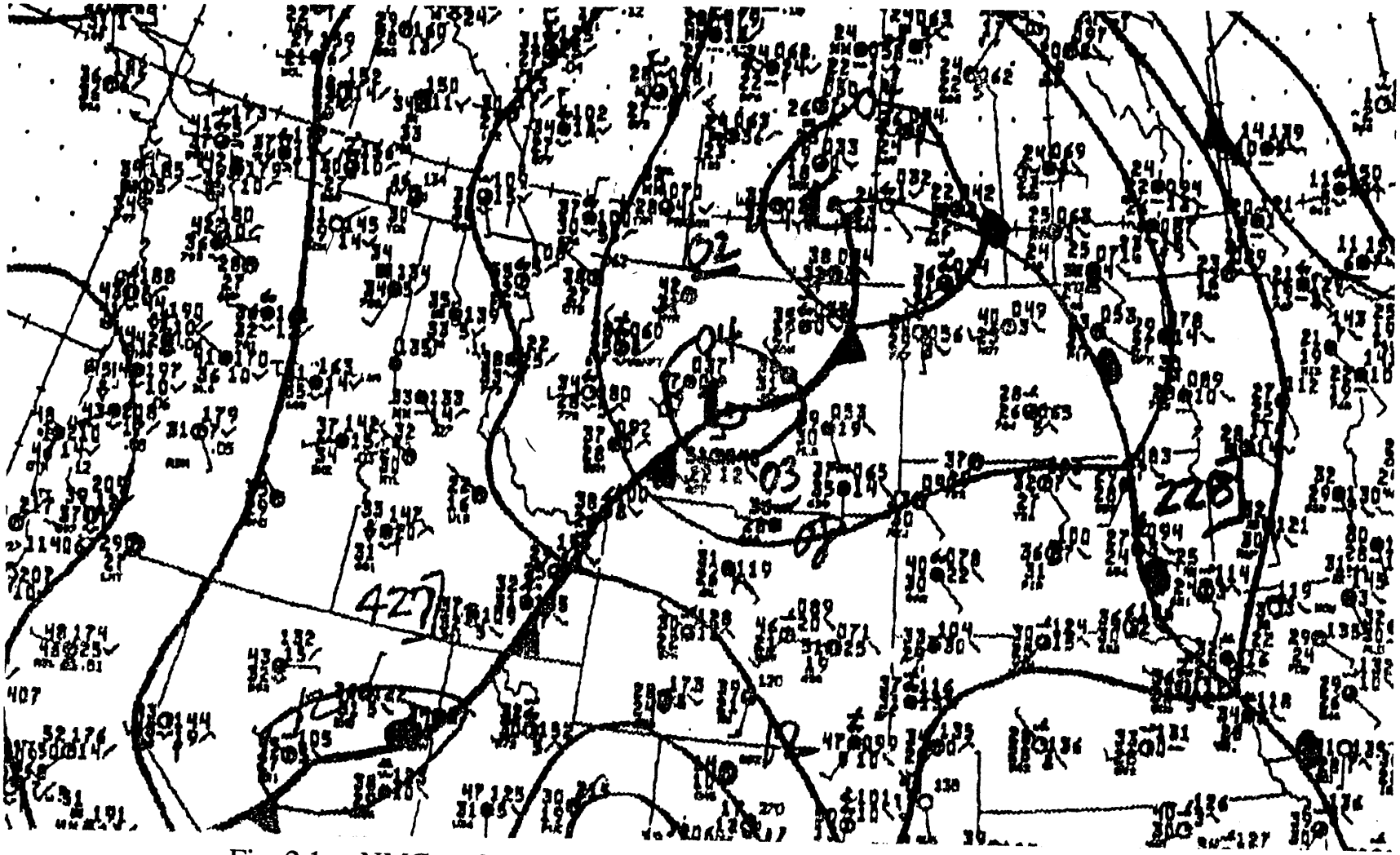

Fig. 2.1c: NMC surface pressure analysis (0600 UTC 20 Jan 1986), showing an example of multiple small-scale low centers within a large-scale cyclone.

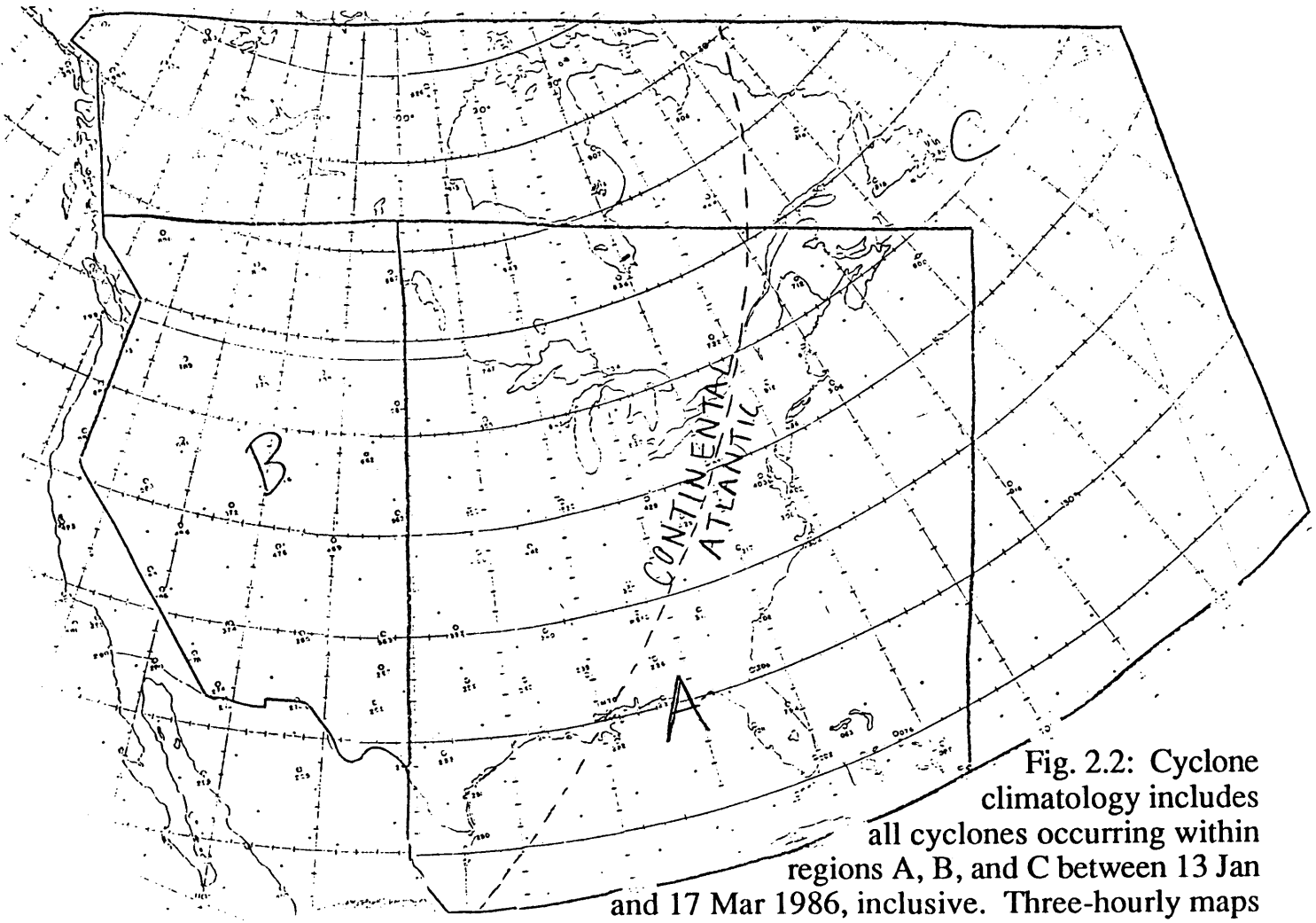

Fig. 2.2: Cyclone climatology includes all cyclones occurring within regions A, B, and C between 13 Jan and 17 Mar 1986, inclusive. Three-hourly maps used for regions A and B; six-hourly maps otherwise. Three-hourly cyclone positions recorded for region A; six-hourly positions otherwise. Dashed line defines genesis regions for Continental and Atlantic cyclones (Section 2.5).

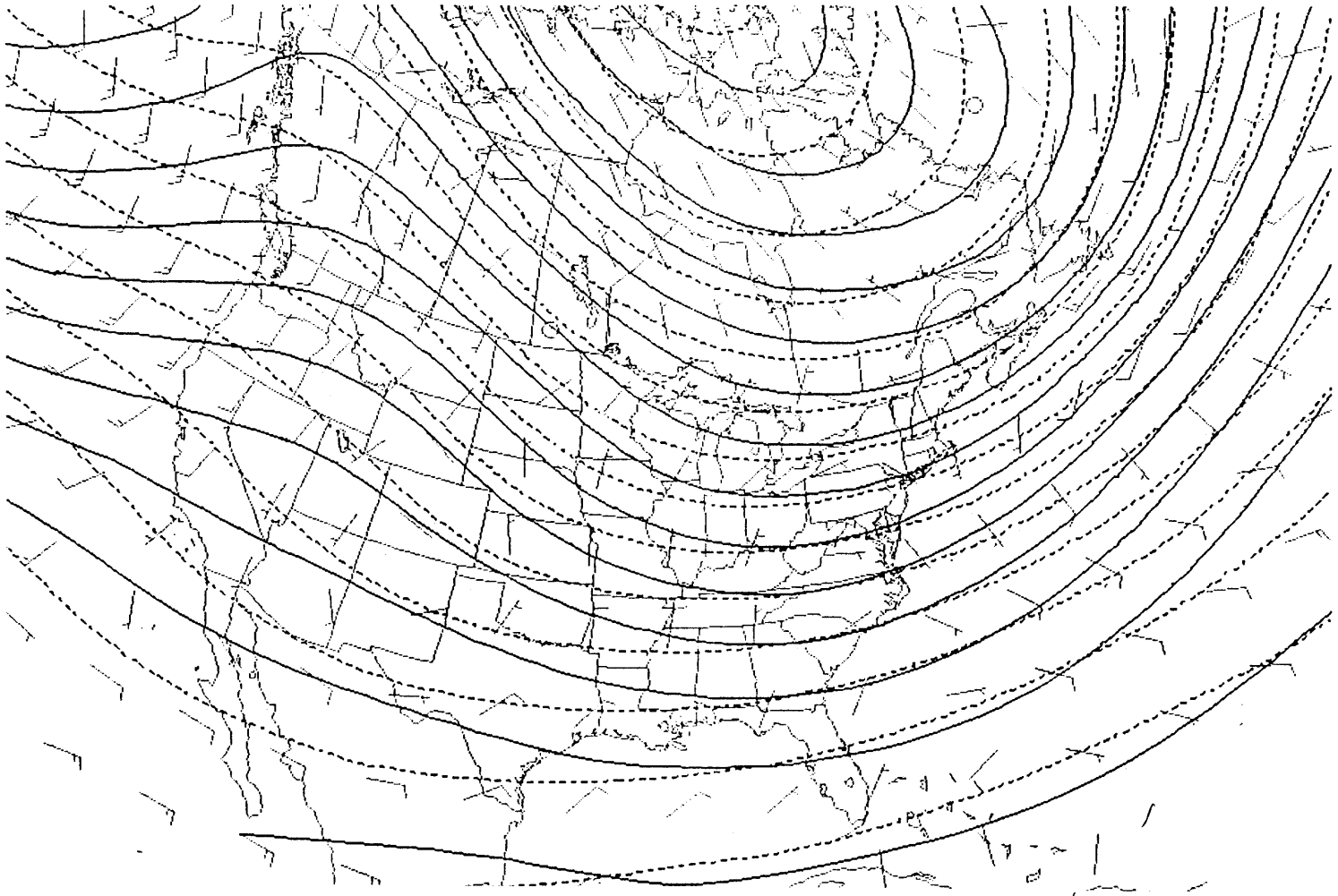

Fig. 2.3: Mean 500 mb geopotential heights during GALE (solid, c.int. 60m); Climatological (1962-1986) heights for GALE period (dashed); geostrophic wind deviation from climatology (standard model, *i. e.* one long barb equals 10 kt (5.2m/s)).

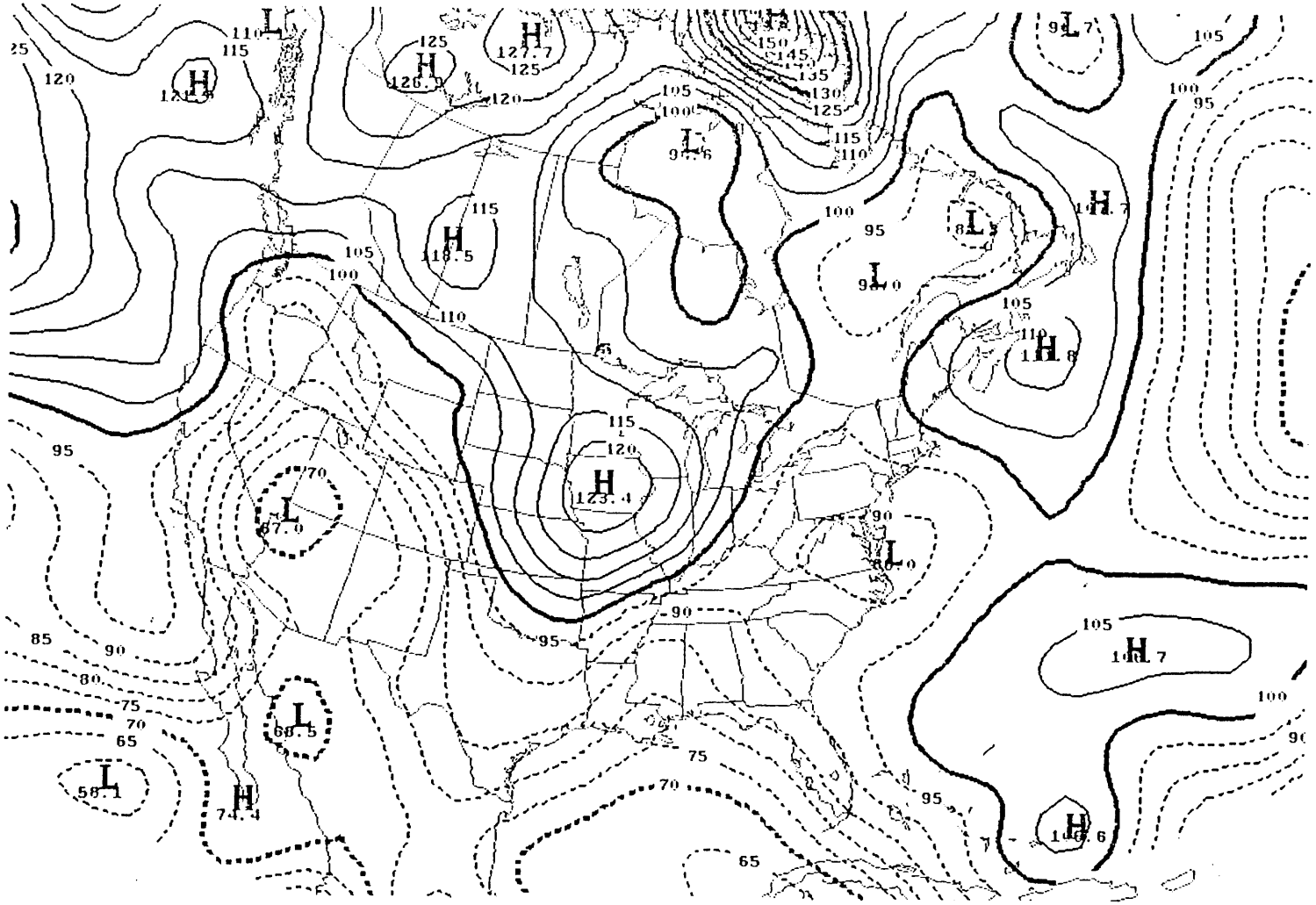

Fig. 2.4: Deviation from climatology of 1000 mb bandpass heights during GALE (see text). Values above (below) 100% indicate anomalously high (low) eddy activity.

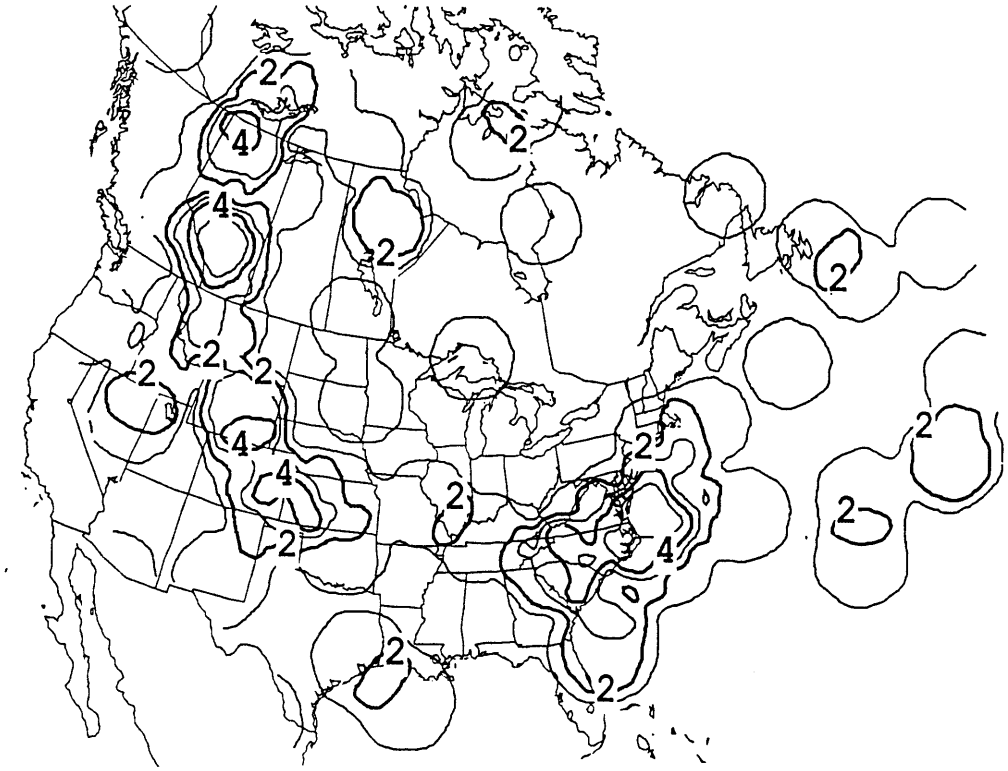

Fig. 2.5a: Number of cyclogenesis events within 300 km radius during GALE. Events filtered (see text) for comparison with Fig. 2.5b.

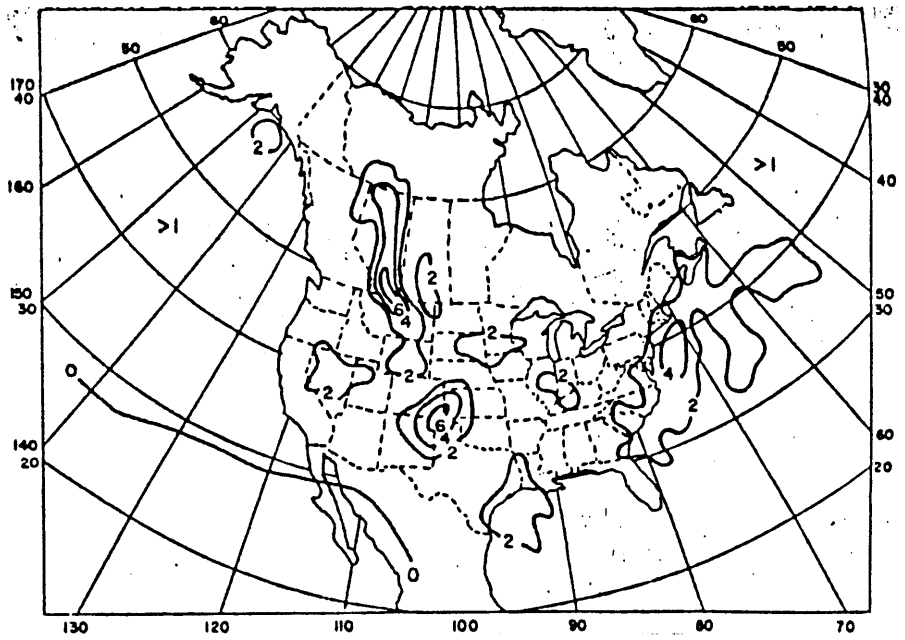

Fig. 2.5b: January climatological cyclogenesis frequency, using 2 degree latitude-longitude bins. From Zishka and Smith (1980).

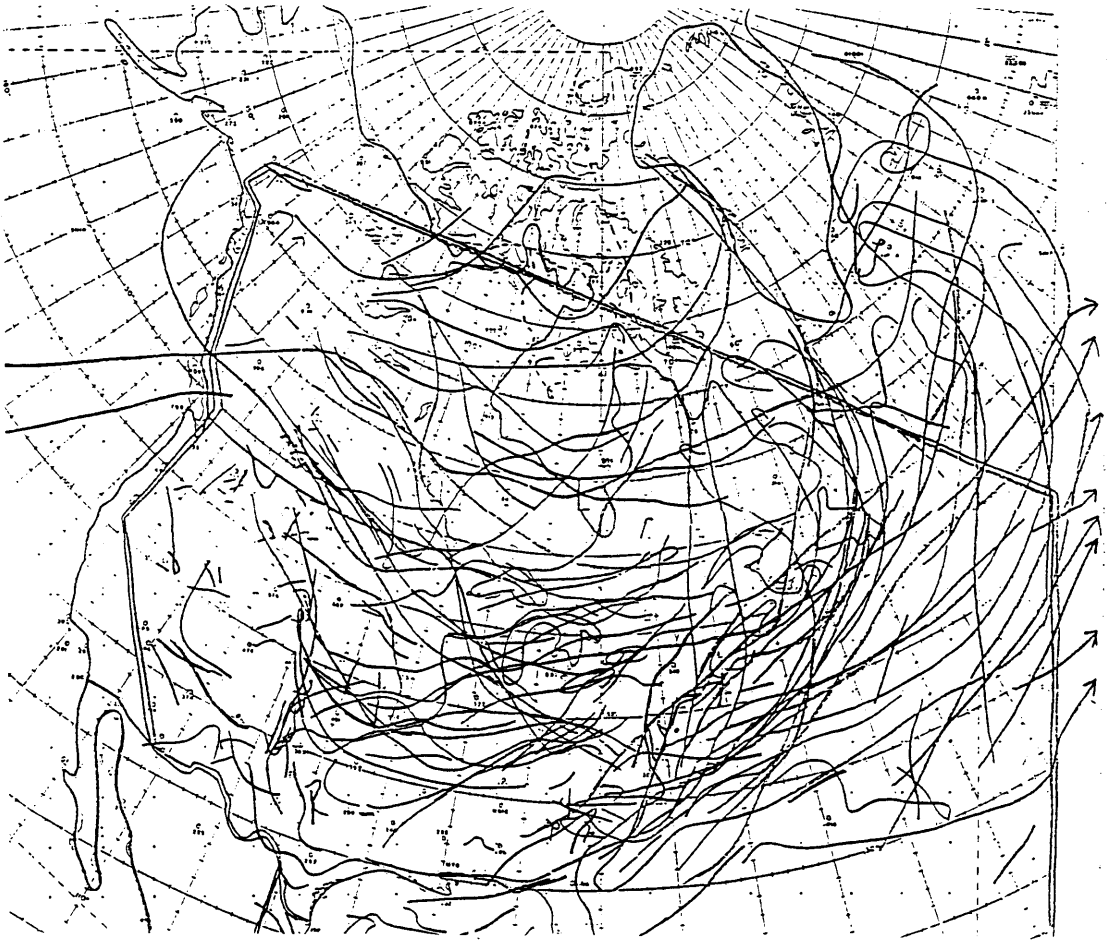

Fig. 2.6: Observed individual cyclone tracks during GALE. Full description in Appendix B.

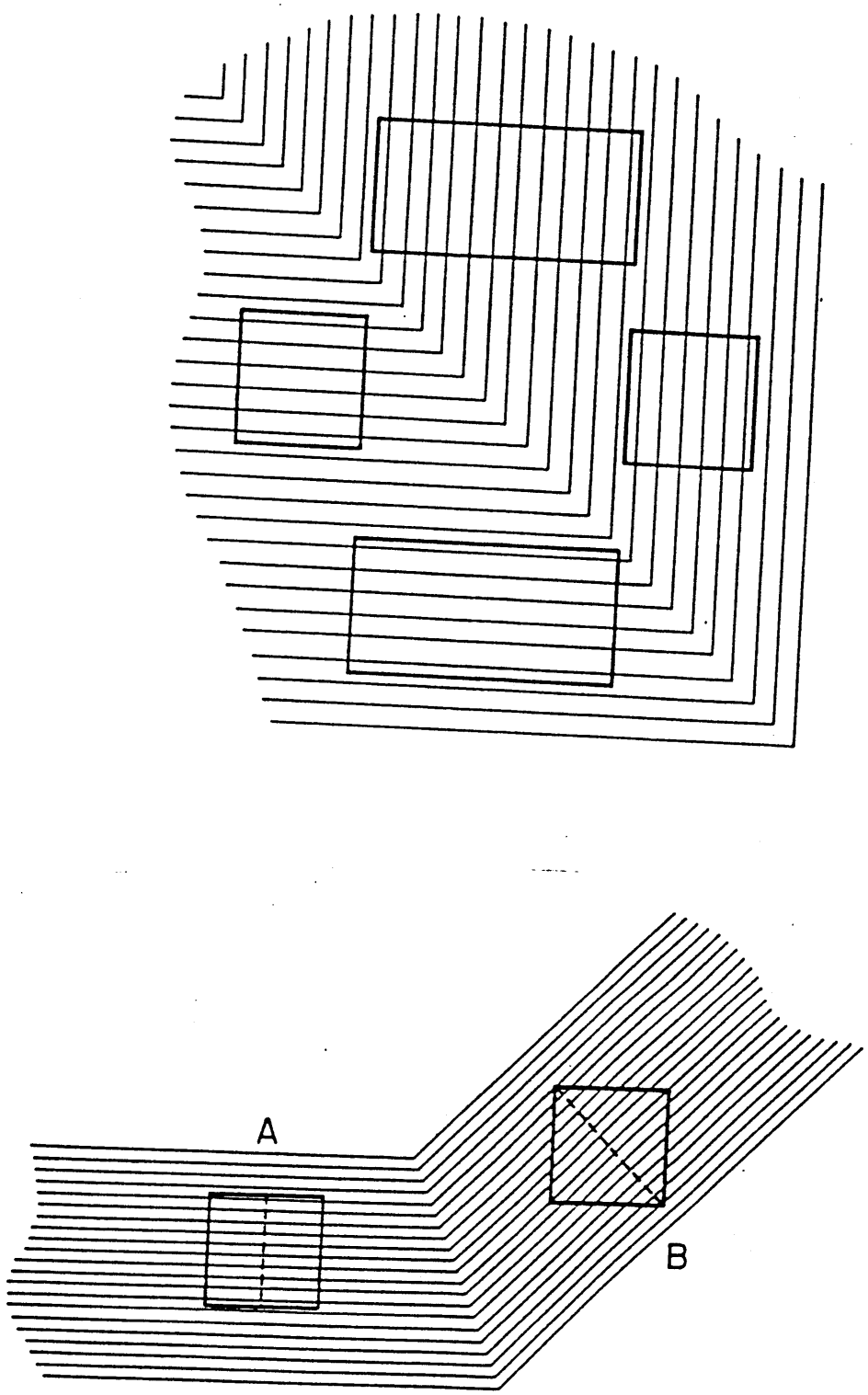

Fig. 2.7: Schematic diagram of sources of error in standard cyclone climatology methods. See Appendix B. From Taylor (1986).

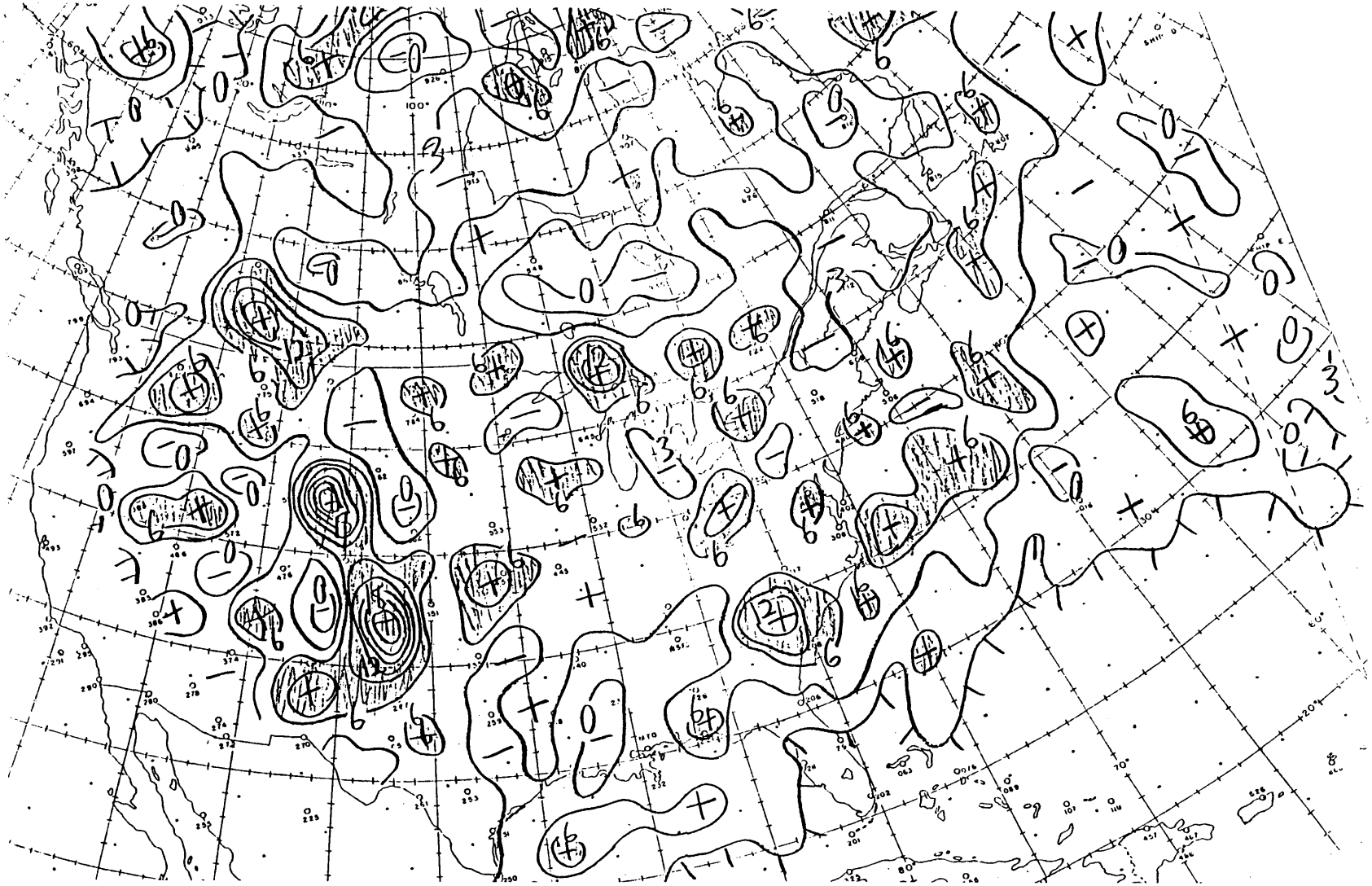

Fig. 2.8: Total number of cyclone centers found on six-hourly maps during GALE within circles of150 km radius.

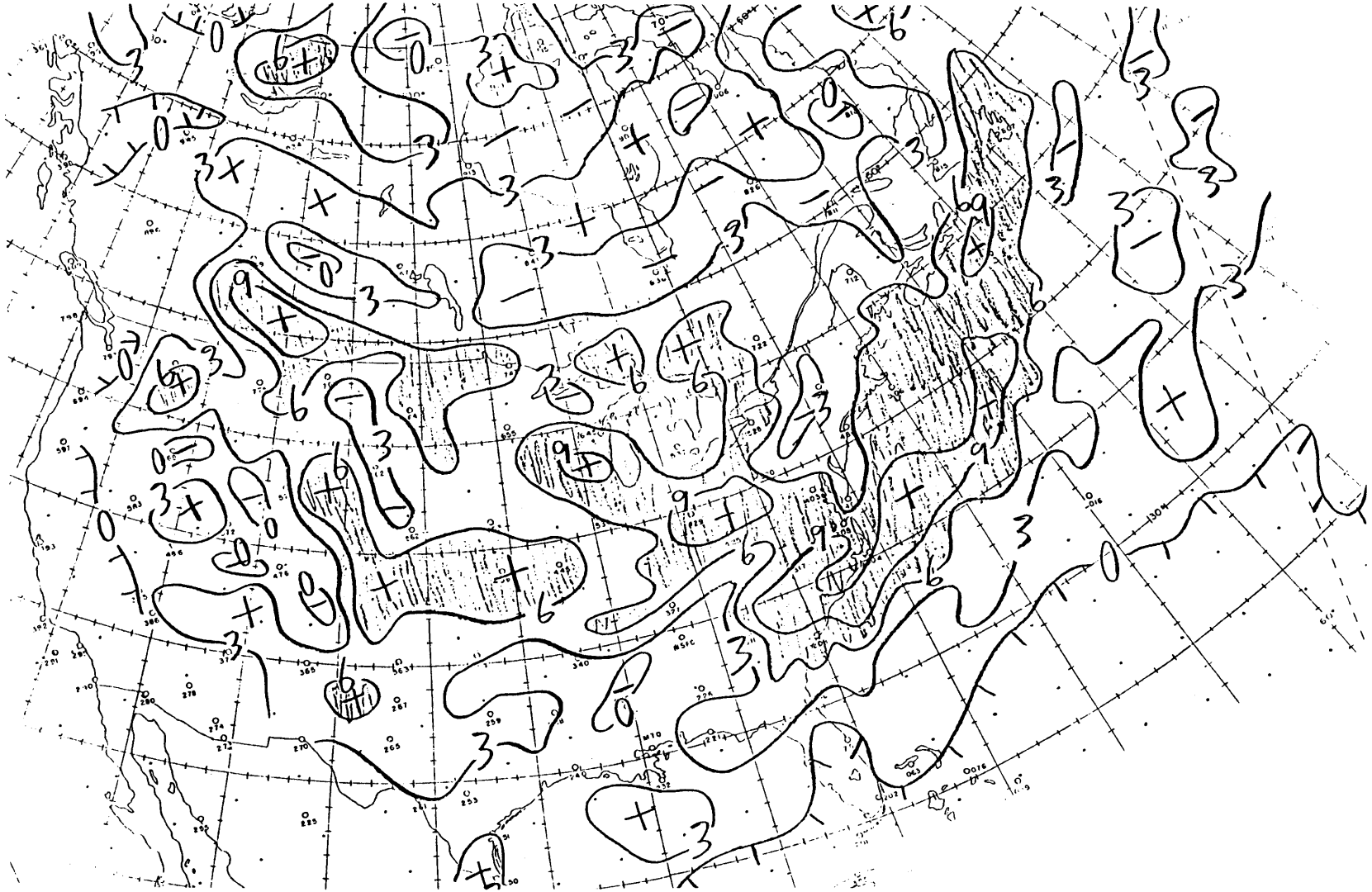

Fig. 2.9: Total number of cyclone tracks passing through circles of 150 km radius during GALE.

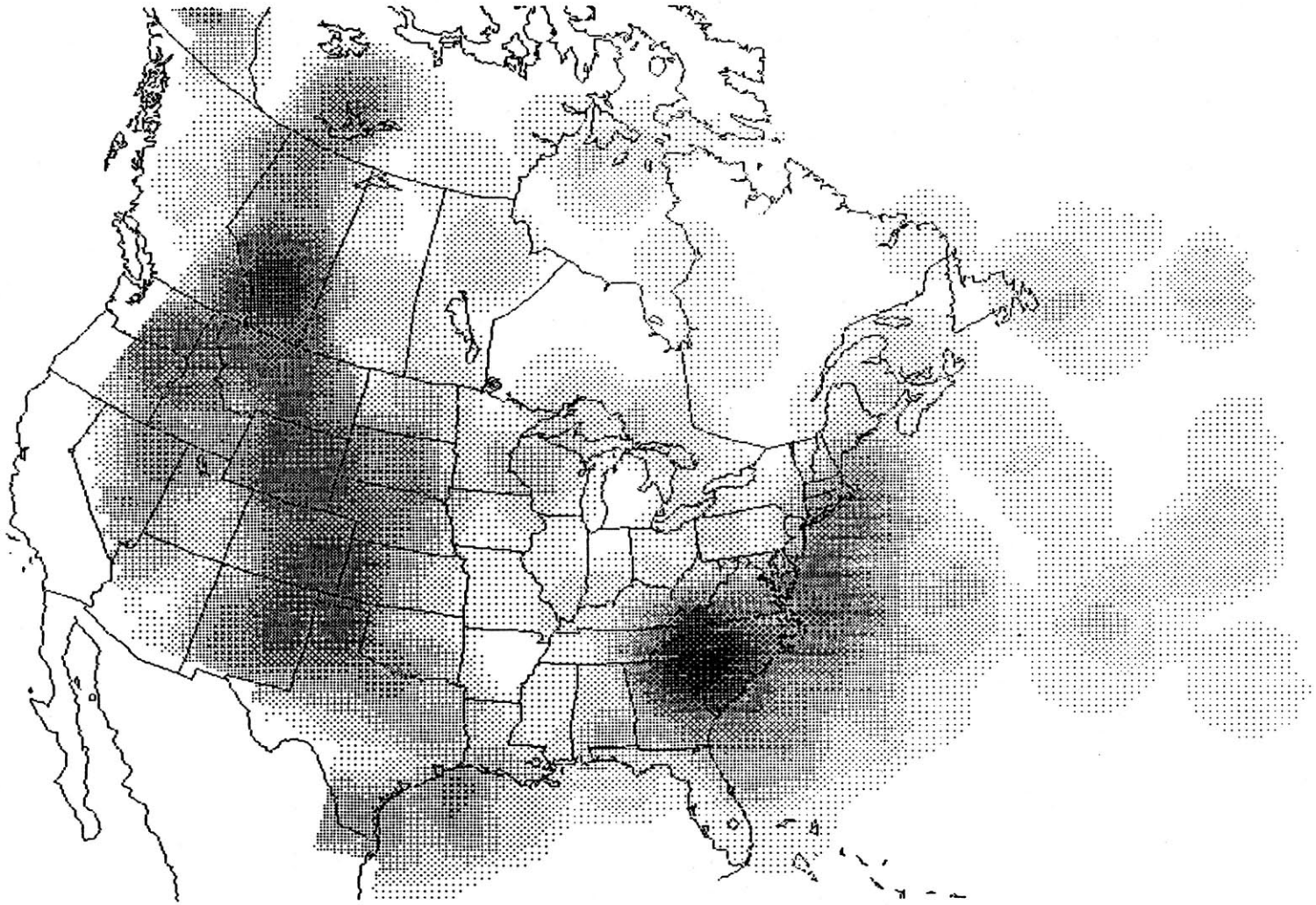

Fig. 2.10: Total number of cyclogenesis events within circles of 150 km during GALE. Shading increment = 1 event (for Figs. 2.10-2.13 & 2.22).

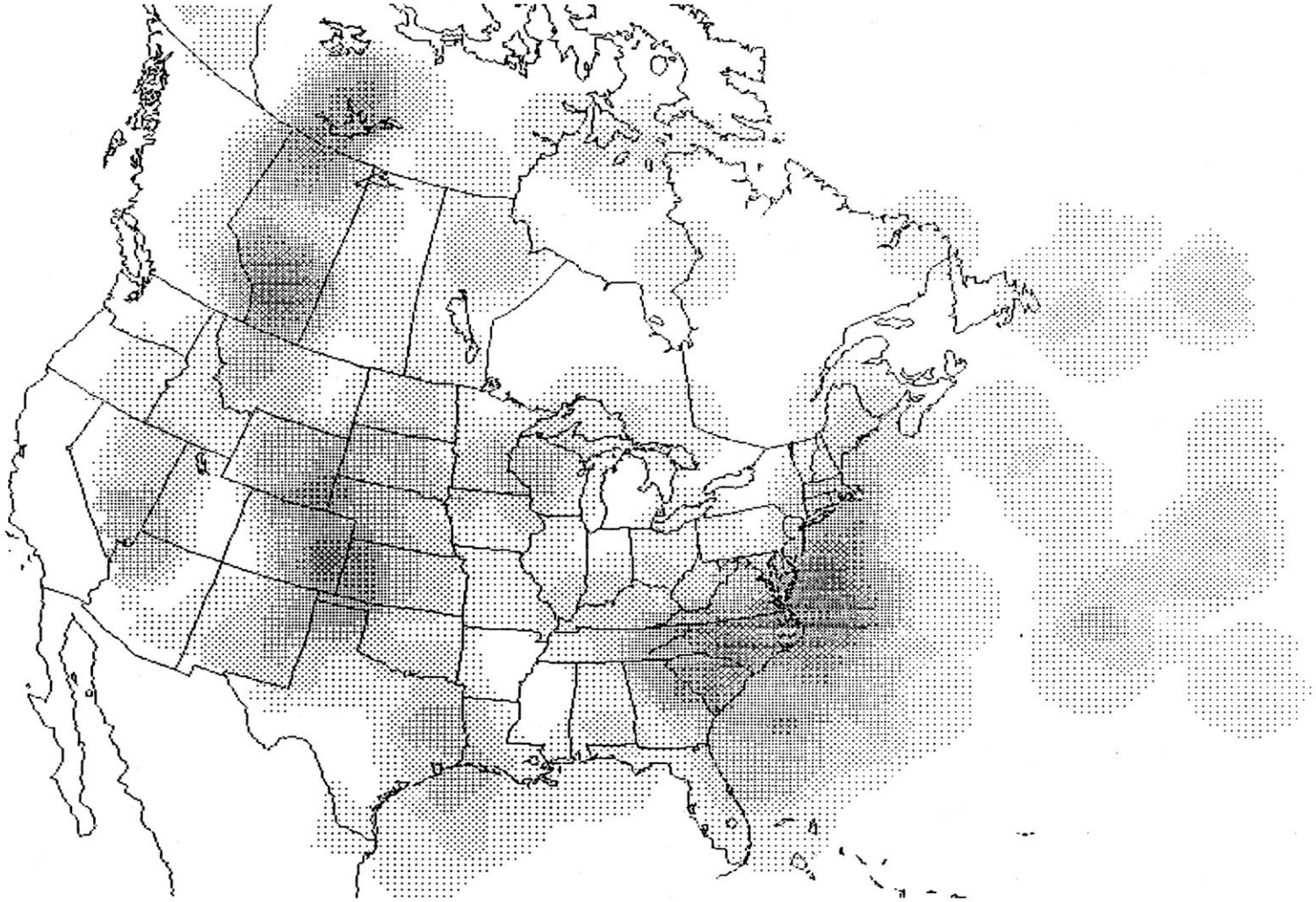

Fig. 2.11: Number of cyclogenesis events during GALE for cyclones which travel at least 400 km from their cyclogenesis location.

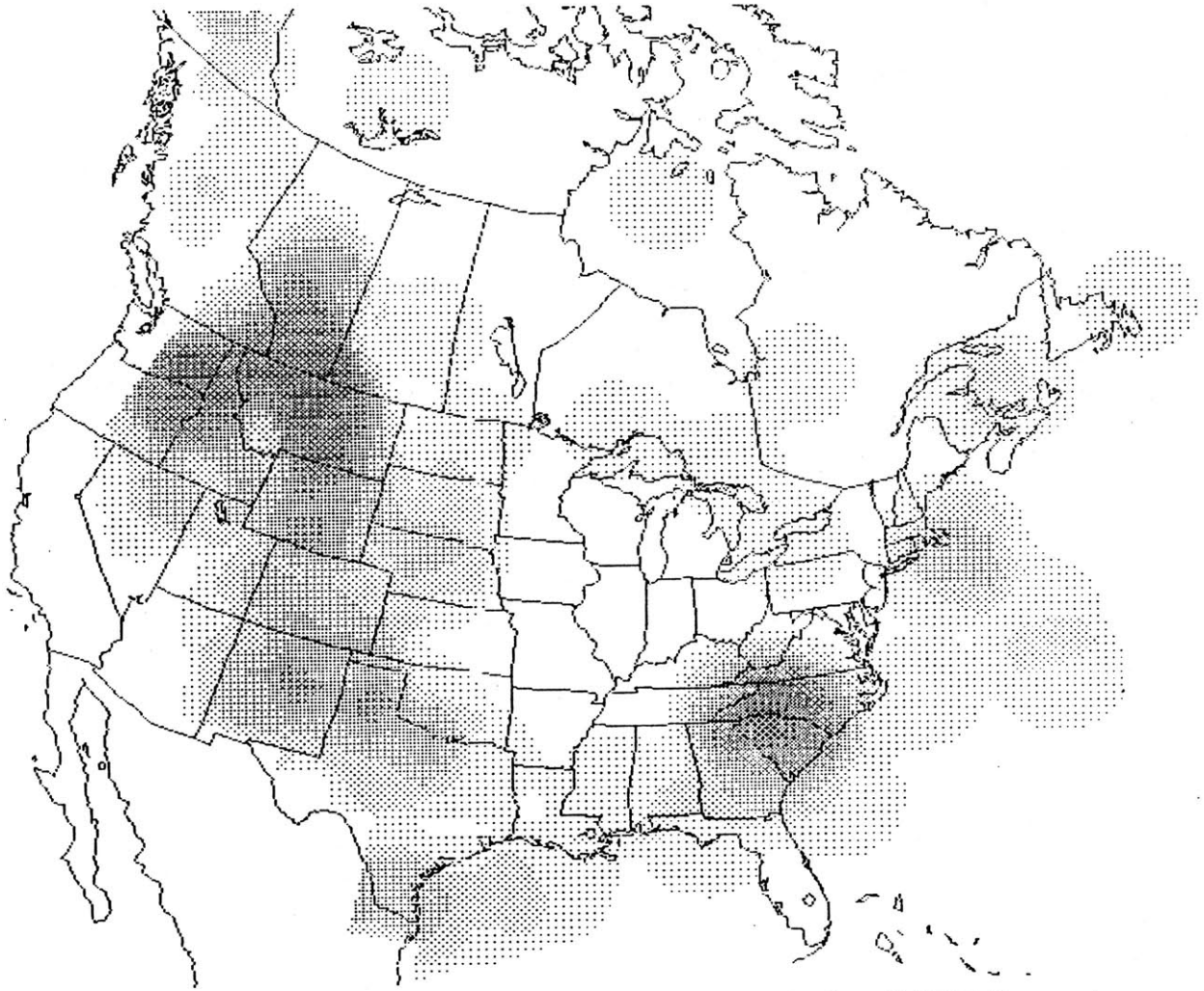

Fig. 2.12: Number of cyclogenesis events during GALE for cyclones which *do not travel 400 km* from their cyclogenesis location. Compare Fig. 2.11.

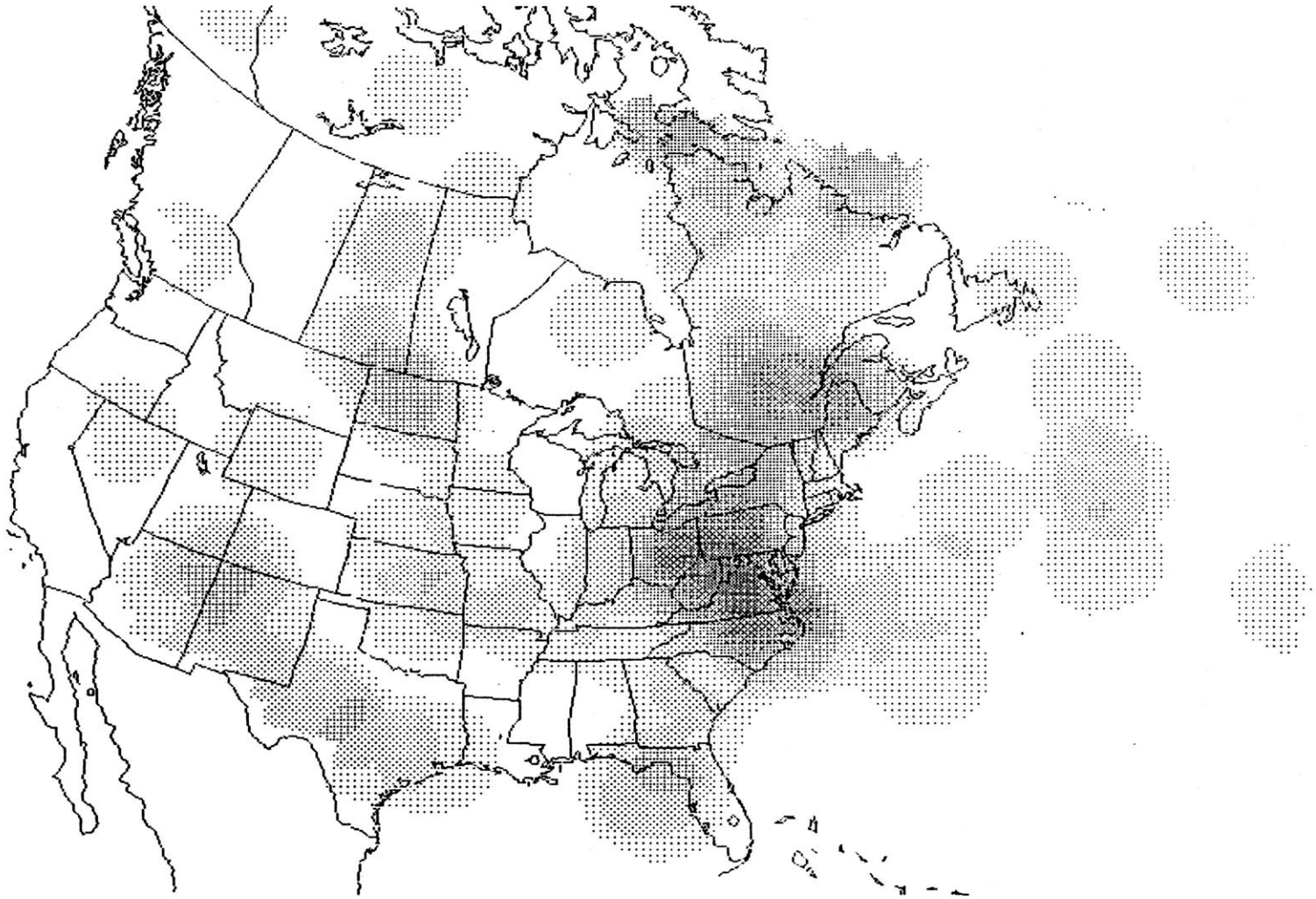

Fig. 2.13: Number of *cyclolysis* events during GALE for cyclones which travel at least 400 km from their cyclogenesis location.

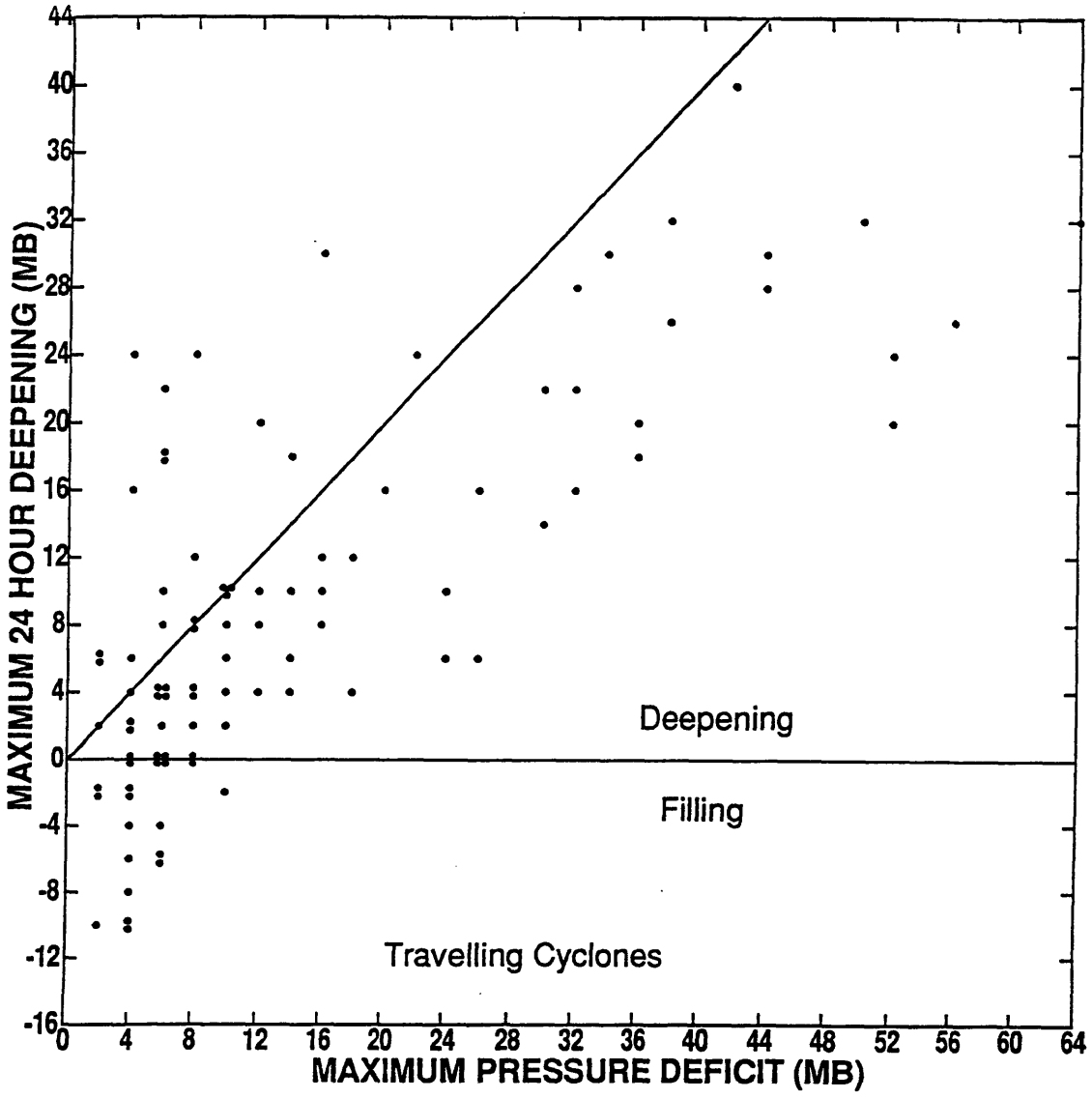

Fig. 2.14. See text for definitions of terms. For each cyclone found above the diagonal line, the largest 24-hour drop in central pressure was greater than the maximum analyzed pressure difference between the cyclone and its environment.

Fig. 2.15.

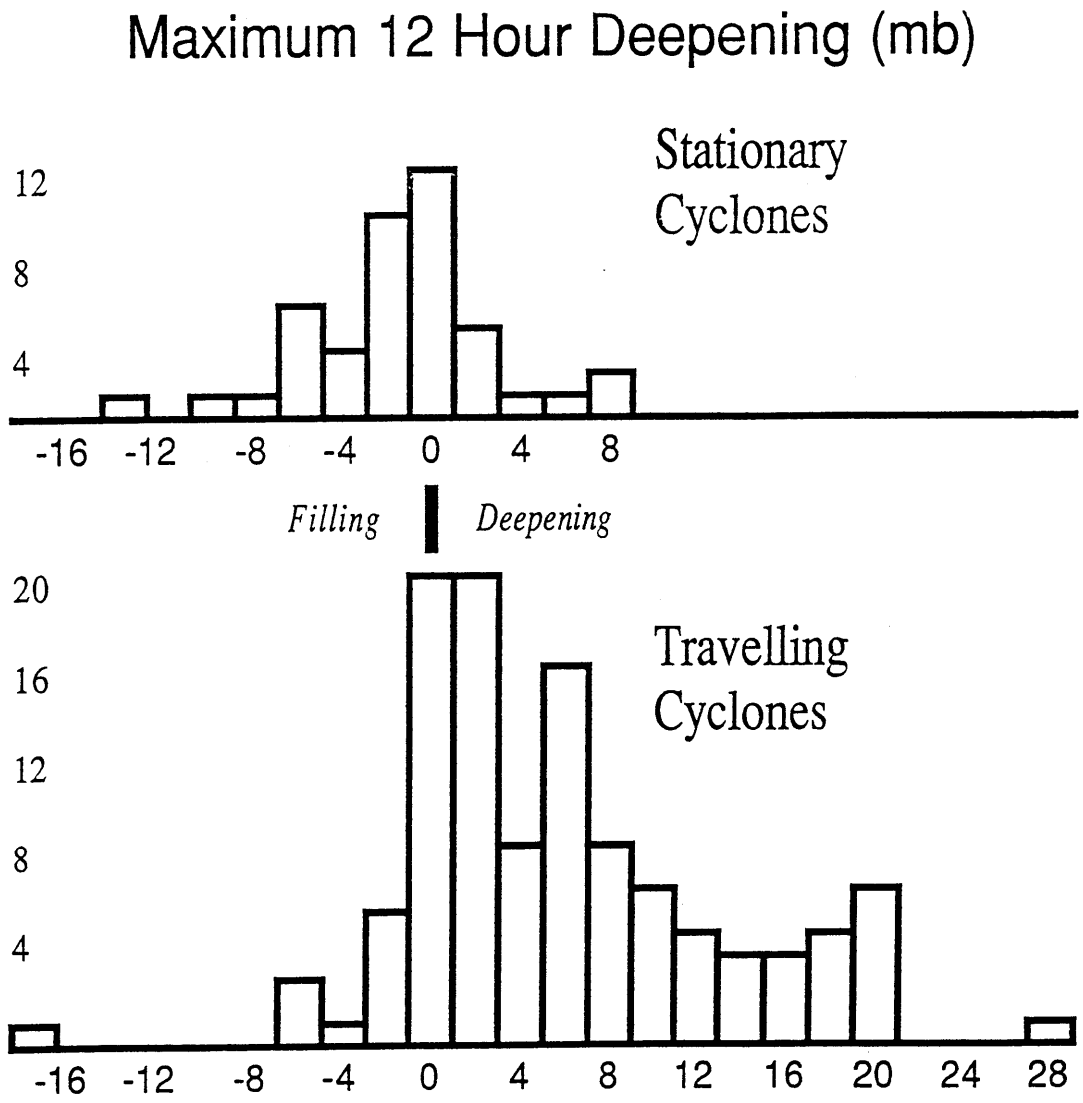
Maximum 12 Hour Deepening (mb)
Stationary Cyclones
12
8
4
-16 -12 -8 -4 0 4 8
Filling
Deepening
20
16
12
8
4
Travelling Cyclones
-16 -12 -8 -4 0 4 8 12 16 20 24 28

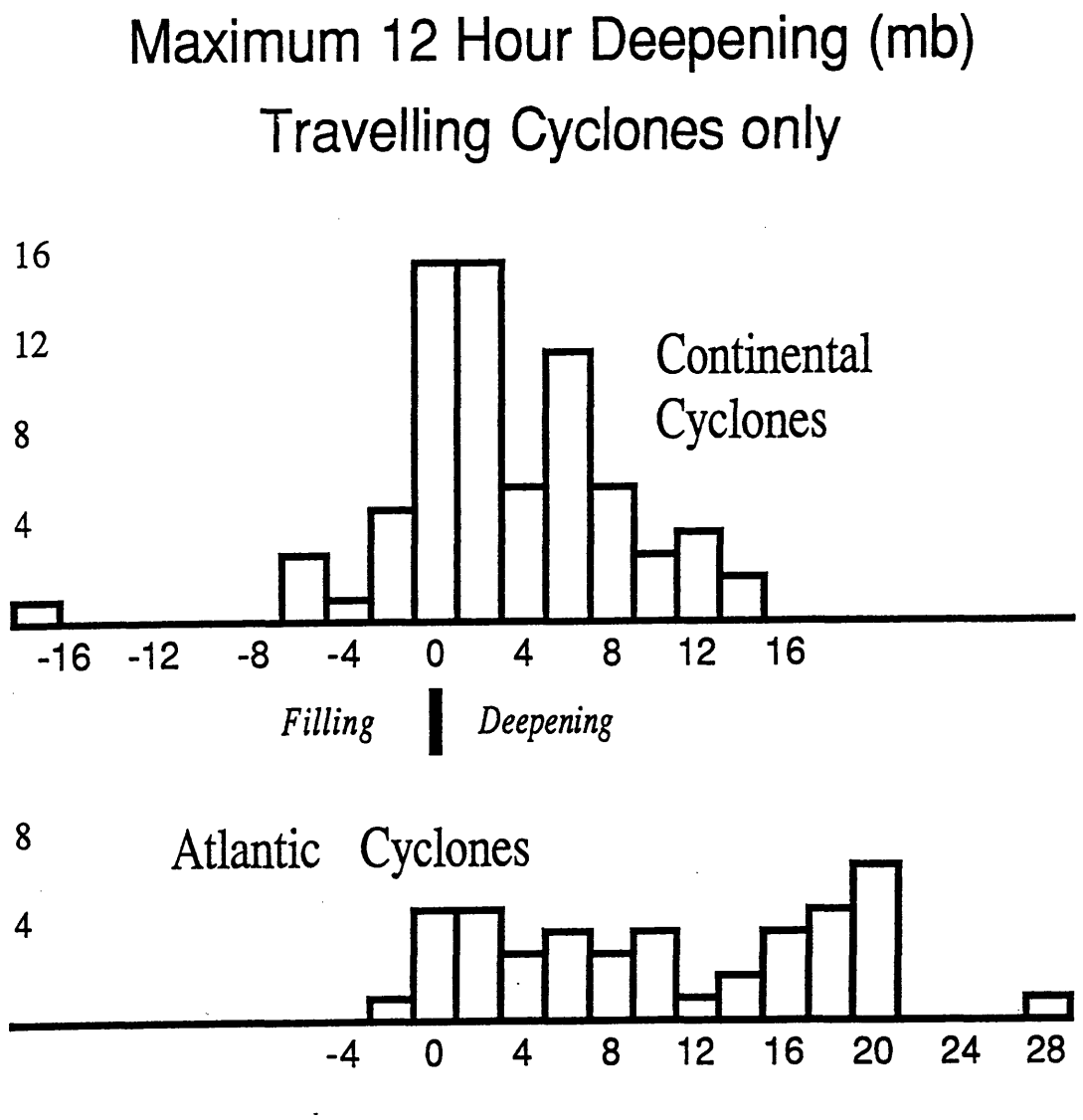

Fig. 2.16. Continental and Atlantic cyclogenesis regions defined in Fig. 2.2.

Fig. 2.17.

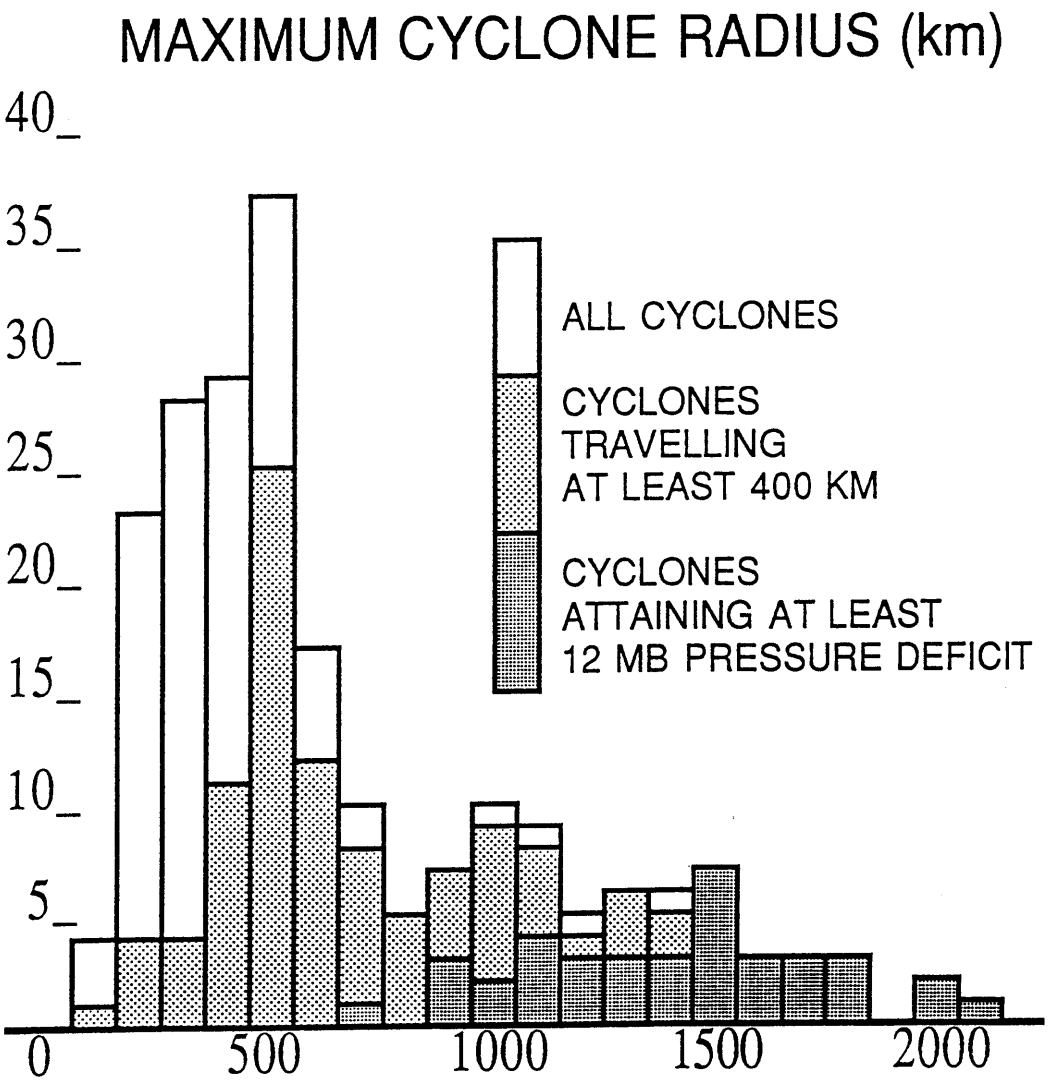
MAXIMUM CYCLONE RADIUS (km)
40
35
30
25
20
15
10
5
0
500
1000
1500
2000
ALL CYCLONES
CYCLONES TRAVELLING AT LEAST 400 KM
CYCLONES ATTAINING AT LEAST 12 MB PRESSURE DEFICIT

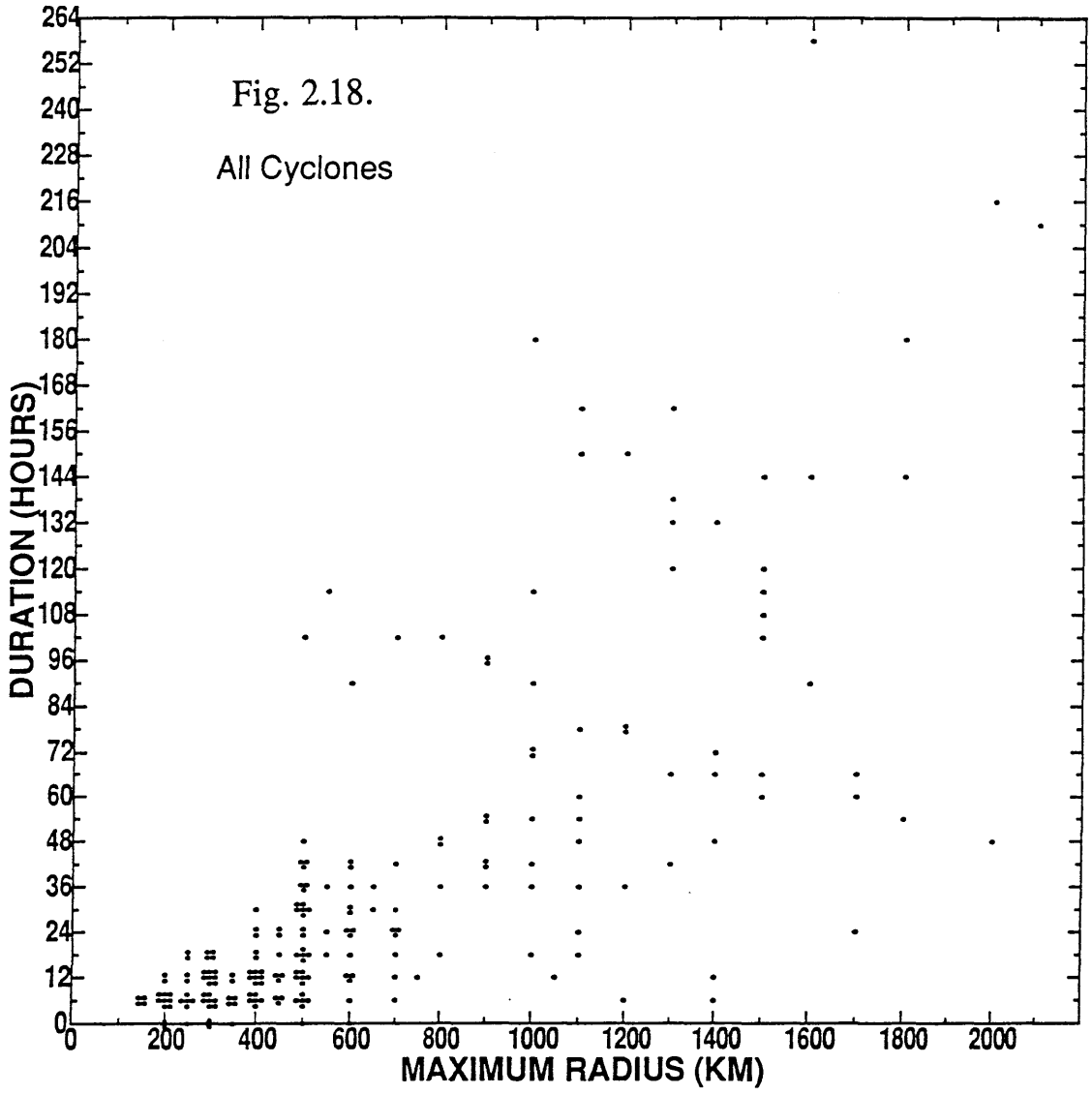

Fig. 2.18.

All Cyclones

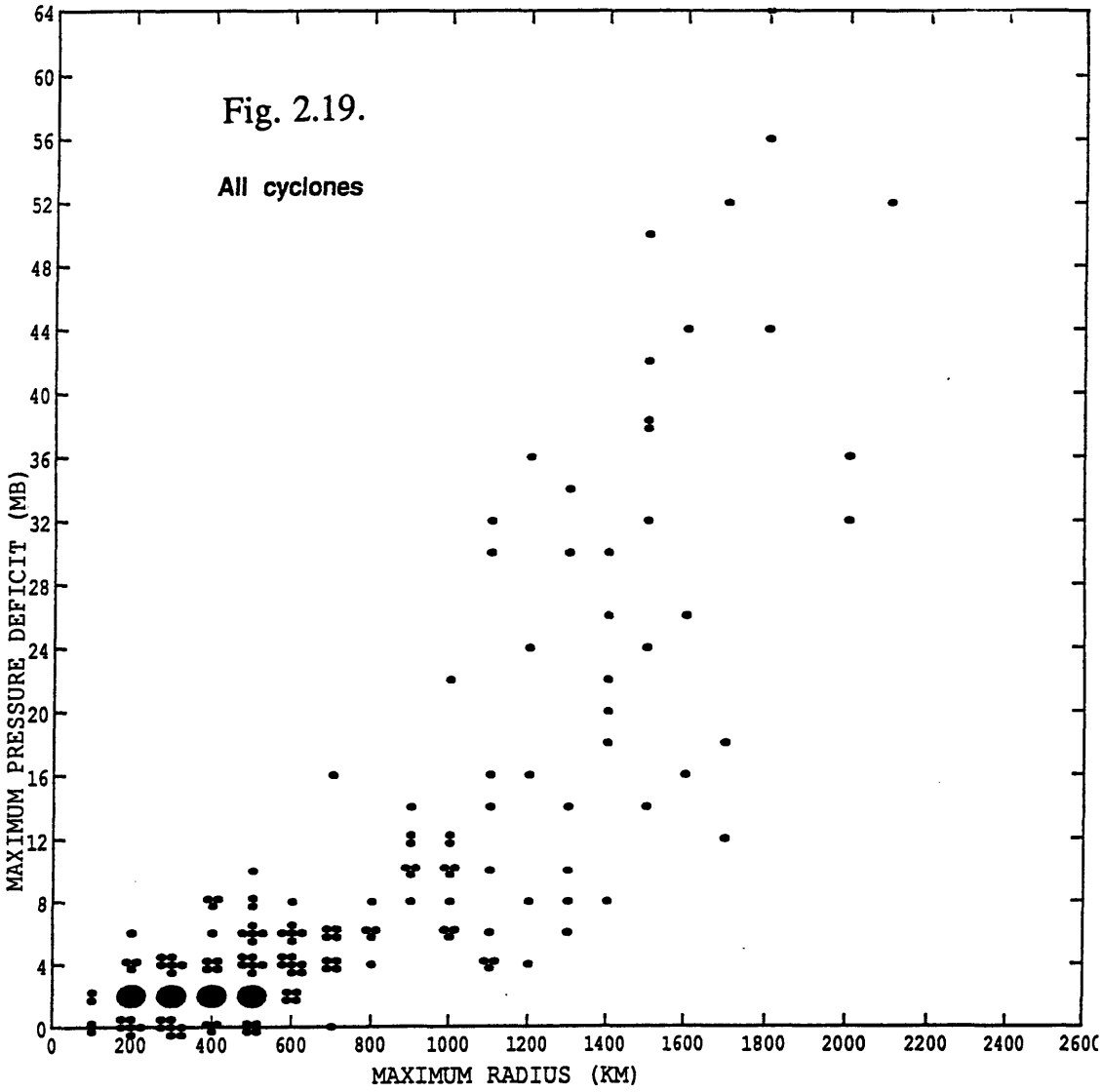
Fig. 2.19.
All cyclones
MAXIMUM PRESSURE DEFICIT (MB)
MAXIMUM RADIUS (KM)
0
4
8
12
16
20
24
28
32
36
40
44
48
52
56
60
64
0
200
400
600
800
1000
1200
1400
1600
1800
2000
2200
2400
2600

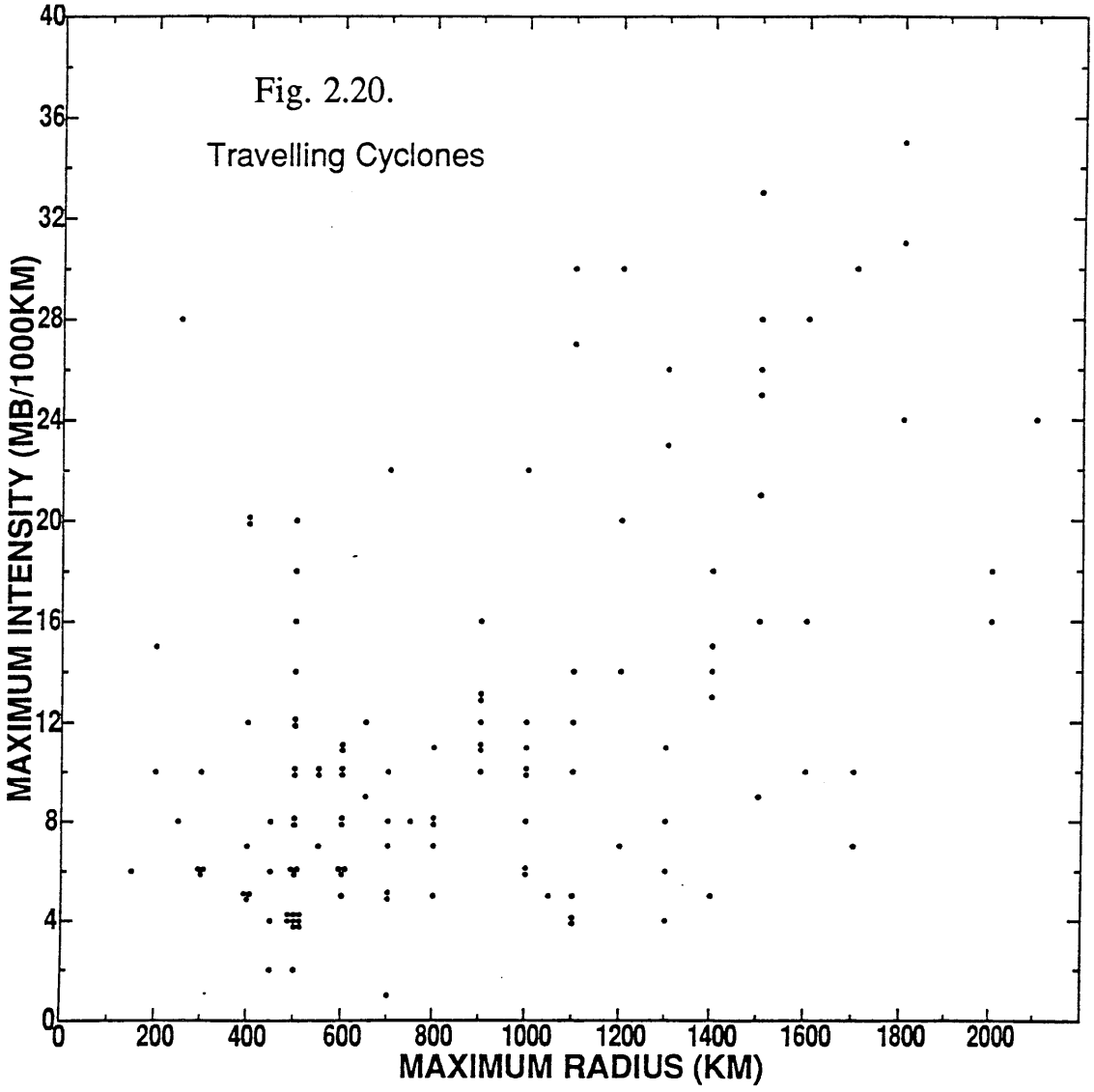

Fig. 2.20.

Travelling Cyclones

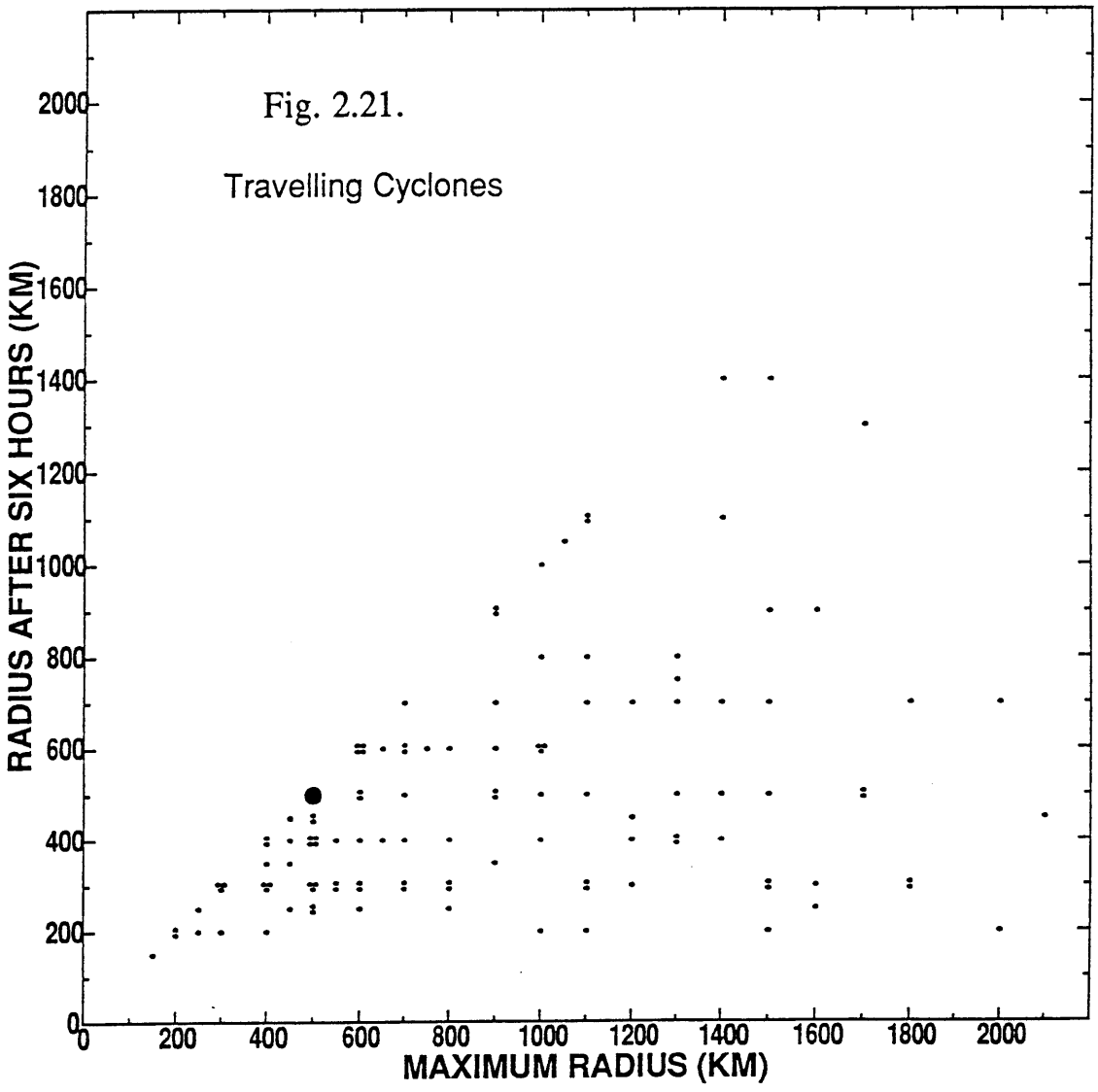
Travelling Cyclones
RADIUS AFTER SIX HOURS (KM)
MAXIMUM RADIUS (KM)
0
200
400
600
800
1000
1200
1400
1600
1800
2000

Fig. 2.21.

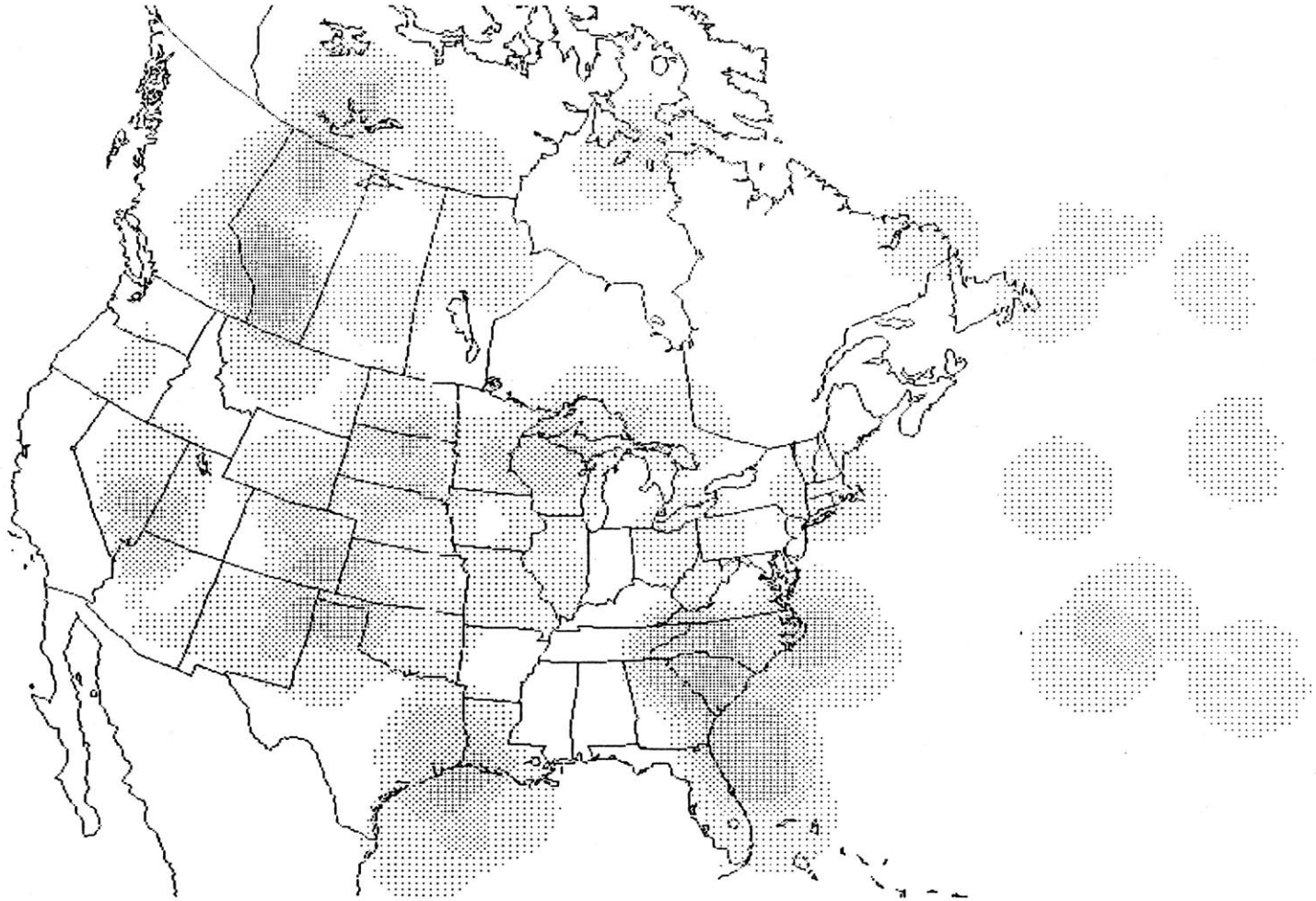

Fig. 2.22: Number of cyclogenesis events during GALE for small-scale cyclones (see text for definition) which travel at least 400 km from their cyclogenesis location. Compare with Figs. 2.10-2.13.

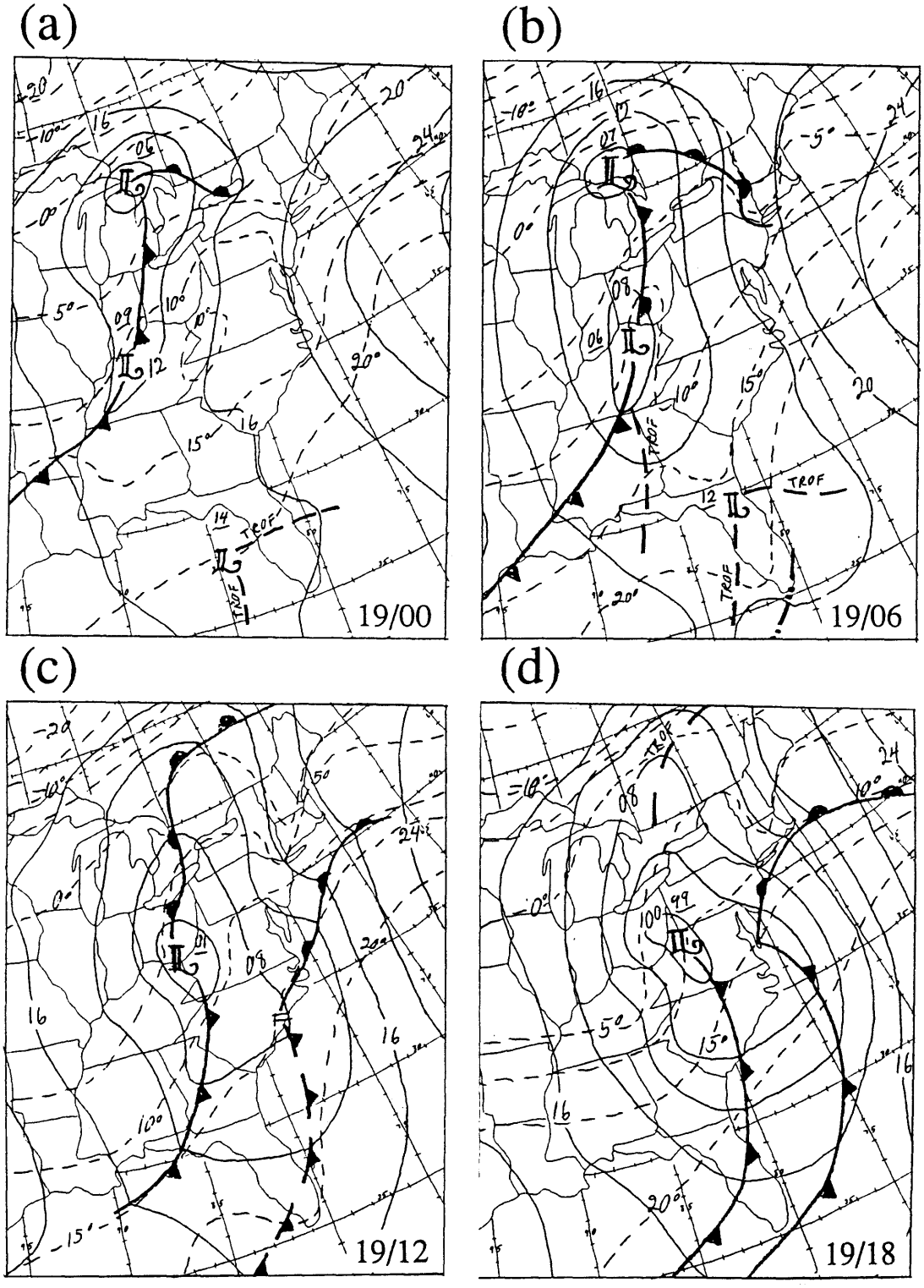

Fig. 3.1 (first of two pages): NMC surface analyses of frontal structure and mean sea level pressure (c.int. 4 mb), with subjective surface temperature analyses (c.int. 5 C) by the author. (a) 00 UTC 19 Jan 1986 (b) 06 UTC 19 Jan 1986 (c) 12 UTC 19 Jan 1986 (d) 18 UTC 19 Jan 1986

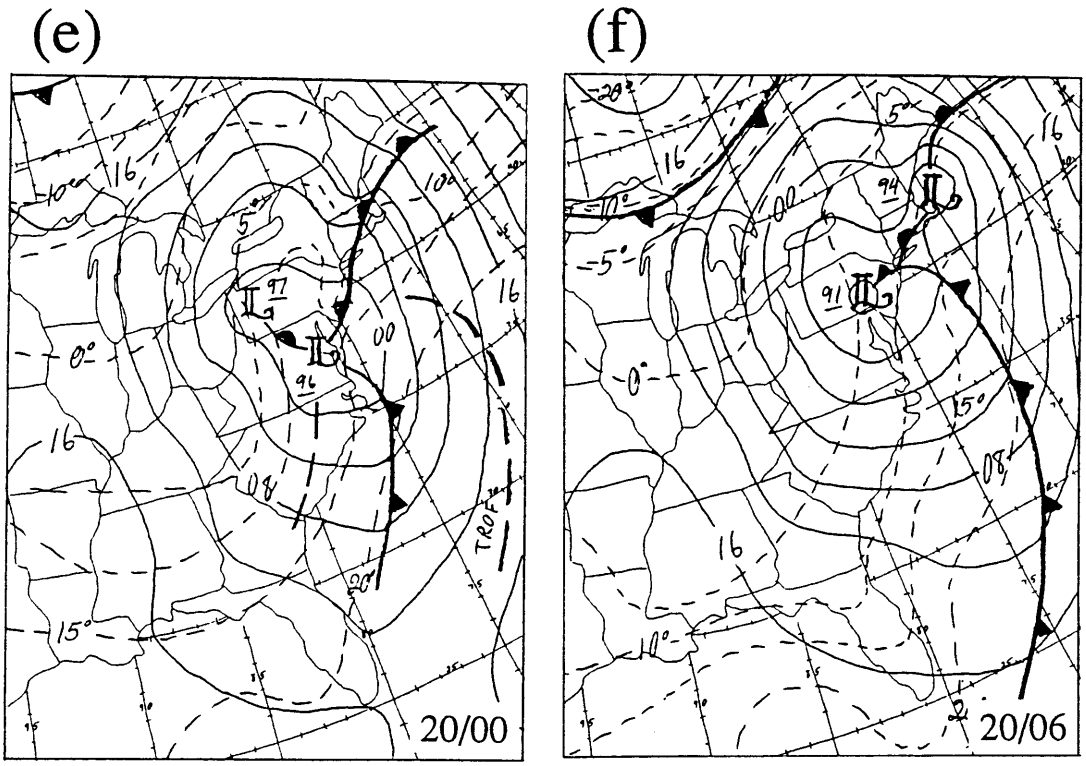

Fig. 3.1 (second of two pages): (e) 00 UTC 20 Jan 1986 (f) 06 UTC 20 Jan 1986

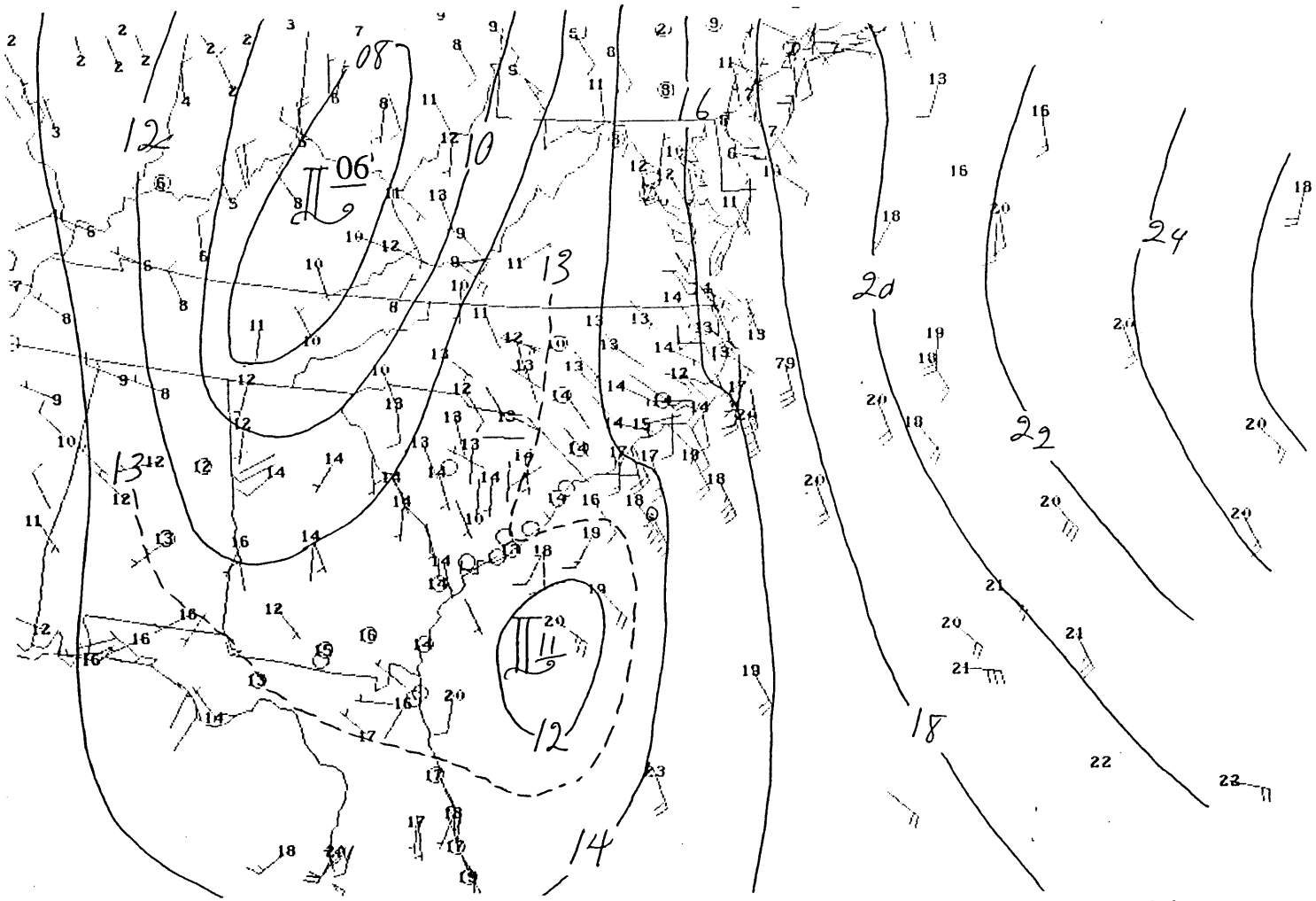

Fig. 3.2: Subjective mean sea level pressure analysis (c.int. 2 mb) for 06 UTC 19 Jan 1986. Observed temperatures (C) and winds (standard model) are plotted at station locations.

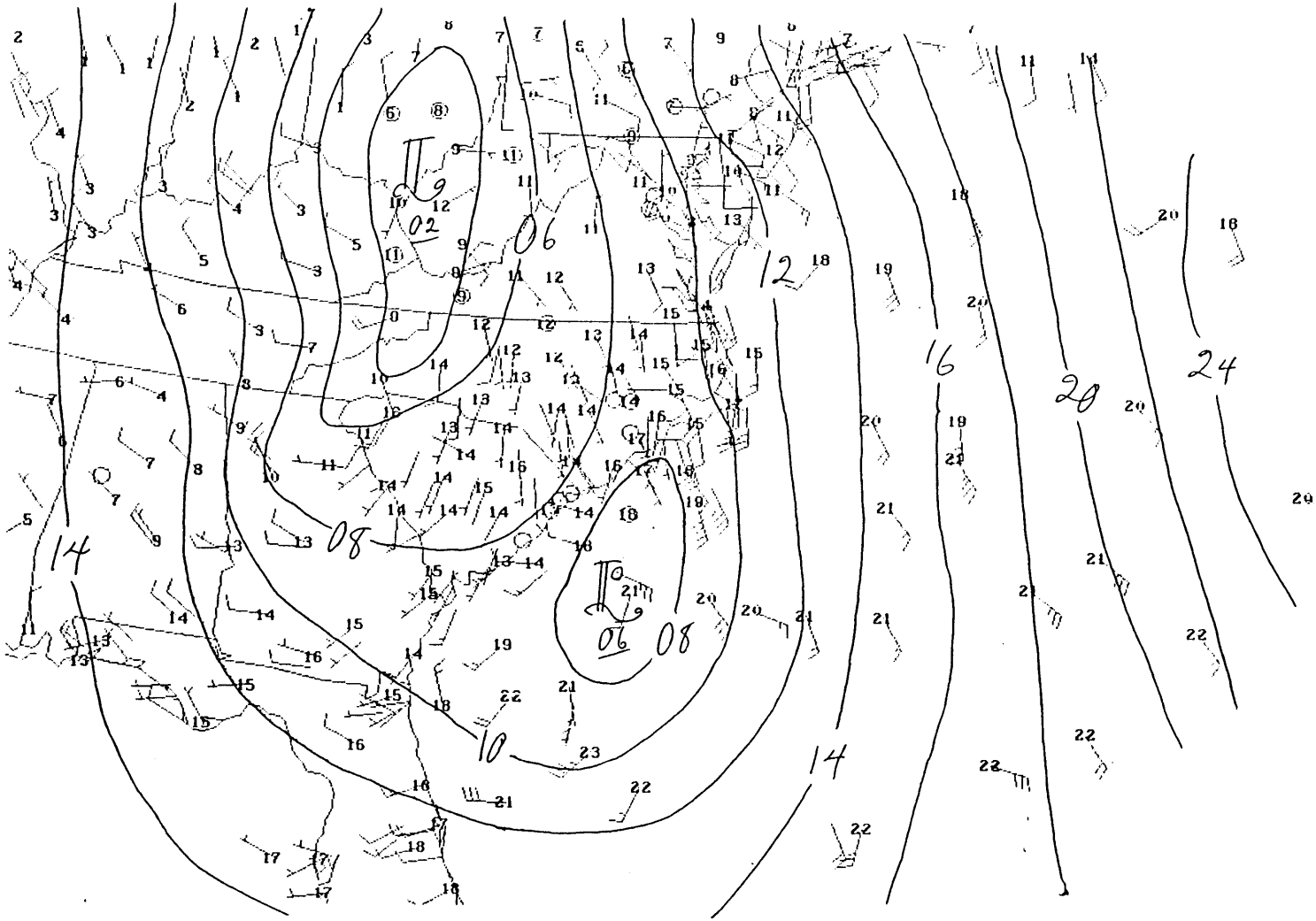

Fig. 3.3: 12 UTC 19 Jan 1986 pressure analysis with temperatures and winds (as in Fig. 3.2)

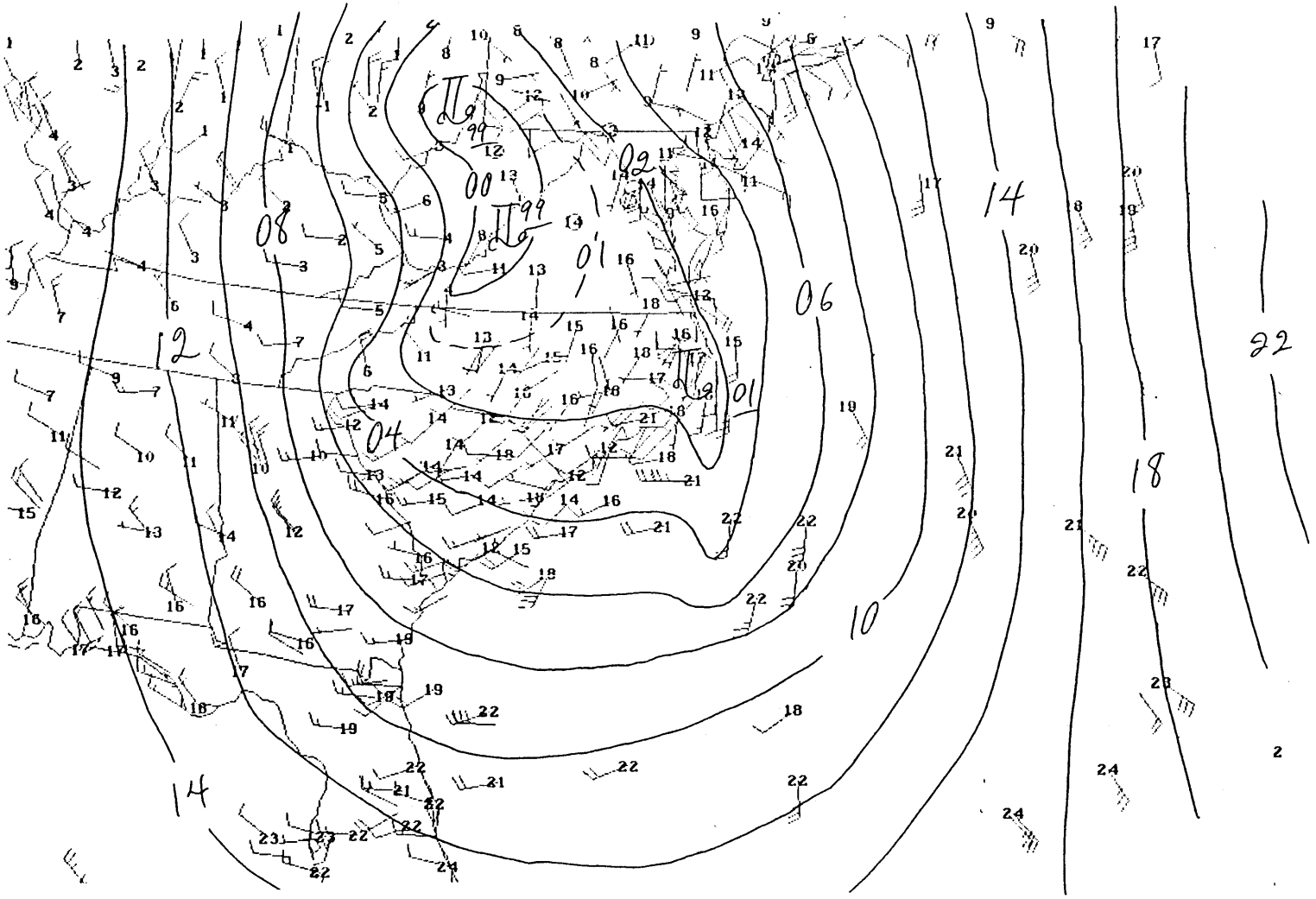

Fig. 3.4: 18 UTC 19 Jan 1986 pressure analysis with temperatures and winds (as in Fig. 3.2)

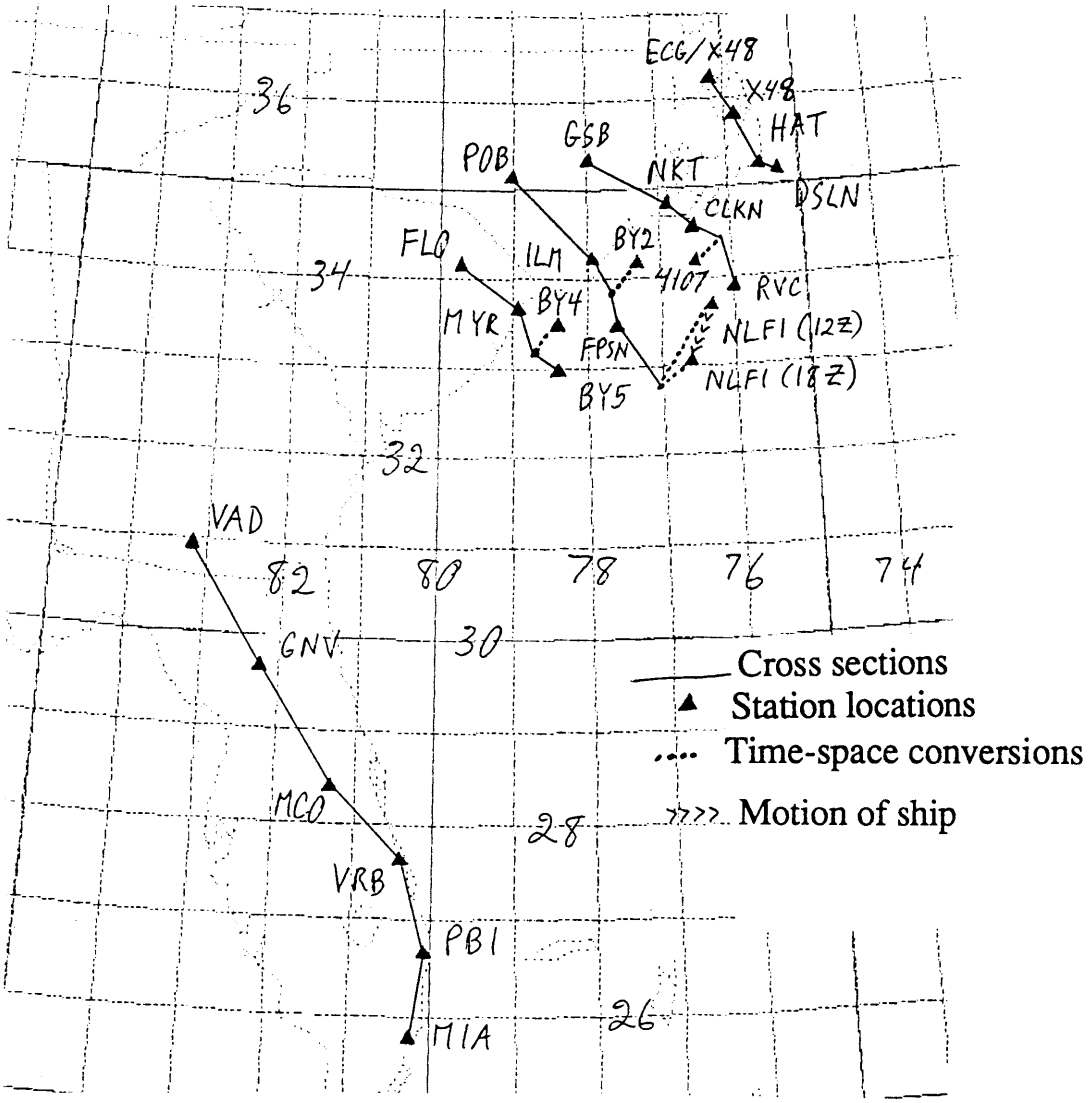

Fig. 3.5: Locations of stations used in time-space cross sections (Figs. 3.6-3.10). Also shown are graphical depictions of time-space conversions used to reduce stations to cross section line (see text for discussion).

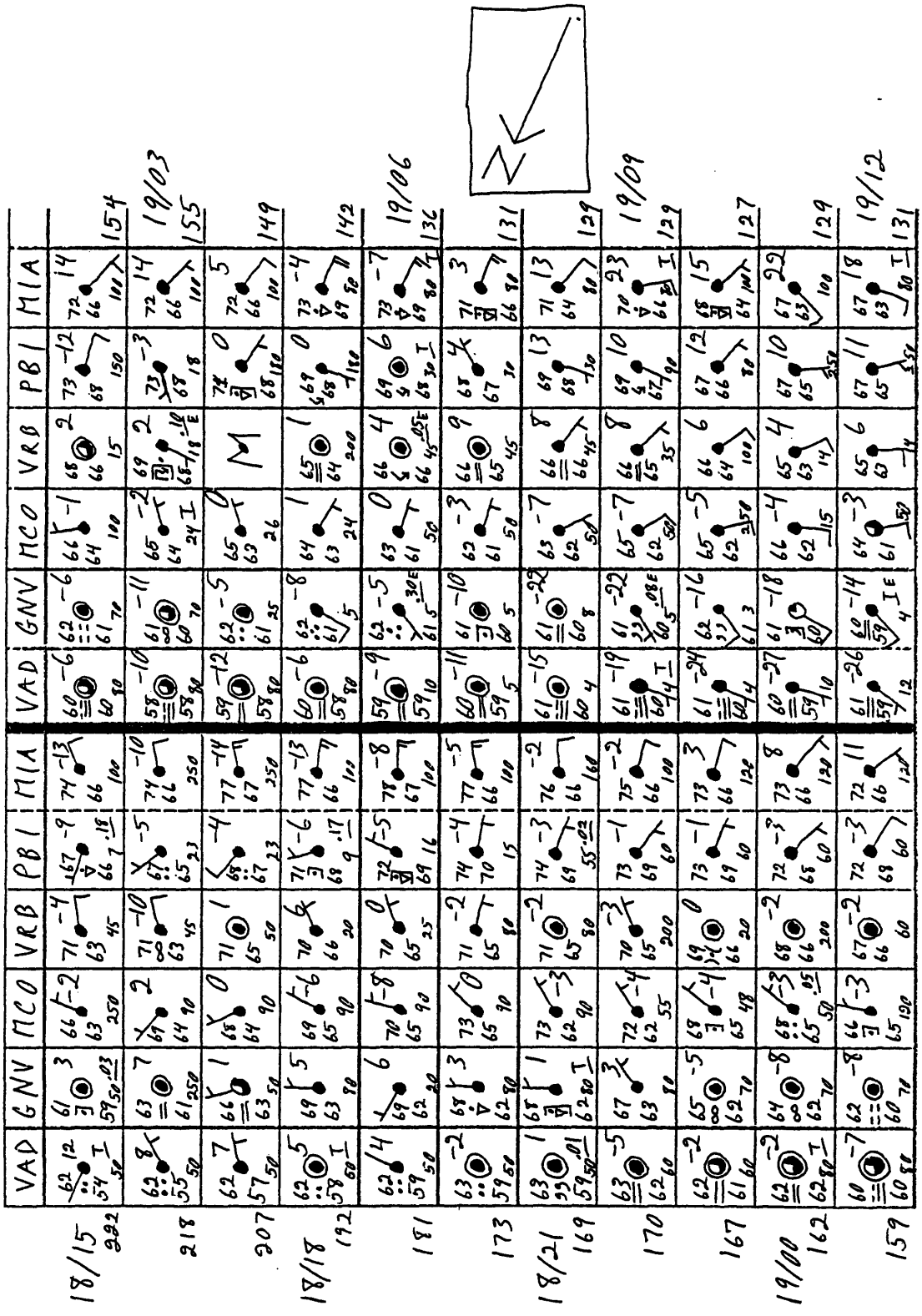

Fig. 3.6: Time-space cross section, VAD-MIA (locations shown in Fig. 3.5), 15 UTC 18 Jan 1986 to 12 UTC 19 Jan 1986, showing stations upstream of small-scale cyclogenesis region. For complete description of Figs. 3.6-3.10, see Appendix B.

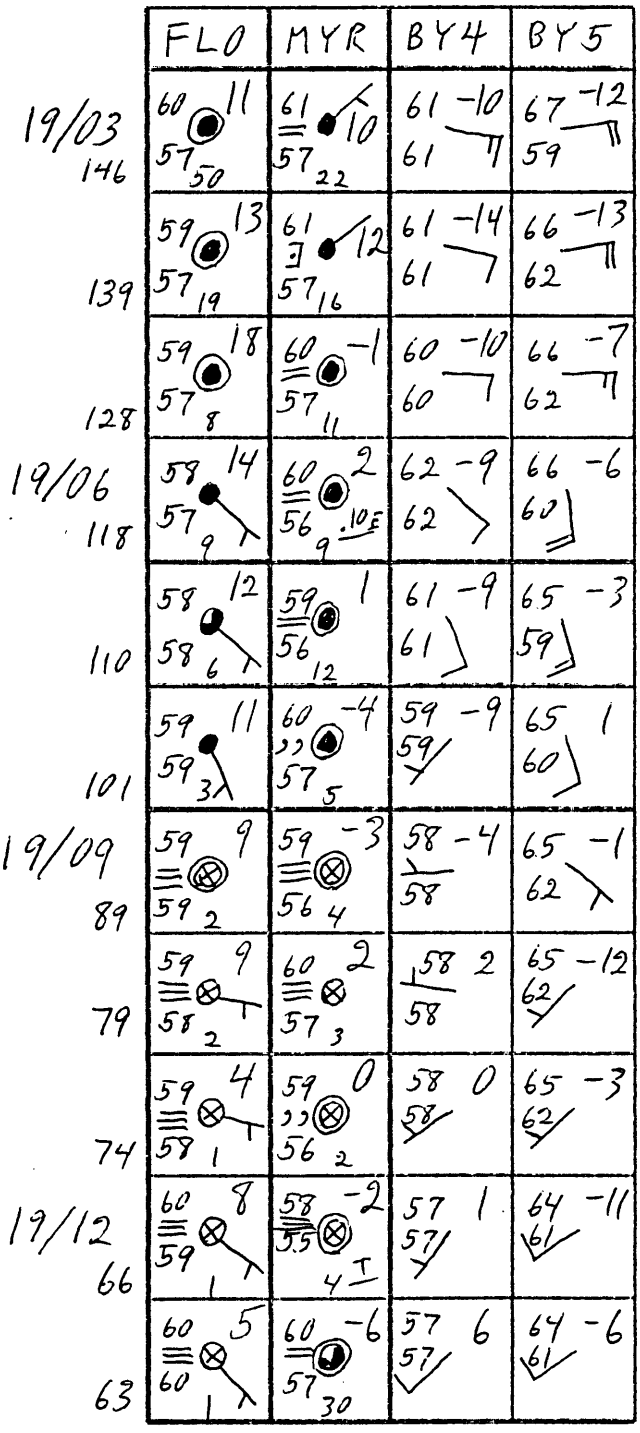

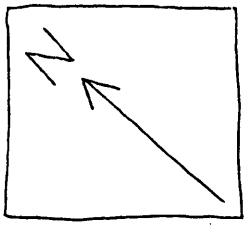

Fig. 3.7: Time-space cross section as in Fig. 3.6, but for FLO-BY5 (locations shown in Fig. 3.5), 03 UTC 19 Jan 1986 to 13 UTC 19 Jan 1986. Observations from BY4 are advanced one hour.

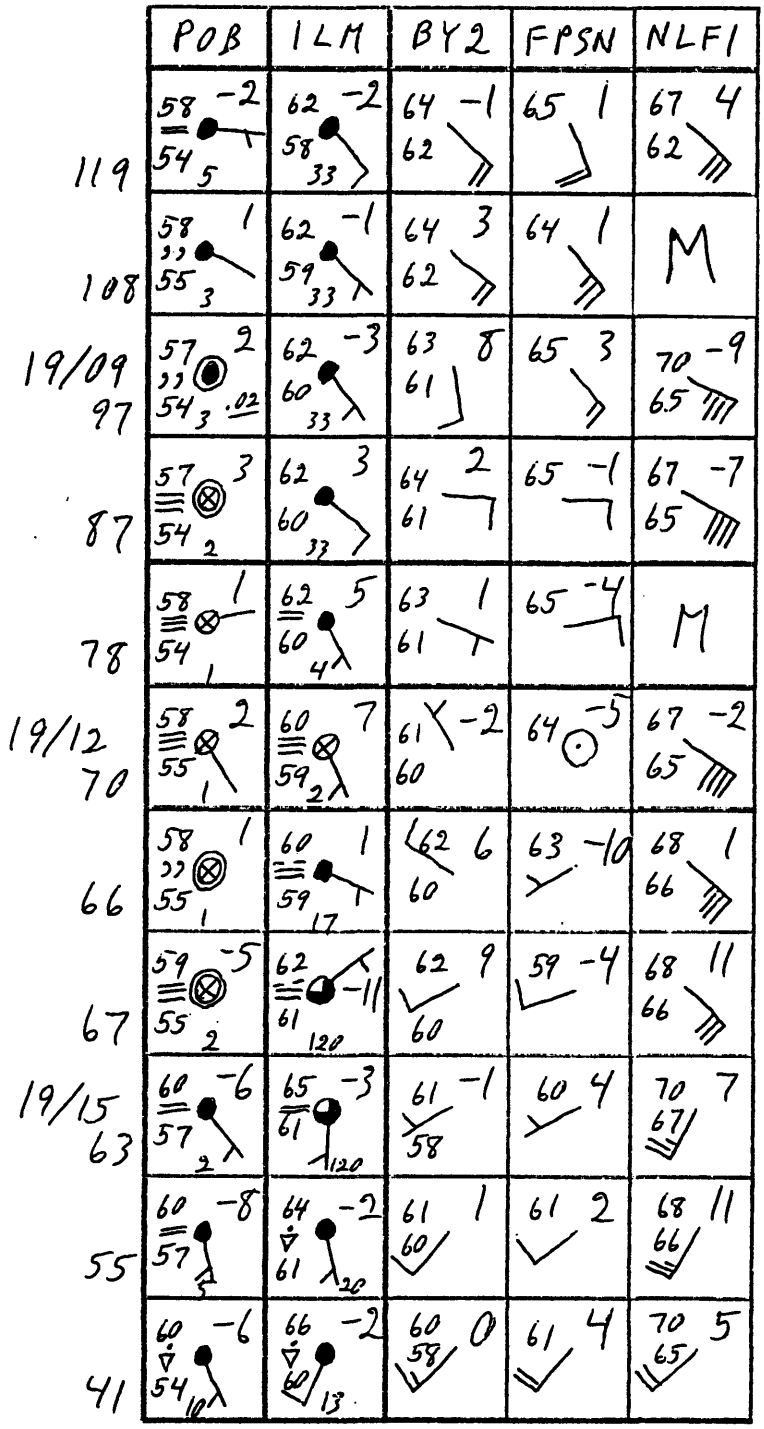

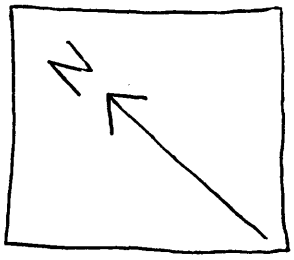

Fig. 3.8: Time-space cross section as in Fig. 3.6, but for POB-NLFI (locations shown in Fig. 3.5), 07 UTC 19 Jan 1986 to 17 UTC 19 Jan 1986. Observations from BY2 are advanced one hour, and observations from ship NLFI are advanced one to three hours.

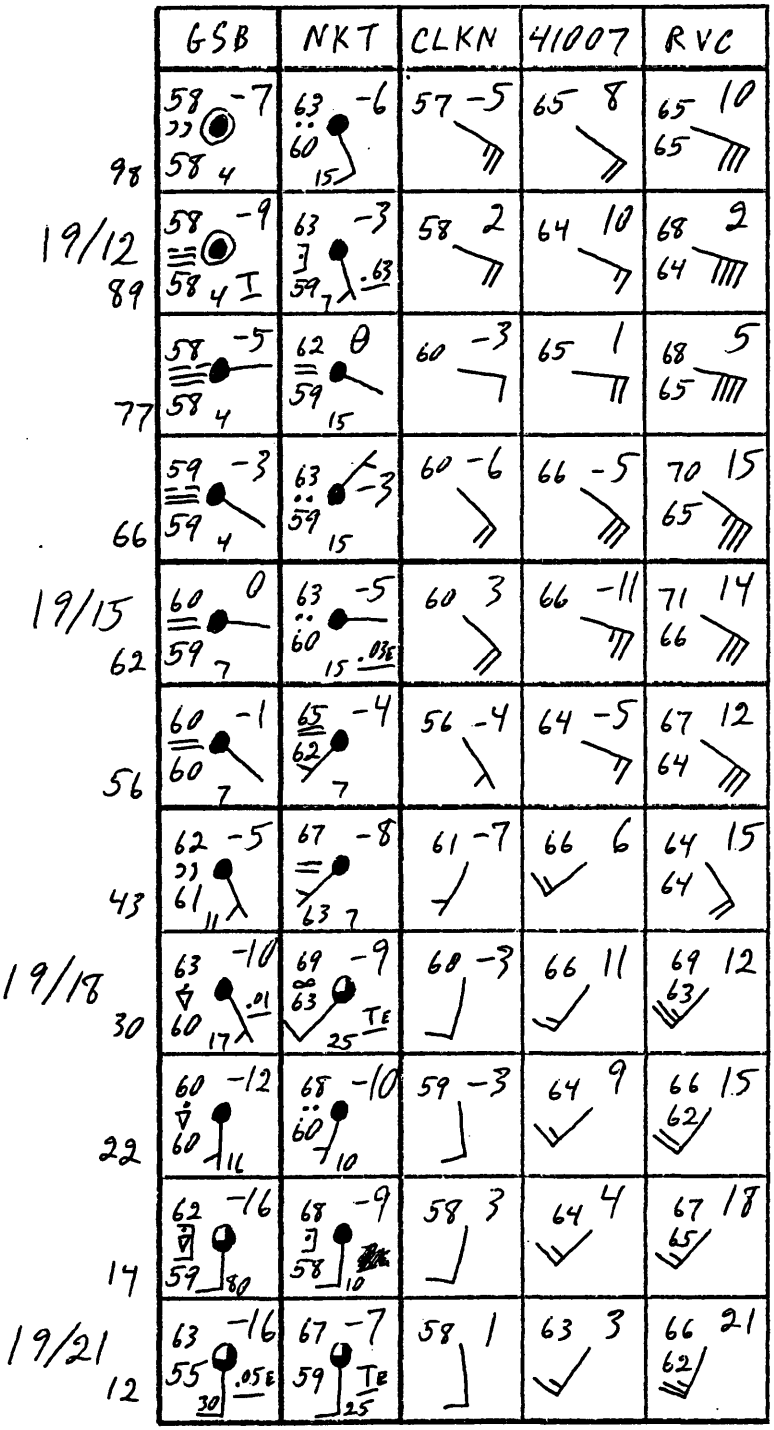

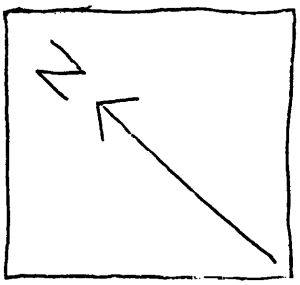

Fig. 3.9: Time-space cross section as in Fig. 3.6, but for GSB-RVC (locations shown in Fig. 3.5), 11 UTC 19 Jan 1986 to 21 UTC 19 Jan 1986. Observations from CLKN are delayed one hour.

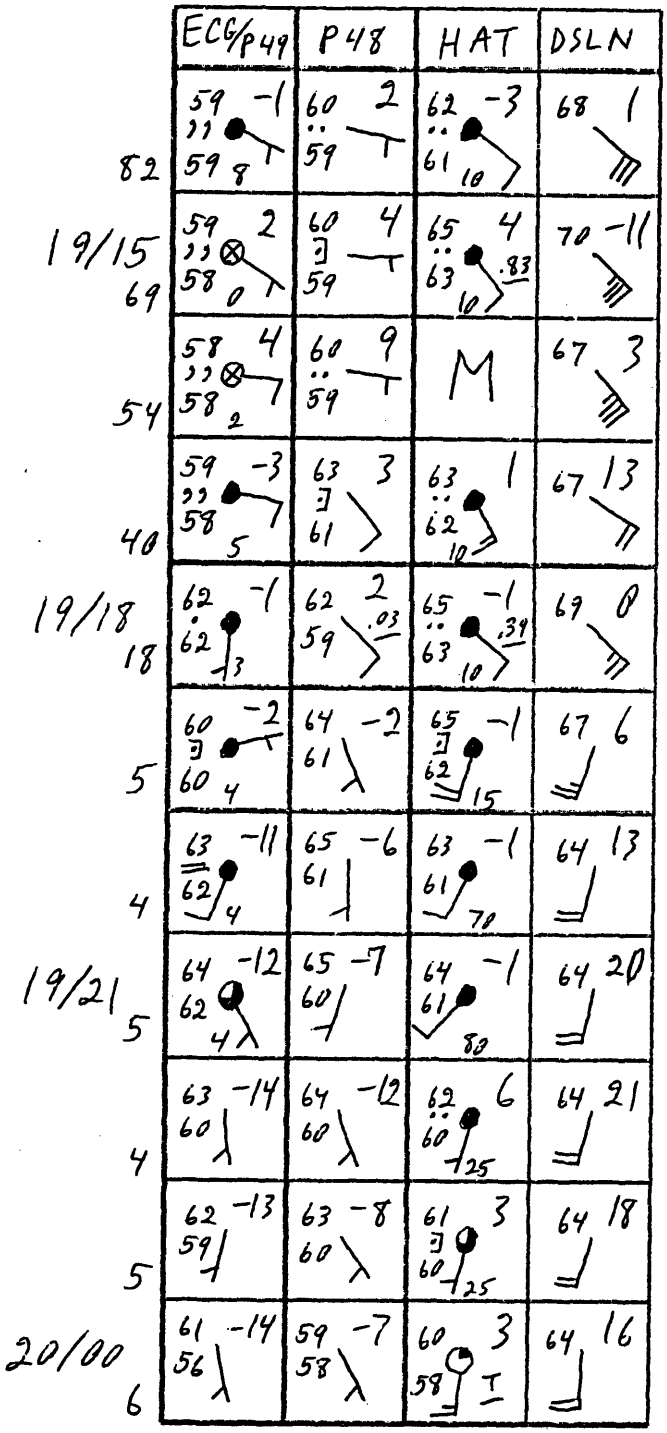

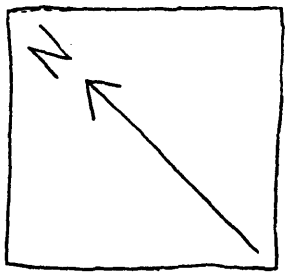

Fig. 3.10: Time-space cross section as in Fig. 3.6, but for ECG-DSLN (locations shown in Fig. 3.5), 14 UTC 19 Jan 1986 to 00 UTC 20 Jan 1986. Observations from ECG are replaced by observations from P49 when ECG stopped reporting after 21 UTC 19 Jan 1986.

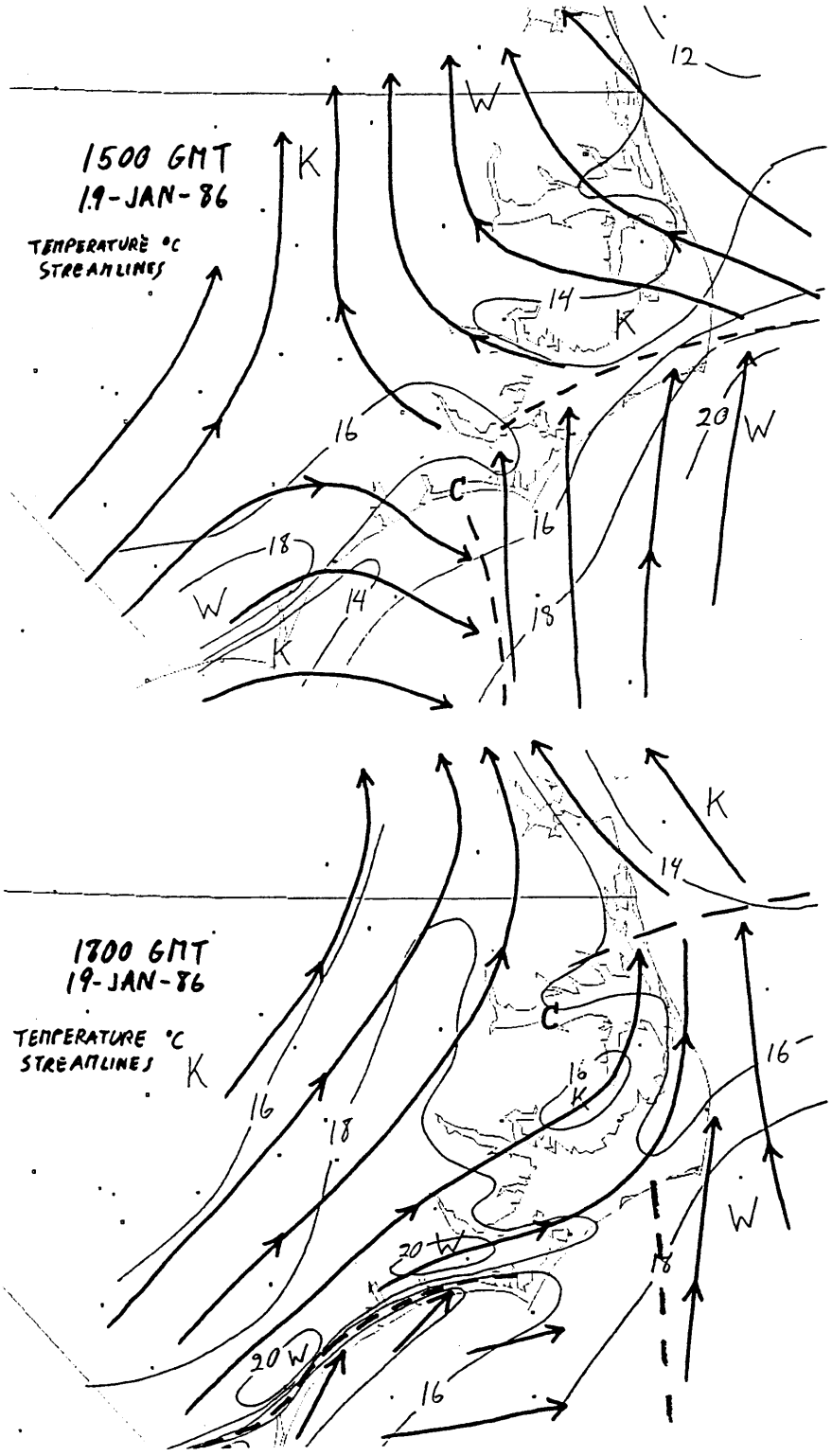

Fig. 3.11: Temperature (c.int. 2 C) and streamline (line spacing not proportional to velocity) analyses of the small-scale cyclone over land. The position of the center of circulation is indicated by a "C".

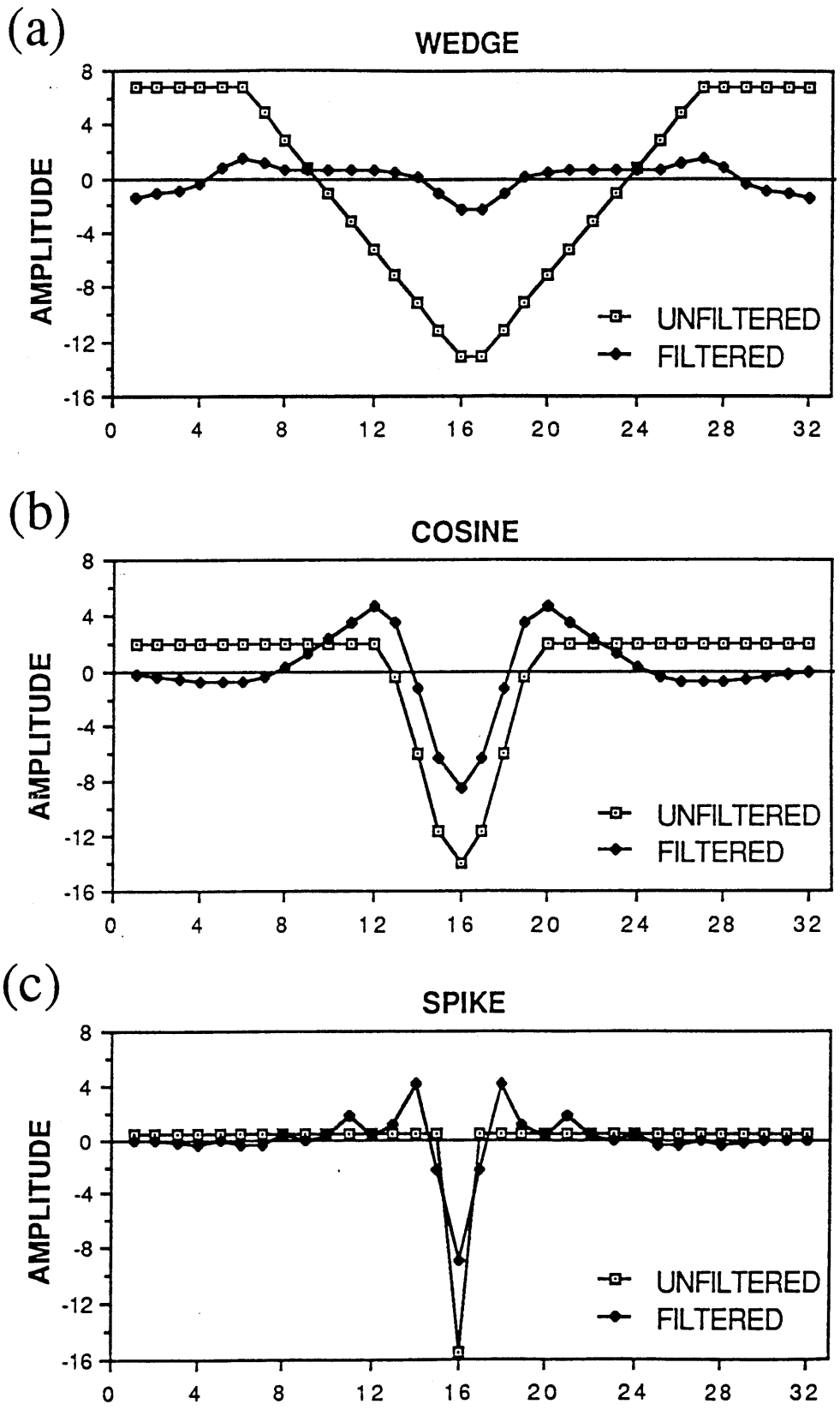

Fig. 3.12: Responses of discrete 32-point Fourier filter to three idealized input signals. See text.

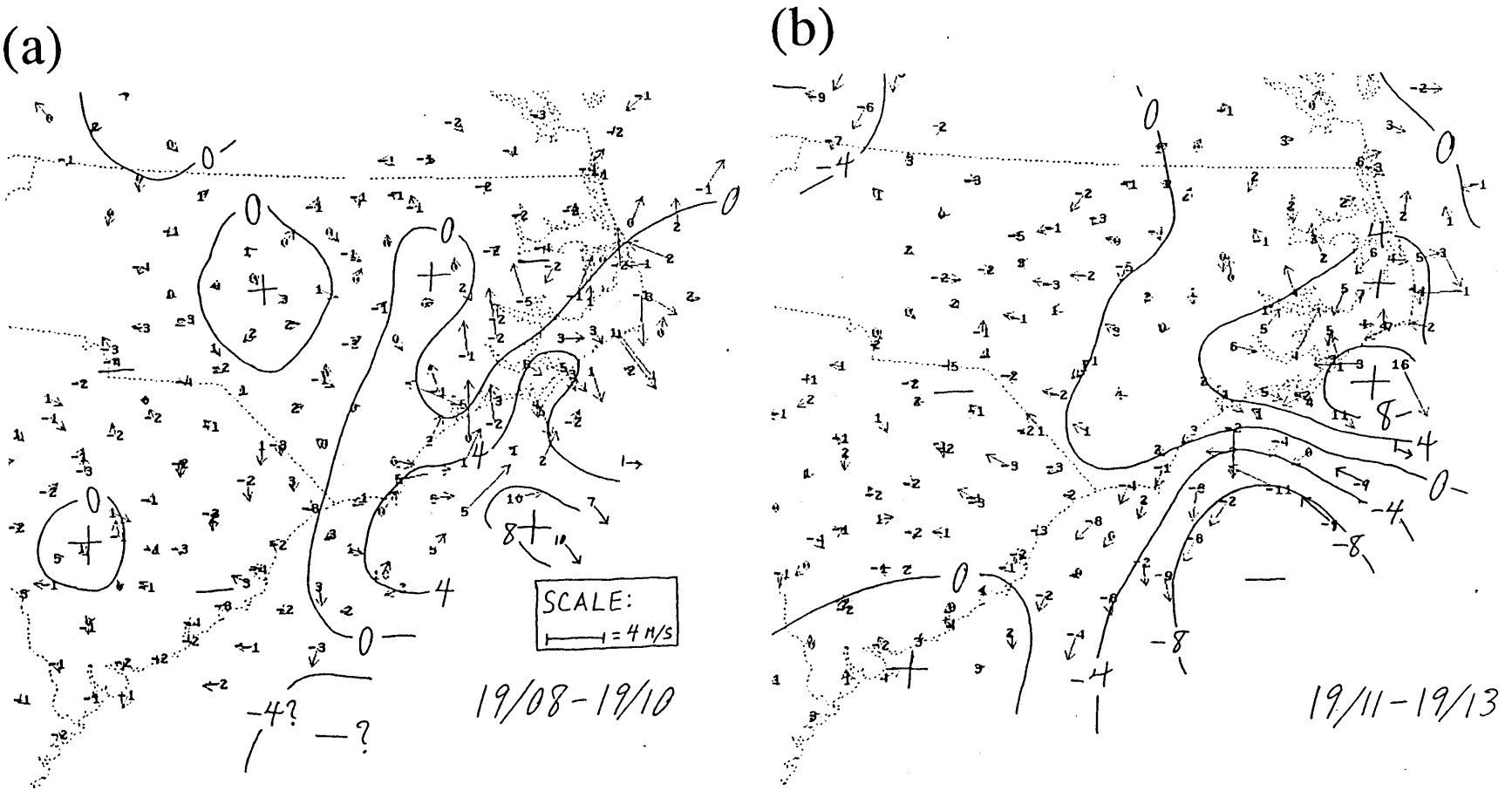

Fig. 3.13 (first of two pages): Subjective analyses of bandpass-filtered (see text) mean sea level pressure (c.int. 0.4 mb). Plotted at station locations are bandpass-filtered pressure (in tenths of mb) and wind (scale for wind vectors given in Fig. 3.13a) Data from three separate hours are plotted on single maps, using a time-space correction of 0.3 degrees of latitude and longitude per hour as described in the text. (a) 08-10 UTC 19 Jan 1986 (b) 11-13 UTC 19 Jan 1986.

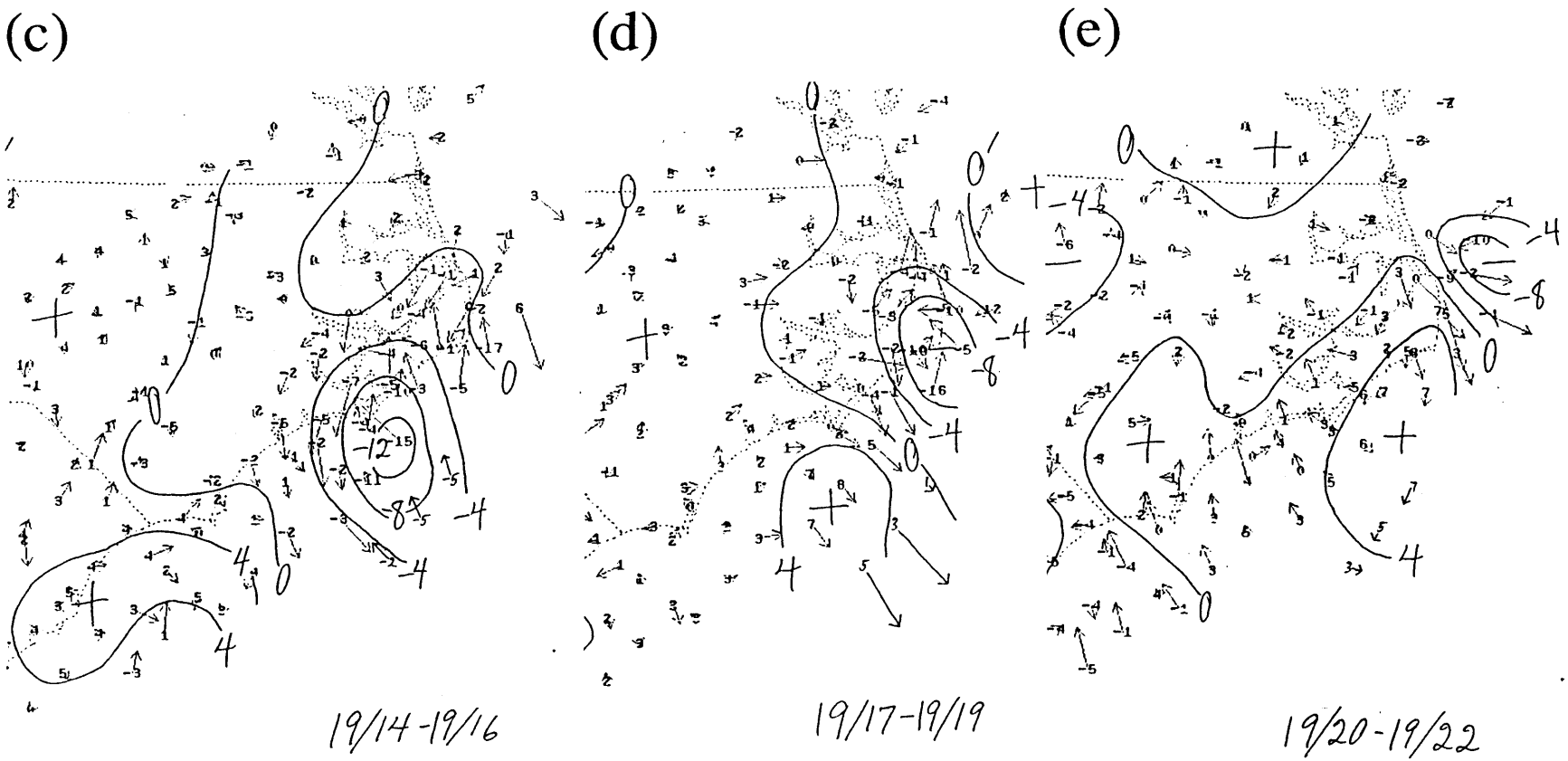

Fig. 3.13 (second of two pages). (c) 14-16 UTC 19 Jan 1986 (d) 15-17 UTC 19 Jan 1986 (e) 18-20 UTC 19 Jan 1986.

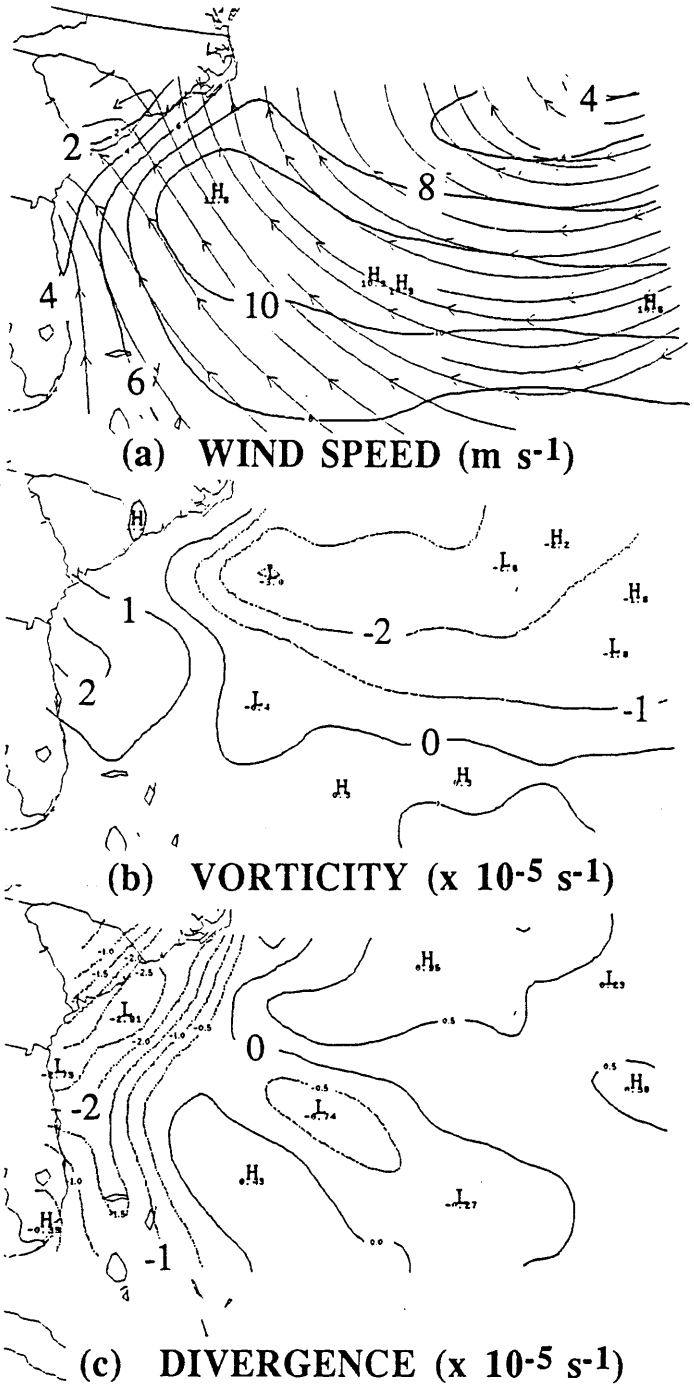

Fig. 3.14: Subjective analysis of offshore winds and derived quantities, 00 UTC 19 Jan 1986. Analysis technique is described in the text. (a) Streamlines and coutours of wind speed (c.int. 2 m s^{-1}) (b) Relative vorticity (c.int. $1x10^{-5}$ s^{-1}, negative contours dashed) (c) Divergence (c.int. $0.5x10^{-5}$ s^{-1}, negative contours dashed). Same format as Figs. 3.15-3.18.

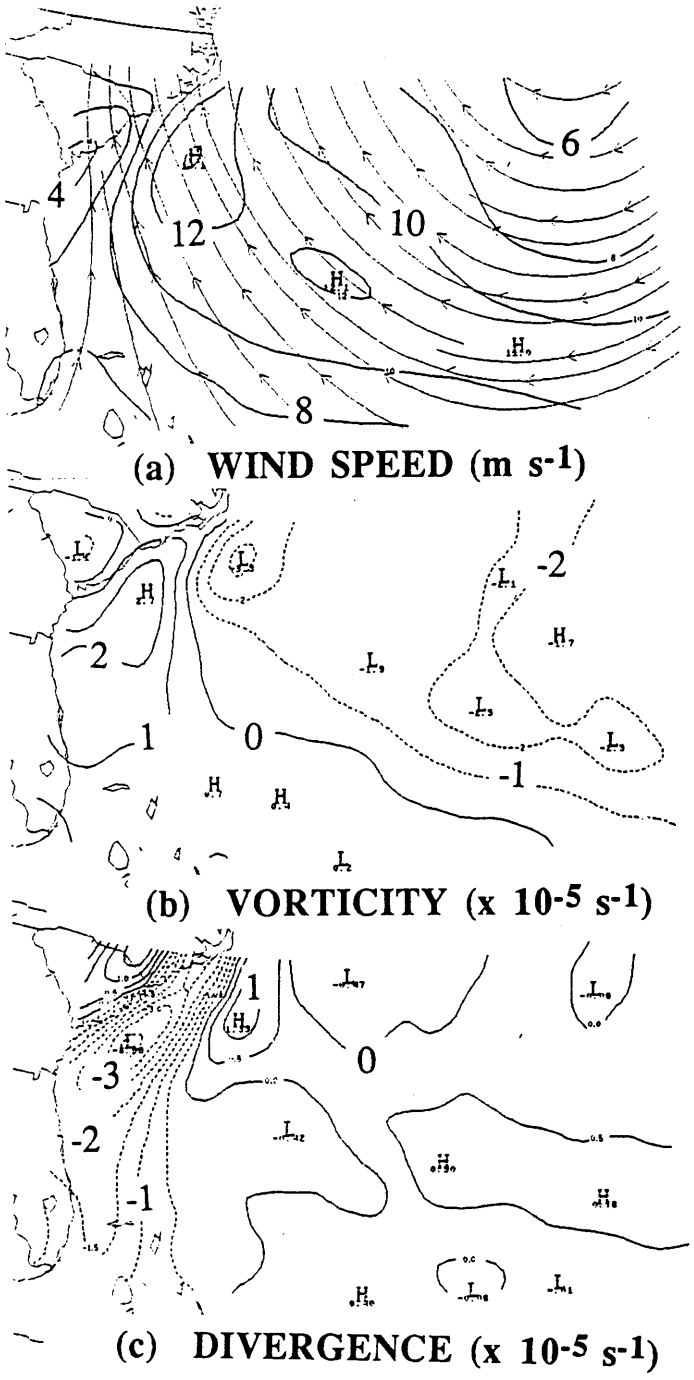

Fig. 3.15: Wind analyses, as in Fig. 3.14, but for 06 UTC 19 Jan 1986.

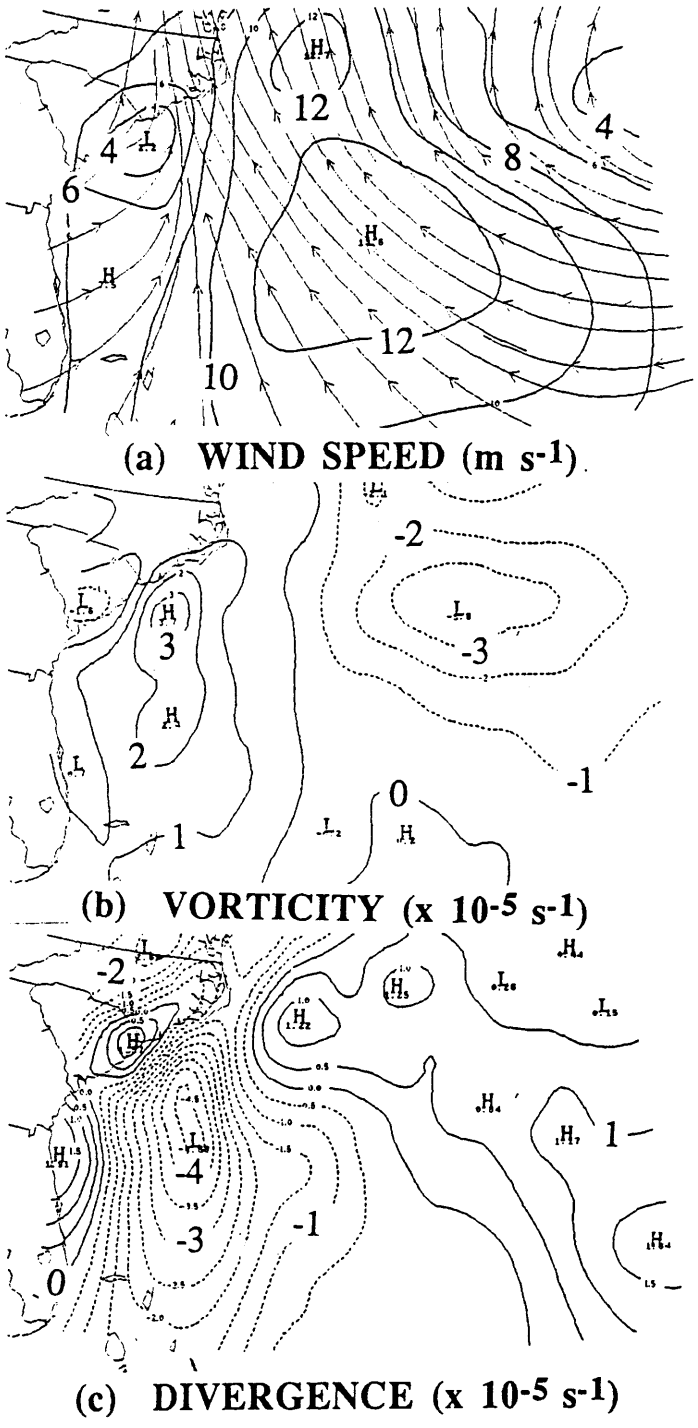

Fig. 3.16: Wind analyses, as in Fig. 3.14, but for 12 UTC 19 Jan 1986.

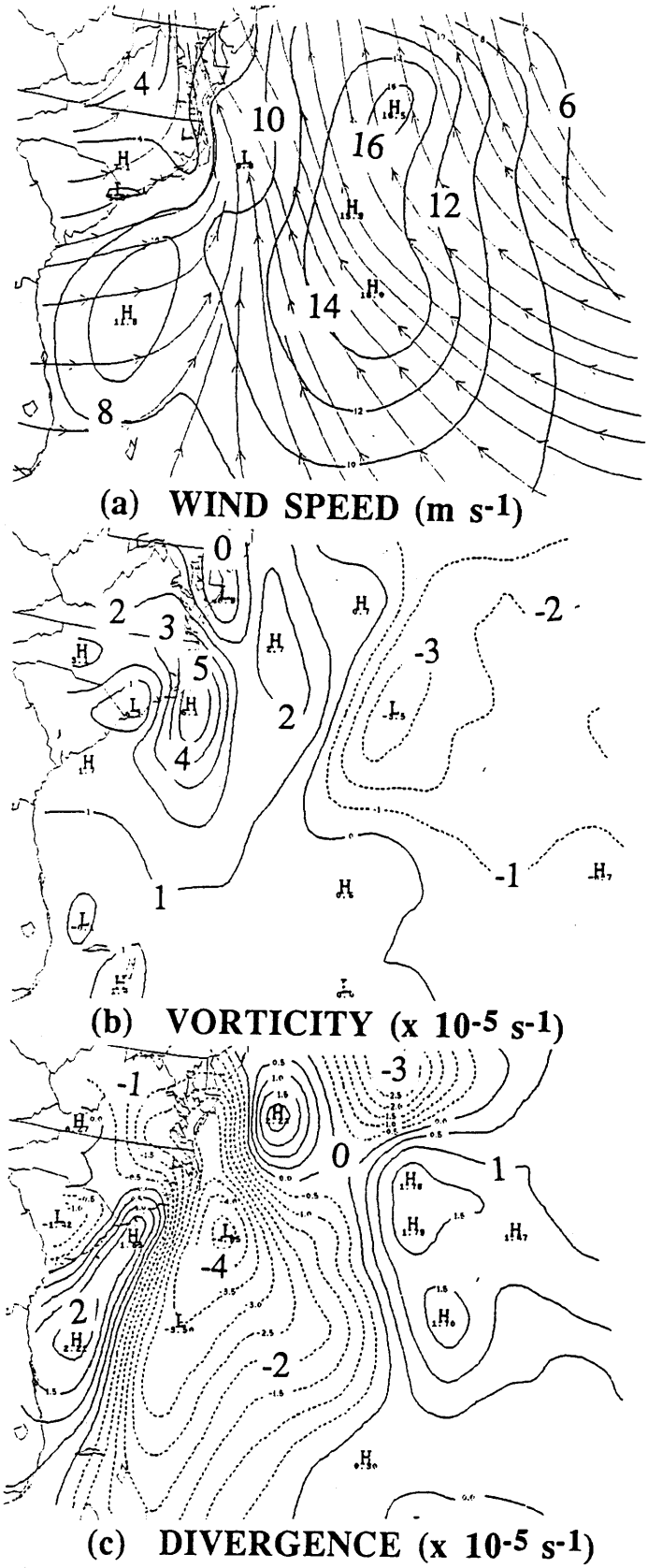

Fig. 3.17: Wind analyses, as in Fig. 3.14, but for 18 UTC 19 Jan 1986.

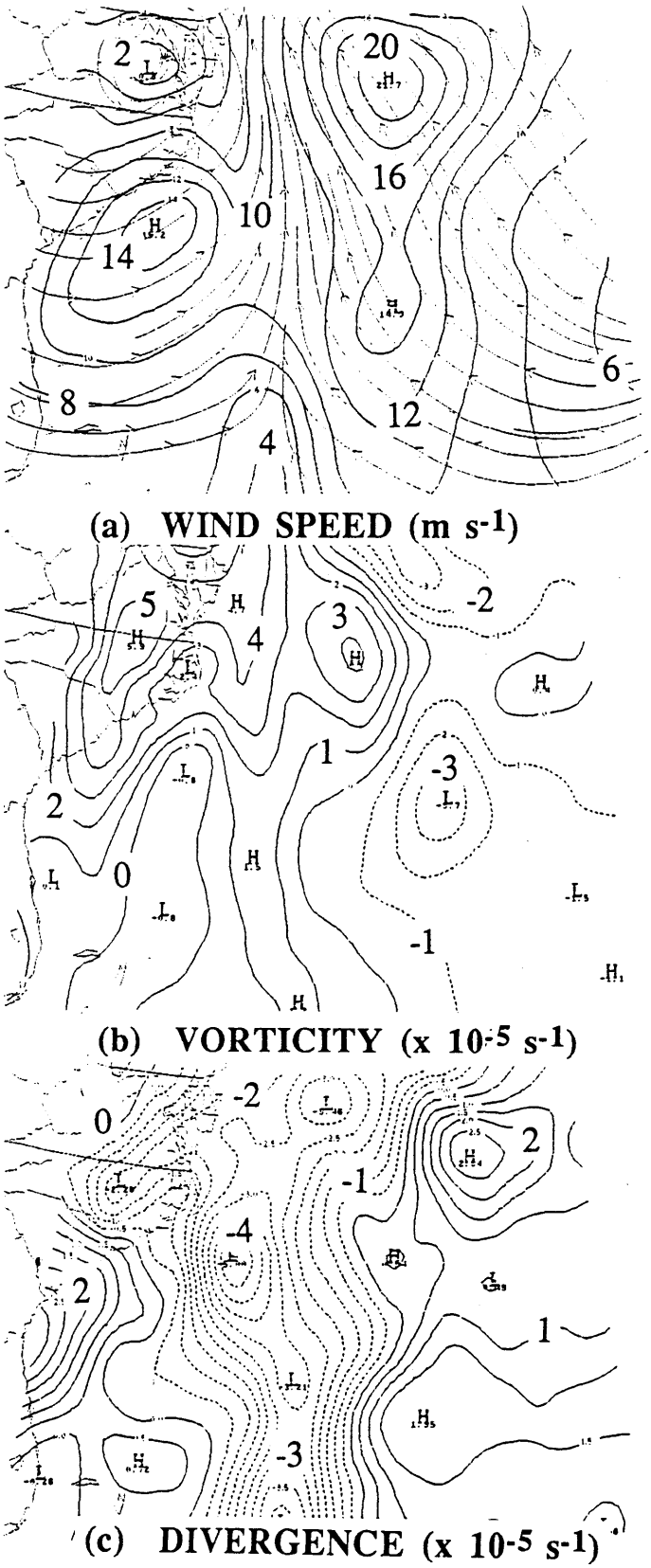

Fig. 3.18: Wind analyses, as in Fig. 3.14, but for 00 UTC 20 Jan 1986.

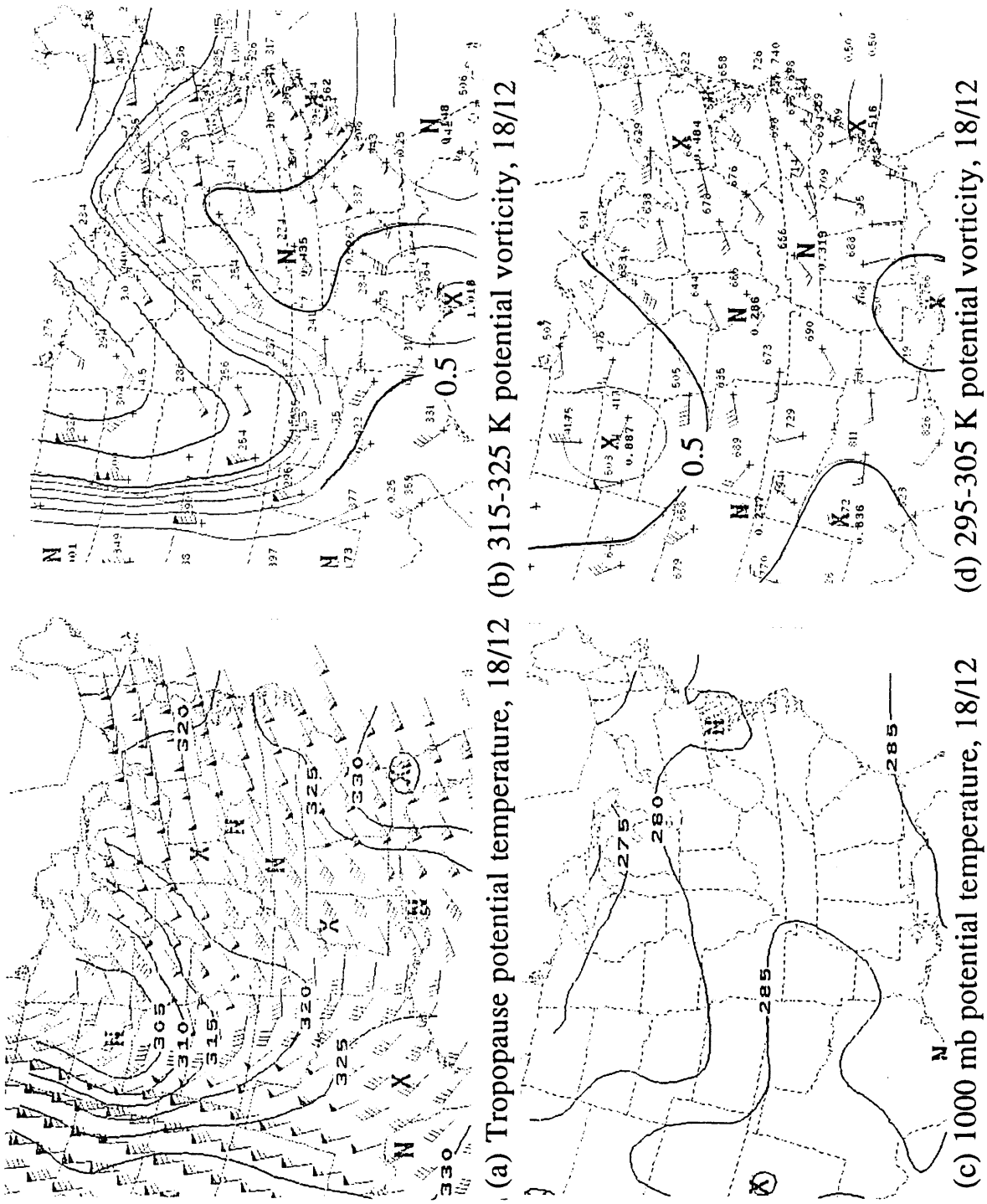

Fig. 3.19: Potential vorticity and potential temperature, 12 UTC 18 Jan 1986. For full description of Figs. 3.19-3.27, see Appendix B.

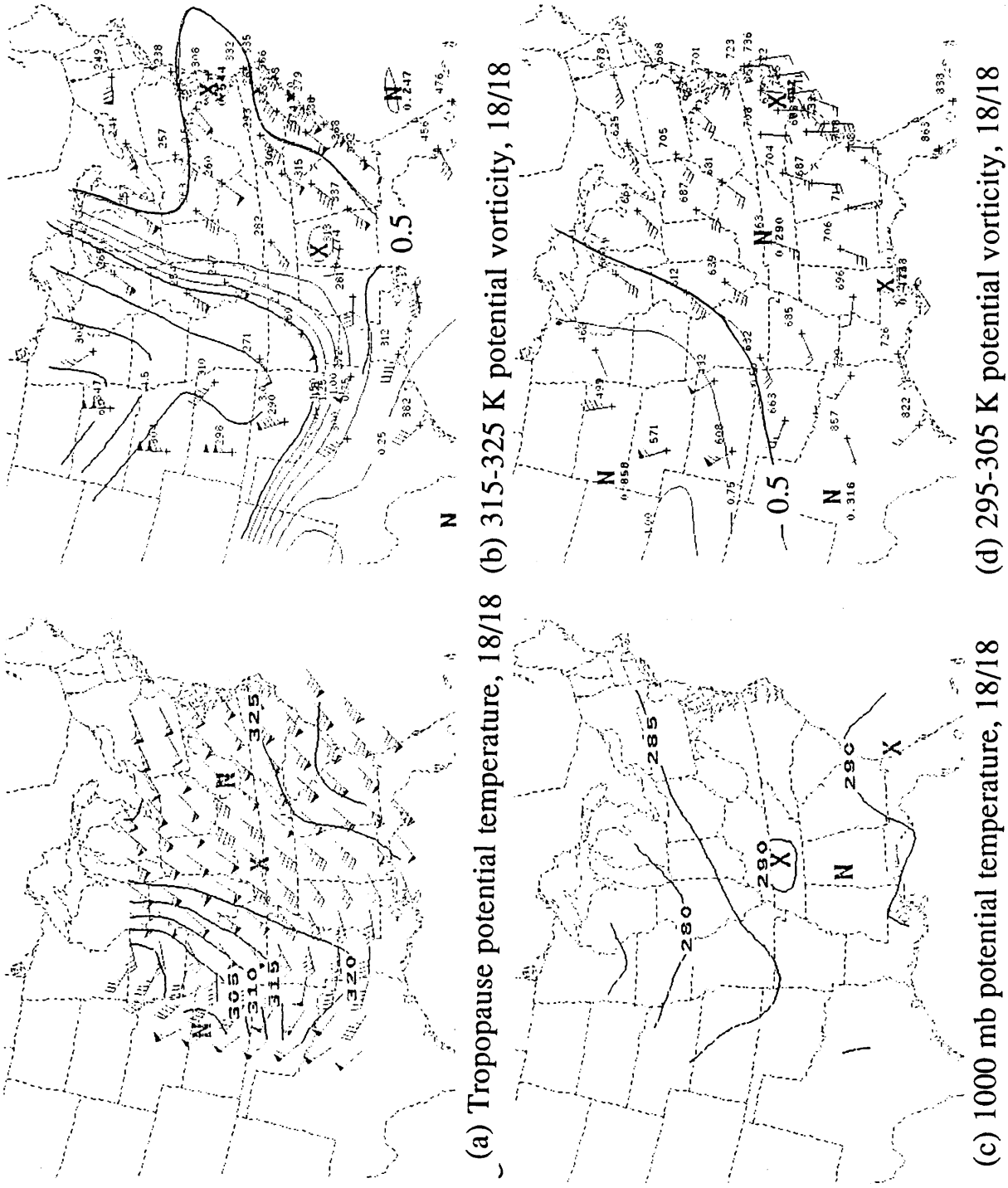

Fig. 3.20: As in Fig. 3.19, but for 18 UTC 18 Jan 1986.

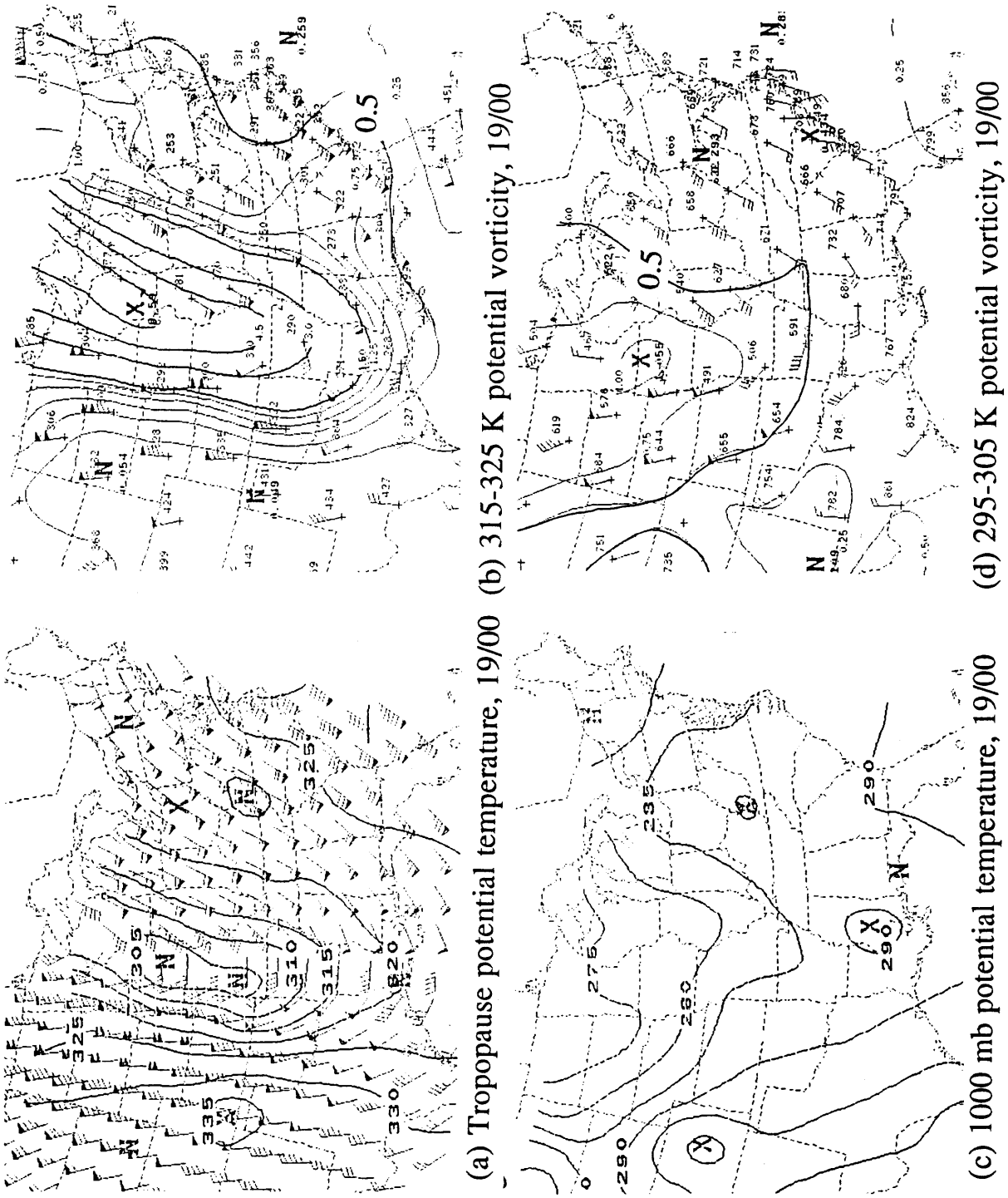

Fig. 3.21: As in Fig. 3.19, but for 00 UTC 19 Jan 1986.

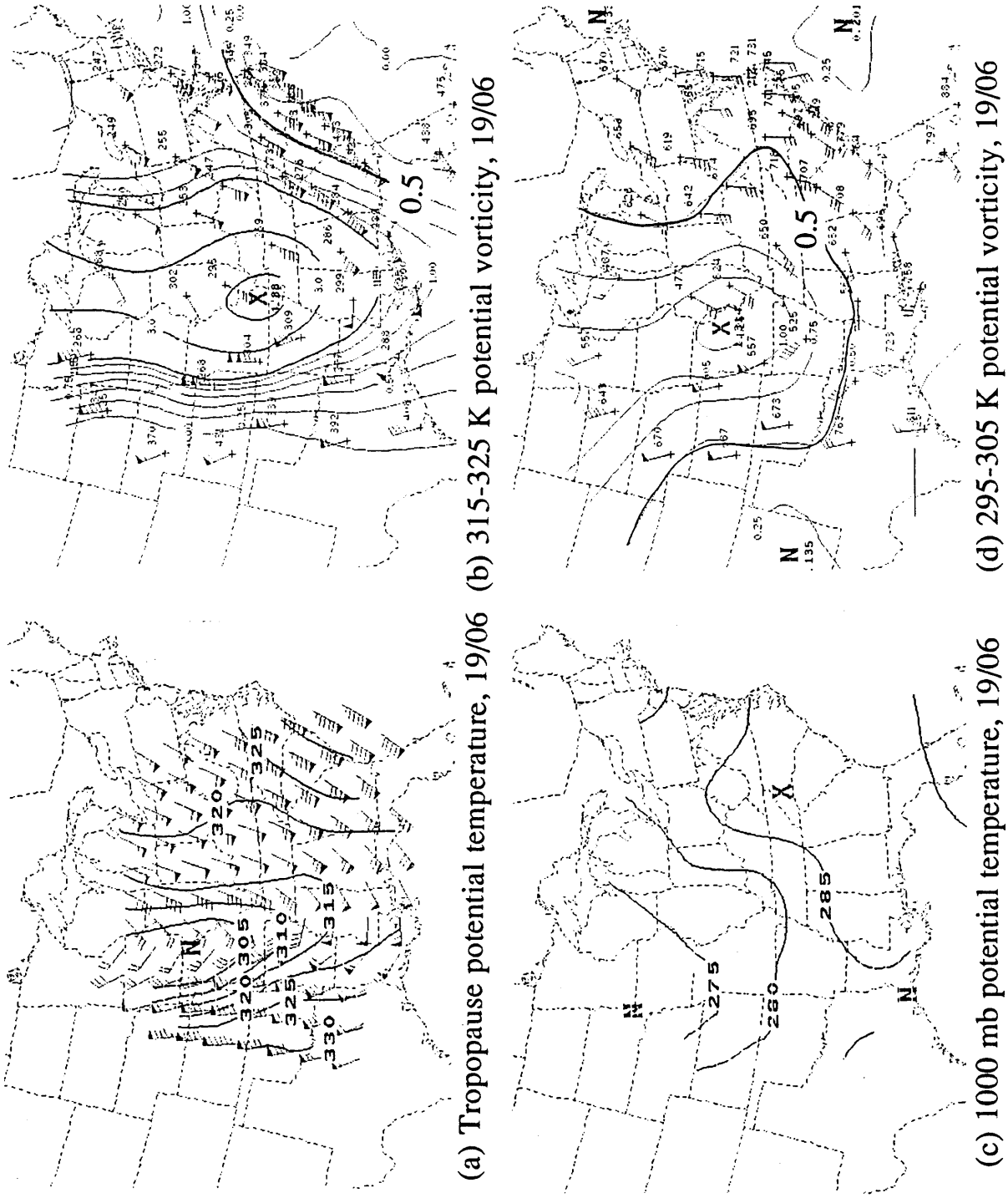

Fig. 3.22: As in Fig. 3.19, but for 06 UTC 19 Jan 1986.

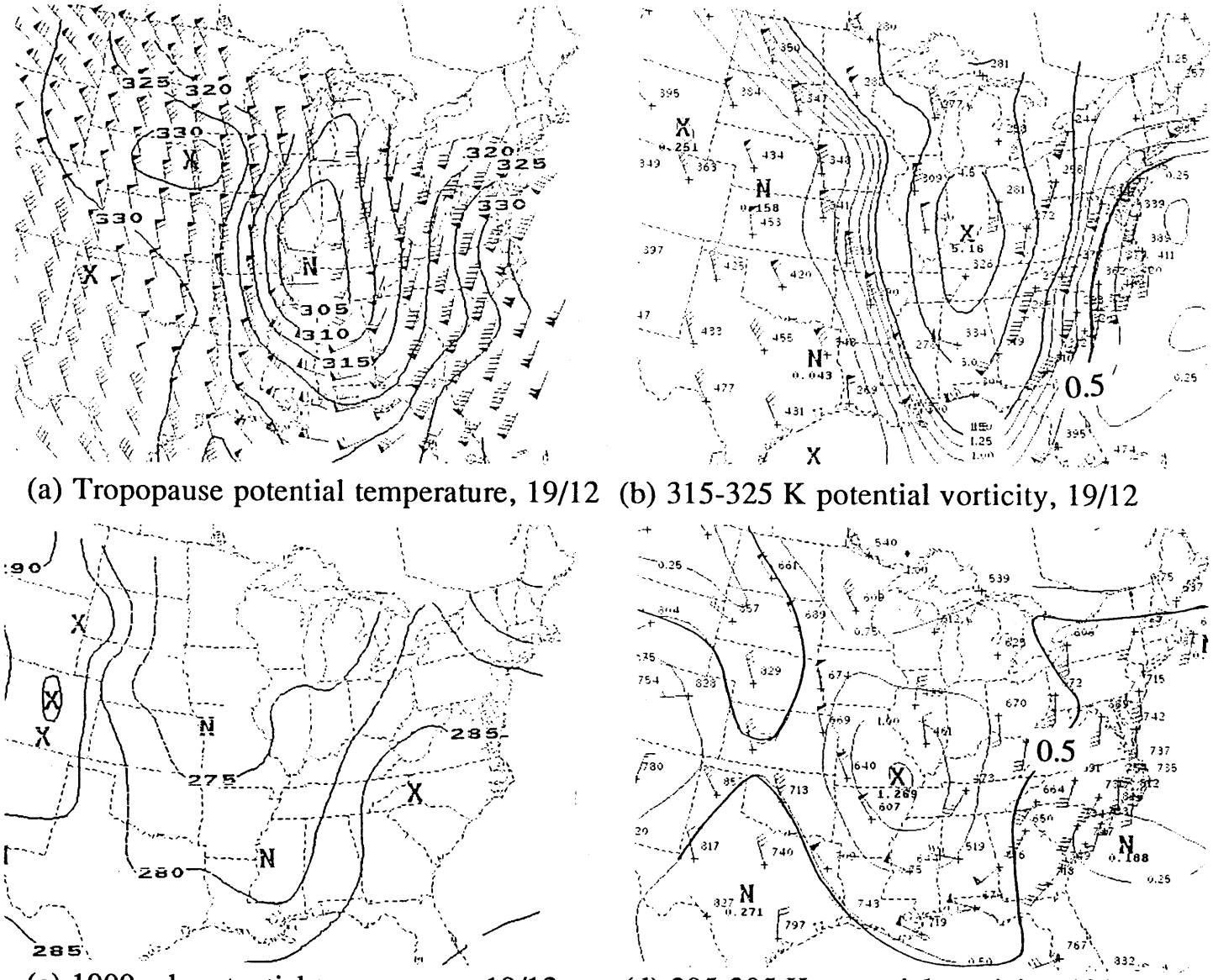

(a) Tropopause potential temperature, 19/12 (b) 315-325 K potential vorticity, 19/12

(c) 1000 mb potential temperature, 19/12 (d) 295-305 K potential vorticity, 19/12

Fig. 3.23: As in Fig. 3.19, but for 12 UTC 19 Jan 1986.

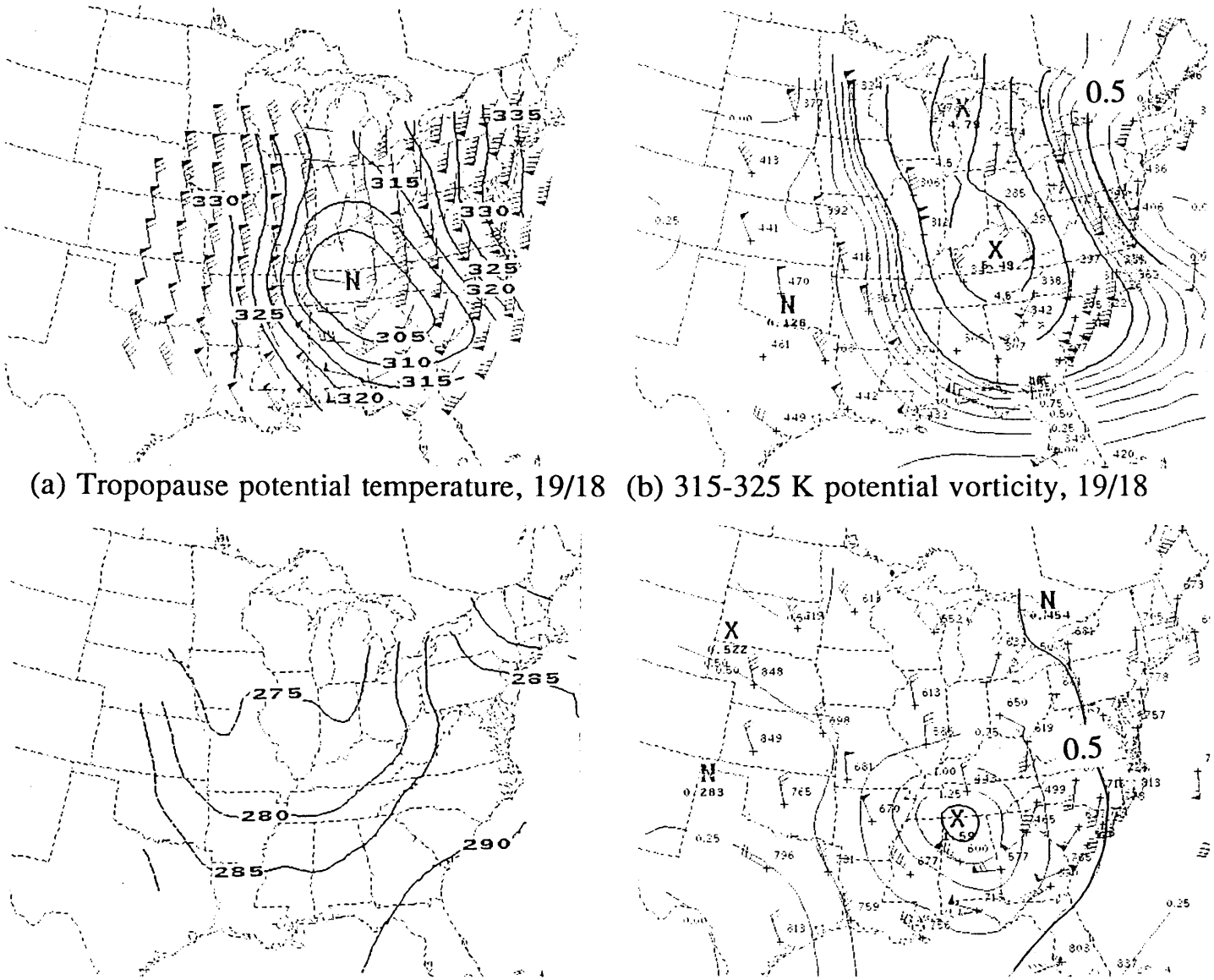

(a) Tropopause potential temperature, 19/18 (b) 315-325 K potential vorticity, 19/18

(c) 1000 mb potential temperature, 19/18 (d) 295-305 K potential vorticity, 19/18

Fig. 3.24: As in Fig. 3.19, but for 18 UTC 19 Jan 1986.

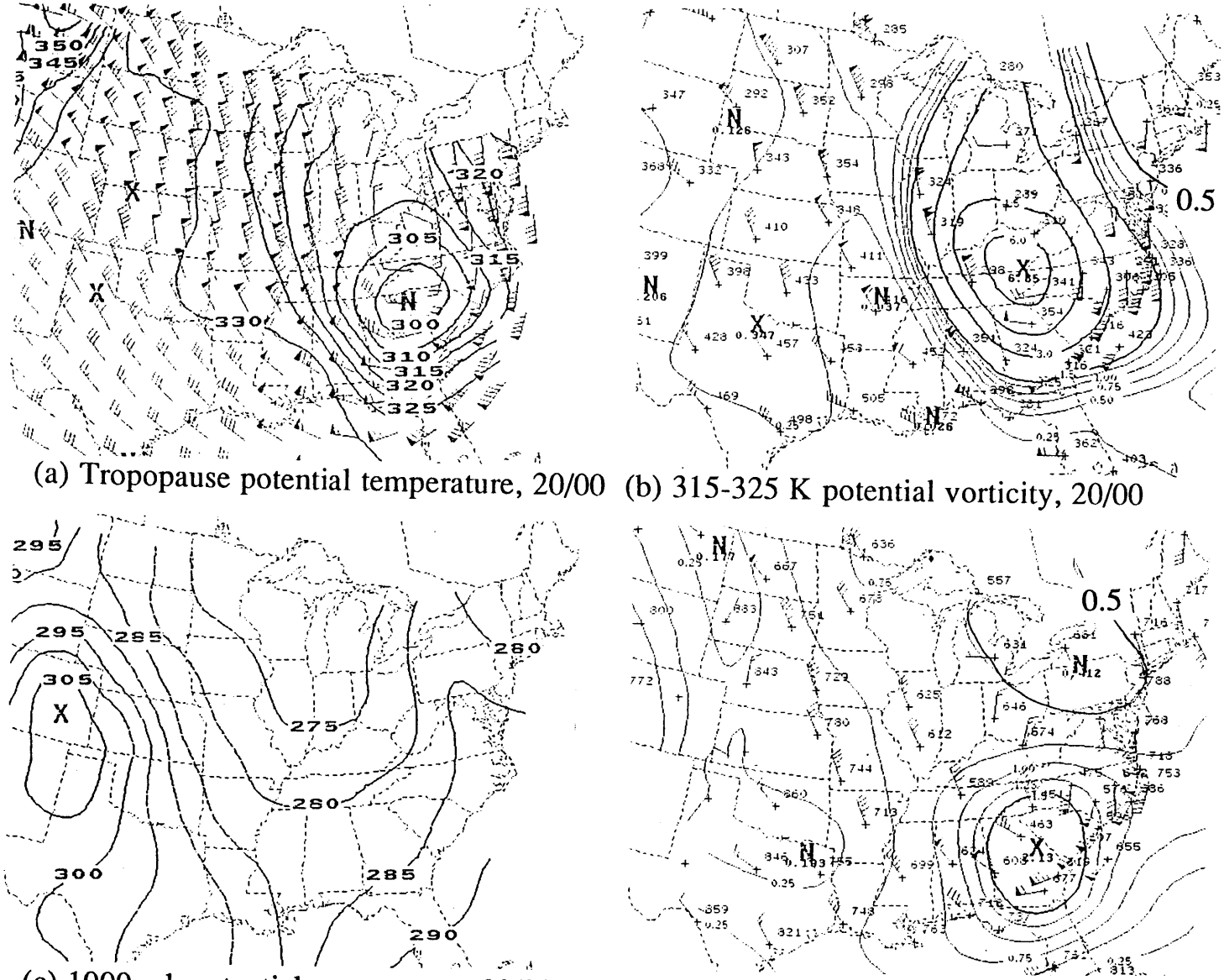

Fig. 3.25: As in Fig. 3.19, but for 00 UTC 20 Jan 1986.

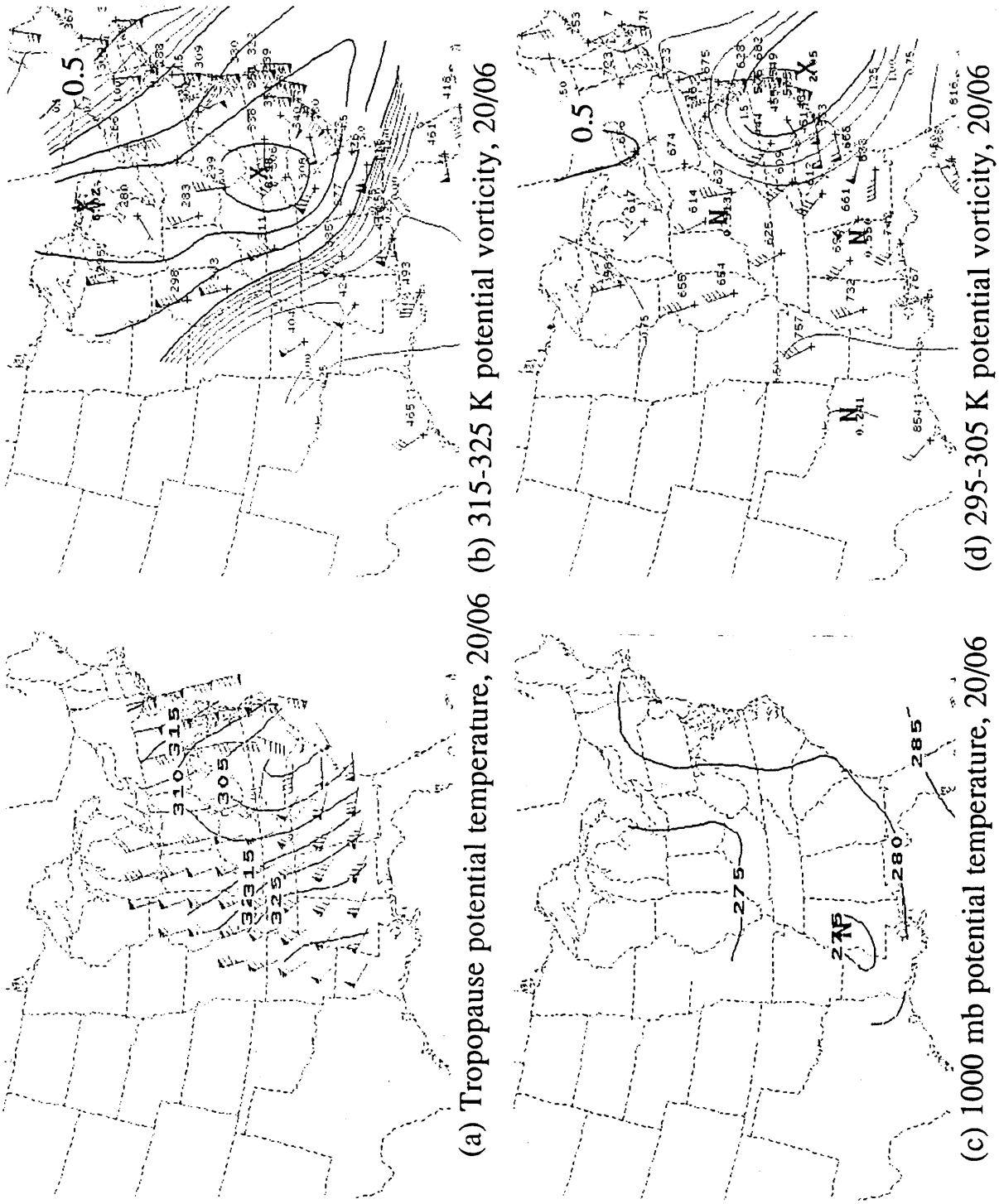

Fig. 3.26: As in Fig. 3.19, but for 06 UTC 20 Jan 1986.

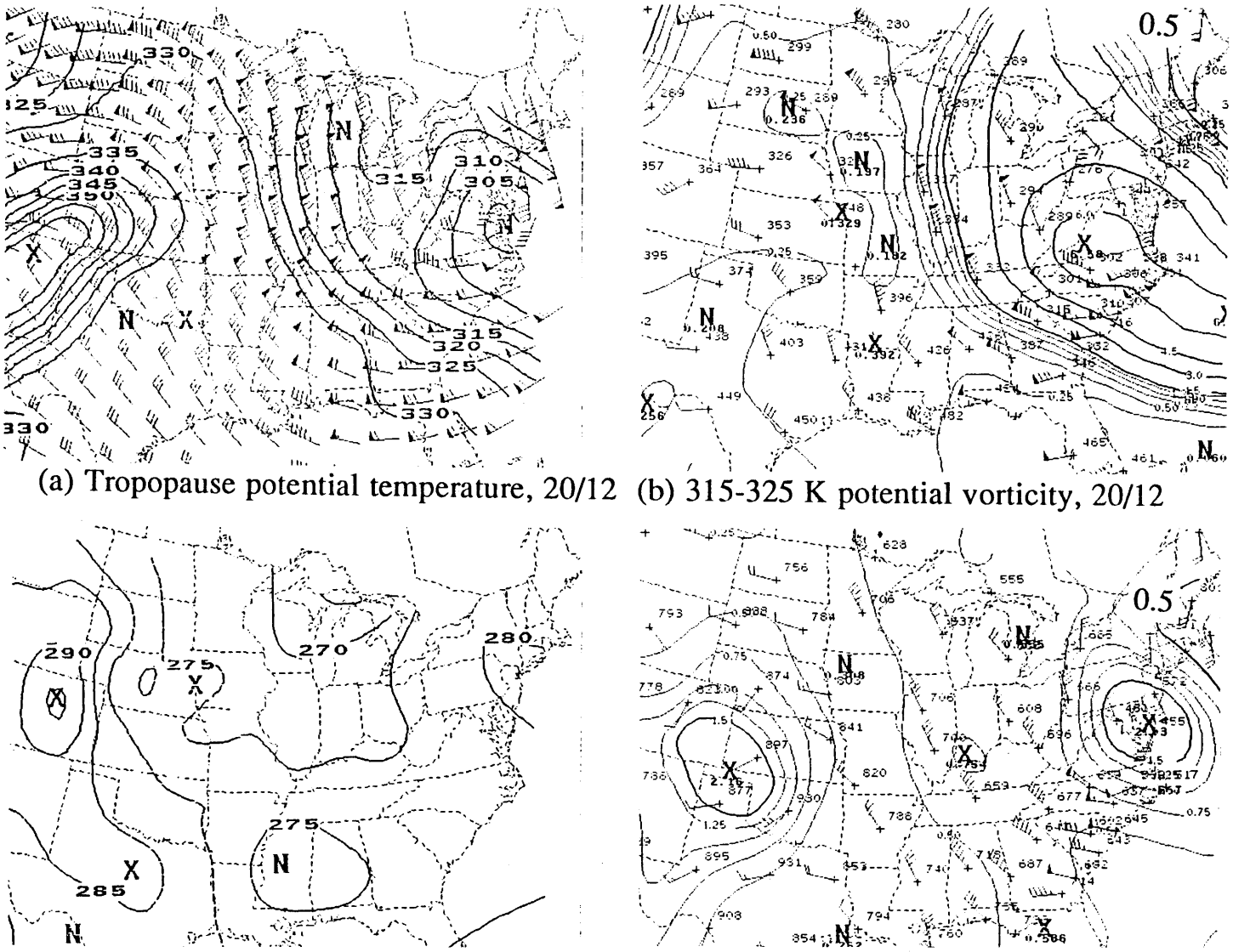

(a) Tropopause potential temperature, 20/12 (b) 315-325 K potential vorticity, 20/12

(c) 1000 mb potential temperature, 20/12 (d) 295-305 K potential vorticity, 20/12

Fig. 3.27: As in Fig. 3.19, but for 12 UTC 20 Jan 1986.

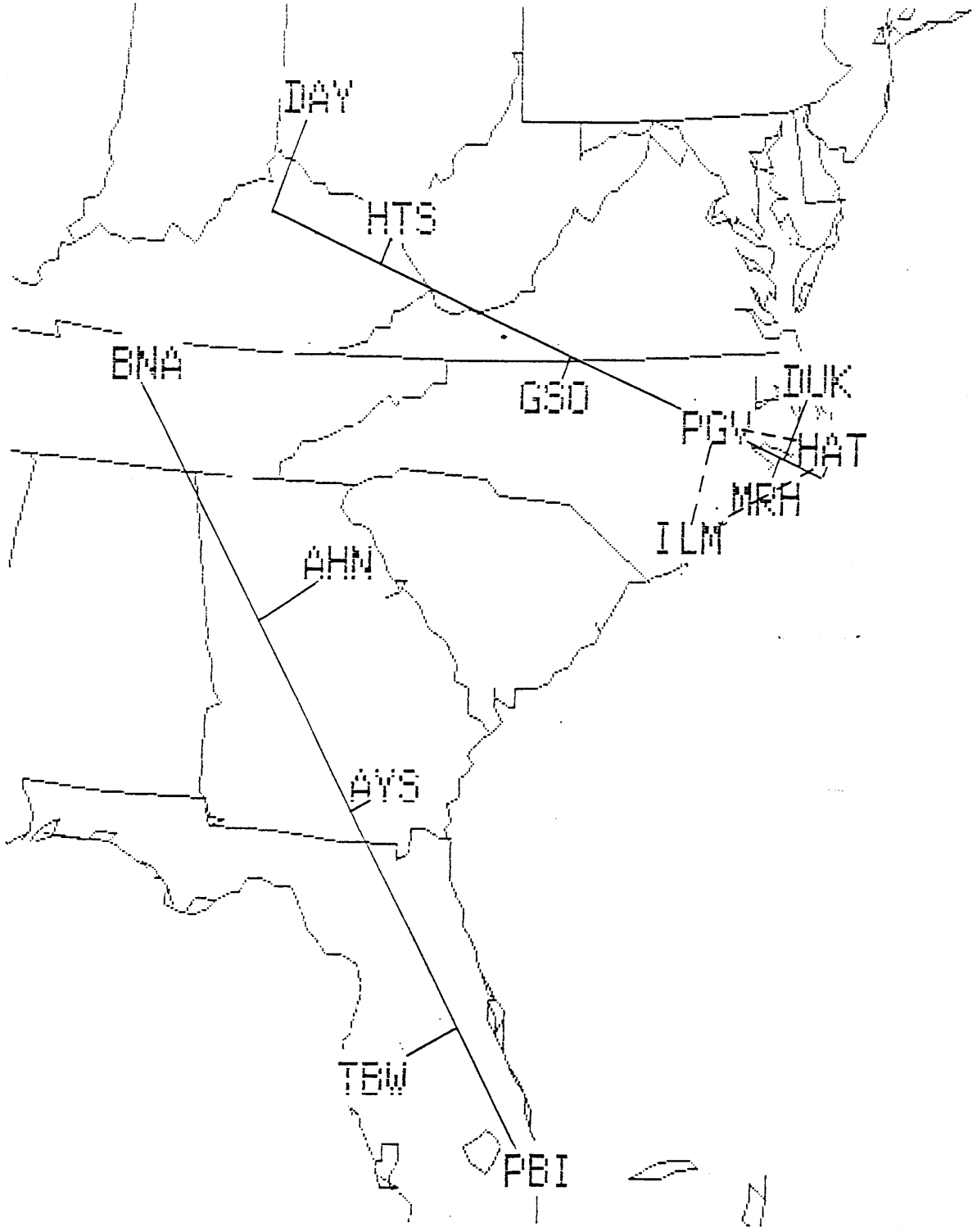

Fig. 3.28: Map showing locations of stations used in cross sections (solid lines) for Figs. 3.28, 3.29, 3.34, and 3.35, and in triangle calculation (Fig. 3.33).

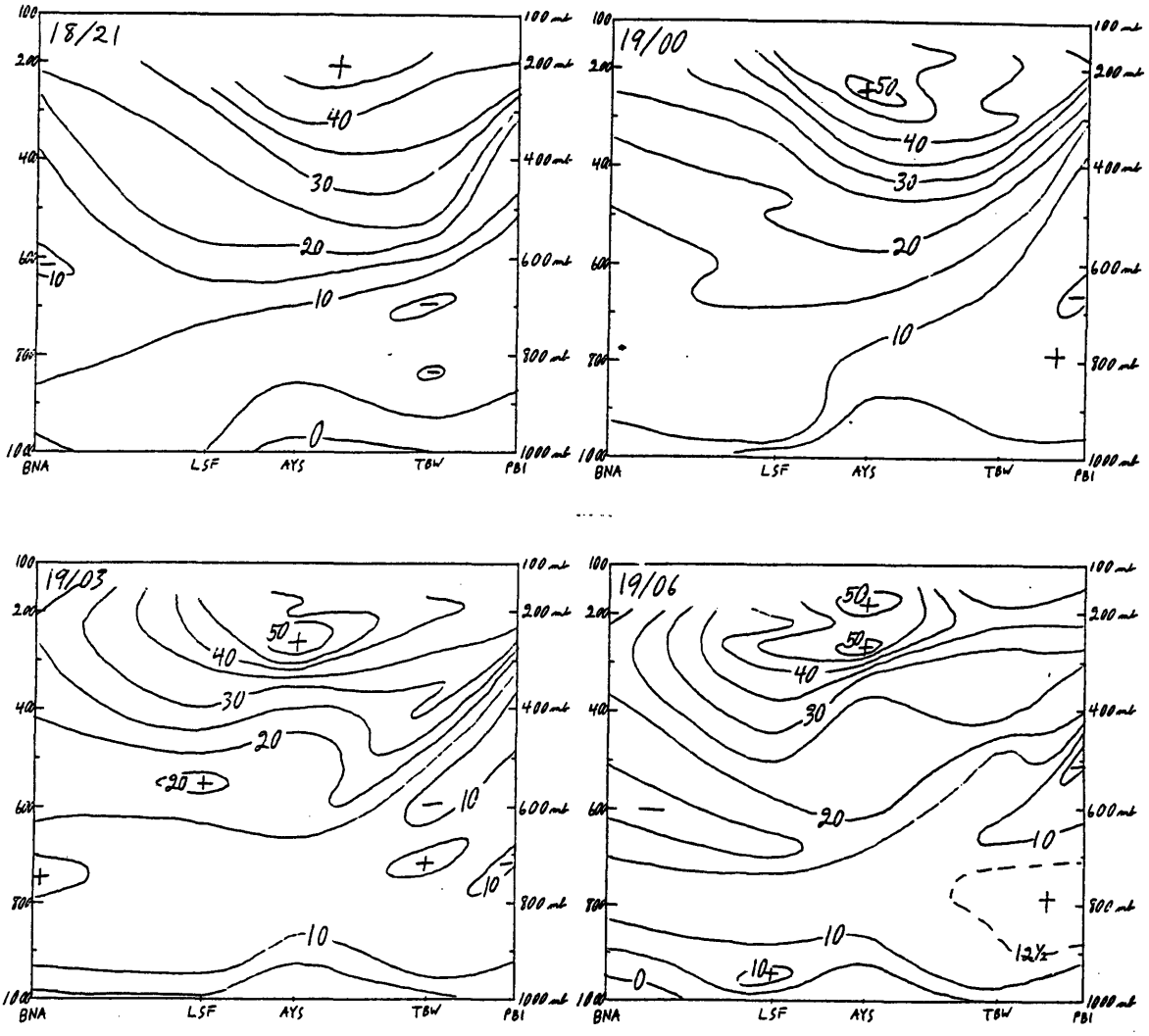

Fig. 3.29: Cross sections, BNA-PBI (station locations in Fig. 3.28), showing cross-section-normal wind (positive toward 55 degrees, c.int. 5 m s^{-1}), 21 UTC 18 Jan 1986 to 06 UTC 19 Jan 1986.

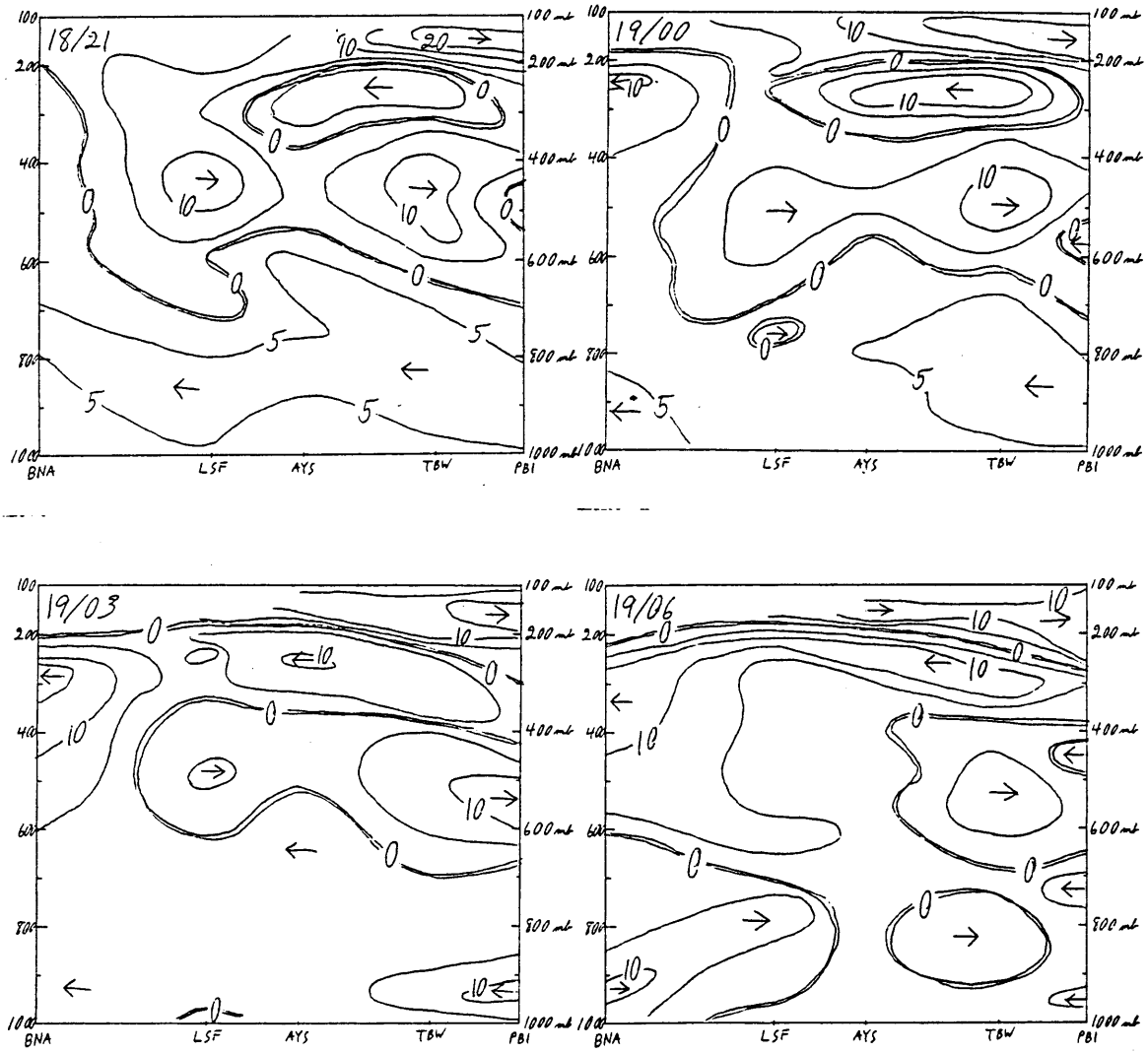

Fig. 3.30: Cross sections, BNA-PBI, showing cross-section-parallel wind (arrows at extrema indicate wind direction, c.int. 5 m s^{-1}), same times as in Fig. 3.29.

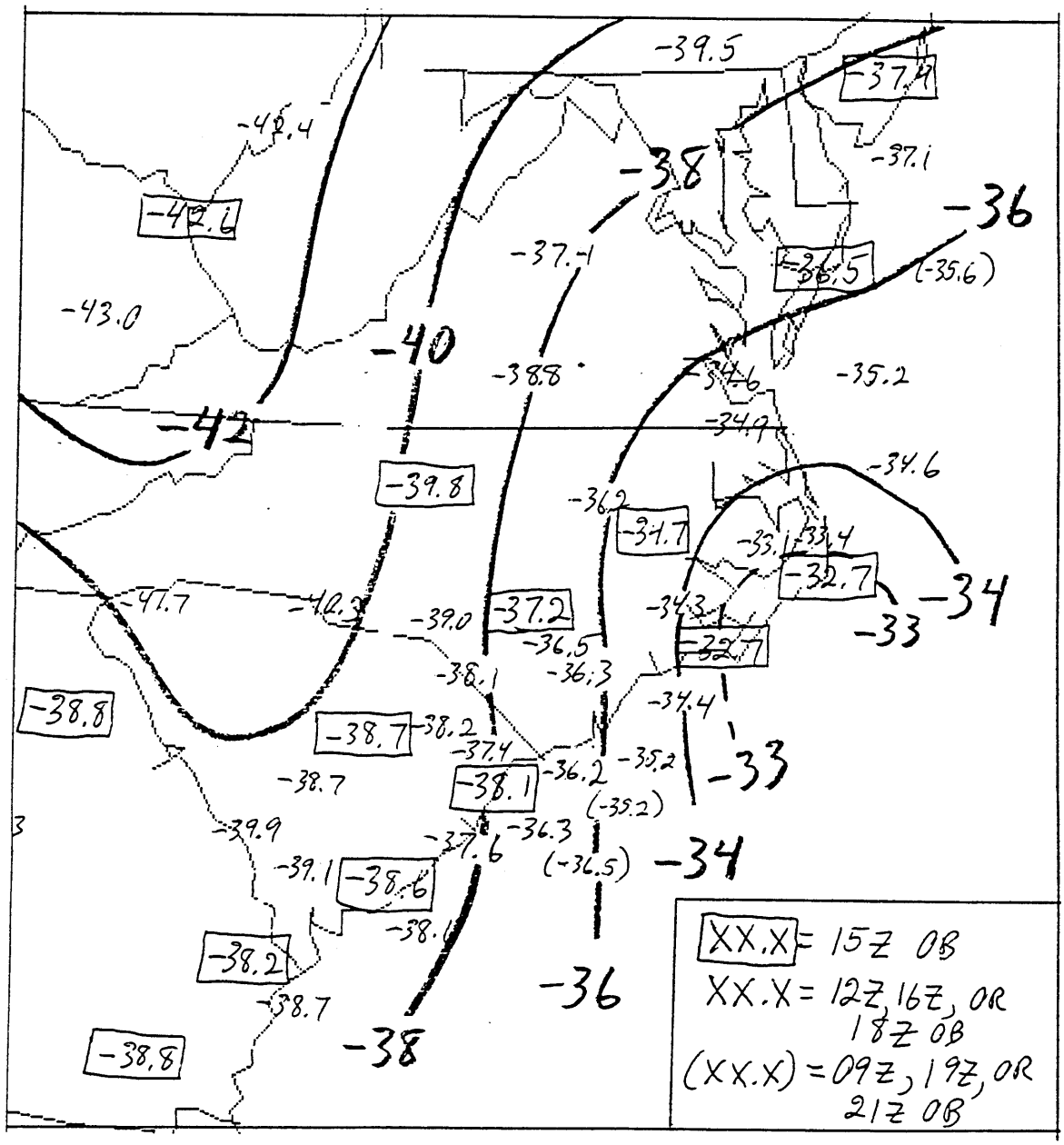

Fig. 3.31: Mean 400-300 mb temperature (c.int. 2 C), computed from observed thicknesses as described in the text. Map time is 15 UTC 19 Jan 1986. Observations from map time and selected observations from up to six hours before and after map time are also plotted (format shown in legend), using the standard time-space conversion of 0.3 degrees latitude and longitude per hour.

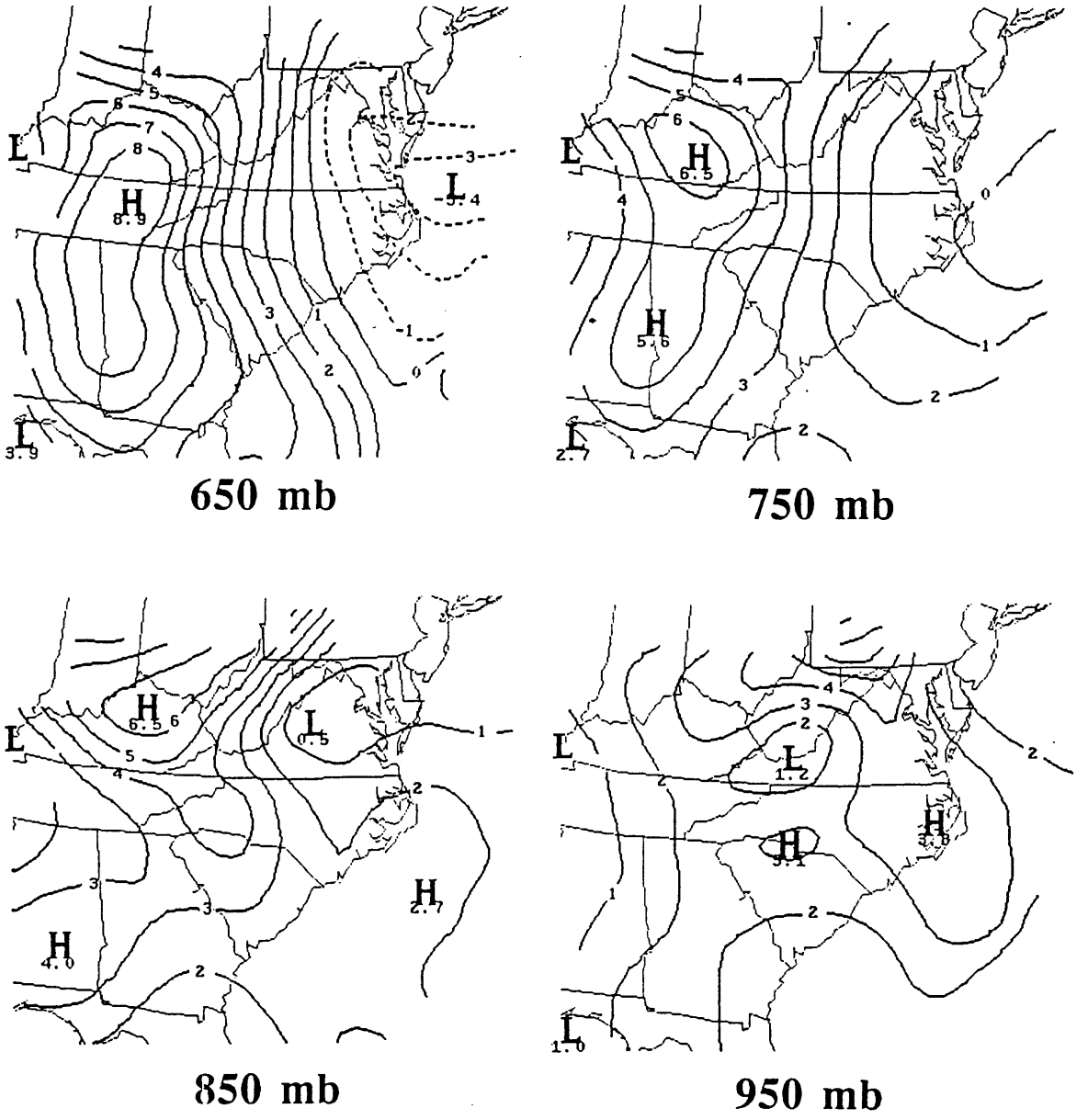

Fig. 3.32: Objectively analyzed relative vorticity (contour interval 1x10^{-5} s^{-1}, negative contours dashed) on constant pressure surfaces, 15 UTC 19 Jan 1986.

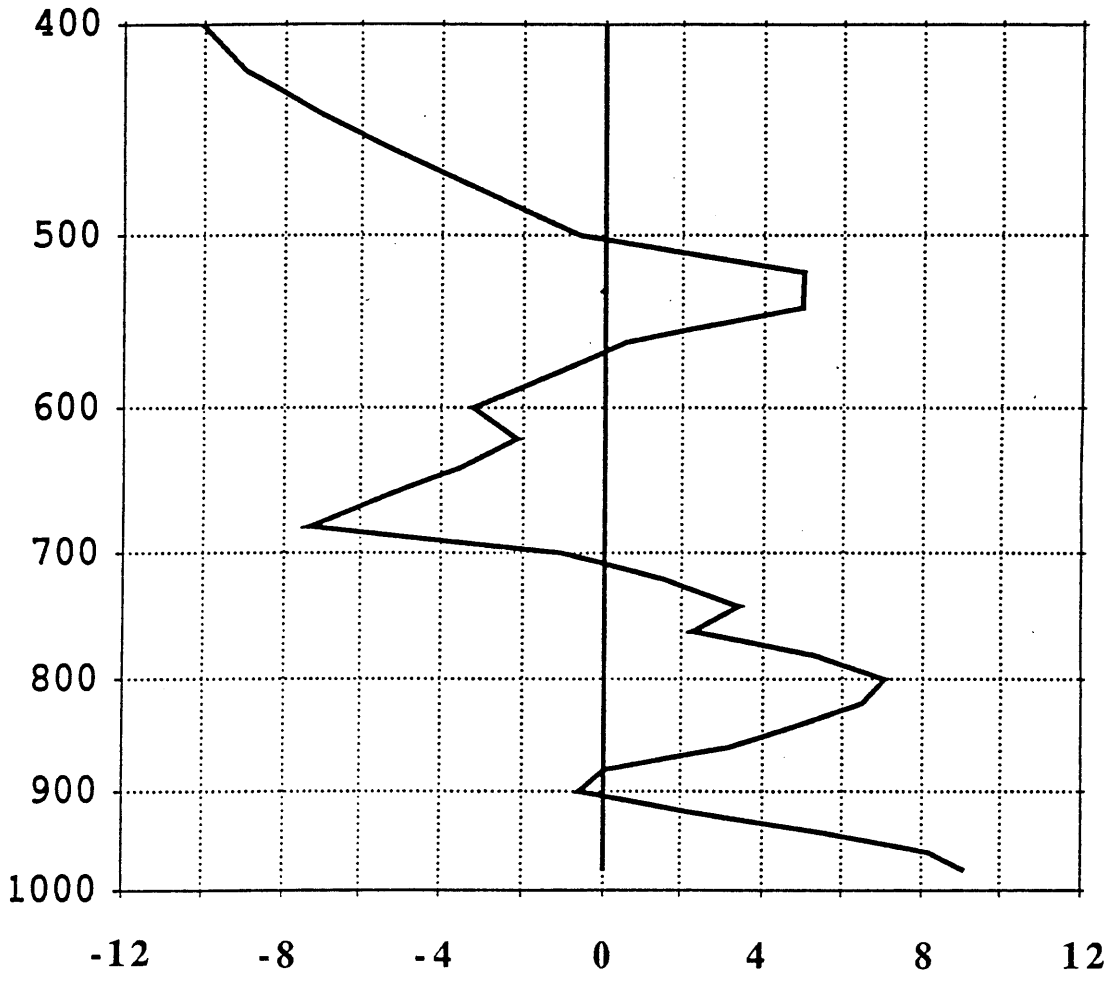

Fig. 3.33: Profile of relative vorticity ($x10^{-5}$ s^{-1}) versus pressure (mb), calculated from ILM-PGV-HAT triangle, 15 UTC 19 Jan 1986. Station locations are shown in Fig. 3.28.

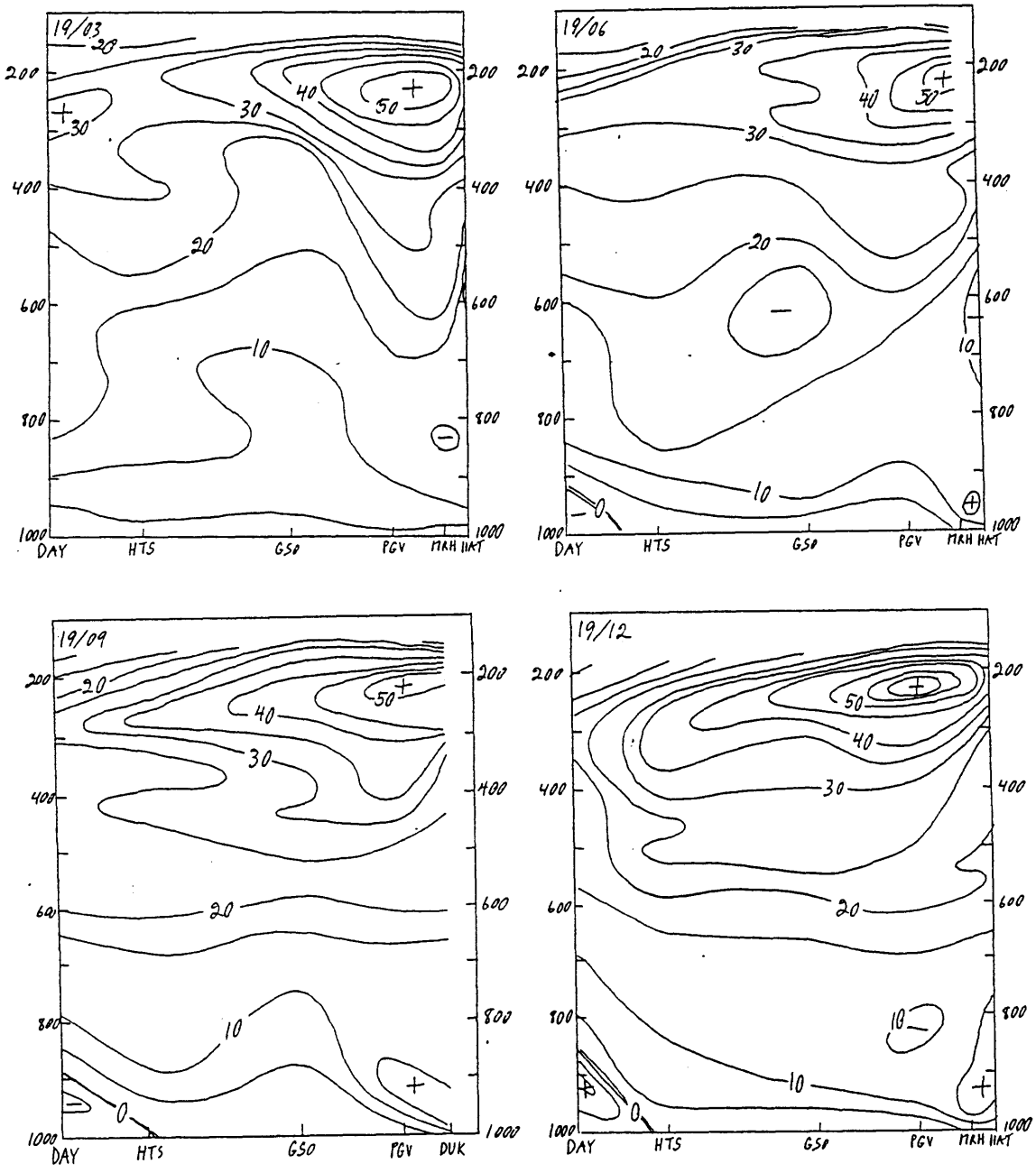

Fig. 3.34 (first of two pages): Cross sections, DAY-HAT (station locations in Fig. 3.28), showing cross-section-normal wind (positive toward 25 degrees, c.int. 5 m s^{-1}), 21 UTC 18 Jan 1986 to 06 UTC 19 Jan 1986.

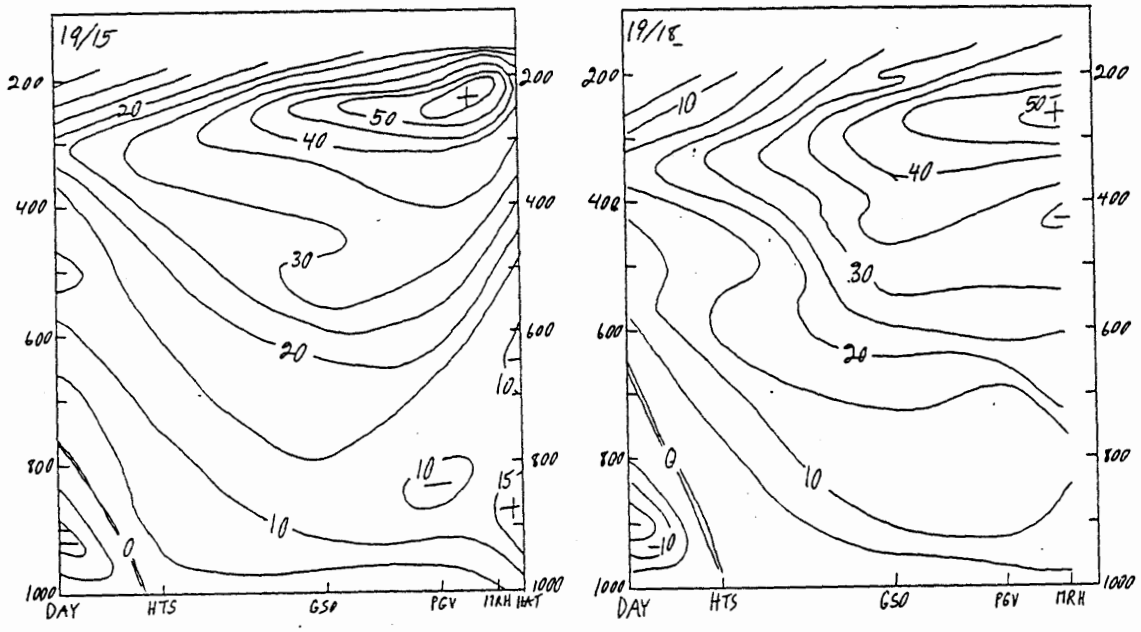

Fig. 3.34 (second of two pages).

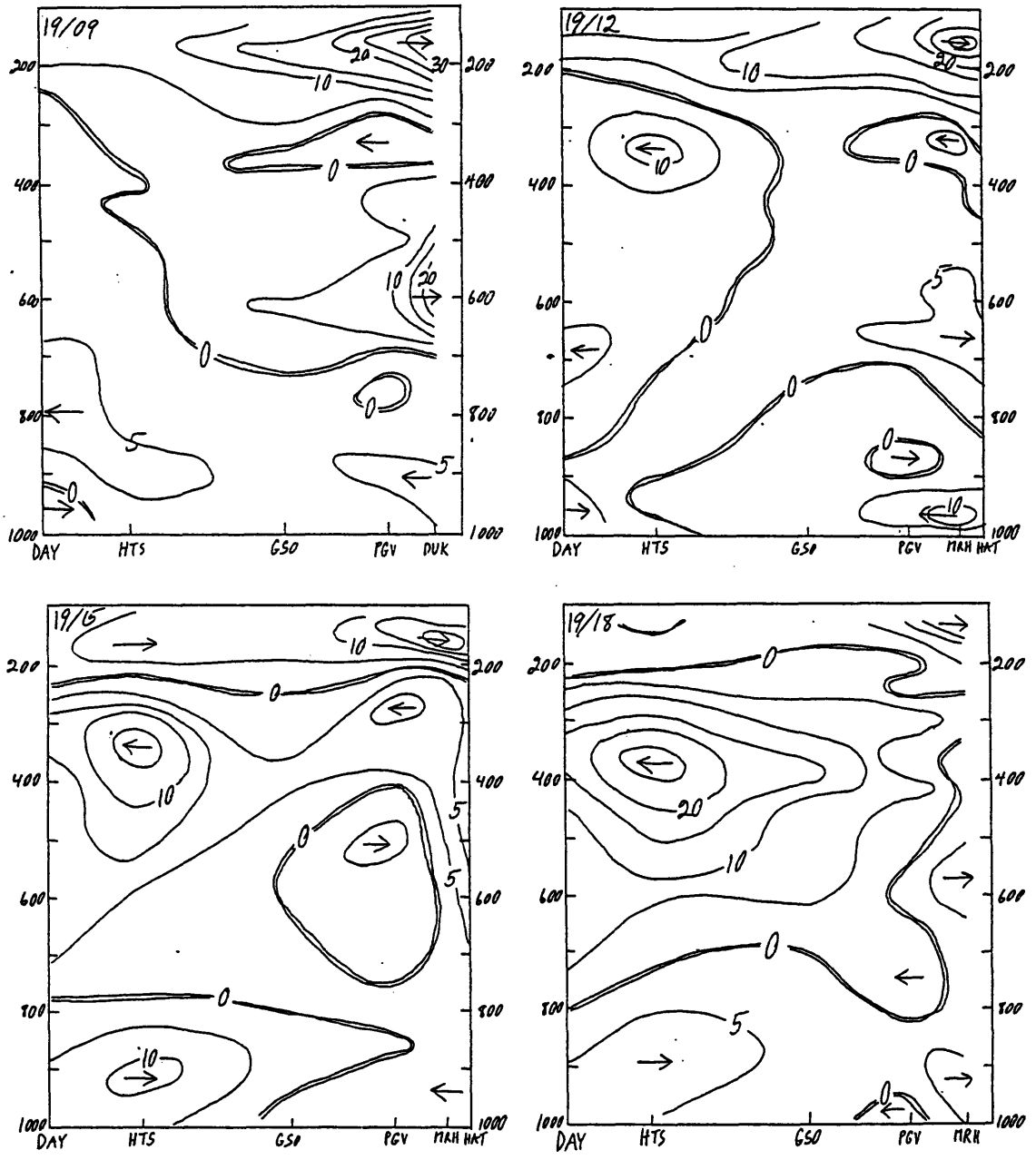

Fig. 3.35: Cross sections, DAY-HAT, showing cross-section-parallel wind (arrows at extrema indicate wind direction, c.int. 5 m s^{-1}), 09 UTC 19 Jan 1986 to 18 UTC 19 Jan 1986. Same times as last four times in Fig. 3.34.

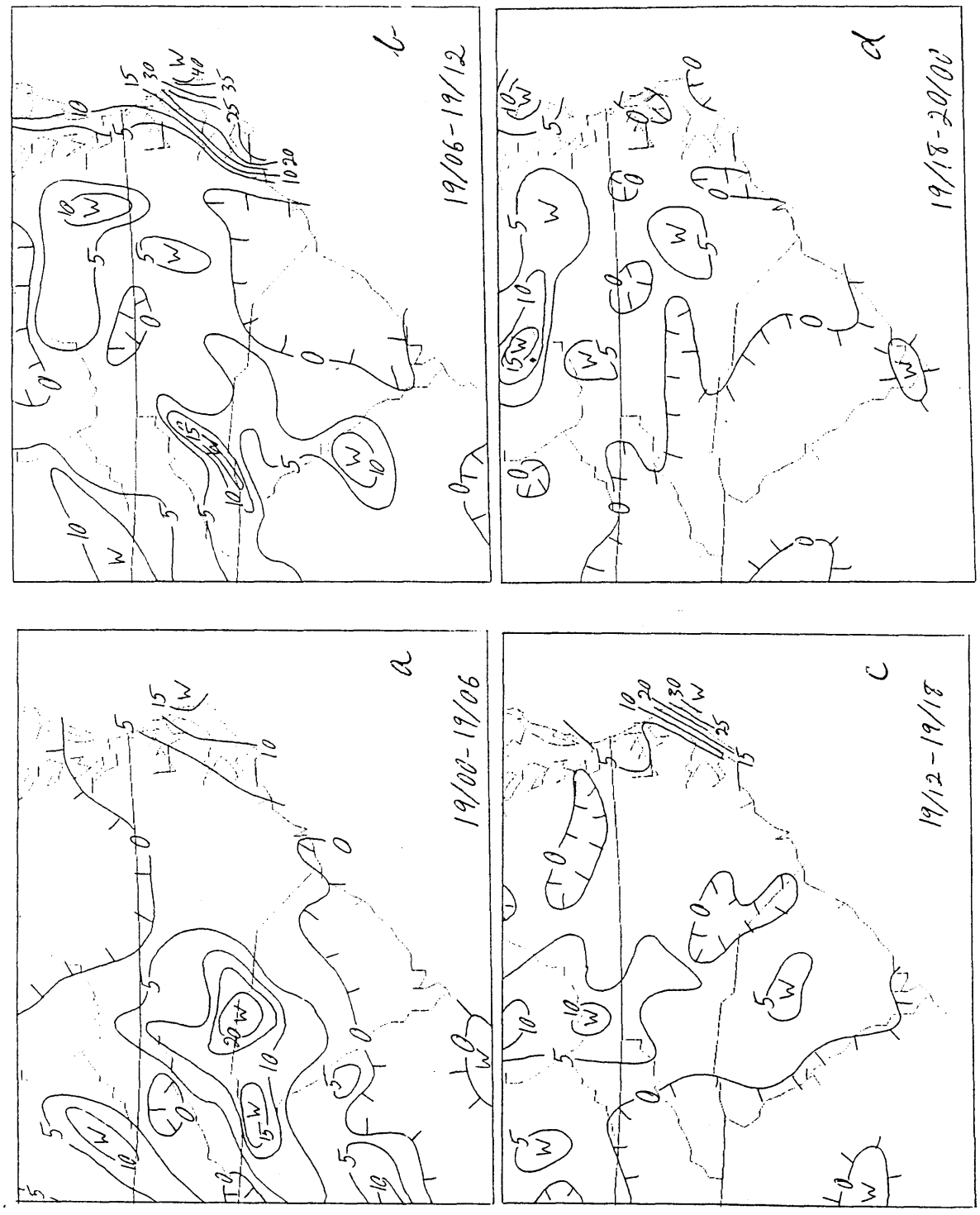

Fig. 3.36: Accumulated six-hour precipitation (c.int. 5 mm). (a) 00 UTC to 06 UTC, 19 Jan 1986. (b) 06 UTC to 12 UTC, 19 Jan 1986. (c) 12 UTC to 18 UTC, 19 Jan 1986. (d) 18 UTC 19 Jan 1986 to 00 UTC 20 Jan 1986.

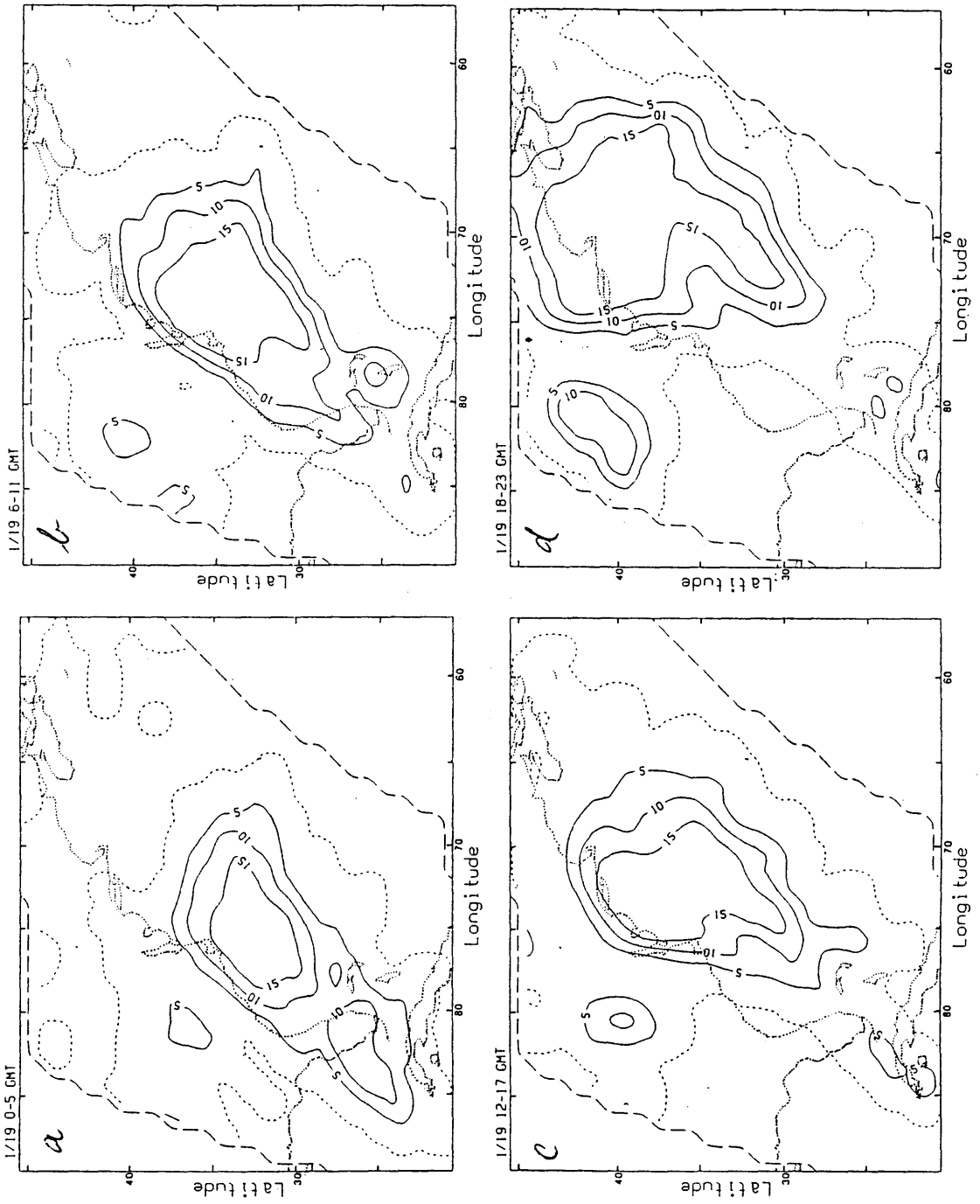

Fig. 3.37: Accumulated six-hour precipitation (c.int. 5 mm), same times as in Fig. 3.36. From Martin *et al.* (1988).

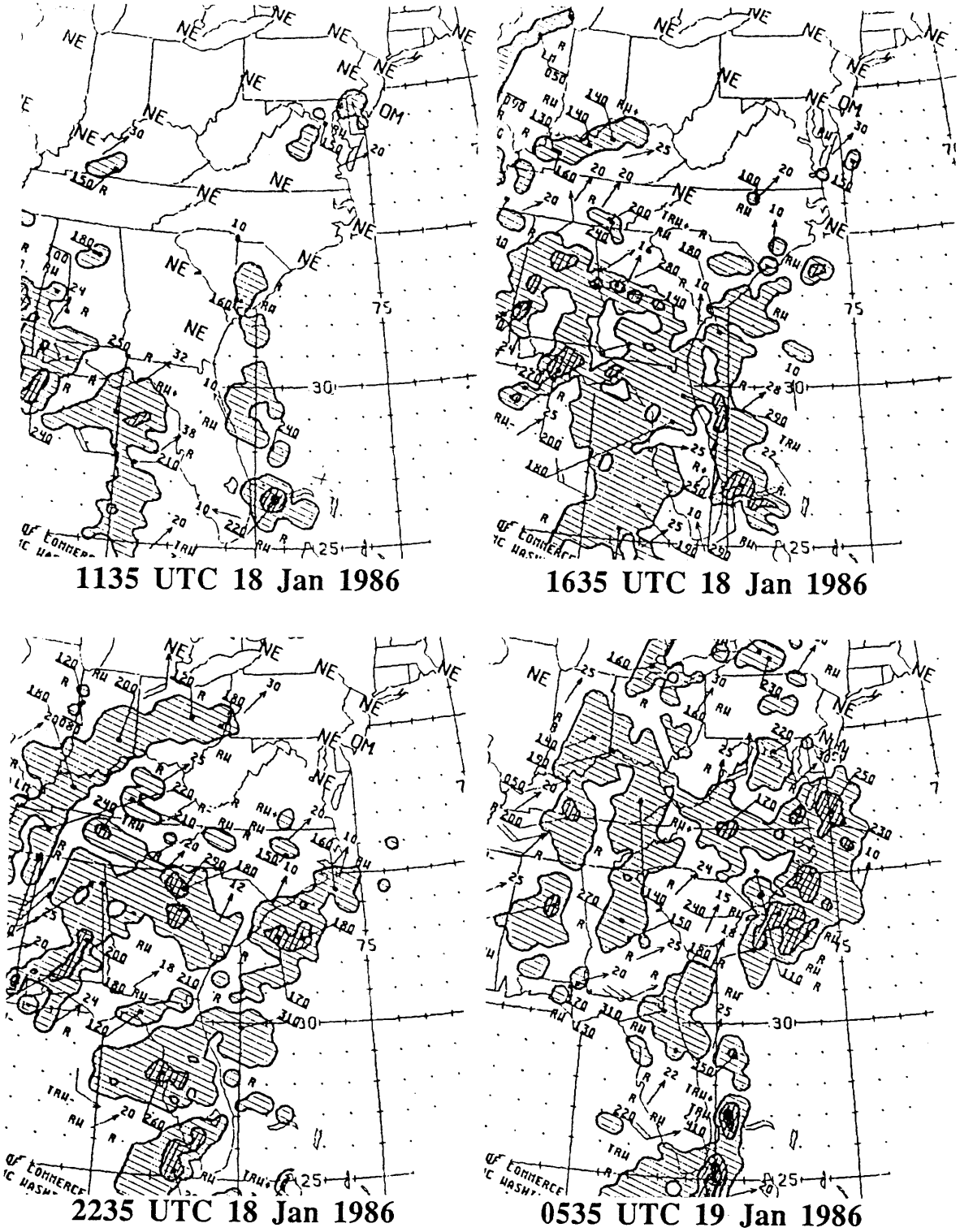

Fig. 3.38 (first of two pages): Portions of National Radar Summaries, 18-20 Jan 1986. Hatching, cross-hatching, and shading indicate VIP levels 1, 3, and 5. Underlined numbers indicate maximum echo heights in hundreds of feet.

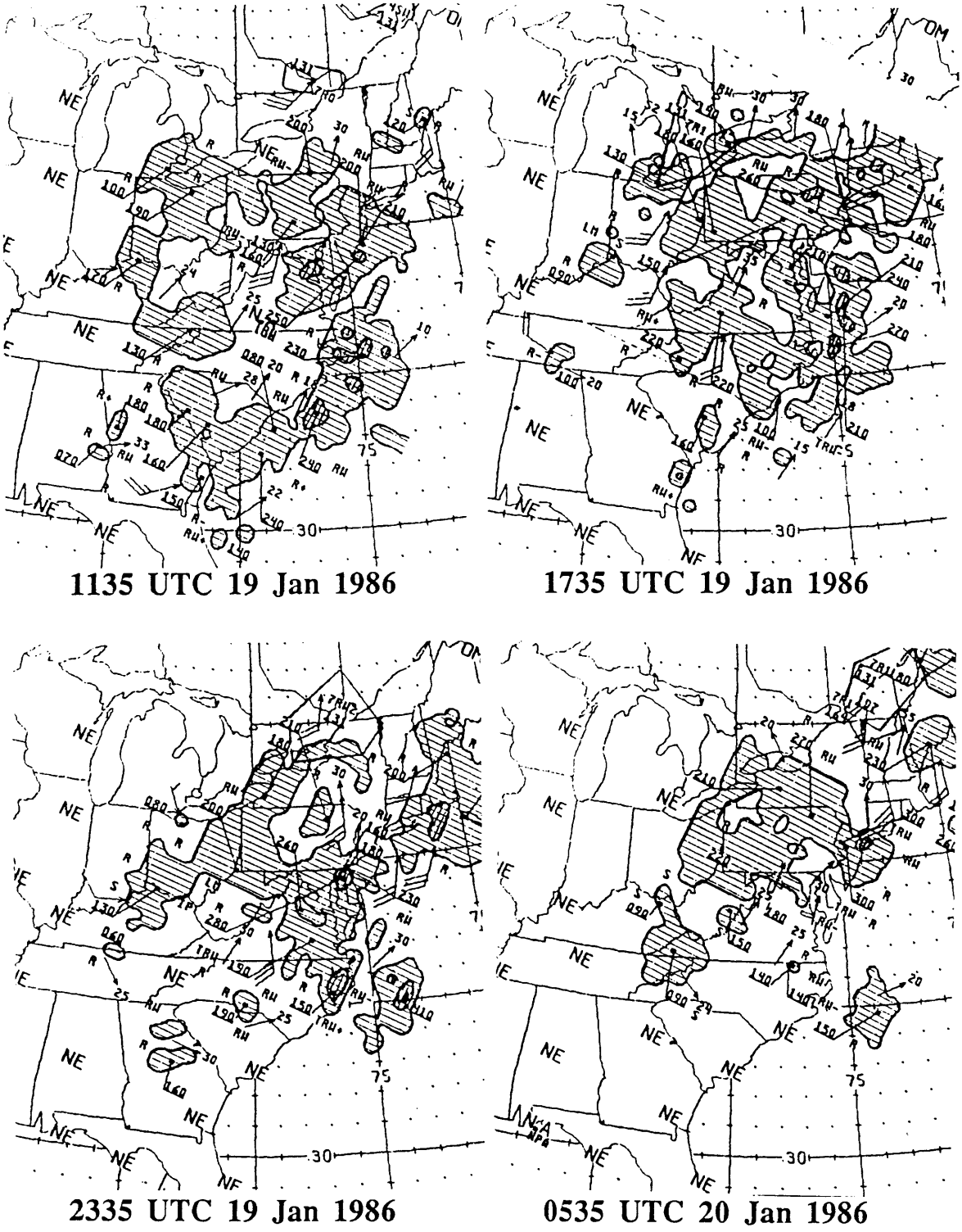

Fig. 3.38 (second of two pages).

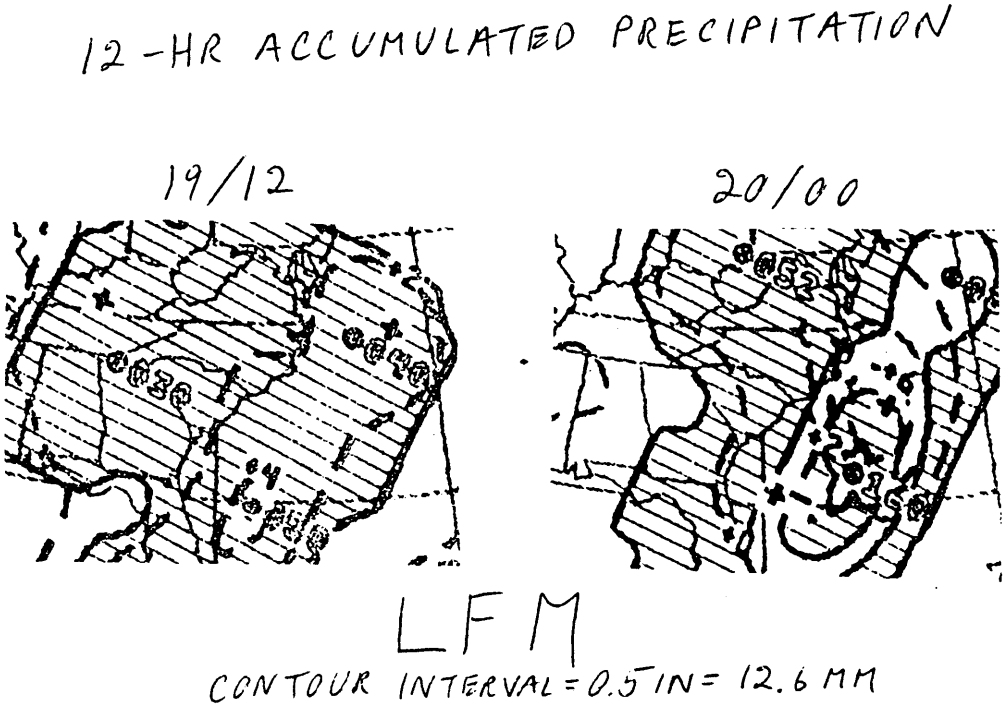
12-HR ACCUMULATED PRECIPITATION
19/12
20/00
LFM
CONTOUR INTERVAL = 0.5 IN = 12.6 MM
19/12
20/00
NGM
CONTOUR INTERVAL = 5 MM

Fig. 3.39.

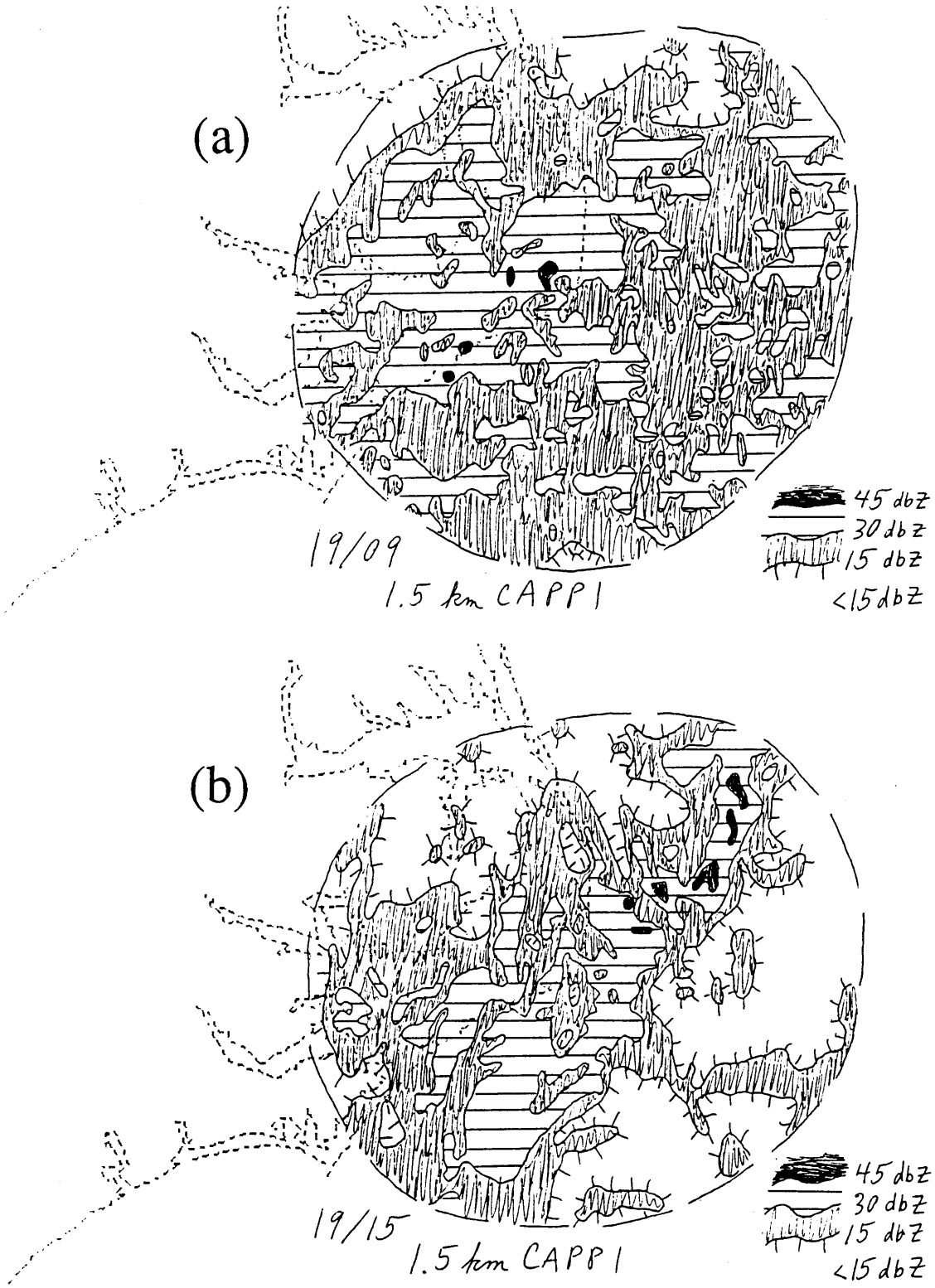

Fig. 3.40: CAPPIs (Constant Altitude Plan-Position Indicators), 1.5 km, from CP4. Reflectivity is contoured at 15 dbZ increments starting at 15 dbZ, as indicated in the legends. Dashed circle indicates extent of areal coverage of radar data. (a) 0900 UTC 15 Jan 1986 (b) 1500 UTC 15 Jan 1986.

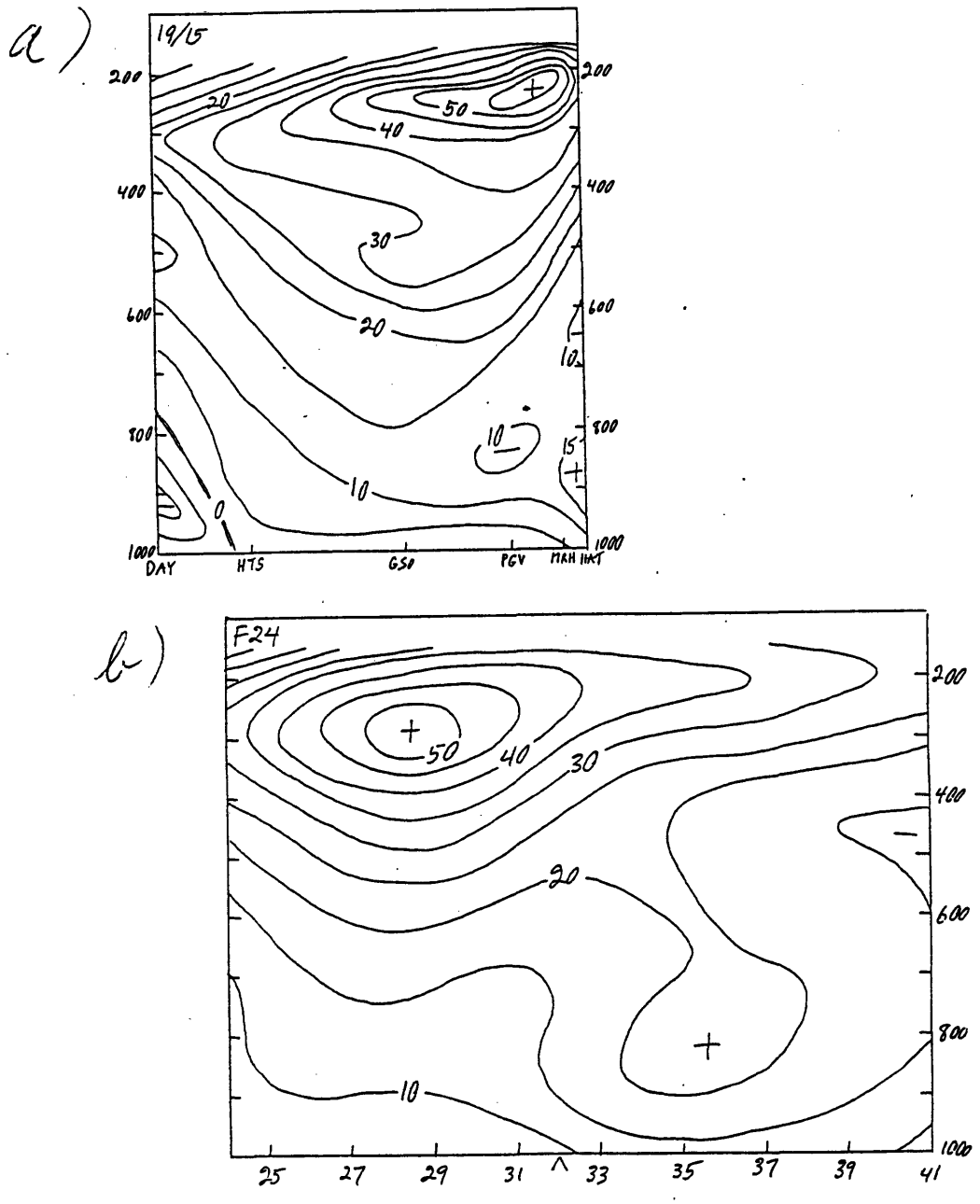

Fig. 4.1: Comparison of observed and NGM cross sections of cross-section-normal wind component (c.int. 5 m s^{-1}) through small-scale cyclone and low-level jet. Horizontal scales are equal. (a) DAY-HAT cross section, 15 UTC 19 Jan 1986, reproduced from Fig. 3.34. (b) Cross section along row 30 of NGM, 24-hour forecast valid 00 UTC 20 Jan 1986. Tick marks at bottom are at every two grid points (spacing approx. 160 km).

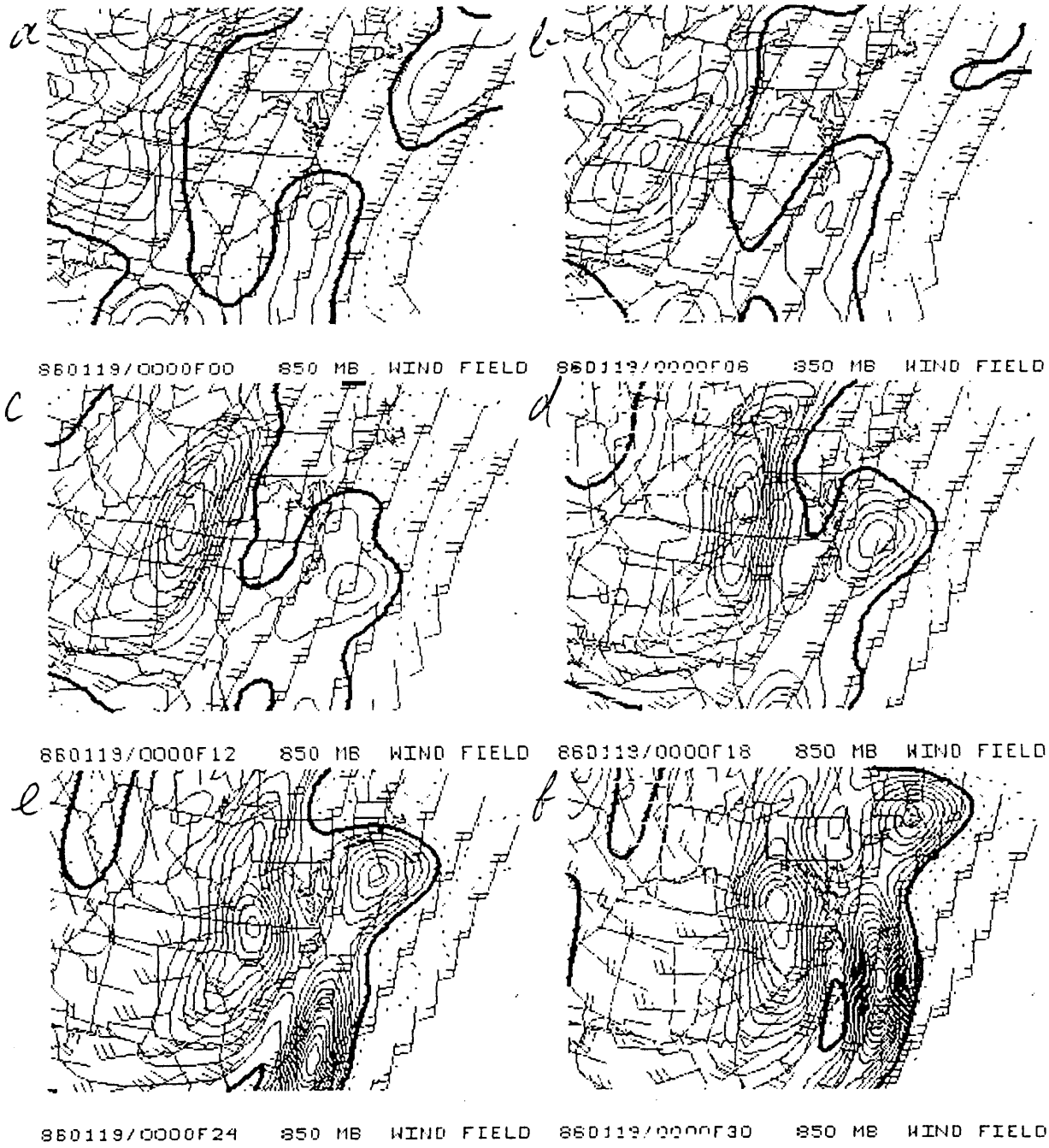

Fig. 4.2: NGM 850 mb relative vorticity (c.int. $1x10^{-5}$ s^{-1}, negative values dotted, zero contour thick), and winds (standard model). In this and succeeding figures, the NGM model run will be the run initialized 00 UTC 19 Jan 1986, and forecast times will be indicated as, for example, F12 for the 12-hour forecast.

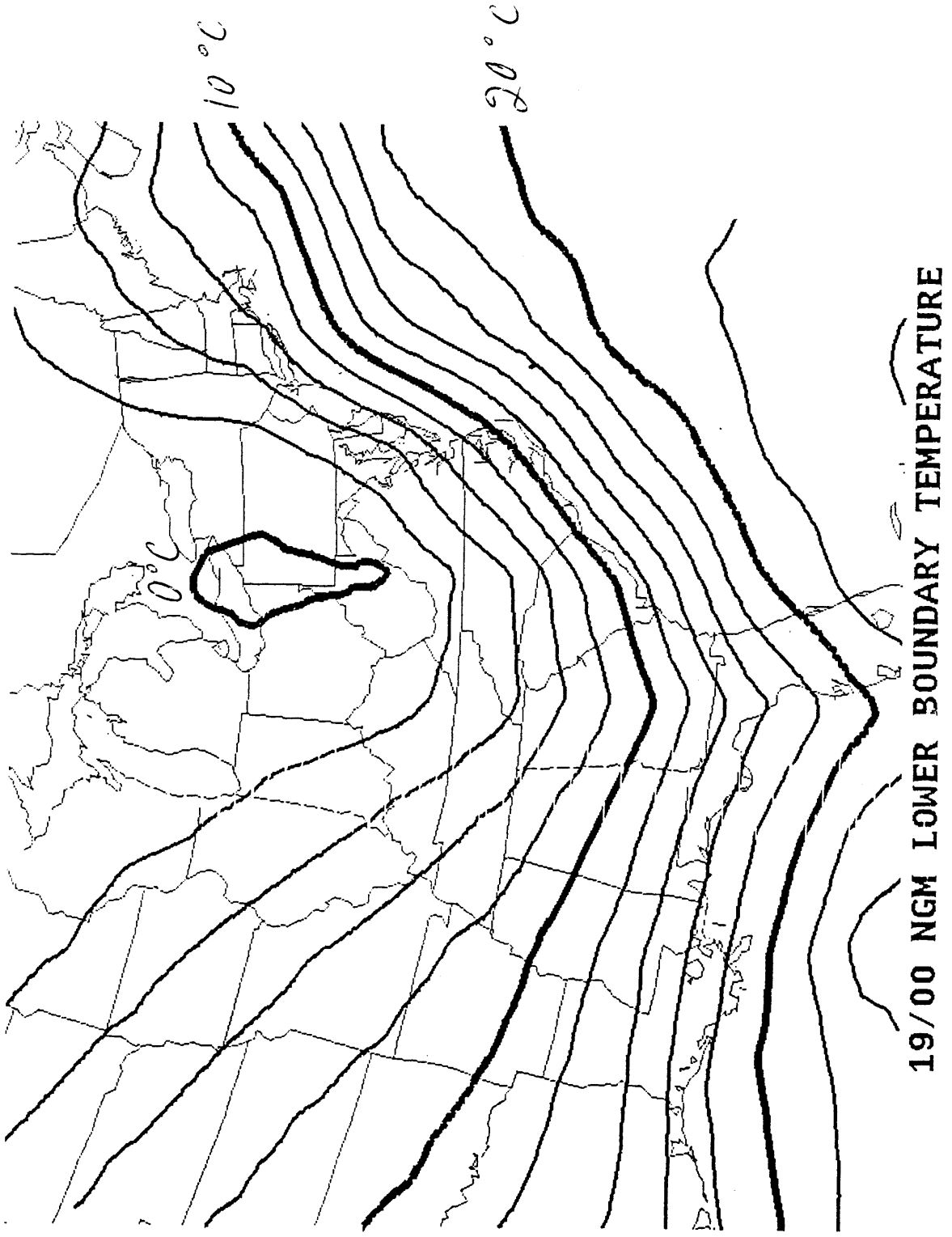

Fig. 4.3: NGM initial surface temperatures (c.int. 2 C), 00 UTC 19 Jan 1986.

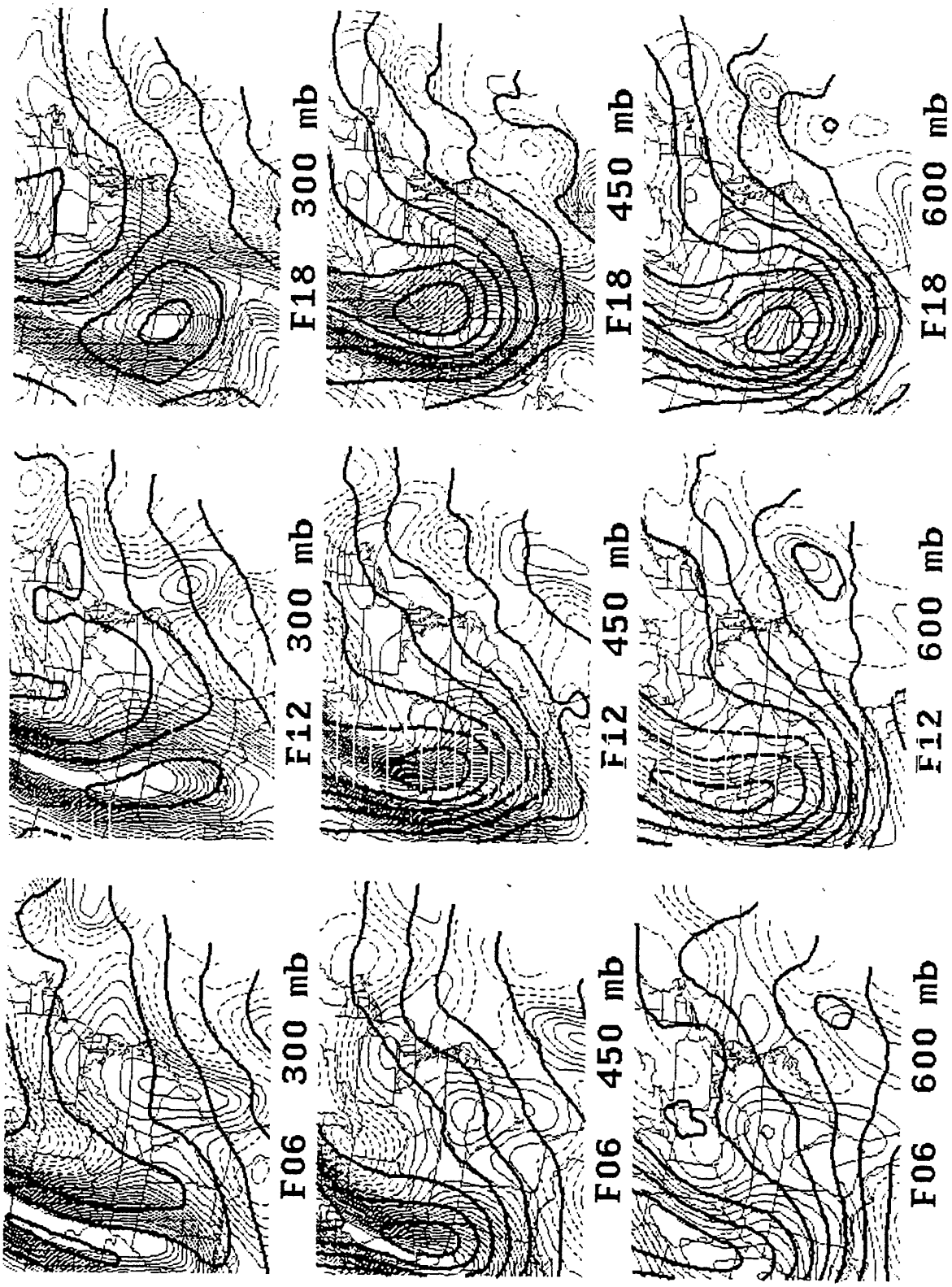

Fig. 4.4: NGM forecast relative vorticity (thin lines, c.int. 1×10^{-5} s^{-1}, negative values dashed) and temperature (thick lines, c.int. 5 C), for various forecast times and pressure levels (as labeled).

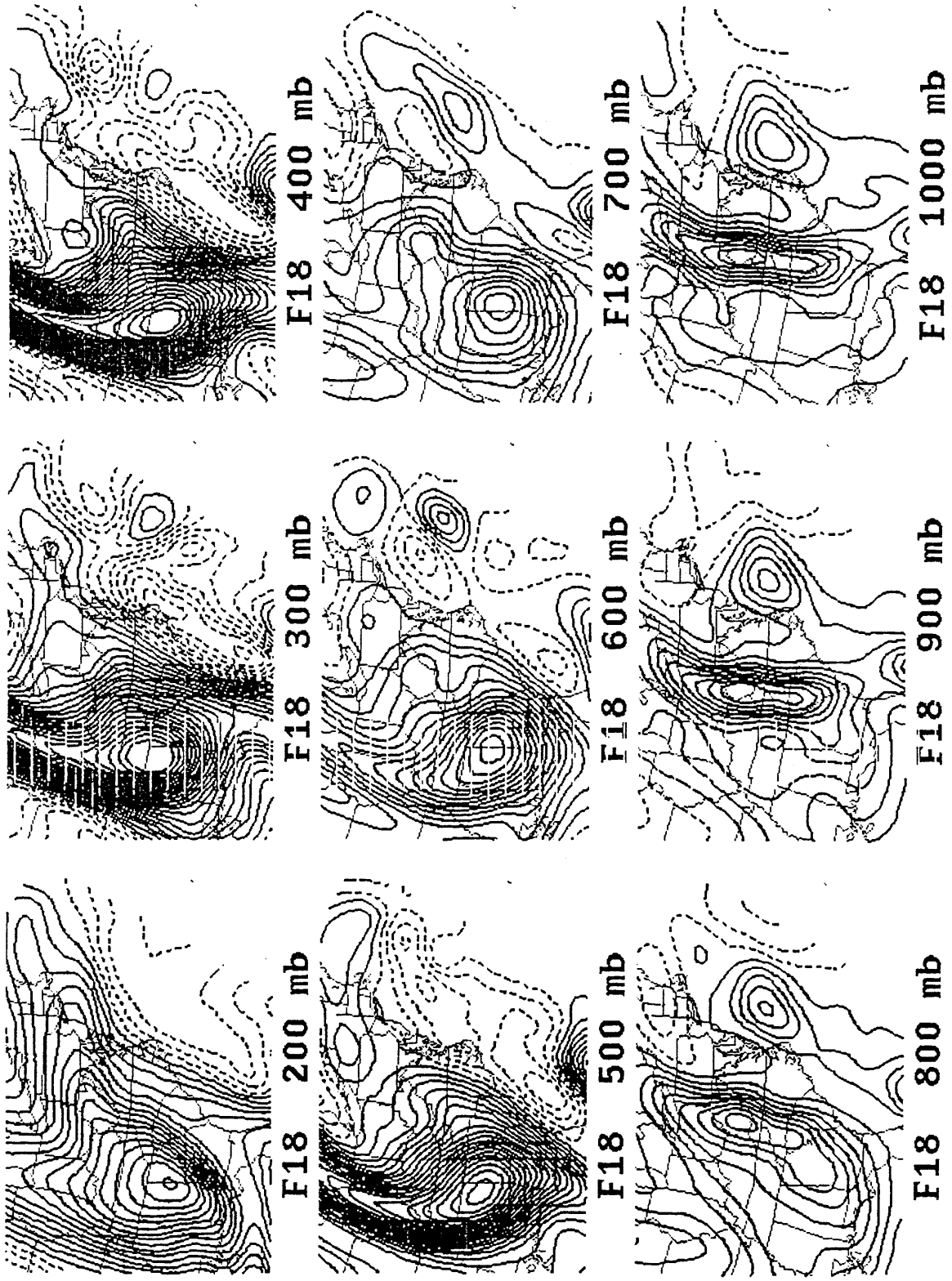

Fig. 4.5: NGM forecast relative vorticity (thin lines, c.int. 1×10^{-5} s^{-1}, negative values dashed), 200 mb to 1000 mb, 18-hour forecast.

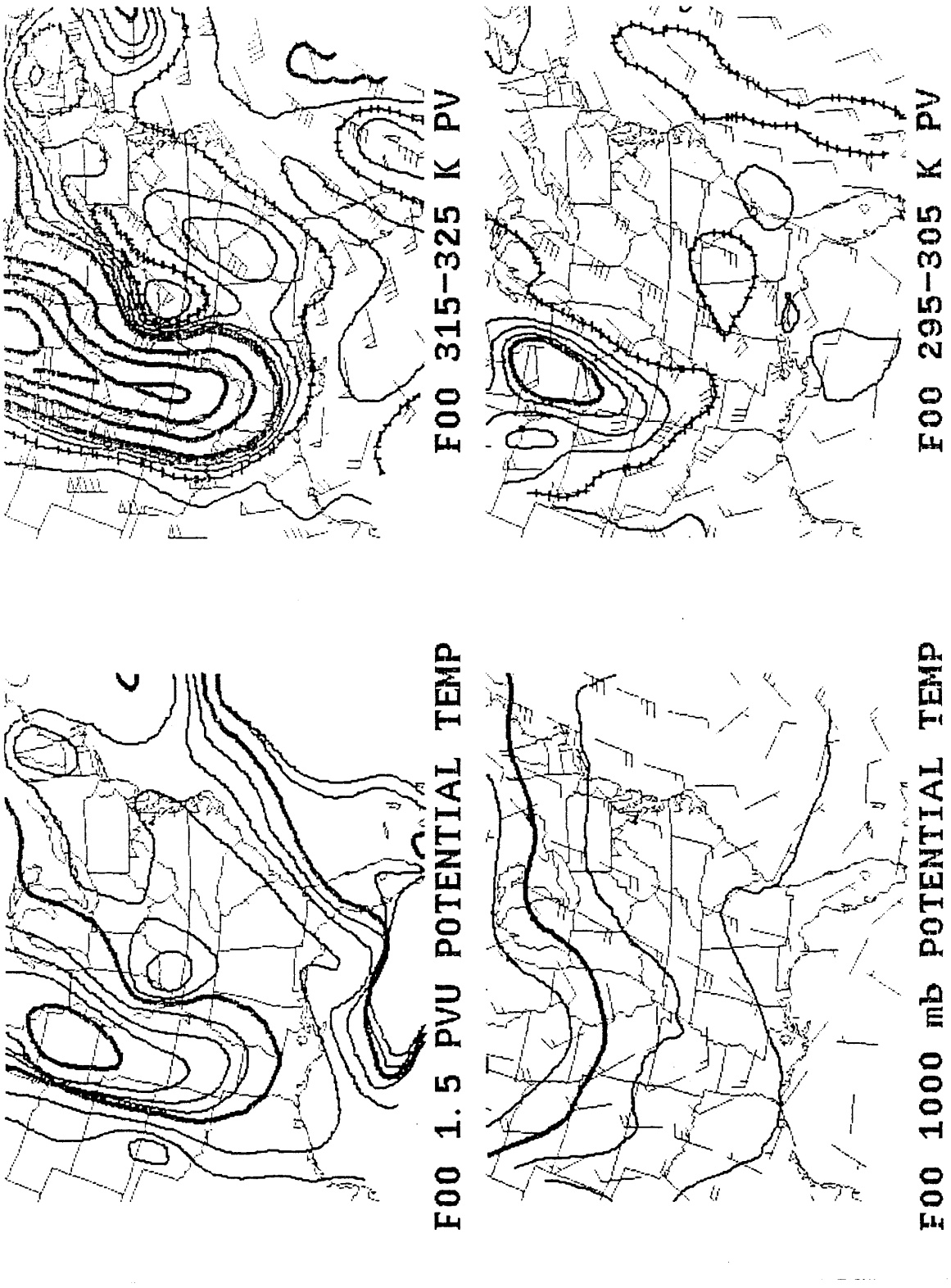

Fig. 4.6: Potential vorticity and potential temperature, NGM initialization (00 UTC 19 Jan 1986). Plotting conventions are similar to Figs. 3.19-3.27. Note that in this and the following figures, the 0.5 PVU contour has been cross-hatched. For full description of Figs. 4.6-4.11, see Appendix B.

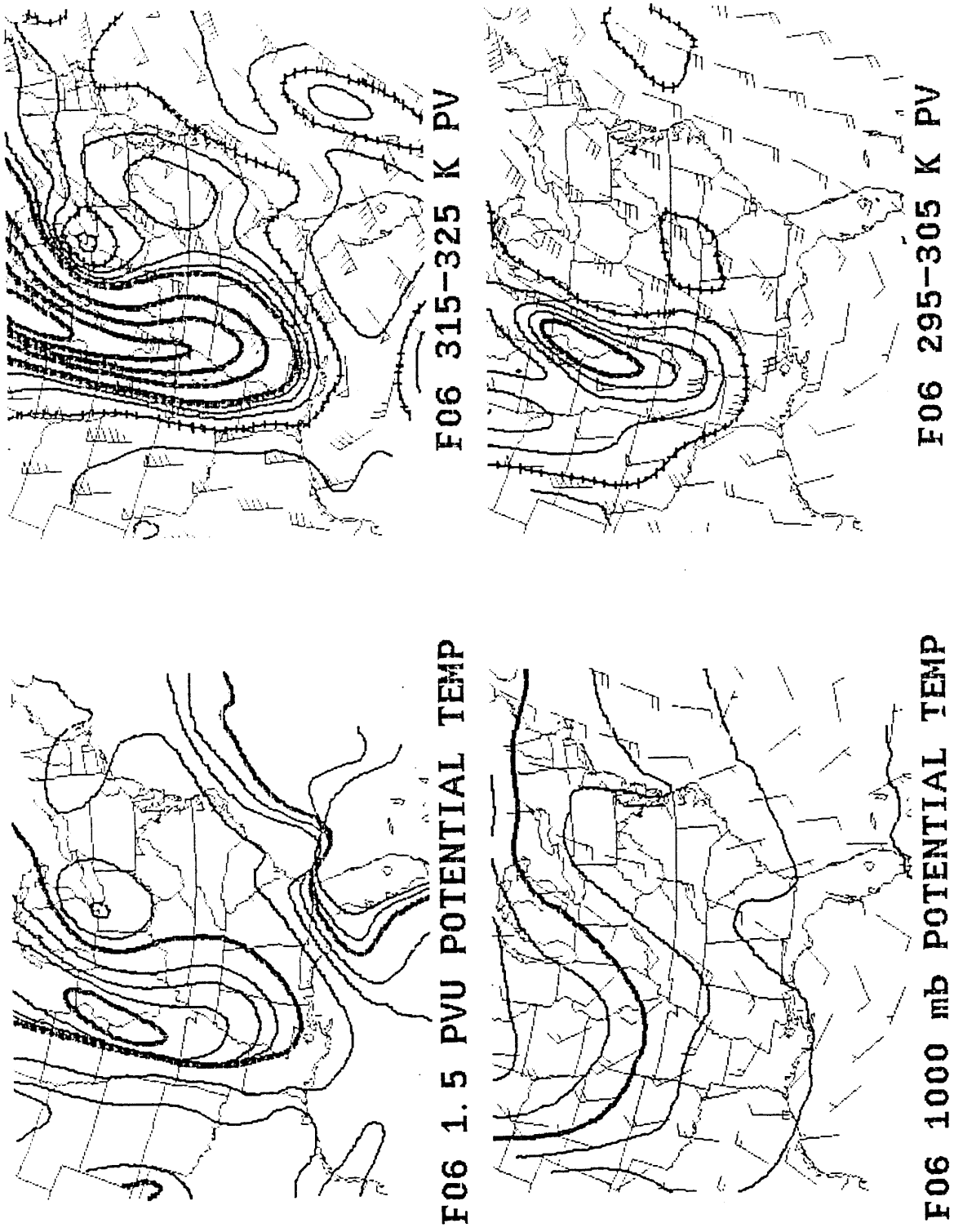

Fig. 4.7: As in Fig. 4.6, but for 6-hour forecast valid 06 UTC 19 Jan 1986.

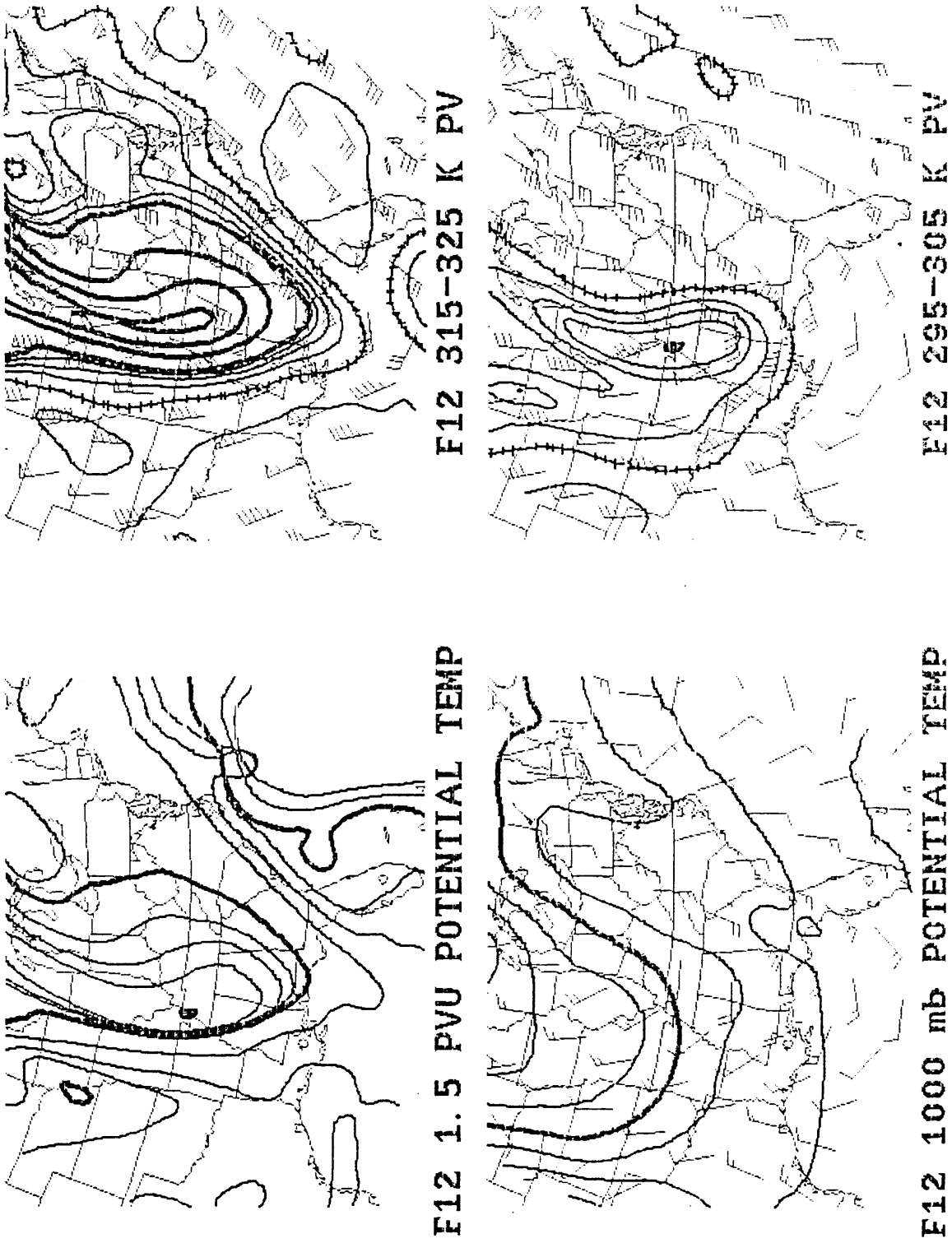

Fig. 4.8: As in Fig. 4.6, but for 12-hour forecast valid 12 UTC 19 Jan 1986.

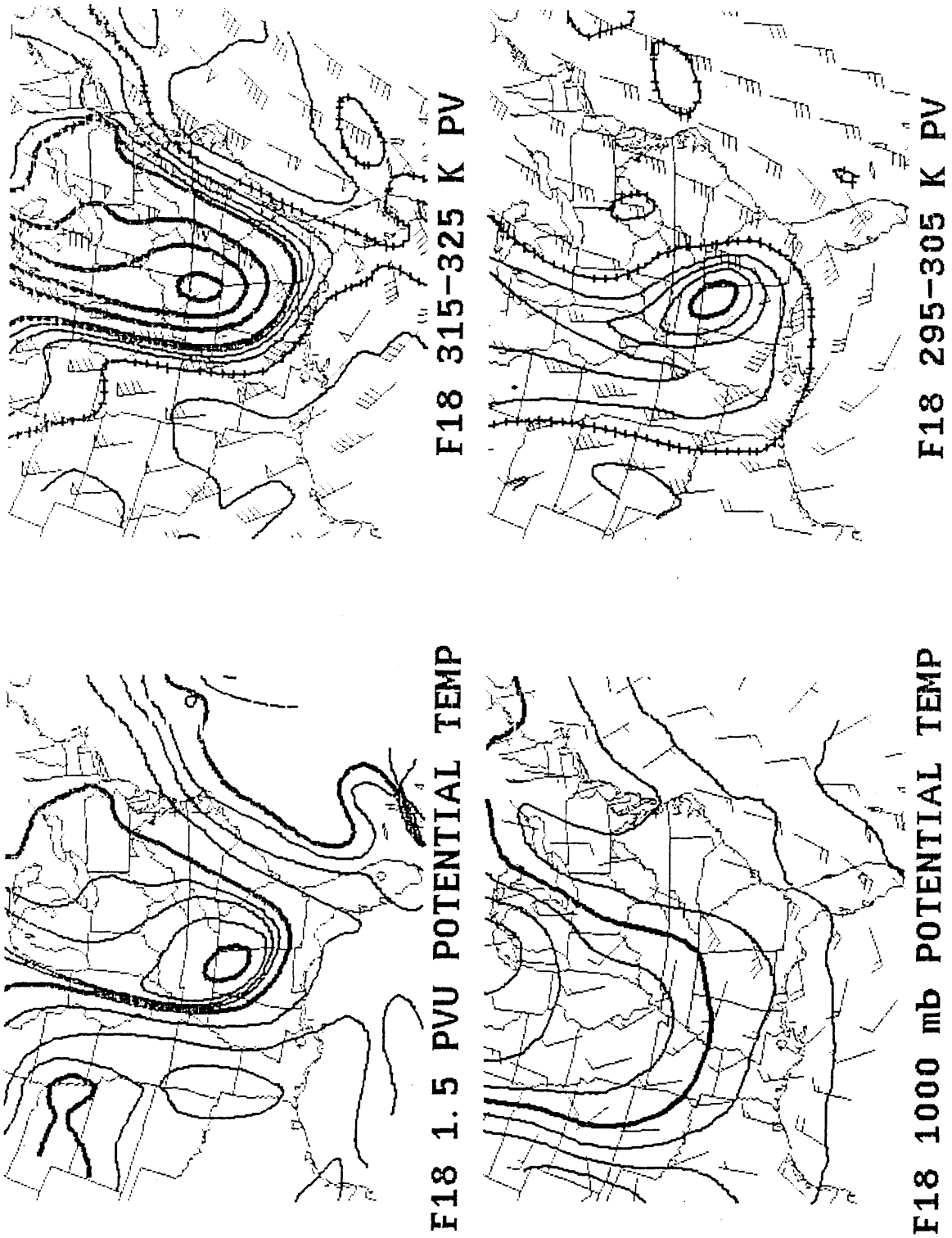

Fig. 4.9: As in Fig. 4.6, but for 18-hour forecast valid 18 UTC 19 Jan 1986.

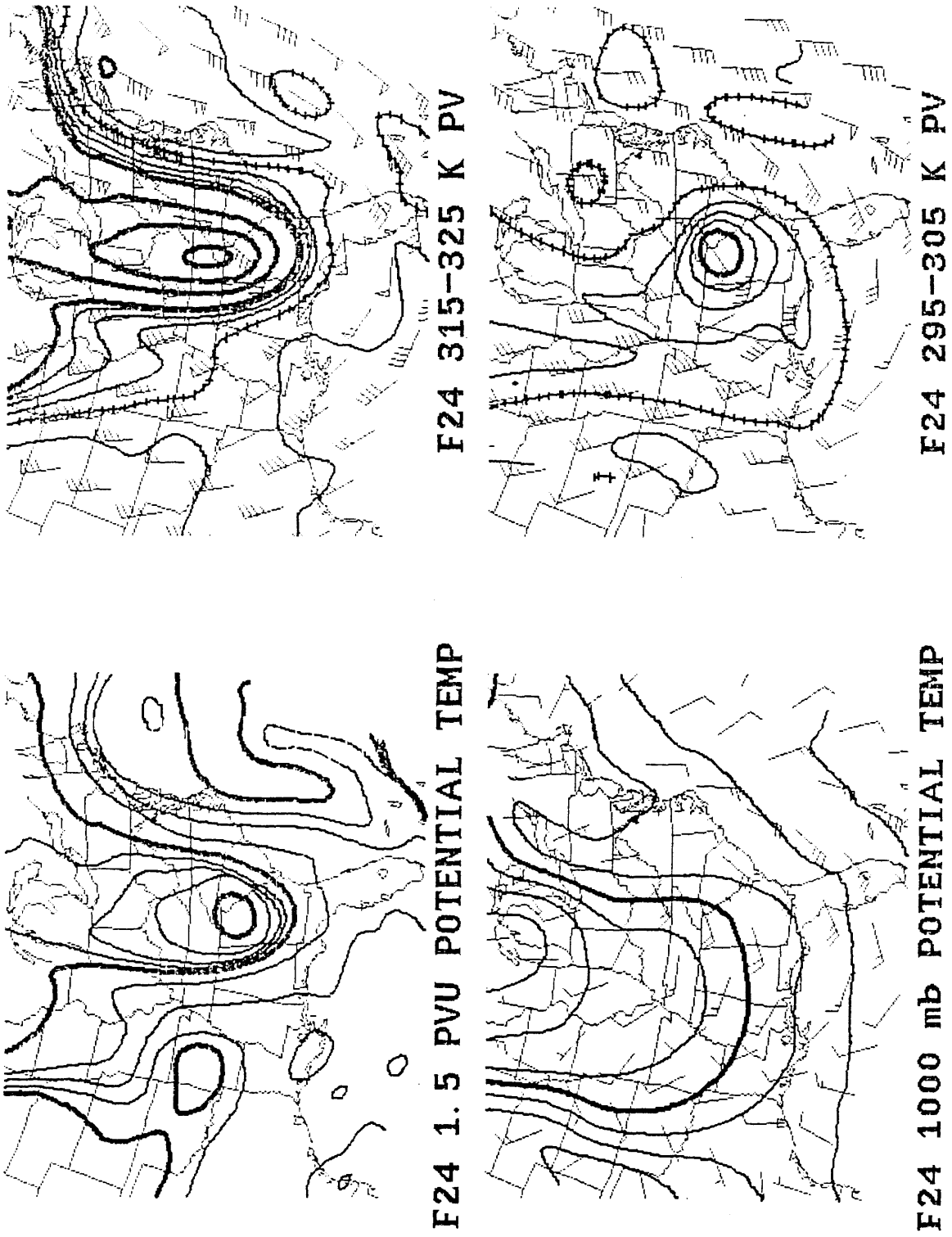

Fig. 4.10: As in Fig. 4.6, but for 24-hour forecast valid 00 UTC 20 Jan 1986.

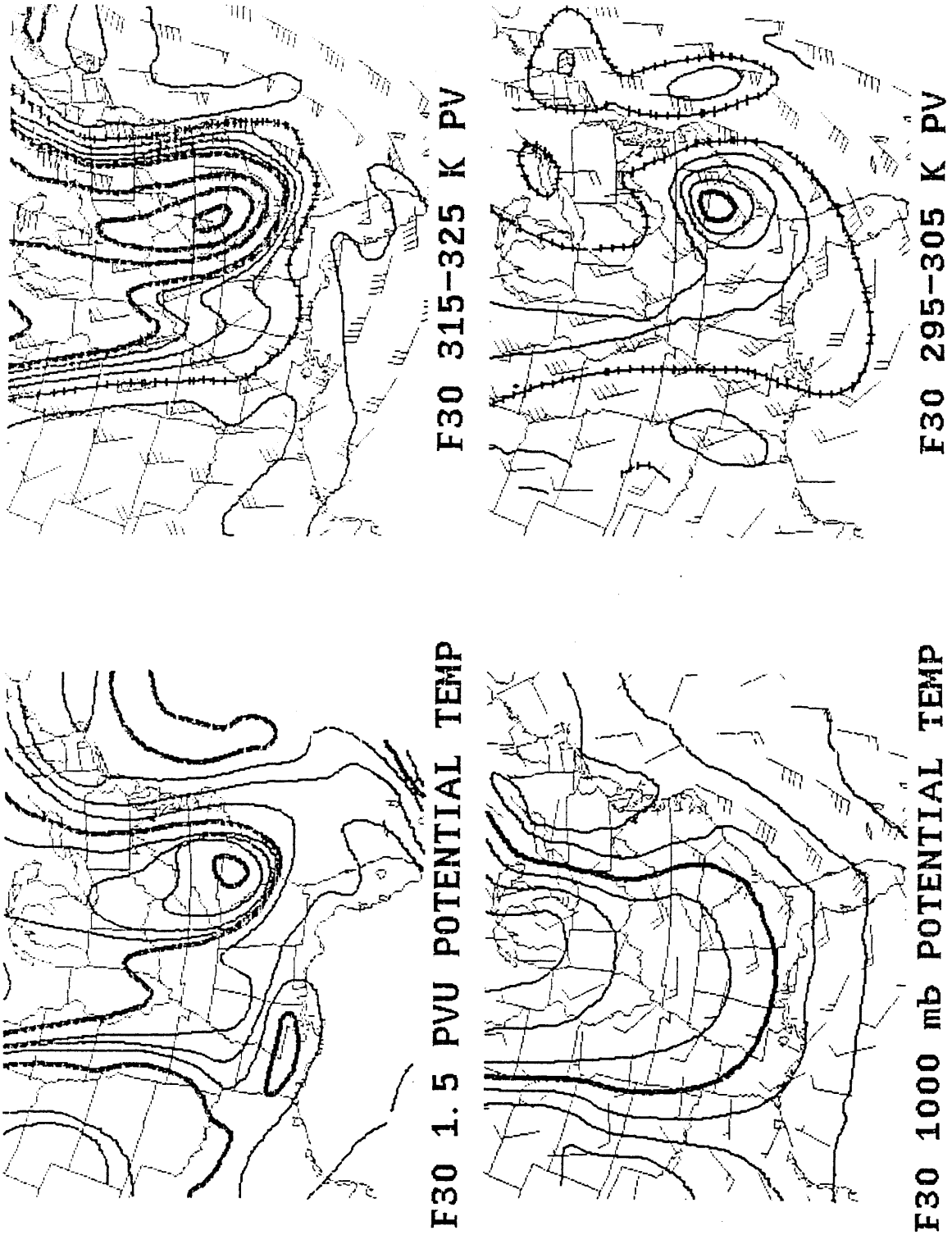

Fig. 4.11: As in Fig. 4.6, but for 30-hour forecast valid 06 UTC 20 Jan 1986.

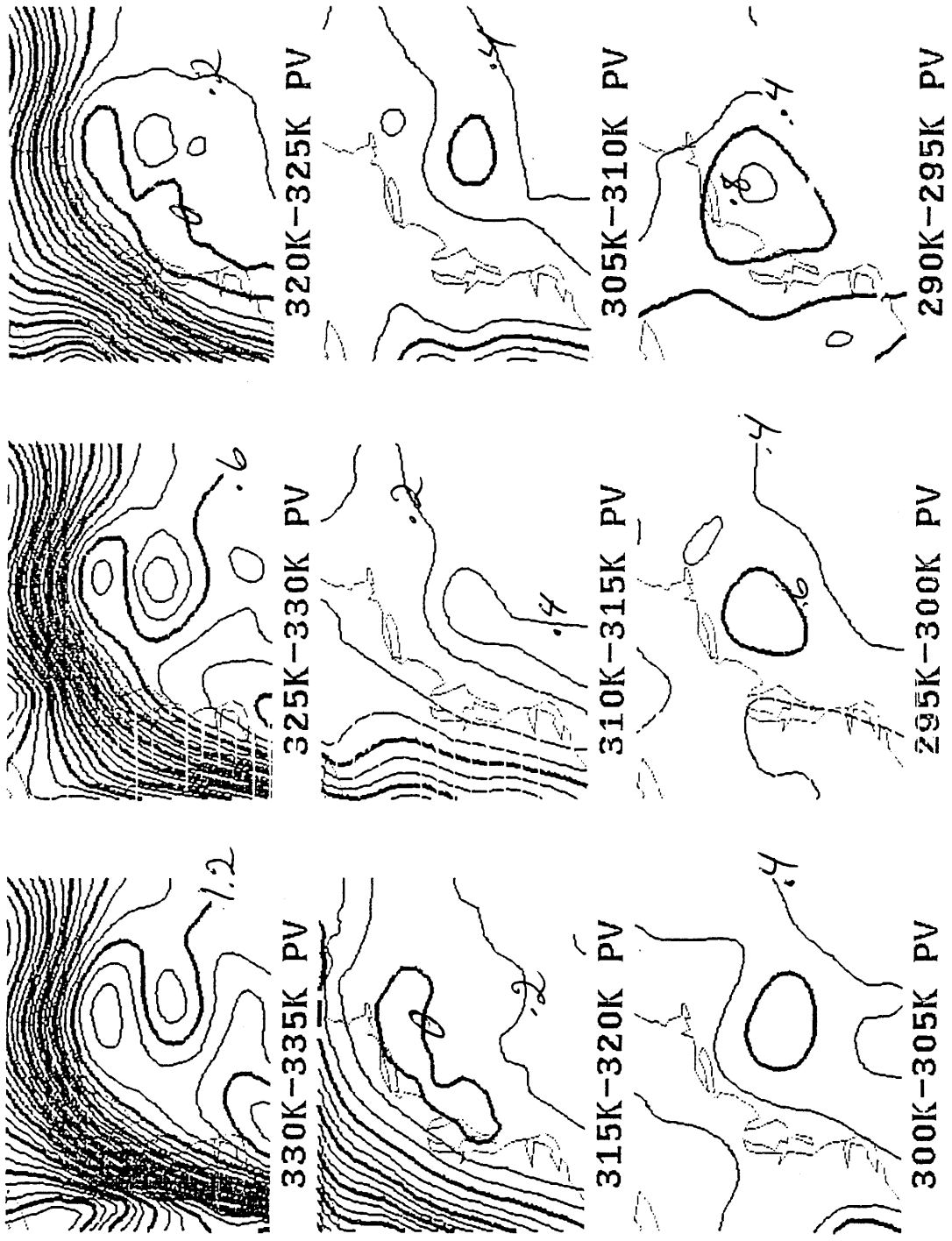

Fig. 4.12: Potential vorticity distribution over small-scale cyclone, NGM 24-hour forecast valid 00 UTC 20 Jan 1986. Contour interval is 0.2 PVU, with every third contour (0.0, 0.6, etc.) thick.

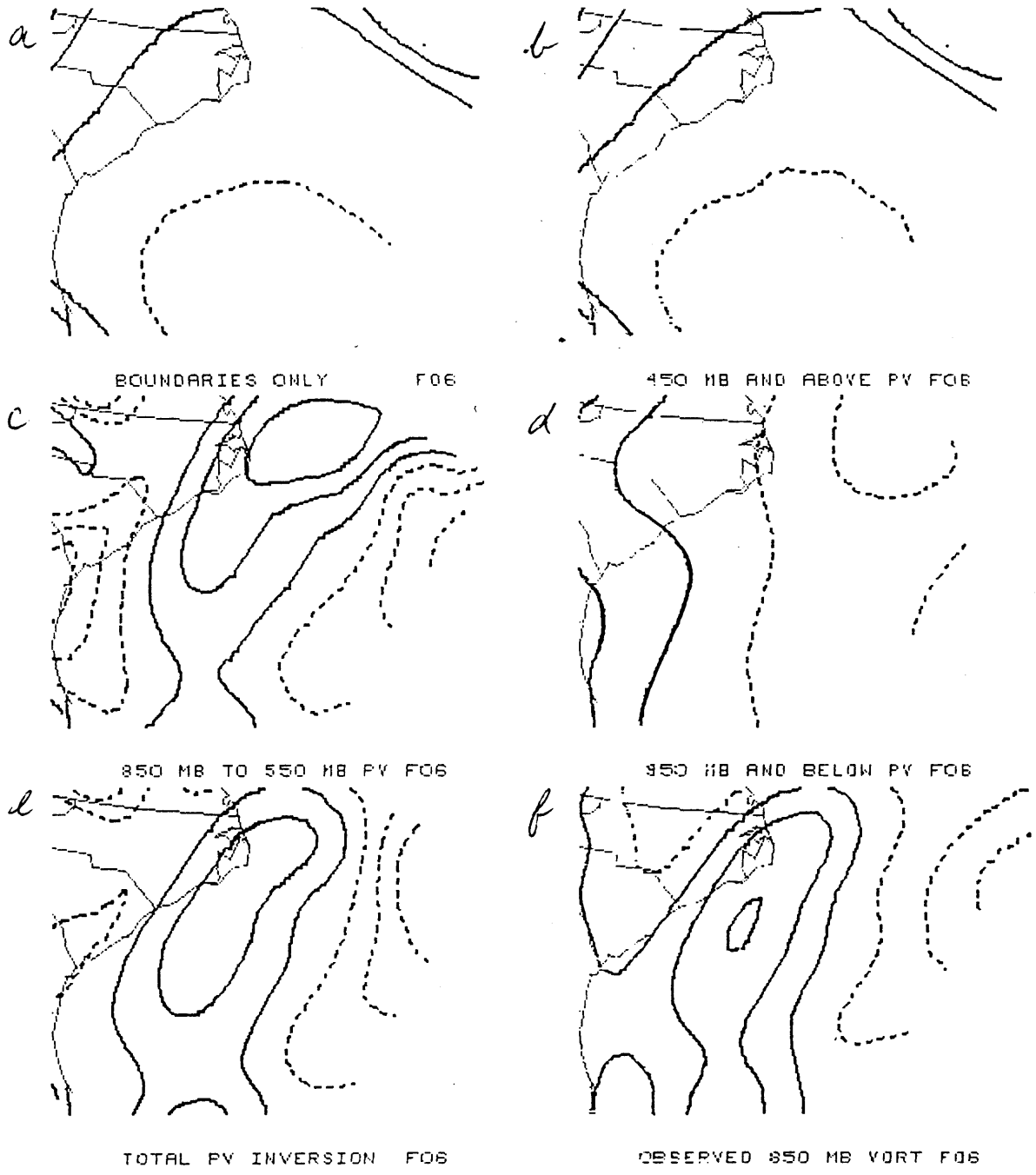

Fig. 4.13: 850 mb relative vorticity (c.int. $1x10^{-5}$ s^{-1}, negative contours dashed) from various bitwise inversions of potential vorticity from the NGM 6-hour forecast valid 06 UTC 19 Jan 1986. For description see Appendix B.

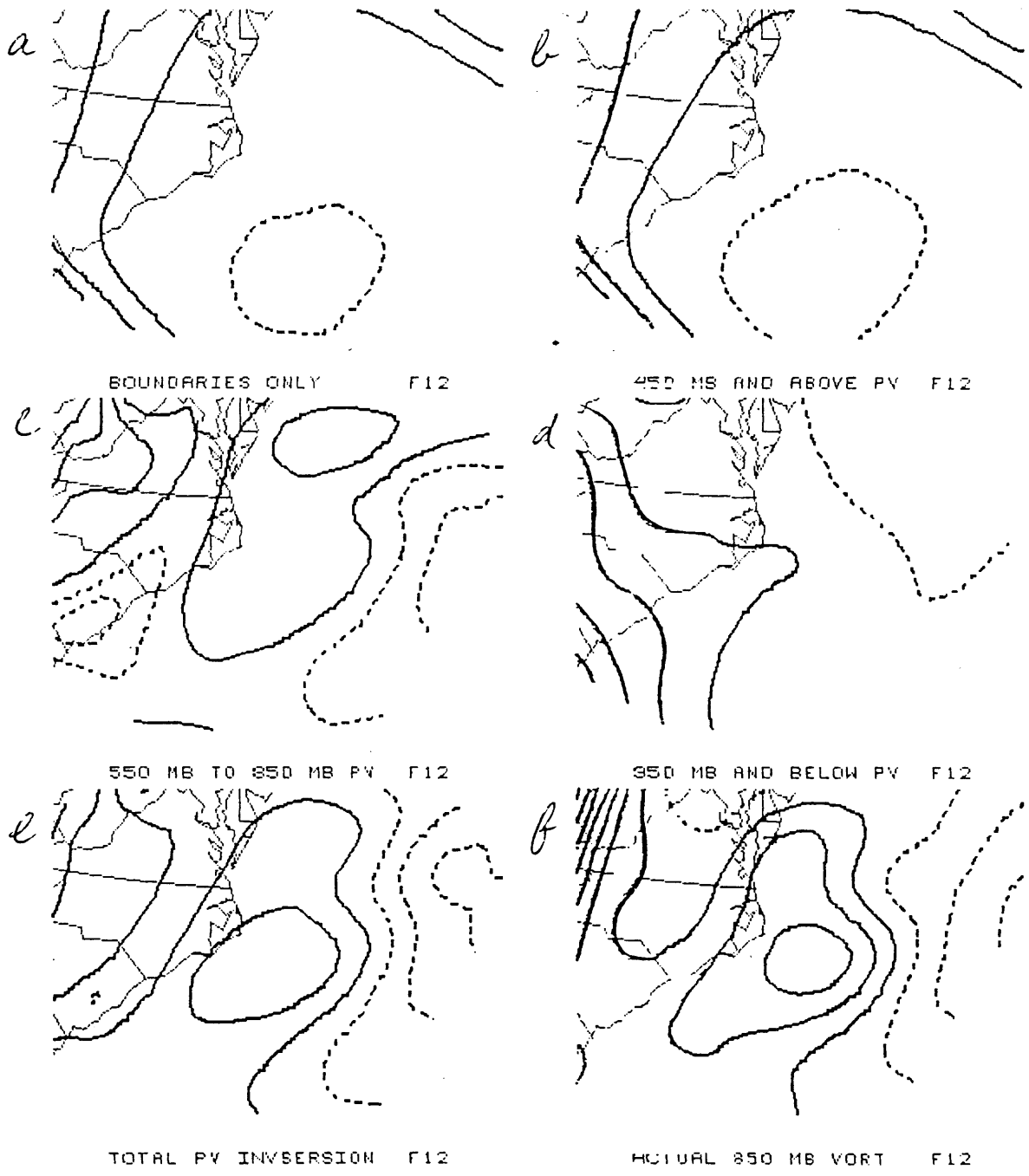

Fig. 4.14: As in Fig. 4.13, but for 12-hour forecast valid 12 UTC 19 Jan 1986.

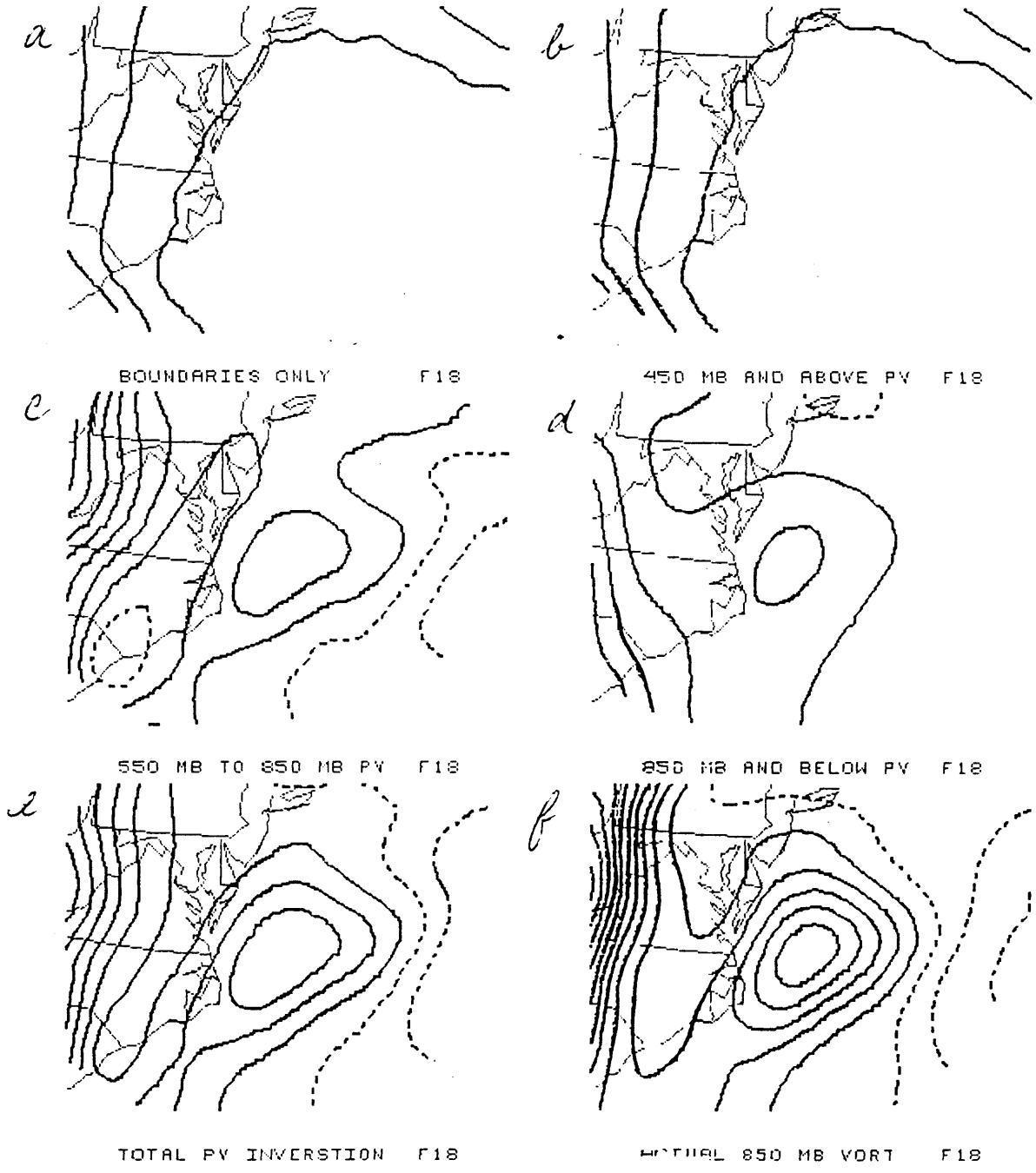

Fig. 4.15: As in Fig. 4.13, but for 18-hour forecast valid 18 UTC 19 Jan 1986.

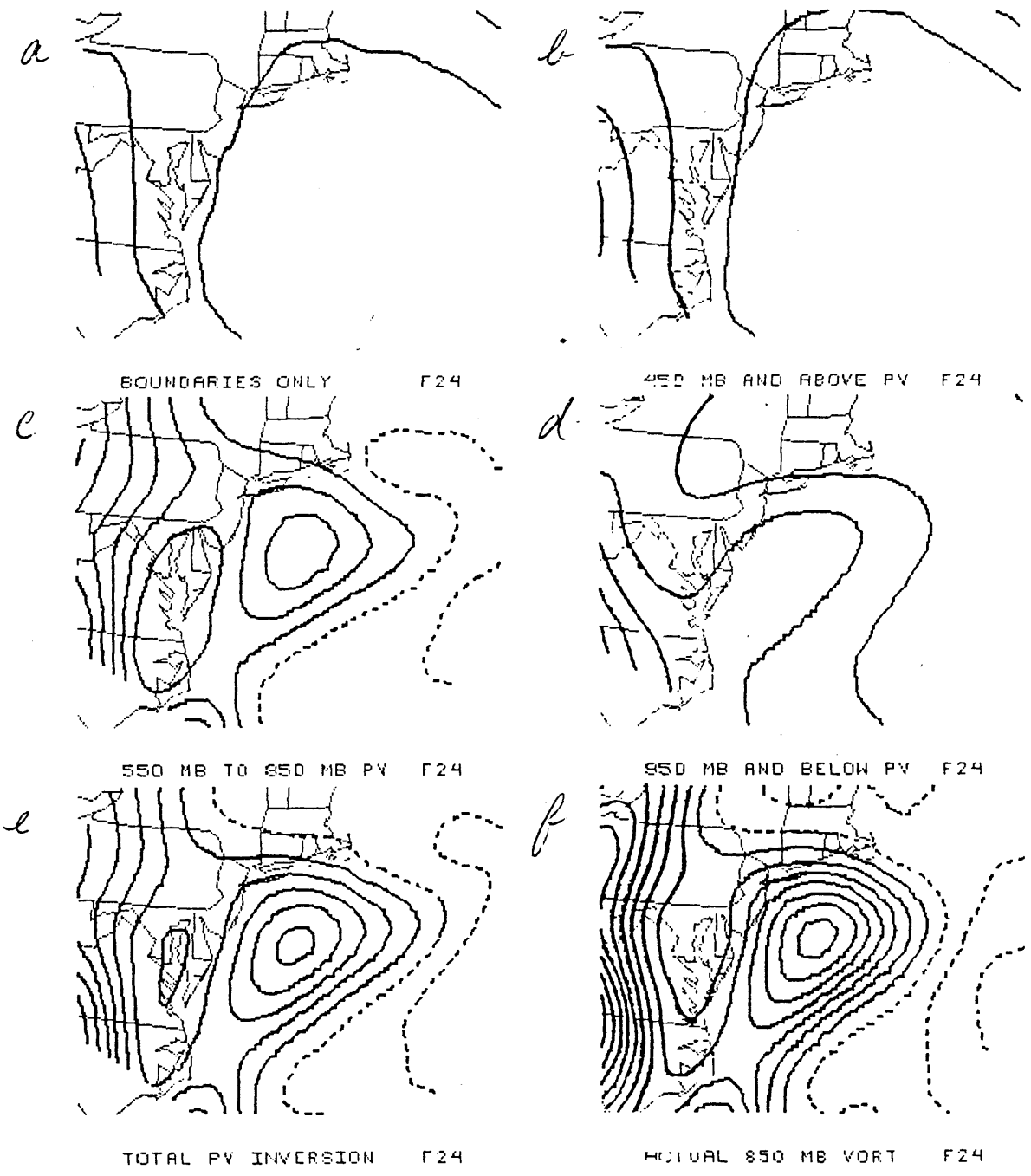

Fig. 4.16: As in Fig. 4.13, but for 24-hour forecast valid 00 UTC 20 Jan 1986.

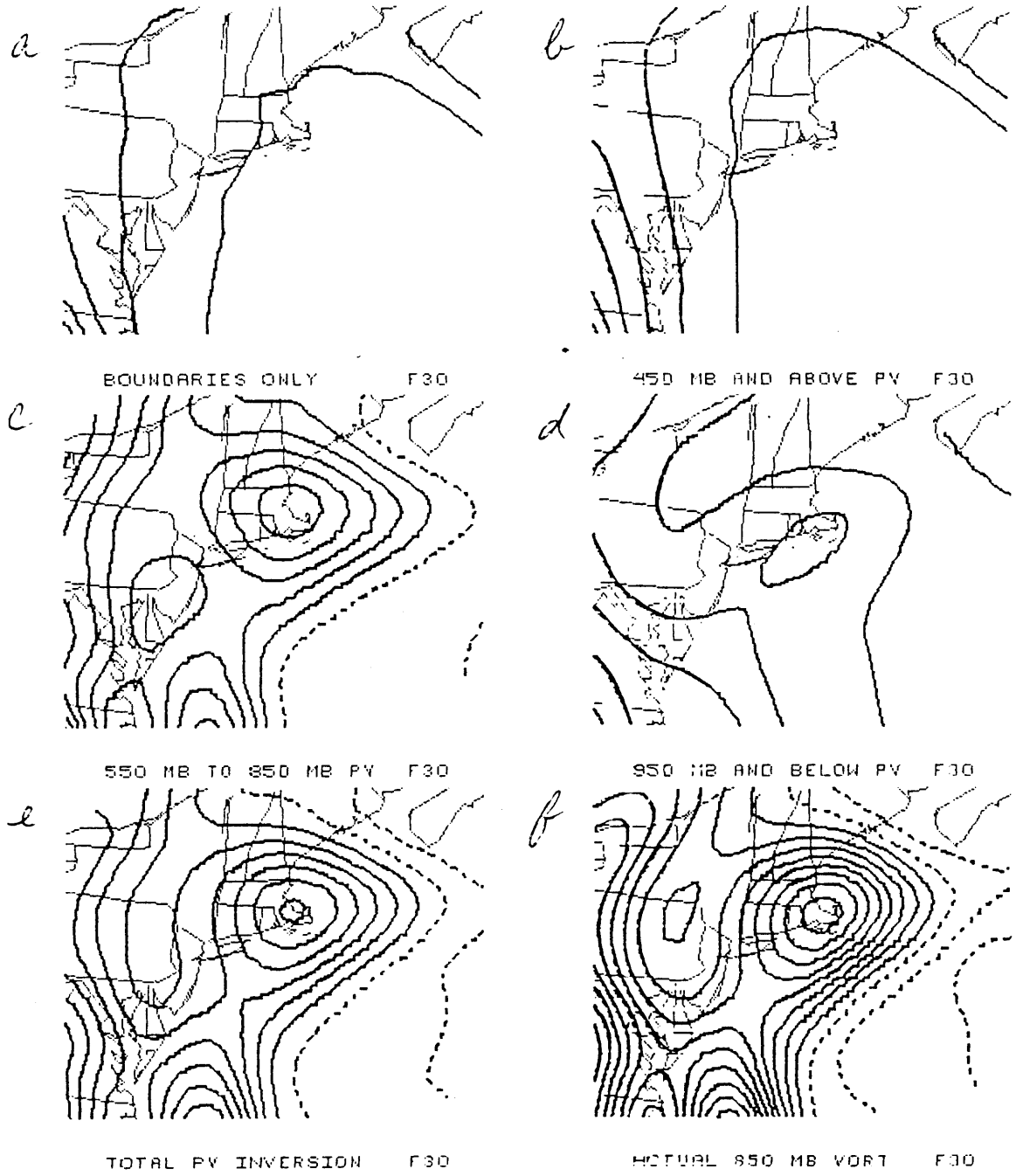

Fig. 4.17: As in Fig. 4.13, but for 30-hour forecast valid 06 UTC 20 Jan 1986.

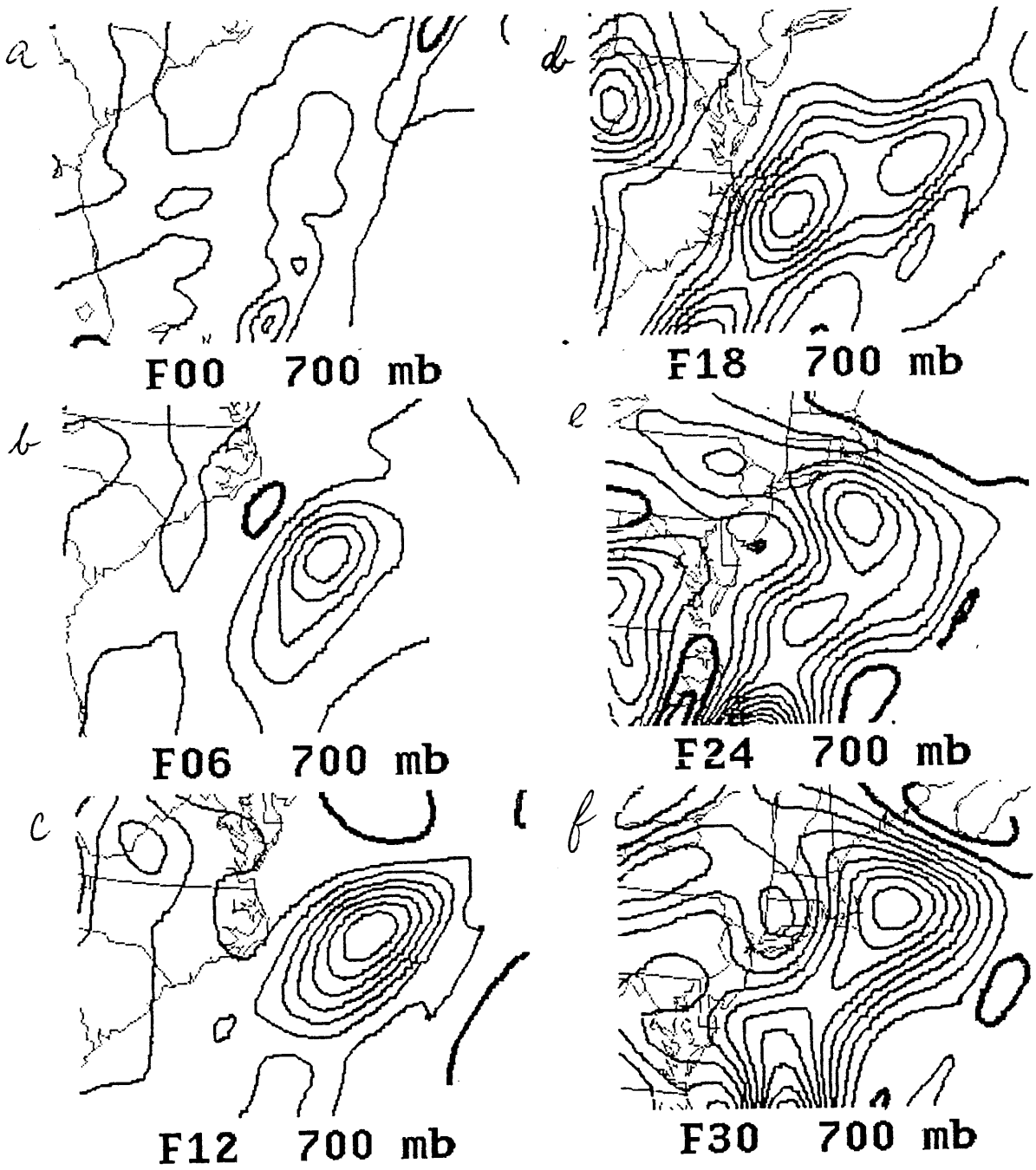

Fig. 4.18: NGM 700 mb omega (vertical motion), c.int. 0.1 Pa s^{-1}, negative (upward) contours thin, other contours thick, for 00 UTC 19 Jan 1986 forecast run. Maps are centered on NGM actual or extrapolated 850 mb small-scale vorticity maximum. Same format as in Fig. 4.19.

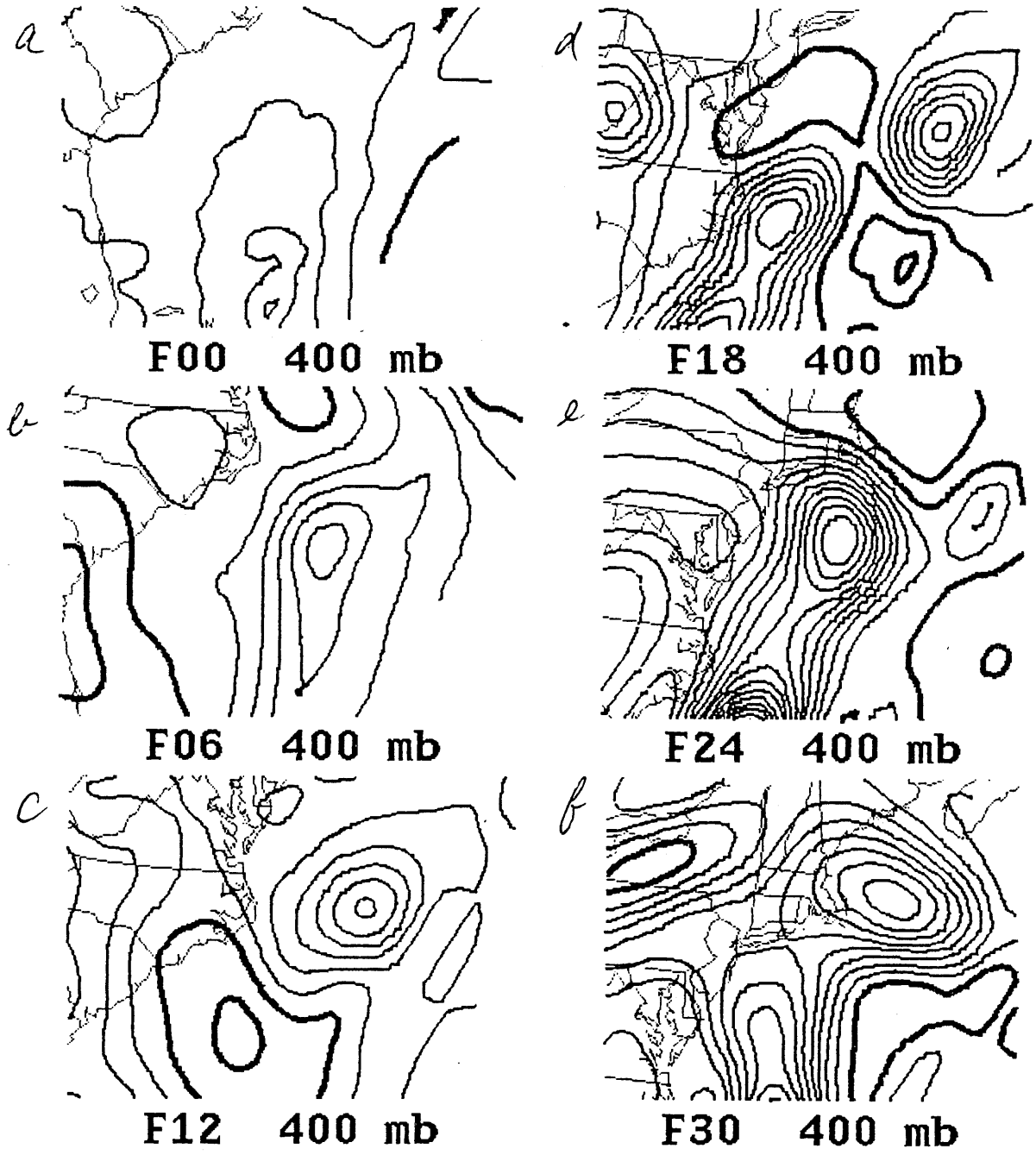

Fig. 4.19: NGM 400 mb omega, as in Fig. 4.18.

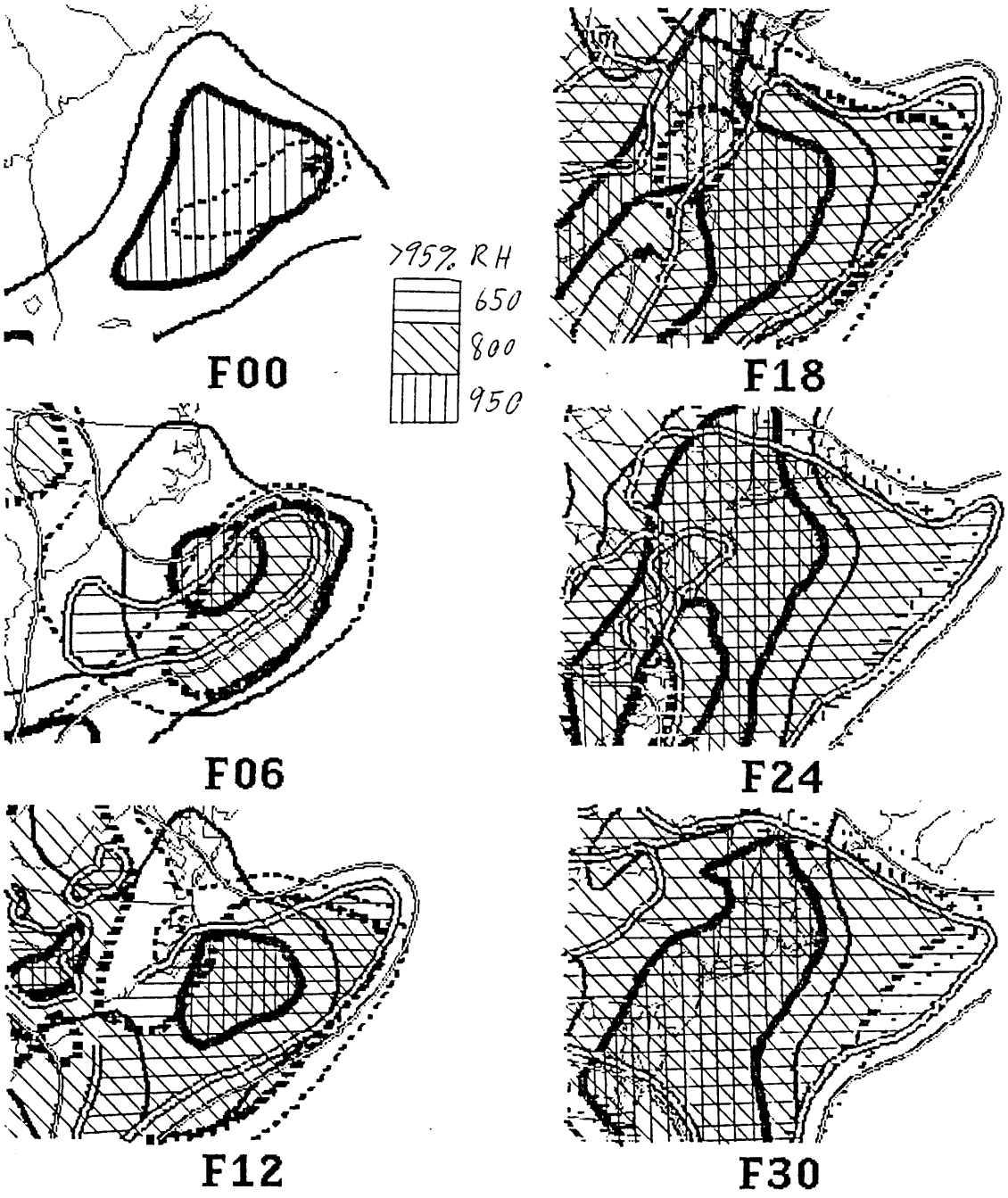

Fig. 4.20: NGM relative humidity, 00 UTC 19 Jan 1986 forecast run. Depicted are relative humidity fields at 950 mb, 800 mb, and 650 mb. At each level, contours of 90% (thin) and 95% (thick) relative humidity are shown. Recall that 95% relative humidity is the start of water condensation in the NGM (see Section 4.2). Also, regions of greater than 95% relative humidity are hatched, using hatching patterns shown in the key.

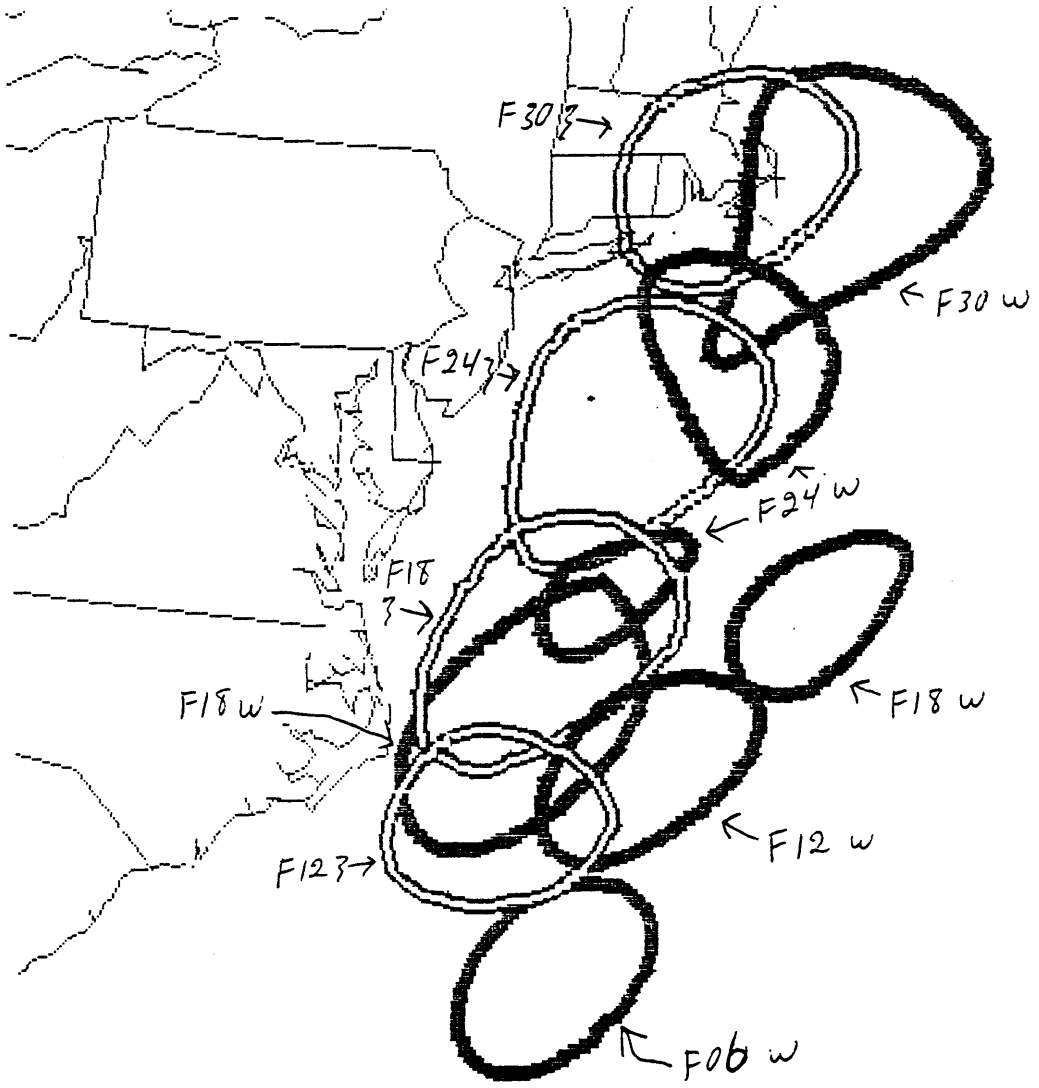

Fig. 4.21: Plots of successive six-hourly positions of selected contours of 700 mb omega (solid lines) and 850 mb relative vorticity (double lines), 00 UTC 19 Jan 1986 forecast run. The purpose of this figure is to show the spatial relationship between the small-scale cyclone and nearby vertical motion maxima. It looks better in color.

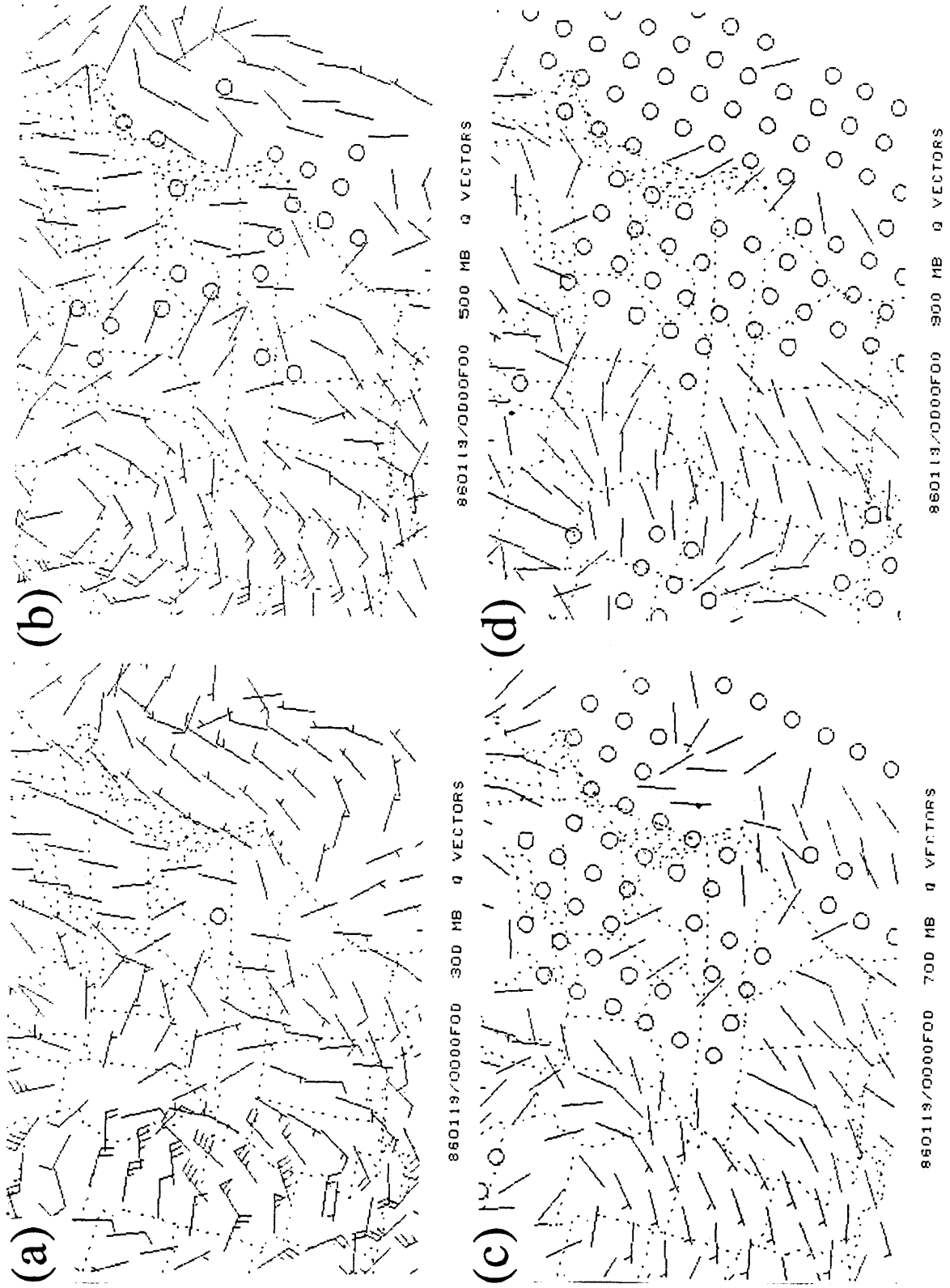

Fig. 5.1: Q-vectors (defined in (5.2)), initialization of NGM 00 UTC 19 Jan 1986 forecast run. Vectors plotted in conventional wind notation, with 1 long barb = 1×10^{-12} m^2 s^{-1} kg^{-1}. (a) 300 mb. (b) 500 mb. (c) 700 mb. (d) 900 mb.

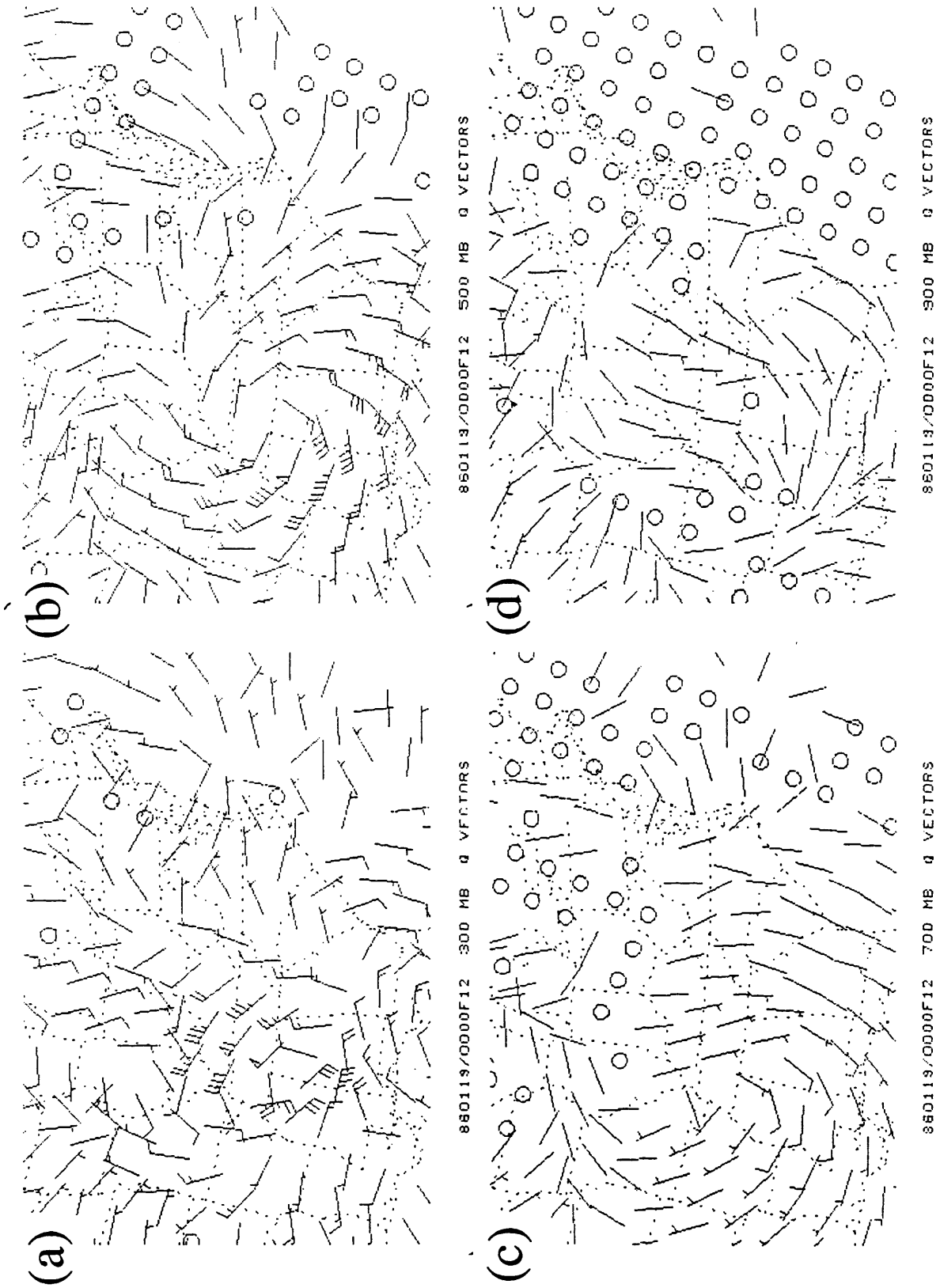

Fig. 5.2: Q-vectors, as in Fig. 5.1, but for 12-hour forecast valid 12 UTC 19 Jan 1986. (a) 300 mb. (b) 500 mb. (c) 700 mb. (d) 900 mb.

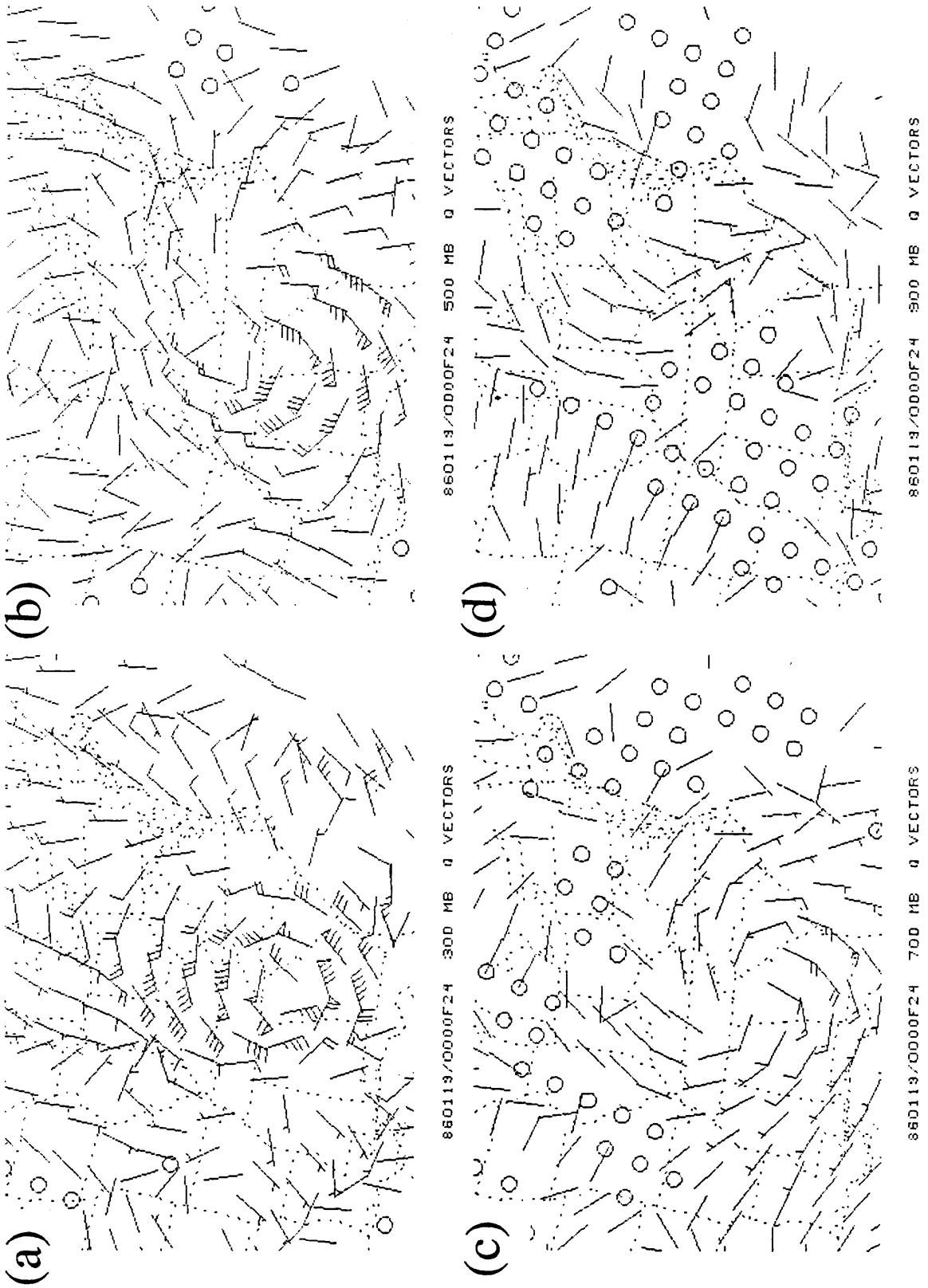

Fig. 5.3: Q-vectors, as in Fig. 5.1, but for 24-hour forecast valid 00 UTC 20 Jan 1986. (a) 300 mb. (b) 500 mb. (c) 700 mb. (d) 900 mb.

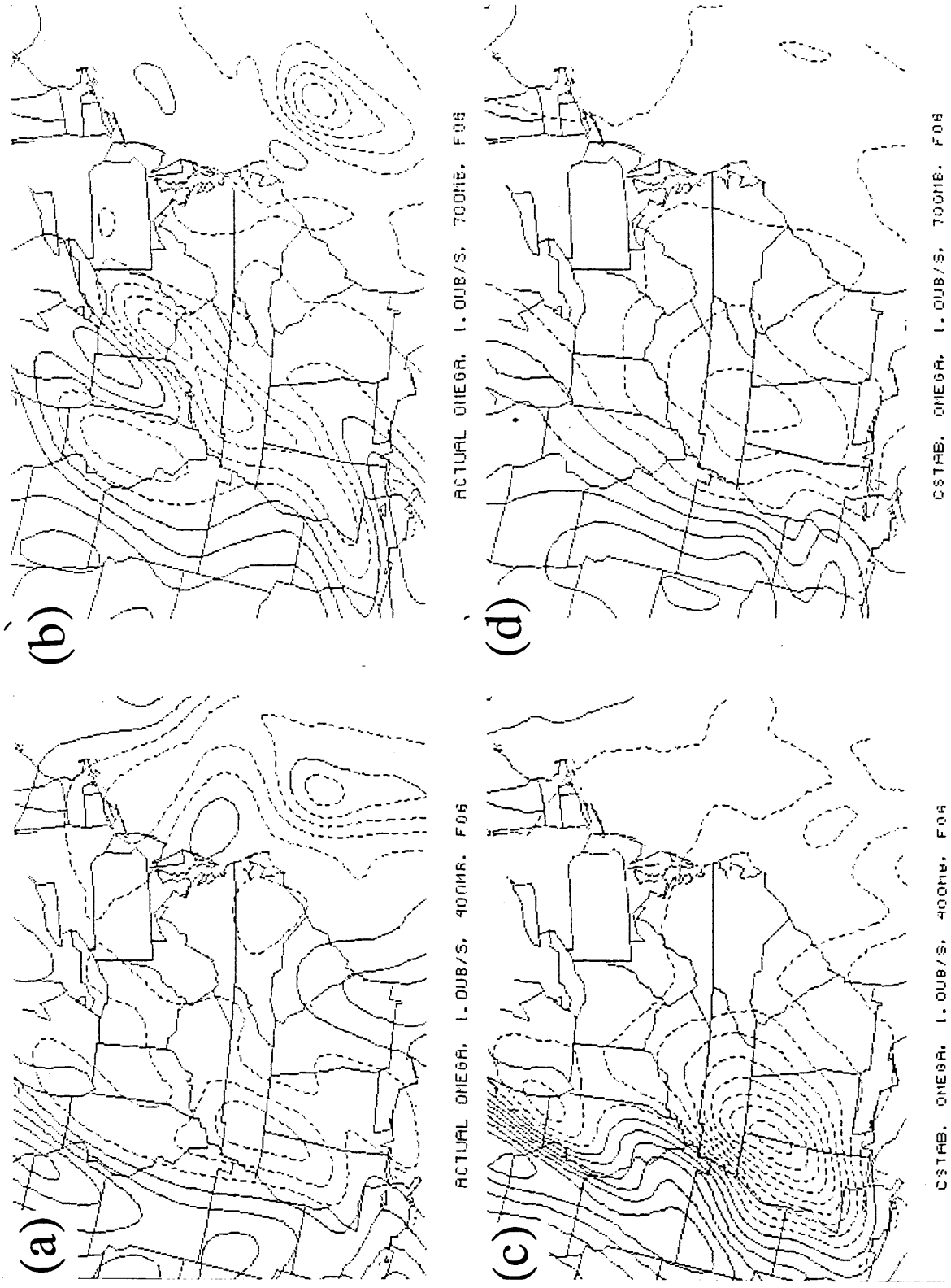

Fig. 5.4: Comparison of quasi-geostrophic and actual ω (c.int. 1×10^{-1} Pa s^{-1}, negative contours dashed), for NGM 6-hour forecast valid 06 UTC 19 Jan 1986. (a) Actual NGM w, 400 mb. (b) Actual NGM ω, 700 mb. (c) Quasi-geostrophic ω, 400 mb. (d) Quasi-geostrophic ω, 700 mb.

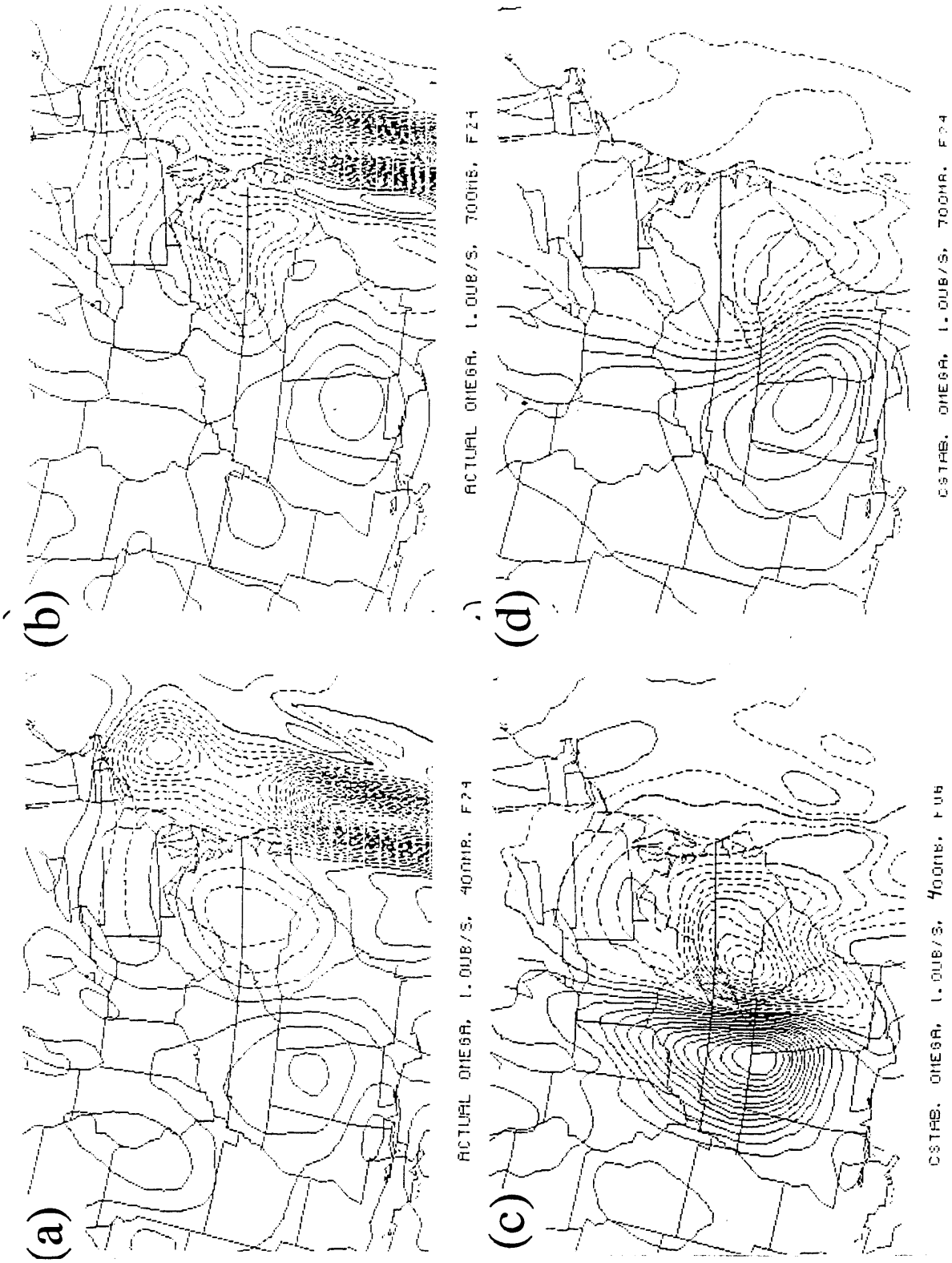

Fig. 5.5: Comparison of quasi-geostrophic and actual ω (c.int. 1×10^{-1} Pa s^{-1}, negative contours dashed), for NGM 24-hour forecast valid 00 UTC 20 Jan 1986. (a) Actual NGM w, 400 mb. (b) Actual NGM ω, 700 mb. (c) Quasi-geostrophic ω, 400 mb. (d) Quasi-geostrophic ω, 700 mb.

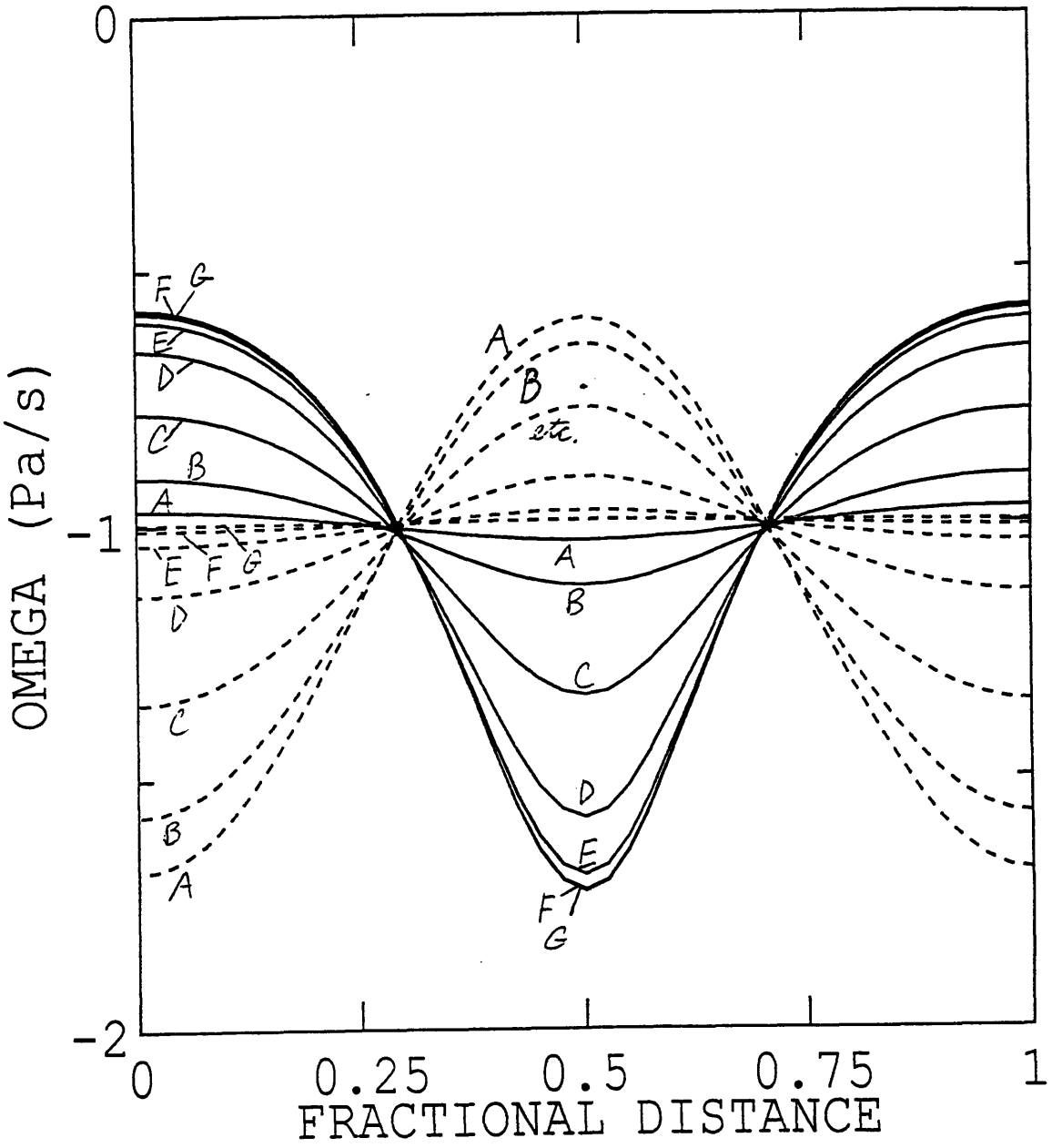

Fig. 5.6: Graph of ω (solid) and $\omega\frac{[\sigma^{-1}]}{\sigma^{-1}}$ (dashed), for negative cosine distribution of stratification and constant forcing. Curves A through G are for varying domain lengths, with A corresponding to a domain length eight times the Rossby radius of deformation and curve G corresponding to a domain length one eighth the Rossby radius of deformation. See text for details.

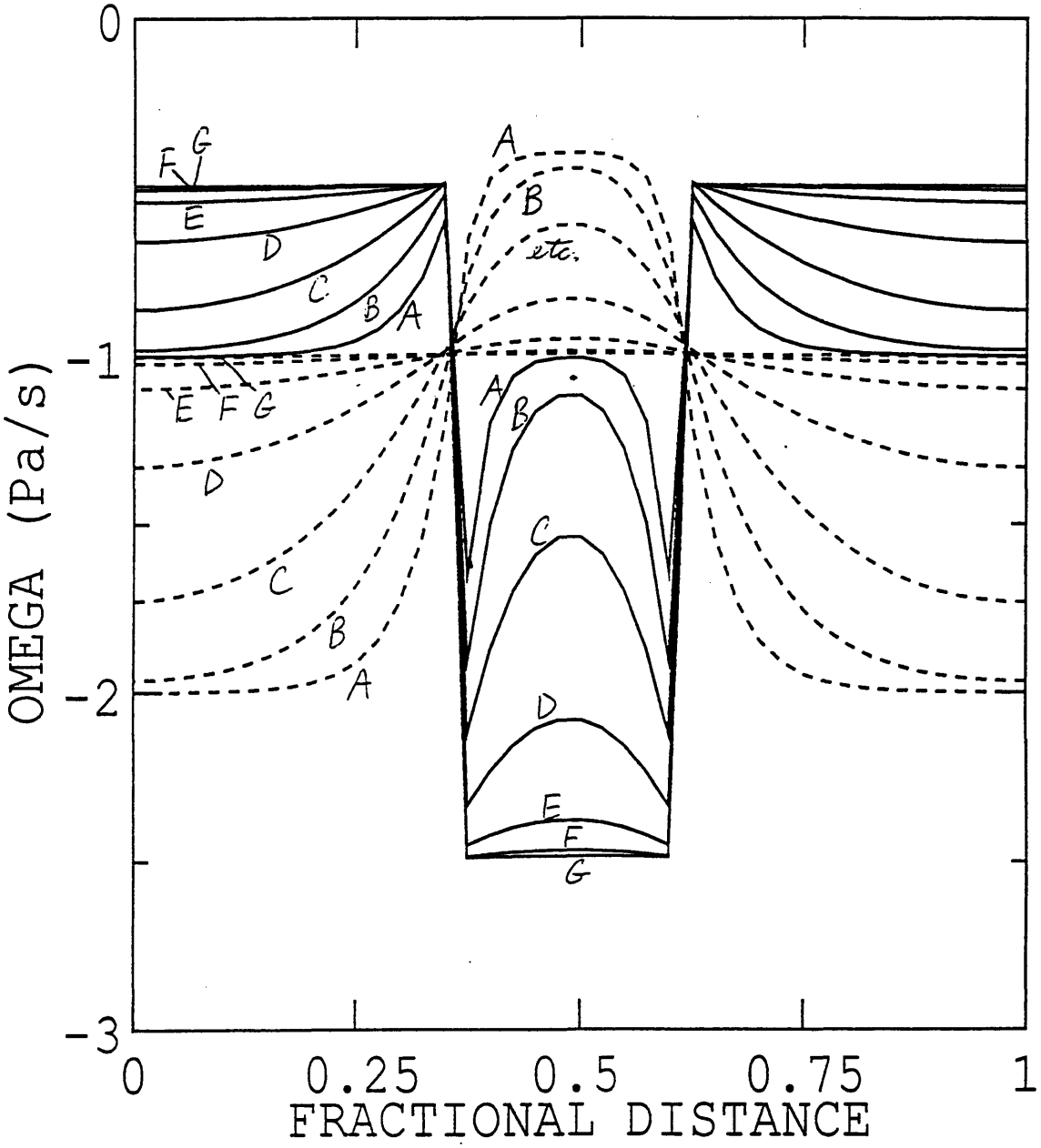

Fig. 5.7: Graph of ω (solid) and $\omega\frac{[\sigma^{-1}]}{\sigma^{-1}}$ (dashed), as in Fig. 5.6, but for inverted top hat distribution of stratification. See text for details.

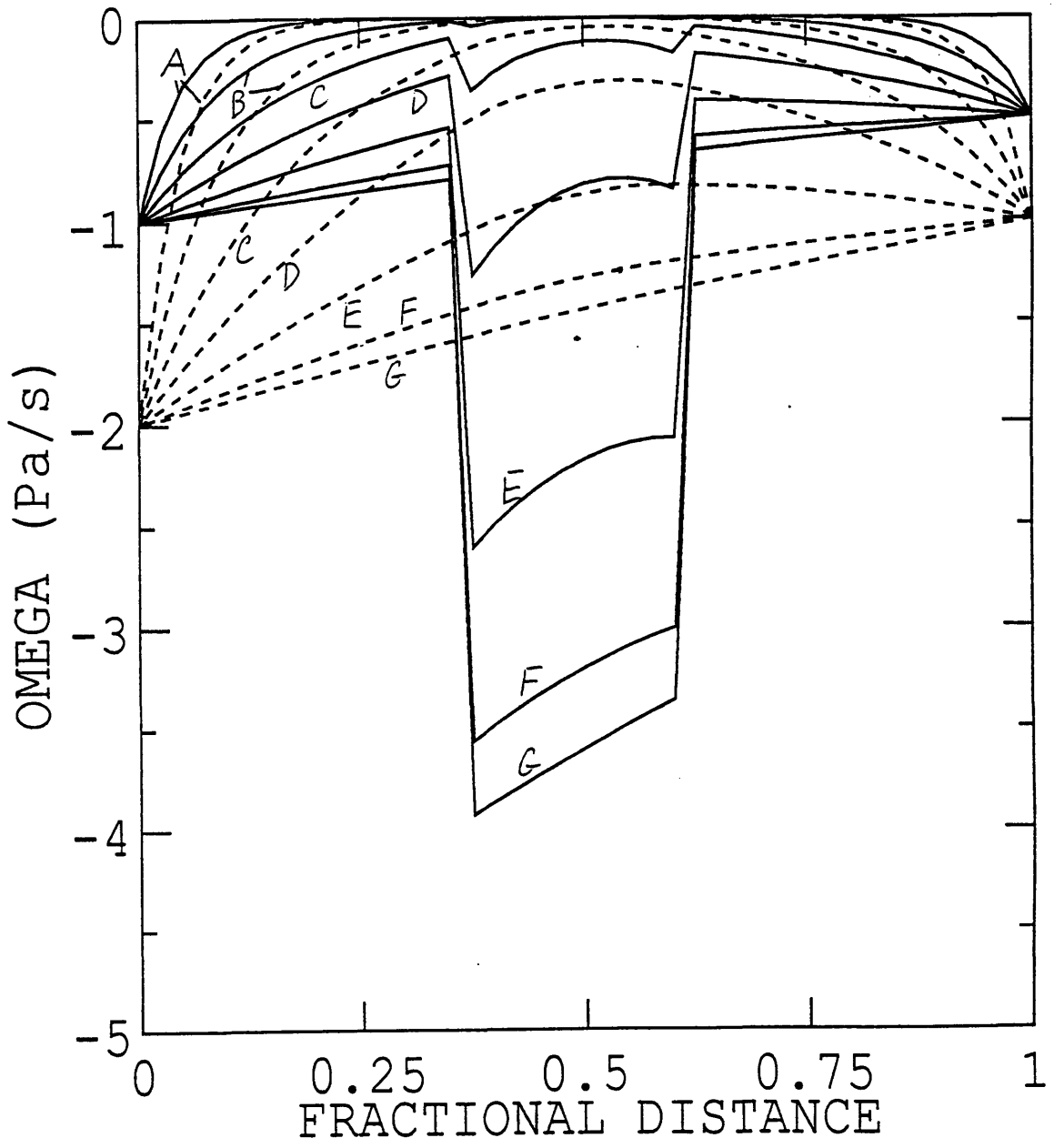

Fig. 5.8: Graph of ω (solid) and $\omega\frac{[\sigma^{-1}]}{\sigma^{-1}}$ (dashed), as in Fig. 5.7 (inverted top hat stratification), but for zero forcing and specified vertical motion on the horizontal boundaries. See text for details.

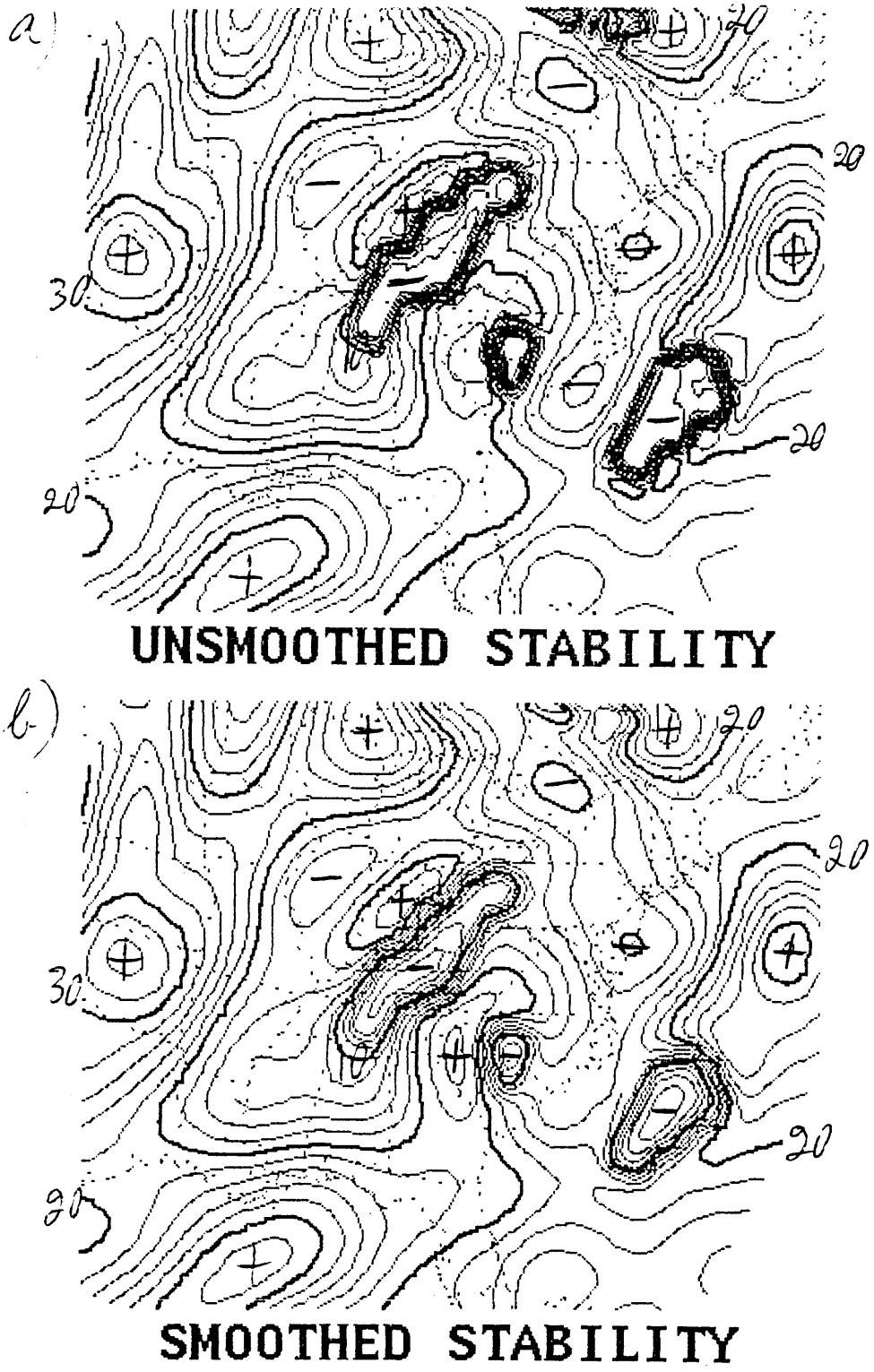

Fig. 5.9: Example of the horizontal distribution of the stratification parameter σ (contour interval 0.2×10^{-6} m^4 s^2 kg^{-2}, thick contours every 1.0×10^{-6}), at 700 mb for the 6-hour forecast from the 19/00 NGM forecast run. (a) Unsmoothed field. (b) Field after being passed through a horizontal low-pass filter.

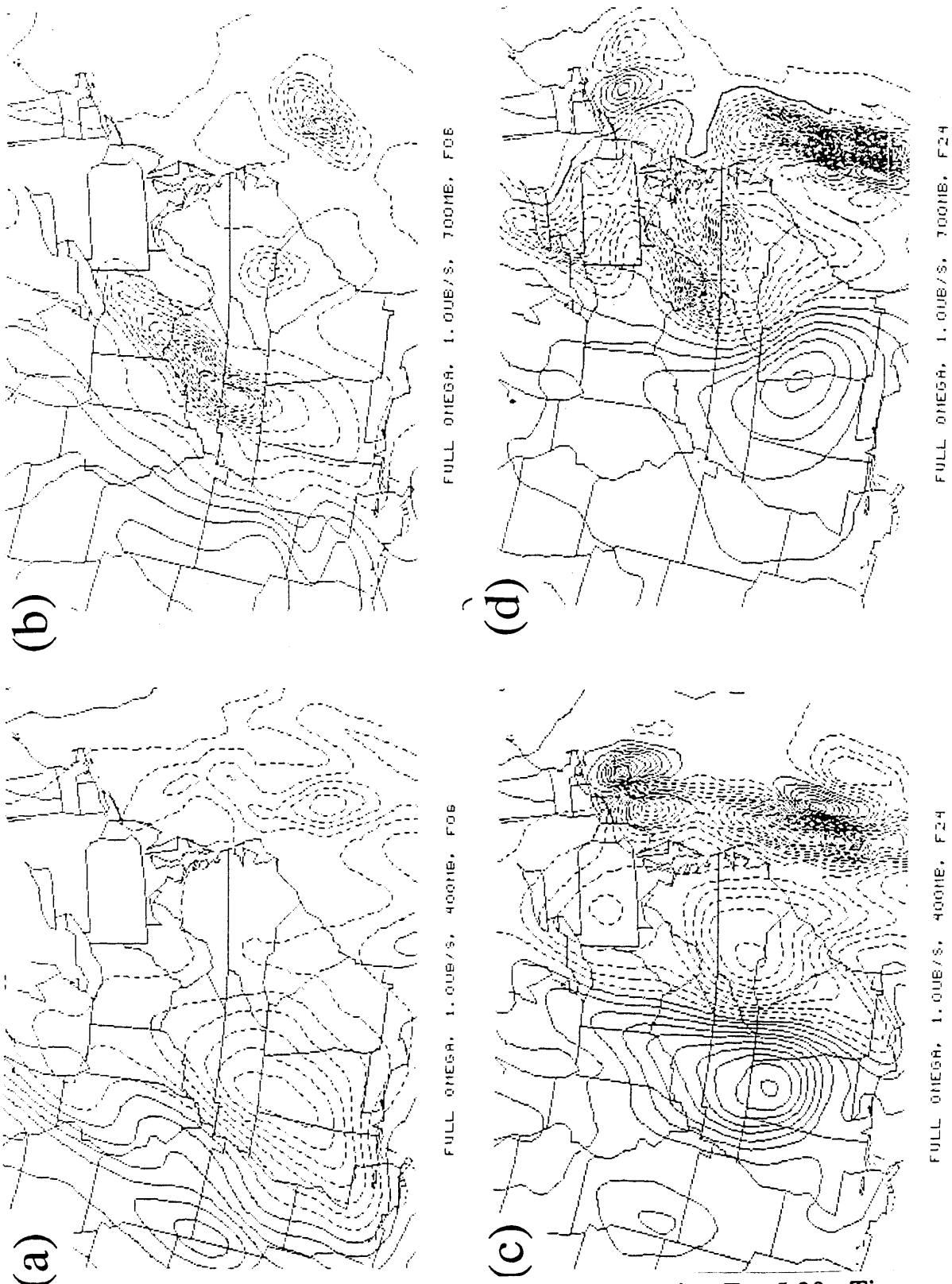

Fig. 5.10: Modified quasi-geostrophic ω calculated using Eq. 5.20. Times and contour conventions are as in Figs. 5.4-5.5. (a) 400 mb, 6-hour forecast. (b) 700 mb, 6-hour forecast. (c) 400 mb, 24-hour forecast. (d) 700 mb, 24-hour forecast.

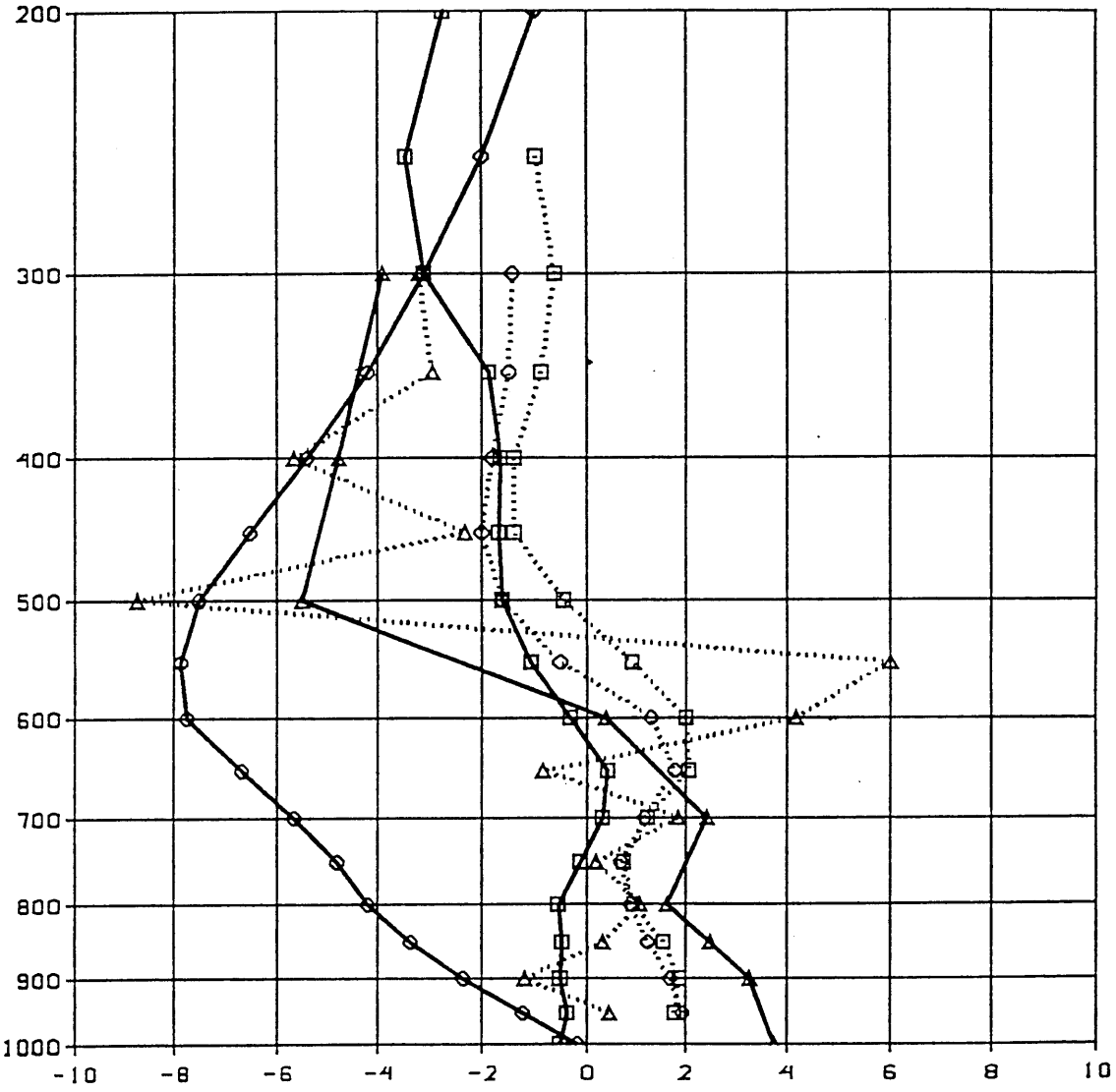

Fig. 5.11: Vertical profiles of various dynamical quantities, for a grid point in the *first updraft, 6-hour forecast* valid 06 UTC 19 Jan 1986. For complete description of Figs. 5.11-5.15, see Appendix B and Section 5.4b. Solid, circles: ω. Solid, squares: ζ. Solid, triangles: ζ_g. Dashed, circles: $Dt(\omega_p)$. Dashed, squares: $Dt(\zeta)$. Dashed, triangles: $Dt(\zeta_{gp})$.

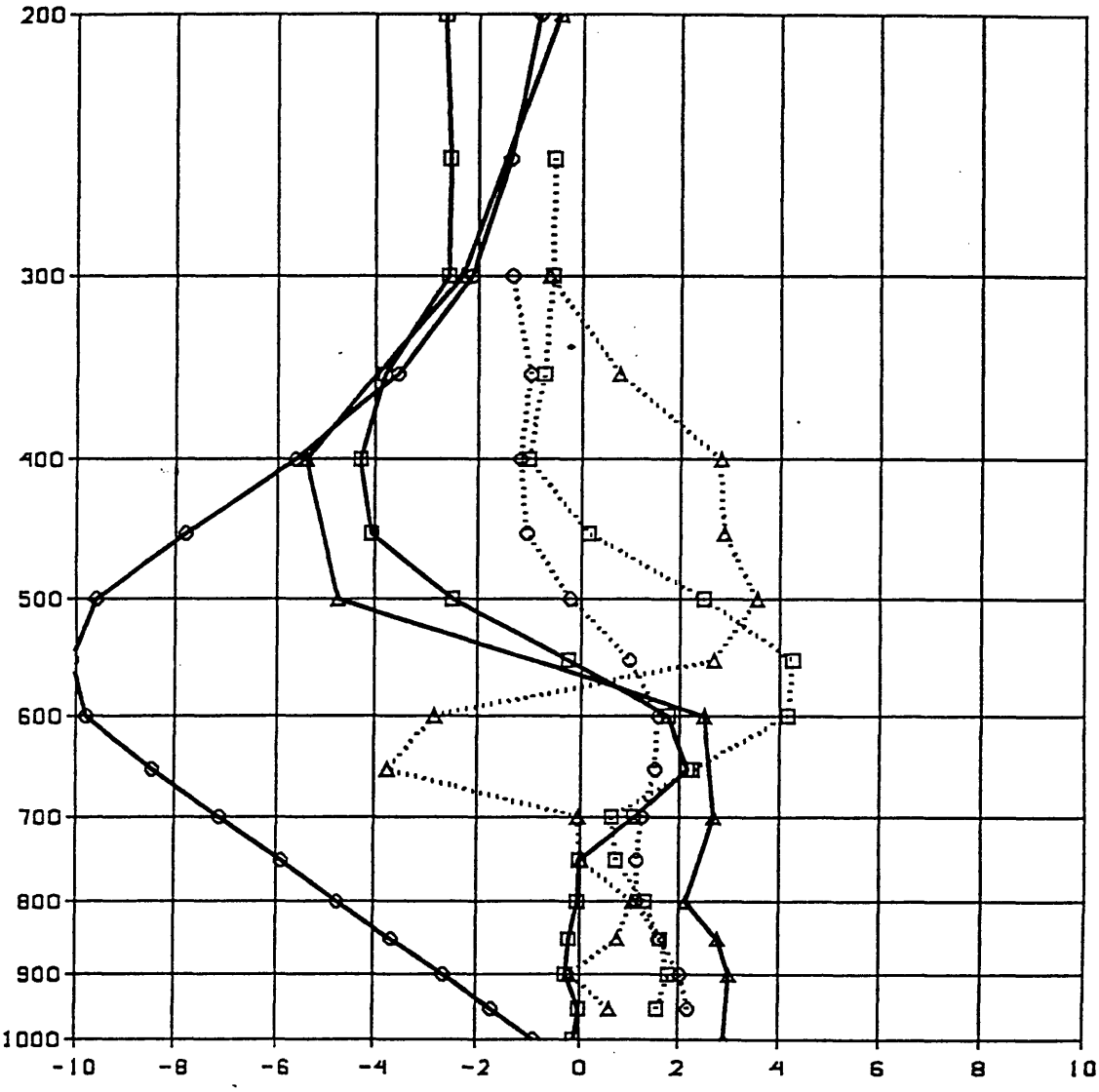

Fig. 5.12: Vertical profiles of various dynamical quantities, for a grid point in the *first updraft, 12-hour forecast* valid 12 UTC 19 Jan 1986. For complete description, see Appendix B and Section 5.4b. Solid, circles: ω. Solid, squares: ζ. Solid, triangles: ζ_g. Dashed, circles: $Dt(\omega_p)$. Dashed, squares: $Dt(\zeta)$. Dashed, triangles: $Dt(\zeta_{gp})$.

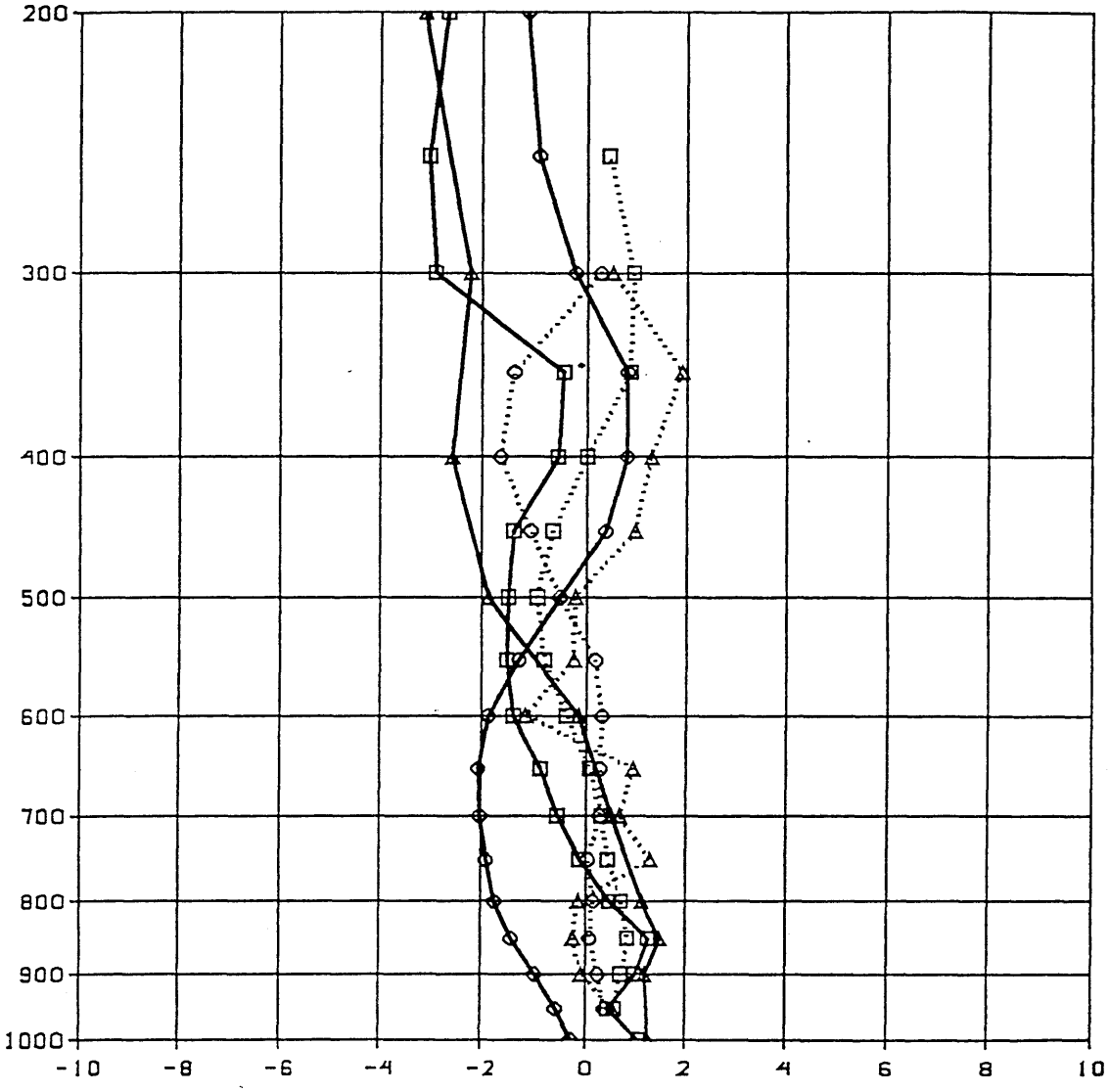

Fig. 5.13: Vertical profiles of various dynamical quantities, for a grid point in the *second updraft, 12-hour forecast* valid 12 UTC 19 Jan 1986. For complete description, see Appendix B and Section 5.4b. Solid, circles: ω. Solid, squares: ζ. Solid, triangles: ζ_g. Dashed, circles: $Dt(\omega_p)$. Dashed, squares: $Dt(\zeta)$. Dashed, triangles: $Dt(\zeta_{gp})$.

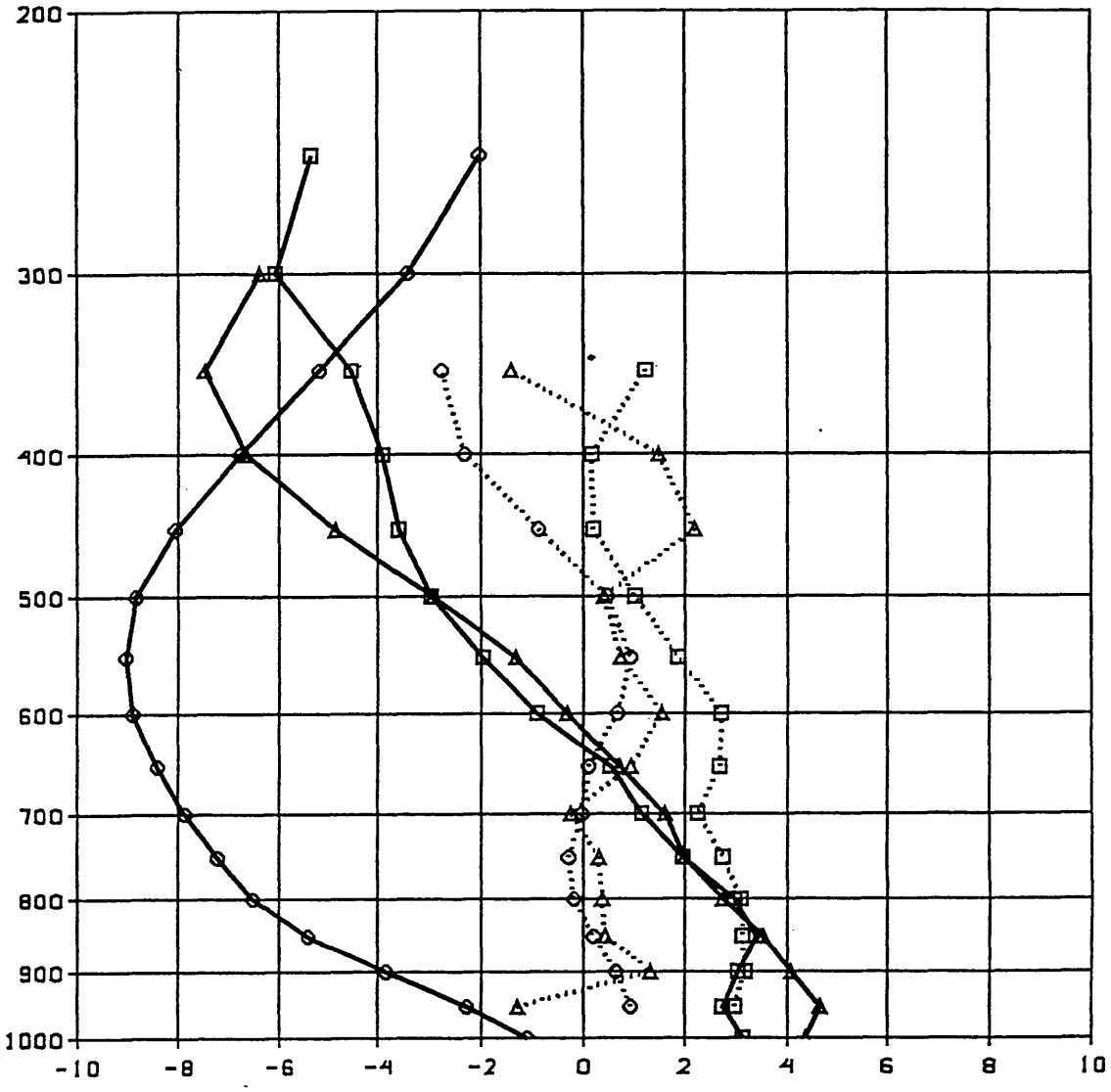

Fig. 5.14: Vertical profiles of various dynamical quantities, for a grid point in the *second updraft, 18-hour forecast* valid 18 UTC 19 Jan 1986. For complete description, see Appendix B and Section 5.4b. Solid, circles: ω. Solid, squares: ζ. Solid, triangles: ζ_g. Dashed, circles: $Dt(\omega_p)$. Dashed, squares: $Dt(\zeta)$. Dashed, triangles: $Dt(\zeta_{gp})$.

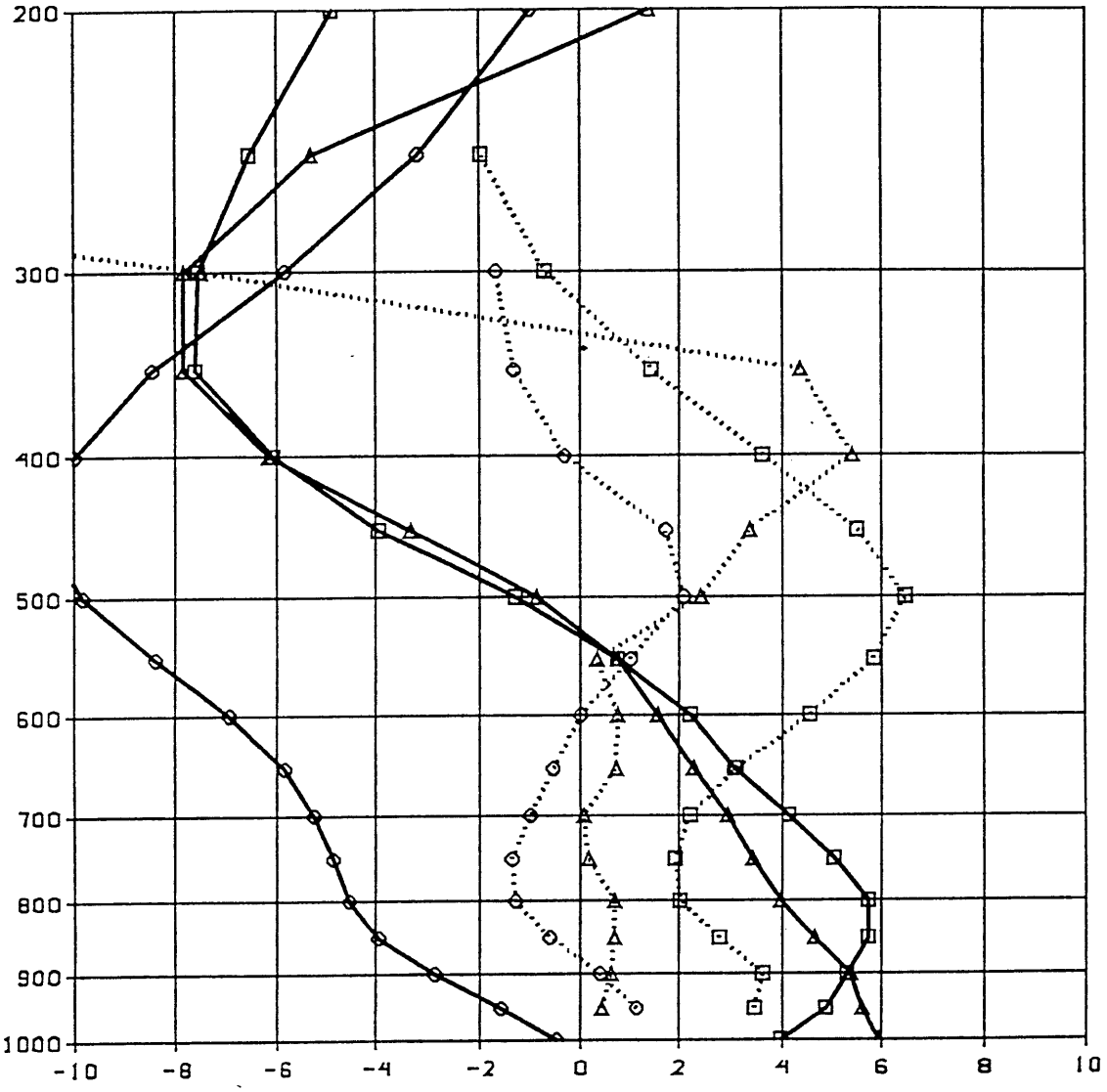

Fig. 5.15: Vertical profiles of various dynamical quantities, for a grid point in the *second updraft, 24-hour forecast* valid 00 UTC 20 Jan 1986. For complete description, see Appendix B and Section 5.4b. Solid, circles: ω. Solid, squares: ζ. Solid, triangles: ζ_g. Dashed, circles: $Dt(\omega_p)$. Dashed, squares: $Dt(\zeta)$. Dashed, triangles: $Dt(\zeta_{gp})$.

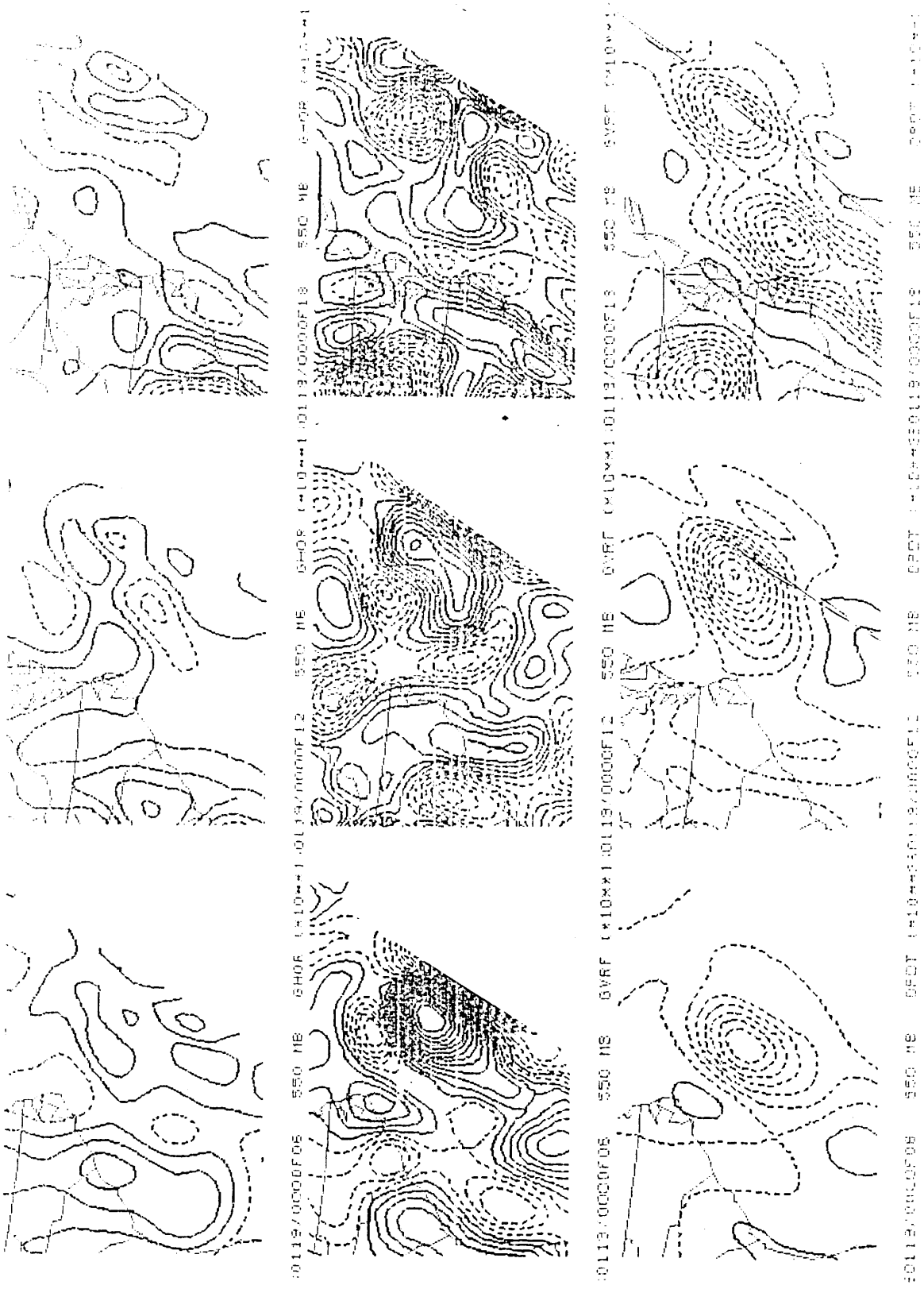

Fig. 5.16: Comparison of terms in the geostrophic vorticity tendency equation, 6-18 hour NGM forecasts, 550 mb. See Appendix B.

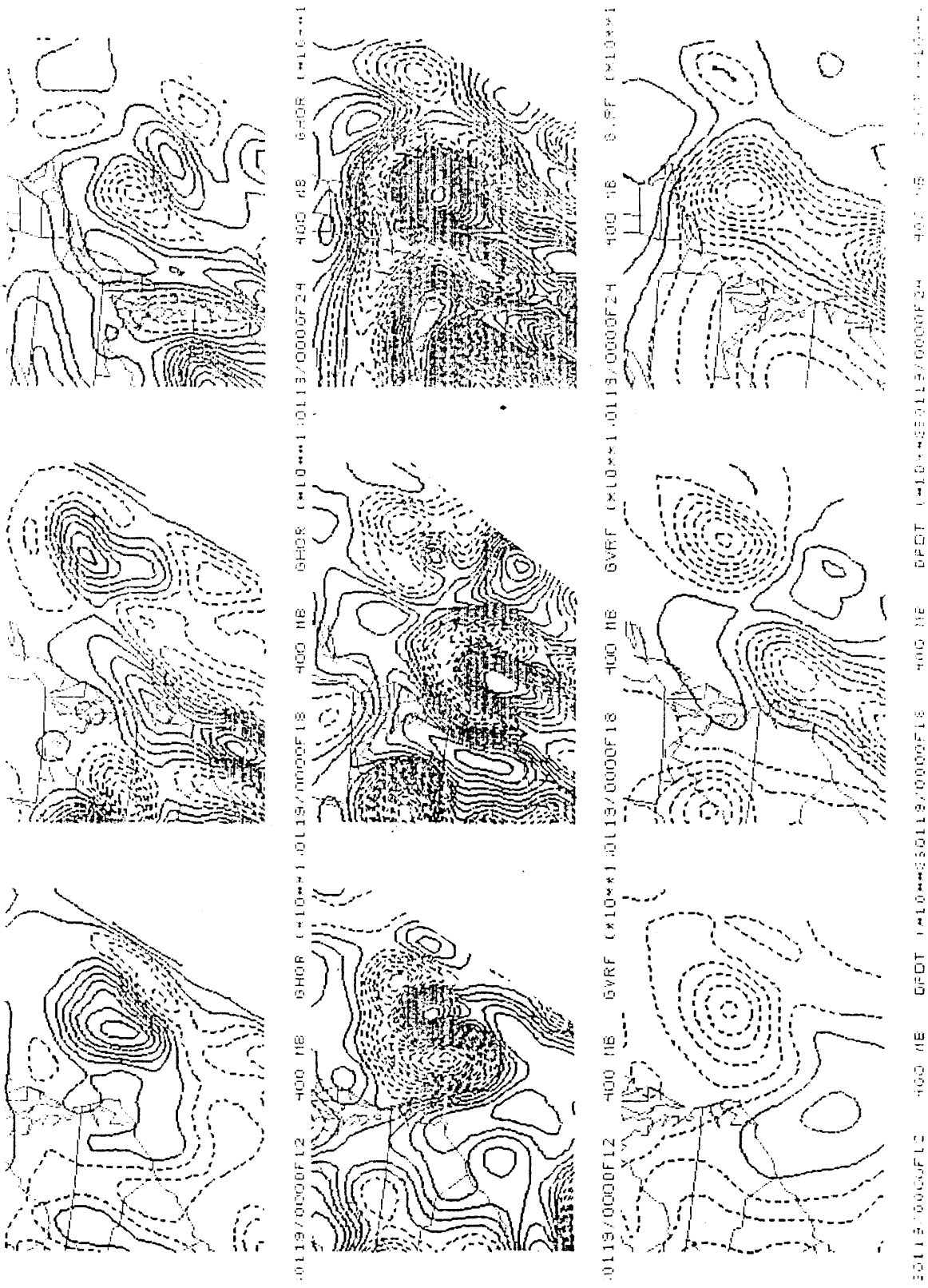

Fig. 5.17: Comparison of terms in the geostrophic vorticity tendency equation, 12-24 hour NGM forecasts, 400 mb. See Appendix B.

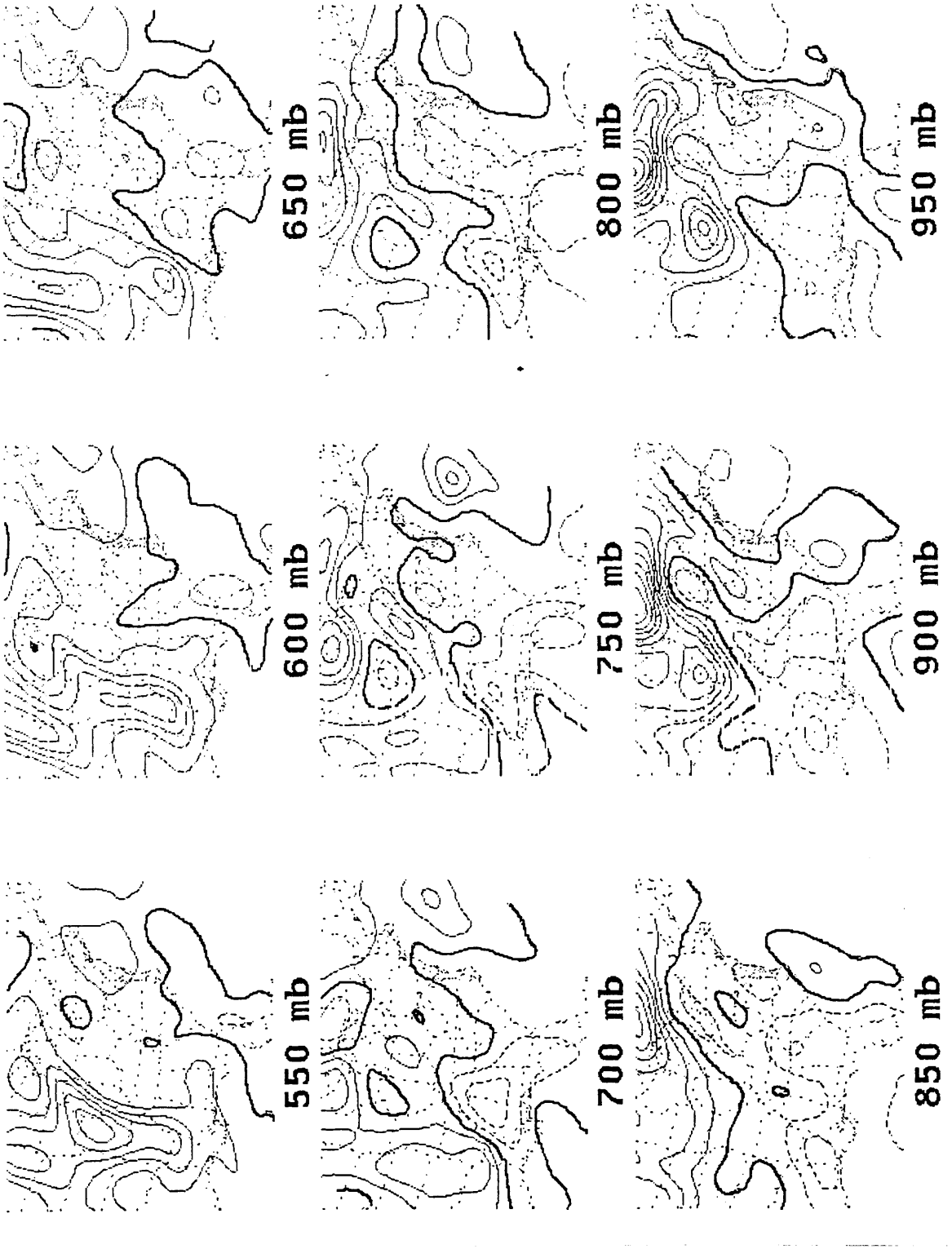

Fig. 5.18: Fields of equivalent potential vorticity, 19/00 NGM forecast run, 6-hour forecast. Contour interval 0.25 PVU, zero contour thick, negative contours dashed.

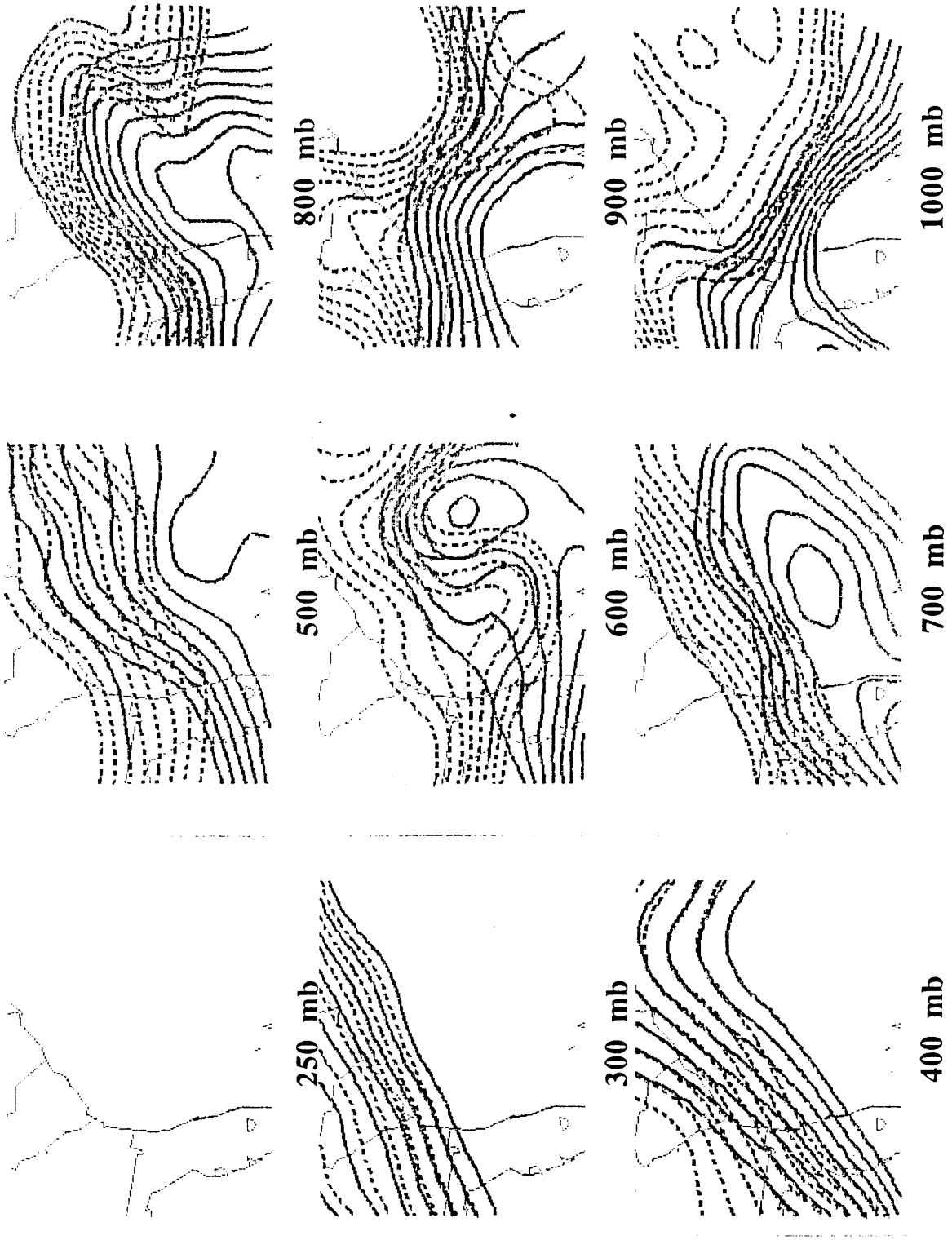

Fig. 5.19: Vertical distribution of θ_e (solid contours) and θ_e* (dashed contours), 250 mb to 1000 mb, initialization, 00 UTC 19 Jan 1986 NGM forecast run. Contours are drawn at 1 K intervals from 318 K to 325 K, with colder temperatures located toward the top of page. See text for interpretation. Same format in Figs. 5.20-5.23.

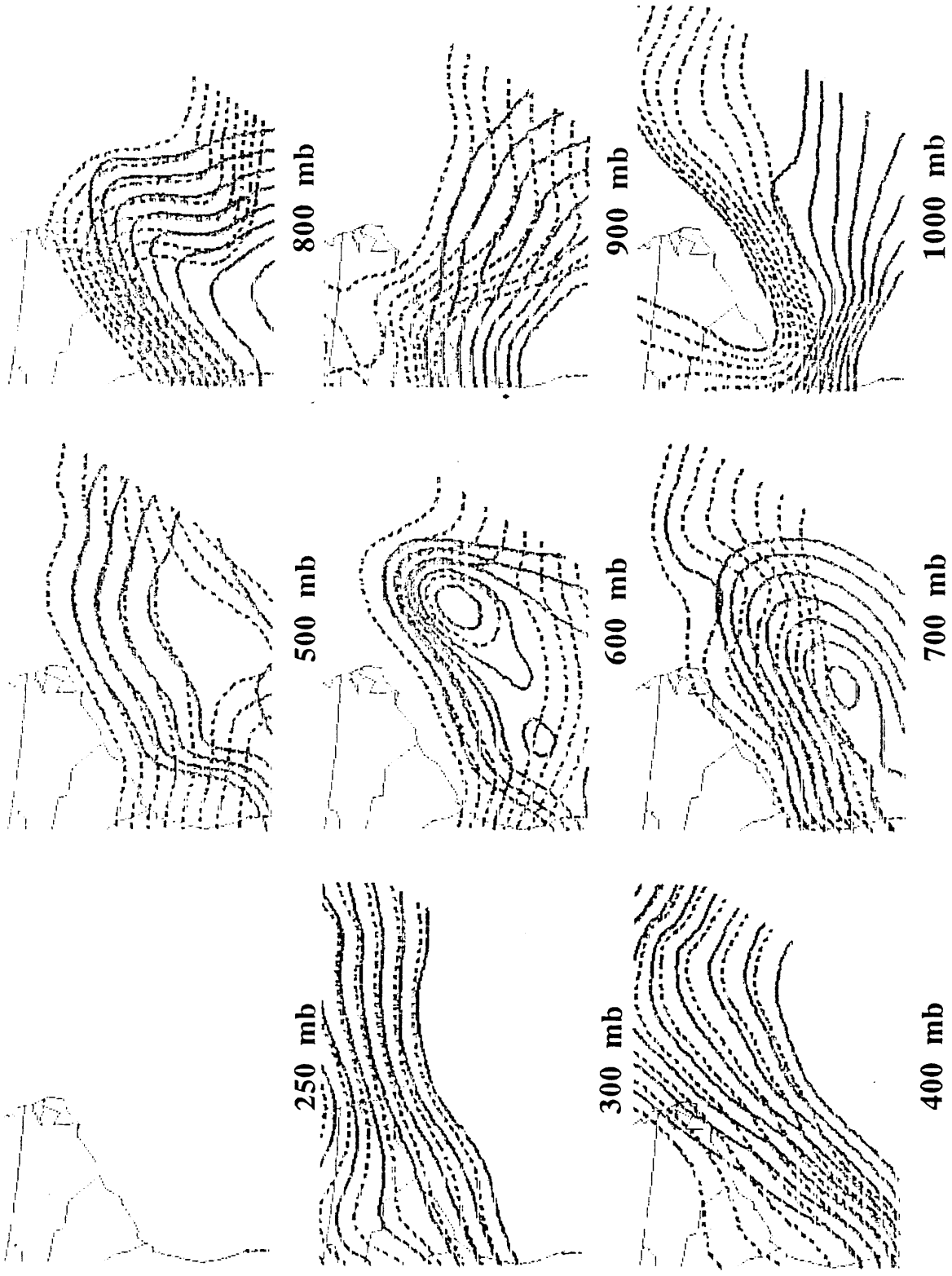

Fig. 5.20: Vertical distribution of θ_e and θ_e*, as in Fig. 5.19, but for 6-hour forecast valid 06 UTC 19 Jan 1986.

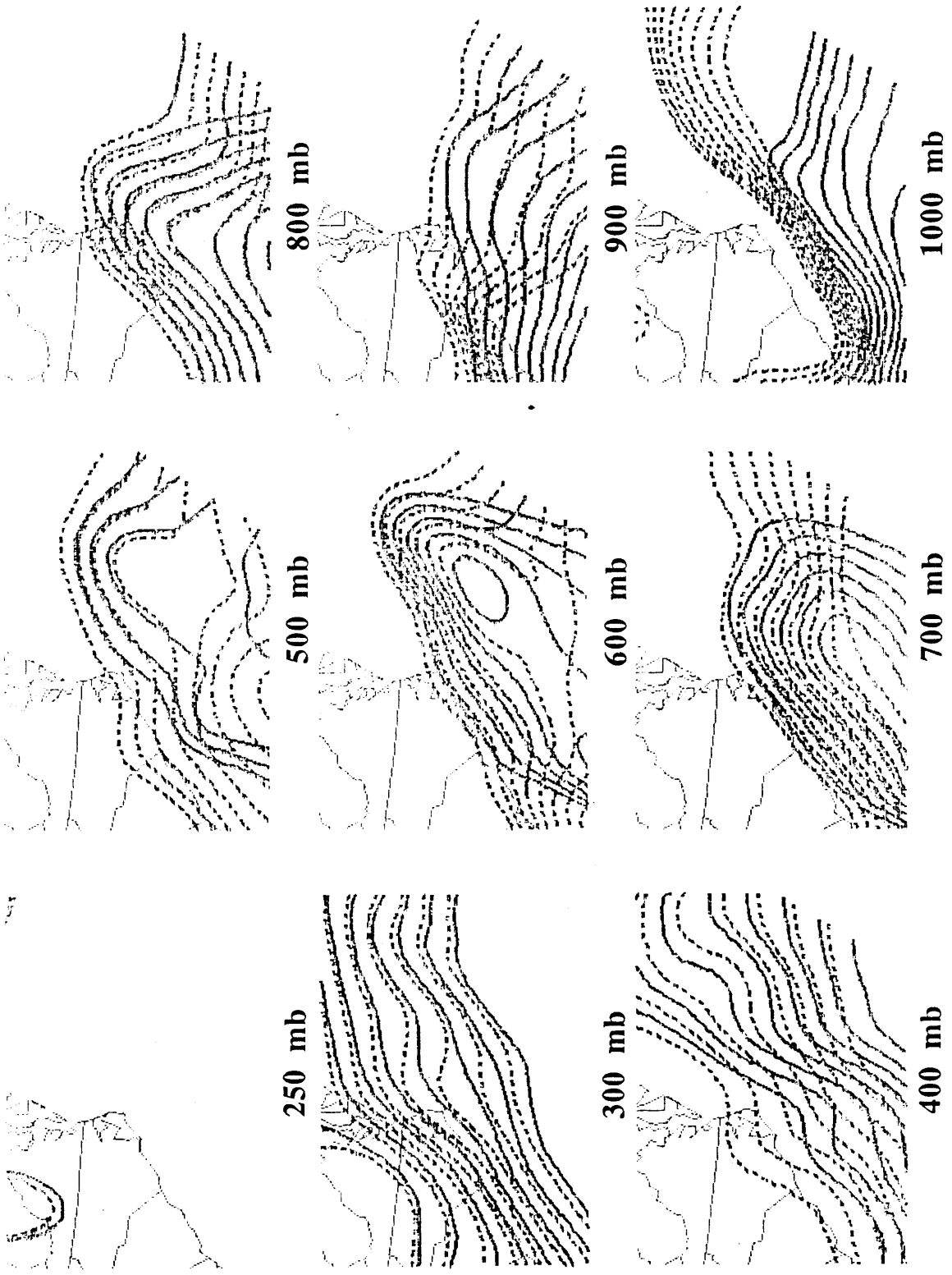

Fig. 5.21: Vertical distribution of θ_e and θ_e*, as in Fig. 5.19, but for 12-hour forecast valid 12 UTC 19 Jan 1986.

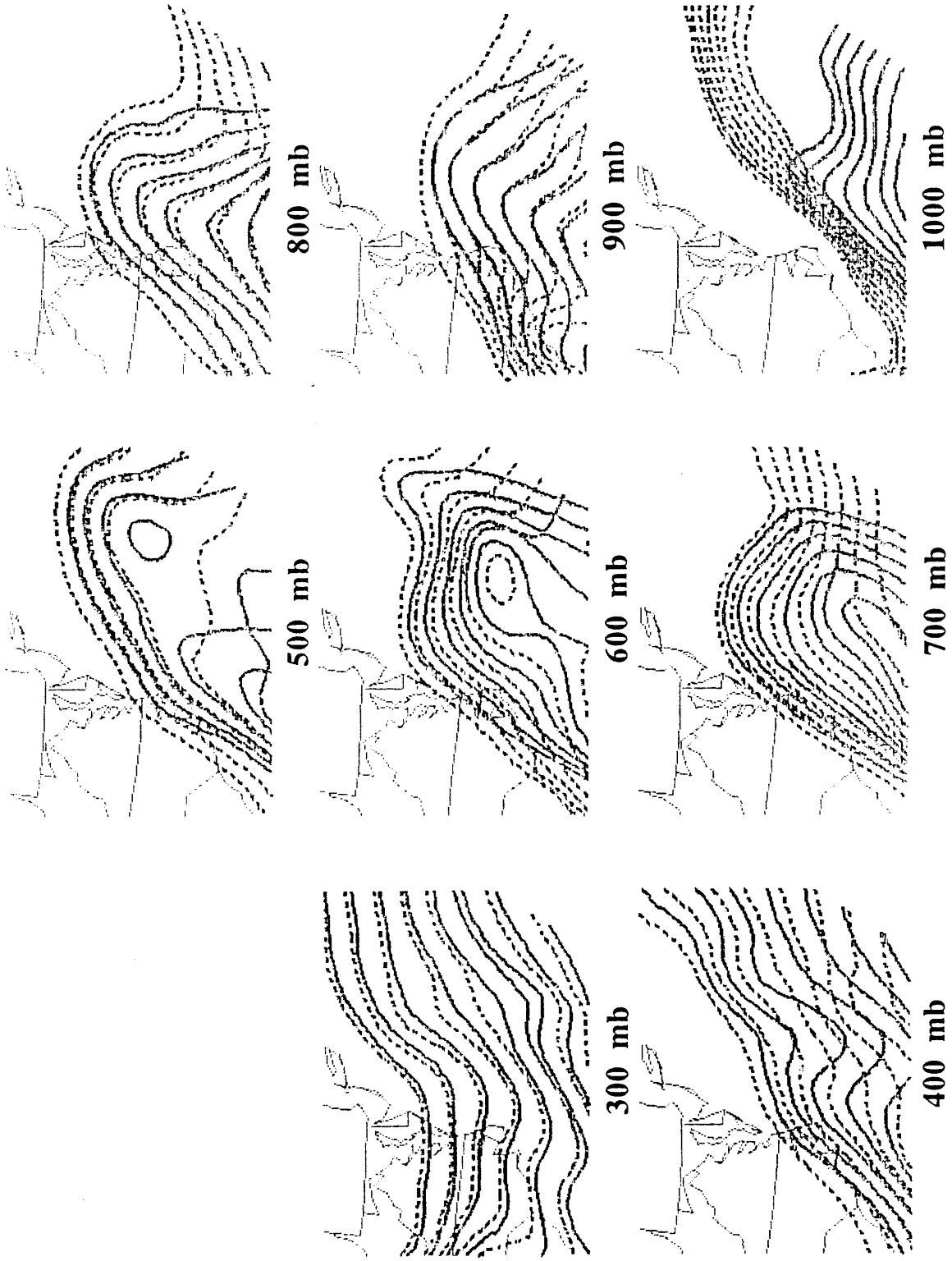

Fig. 5.22: Vertical distribution of θ_e and θ_e*, as in Fig. 5.19, but for 18-hour forecast valid 18 UTC 19 Jan 1986.

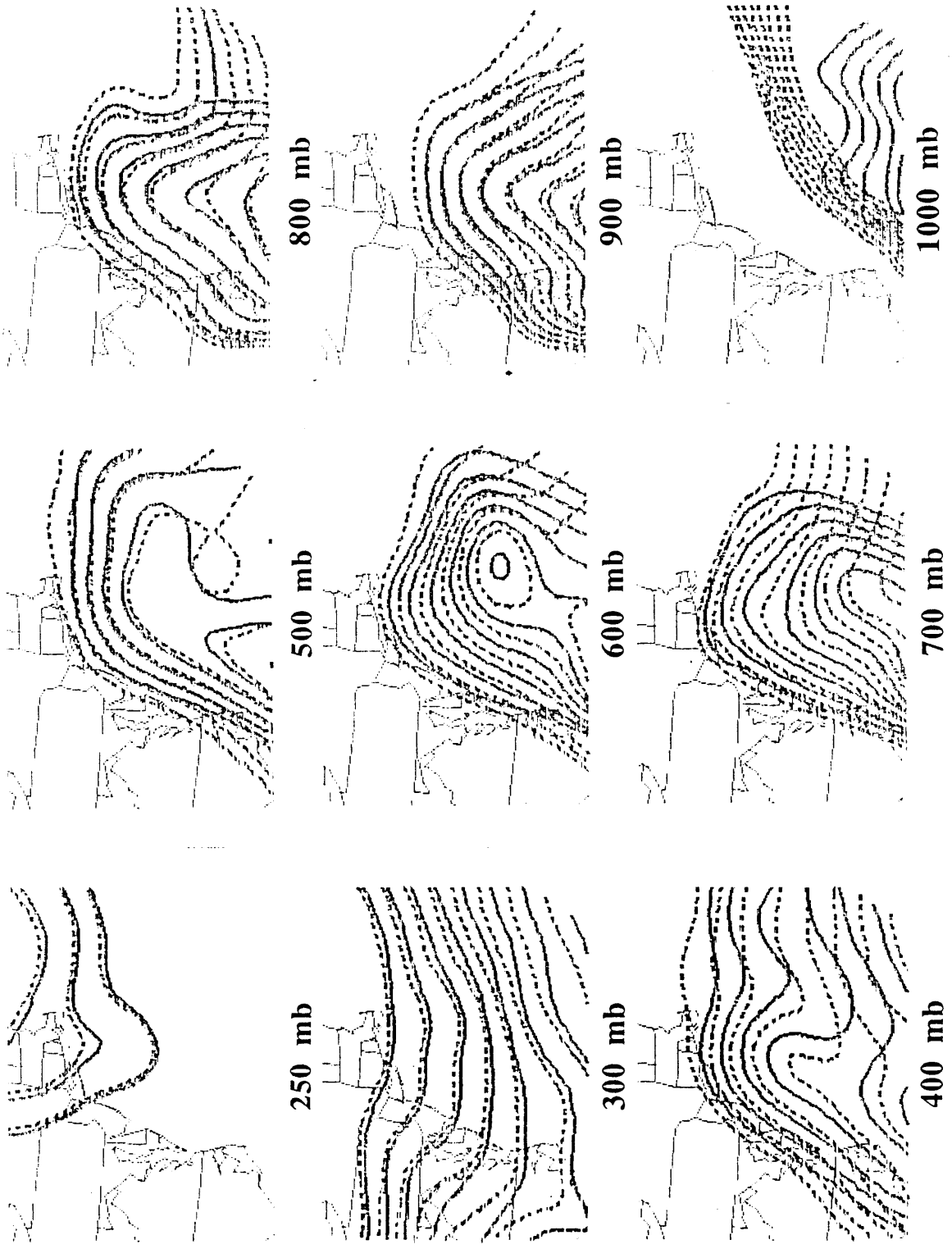

Fig. 5.23: Vertical distribution of θ_e and θ_e*, as in Fig. 5.19, but for 24-hour forecast valid 24 UTC 19 Jan 1986.

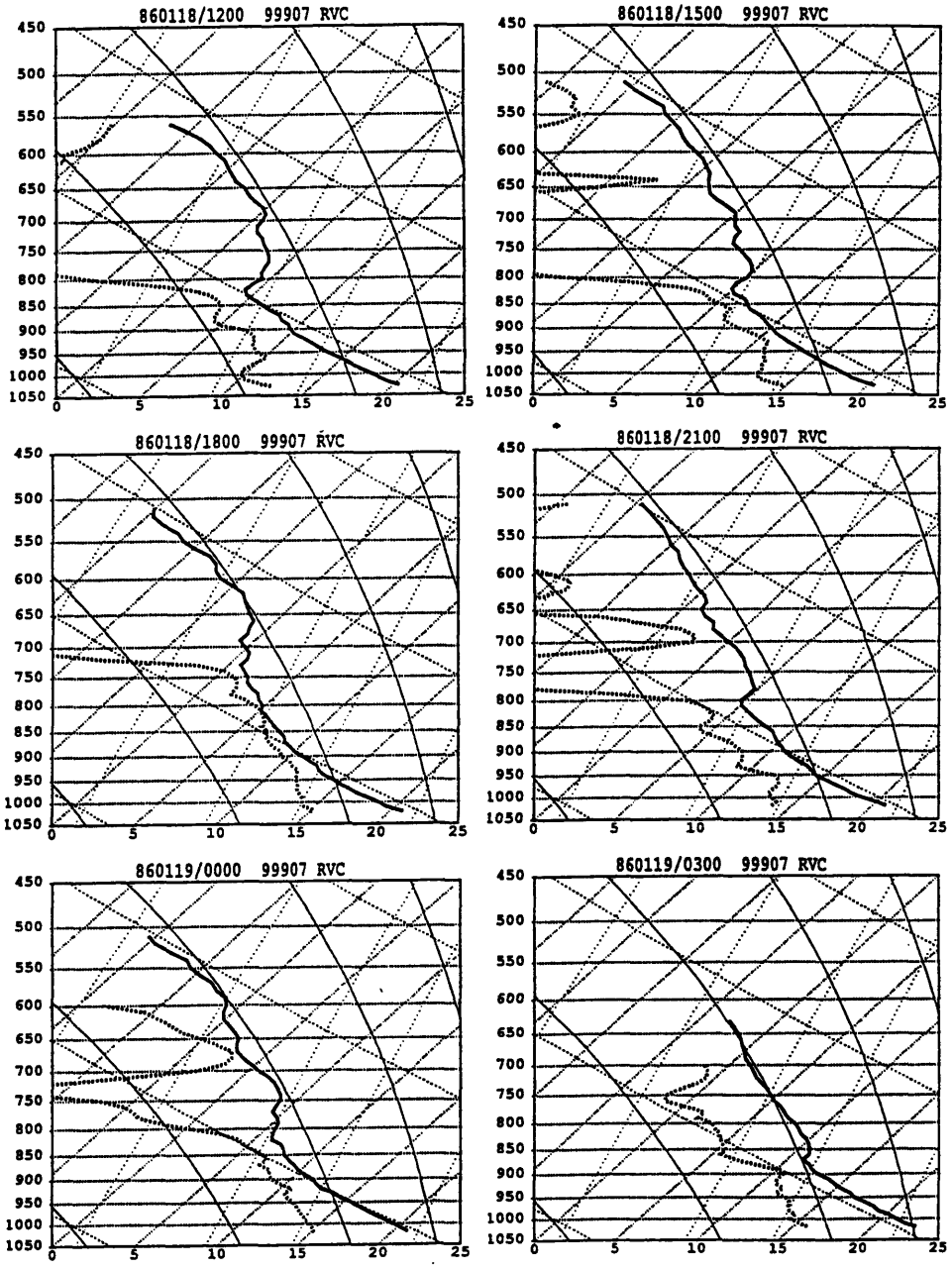

Fig. 5.24 (first of two pages): Skew-*T* log-*p* sounding diagrams for station RVC (station location shown in Fig. 3.5), 12 UTC 18 Jan 1986 to 00 UTC 20 Jan 1986, showing temperature (thick solid) and dew point (thick dashed). Background lines include pressure (horizontal, fine dashes), temperature (sloping to the right, fine dashes), dry adiabats (sloping to the left, dashes), moist adiabats (sloping to the left, solid), and isolines of mixing ratio (sloping to the right, dots). Same format as in Figs. 5.25-5.27.

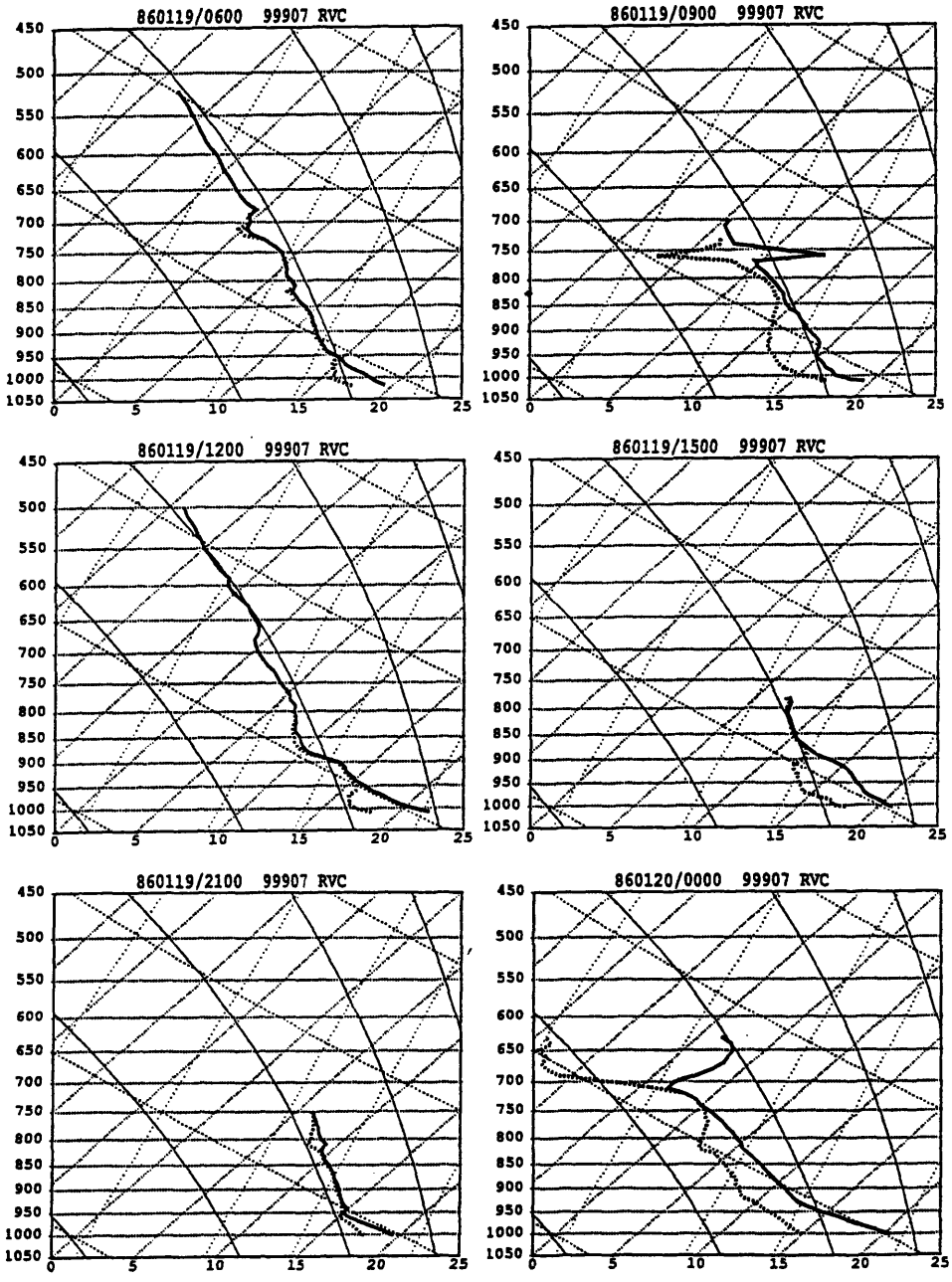

Fig. 5.24 (second of two pages): RVC soundings.

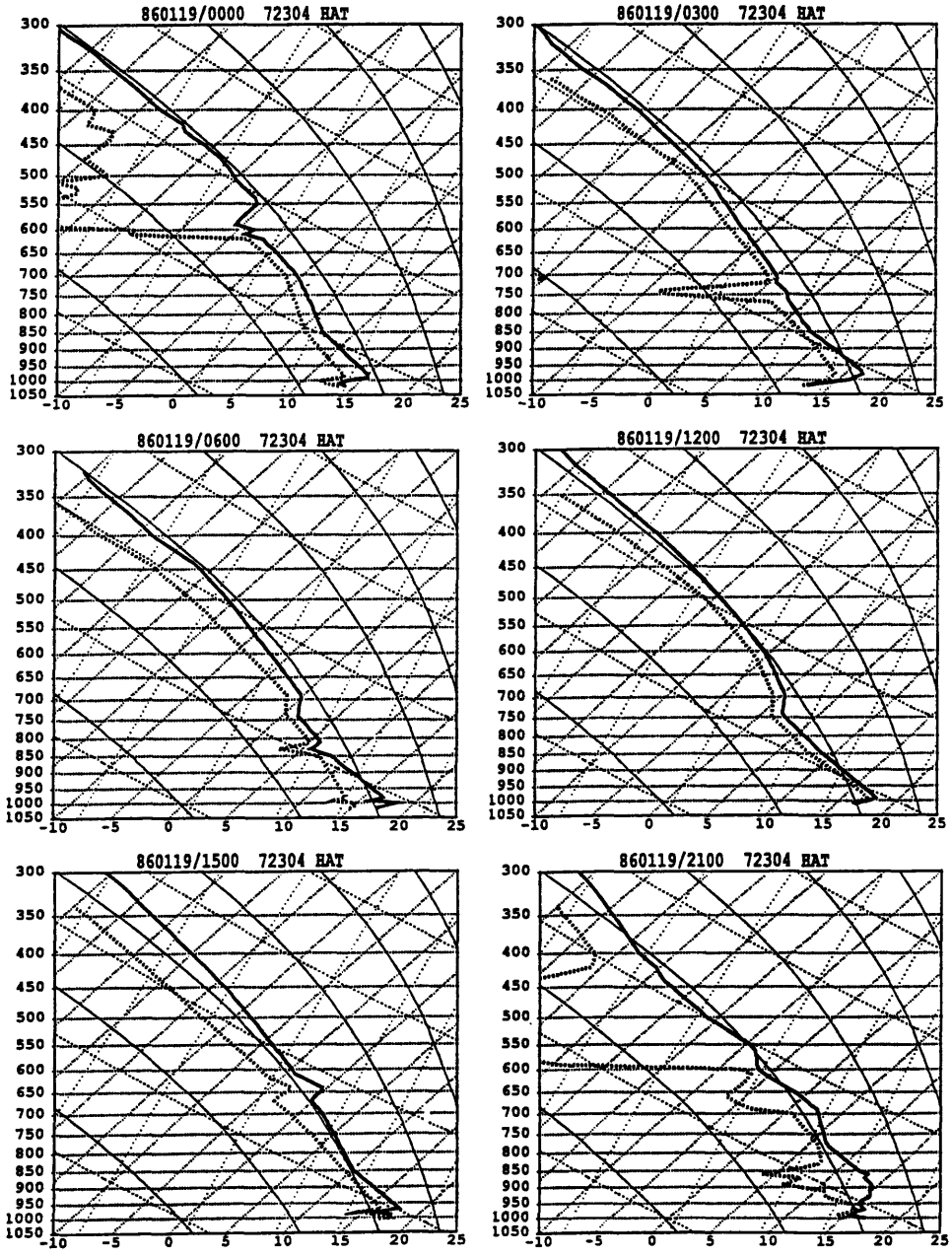

Fig. 5.25: Sounding diagrams for HAT (station location shown in Fig. 3.28), 00 UTC 19 Jan 1986 to 21 UTC 19 Jan 1986. For description of sounding format, see Fig. 5.24.

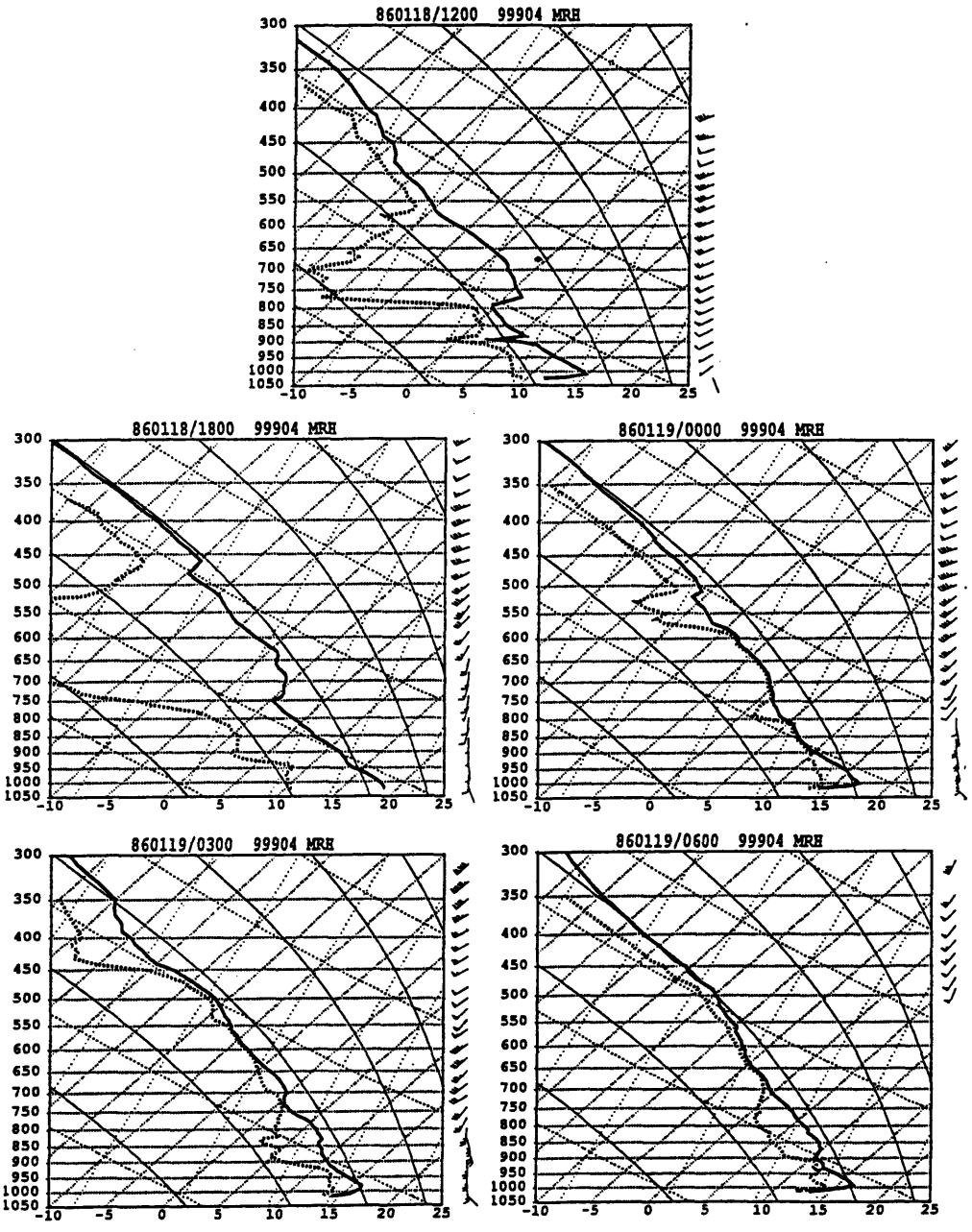

Fig. 5.26 (first of two pages): Sounding diagrams for MRH (station location shown in Fig. 3.28), 12 UTC 18 Jan 1986 to 21 UTC 19 Jan 1986. For description of sounding format, see Fig. 5.24.

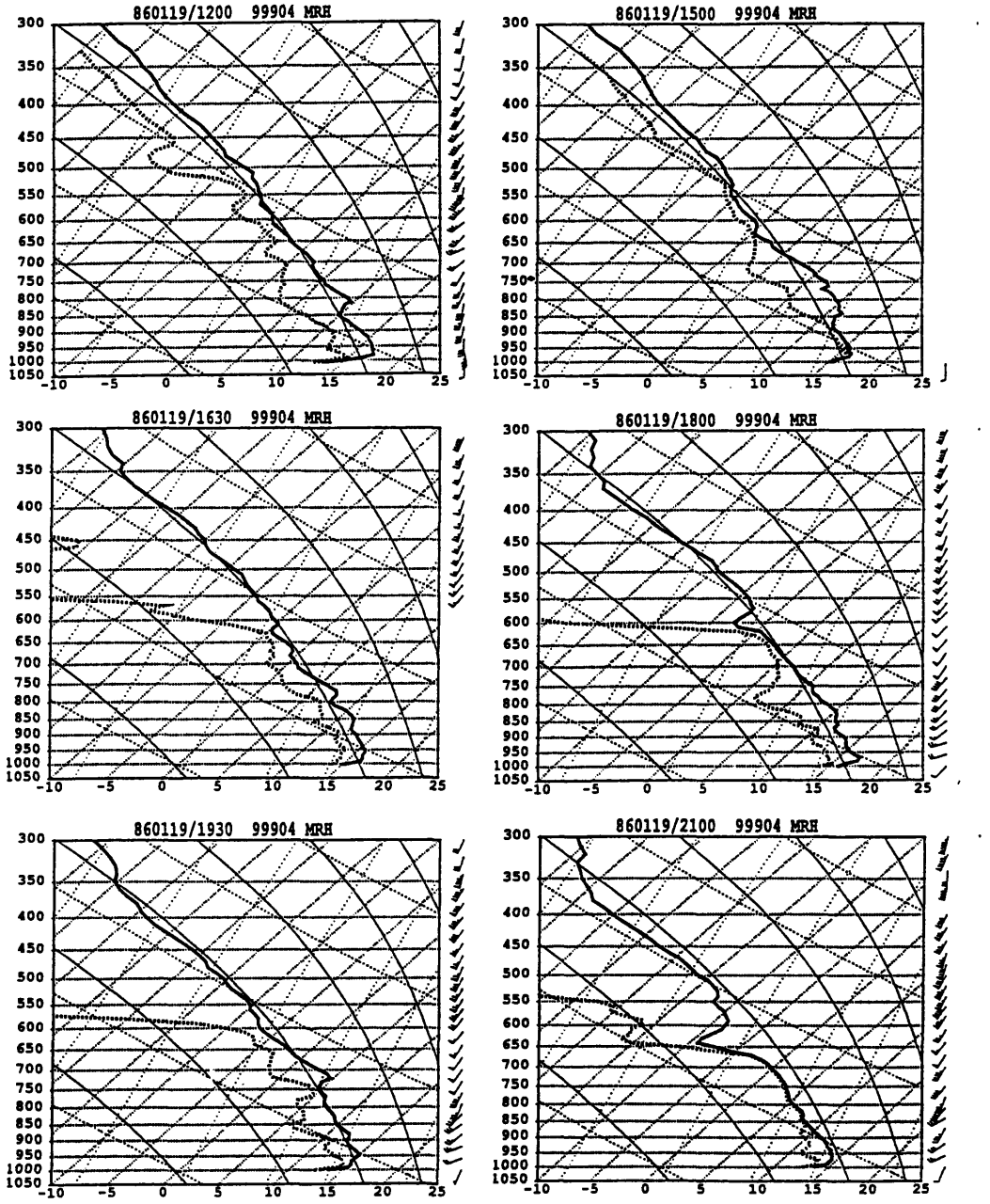

Fig. 5.26 (second of two pages): MRH soundings.

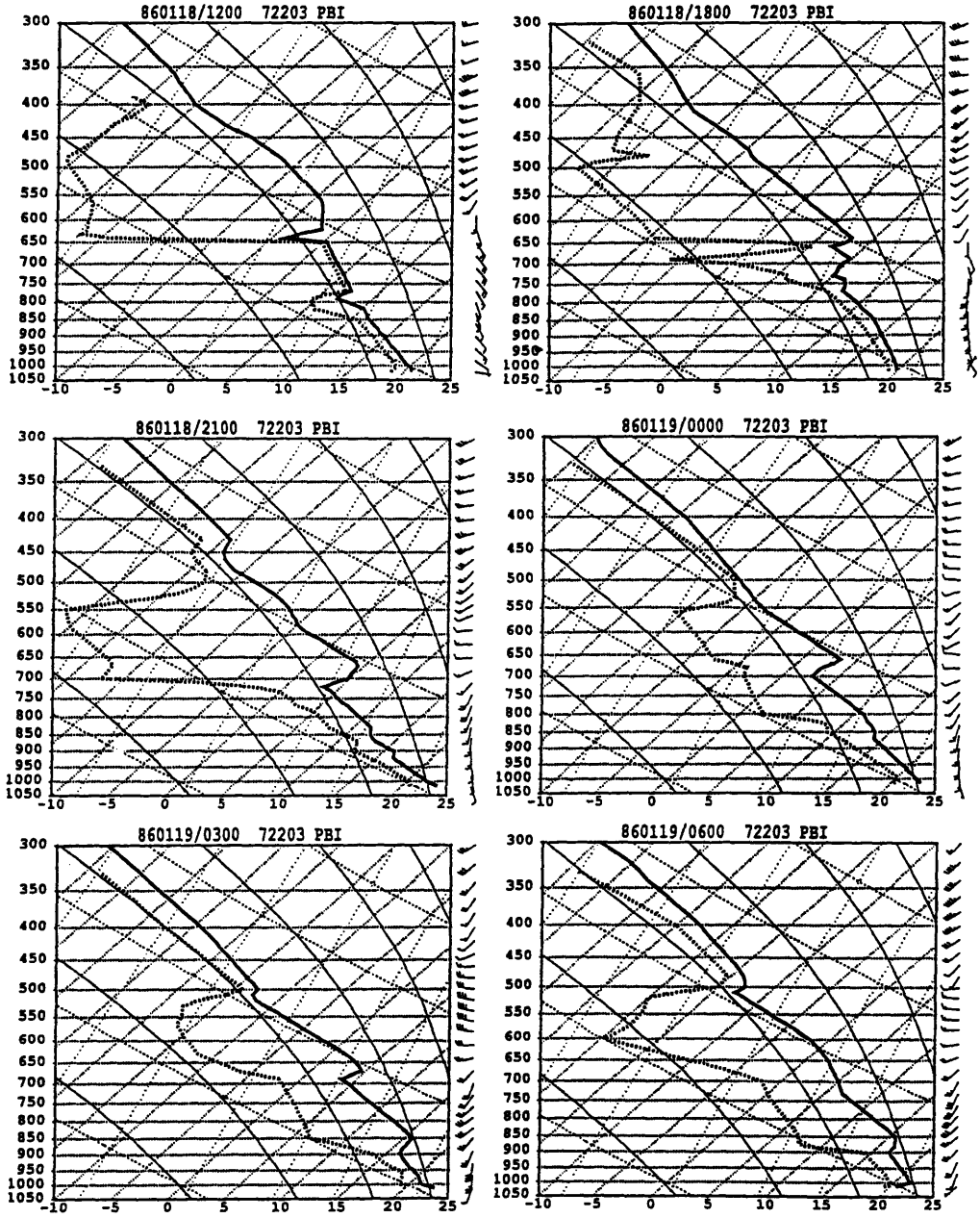

Fig. 5.27: Sounding diagrams for PBI (station location shown in Fig. 3.28), 12 UTC 18 Jan 1986 to 06 UTC 19 Jan 1986. For description of sounding format, see Fig. 5.24.

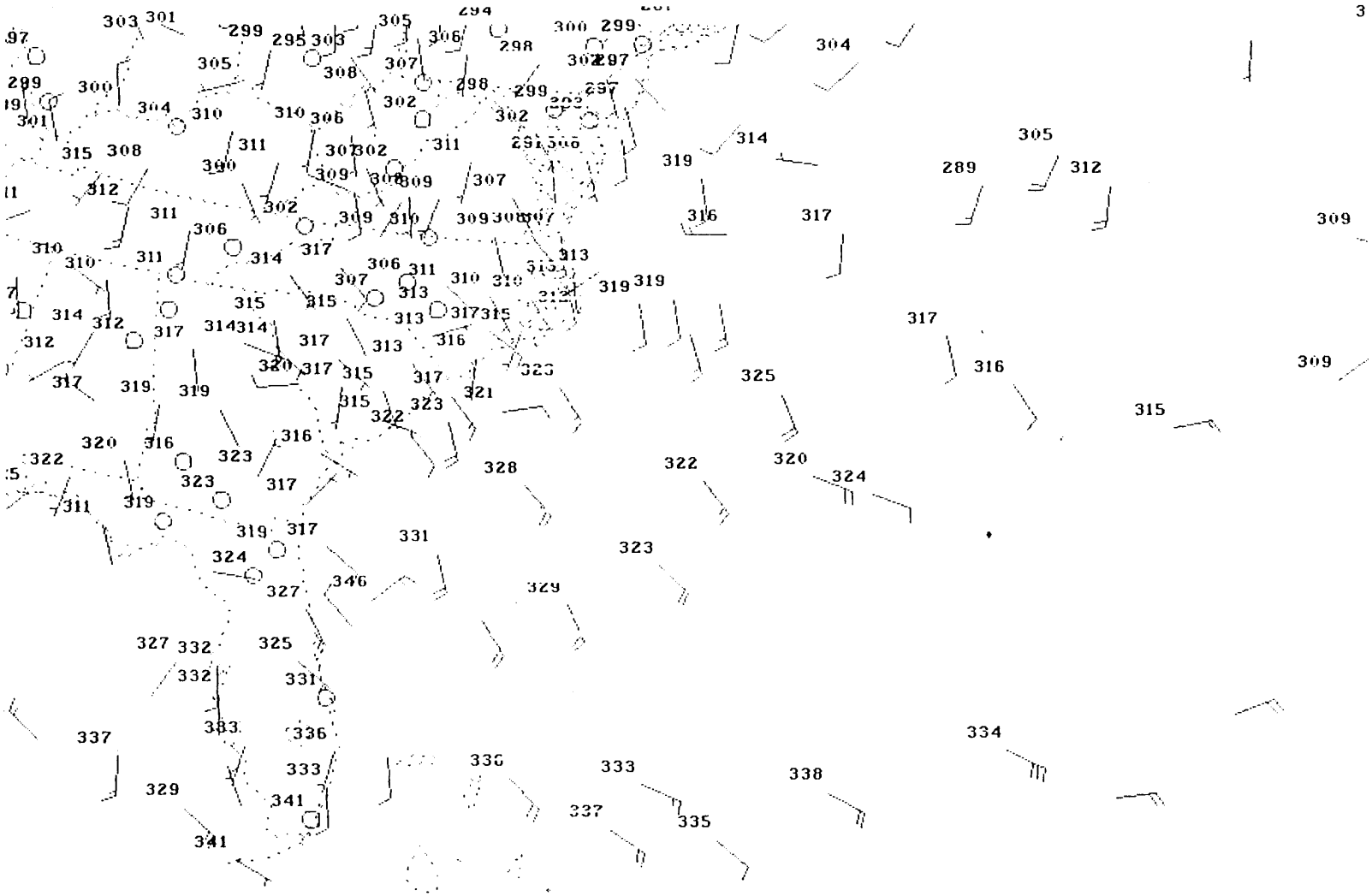

Fig. 5.28: Surface map of equivalent potential temperature (K) and winds (standard model), 00 UTC 19 Jan 1986.

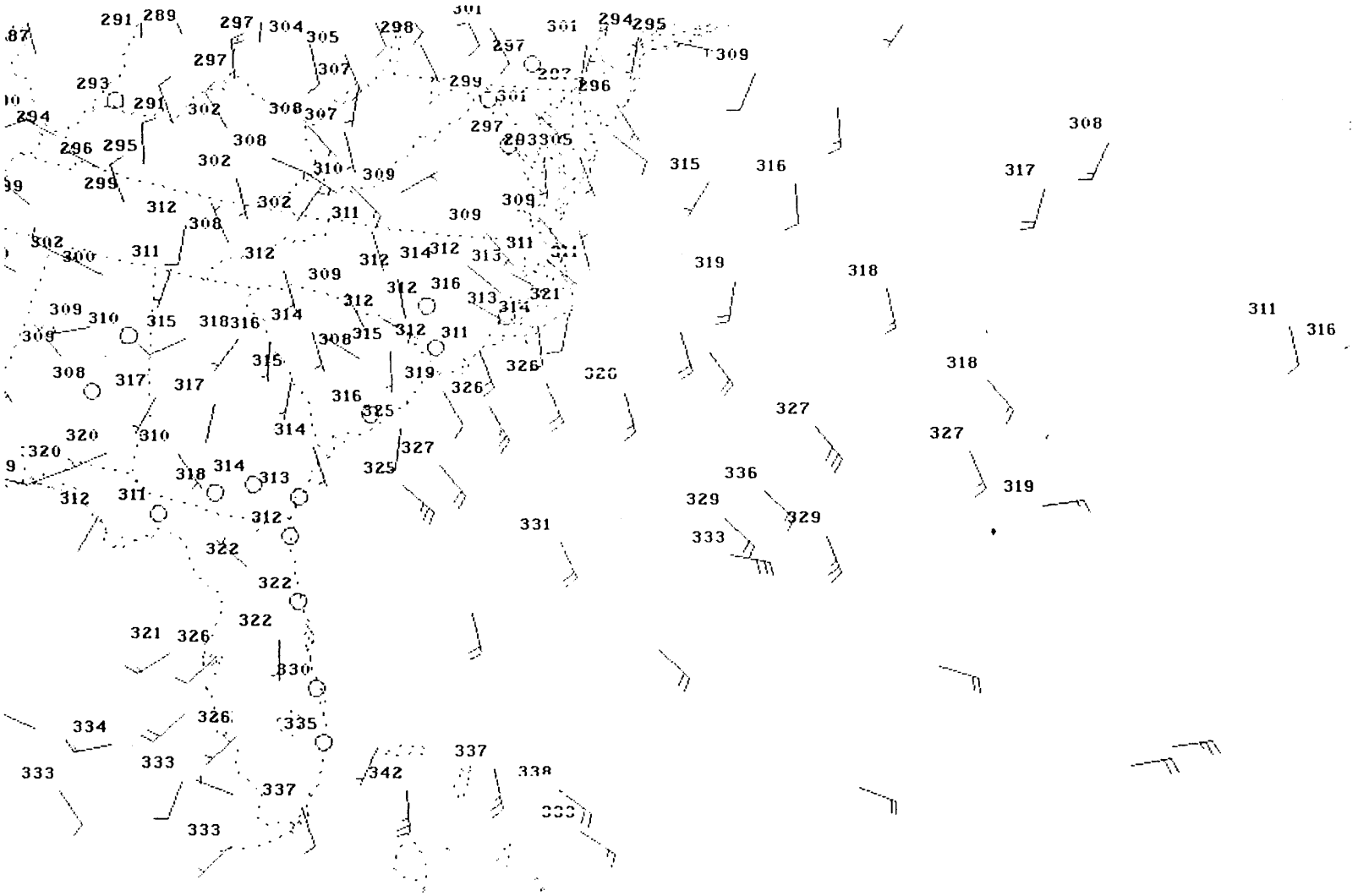

Fig. 5.29: Surface map of equivalent potential temperature (K) and winds (standard model), 06 UTC 19 Jan 1986.

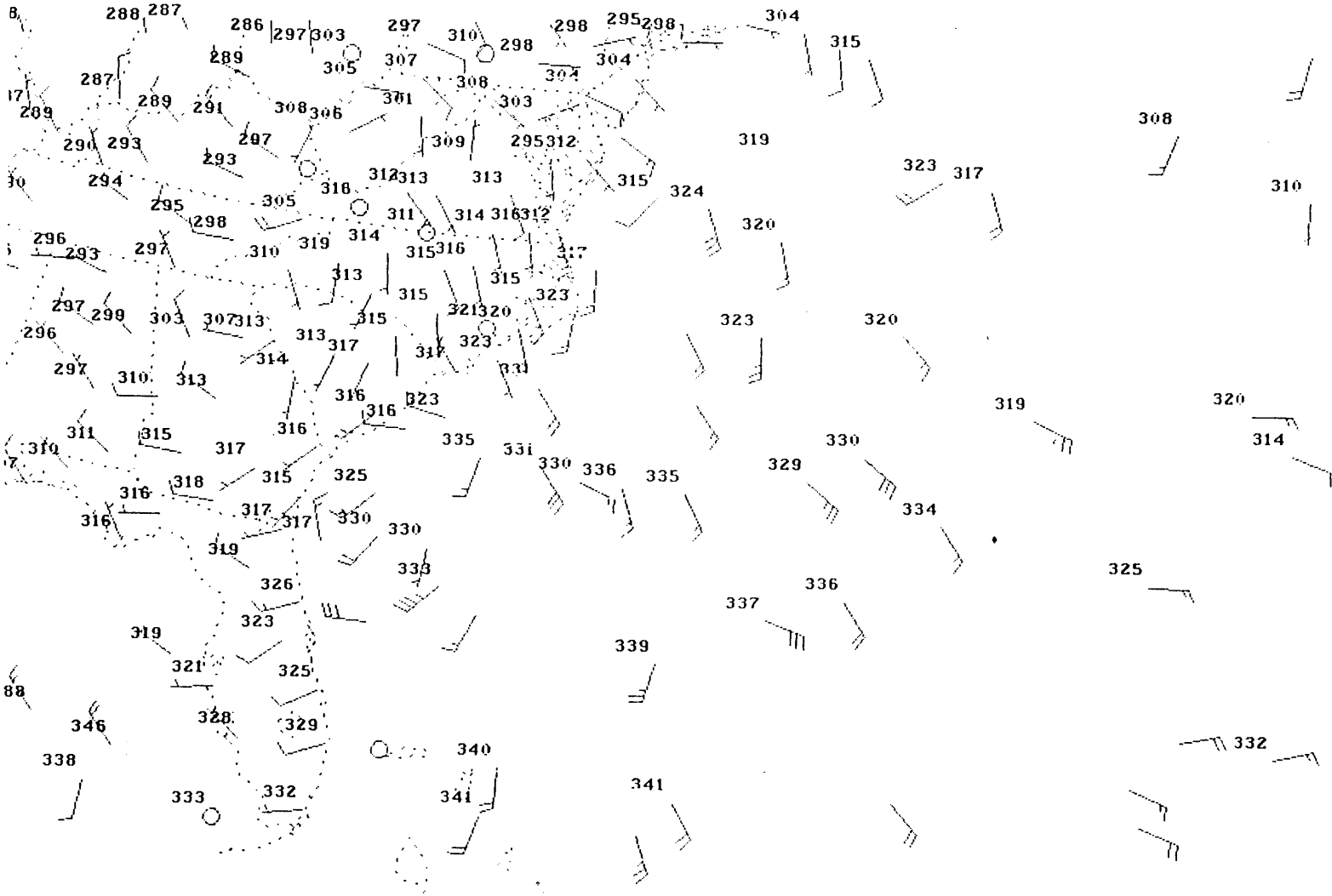

Fig. 5.30: Surface map of equivalent potential temperature (K) and winds (standard model), 12 UTC 19 Jan 1986.

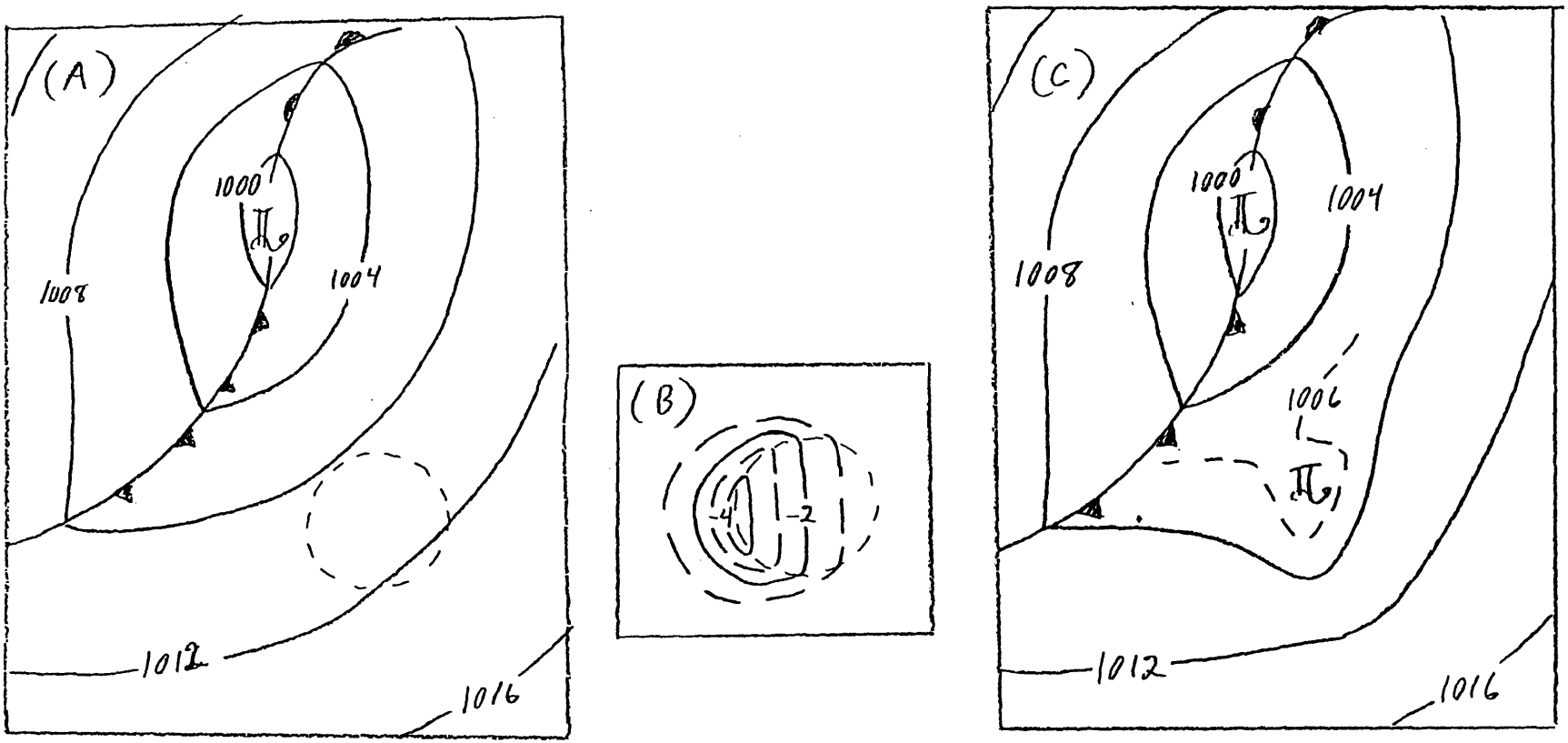

Fig. 5.31: Schematic diagram, showing superposition of surface pressure fields of large scale cyclone and localized heating region. (a) Surface pressure distribution (mb) of large-scale cyclone. Dashed circle shows region of localized heating. (b) Surface pressure change associated with localized heating. (c) Graphical addition of large-scale pressure field and localized pressure change. See text for interpretation.

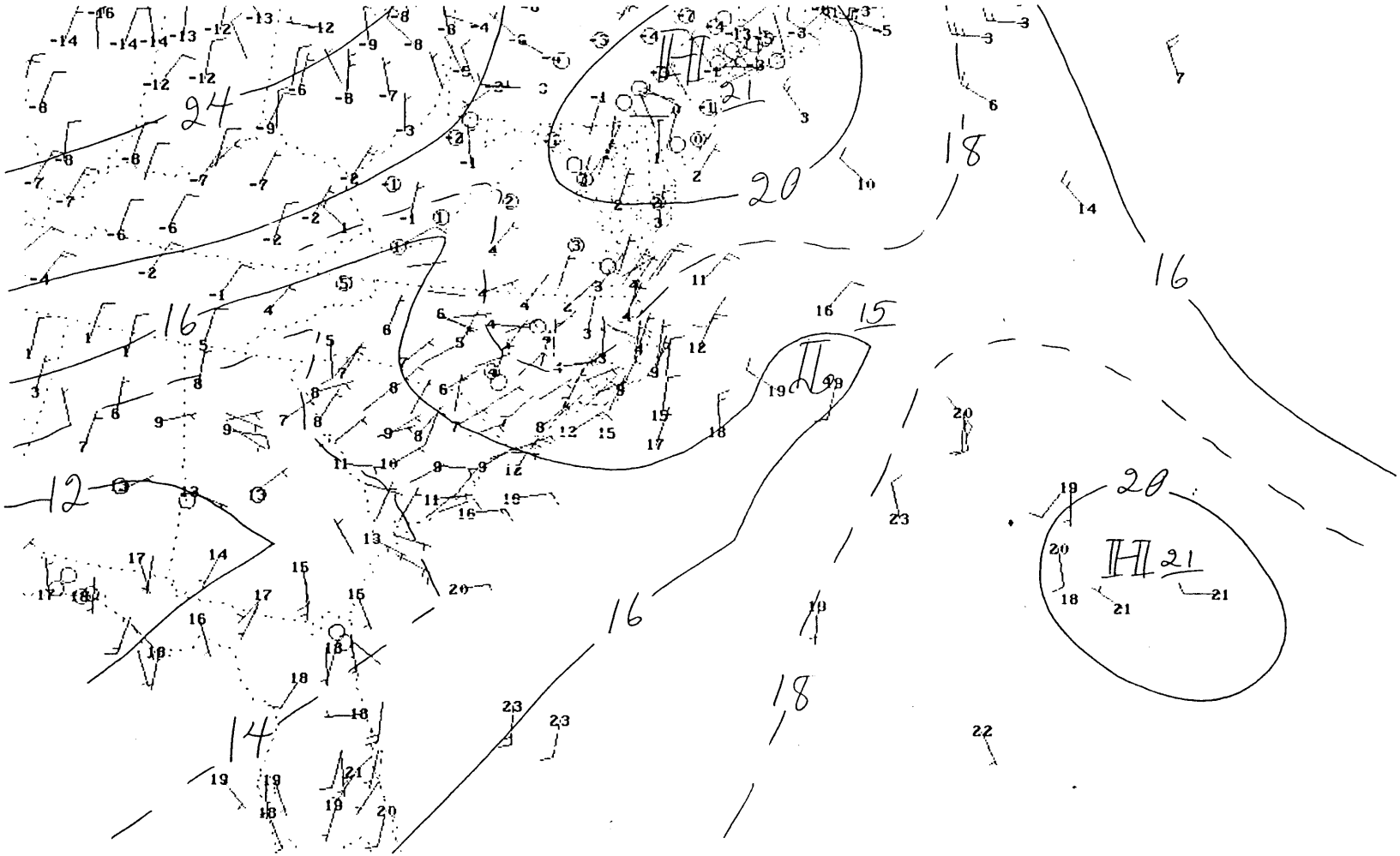

Fig. 6.1: Subjective mean sea level pressure analysis (c.int. 2 mb) for 12 UTC 10 Feb 1986. Observed temperatures (C) and winds (standard model) are plotted at station locations. Same format as in Figs. 6.2-6.4.

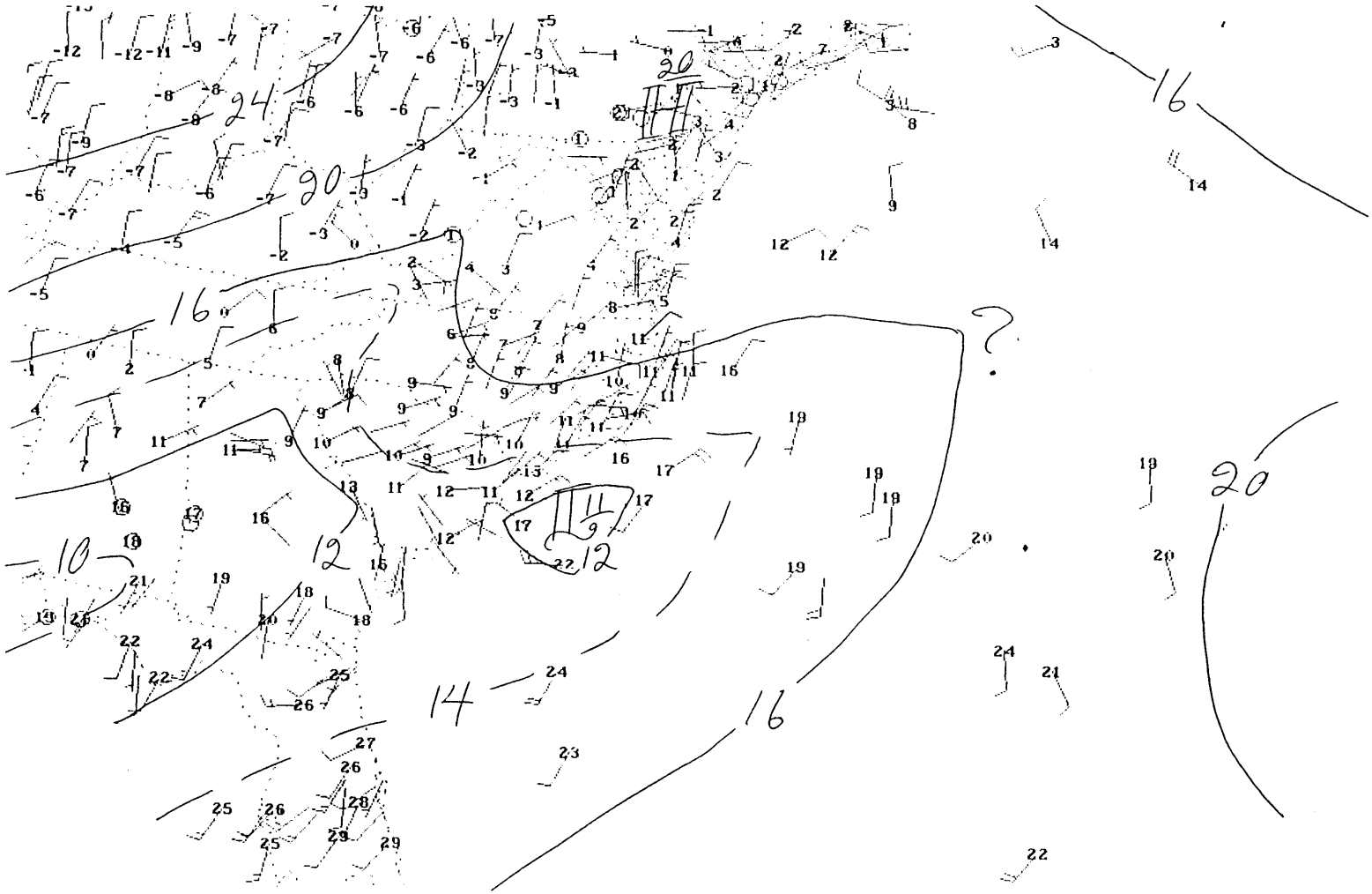

Fig. 6.2: 18 UTC 10 Feb 1986 pressure analysis with temperatures and winds (as in Fig. 6.1).

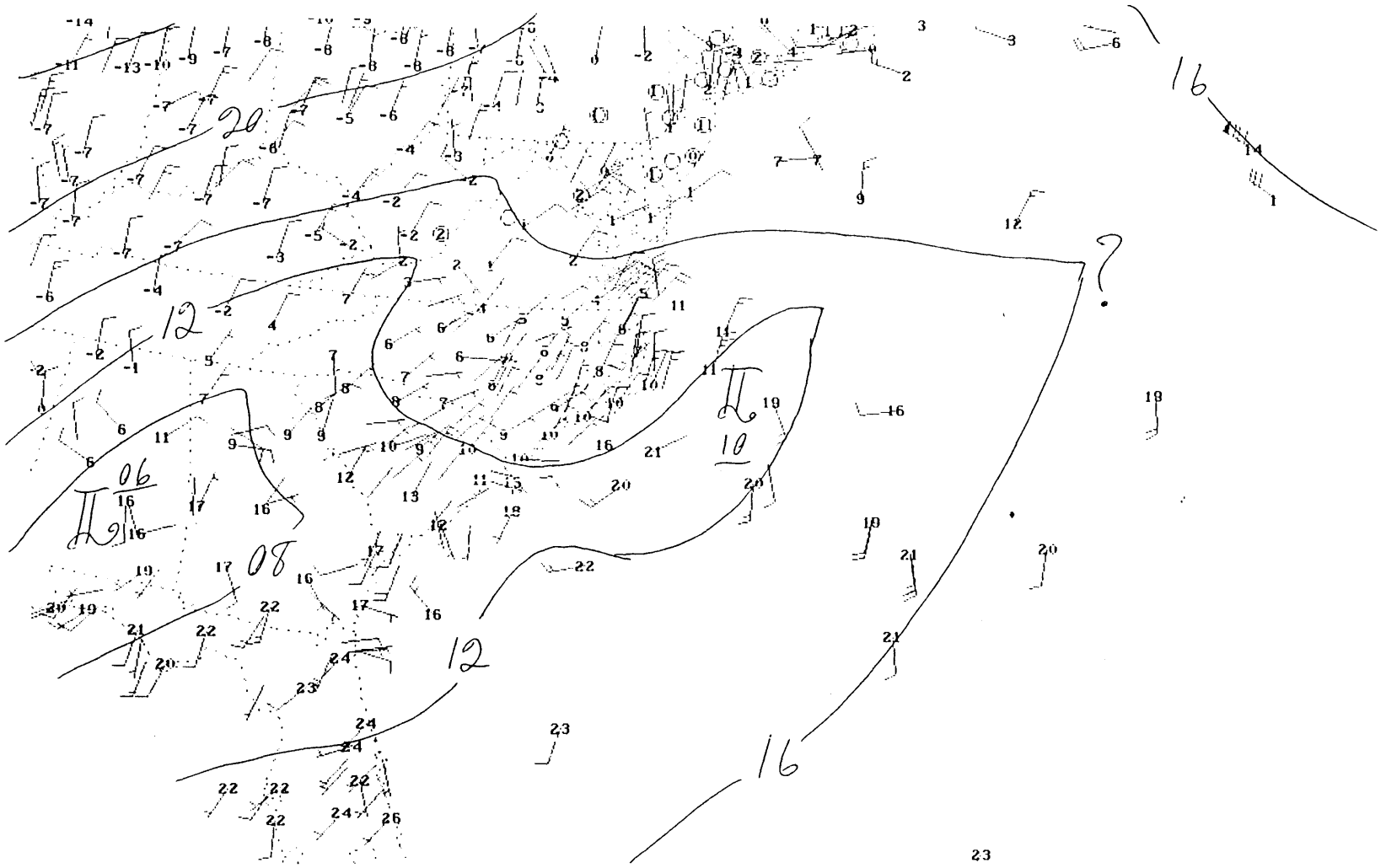

Fig. 6.3: 00 UTC 11 Feb 1986 pressure analysis with temperatures and winds (as in Fig. 6.1).

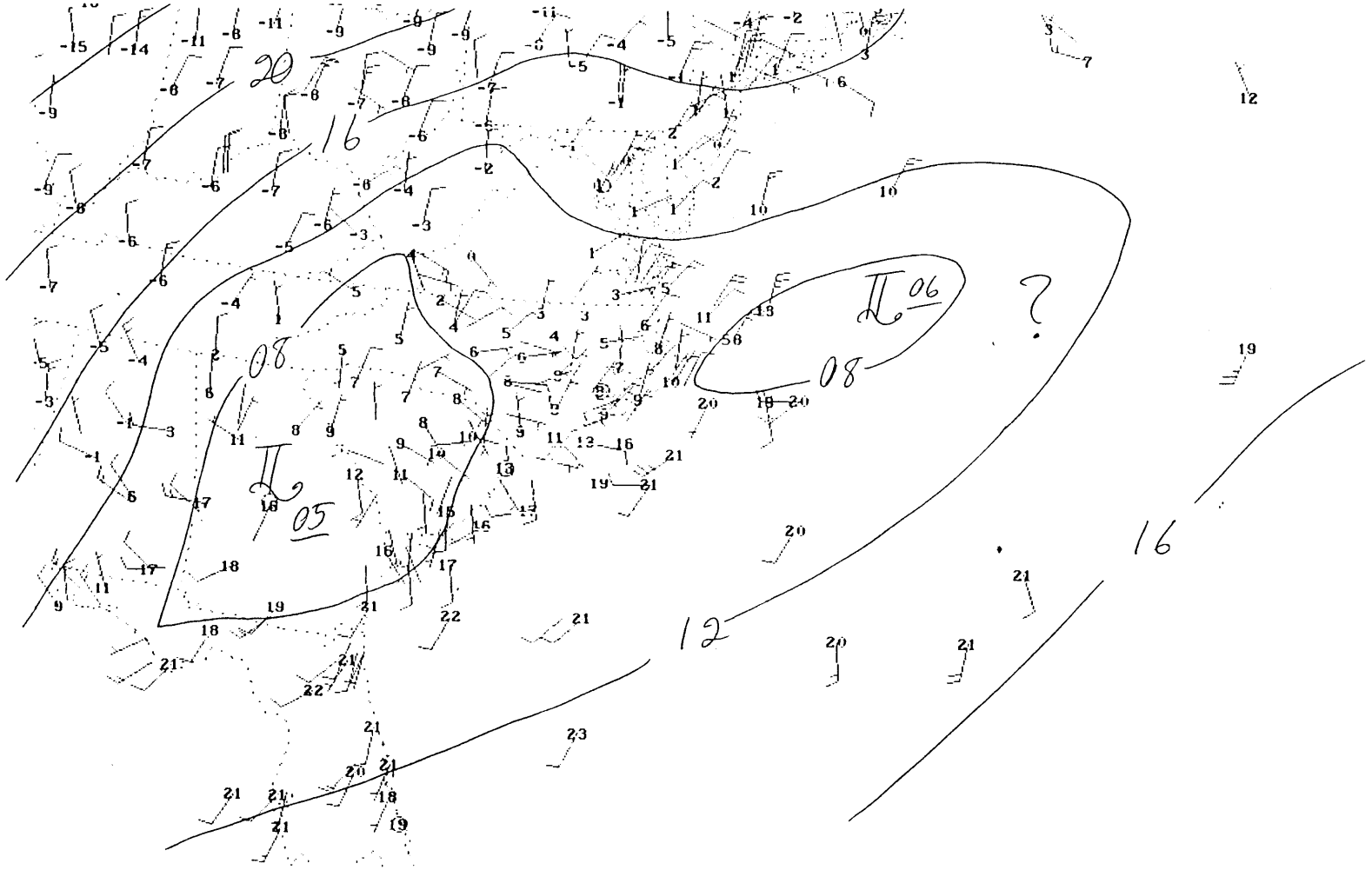

Fig. 6.4: 06 UTC 11 Feb 1986 pressure analysis with temperatures and winds (as in Fig. 6.1).

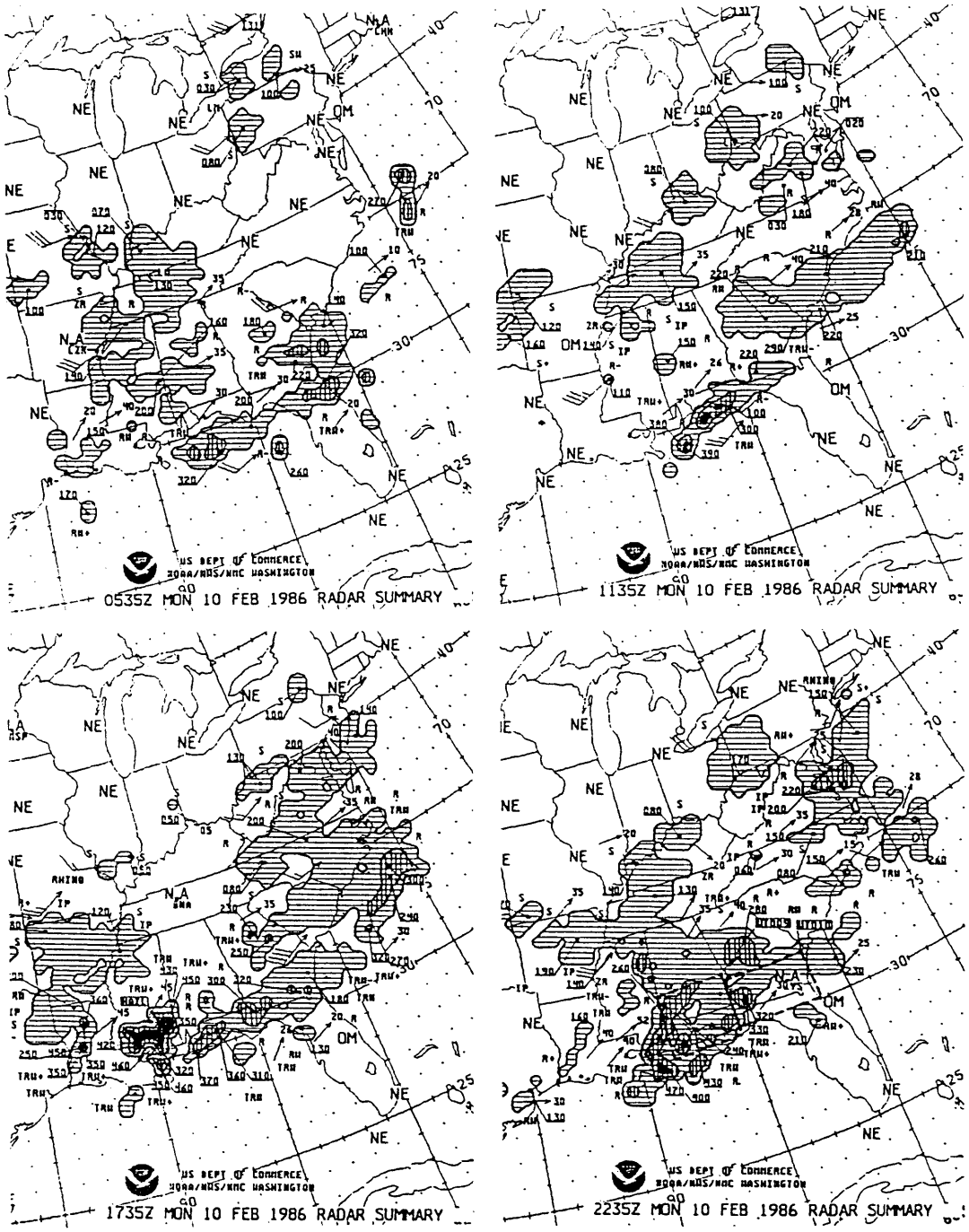

Fig. 6.5: Portions of National Radar Summaries, 10 Feb 1986. Hatching, cross-hatching, and shading indicate VIP levels 1, 3, and 5. Underlined numbers indicate maximum echo heights in hundreds of feet. Dashed box indicates location of tornado watch area.

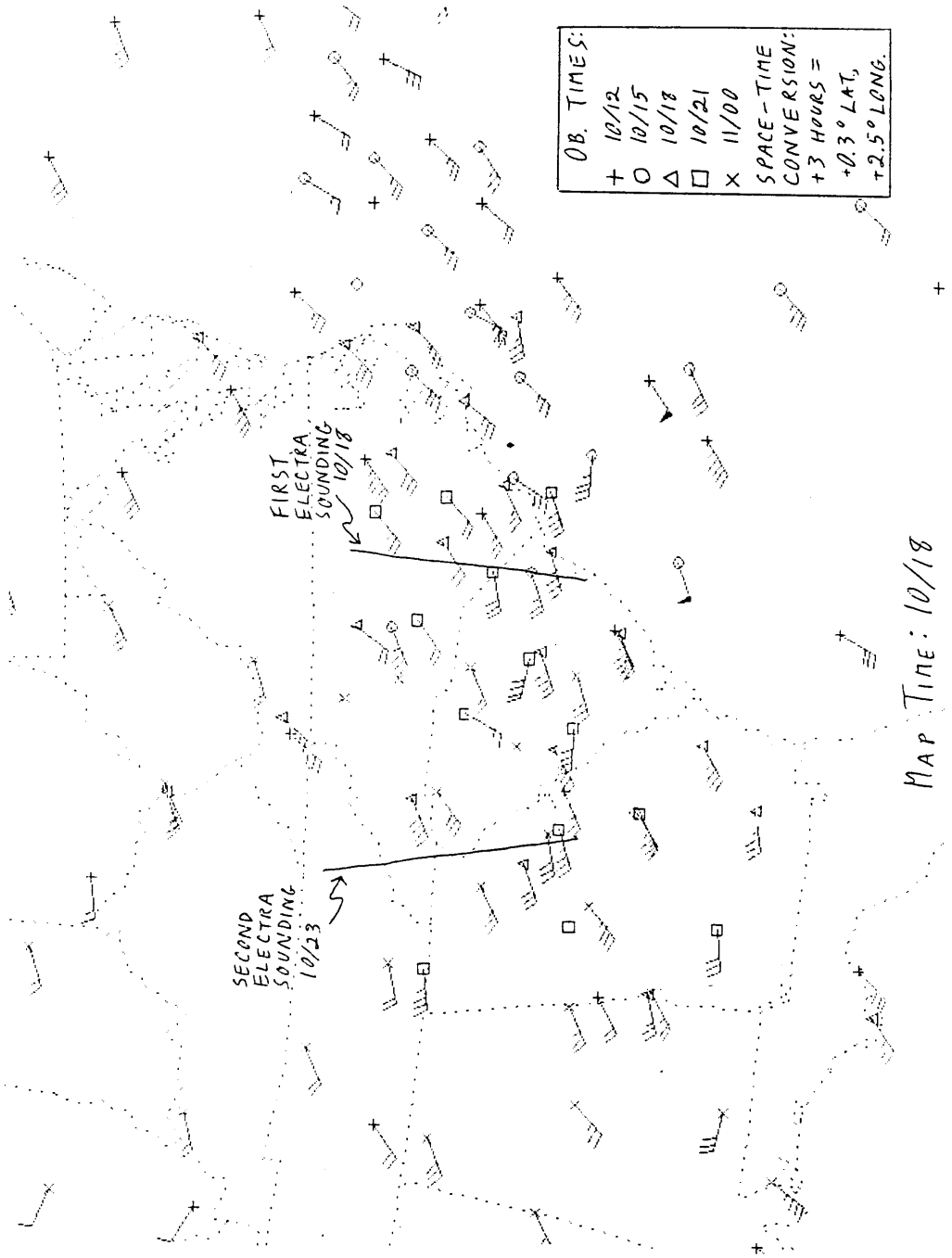

Fig. 6.6: Observed winds (standard model), 800 mb. Nominal map time is 18 UTC 10 Feb 1986. Observations from 10/12 to 11/00 are included in the figure and are plotted according to a space-time conversion of 0.3 degrees latitude and 2.5 degrees longitude per three hours. Also indicated are the locations of the aircraft *M*-surface cross sections shown in Figs. 6.7 and 6.8.

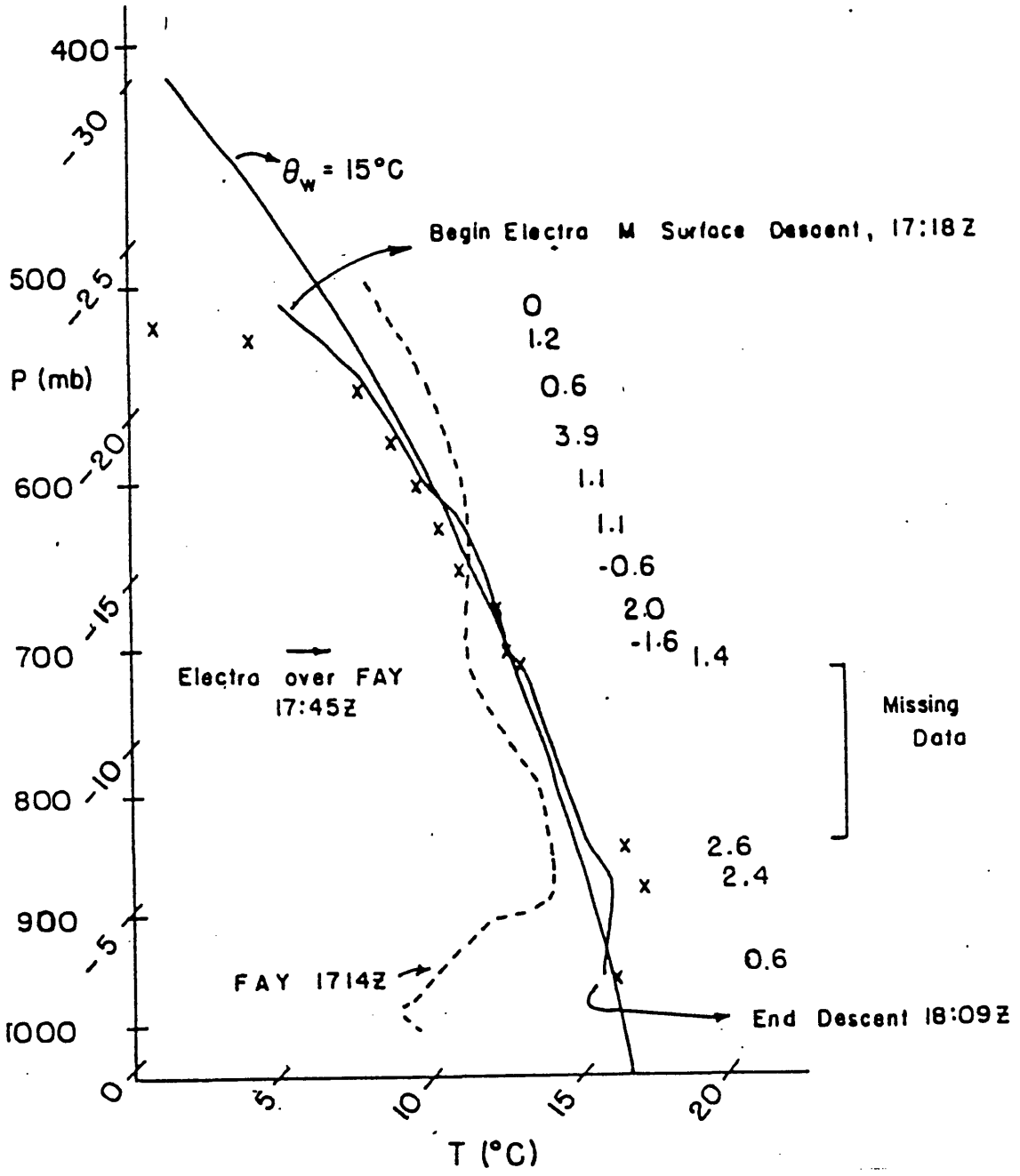

Fig. 6.7: *M*-surface sounding by NCAR Electra aircraft, 1718-1809 UTC 10 Feb 1986. Solid line shows temperature while x's denote dew point. Numbers to right show departures of *M* (m s^{-1}) from initial value. Dashed line is the 18 UTC temperature sounding from FAY.

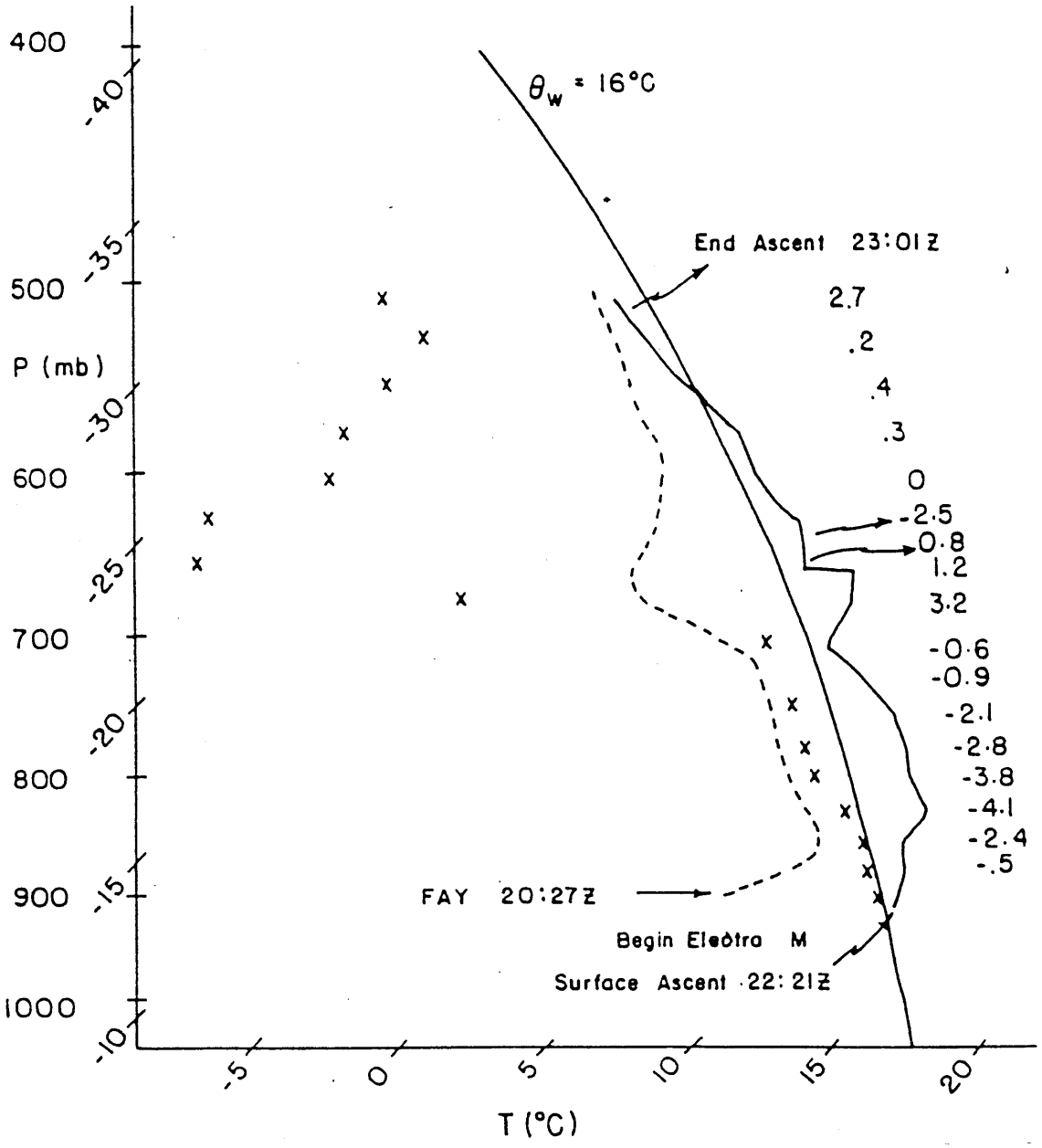

Fig. 6.8: *M*-surface sounding by NCAR Electra aircraft, 2221-2301 UTC 10 Feb 1986. Solid line shows temperature while x's denote dew point. Numbers to right show departures of M (m s^{-1}) from initial value. Dashed line is the 21 UTC temperature sounding from FAY.

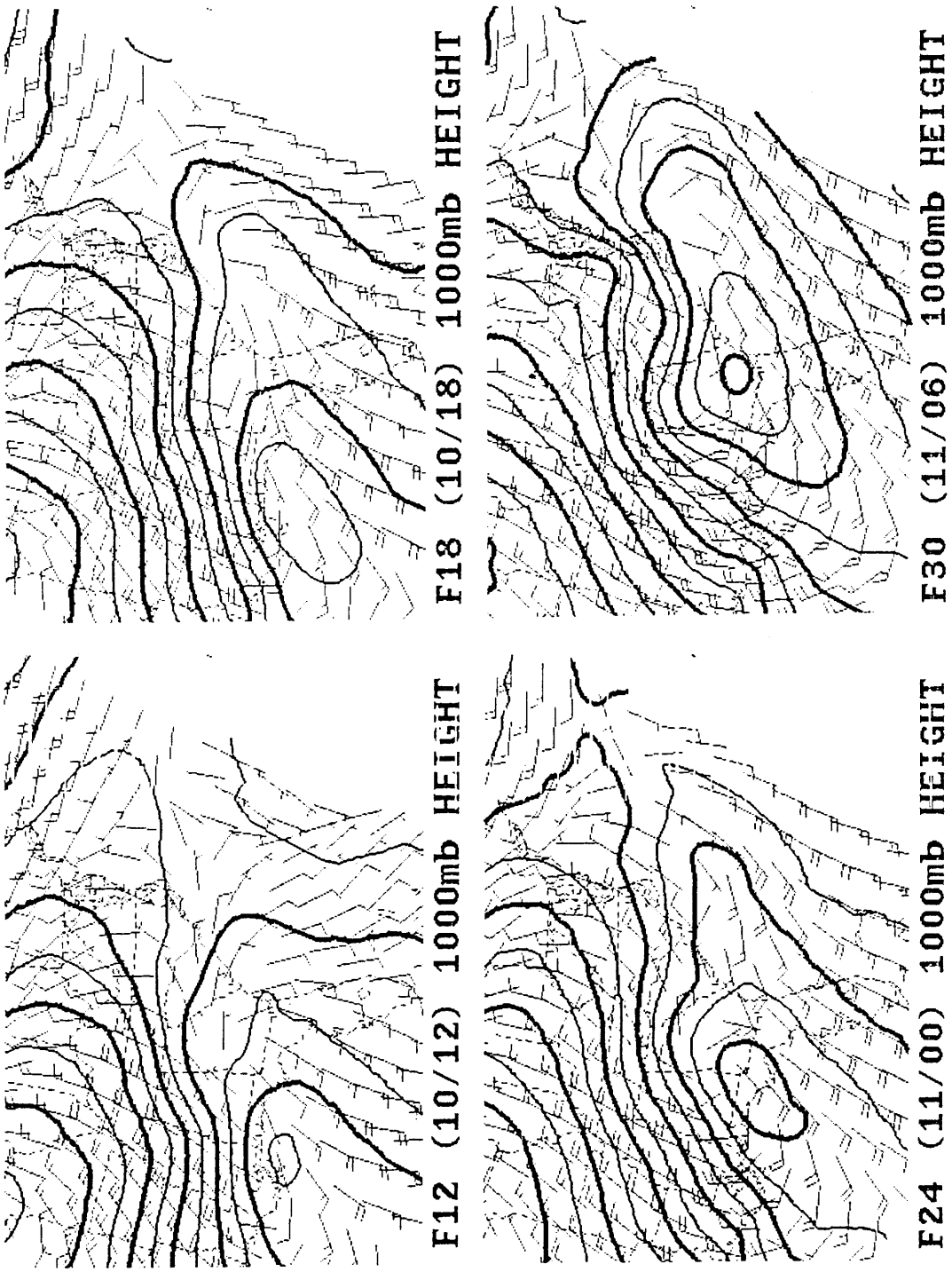

Fig. 6.9: Plots of 1000 mb height (c.int. 1.5 dam) and wind (standard model) from the 00 UTC 10 Feb 1986 NGM run. Compare with Figs. 6.1-6.4.

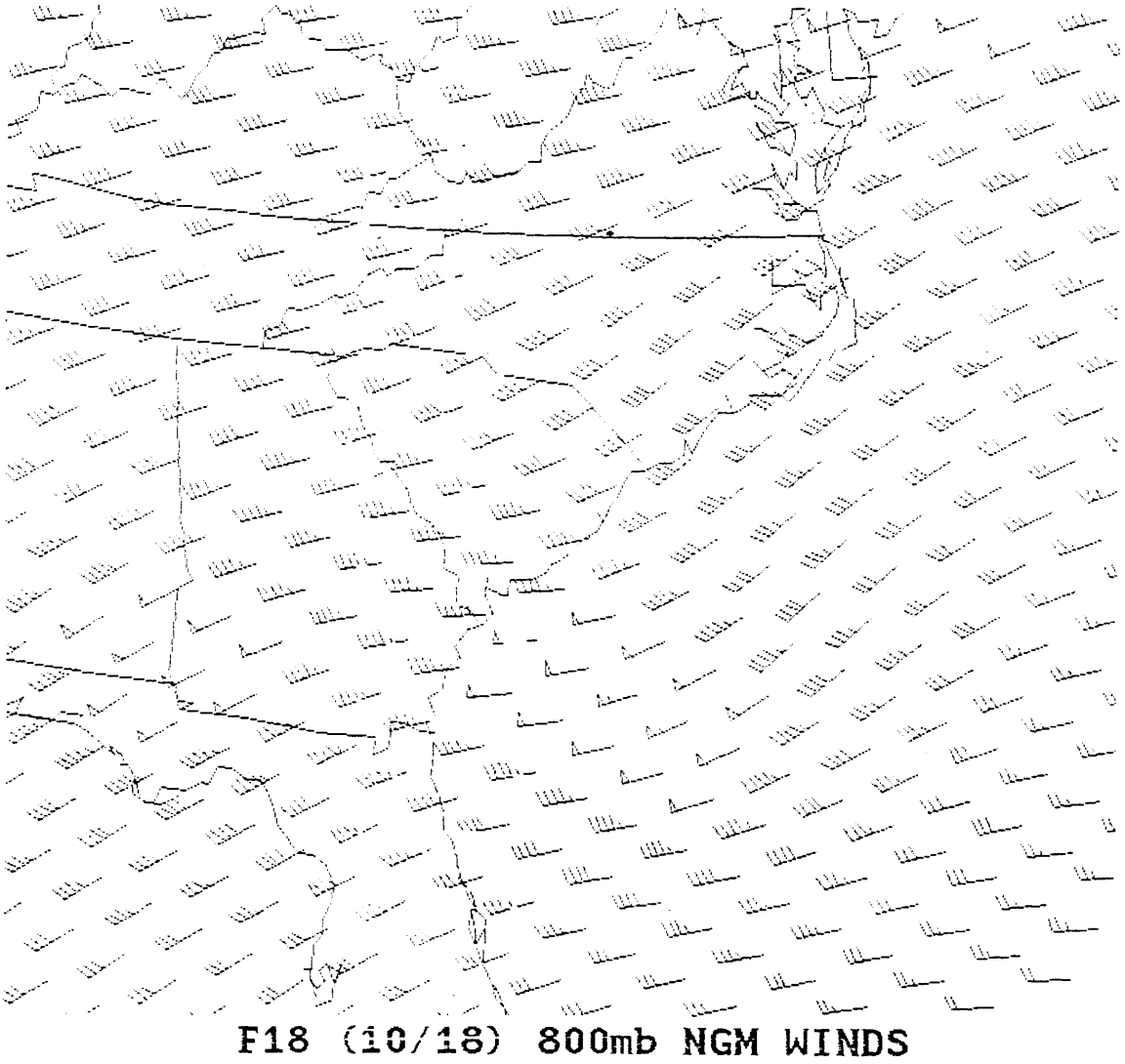

Fig. 6.10: Plot of 800 mb wind (standard model) from the NGM 18-hour forecast valid 18 UTC 10 Feb 1986. Compare with Fig. 6.6.

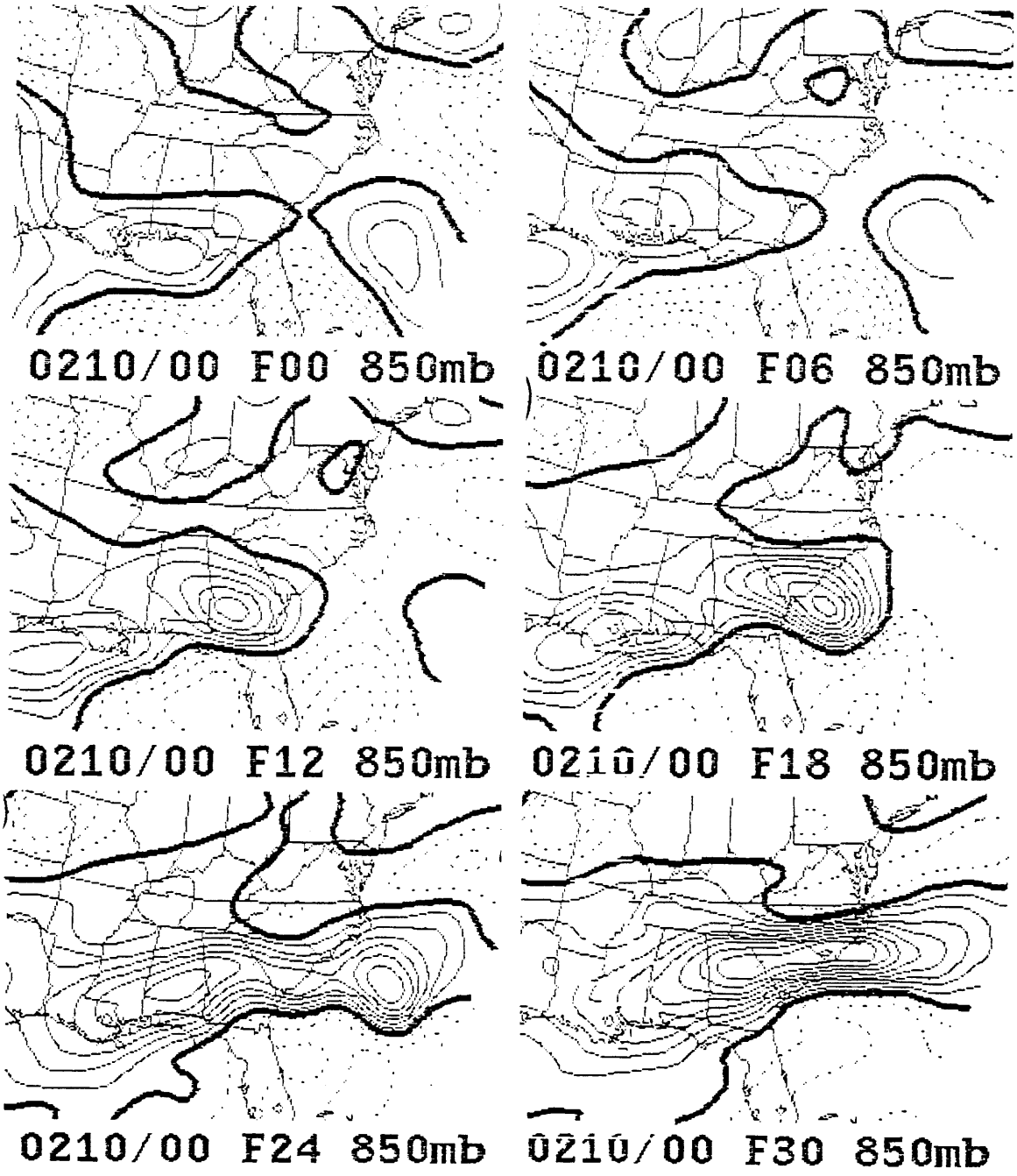

Fig. 6.11: NGM 850 mb relative vorticity (c.int. $1x10^{-5}$ s^{-1}, negative values dotted, zero contour thick), 00 UTC 10 Feb 1986 model run.

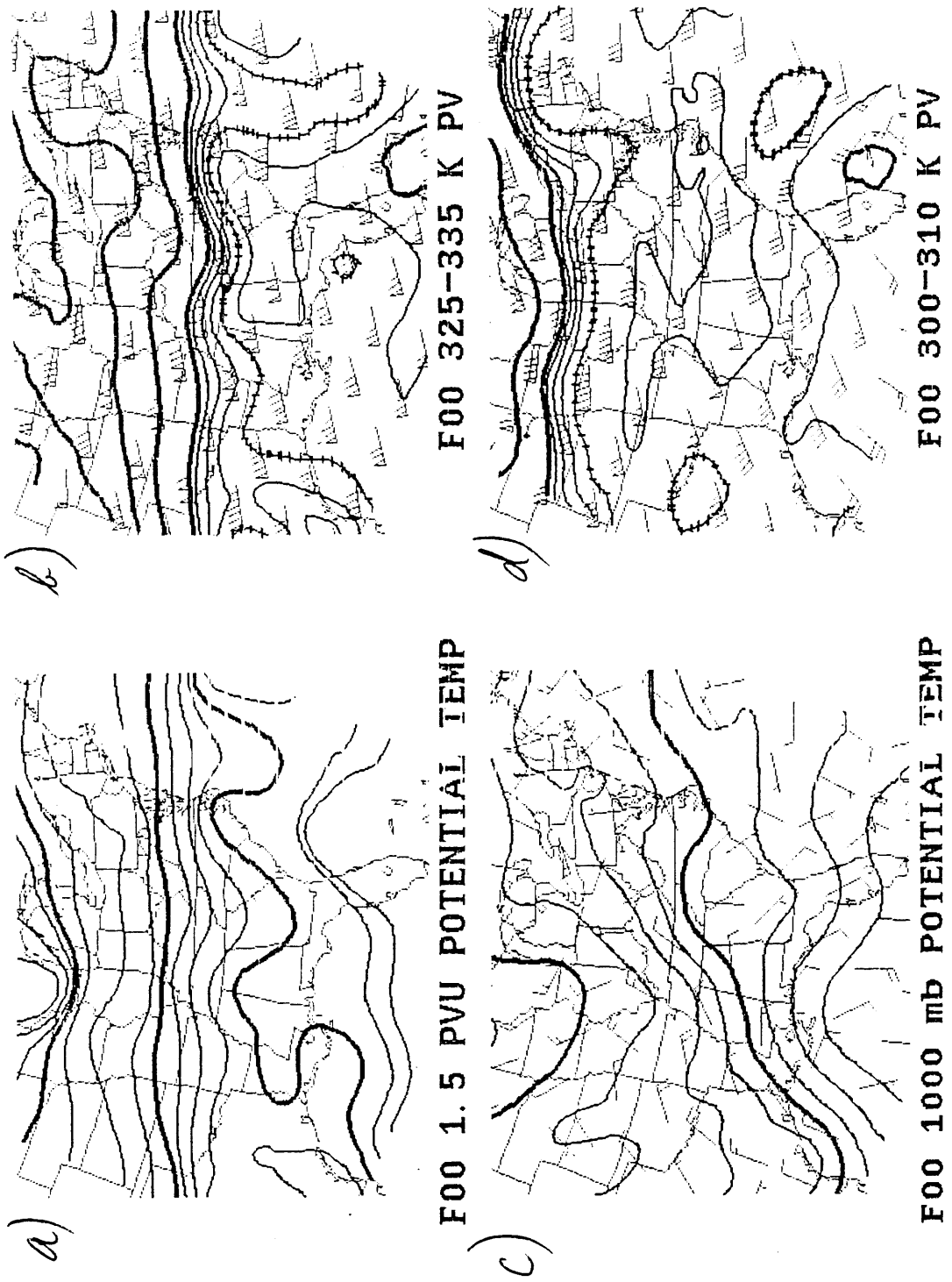

Fig. 6.12: Potential vorticity and potential temperature, NGM initialization (00 UTC 10 Feb 1986). Plotting conventions are similar to Figs. 4.6-4.11 (see Appendix B), except that (b) shows PV on the 325-335 K layer and winds on the 330 K level, and (d) shows PV on the 300-310 K layer and winds on the 305 K level. Same format as in Figs. 6.13-6.15.

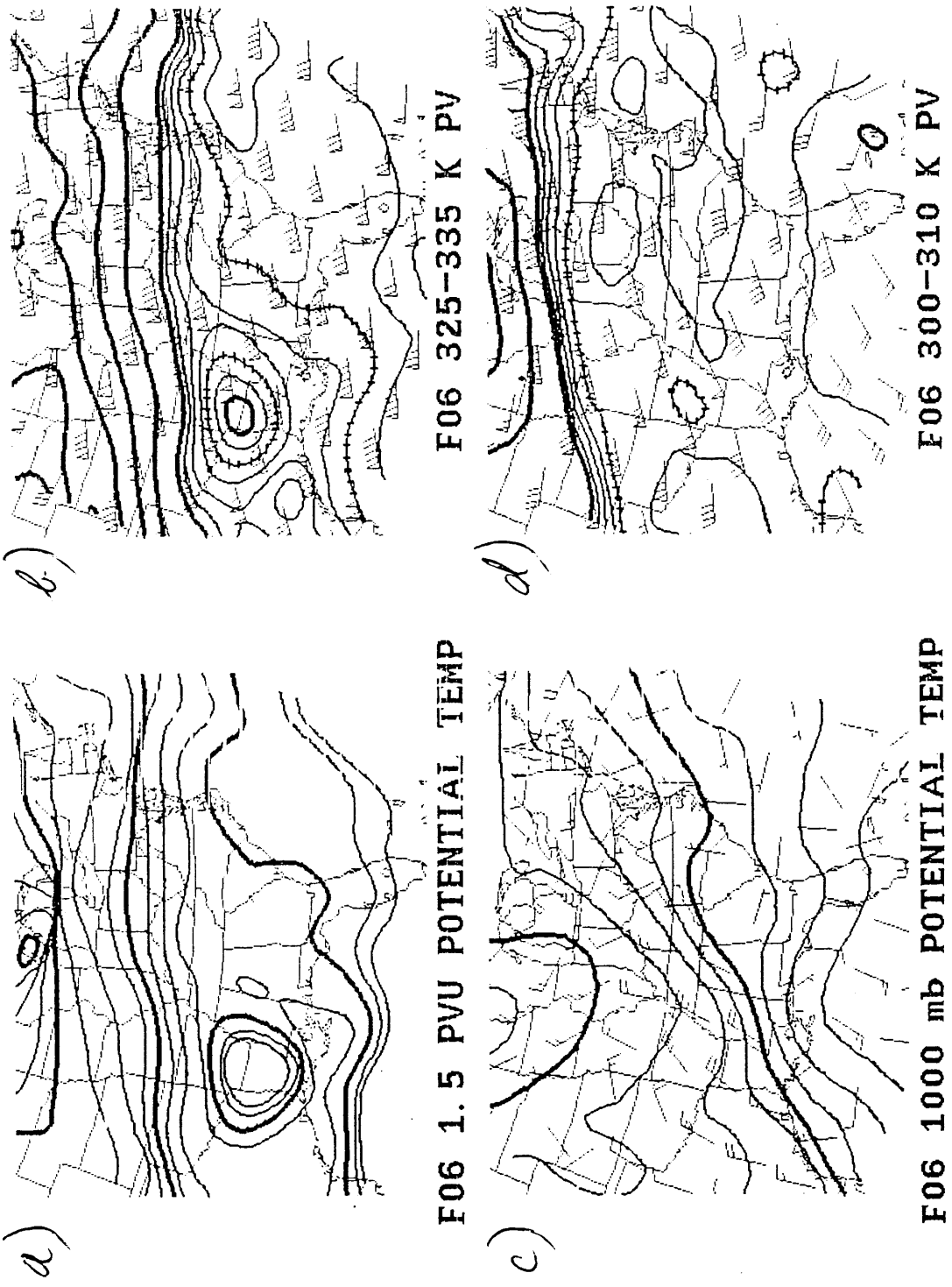

Fig. 6.13: As in Fig. 6.12, but for 6-hour forecast valid 06 UTC 10 Feb 1986.

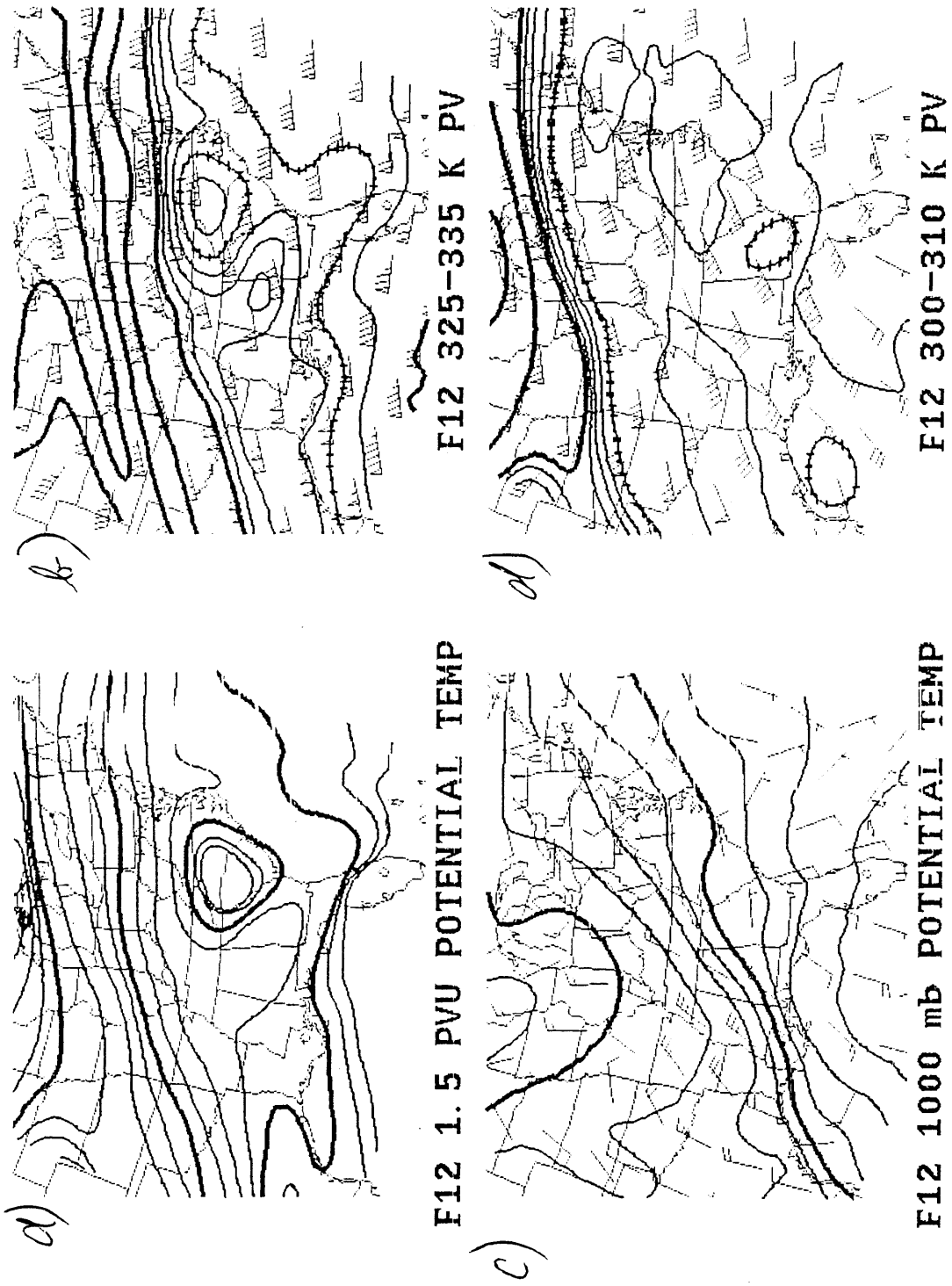

Fig. 6.14: As in Fig. 6.12, but for 12-hour forecast valid 12 UTC 10 Feb 1986.

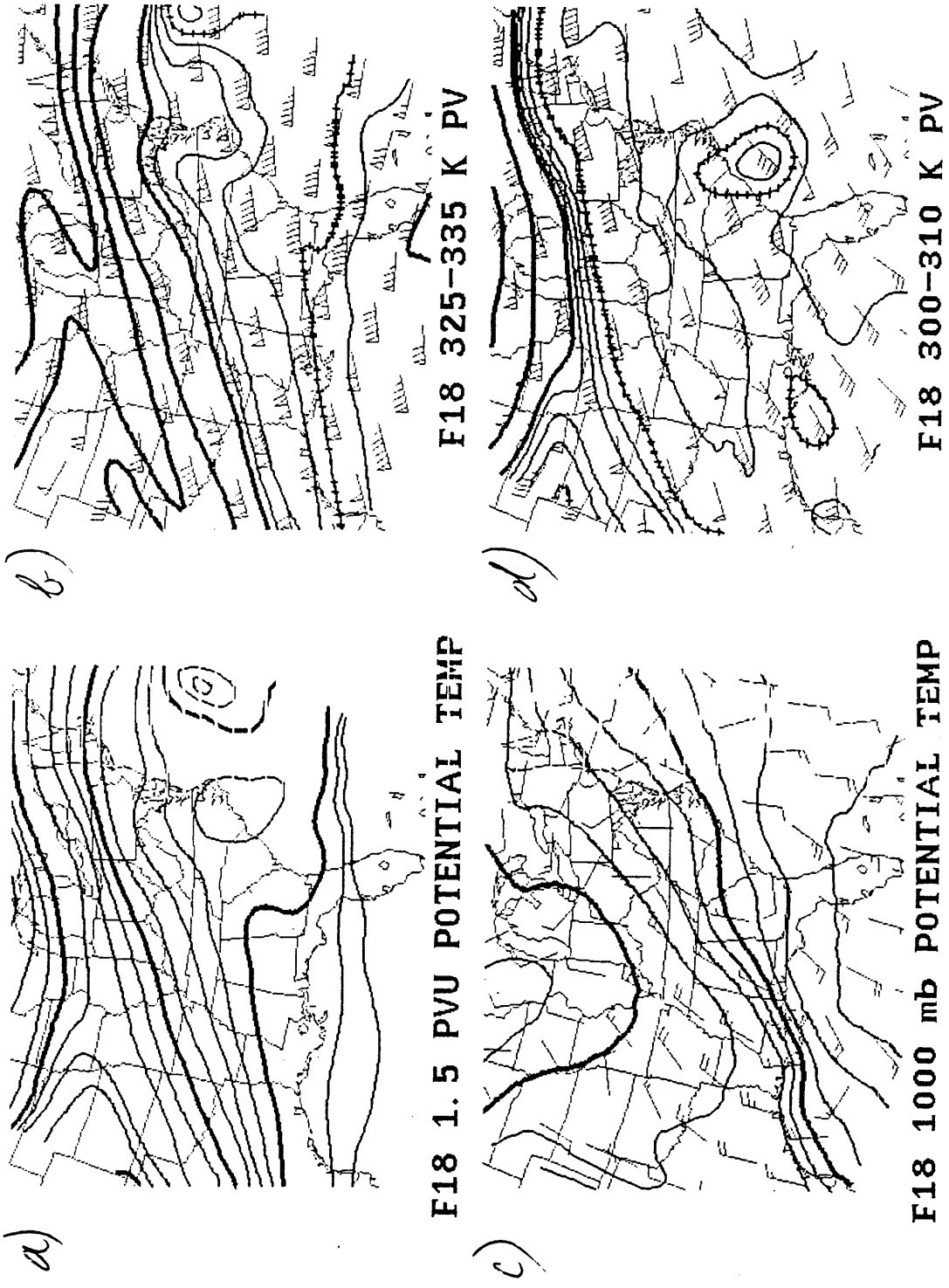

Fig. 6.15: As in Fig. 6.12, but for 18-hour forecast valid 18 UTC 10 Feb 1986.

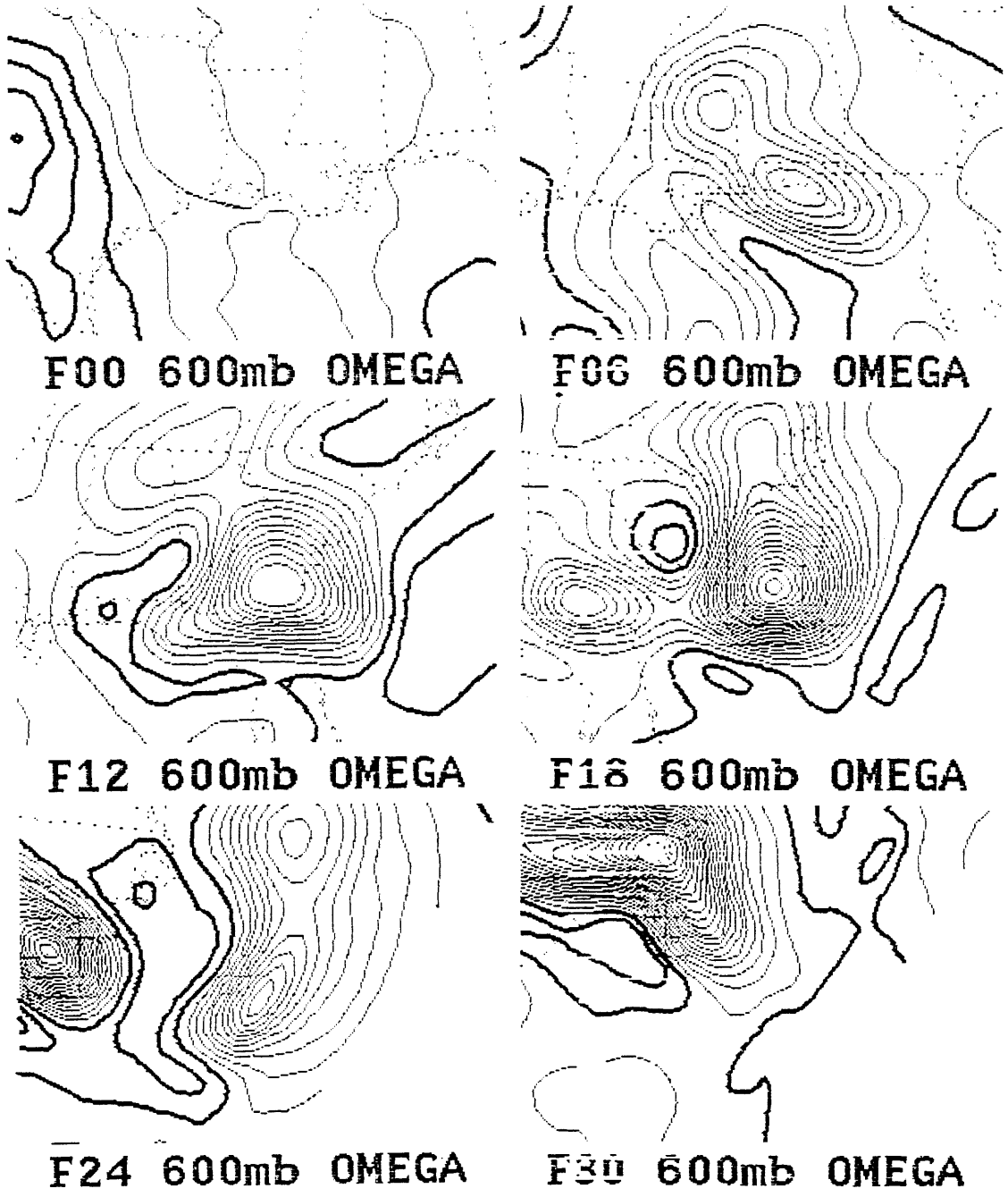

Fig. 6.16: NGM 600 mb omega (vertical motion), contour interval $1x10^{-1}$ Pa s^{-1}, zero contour and all positive contours (downward motion) thick, for 00 UTC 10 Feb 1986 forecast run.

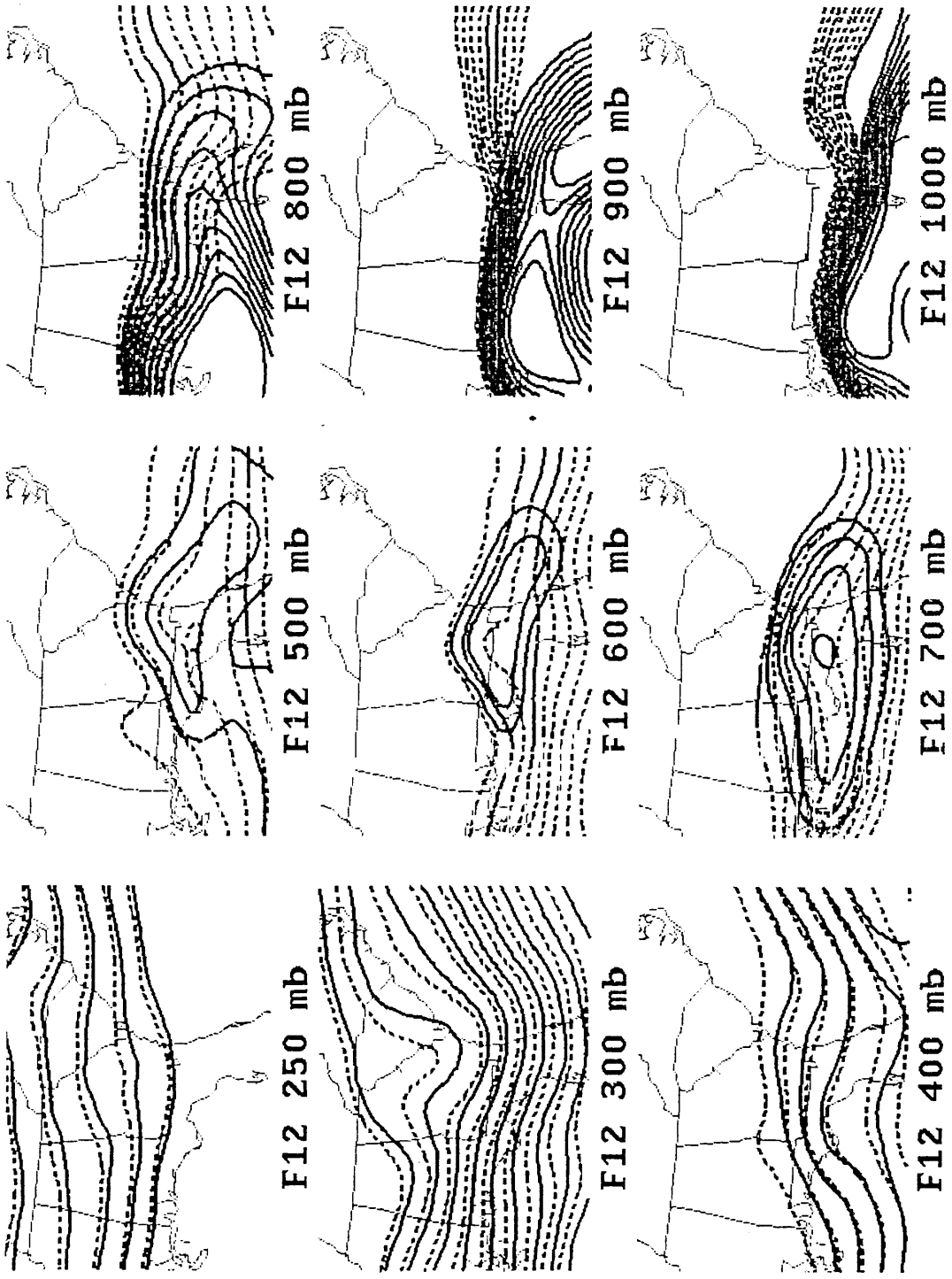

Fig. 6.17: Vertical distribution of θ_e (solid contours) and θ_e* (dashed contours), 250 mb to 1000 mb, NGM 12-hour forecast valid 12 UTC 10 Feb 1986. Contours are drawn at 1 K intervals from 325 K to 333 K, with colder temperatures located toward the top of page. See text for interpretation. Similar format to Figs. 5.19-5.23.

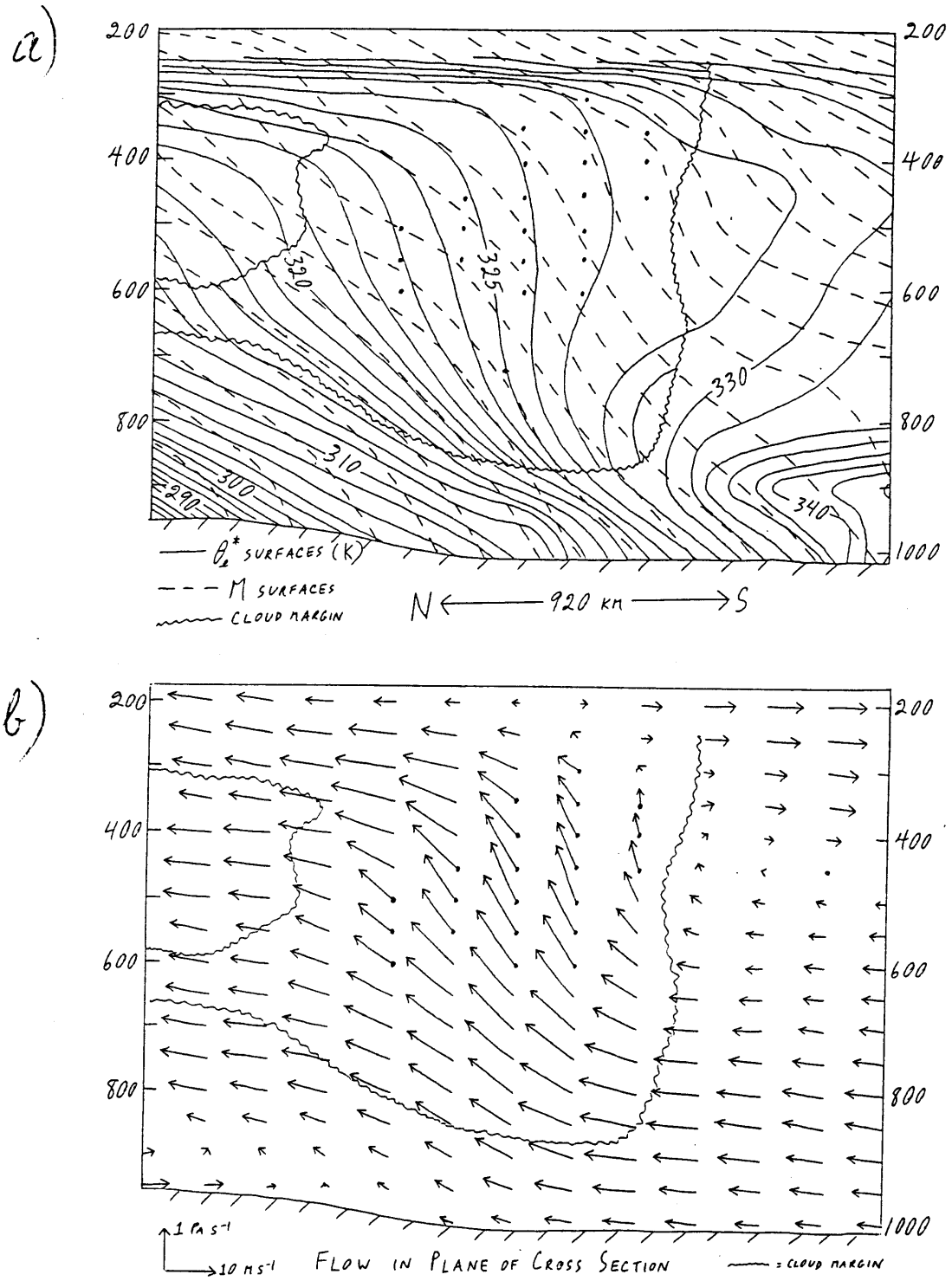

Fig. 6.18: Cross sections through updraft across shear and track of cyclone, NGM 12-hour forecast valid 12 UTC 10 Feb 1986. For description see Appendix B.

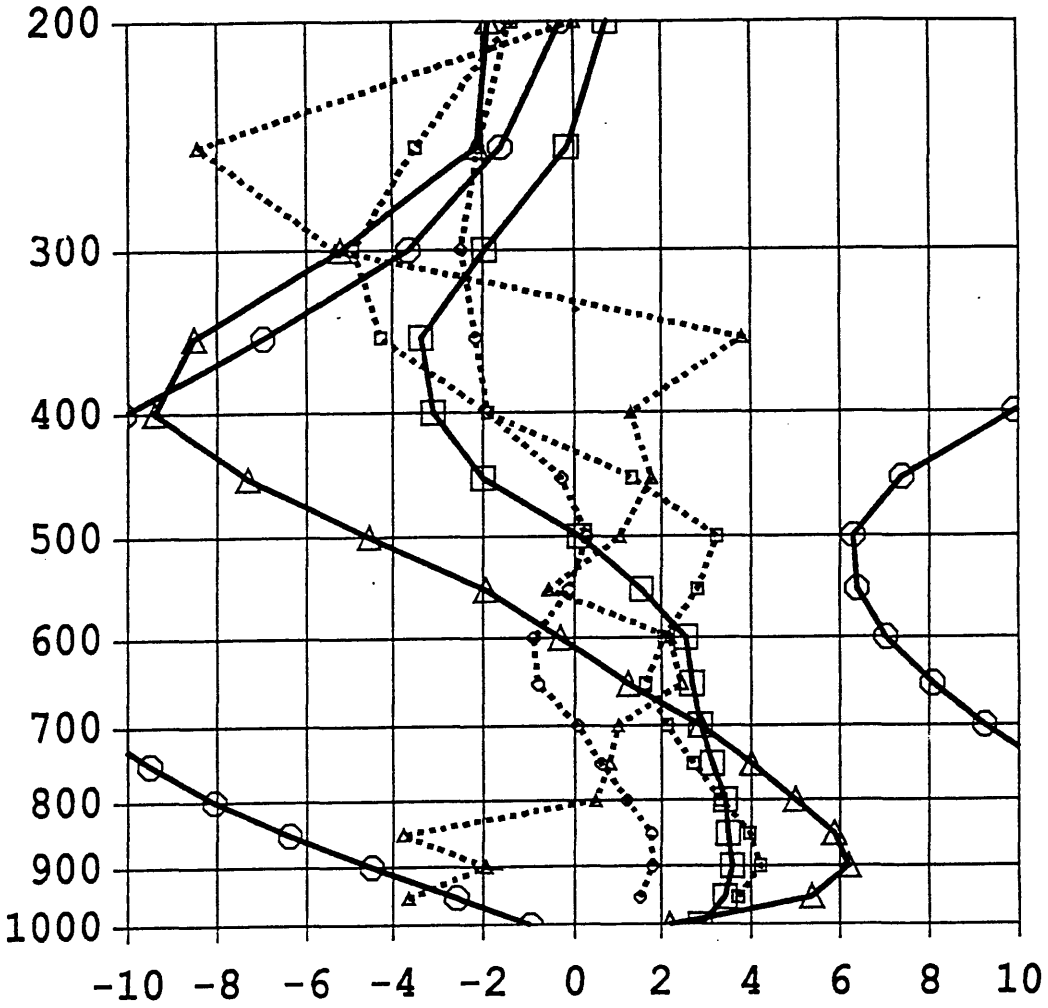

Fig. 6.19: Vertical profiles of various dynamical quantities, for a grid point in the developing updraft, NGM 12-hour forecast valid 12 UTC 10 Feb 1986. For complete description, see description of Fig. 5.11 inAppendix B. Solid, circles: ω. Solid, squares: ζ. Solid, triangles: ζ_g. Dashed, circles: $Dt(\omega_p)$. Dashed, squares: $Dt(\zeta)$. Dashed, triangles: $Dt(\zeta_{gp})$.